UNIVERSITÀ DEGLI STUDI DI PAVIA
Dipartimento di Scienze della Terra e dell'Ambiente

PhD Program in Earth and Environmental Sciences
Dottorato di ricerca in Scienze della Terra e dell'Ambiente
XXXVI Series

The geodynamic evolution of the Gondwana–Laurasia boundary in Triassic times: Constraints from the tectono-magmatic cycles of the Southern Alps

PhD thesis of

Abimbola Chris Ogunyele

Tutor
Dr. Alberto Zanetti

Coordinator
Prof. Silvio Seno

Academic year 2022/2023

Thesis Declaration

I, Abimbola Chris Ogunyele, certify that:

This thesis has been accomplished by me during enrolment for the PhD degree in Earth and Environmental Sciences at the University of Pavia, Italy.

This thesis does not contain material which has been submitted for the award of any other degree or diploma in my name, in any university or other tertiary institution.

This thesis contains published article and four manuscripts prepared for publication by me in collaboration with other co-authors.

This thesis does not contain any material previously published or written by another person, except where due reference has been made in the text.

This thesis does not violate or infringe any copyright, patent, trademark, or other rights whatsoever of any person.

Pavia, Italy; 9 February, 2024

Abimbola Chris Ogunyele

PhD Student

Alberto Zanetti

Tutor

Acknowledgements

If I have seen further, it is by standing on the shoulders of giants (Sir Isaac Newton, 1675). The success of my PhD journey is the result of the cumulative efforts and kindness of so many people. The greatest Giant who has helped me this far in my academic pursuit is the Almighty God. I remain eternally grateful to Him for His guidance, wisdom and provision.

I am grateful to my supervisor, Alberto Zanetti, who is a kind and resourceful intellectual. In collaboration with Alessio Sanfilippo and Vincent Salters, he brought the best out of me. I also thank Vincent Salters for hosting me at the National High Magnetic Field Laboratory at the Florida State University, USA where I performed some of the experiments reported in this thesis.

I would like to extend my thanks to Mattia Bonazzi who taught me how to use many analytical facilities and techniques at the CNR–IGG Pavia. My sincere appreciation also goes to the many other scientists whom I collaborated with during the doctorate, especially Tommaso Giovanardi and Maurizio Mazzucchelli.

I thank my examiners – Riccardo Tribuzio, Angelo De Min, Massimo Coltorti and Tommaso Giovanardi for their expert reviews and constructive comments throughout the research.

This PhD is funded by a scholarship from the University of Pavia for which I am grateful. The CNR–IGG Pavia also provided analytical facilities and funding to attend numerous national and international conferences, schools and workshops. Additional travel and conference grants from the European Association of Geochemistry, European Geosciences Union and the Società Italiana di Mineralogia e Petrologia are acknowledged.

My sincere gratitude goes to my wife, Imoleayo and son, Ariyo for their unflinching love, understanding, support and prayers. I couldn't have come this far without the both of you! I love you always. Many thanks also to my parents, Pastor Abayomi and Dcns. Yemisi Ogunyele, and my siblings. You are the best!

My story would be incomplete without the mention of the efforts and influence of my teacher and mentor, Olatunde Adegbuyi (of blessed memory). He was a great and influential teacher who inspired me a lot. Today, I am studying the petrology and geochemistry of "hard" rocks mainly because of his many wonderful teachings and illustrations while I was an undergraduate. I miss you greatly Sir.

Last but not least, I want to thank myself (I think I deserve it!). I want to thank myself for not giving up, for making a lot of sacrifices and for making myself and my family proud! Yes, you did it, Abimbola!

Extended Abstract

The Triassic geodynamic evolution at the Gondwana–Laurasia boundary in the area now corresponding to the Southern Alps has been a subject of debate in the last five decades. The Southern Alps located at the northern margin of the Adriatic Plate was marked by the development of carbonate platforms and basins, and widespread magmatic activity during the Triassic. Detailed petrological and geochemical studies of these Triassic magmatic events have been conducted mainly in the eastern sector (e.g., Dolomites, Julian Alps, Vicentinian Alps, etc) of the region. However, many details and datasets on the Triassic magmatic events in the Southern Alps especially in the western (Ivrea-Verbano Zone, IVZ) and central (Brescian Prealps) sectors are still lacking, hence, a complete picture of the geodynamic framework of the region is unavailable. This issue is further complicated by the complex paleogeography of the Adriatic Plate during and after the Variscan orogenic cycle, and the widespread hydrothermal alteration of Triassic outcrops in the region.

These knowledge and data gaps were addressed in this thesis. The thesis reports the outcomes of detailed petrological, geochemical and radiogenic isotopic studies on the Triassic–Early Jurassic magmatism which occurred in the Southern Alps, particularly in the westernmost (IVZ) and eastern (Dolomites) sectors in order to provide further constraints on the geodynamic evolution of the Gondwana–Laurasia boundary in Triassic times prior to the breakup of the Pangea. Invaluable insights were also provided by the study of the lherzolitic and harzburgitic mantle massifs outcropping in the IVZ.

The detailed petrochemical and amphibole Nd-Sr-Hf-Pb isotopic study conducted on Early Mesozoic (Middle Triassic–Early Jurassic) alkali-rich dyke swarms which intruded the Finero Phlogopite Peridotite in the northernmost part of the IVZ, western Southern Alps

highlights the complex tectono-magmatic events which occurred throughout the Southern Alps during this timeframe (Chapter 2). The dykes document a shift of the IVZ magmatism from orogenic-like to anorogenic alkaline affinity during the Late Triassic, similar to what has been observed in the eastern and central sectors of the Southern Alps. This geochemical shift is related to a change of the mantle sources of these contrasting magmatisms from a predominantly metasomatized lithospheric mantle containing significant amount of recycled continental crust components (similar to Finero phlogopite peridotite) to a depleted asthenospheric mantle. New trace elements, U-Pb geochronology and in-situ Hf isotopes data on zircons from the IVZ anorogenic alkaline dykes (Chapter 3) further support their derivation largely from an upwelling depleted asthenosphere but also containing and/or interacting with relatively minor amounts of recycled enriched components. To reconcile the geochemical and isotopic signatures of the Southern Alps Triassic–Early Jurassic magmatisms with geodynamic aspects, we proposed a model in which the magmatisms were triggered by the Paleotethys subduction but the recycled continental crust materials in the mantle sources of these magmatisms are related to crustal materials brought down to mantle depths by the Variscan and/or older subduction events, as well as by delamination of the roots of the Variscan chain.

In the Dolomites (eastern Southern Alps), a new collection of Middle Triassic high-K calc-alkaline to shoshonitic lavas and dykes were investigated for Nd-Sr-Hf-Pb isotopes and trace elements composition (Chapter 4). The lavas and dykes show “crust-like” isotopic and trace element signatures, similar to the IVZ orogenic-like dykes. They provide additional evidence that the Southern Alps subcontinental mantle which generated the Triassic magmatisms is heterogeneous and contains variable amounts of recycled continental (and oceanic?) crustal materials. A strong correlation between the Middle Triassic magmatism in the Dolomites and the

orogenic-like magmatism in the IVZ was proposed on the basis of similarity in isotopic and trace element signatures.

The geochemical and isotopic study of the orogenic mantle massifs in the IVZ provided first-hand details on the nature, evolution and relationship of the subcontinental lithospheric mantle (SCLM) beneath the IVZ area with respect to the Triassic–Early Jurassic magmatisms of the Southern Alps. Trace elements and Nd-Hf isotopes data coupled with geochemical modeling of the lherzolitic mantle massifs in the central to southern parts of IVZ (Chapter 5) revealed that the Adriatic Plate was in a back-arc setting in the Upper Devonian (ca. 370 Ma) during Pangea amalgamation. It was in this timeframe and setting that the IVZ lherzolitic massifs were accreted to the Adriatic SCLM, with a petrochemical evolution characterized by low-degree (~5–12%) depletion and nearly contemporaneous pervasive to focused melt migration. The lithospheric accretion putatively took place through asthenospheric upwelling triggered by Variscan intra-continental extension in a back-arc setting related to the subduction of the Rheic Ocean. On the other hand, the harzburgitic mantle massif of Finero in northern IVZ (Chapter 6) tells a more complex and different geological history involving relatively higher degree of partial melting (~18%) and pervasive metasomatism by hydrous silica-saturated melts carrying DUPAL isotope anomaly. We hypothesize, based on isotopic and geodynamic arguments, that the metasomatizing melts carrying the DUPAL isotope anomaly was derived from the partial melting of continental crust subducted and/or delaminated into the upper mantle. We conclude that the recycling of continental crust materials within the Southern Alps upper mantle, as testified by the Finero mantle peridotite massif, plausibly explains the development of magmatism derived from mantle sources containing continental crust components in the IVZ and throughout the Southern Alps during the Triassic–Jurassic period.

Table of Contents

CHAPTER 1

Introduction

1.1 Scientific background

In the Late Carboniferous, around ca. 340 Ma, the convergence of Gondwana and Laurasia during the closure of the Rheic Ocean led to the assembly of the Pangea Supercontinent in what is known as the Variscan collision (e.g., Matte, 1986; Dal Piaz et al., 2003; Nance, 2010; Nance et al., 2012; Warr, 2012; Kroner and Romer, 2013; Muttoni and Kent, 2019; van Hinsbergen et al., 2020; De Min et al., 2020). Prior to the Variscan collision, around 400–370 Ma (in the Devonian), three distinct terrane assemblages – Ligeria, Armorica and Galatia were detached from the northern margin of Gondwana and accreted to the southern margin of Laurasia (Stampfli et al., 2002; von Raumer et al., 2013). The Adriatic Plate, in which the Southern Alps (present study area, Figure 1.1) are located, is one of the many geodynamic units of the Galatian assemblage. Other units belonging to the Galatian assemblage include Austroalpine, Carnic Alps, Helvetic, Briançonnais east and west, Sardinia, West Carpathians, etc (von Raumer et al., 2013).

The Variscan collision produced a large E-W-trending orogenic belt that ranged from the southern Appalachians and Ouachitas in North America to the Variscan belt in Western Europe and to the Caucasus in the east (von Raumer, 1998; Mayringer et al., 2011; Soder and Romer, 2018; De Min et al., 2020). In the Southern Alps within the Adriatic lithosphere, Variscan-related metamorphism and crustal melting are also well documented (Muttoni et al., 1996; von Raumer, 1998; Handy et al., 1999; Roda et al., 2023).

A reactivation of the suture zone between Gondwana and Laurasia occurred during the Permian. This reactivation affected the eastern coast of North America, the northern part of South America, northwestern Africa and the northern margin of Adria (Cassinis et al., 2008; Muttoni et al., 2009) and was associated with significant magmatic activity (e.g., Lago

et al., 2004). In the Southern Alps at the northern border of Adria, this magmatic activity is documented by the Mafic Complex in the Ivrea-Verbano lower crustal section (westernmost part of Southern Alps; Quick et al., 2009; Peressini et al., 2007; Klötzli et al., 2014) and by volcanics and/or granitoid intrusions in the western, central and eastern parts of the Southern Alps (e.g., Rottura et al., 1998; Schaltegger and Brack, 2007; Cassinis et al., 2008; Bellieni et al., 2010; Lustrino et al., 2019) (Figure 1.1).

The Permian period was also characterized by transtensional to extensional tectonics in Western Europe, Adria and neighboring areas. The subduction of the Paleotethys Ocean in the east beneath the Euroasiatic margin also started in this time (e.g. Stampfli et al., 2002; Muttoni et al., 2009). These events continued until the Triassic–Jurassic period (Schettino and Turco, 2011; Denyszyn et al., 2018). Notably, the Southern Alps in the northern part of Adria and neighboring areas (e.g., Dinarides, Karawanken, Alcapa, Corsica) witnessed the development of carbonate platforms and basins, and widespread magmatic activity during the Triassic in response to prevalent extensional to strike-slip tectonics (e.g. Doglioni, 1987; Gianolla et al., 1998; Beltrando et al., 2015; Lustrino et al., 2019; De Min et al., 2020; Velicogna et al., 2022) (Figure 1.1).

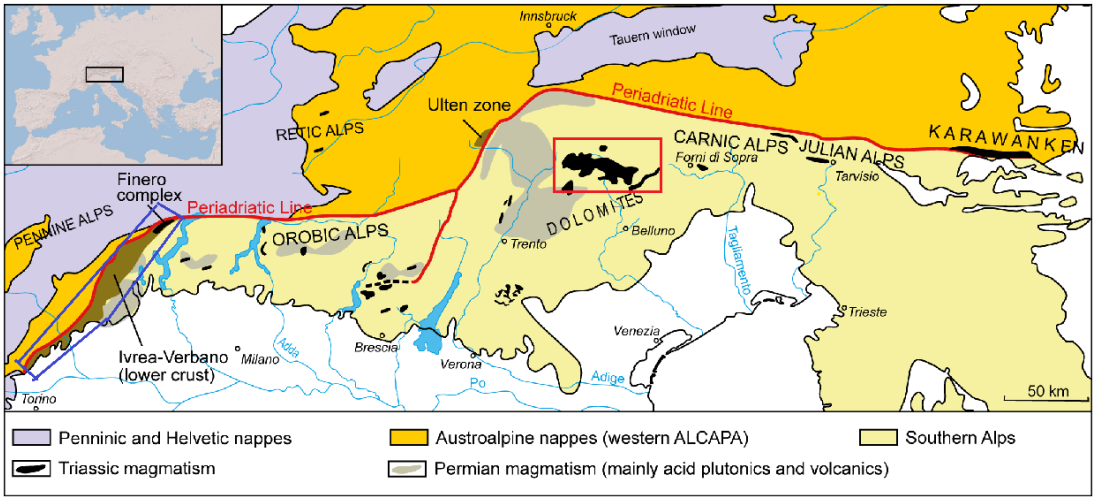

Figure 1.1: Generalized geological map of the Southern Alps (modified after De Min et al., 2020) showing the locations of the Ivrea-Verbano Zone (marked in blue) and the Dolomites (marked in red), focus of the present research.

The Triassic magmatism in the Southern Alps, largely studied in detail in the eastern sector (e.g., Dolomites, Vicentinian Alps, Julian Alps, Val di Non, etc) occurred in two major cycles. The first cycle, from the Middle to early Late Triassic (~243-235 Ma), was characterized by emplacement of volcanics and intrusions of high-K calc-alkaline to shoshonitic geochemical signatures (Bonadiman et al., 1994; Casetta et al., 2018, 2021; Lustrino et al., 2019; Storck et al., 2019, 2020; De Min et al., 2020; Nardini et al., 2022). This was followed, in the Late Triassic to Early Jurassic (~230-190 Ma) by a magmatic cycle with geochemical affinities varying from alkaline to transitional and tholeiitic (e.g., Cassinis et al., 2008; Casetta et al., 2019; De Min et al., 2020). In the central and western parts of the Southern Alps, many details and datasets on the Triassic magmatism are however unavailable (e.g., Cassinis et al., 2008; Stähle et al., 1990; 2001; Mazzucchelli et al., 2010; Schaltegger et al., 2015; Denyszyn et al., 2018; Galli et al., 2019; Bonazzi et al., 2020; Giovanardi et al., 2013, 2020). Due to this situation and the widespread hydrothermal alteration of outcrops, substantive correlation of the magmatic events that occurred in the different sectors of the Southern Alps (at the Gondwana–Laurasia boundary) during the Triassic is currently lacking. The relation of these magmatic events of the Southern Alps to the geodynamic environment during the Triassic is also complicated and strongly debated, particularly with respect to the Middle Triassic magmatism exhibiting high-K calc-alkaline to shoshonitic geochemical affinity in contrast to the extensional to strike-slip tectonics (e.g. Doglioni, 1987; Gianolla et al., 1998; Beltrando et al., 2015) which was prevalent during this time.

Hence, to provide further constraints on the geodynamic evolution of the Gondwana–Laurasia boundary in Triassic times prior to the breakup of the Pangea, this thesis documents the results of detailed research on the Triassic–Early Jurassic magmatism which occurred in the Southern Alps, particularly in the westernmost and eastern sectors. The orogenic mantle sequences exposed in the westernmost sector of the Southern Alps were also studied to

provide constraints on the nature and evolution of the possible mantle sources of the Triassic magmatism in this area. A multidisciplinary approach including sampling and field observations, detailed petrography, geochemistry, geochemical modeling, geochronology and radiogenic isotope systematics was employed.

To overcome the limitation imposed by high degree of alteration of outcrops in the Southern Alps, we focused geochemical characterization of sampled rocks on the analysis of mineral phases after detailed petrography. The analysis of different generation of minerals and the systematic core-to-rim analysis also provided the opportunity for tracing geochemical changes in the studied rocks.

1.2 Research objectives

The key objectives of this research included:

1) Comparison of the tectono-magmatic evolution of the westernmost Southern Alps (Ivrea-Verbano Zone) with respect to the eastern (Dolomites) and central (Brescian PreAlps) sectors.
2) Detailed characterization of the poorly-studied Late Triassic tectono-magmatic events of the Southern Alps. In this frame, invaluable constraints were provided by the investigation of the deep intrusions in the Ivrea-Verbano Zone.
3) Provide new geochronological and isotopic constraints (U-Pb, Lu-Hf, Sm-Nd, Rb-Sr, Pb-Pb) on the Southern Alps tectono-magmatic events.
4) Determine the origin and nature of crustal components in uprising mantle melts in the Southern Alps.
5) Unravel the nature, heterogeneity and evolution of the subcontinental lithospheric mantle beneath the Southern Alps. In this case, unique insights were also provided by the study of the Ivrea-Verbano Zone mantle peridotites.

1.3 Thesis structure

This thesis is divided into two main parts. The first part comprises three Chapters and is focused on Triassic to Early Jurassic magmatism which occurred in the western (Ivrea-Verbano Zone) and eastern (Dolomites) sectors of the Southern Alps. The second part is composed of two Chapters dealing with the orogenic mantle massifs outcropping in the Ivrea-Verbano Zone, western Southern Alps.

Chapter 1 is introductory and provides the scientific background and objectives of the research.

Chapter 2 is an original article published in **Gondwana Research**, vol. 129, pp. 201-219, https://doi.org/10.1016/j.gr.2023.12.011. It deals with the transition of the Triassic magmatism in the Ivrea-Verbano Zone from orogenic-like to anorogenic signatures.

Chapter 3 is a manuscript submitted to **Lithos** for peer-review and possible publication. The chapter focuses on the Late Triassic to Early Jurassic alkaline magmatism which occurred in the Ivrea-Verbano Zone.

Chapter 4 is a manuscript in preparation for submission to a journal for review and possible publication. It focuses on the Middle Triassic high-K calc-alkaline to shoshonitic magmatism in the Dolomites.

Chapter 5 is a manuscript submitted to **Scientific Reports** for peer-review and possible publication. The chapter presents new geochemical and Nd-Hf isotopes on the lherzolitic mantle massifs from Ivrea-Verbano Zone.

Chapter 6 is a manuscript in preparation for submission to a journal for peer-review and possible publication. It reports, for the first time, the occurrence of the DUPAL isotope anomaly in the Finero phlogopite peridotite massif, Ivrea-Verbano Zone and relates the recycling of subducted and/or delaminated continental crust within the Southern Alps upper

mantle to the development of magmatism derived from mantle sources containing continental crust components throughout the Southern Alps during the Triassic–Jurassic period.

Chapter 7 is conclusions and recommendations.

References

Bellieni, G., Fioretti, A.M., Marzoli, A.,Visonà, D., 2010. Permo–Paleogene magmatism in the eastern Alps. Rendiconti Lincei 21, 51–71.

Beltrando, M., Stockli, D.F., Decarlis, A., Manatschal, G., 2015. A crustal-scale view at rift localization along the fossil Adriatic margin of the Alpine Tethys preserved in NW Italy. Tectonics 34. https://doi.org/10.1002/2015TC003973.

Bonazzi, M., Langone, A., Tumiati, S., Dellarole, E., Mazzucchelli, M., Giovanardi, T., Zanetti, A., 2020. Mantle-derived corundum-bearing felsic dykes may survive only within the lower (refractory/inert) crust: Evidence from zircon geochemistry and geochronology (Ivrea–Verbano Zone, Southern Alps, Italy). Geosciences 10, 281. https://doi.org/10.3390/geosciences10080281.

Casetta, F., Coltorti, M., Marocchino, E. 2018. Petrological evolution of the Middle Triassic Predazzo Intrusive Complex, Italian Alps. Inter. Geol. Rev. 60, 977–97. https://doi.org/10.1080/00206814.2017.1363676.

Casetta, F., Ickert, R.B., Mark, D.F., Bonadiman, C., Giacomoni, P.P., Ntaflos, T., Coltorti, M., 2019. The alkaline lamprophyres of the Dolomitic Area (Southern Alps, Italy): markers of the late Triassic change from orogenic-like to anorogenic magmatism. J. Petrol. 60, 1263–1298. https://doi.org/10.1093/petrology/egz031.

Casetta, F., Ickert, R.B., Mark, D.F., Giacomoni, P.P., Bonadiman, C., Ntaflos, T., Zanetti, A., Coltorti, M., 2021. The Variscan subduction inheritance in the Southern Alps Sub-Continental Lithospheric Mantle: Clues from the Middle Triassic shoshonitic magmatism of the Dolomites (NE Italy). Lithos 380-381. https://doi.org/10.1016/j.lithos.2020.105856.

Cassinis, G., Cortesogno, L., Gaggero, L., Perotti, C.R., Buzzi, L., 2008. Permian to Triassic geodynamic and magmatic evolution of the Brescian Prealps (Eastern Lombardy, Italy). Ital. J. Geosci. 127, 501–518.

Dal Piaz, G.V., Bistacchi, A., Massironi, M., 2003. Geological outline of the Alps. Episodes 26, 175-180.

De Min, A., Velicogna, M., Ziberna, L., Chiaradia, M., Alberti, A., Marzoli, A., 2020. Triassic magmatism in the European Southern Alps as an early phase of Pangea break-up. Geol. Mag. 157, 1–23. https://doi.org/10.1017/S0016756820000084.

Denyszyn, S.W., Fiorentini, M.L., Maas, R., Dering, G., 2018. A bigger tent for CAMP. Geology 46, 823–826. https://doi.org/10.1130/G45050.1.

Doglioni, C., 1987. Tectonics of the Dolomites (Southern Alps, Northern Italy). J. Struct. Geol. 9, 181–193.

Galli, A., Grassi, D., Sartori, G., Gianola, O., Burg, J.P., Schmidt, M.W., 2019. Jurassic carbonatite and alkaline magmatism in the Ivrea zone (European Alps) related to the breakup of Pangea. Geology 47, 199-202. https://doi.org/10.1130/G45678.1.

Gianolla, P., De Zanche, V., Mietto, P., 1998. Triassic Sequence Stratigraphy in the Southern Alps. Definition of sequences and basin evolution, *in* de Graciansky, P.C., Hardenbol, J., Jacquin, T., Vail, P.R., Ulmer-Scholle, D., eds., Mesozoic-Cenozoic Sequence Stratigraphy of European Basins, SEPM Special Publication 60, 723–751, Tulsa/Oklahoma.

Giovanardi, T., Morishita, T., Zanetti, A., Mazzucchelli, M., Vannucci, R., 2013. Igneous sapphirine as a product of melt-peridotite interactions in the Finero Phlogopite Peridotite Massif, Western Italian Alps. Eur. J. Miner. 25, 17–31. https://doi.org/10.1127/0935-1221/2013/0025-2251.

Giovanardi, T., Zanetti, A., Dallai, L., Morishita, T., Hémond, C., Mazzucchelli, M., 2020. Evidence of subduction-related components in sapphirine-bearing gabbroic dykes (Finero phlogopite–peridotite): Insights into the source of the Triassic–Jurassic magmatism at the Europe–Africa boundary. Lithos 356–357, 105366. https://doi.org/10.1016/j.lithos.2020.105366.

Handy, M., Franz, L., Heller, F., Janott, B., Zurbriggen, R., 1999. Multistage accretion, orogenic stacking, and exhumation of continental crust (Ivrea crustal section, Italy and Switzerland). Tectonics 18, 1154-1177.

Klötzli, U.S., Sinigoi, S., Quick, J.E., Demarchi, G., Tassinari, C.C.G., Sato, K., Günes, Z., 2014. Duration of igneous activity in the Sesia Magmatic System and implications for

high-temperature metamorphism in the Ivrea–Verbano deep crust. Lithos 206–207, 19-33. https://doi.org/10.1016/j.lithos.2014.07.020.

Kroner, U., Romer R.L., 2013. Two plates – Many subduction zones: The Variscan orogeny reconsidered. Gondwana Res. 24, 298-329. https://dx.doi.org/10.1016/j.gr.2013.03.001

Lago, M., Arranz, E., Pocovì, A., Galè, C., Gil-Imaz, A., 2004. Permian magmatism and basin dynamics in the southern Pyrenees: a record of the transition from late Variscan transtension to early Alpine extension. *in* Wilson, M., Neumann, E.-R., Davies, G.R., Timmerman, M.Y., Heeremans, M., Larsen, B.T., eds., Permo-Carboniferous Magmatism and Rifting in Europe. Geological Society of London, Special Publication 223, 439–464.

Lustrino, M., Abbas, H., Agostini, S., Caggiati, M., Carminati, E., Gianolla, P., 2019. Origin of Triassic magmatism of the Southern Alps (Italy): Constraints from geochemistry and Sr-Nd-Pb isotopic ratios. Gondwana Res. 75, 218–238. https://doi.org/10.1016/j.gr.2019.04.011.

Matte, P., 1986. Tectonics and plate tectonics model for the Variscan belt of Europe. Tectonophysics 126, 329-332.

Mayringer, F., Treloar, P.J., Gerdes, A., Finger, F., Shengelia, D., 2011. New age data from the Dzirula massif, Georgia: implications for the evolution of the Caucasian Variscides. Am. J. Sci. 311, 404-441.

Mazzucchelli, M., Zanetti, A., Rivalenti, G., Vannucci, R., Correia, C.T., Tassinari, C.C.G., 2010. Age and geochemistry of mantle peridotites and diorite dykes from the Baldissero body: Insights into the Paleozoic-Mesozoic evolution of the Southern Alps. Lithos 119, 485–500. https://doi.org/10.1016/j.lithos.2010.08.002.

Muttoni, G., Gaetani, M., Kent, D.V., Sciunnach, D., Angiolini, L., Berra, F., Garzanti, E., Mattei, M., Zanchi, A., 2009. Opening of the Neo-Tethys Ocean and the Pangea B to Pangea A transformation during the Permian. GeoArabia 14, 17–48.

Muttoni, G., Kent, D.V., 2019. Adria as promontory of Africa and its conceptual role in the Tethys Twist and Pangea B to Pangea A Transformation in the Permian. Riv. Ital. Paleontologia Strat. 125, 249-269.

Muttoni, G., Kent, D.V., Channell, J.E.T., 1996. Evolution of Pangea: Paleomagnetic

constraints from the Southern Alps, Italy. Earth Planet. Sci. Lett. 140, 97-112.

Nance, R.D., 2010. The Rheic Ocean: Palaeozoic evolution from Gondwana and Laurussia to Pangaea–Introduction. Gondwana Res. 17, 189-192.

Nance, R.D., Gutierrez-Alonso, G., Keppie, J.D., Linnemann, U., Murphy, J.B., Quesada, C., Strachan, R.A., Woodcock, N.H., 2012. A brief history of the Rheic Ocean. Geoscie. Front. 3, 125-135. https://doi.org/10.1016/j.gsf.2011.11.008.

Nardini, N., Casetta, F., Ickert, R.B., Mark, D.F., Ntaflos, T., Zanetti, A., Coltorti, M., 2022. From the Middle Triassic Cima Pape complex (Dolomites; Southern Alps) to the feeding systems beneath active volcanoes: Clues from clinopyroxene textural and compositional zoning. J. Volcan. Geotherm. Res. 422. https://doi.org/10.1016/j.jvolgeores.2021.107459.

Peressini, G., Quick, J.E., Sinigoi, S., Hofmann, A.W., Fanning, M., 2007. Duration of a large mafic intrusion and heat transfer in the lower crust: a SHRIMP U/Pb zircon study in the Ivrea–Verbano Zone (Western Alps, Italy). J. Petrol. 48, 1185-1218, https://doi.org/10.1093/petrology/egm014.

Roda, M., Spalla, M.I., Filippi, M., Lardeaux, J.-M., Rebay, G., Regorda, A., Zanoni, D., Zucali, M., Gosso, G., 2023. Metamorphic Remnants of the Variscan Orogeny across the Alps and Their Tectonic Significance. Geosciences 13.

Rottura, A., Bargossi, G.M., Caggianelli, A., Del Moro, A., Visonà, D., Tranne, C.A., 1998 Origin and significance of the Permian high-K calc-alkaline magmatism in the central-eastern Southern Alps, Italy. Lithos 45, 329–348.

Schaltegger, U., Brack, P., 2007. Crustal-scale magmatic systems during intracontinental strike-slip tectonics: U, Pb and Hf isotopic constraints from Permian magmatic rocks of the Southern Alps. Inter. J. Earth Sci. 96, 1131–1151.

Schaltegger, U., Ulianov, A., Müntener, O., Ovtcharova, M., Peytcheva, I., Vonlanthen, P., Vennemann, T., Antognini, M., & Girlanda, F. (2015). Megacrystic zircon with planar fractures in miaskite-type nepheline pegmatites formed at high pressures in the lower crust (Ivrea Zone, southern Alps, Switzerland). Am. Mineral. 100, 83-94. https://doi.org/10.2138/am-2015-4773.

Schettino, A., Turco, E., 2011. Tectonic history of the western Tethys since the Late Triassic. GSA Bull. 123, 89–105. https://doi.org/10.1130/B30064.1.

Soder, C.G., Romer, R.L., 2018. Post-collisional potassic-ultrapotassic magmatism of the Variscan orogen: Implications for mantle metasomatism during continental subduction. J. Petrol. 59, 1007-1034. https://doi.org/10.1093/petrology/egy053.

Stähle, V., Frenzel, G., Hess, J.C., Saupé, F., Schmidt, S.T., Schneider, W., 2001. Permian metabasalt and Triassic alkaline dykes in the Northern Ivrea Zone: clues to the post-Variscan geodynamic evolution of the Southern Alps. Schweizerische Mineralogische Petrographische Mitteillungen 81, 1–21.

Stähle, V., Frenzel, G., Kober, B., Michard, A., Puchelt, H., Schneider, W., 1990. Zircon syenite pegmatites in the Finero peridotite (Ivrea Zone): evidence for a syenite from a mantle source. Earth Planet. Sci. Lett. 101, 196–205. https://doi.org/10.1016/0012-821X(90)90153-O.

Stampfli, G.M., Borel, G.D., 2002, A plate tectonic model for the Paleozoic and Mesozoic constrained by dynamic plate boundaries and restored synthetic oceanic isochrones. Earth Planet. Sci. Lett. 196, 17–33. https://doi.org/10.1016/S0012-821X(01)00588-X.

Stampfli, G.M., Von Raumer, J.F., Borel, G.D., 2002. Paleozoic evolution of pre-Variscan terranes: from Gondwana to the Variscan collision, *in* Catalan, J.R.M., Hatcher, R.D., Arenas, R., Garcia, F.D., eds., Variscan-Appalachian dynamics: The building of the late Paleozoic basement. GSA Special Paper 364, 263–280. https://doi.org/10.1130/0-8137-2364-7.263.

Storck, J.-C., Brack, P., Wotzlaw, J.F., Ulmer, P. (2019). Timing and evolution of Middle Triassic magmatism in the Southern Alps (northern Italy). J. Geol. Soc. 176, 253-268. https://doi.org/10.1144/jgs2018-123.

Storck, J.C., Wotzlaw, J.F., Karakas, Ö., Brack, P., Gerdes, A., Ulmer, P., 2020. Hafnium isotopic record of mantle-crust interaction in an evolving continental magmatic system. Earth Planet. Sci. Lett. 535, 116100.

van Hinsbergen, D.J.J., Torsvik, T.H., Schmid, S.M., Maţenco, L.C., Maffione, M., Vissers, R.L.M., Gürer, D., Spakman, W., 2020. Orogenic architecture of the Mediterranean region and kinematic reconstruction of its tectonic evolution since the Triassic. Gondwana Res. 81, 79-229. https://doi.org/10.1016/j.gr.2019.07.009.

Velicogna, M., De Min, A., Prašek, M.K., Ziberna, L., Brombin, V., Jourdan, F., Renne, P.R., Balen, D., Grégoire, M., Marzoli, A., 2022. The Norian magmatic rocks of Jabuka,

Brusnik and Vis Islands (Croatia) and their bearing on the evolution of Triassic magmatism in the Northern Mediterranean. Int. Geol. Rev. 65.

von Raumer, J.F., 1998. The Palaeozoic evolution in the Alps: from Gondwana to Pangea. Geol. Rund. 87, 407–35.

von Raumer, J.F., Bussy, F., Schaltegger, U., Schulz, B., Stampfli, G.M., 2013. Pre-Mesozoic Alpine basements – Their place in the European Paleozoic framework. GSA Bull. 125, 89–108. https://doi.org/10.1130/B30654.1.

Warr, L.N., 2012. The Variscan Orogeny: the Welding of Pangaea, *in* Woodcock, N., Strachan, R., eds., Geological History of Britain and Ireland, 274-298.

PART 1

CHAPTER 2

Transition from orogenic-like to anorogenic magmatism in the Southern Alps during the Early Mesozoic: Evidence from elemental and Nd-Sr-Hf-Pb isotope geochemistry of alkali-rich dykes from the Finero Phlogopite Peridotite, Ivrea-Verbano Zone

Abimbola C. Ogunyele[1,2], Mattia Bonazzi[2], Tommaso Giovanardi[3], Maurizio Mazzucchelli[2,3], Vincent J.M. Salters[4], Alessandro Decarlis[5], Alessio Sanfilippo[1,2], Alberto Zanetti[2]

[1] Department of Earth and Environmental Sciences, University of Pavia, Via Ferrata 1, 27100 Pavia, Italy

[2] CNR – Istituto Geoscienze e Georisorse, Via Ferrata 1, 27100 Pavia, Italy

[3] Department of Chemical and Geological Sciences, University of Modena and Reggio Emilia, Via Campi 103, 41125 Modena, Italy

[4] National High Magnetic Field Laboratory, Department of Earth, Ocean and Atmospheric Sciences, Florida State University, Tallahassee, FL 32310, USA

[5] RICH Center, Earth Sciences Department, Khalifa University of Science and Technology, P.O. Box 12788, Abu Dhabi, United Arab Emirates

Declaration

This chapter is published as an original article in **Gondwana Research**, vol. 129, pp. 201-219, https://doi.org/10.1016/j.gr.2023.12.011. The study was conducted in collaboration with the co-authors cited above. The contribution of each author is given below.

ACO: Data curation, Formal analysis, Investigation, Methodology, Validation, Visualization, Writing - original draft, Writing - review & editing; **MB**: Formal analysis, Investigation, Methodology, Writing - review & editing; **TG**: Data curation, Formal analysis, Investigation, Methodology, Validation, Visualization, Writing - review & editing; **MM**: Conceptualization, Funding acquisition, Investigation, Supervision, Writing - review & editing; **VJMS**: Funding acquisition, Investigation, Supervision, Writing - review & editing; **AD**: Funding acquisition, Writing - review & editing; **AS**: Supervision, Writing - review & editing; **AZ**: Conceptualization, Funding acquisition, Methodology, Project administration, Resources, Supervision, Validation, Visualization, Writing - review & editing.

Abstract

The Ivrea-Verbano Zone (IVZ) in the westernmost sector of the Southern Alps is an iconic upper mantle to lower continental crust sequence of the Adriatic Plate and provides a geological window into the tectono-magmatic events that occurred at the Gondwana–Laurussia boundary from Late Paleozoic to Early Mesozoic. In this work, we document new geochemical and Nd-Sr-Hf-Pb isotopic data for Early Mesozoic alkali-rich dyke swarms which intruded the Finero Phlogopite Peridotite (northern IVZ) to provide geological constraints on the nature, origin and evolution of Early Mesozoic magmatism in the Southern Alps. The studied dykes are amphibole-phlogopite-bearing and show geochemical features varying between two end-member groups. A dyke group is characterized by HFSE-poor, Al-rich amphibole (Al_2O_3 up to 16 wt.%) with high LILE and LREE contents, high radiogenic $^{87}Sr/^{86}Sr_{(i)}$ (0.704732 to 0.704934) and low radiogenic Nd isotopes ($\varepsilon Nd_{(i)}$ from –0.1 to –0.7), which support the occurrence of significant amounts of recycled continental crust components in the parental mantle melts and impart an overall "orogenic-like" affinity. This dyke group was largely derived from metasomatized lithospheric mantle sources. The second group is HFSE-rich with Al-poorer amphibole enriched in LILE and LREE, low radiogenic $^{87}Sr/^{86}Sr_{(i)}$ (0.703761–0.704103) and higher radiogenic Nd isotopes ($\varepsilon Nd_{(i)}$ from +3.4 to +5.4) pointing to an "anorogenic" alkaline affinity and asthenospheric to deep lithospheric mantle sources. Some dykes show both orogenic and anorogenic affinities, providing evidence that the orogenic-like magmatism in the IVZ predates the alkaline anorogenic magmatism. The Finero dyke swarms therefore record a geochemical change of the Early Mesozoic magmatism of the Southern Alps from orogenic-like magmatism, typical of post-collisional settings, to anorogenic alkaline magmatism, common in intraplate to extensional settings, and places a temporal correlation of Early Mesozoic magmatism in the IVZ to those in the eastern and central sectors of the Southern Alps.

2.1 Introduction

The geodynamic processes that trigger a shift from orogenic-like calc-alkaline magmatism to alkaline OIB-like magmatism in syn- to post-collisional settings are enigmatic, ranging from asthenospheric upwelling to lithospheric delamination, mantle plumes, plume-arc interaction, slab roll-back, slab tearing, and incorporation of exotic enriched mantle components, etc (Marquez et al., 1999; Agostini et al., 2007; Handy et al., 2019; Deng et al., 2023). Such a shift and processes are well-documented in several localities around the Alpine-Mediterranean region and in most subduction zones worldwide (e.g., Coltorti et al., 2007; Agostini et al., 2007; Harangi et al., 2007; Lustrino et al., 2013; Zheng, 2019; Deng et al., 2023). One of such areas in the Alpine-Mediterranean region is the Southern Alps where significant magmatic activities occurred during the Late Paleozoic to Early Mesozoic, particularly from the Middle to Late Triassic (ca. 243–237 Ma) (Lustrino et al., 2019; Storck et al., 2019; De Min et al., 2020; Casetta et al., 2021). Petrological and geochemical studies focused on the Middle Triassic volcano-plutonic sequences emplaced at shallow crustal depths and erupted at the surface in the eastern (e.g. Dolomites) and central (Brescian Prealps) sectors of the Southern Alps confirm a K-rich calc-alkaline to shoshonitic affinity of the uprising melts, commonly interpreted as the result of the partial melting of mantle sources presumably subduction-modified during the "Variscan cycle" with negligible crustal contamination (e.g., Lustrino et al., 2019; De Min et al., 2020; Casetta et al., 2021; Nardini et al., 2022). In this case, "Variscan" is used in the broadest sense of the term. In the Late Triassic, the subduction-related magmatism was followed by alkaline OIB-type magmatism represented by the ca. 219 Ma alkaline lamprophyre dykes in the Dolomites (Casetta et al., 2019) and the ca. 217 Ma transitional basaltic dykes in the Brescian Prealps (Cassinis et al., 2008) indicating a significant variation of the mantle sources and geodynamic environment

subsequently leading to the opening of the Alpine Tethys during the Lower Jurassic (Cassinis et al., 2008; Casetta et al., 2019).

The opportunity of characterizing different cycles of Early Mesozoic magmatism, their source changes and relationship with the evolution of the geodynamic environment is also possible in the westernmost sector of the Southern Alps in the Ivrea-Verbano Zone (IVZ). The IVZ forms a spectacular exposure of lower to middle continental crust with the widespread occurrence of mantle peridotite lenses (Figure 2.1) that provides a unique natural laboratory to study deep crustal and mantle rocks of Late Paleozoic to Early Mesozoic age. The petrochemical record of Triassic–Jurassic magmatism in the IVZ was only recently recognized, and it is particularly relevant in the Finero Complex. The IVZ Triassic–Jurassic magmatism is recorded by a variety of intrusive bodies (mainly veins, dykes and pods) emplaced into the lower crust and mantle peridotites (Stähle et al., 1990; 2001; Grieco et al., 2001; Mazzucchelli et al., 2010; Zanetti et al., 2013; Schaltegger et al., 2015; Denyszyn et al., 2018; Galli et al., 2019; Bonazzi et al., 2020; Giovanardi et al., 2013, 2020; Decarlis et al., 2023). Tuffitic horizons within carbonate platform sequences close to IVZ and some mafic dykes in the adjacent Serie dei Laghi (Zurbriggen, 1996; Handy et al., 1999) also provide evidence of Early Mesozoic magmatism in the westernmost Southern Alps.

However, the Mesozoic magmatism in the Finero Complex and the IVZ at large is still poorly constrained due to the intrinsic complication of its poly-phasic emplacement that occurred between two major orogenic cycles (i.e. the demise of the Variscan belt and onset of the Alpine Tethys). In addition, Mesozoic melts migration started when the Finero Complex was still placed at P-T conditions typical of a continental crust-mantle transition (~1 GPa) and this promoted the re-opening of the geochronological clocks widening time interval brackets of absolute dating (Zanetti et al., 2016). Previous geochemical studies on the Early Mesozoic magmatism of the IVZ point to the variable geochemical signatures of the parental

mantle melts from tholeiitic to OIB affinity, often containing continental crustal components (e.g., Giovanardi et al., 2020). Unlike the magmatisms in the Brescian Prealps and Dolomitic areas, the IVZ Triassic magmatism is mostly younger than 235 Ma, providing an opportunity to better characterize the Late Triassic tectono-magmatic cycle below or at crust-mantle transition depths. Moreover, the Mesozoic intrusive bodies emplaced in the IVZ mainly show limited interaction with the continental crust. As a consequence, they preserve the primary geochemical features, which allow to provide straightforward constraints on their mantle source compositions.

Here, we present the geochemistry of Early Mesozoic dyke swarms cross-cutting the Finero Phlogopite Peridotite in northern IVZ to: (i) study the origin and evolution of mantle melts and the role of continental crust recycling, highlighting the heterogeneity of the subcontinental lithospheric mantle beneath the Southern Alps, and (ii) to further understand the nature of Triassic–Jurassic magmatism in the Southern Alps tectonic context in the light of the existing literature.

2.2 Geological settings of the Ivrea-Verbano Zone and Finero Complex

The Ivrea-Verbano Zone (IVZ) is the westernmost sector of the Southern Alps and represents a continuously exposed section of lower to intermediate continental crust (Schmid, 1993; Zanetti et al., 2013; Decarlis et al., 2023; Figure 2.1). The IVZ was part of the Mesozoic continental margin of the Adriatic Plate during the opening of the Alpine Tethys and provides a unique opportunity to investigate the Paleozoic to Mesozoic geodynamic evolution of the Gondwana and Laurasia boundary from a lower continental crust perspective (Stampfli and Borel, 2002, 2004; Handy et al., 2010). The present-day exposure of the IVZ results from a 90-degree tilting generated by a series of deformation events that likely started during Permian-Triassic stages of lithospheric thinning in the Variscan post-collisional realm.

Pronounced exhumation and blocks rotation took place during the opening of the Jurassic Alpine Tethys (Decarlis et al., 2023 and references therein) and concluded with the Alpine collision (Handy et al., 1999).

The IVZ comprises three main units: (i) the Kinzigite Formation, (ii) the Mafic Complex and (iii) the Mantle Peridotites. The Kinzigite Formation is an amphibolite- to granulite-facies volcano-sedimentary succession underplated and intruded by the trans-crustal Mafic Complex during the late Carboniferous-early Permian (Peressini et al., 2007). The Mafic Complex represents a large magmatic system that progressively grew due to a continued input of new magmas. The Valsesia area roughly corresponds to the major axis of the magmatic chamber, reaching a maximum thickness of about 11 km. Several orogenic mantle peridotite bodies line up along the NW margin of the Mafic Complex and parallel to the Insubric Line. The largest and more famous of the Ivrea-Verbano mantle peridotites are, from south to north, the Baldissero, Balmuccia, Premosello and Finero massifs (Figure 2.1).

The Finero Complex lies in the northernmost segment of the IVZ (Figure 2.1a-b). It is a large (12 x 3 km), lens-shaped succession including a mantle peridotite (the Finero Phlogopite Peridotite; FPP) at the centre surrounded by a layered gabbroic to ultramafic body (the Finero Mafic Complex; FMC). The Finero Complex is bordered by the Insubric Line to the N-NW and by the Kinzigite Formation to the S-SE (e.g. Zanetti et al., 1999; 2013). The FPP is a pervasively metasomatized harzburgitic body (roughly 11 x 1 km) characterized by the widespread occurrence of amphibole and phlogopite (see Decarlis et al., 2023 for an overview). The FMC can be subdivided into three units, from base to top: (1) the Internal Gabbro, overlying the FPP; (2) the Amphibole Peridotite; and (3) the External Gabbro (Siena and Coltorti, 1989). The Internal Gabbro, also called Layered Internal Zone, is ~70-120 m thick and mainly consists of garnet-bearing hornblendite with subordinate garnet-bearing amphibole gabbro, anorthosite, pyroxenite and peridotite. The Amphibole Peridotite unit is

~400 m thick and is constituted by amphibole-bearing cumulus peridotite (dunite, wehrlite and subordinately lherzolite), pyroxenite and hornblendite. The External Gabbro unit is ~400-500 m thick and mainly consists of amphibole gabbro and diorite, with minor pyroxenite and anorthosite bands. The contact between the Amphibole Peridotite and External Gabbro is tectonic (Langone et al., 2018). Many discordant dyke swarms of ultramafic to felsic compositions intrude the FPP and the FMC (Stähle et al., 1990; 2001; Giovanardi et al., 2013, 2020; Grieco et al., 2001; Schaltegger et al., 2015; Langone et al., 2017), some of which are the subject of the present investigation.

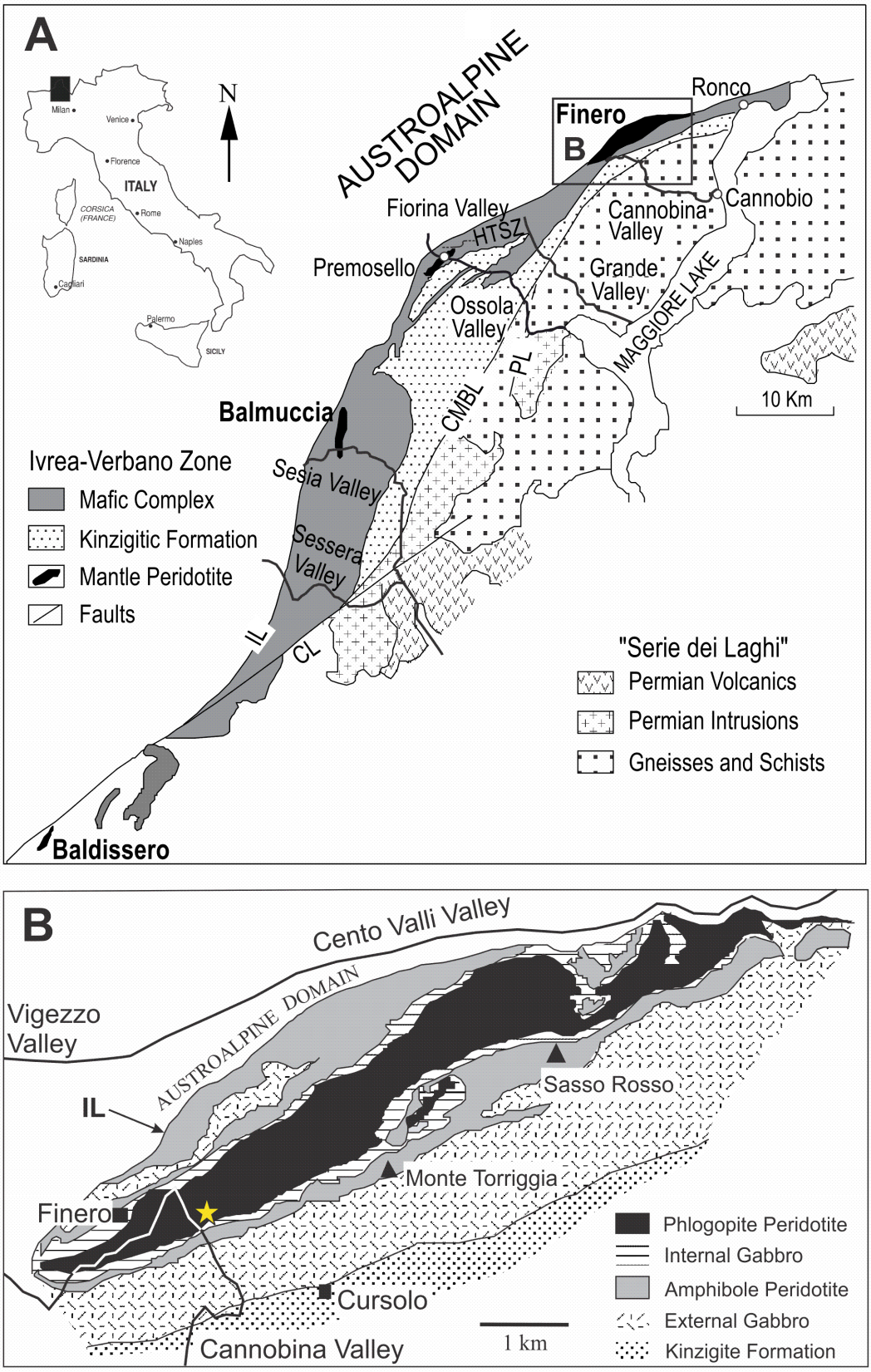

Figure 2.1: Geological maps of (a) the Ivrea-Verbano Zone and (b) the Finero Complex with sampling location (yellow star) of the studied dykes around Rio Creves. IL – Insubric Line, CMBL – Cossato-Mergozzo-Brissago Line, PL – Pogallo Line (after Zanetti et al., 1999).

2.3 Field relationships, samples and petrography

The dyke swarms studied in this work are well-exposed in and around a quarry located along the right flank of the Rio Creves, near the contact between the FPP and the FMC (46°06'27.90"N; 8°32'38.76"E; Figure 2.1b). The outcrops of the dykes are tens to hundreds of meters far from the outcrops of the sapphirine-bearing gabbroic dykes investigated by Giovanardi et al. (2013, 2020), and few hundreds of meters from the outcrops of mantle peridotite intruded by phlogopite-bearing websterites studied by Zanetti et al. (1999).

Most of the alkali-rich dykes of this study cross-cut at a high angle and show sharp contacts with the Paleozoic mantle foliation of the FPP (frequently at right angle; e.g., Figure 2.2a), similar to what is observed for the sapphirine-bearing gabbroic dykes (Giovanardi et al., 2013, 2020). Some alkali-rich dykes are found in shear zones, with sub-parallel to discordant strike to the mantle foliation and testify to a multistage evolution (e.g., Figure 2.2b; Corvò et al., 2020). The dykes show extremely variable composition and they are best classified based on their geochemistry. Hence, due to the occurrence of amphibole in all the dyke samples and the variable contents of the High Field Strength Elements (particularly Nb and Ta) in this mineral phase, the studied dykes are categorized into three groups: (1) HFSE-rich dyke group; (2) HFSE-poor dyke group; and (3) composite HFSE-poor and -rich dyke group (Table 3.1).

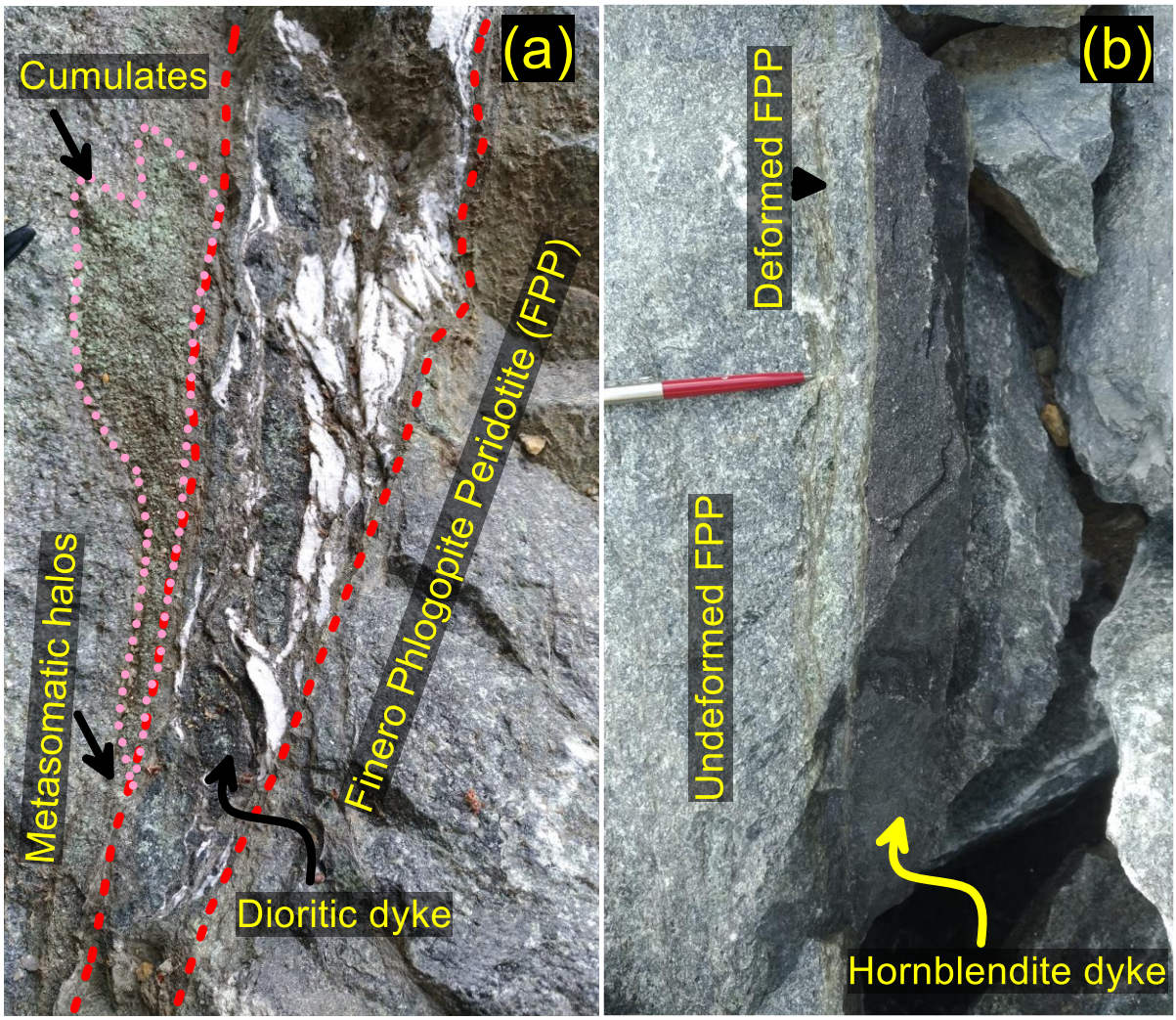

Figure 2.2: Field aspects of alkali-rich dykes cross-cutting the host rock, a phlogopite peridotite in Finero, Ivrea-Verbano Zone. (a) Dioritic dyke in which the magmatic structure has been highly deformed by syn-magmatic volatile-driven overpressure in the conduit; and (b) hornblendite dyke within a shear zone which underwent multistage evolution.

Table 2.1: Description of selected samples of Finero dykes and analytical methods of investigation

Sample ID	Rock type	Grouping	Major mineral phases	Textures	SEM-EDS	EPMA	LA-ICP-MS	Nd-Sr-Hf-Pb isotopes on Amph
FI1603	Diorite	HFSE-rich	Amph + Pl + Phl + Ap + (Cpx)	Magmatic to porphyroclastic	X	X	X	X
FI1604	Diorite	HFSE-rich			X	X	X	
FI1605	Diorite	HFSE-rich			X	X	X	
FI2102	Diorite	HFSE-rich			X	X	X	
FI2103	Diorite	HFSE-rich				X	X	X
FI2104	Diorite	HFSE-rich				X	X	
FI2105	Diorite	HFSE-rich			X	X	X	
FI1501	Hornblendite (with olivine layer)	HFSE-rich	Amph + Phl + Ap + (Ol)	Hypidiomorphic	X	X	X	X
FI1612	Hornblendite	HFSE-rich	Amph + Phl + Ap + (Cpx)			X	X	
FI19A01	Albite-dominated anorthosite	HFSE-rich	Pl + Ap ± Amph ± Phl	Hypidiomorphic to glomerophyric			X	
FI19A02	Albite-dominated anorthosite	HFSE-rich			X	X	X	
FI19A04	Albite-dominated anorthosite	HFSE-rich			X	X	X	
FI1608	Hornblendite	HFSE-poor	Amph + Phl + Ap	Mylonitic to ultramylonitic	X	X	X	
FI2101	Gabbro bordered by orthopyroxenite	HFSE-poor	Amph + Phl + Ap + (Opx)	Banded		X	X	X
FI2106	Diorite	Composite HFSE-poor and -rich	Amph + Pl + Phl + Ap	Porphyroclastic	X	X	X	
FI1607	Hornblendite dyke with cumulus peridotite		Amph + Phl + Ap + (Ol)	Porphyroclastic	X	X	X	X

*Phases in brackets are minerals present in cumulates associated with the dykes (mineral abbreviations after Kretz, 1983)

2.3.1 HFSE-rich (HR) dyke group

Dykes of the HR group contain amphibole with high HFSE content (e.g., Nb >70 ppm). They consist of diorite, albite-dominated anorthosite and hornblendite (Figure 2.3). The diorites (samples FI1603, FI1604, FI1605, FI2102, FI2103, FI2104 and FI2105) show variable proportion (~10-40 vol. %) of leucocratic patches/layers associated with melanocratic segregates. They cross-cut the host peridotite foliation and show a magmatic structure often deformed by syn-magmatic volatile-driven overpressure that took place in the conduits (Figure 2.2a). The texture is variable but commonly porphyroclastic, with magmatic domains and fine-grained mosaic textures (Figure 2.4a-f). Mafic phases in the melanocratic layers of the diorites range from ~90 vol. % amphibole to ~90 vol. % phlogopite. Amphiboles are commonly green to brown, locally fractured and filled by fine-grained phlogopite, plagioclase, apatite, Nb-Ta oxides and calcite. Leucocratic patches formed by plagioclase and apatite show evidence of plastic flow, rotation and grinding. The melanocratic parts locally contain clinopyroxenite cumulates (Figure 2.3b).

Anorthosites (samples FI19A01, FI19A02 and FI19A04) are essentially composed of albite (>90 vol. %) and oligoclase with subordinate brown amphibole, phlogopite and apatite. Zircon, titanite, allanite, calcite and Nb-Ta oxides are common accessory minerals. The texture is hypidiomorphic to glomerophyric. HFSE-rich hornblendites (samples FI1501 and FI1612; Figure 2.3d-e) are almost wholly composed of brown amphibole (>90 vol. %) with hypidiomorphic texture that locally contains thin layers and/or pods of olivine, clinopyroxene, sulphides, and phlogopite. Phlogopite, apatite, Nb-Ta oxides and calcite are subordinate.

U-Pb dating of zircons from some HR dioritic and anorthosite dykes show wide age intervals ranging from 221 ± 9 Ma to 192 ± 8 Ma with peak concordant ages around 200 Ma (Ogunyele et al., 2021; Bonazzi et al., 2022).

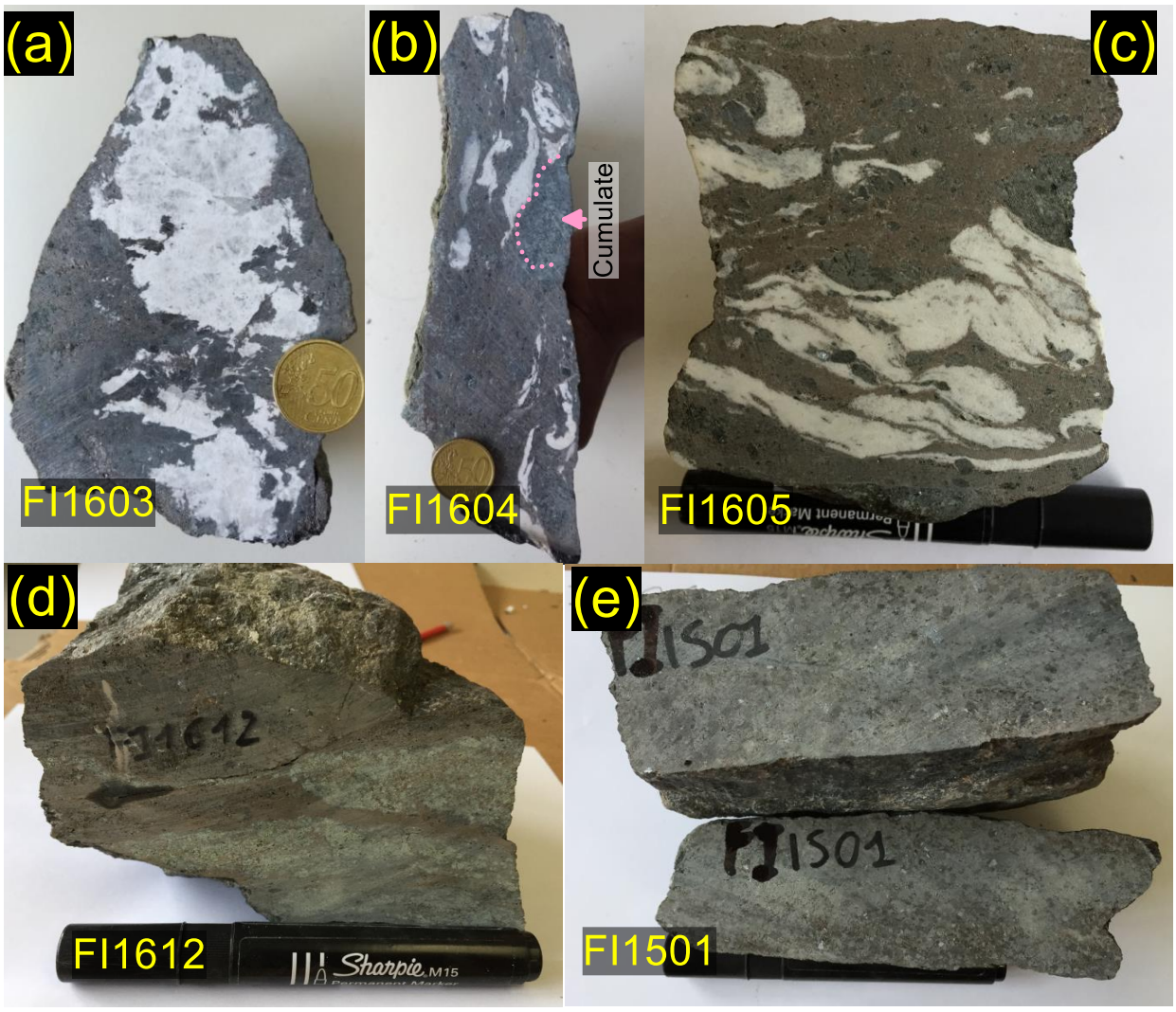

Figure 2.3: Mesoscopic aspects of the Finero HFSE-rich dykes. (a, b, c) HFSE-rich dioritic dyke samples showing leucocratic patches/layers associated with ultramafic segregates and xenoliths of cumulus clinopyroxenite; (d, e) HFSE-rich hornblendite dyke samples. Cumulus clinopyroxenites are also present in the hornblendite dyke sample FI1612.

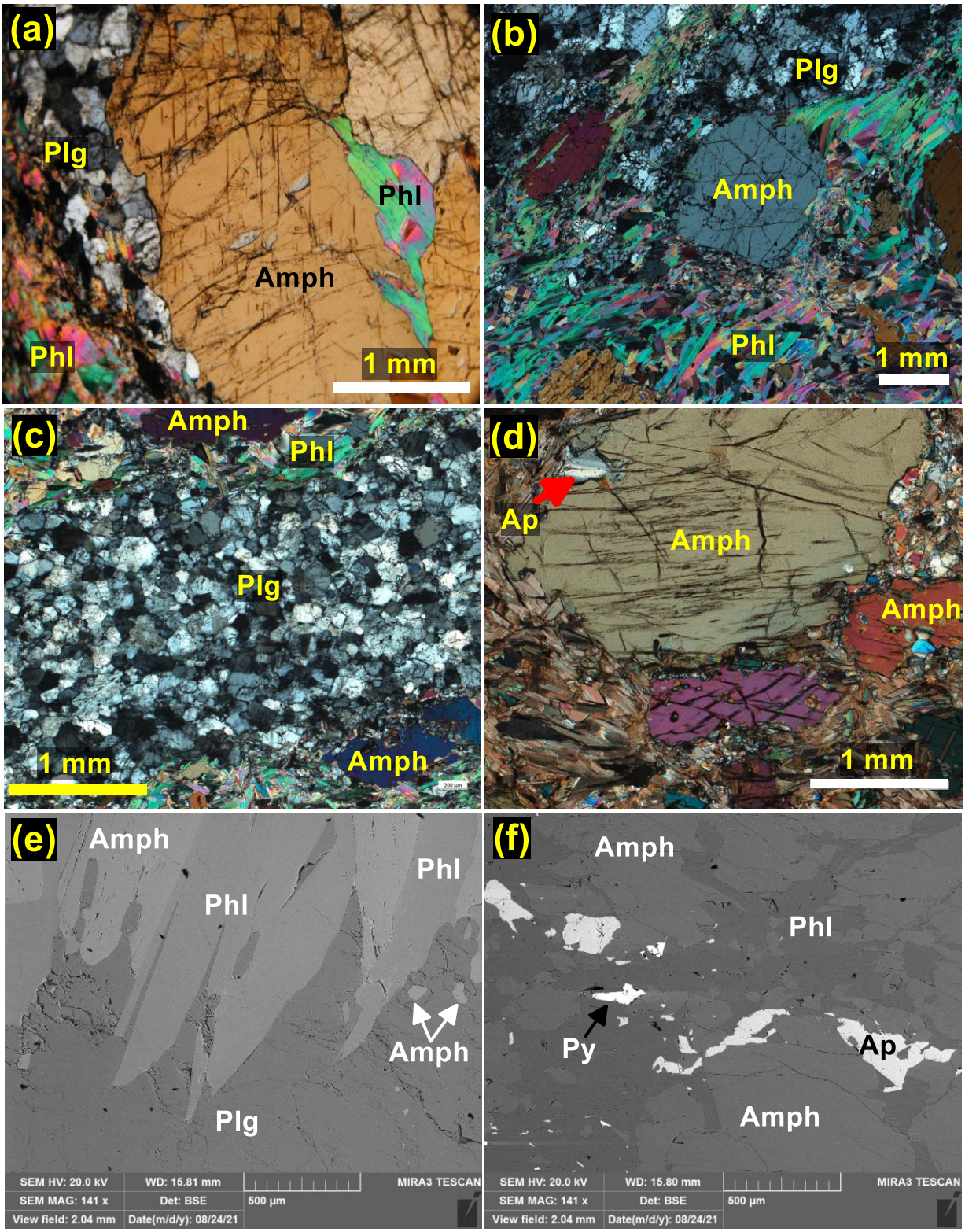

Figure 2.4: Microscopic aspects of the Finero HFSE-rich dioritic dykes. Photomicrographs showing (a) large magmatic amphiboles within plagioclase and fine-grained phlogopite. The

amphibole contains fractures filled by phlogopite, plagioclase and apatite; (b) amphibole porphyroclasts embedded within a groundmass of fine-grained phlogopite, amphibole and plagioclase; (c) leucocratic layer of medium- to fine-grained plagioclase and apatite within melanocratic layers made by amphibole porphyroclasts and fine-grained phlogopite; (d) amphibole porphyroclasts containing apatite wrapped around by fine-grained phlogopite and plagioclase; (e) BSE image showing plagioclase "permeating" amphibole + phlogopite layer; and (f) BSE image showing the interstices of amphiboles filled by phlogopite, apatite and pyrite.

2.3.2 HFSE-poor (HP) dyke group

Dykes of the HP group are characterized by amphibole with low contents of HFSE (e.g., Nb <9 ppm). They include hornblendite (FI1608) and gabbro (FI2101), both of which outcrop in shear zones within the host peridotite. The hornblendite is a mylonitic to ultramylonitic rock almost entirely composed of fine to very fine amphiboles (Figure 2.5a). It is formed by a peculiar alternation of fine-grained amphibole and olivine-rich horizons sandwiched between mylonitic amphibole layers. Phlogopite, apatite and sulphide occur as accessories. The gabbro is similar in structure and mineralogy to sapphirine-bearing gabbroic dykes studied by Giovanardi et al. (2013, 2020). It consists of outer orthopyroxene layers bordering internal layers of brown to greenish amphiboles and plagioclase (Figure 2.5b). Phlogopite, apatite, sapphirine, spinel, and calcite are present. Zircon is however absent in both samples.

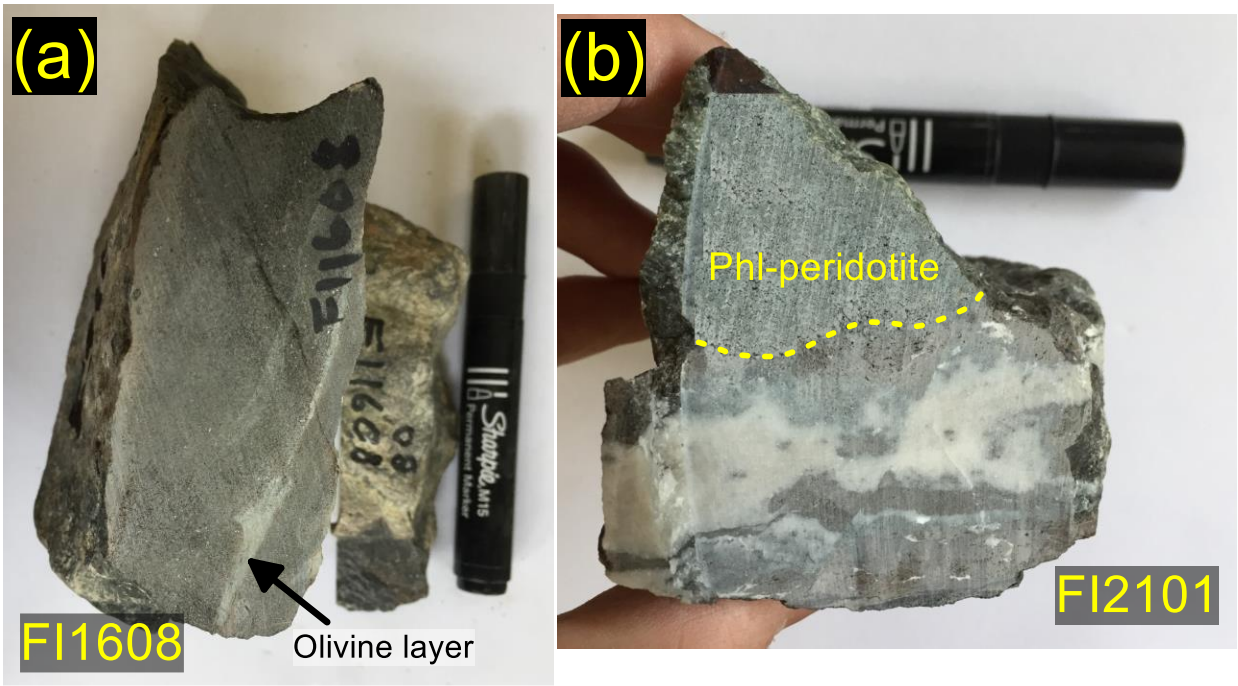

Figure 2.5: Mesoscopic aspects of the Finero HFSE-poor dykes. (a) HFSE-poor hornblendite dyke sample showing mylonitic to ultramylonitic texture. In this sample, ultramylonitic amphibole and olivine-rich layers are sandwiched between fine-grained mylonitic amphibole layers. (b) HFSE-poor gabbroic dyke sample with the host phlogopite peridotite. Between the host peridotite and the gabbroic dyke, an orthopyroxenite layer is present.

2.3.3 Composite HFSE-poor and -rich (HC) dyke group

Dykes belonging to the HC group contain amphiboles ranging from HFSE-poor to HFSE-rich compositions. The two sampled dykes are a diorite (sample FI2106) and a hornblendite with cumulus peridotite (FI1607), both outcropping in shear zones. The diorite (FI2106) is a porphyroclastic amphibole-dominated rock cut by leucocratic layers of plagioclase and apatite. Phlogopite, sulphides and calcite occur as accessories in the dyke (Figure 2.6). Amphibole in the central part of the dyke is enriched in HFSE and grades to HFSE-poor composition towards the margins, suggesting that an HFSE-poor dyke was intruded and overprinted by HFSE-rich melt(s). This observation is crucial to assess the relative timing of HFSE-rich and HFSE-poor

dykes' emplacement, as field cross-cutting relationships are missing at present and zircons are absent in the HFSE-poor dykes.

Sample FI1607 is composed of a 3 cm thick cumulus peridotite layer and a 20 cm thick porphyroclastic hornblendite. The latter is formed by brown amphibole, phlogopite, apatite, calcite and sulphides. Interstitial clino- and orthopyroxene, probably resulting from the dehydration of amphibole at high PT conditions are present. Veinlets of brown amphibole also occur within the porphyroclastic cumulus olivine-dominated peridotite.

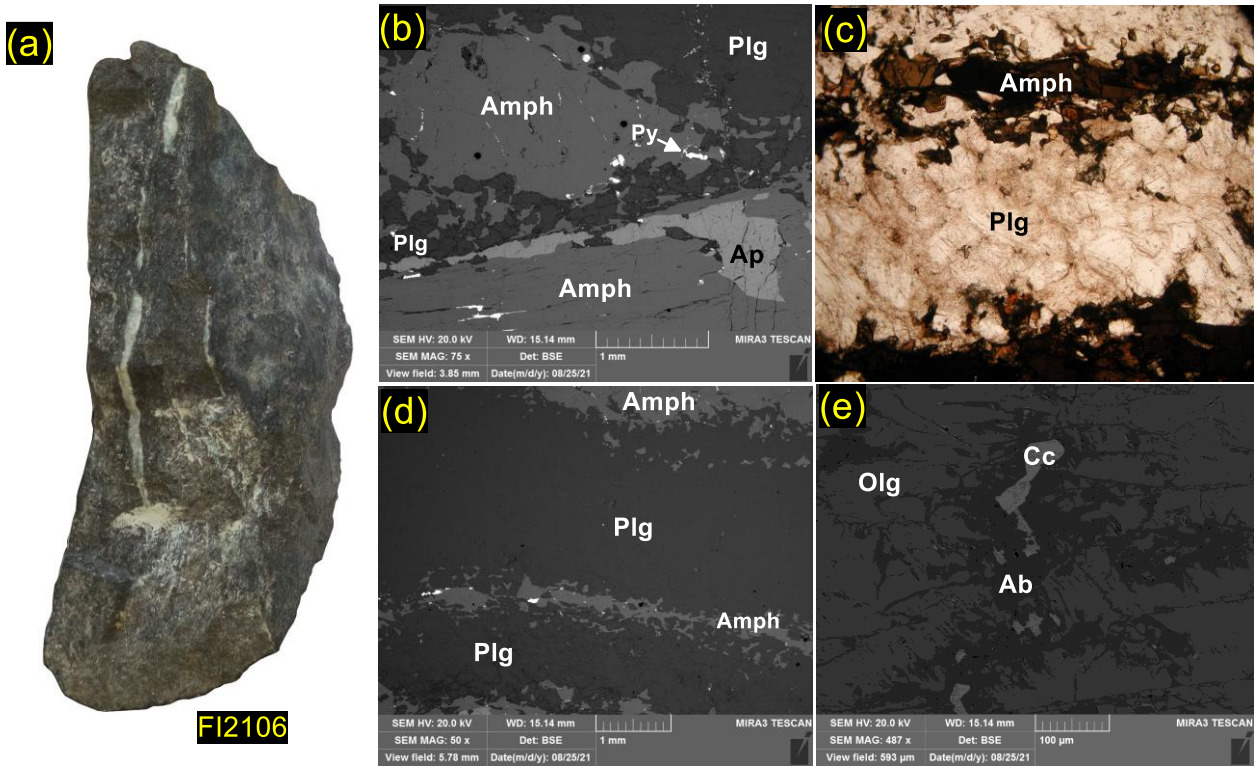

Figure 2.6: (a) Representative sample of the Finero composite HFSE-poor and -rich dioritic dyke (FI2106) showing thin leucocratic layers within the melanocratic rock; (b) BSE image of the dyke showing porphyroclasts of amphiboles and plagioclase within a groundmass made by similar minerals and apatite. Apatite appears to vein an amphibole porphyroclast; (c-d) photomicrograph and BSE image showing a leucocratic layer made by plagioclase within

amphibole layers. The leucocratic layer is also cut by veinlets of fine-grained amphiboles and sulphides; and (e) BSE image showing albite and calcite veinlets within oligoclase in the dyke.

2.4 Analytical methods

Petrographic features and mineral assemblages of the dyke samples were assessed by polarized light microscopes and SEM-EDS at Dipartimento di Scienze della Terra e dell'Ambiente (DSTA), University of Pavia, and at Dipartimento di Scienze Chimiche e Geologiche (DSCG), University of Modena and Reggio Emilia. The SEM-EDS at DSTA UNIPV comprises a Tescan Mira3 XMU-series FESEM equipped with an EDAX-EDX operated at an accelerating voltage of 20 kV, beam intensity of 16.5 nA, spot area of 100 × 100 μm, counts of 100 s., and a working distance of 15.8 mm. Data were processed with EDAX Genesis software using the ZAF algorithms.

Mineral major element compositions were measured by electronprobe microanalysis with a JEOL JXA-8200 Superprobe equipped with five WDS spectrometers operating in wavelength dispersive mode, housed at Dipartimento di Scienze della Terra "Ardito Desio", University of Milan. Operating conditions were 15 kV accelerating voltage, 15 nA beam current, 1-5 μm spot size, and counting time of 30 s on the peaks and 10 s on the backgrounds. Natural minerals (olivine for Mg; omphacite for Na; ilmenite for Ti; rhodonite for Mn; K-feldspar for K; anorthite for Al and Ca; wollastonite for Si; fayalite for Fe and niccolite for Ni) and synthetic chromite were used as standards. The results were corrected for matrix effects using the conventional ZAF method provided by JEOL software package. Results are considered to be accurate within 2–6%.

Trace element contents of mineral phases (amphibole, phlogopite, plagioclase, apatite, pyroxenes and olivine) in thin sections and separates of the dyke samples were determined with LA-ICP-MS housed at Centro Interdipartimentale Grandi Strumenti (CIGS) of the University of

Modena and Reggio Emilia and at Istituto di Geoscienze e Georisorse, Consiglio Nazionale delle Ricerche, Sede Secondaria di Pavia (CNR-IGG Pavia). The instrument at the CIGS consists of an ICP-MS X Series II (ThermoFisher Scientific) coupled to a 213 nm Nd:YAG laser ablation system (New Wave Research™). The ICP-MS was tuned using NIST SRM 612 synthetic glass standard to optimize the signal intensity and stability, monitoring ^{139}La, ^{238}U and the ^{232}Th/^{248}ThO ratio. NIST SRM 614, NIST SRM 612 and NIST SRM 610 were used as external standards during the analytical session. Data reduction was performed using the PlasmaLab software. LA-ICP-MS at the CNR-IGG Pavia coupled a 266 nm Nd:YAG laser ablation system (Quentel^{TM}) to a Triple-quadrupole ICP-MS system (Agilent™ Series 8900). The ICP-MS was tuned using NIST SRM 610 synthetic glass to optimize the signal intensity and stability and remove molecular interferences by monitoring ^{24}Mg, ^{115}In, ^{238}U and the ^{232}Th/^{248}ThO ratio. Data reduction was done with the GLITTER software (Griffin et al., 2008). NIST SRM 610 was used as external standard and USGS reference sample BCR2g was used as unknown. The laser was operated with a 10 Hz repetition rate, 10 J/cm^2 fluence and 50-60 μm spot size. ^{44}Ca was used as an internal standard for amphibole, apatite, and clinopyroxene; and ^{29}Si for plagioclase, phlogopite, orthopyroxene and olivine. Precision and accuracy are at ±5% and ±10%, respectively.

Nd, Hf, Sr and Pb isotopes measurements were performed on amphiboles separated from three HFSE-rich samples [FI1603, FI2103 (diorites), FI1501 (hornblendite)], one HFSE-poor gabbro (FI2101) and one composite dyke (i.e., the HFSE-poor amphiboles of hornblendite dyke FI1607). About 100 mg of amphibole separate for each sample was leached, dissolved, processed through ion exchange columns and measured for isotopes at the National High Magnetic Field Laboratory, Florida State University. The separates were leached in 5 ml 2.5N HCl and <30%

H_2O_2 for 60 min at room temperature to remove any alteration products. The leached separates were rinsed several times with quartz sub-boiling distilled water. Subsequent dissolution and column chemistry was performed after procedures described by Stracke et al. (2003) and Woelki et al. (2023). Sr isotope compositions were measured by thermal ionization mass spectrometry (TIMS) using a Finnigan MAT 262 RPQ system. Measurements of the Eimer & Amend (E&A) $SrCO_3$ standard provided a $^{87}Sr/^{86}Sr$ ratio of 0.708010 ± 0.000010 (2σ, n = 3). The $^{87}Sr/^{86}Sr$ ratios are corrected for mass bias using a $^{88}Sr/^{86}Sr$ value of 0.1194 and reported relative to the E&A $SrCO_3$ standard value of $^{87}Sr/^{86}Sr$ = 0.708000. Blanks for Sr were less than 100 pg. Nd, Hf and Pb isotopes were measured using a ThermoFisher Neptune Multi-Collector ICP-MS system. Repeated measurements of the La Jolla standard yielded $^{143}Nd/^{144}Nd$ ratio of 0.511790 ± 0.000012 (2σ, n = 17). The $^{143}Nd/^{144}Nd$ ratios are corrected for mass bias using a $^{146}Nd/^{144}Nd$ ratio of 0.7219 and are reported relative to the La Jolla standard of 0.511850. Blanks for Nd were less than 10 pg. Measured value of the JMC-475 standard is $^{176}Hf/^{177}Hf$ = 0.282150 ± 0.000008 (2σ, n = 20). The $^{176}Hf/^{177}Hf$ ratios are corrected for mass bias using a $^{179}Hf/^{177}Hf$ ratio of 0.7325 and reported relative to JMC-475 value of $^{176}Hf/^{177}Hf$ = 0.282150. Blanks for Hf were less than 40 pg. Ten measurements of NBS 981 provided $^{206}Pb/^{204}Pb$, $^{207}Pb/^{204}Pb$, and $^{208}Pb/^{204}Pb$ ratios and 2σ of 16.9332 ± 0.0073, 15.4847 ± 0.0121, and 36.6744 ± 0.0434, respectively. The measured Pb isotopes were normalized to NBS 981 $^{206}Pb/^{204}Pb$, $^{207}Pb/^{204}Pb$, and $^{208}Pb/^{204}Pb$ ratios of 16.9356, 15.4891, and 36.7006, respectively. Blanks for Pb were less than 30 pg. $^{87}Rb/^{86}Sr$, $^{147}Sm/^{144}Nd$, $^{176}Lu/^{177}Hf$, $^{238}U/^{204}Pb$, $^{235}U/^{204}Pb$ and $^{232}Th/^{204}Pb$ ratios were calculated from the Rb, Sr, Sm, Nd, Lu, Hf, Pb, U and Th concentrations measured on the amphibole samples by LA-ICP-MS.

2.5 Analytical results

2.5.1 Mineral major element composition

The full dataset of major and minor elements in mineral phases from the studied dyke samples including each mineral analysis is reported in Appendix 2.1.

2.5.1.1 Amphibole

Following the normalization scheme of Ridolfi et al. (2018) and the classification scheme of Hawthorne et al. (2012), amphiboles are pargasites in all the HR, HP and HC group samples (Figure 2.7). Amphiboles from the HR dyke group (diorites and associated clinopyroxenite cumulates, hornblendites and anorthosites) are characterized by magnesium numbers (Mg# = molar $[Mg/(Mg + Fe_t)] * 100$) from 73 to 85, and contain 9-13 wt. % Al_2O_3, 0.2-2.1 wt. % TiO_2, and 0.2-1.4 wt. % K_2O.

Amphiboles from the HP dykes are more enriched in Al_2O_3 (13-16 wt. %) and TiO_2 (1.3-2.6 wt. %), and show contrasting major elements chemistry from the HR dykes. Mg# of amphiboles from the HP hornblendite and gabbro shows significant variations from 63 to 71 and 74 to 88, respectively. K_2O ranges from 0.15 to 0.57 wt. %. The composition of amphiboles from the gabbroic dyke is similar to those reported for sapphirine-bearing gabbroic dykes from FPP (Giovanardi et al., 2013, 2020).

In the HC group, amphiboles are Al- and Ti-rich pargasites showing no systematic major element variation between HFSE-rich and HFSE-poor amphiboles. Generally, they contain 13-15 wt. % Al_2O_3, 2.1-2.7 wt. % TiO_2 and 0.4-0.6 wt. % K_2O. The composite diorite dyke (FI2106) contains amphiboles with Mg# from 60 to 64, whereas amphiboles from the composite hornblendite dyke with cumulus peridotite (FI1607) have Mg# varying from 58 to 73.

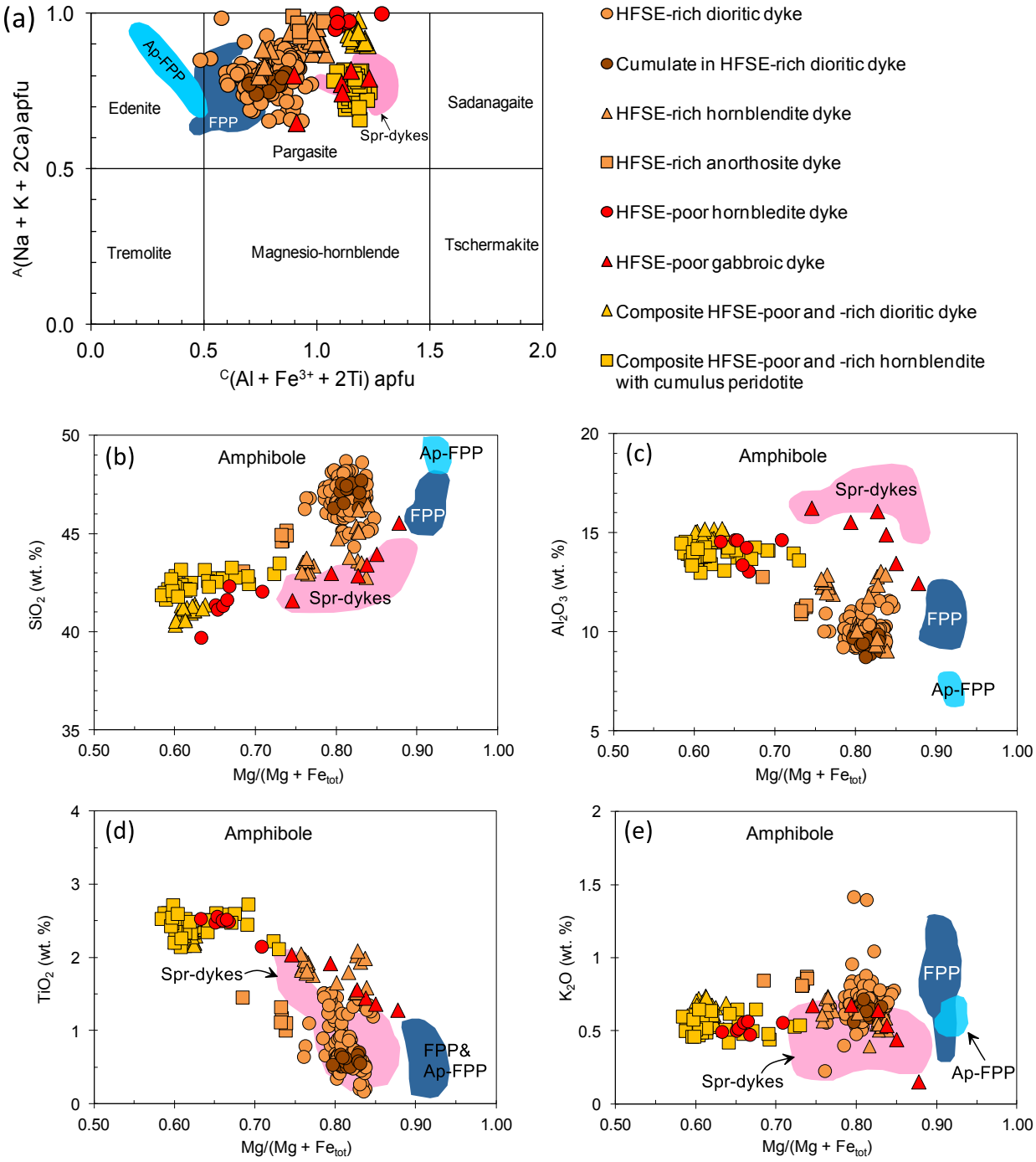

Figure 2.7: (a) Classification (after Hawthorne et al., 2012); and (b) major elements discrimination of amphiboles from the alkali-rich dykes of Finero. Plotted literature data are: Finero Phlogopite Peridotite (FPP) and Apatite-bearing Phlogopite Peridotite (Ap-FPP) from Zanetti et al. 1999 and Giovanardi et al. 2020; and sapphirine-bearing gabbroic dykes (Spr-dykes) from Giovanardi et al. 2020.

2.5.1.2 Plagioclase

In HR dioritic and anorthosite dykes, plagioclase is predominantly albite (An 6-11), as in corundum-bearing felsic dykes from central IVZ (Bonazzi et al., 2020) and nepheline-bearing alkaline dyke from FPP (Stähle et al., 1990). Plagioclase in HP gabbroic dyke, is labradorite to bytownite (An 69-87), similar to what was reported by Giovanardi et al. (2013, 2020) for sapphirine-bearing gabbroic dykes from FPP. Oligoclase (An 23-30) occurs in the HC dioritic dyke (Figure 2.8a). Albite and calcite veinlets are found within the oligoclase bands (Figure 2.6e).

2.5.1.3 Phlogopite

Mica is phlogopite in all the dyke groups (Figure 2.8b). Phlogopites from the HR dykes have Mg# from 76 to 89, 13-16 wt. % Al_2O_3 and 0.3-3.1 wt. % TiO_2. Phlogopite is scarce in the HP dykes and was not analyzed for major elements in this study. However, analysis of phlogopites from the sapphirine-bearing gabbroic dykes from FPP by Giovanardi et al. (2013, 2020) showed they contain 16-20 wt. % Al_2O_3, 0.6-3.4 wt. % TiO_2 and Mg# from 70 to 93.

In the HC dioritic dyke, phlogopite shows high Al_2O_3 (~17 wt. %) and TiO_2 (~4 wt. %) contents with Mg# between 71 and 73. Phlogopite from the HC hornblendite dyke shows a progressive increase in Mg# passing from the hornblendite (79-81) to the cumulus peridotite (87-88). Al_2O_3 and TiO_2 contents in both domains are similar, ranging from 15-17 wt. % and 2-4 wt. %, respectively.

2.5.1.4 Apatite

Apatite in the HR dykes is rich in Cl (0.3-3.5 wt. %) and locally in F (up to 3.10 wt. %) and LREE (La-, Ce-, Nd-oxides). Apatite from the HP hornblendite contains less Cl (~0.6 wt. %). In the HC dykes, apatite contains 0.5-1.9 wt. % Cl and 1.6-1.9 wt. % F.

2.5.1.5 Pyroxenes

The clinopyroxenite cumulates associated with HR dioritic dykes are composed of diopside with 21–23 wt. % CaO, 0.2–0.5 wt. % Cr_2O_3, 0.9–2.2 wt. % Al_2O_3, <0.1 wt. % TiO_2, 7–20 Cr# (Cr# = molar [Cr /(Cr + Al)]∗100) and 84–89 Mg#. Interstitial clinopyroxene of diopside composition and orthopyroxene (enstatite: 62-63; Mg#: 62-64) also occur in the HC hornblendite dyke, probably resulting from dehydration of amphibole rim. Orthopyroxenes from orthopyroxenite layers around the HP gabbroic dyke (FI2101) have enstatite content of 82-88 and Mg# of 83-89 (Figure 2.8c).

2.5.1.6 Olivine

Olivine from the cumulus peridotite (FI1607) and olivine layer in hornblendite (FI1501) shows Fe-enriched composition with forsterite content **(**Fo = molar [Mg/(Mg + Fe_t)]∗100**)** from 77 to 82.

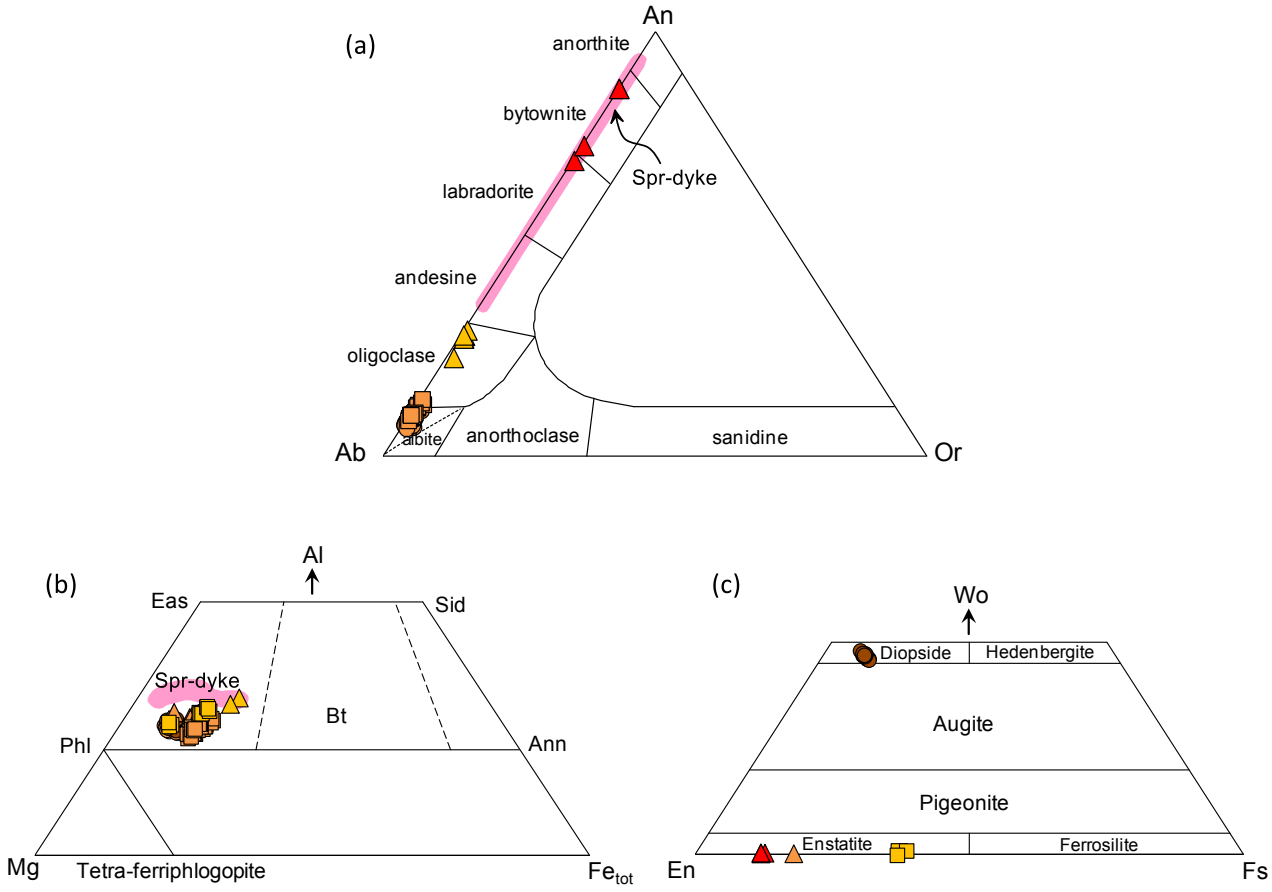

Figure 2.8: Classification of (a) plagioclase; (b) phlogopite; and (c) pyroxenes from the alkali-rich dykes of Finero. Sample symbols are as in Figure 2.7. Plotted literature data are sapphirine-bearing gabbroic dykes from Giovanardi et al. (2020).

2.5.2 Mineral trace element composition

The complete trace element dataset, including each mineral analysis for the three dyke groups is reported in Appendix 2.2.

2.5.2.1 Amphibole

Amphiboles from the HR dykes are generally enriched in incompatible trace elements relative to the composition of the primitive mantle (PM, McDonough and Sun, 1995; Figure 2.9a-d). The amphiboles from all the HR dyke samples are high in Ba, Rb, Sr, Nb, Ta, Zr, Hf, Ti; low in Th, U and Cs; and show strongly positive anomalies in Nb and Ta, weakly negative to strongly positive anomalies in Zr and Hf, and distinct negative Ti and Pb anomalies on the PM-normalized plot. Amphibole shows L-MREE-enriched CI-normalized patterns, which are almost flat for LREE and HREE with strong fractionation among MREE and a weak positive anomaly in Eu (Eu_N/Eu_N^* = 1.02–1.39; CI chondrite-normalized, Lyubetskaya and Korenaga, 2007). They also show subchondritic Ti/Nb (7–151) and Zr/Nb (0.7–4.1) ratios. The geochemical signature of the amphiboles from samples of the HR group is consistent with amphiboles from intraplate settings (I-Amph) (Moine et al., 2001; Witt-Eickschen et al., 2003; Coltorti et al., 2004, 2007).

Amphiboles from the HP dykes are also enriched in incompatible trace elements (e.g. Ba, Rb, Sr, Pb). However, these samples show contrasting HFSE contents and patterns compared to the amphiboles from the HR dykes. The HP hornblendite and gabbroic dykes are characterized by amphibole showing distinct negative anomalies in Nb, Ta, Zr and Hf with a typical fractionation pattern of $Ba_N > Nb_N > Ta_N$ (Figure 2.9e). They also display an L-MREE-enriched convex-upward pattern (Figure 2.9f) and relatively lower ΣREE abundances compared to amphiboles from the HR dykes. In contrast to those of the HR dykes, amphibole from the HP

dykes shows suprachondritic Ti/Nb (1030–4876) and Zr/Nb (4.3–11.4) ratios typical for suprasubduction settings (S-Amph) (Zanetti et al., 1999; Gregoire et al., 2001; Ishimaru et al., 2007; Coltorti et al., 2007; Zheng, 2019).

The HC dioritic dyke (FI2106) contains amphiboles with HFSE-rich and HFSE-poor compositions. Both amphibole compositions are enriched in incompatible trace elements (e.g. Ba, Rb, Sr, Pb) and show variable Nb, Ta, Zr and Hf contents. The margins of the dyke contain amphibole poor in Nb, Ta, Zr and Hf displaying negative anomalies in these elements, with fractionation patterns of $Ba_N > Nb_N > Ta_N$ and suprachondritic Ti/Nb and Zr/Nb very similar to the amphibole of the HFSE-poor hornblendite and gabbroic dykes. Geochemical analysis on amphibole conducted from the margins to the center of the dyke revealed a progressive increase in the HFSE towards the centre. Amphibole in the central part of the dyke is enriched in Nb, Ta, Zr and Hf showing strongly positive anomalies in these elements, with subchondritic Ti/Nb and Zr/Nb very similar to amphibole from the HFSE-rich dykes (Figure 2.10a). In addition, amphibole shows a geochemical gradient in REE from the margins to the centre where ΣREE abundances are markedly higher (Figure 2.10b).

In the composite dyke FI1607, amphibole in hornblendite farther away from the cumulus peridotite shows relatively LILE-, HFSE- and LREE-depleted composition. The LILE, HFSE and REE increase towards the margin with the cumulus peridotite (Figure 2.10c-d). Amphibole veinlets in the cumulus peridotite, however exhibit strongly positive Nb anomaly; a strong decoupling between Nb and Ta; negative Zr, Hf, Ti and Pb anomalies, and highest ΣREE abundances (Figure 2.10c-d).

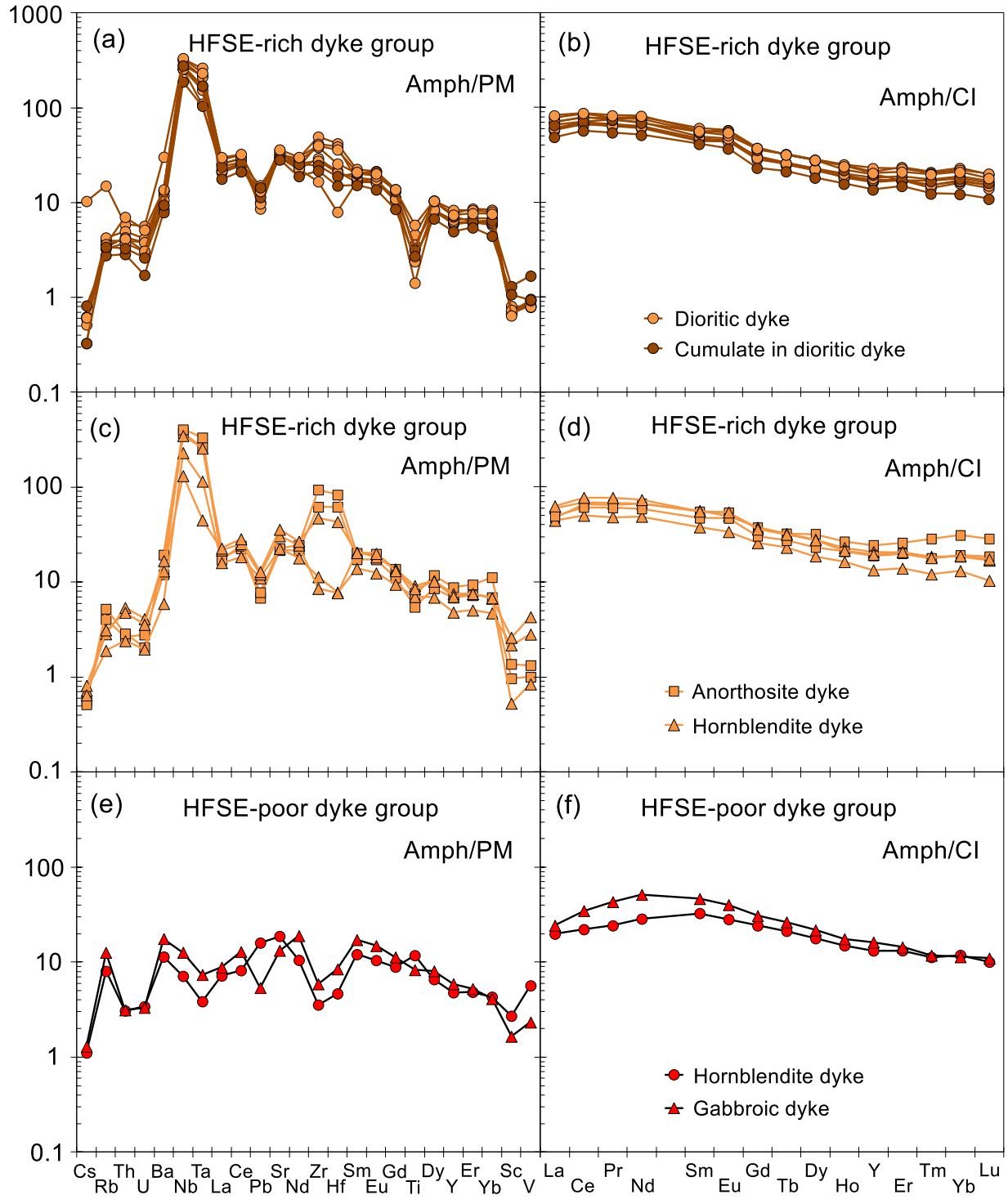

Figure 2.9: Incompatible trace elements and REE patterns of amphiboles from (a-b) HFSE-rich dioritic dykes and associated clinopyroxenite cumulates; (c-d) HFSE-rich hornblendite and anorthosite dykes; and (e-f) HFSE-poor hornblendite and gabbroic dykes of Finero. Shown are

the compositional averages for each dyke sample. PM and CI-chondrite values are from McDonough and Sun (1995) and Lyubetskaya and Korenaga (2007).

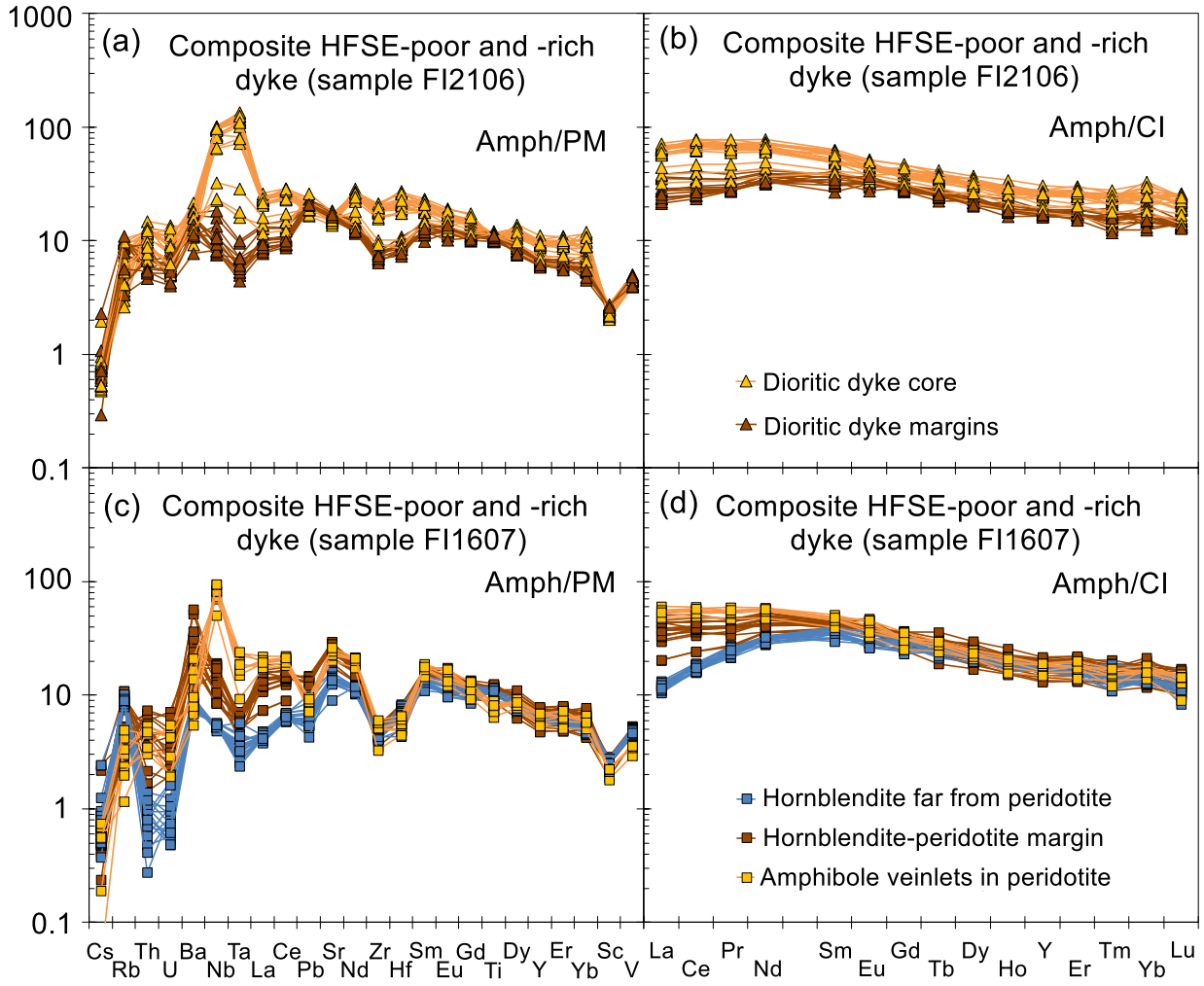

Figure 2.10: Incompatible trace elements and REE patterns of amphiboles from (a-b) composite HFSE-poor and -rich dioritic dyke (FI2106); and (c-d) composite HFSE-poor and -rich hornblendite dyke with cumulus peridotite (FI1607) of Finero. Shown are the individual mineral analyses for each dyke sample. PM and CI-chondrite values are from McDonough and Sun (1995) and Lyubetskaya and Korenaga (2007).

2.5.2.2 Phlogopite

Similar to amphibole, phlogopites from all HR dykes are strongly enriched in Nb and Ta. Phlogopite from the margin between hornblendite and cumulus peridotite in the composite dyke sample FI1607, however is less enriched in Nb-Ta. All analyzed phlogopites are enriched in Li, Cs, Rb, Ba, Pb, Sr and Ti; and depleted in Zr, Hf, Th, U, REE, and Sc.

2.5.2.3 Plagioclase

Albite from all HR diorite and anorthosite dykes is enriched in LREE, strongly depleted in M-HREE (often below the detection limit) and shows the typical strong positive anomaly in Eu. Plagioclase from the HP gabbroic dyke and HC diorite dyke shows similar REE patterns to the HR dykes, but with higher absolute abundances of L-MREE.

2.5.2.4 Apatite

Apatite from all dyke groups is characterized by strong enrichments in REE, Th, U, Sr and Pb. In chondrite-normalized patterns, all apatites show strong enrichment in LREE relative to MREE and HREE. Apatite from the HR dykes shows the highest content of REE.

2.5.2.5 Pyroxenes

Clinopyroxenes from clinopyroxenite cumulates in HR diorite dykes show trace element contents and patterns that are similar to amphibole in the cumulates and diorites, except for Rb, Ba, Cs, Nb, Ta and Ti, which are strongly depleted, according to crystallochemical constraints. Clinopyroxene from the composite hornblendite sample FI1607 shows a convex-upward REE

pattern similar to co-existing amphiboles but with lower elemental abundances. Orthopyroxenes show strongly depleted LREE contents relative to M-HREE.

2.5.2.6 Olivine

Olivine from the cumulus peridotite (FI1607) and olivine layer in hornblendite (FI1501) is depleted in most trace elements relative to the primitive mantle. Ni, Co and Ti range from 941-2076 ppm, 107-145 ppm, and 3-7 ppm, respectively. The low Ni/Co (<20) and Ni/Mn (<2) values are typical of magmatic olivines (Wang et al., 2021).

2.5.3 Nd-Sr-Hf-Pb isotopes

The measured and initial Nd-Sr-Hf-Pb isotopic compositions of amphibole from selected dyke samples are reported in Appendix 2.3 and Figure 2.11. The initial isotopic ratios of the selected HFSE-rich dyke samples were corrected to 200 Ma in accordance with U-Pb peak ages of zircons from the HFSE-rich diorites and anorthosites (Ogunyele et al., 2021; Bonazzi et al., 2022) and to other published zircon ages of alkaline magmatism in the IVZ straddling the Triassic–Jurassic boundary (e.g., Schaltegger et al., 2015; Galli et al., 2019). The HFSE-poor dyke samples, in the absence of precise emplacement ages, were also corrected to 200 Ma, however, correction using this age results in only minor uncertainties: for example, if an age of 225 Ma were used (similar to the age used by Giovanardi et al., 2020 for the sapphirine-bearing gabbroic dykes), calculated $\varepsilon Nd_{(i)}$, $\varepsilon Sr_{(i)}$, and $\varepsilon Hf_{(i)}$ values would be higher by ~0.1, ~0.3 and ~0.3, respectively.

Amphibole from the HFSE-rich diorites and hornblendite shows Nd and Sr isotopic compositions significantly different from those of the HFSE-poor dykes. On the Nd-Sr isotopic

diagram (Figure 2.11a), the HFSE-rich dykes ($\varepsilon Nd_{(i)}$: +3.4 to +5.4; $^{87}Sr/^{86}Sr_{(i)}$: 0.703761 to 0.704103) plot very close to the nepheline-bearing alkaline dykes of FPP and alkaline lamprophyres from Predazzo, Dolomites (Stähle et al., 2001; Casetta et al., 2019) whereas the HFSE-poor dykes ($\varepsilon Nd_{(i)}$: -0.1 to -0.7; $^{87}Sr/^{86}Sr_{(i)}$: 0.704732 to 0.704934) plot within the field of the Middle Triassic igneous rocks of Dolomites (SATIR in Figure 2.11a; Lustrino et al., 2019; Casetta et al., 2021; Nardini et al., 2022). On the Nd-Hf isotopic diagram (Figure 2.11b), the two dyke groups plot differently along the Nd-Hf mantle array with the HFSE-rich dykes plotting within the OIB field and the HFSE-poor dykes at the end of the OIB field. Both dyke groups however exhibit similar EMII-like Pb isotopic composition ($^{206}Pb/^{204}Pb$=18.4–18.7; $^{207}Pb/^{204}Pb$=~15.6; $^{208}Pb/^{204}Pb$=38.4–38.5) (Figure 2.11c-d).

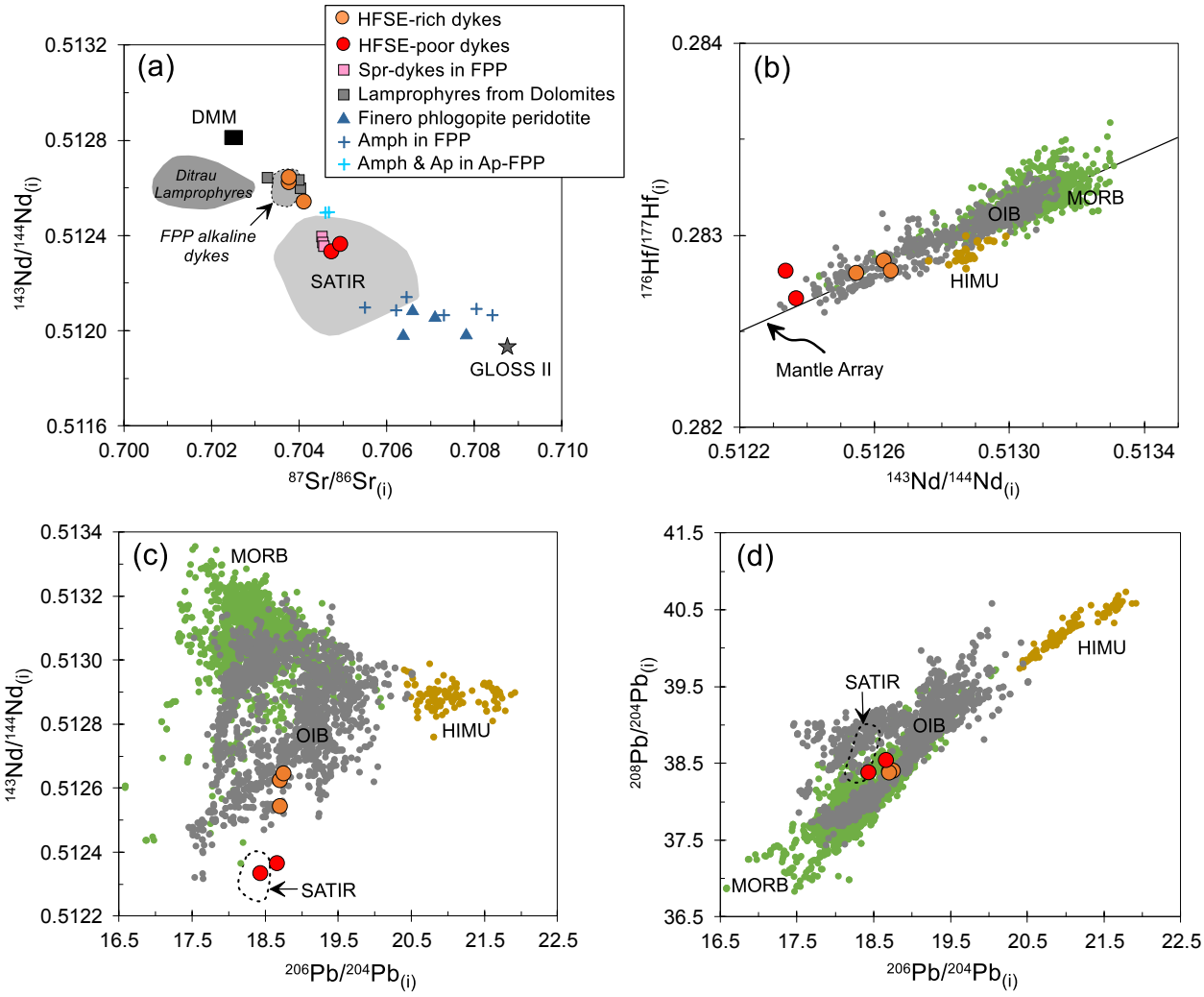

Figure 2.11: Diagrams of (a) $^{87}Sr/^{86}Sr$ vs. $^{143}Nd/^{144}Nd$ (b) $^{143}Nd/^{144}Nd$ vs. $^{176}Hf/^{177}Hf$ (c) $^{206}Pb/^{204}Pb$ vs $^{143}Nd/^{144}Nd$ and (d) $^{206}Pb/^{204}Pb$ vs $^{208}Pb/^{204}Pb$ for amphiboles from the Finero HFSE-rich and HFSE-poor dyke samples (corrected to 200 Ma) compared to the Finero phlogopite peridotite (FPP, whole-rock, 295 Ma; Voshage et al., 1987), metasomatic amphiboles in the FPP (295 Ma; Obermiller, 1994; Giovanardi et al., 2020), amphibole and apatite from apatite-bearing layers in the FPP (215 Ma; Morishita et al., 2008), alkaline dykes in the FPP (225 Ma; Stähle et al., 2001), sapphirine-bearing gabbroic dykes in FPP (225 Ma; Giovanardi et al., 2020), alkaline lamprophyres from Predazzo, Dolomites (219 Ma; Casetta et al., 2019), Southern Alps Mid-Triassic igneous rocks (SATIR; 230 Ma; Lustrino et al., 2019; Casetta et al., 2021), Ditrau lamprophyres (220 Ma; Batki et al., 2014), modern MORB, OIB and HIMU (Stracke, 2012), DMM (Salters and Stracke, 2004; corrected to 200 Ma), GLOSS-II (average global subducting sediments II; Plank, 2014; corrected to 320 Ma).

2.6 Discussion

2.6.1 Multistage and prolonged injection of melts into the subcontinental lithospheric mantle during the Early Mesozoic

Field, petrographic and geochemical evidence suggest that the intrusion of the studied Finero dyke swarms into the host phlogopite peridotite (FPP) occurred as multistage, multiphase and prolonged magmatic events during the Early Mesozoic. The HFSE-rich dykes, in particular the diorite dykes, show clear field and petrographic evidence of multiple melt percolations into their conduits, such as:

(i) Injection of leucocratic layers of plagioclase and apatite into melanocratic segregates of amphibole and phlogopite.

(ii) Small inclusions of melanocratic segregates of mainly amphibole within leucocratic layers.

(iii) Deformation of the original magmatic structure of the dykes by syn-magmatic volatile-driven overpressure, probably caused by a high-energy, focused injection of extremely differentiated, maybe exsolved, volatile-rich melts. This event may also be related to pervasive fluid circulation causing the replacement of the melanocratic segregates initially made of amphiboles by phlogopite.

(iv) Occurrence of olivine-dominated peridotite and clinopyroxenite layers, inclusions and pods in the dykes, probably representing cumulates fractionated during early stages of melt percolation and crystallization.

(v) Chloritization of phlogopite and occurrence of allanite (especially in anorthosites) documenting late-stage fluid circulation.

The symmetric layering of the HFSE-poor gabbro and hornblendite dykes also suggests that their emplacement was due to several events of melt percolation and deformation along

shear zones. Several amphibole crystals in the gabbro are cut by leucocratic layers of plagioclase evidencing that a forceful magma injection led to the enlargement of the conduits, as previously highlighted by Giovanardi et al. (2013, 2020). The composite dykes containing amphiboles with both HFSE-poor and -rich compositions undoubtedly confirm that the dykes' conduits were percolated by multiple melts with different geochemical compositions and affinities. The observed geochemical gradient in amphibole (HFSE and REE) from the core to margins of the composite diorite (FI2106) clearly indicates that an older HFSE-poor rock was percolated and overprinted by HFSE-rich melt(s) which produced HFSE-rich amphiboles.

In summary, the formation of the Finero dykes involved several melts with different compositions episodically percolating conduits within the FPP over a prolonged period. Injected mafic mantle melts, in the early stages of crystallization, probably segregated cumulus peridotites and clinopyroxenites, some of which are preserved as relics in the dykes' conduits. These mafic mantle melts after the fractionation of olivine, clinopyroxene and probably spinel became more evolved and segregated amphiboles and other phases present in the dykes. The amphibole + phlogopite + apatite ± plagioclase-dominated mineralogy of all the dykes coupled with the occurrence of primary calcite in them supports the assertion that they were derived from evolved mantle melts rich in volatiles (e.g. H_2O, P, CO_2, S, Cl, F).

2.6.2 Geochemical signatures and nature of parental melts

Major, trace and Nd-Sr isotopic compositions of amphiboles point to two distinct geochemical affinities of the melts that segregated the Finero dykes. The low HFSE content (Nb=3.2-8.7 ppm; Ta=0.1-0.3 ppm) coupled to the enrichment of LILE relative to HFSE (e.g. high Ba/Nb=8-22) and suprachondritic Ti/Nb and Zr/Nb ratios of amphibole from the HFSE-poor dykes indicates amphibole segregation from calc-alkaline melts with orogenic-like affinity (Coltorti et al., 2007). Amphibole from the HFSE-rich dykes, on the other hand, is characterized by high HFSE contents (Nb=70-270 ppm; Ta=1-12 ppm), enrichment in HFSE relative to LILE (e.g. low Ba/Nb commonly < 0.7), and chondritic to subchondritic Ti/Nb and Zr/Nb ratios, pointing to an alkaline to ultra-alkaline affinity of the parental melts. This assertion is further supported by (i) the occurrence of Nb-Ta-rich phlogopite, Nb-Ta oxides (e.g. columbite) and accessory titanite and ilmenite in the HFSE-rich dykes; and (ii) the common association of ultra-alkaline (-carbonatitic) magmatism, Nb-Ta deposits and albite-dominated anorthosites (or albitite) that is well-documented in literature (e.g., Pin et al., 2006; Galli et al., 2019).

The Nd and Sr isotopic compositions of the HFSE-rich and HFSE-poor dykes are also very different, supporting different melts affinities and sources (Figure 2.11a). Amphibole from the HFSE-poor dykes is characterized by high radiogenic $^{87}Sr/^{86}Sr_{(200)}$ (0.704732 to 0.704934) and low radiogenic Nd isotopes ($\varepsilon Nd_{(200)}$ from –0.1 to –0.7). These values are very similar to those reported for the sapphirine-bearing gabbroic dykes from FPP (Giovanardi et al., 2020) and the Middle Triassic high-K calc-alkaline to shoshonitic lavas from Dolomites (Lustrino et al., 2019; Casetta et al., 2021; Nardini et al., 2022). This signature may be interpreted as the result of the interaction of ascending mantle melts with continental crust. Alternatively, it may be derived from ancient mantle sources that have experienced variable degrees of melt extractions and/or

modifications in the form of digestion of subducted and/or delaminated material (e.g., Lustrino et al., 2011; Lustrino and Anderson, 2015; Lustrino et al., 2019; Giovanardi et al., 2020; Velicogna et al., 2022). The FPP and its constituent amphibole exhibits more radiogenic $^{87}Sr/^{86}Sr_{(i)}$ and unradiogenic $^{143}Nd/^{144}Nd_{(i)}$ (Giovanardi et al., 2020; Zanetti et al., 1999; Obermiller, 1994; Figure 2.11a) indicating that the FPP had a larger fraction of crustal components than the melts that segregated the HFSE-poor dykes. However, the melts which formed the apatite-bearing layers within the FPP (Morishita et al., 2008; Figure 2.11a) may be similar to the melts that segregated the HFSE-poor dykes. The Nd-Sr isotopic composition and high Al_2O_3, TiO_2 and K_2O contents of the HFSE-poor dykes, combined with those of the sapphirine-bearing gabbroic dykes and FPP, points to mantle sources containing significant amounts of continental crustal components. The radiogenic Pb isotopic composition of amphiboles from the HFSE-poor dykes ($^{206}Pb/^{204}Pb$=18.4–18.6; $^{207}Pb/^{204}Pb$=15.6; $^{208}Pb/^{204}Pb$=38.4–38.5) overlaps the field of OIB recording EMII-like characteristics of the mantle source, attesting to the involvement of significant amounts of recycled continental crust Pb components in the mantle source(s) of their parental melts. In the Nd-Pb diagram, the HFSE-poor dykes lie within the peculiar field defined by Southern Alps Middle Triassic Rocks (SATIR; Figure 2.11c). The plot of the HFSE-poor dykes at the end of the OIB field on the Nd-Hf mantle array (Figure 2.11b) and oxygen isotopic composition of amphibole and plagioclase from the sapphirine-bearing gabbroic dykes ($\delta^{18}O$ Amph=6.86-6.94 ‰ SMOW; $\delta^{18}O$ Plag=8.6 ‰ SMOW; Giovanardi et al., 2020) heavier than mantle composition (e.g., $\delta^{18}O$ of mantle peridotite, pyroxenite, and MORB = 5.7 ± 0.2‰ SMOW; Bindeman, 2008) are further evidence for the presence of substantial amounts of recycled continental crust components in the mantle sources and melts of the orogenic-like, HFSE-poor magmatism of Finero.

In contrast, amphibole from the HFSE-rich dykes exhibits relatively low radiogenic $^{87}Sr/^{86}Sr_{(200)}$ (0.703761–0.704103) and relatively high radiogenic Nd isotopes ($\varepsilon Nd_{(200)}$ from +3.4 to +5.4) plotting close to the DMM end-member and closely similar to the compositions of nepheline-bearing alkaline dykes from FPP and the alkaline lamprophyres from Predazzo, Dolomites (Stähle et al., 2001; Casetta et al., 2019). This signature is consistent with derivation from a more depleted mantle source. The Pb isotope data of amphiboles from the HFSE-rich dykes ($^{206}Pb/^{204}Pb$=18.7; $^{207}Pb/^{204}Pb$=15.6; $^{208}Pb/^{204}Pb$=38.4) are similar to those of the HFSE-poor dykes. This suggests that the mantle sources of both dyke groups contained recycled continental crustal components. However, the HFSE-rich dykes most probably incorporated less crustal components as indicated by its more depleted Nd, Sr and Hf isotopic compositions. It is also important to highlight here that we find no evidence of HIMU components in any of the investigated dykes from Finero, as suggested by Stälhe et al. (2001).

Equilibrium melts composition calculated from the trace element contents of amphiboles from representative samples of HFSE-poor and HFSE-rich dykes using experimentally determined amphibole-melt partition coefficients (dataset 47S; Tiepolo, 1999) are shown in Figure 2.12 and are compared to the bulk-rock composition of Middle Triassic lavas and Late Triassic alkaline lamprophyres from the Dolomites. The incompatible trace element fractionation of the calculated HFSE-poor melt mimics that of the Middle Triassic high-K calc-alkaline to shoshonitic lavas from the Dolomites (Casetta et al., 2021). The major difference between our calculated HFSE-poor melt and the Dolomites shoshonites relates to absolute abundances particularly in Th, U, Nb, Ta and Pb which are higher in the calculated HFSE-poor melt. Notwithstanding, Nb-Ta in the HFSE-poor melt are less than the concentration in the alkaline lamprophyre from Predazzo, Dolomites (Casetta et al., 2019). The Predazzo alkaline

lamprophyres however have significantly lower trace element content including Nb-Ta compared to the calculated HFSE-rich melt which appears ultra-alkaline and highly enriched in Nb, Ta, Zr and Hf **(**Figure 2.12**)**.

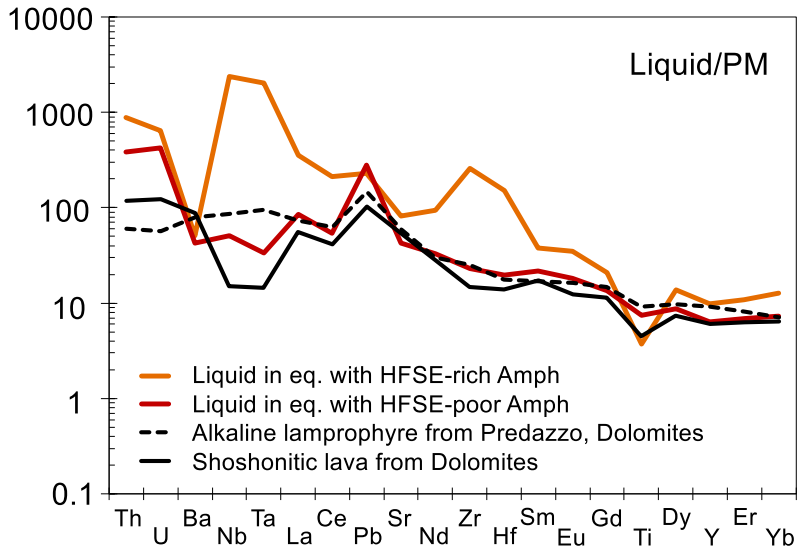

Figure 2.12: Incompatible trace element patterns of melts calculated in equilibrium with amphiboles from representative samples of Finero HFSE-rich and HFSE-poor dykes. The bulk-rock composition of Late Triassic alkaline lamprophyre (Casetta et al., 2019) and Mid-Triassic shoshonitic lava (Casetta et al., 2021) from the Dolomites are also plotted for comparison. PM values are from McDonough and Sun (1995).

According to Coltorti et al. (2007), the geochemical features of calc-alkaline and intraplate magmatism can be reconciled by HFSE-depleted fluids coming off subducted crustal slab(s), leaving a rutile-bearing eclogite residuum rich in HFSE (mainly Nb, Ta and Ti). As the subduction process continues, the rutile-bearing eclogite further descends into the lower part of the upper mantle (or even below), generating a subchondritic Ti/Nb or Zr/Nb reservoir. Decarlis et al. (2023) suggested that crustal delamination processes may have occurred in the IVZ during the collapse of the Variscan chain far to the North, as testified by widespread metasomatism of the FPP. Following both hypotheses, the partial incorporation of crustal materials to different

mantle domains via subduction and/or delamination may explain the genesis of the Finero HFSE-poor and HFSE-rich dykes and the crustal components might be related to the Variscan and/or older orogenic cycles which were later triggered or remobilized until the Early Mesozoic. The presence of primary calcite in all the dykes supports the derivation of their parental melts from mantle sources probably containing some carbonatitic components. The possibility of assimilation of crustal rocks by the mantle-derived melts which segregated the Finero dykes is severely limited as they were very likely emplaced into the host mantle peridotite (FPP) when it was still at mantle levels (Zanetti et al., 2016; Decarlis et al., 2023). The idea of the FPP still at mantle levels under P ≥1.1 GPa until Mesozoic times is attested to by (i) the occurrence of sapphirine in our HFSE-poor gabbro sample and those investigated by Giovanardi et al. (2013, 2020), and (ii) amphibole-plagioclase thermometric calculation (Holland and Blundy, 1994) providing P-T conditions of dykes' emplacement at ~660-1000 °C and ~1 GPa. The geochemical signatures of the dykes are therefore primary features inherited from their mantle sources. The crustal imprints in mantle melts recorded by the studied dykes and the metasomatizing agents of the FPP could consequently imply that the subcontinental mantle sources beneath the Finero Complex and the IVZ at large continuously retained enriched subduction-related (Zanetti et al., 1999; Selverstone and Sharp, 2017; Cannaò et al., 2022) and/or delaminated crustal components (Decarlis et al., 2023) over a prolonged period of time. This contradicts an earlier conclusion by Casetta et al. (2019, 2021) that the generation of the Middle Triassic high-K calc-alkaline to shoshonitic magmas represents the exhaustion of the subduction-related signature in the Southern Alps lithosphere.

Based on petrographic, geochemical and isotopic data, and petrological reasoning, we recognize that the HFSE-poor magmatism occurred shortly before the HFSE-rich magmatism in

Finero and IVZ. Therefore, there is no possibility of HFSE-poor magmas directly fractionating to HFSE-rich melts. We also exclude the possibility of the HFSE-poor dykes being products of residual melts after fractional crystallization and segregation of the HFSE-rich dykes. These hypotheses are premised on (i) the trace elements gradients observed in amphiboles and apatites from the composite dykes lending credence to the overprinting of older HFSE-poor amphiboles by HFSE-rich melts; (ii) close similarity of the geochemical and isotopic signatures of the HFSE-poor dykes with the Middle Triassic calc-alkaline to shoshonitic magmatism of Dolomites; (iii) similarity of the age, and geochemical and isotopic signatures of the HFSE-rich dykes with the Late Triassic alkaline lamprophyres of Dolomites and nepheline-bearing alkaline dykes from FPP; and (iv) the well-established temporal sequence of subduction, calc-alkaline volcanism and intraplate magmatism that has been documented in the Dolomites and several localities around the Mediterranean areas and in most subduction zones worldwide (Coltorti et al., 2007; Agostini et al., 2007; Zheng, 2019; Deng et al., 2023).

Hence, as a whole, the Finero dyke swarms record a geochemical change from orogenic-like magmatism, typical of post-collisional settings, to anorogenic alkaline magmatism, common in intraplate to extensional settings, pointing to a progressive variation of the mantle sources of the Southern Alps magmatism in response to the change of geodynamic environment during Early Mesozoic times.

2.6.3 Origin of cumulates in dykes

As earlier highlighted in section 2.6.1, olivine-dominated peridotite and clinopyroxenite layers, inclusions and pods occurring in the Finero dykes (e.g., Figure 2.2a) are probably relics of cumulates segregated in the early stages of crystallization from the mantle-derived melts which evolved to produce the amphibole-dominated dykes. It is very likely that both HFSE-poor and HFSE-rich mantle-derived melts which percolated the FPP conduits crystallized and fractionated at least olivine at the beginning of crystallization leading to melts' evolution and subsequent crystallization of amphiboles and other mineral phases. Therefore, the composition of these cumulates and their relation to subsequent HFSE-poor and HFSE-rich amphiboles derived from more evolved melts is crucial to decipher the processes controlling the early stages of the magmatisms.

Olivine-dominated peridotite pods and inclusions occur in all the dyke groups and show similar composition, with forsterite (77-82), NiO (commonly < 0.32 wt. %) and FeO_t (17-21 wt. %) contents of olivine significantly outside the array of primary mantle peridotites (e.g., FPP olivine Fo=90-92; NiO=0.25-0.47 wt. %; FeO_t=~9 wt. %; Zanetti et al., 1999; Giovanardi et al., 2020). Low-forsterite olivine can be regarded as a product of (i) melt-rock interaction or (ii) crystallization from Fe-enriched evolved mantle melts. Melt-rock interaction can modify the composition of primary mantle peridotites; however, the forsterite content of the constituent mantle olivine can only be significantly decreased after interaction with very large amount of highly-evolved melts (Berno et al., 2019). A typical example is the FPP, which retains a highly depleted olivine composition (olivine Fo=90-92) after multiple episodes of metasomatic modifications. On the other hand, during crystallization from primitive mantle-derived magmas containing > 6 wt % MgO, spinel (Cr-spinel and chromite) and high forsterite olivine are often

the first phases to crystallize (Roeder et al., 2001, 2006). When these high-Mg# and Cr# phases separate, the residual melt evolves toward a Fe-enriched composition which can crystallize low-forsterite olivine. The olivine composition of the peridotites within the studied dykes can therefore result from crystallization from evolved Fe-enriched melts after the fractional crystallization and separation of high forsterite olivine and spinel. The absence of spinel in the olivine-dominated peridotites probably attests to their earlier fractionation out of the melts. Additionally, the low Ni/Co (<20) and Ni/Mn (<2) values of the olivines are typical of magmatic olivines (Wang et al., 2021).

Fe/Mn and Zn/Fe ratios in olivine are good proxies to decipher the signature of the mantle source region (peridotite or pyroxenite source) because the Fe/Mn ratio is largely unchanged by olivine fractionation (e.g., Søager et al., 2015) and Zn/Fe ratio appears to be temperature-independent within error (e.g., Le Roux et al., 2010). The Fe/Mn (~60-70) and $Zn*10^4/Fe$ (9-11) ratio of olivines from our cumulate peridotite pods exhibit values typical of magmas derived from the partial melting of primary mantle peridotites. The abundance of pyrite and pentlandite associated with the olivines reflects the metal (e.g., Fe and Ni) enrichment of the mantle melts and suggests derivation from a metal-rich source region. The occurrence of the olivine-dominated peridotite as pods and thin layers within the dykes also indicates that they are preserved relics after multiple percolations and interaction with subsequent HFSE-poor and HFSE-rich mantle melts. The formation of fine-grained interstitial orthopyroxene between olivines and amphiboles indicates interaction between the olivine-dominated peridotite and subsequent melts. We therefore, tentatively suggest that the olivine-dominated peridotite pods/layers are related to their host dykes, whether HFSE-poor or -rich, by fractionation process.

Clinopyroxenite cumulates are only associated with the HFSE-rich dykes (in diorites and hornblendites) probably documenting an additional mineral phase (clinopyroxene) fractionated after olivine from HFSE-rich melts in the FPP conduits. Clinopyroxenes from the clinopyroxenite cumulates exhibit similar REE contents and chondrite-normalized patterns with the amphiboles from the HFSE-rich dykes. This suggests an equilibrium between the clinopyroxenes and amphiboles pointing to cognate alkaline melt sources. On this basis, the clinopyroxenites are inferred to be segregates fractionated from HFSE-rich melts pulses intruded into FPP during Early Mesozoic times.

2.6.4 Is the Finero phlogopite peridotite a possible mantle source of the Early Mesozoic magmatism in the Southern Alps?

Conceição and Green (2004) have demonstrated via high-pressure and -temperature melting experiments that primary shoshonitic magmas may be produced by decompression melting of phlogopite- and pargasite-bearing peridotites at ~1 GPa and 1050–1150°C. On the other hand, alkaline, volatile-rich magmas segregating amphibole-rich rocks have also been modelled to originate by low-degree partial melting of similar mantle domains, but at higher pressures (≥3 GPa), possibly at the asthenosphere–lithosphere boundary (Foley, 1990; Tappe et al., 2006). In light of these experimental constraints coupled with the Nb-Ta-Ti-depleted composition and mineralogical make-up of the FPP by metasomatic amphibole, phlogopite, and sometimes apatite and carbonates, an assumption of the generation of the melts segregating the studied HFSE-poor dykes from a similar metasomatized lithospheric mantle is reasonable. The modeling of the source composition of the Middle Triassic shoshonitic magmatism of Dolomites by Casetta et al. (2021) suggests that the Finero phlogopite peridotite is the best approximation

of the mantle source of the HFSE-poor, shoshonitic magmatism during this time. The HFSE-rich alkaline melts may also be generated from a Finero-like mantle but with enrichments in Nb-Ta from a deeply subducted/recycled rutile-bearing eclogitic slab at asthenospheric to deep lithospheric depths. The depleted Nd, Sr and Hf isotopic compositions of the HFSE-rich dykes suggests that they were predominantly derived from an asthenospheric mantle source; however, the contribution of a deep lithospheric mantle source to their parental melts cannot be excluded. Possible mechanisms of formation of the HFSE-rich alkaline melts may include: (i) partial melting of an upwelling depleted asthenosphere interacting with enriched/metasomatized deep lithospheric mantle components (e.g., Casetta et al., 2019); (ii) partial melting of an upwelling depleted asthenosphere interacting with small volumes of enriched melts derived from melting of deeply subducted rutile-bearing eclogitic slab; and/or (iii) partial melting of enriched asthenosphere. A good approximation of the mantle source lithology could be a garnet peridotite with or without phlogopite, K-richterite and calcite (e.g., Tappe et al., 2006).

2.6.5 Geodynamic perspective

The Early Mesozoic orogenic-like magmatism of the Ivrea-Verbano Zone originated by decompression partial melting of metasomatized lithospheric mantle sources at relatively lower pressures. The subsequent alkaline anorogenic magmatism was possibly derived by low-degree partial melting of asthenospheric to deep lithospheric mantle sources. This transition clearly indicates that the mantle source regions in the IVZ changed through times. The heterogeneity of the mantle beneath the eastern (e.g., Dolomites) and central (e.g., Brescian Prealps) sectors of the Southern Alps has also been documented by a change in the geochemical signatures of the Early Mesozoic magmatism from high-K calc-alkaline to shoshonitic affinity during the Middle

Triassic to alkaline affinity during the Late Triassic (e.g., Cassinis et al., 2008; De Min et al., 2020; Casetta et al., 2019, 2021). This correlation and similarity in geochemical signatures strongly indicate that similar tectonic and magmatic processes/events occurred throughout the Southern Alps after the Variscan orogeny s.s.

Variscan orogeny in the European area resulted from a complex setting which details is still a matter of debate. The principal components of this tectonic scenario were Gondwana s.l. (to the South) and Laurussia continental plates (to the North). Their collision in the Carboniferous resulted in the formation of the Hercinian-Variscan Cordillera, following the closure of the Rhenohercinian Ocean (e.g., Stampfli and Borel, 2004 and references therein). The Hercinian-Variscan belt was connected to the Appalachian region to the west by a complex range, probably dominated by wrench tectonics. Following one of the most popular paleogeographic interpretation of the Alpine region (e.g., Stampfli and Kozur, 2006), the Variscan collision in the present-day Western European area occurred between Laurussia and the Hunic/Galatian superterrane (Stampfli et al., 2002; von Raumer et al., 2013), a sector of Gondwana that drifted away from the main continent after the onset of the Paleotethys ocean during the Devonian (Stampfli and Borel, 2004; von Raumer et al., 2013). Adria microplate was located at the southern termination of this superterrane, and rested in the outskirts of the Variscan Cordillera s.s. during Late Carboniferous collision (Figure 2.13a-b).

Thus, the Southern Alps (and the IVZ at depths) were located between the Variscan collisional system to the North and a mature Paleotethys oceanic system to the South. During the Late Carboniferous, the overthickened Variscan crust started to collapse in a post-collisional environment (Figure 2.13b-c; Burg et al., 1994). Following the interpretation of Decarlis et al. (2023), the delamination of the lower crust led to the detachment of wide slabs from the root of

the chain that sunk into the mantle favouring mixing of the mantle with continental melts, as possibly documented by the ca. 315-310 Ma pervasive metasomatism of the FPP mantle section (Figure 2.13b-c). This event was concomitant to the widespread eruption of K-rich lamprophyres throughout the Variscan realm in the 340-280 Ma time interval following the Variscan orogeny peak (Soder and Romer, 2018). The presence of continental crust component is also documented in primary mantle magmas intruded into the Southern Variscides (Southern Alps and Corsica) in the Lower Permian post-collisional magmatic climax (290-280 Ma; Boscaini et al., 2020).

Later on, following the interpretation of Casetta et al. (2021), the influence of the Paleotethys active margin became more and more relevant in the Alpine region and eventually, in the Triassic, the Paleotethys subduction system triggered the magmatism of the Southern Alps. This setting, still ascribed by several authors to the "Variscan cycle", may be regarded as the paleotectonic scenario in which the Early Mesozoic Finero dykes with orogenic-like affinity, object of the present study, may have developed (Figure 2.13d).

It is very difficult and beyond the scope of this paper, to assess the exact paleogeographic context of the region. Several solutions were proposed to explain the continuous extension in the Southalpine domain during the Triassic and the relationships with the subduction of Paleotethys and/or later oceanic troughs (e.g., Channell and Kozur, 1997; Stampfli and Borel, 2004; Handy et al. 2010; van Hinsbergen et al. 2020). The solution in Figure 2.13c-d may represent a mere oversimplification of the real system (taken from Casetta et al., 2021 and Stampfli and Borel, 2004; modified). However, this interpretation is at the moment purely speculative and requires further investigation. The relatively long distance of the Southalpine domain from the subduction area may represent a limitation and open the possibility that other factors may have contributed to the continental contamination of the Finero mantle section (e.g. late melting or reaction of

remnant of slabs of the Variscan belt present in the mantle). Especially, the major challenge is represented by the peculiar position occupied by the Adriatic plate during the Variscan and early Alpine cycles, which since Late Carboniferous onward, remained at the North-westernmost termination of the Paleotethys. The area was at first characterized by a wrenching connection with the westernmost sectors (Figure 2.13b-c), then possibly acted as a "pivot" for the Cimmerian Terranes (Figure 2.13c-d) and finally underwent extreme extension leading to the opening of the Alpine Tethys (Figure 2.13e; Decarlis et al., 2017; Beltrando et al., 2015). It was in this latter context that the studied anorogenic dykes were probably emplaced. In fact, starting from the late Triassic onwards (Beltrando et al., 2015), the thermal structure of the Adriatic lithosphere underwent a profound reorganization. Changes started early at mantle depths, as testified by the evidence of the Finero magmatism, and later became evident in the upper crust as a progressive increase of stretching that culminated with hyperextension and exhumation of the mantle to the surface (e.g., Decarlis et al., 2015; 2017; Petri et al., 2023). This dynamics was tentatively simulated using numerical modelling by Chenin et al. (2019).

On a final note, both the orogenic-like and alkaline anorogenic magmatisms in the IVZ and those in the central and eastern sectors of the Southern Alps occurred during a period of protracted extension in the Early Mesozoic that started at ca. 245 Ma and continued up to ca. 170-160 Ma culminating with the Alpine Tethys emplacement (Schettino and Turco, 2011; Denyszyn et al., 2018). However, notwithstanding the occurrence of the orogenic-like magmatism of the Southern Alps in transtensional to extensional settings, its geochemical signature is typical of post-collisional tectonic settings (Stampfli and Borel, 2002, 2004; Doglioni, 2007; Zanetti et al., 2013; Casetta et al., 2018; De Min et al., 2020). On the other hand, the successive alkaline to ultra-alkaline magmatism are more frankly related to a rift-related

asthenospheric upwelling event in an intraplate geodynamic setting, and probably represent a precursor of the rifting stage connected to the Alpine Tethys opening in the western Mediterranean region (Stälhe et al., 2001; Mazzucchelli et al., 2010; Schaltegger et al., 2015; Galli et al., 2019; Casetta et al., 2019; Bonazzi et al., 2020; De Min et al., 2020).

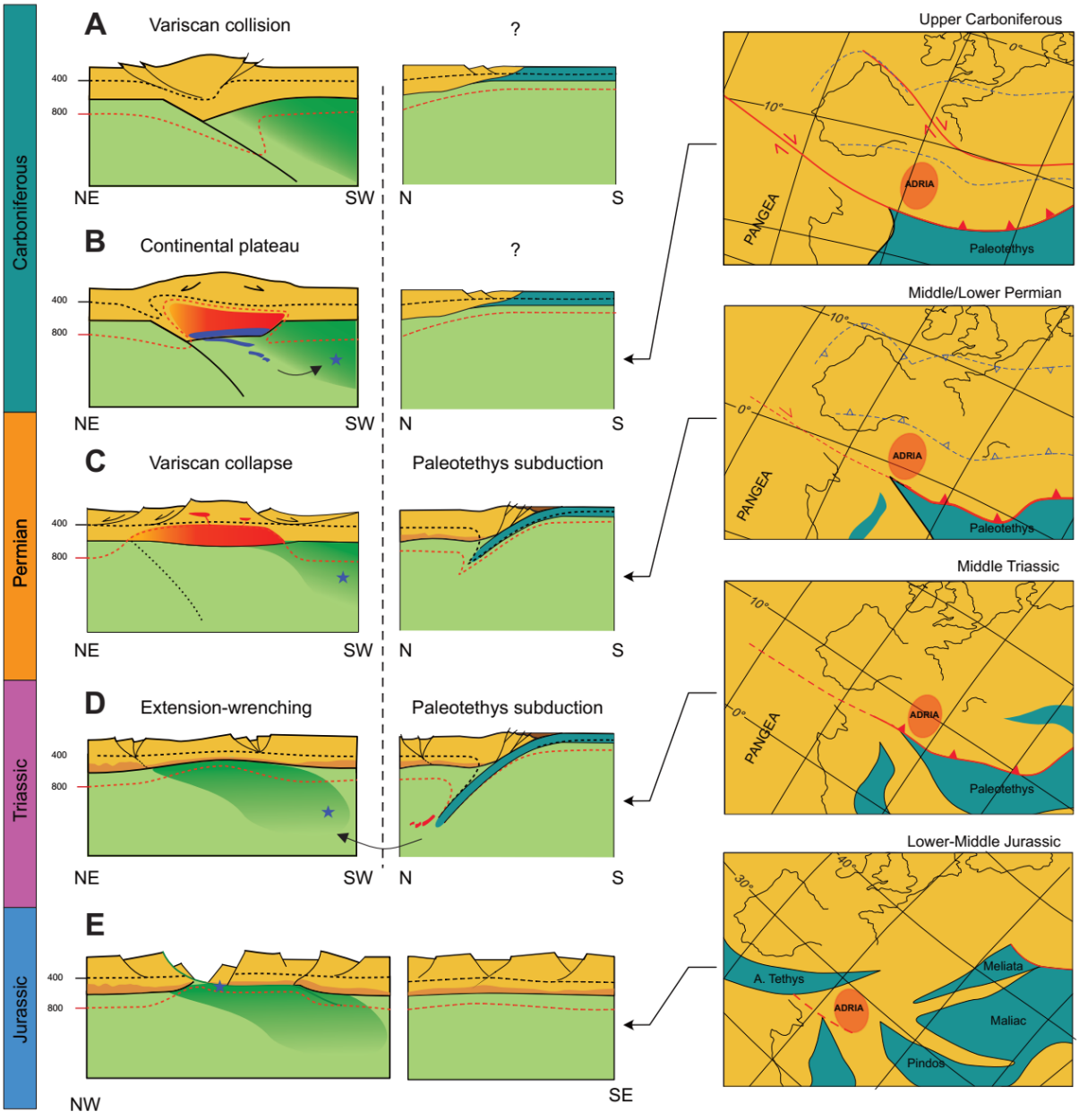

Figure 2.13: Schematic diagrams of the possible evolution of the Southalpine domain during the Late Paleozoic-Early Mesozoic interval derived from literature and personal observations in the

Ivrea-Verbano Zone (blue star: suggested position of the Finero massif). (a, b) Late Variscan cycle, progressive thickening of the continental crust leading to delamination and contamination of the Finero peridotite (from Decarlis et al., 2023; Casetta et al., 2021; Stampfli and Kozur, 2006); (c) Collapse of the Variscan belt to the west accompanied by subduction of the Paleotethys oceanic domain in the southernmost sector (Casetta et al., 2021); (d) Diffused extensional tectonics in the western-central Southalpine sector and protracted Paleotethys subduction to the south; triggering of Southalpine magmatism and possible mantle crustal contamination (Casetta et al., 2021); (e) Initiation of Alpine Tethys rifting and formation of the distal margin in the Western Southalpine domain (e.g. Beltrando et al., 2015; Decarlis et al., 2017 and references therein). To the southeast, the system passes to a complex tectonic scenario, still matter of debate, in which different extensional basins may have existed (e.g. Channell and Kozur, 1997), here oversimplified with a generalized extension. See text for detailed descriptions. Paleogeographic plate reconstructions are modified from Borel and Stampfli (2004) and Stampfli and Kozur (2006).

2.7 Concluding remarks

Detailed geochemical and isotopic characterization of Early Mesozoic dyke swarms cross-cutting the Finero phlogopite peridotite in the Ivrea-Verbano Zone identified three varieties on the basis of their HFSE enrichments: HFSE-poor, HFSE-rich and composite HFSE-poor and -rich dykes. These dykes record a geochemical change from orogenic-like calc-alkaline magmatism derived from metasomatized lithospheric mantle sources at relatively lower pressures, to alkaline anorogenic magmatism possibly derived from low-degree partial melting of asthenospheric to deep lithospheric mantle sources indicating a progressive variation of the mantle sources of the Southern Alps magmatism during Early Mesozoic times. These Early Mesozoic magmatisms also provide evidence that the mantle sources beneath the Southern Alps continuously retained subduction-related and/or delaminated crustal components over a prolonged period of time probably from the Variscan and/or older times up to the Triassic–

Jurassic boundary. The transition of the geochemical affinities of the Early Mesozoic magmatism in the IVZ in combination with geochemical records from the Dolomites and the Brescian Prealps further attests to the complex and diverse magmatic events that characterizes the Southern Alps in response to changing geodynamic regimes after the Variscan orogeny and shortly before the break-up and dispersal of the Pangea.

Declaration of Competing Interest

The authors declare that they have no known competing financial interests or personal relationships that could have appeared to influence the work reported in this paper.

Acknowledgements

ACO acknowledges the support of the University of Pavia for a doctoral scholarship and an international mobility grant to visit the National High Magnetic Field Laboratory to conduct some analytical work reported in this manuscript. VJMS was supported by NSF grant OCE 2126496. Part of this work was performed at the National High Magnetic Field Laboratory, which is supported by National Science Foundation Cooperative Agreement No. DMR-1157490 and the State of Florida. A.Z. was supported by the Italian "Programma di Rilevante Interesse Nazionale" project PRIN_20178LPCPW. MM and TG were supported by FAR 2023 project of the Università di Modena e Reggio Emilia. The Editor, Taras Gerya, and two anonymous reviewers are thanked for their constructive reviews.

References

Agostini, S., Doglioni, C., Innocenti, F., Manetti, P., Tonarini, S., Savasçin, M.Y., 2007. The transition from subduction-related to intraplate Neogene magmatism in the Western Anatolia and Aegean area, *in* Beccaluva, L., Bianchini, G., and Wilson, M., eds., Cenozoic Volcanism in the Mediterranean Area. Geol. Soc. Am. Spec. Paper 418, 1–15. https://doi.org/10.1130/2007.2418(01).

Batki, A., Pal-Molnar, E., Dobosi, G., Skelton, A., 2014. Petrogenetic significance of ocellar camptonite dykes in the Ditrau Alkaline Massif, Romania. Lithos 200, 181–196. https://doi.org/10.1016/j.lithos.2014.04.022.

Beltrando, M., Stockli, D.F., Decarlis, A., Manatschal, G., 2015. A crustal-scale view at rift localization along the fossil Adriatic margin of the Alpine Tethys preserved in NW Italy. Tectonics 34. https://doi.org/10.1002/2015TC003973.

Berno, D., Tribuzio, R., Zanetti, A., Hémond., C., 2020. Evolution of mantle melts intruding the lowermost continental crust: constraints from the Monte Capio–Alpe Cevia mafic–ultramafic sequences (Ivrea–Verbano Zone, northern Italy). Contrib. Miner. Petrol. 175. https://doi.org/10.1007/s00410-019-1637-8.

Bindeman, I., 2008. Oxygen isotopes in mantle and crustal magmas as revealed by single crystal analysis. Rev. Miner. Geochem. 69, 445–478. https://doi.org/10.2138/rmg.2008.69.12.

Bonazzi, M., Langone, A., Tumiati, S., Dellarole, E., Mazzucchelli, M., Giovanardi, T., Zanetti, A., 2020. Mantle-derived corundum-bearing felsic dykes may survive only within the lower (refractory/inert) crust: Evidence from zircon geochemistry and geochronology (Ivrea–Verbano Zone, Southern Alps, Italy). Geosciences 10, 281. https://doi.org/10.3390/geosciences10080281.

Bonazzi, M., Ogunyele, A.C., Giovanardi, T., Mazzucchelli, M., Zanetti, A., 2022. Geochemistry and U-Pb geochronology of zircons from diorite to anorthosite dykes intruding the Finero Phlogopite Peridotite (Ivrea-Verbano Zone): Evidence for a prolonged mantle-derived alkaline magmatism from the Upper Triassic to the Lower Jurassic in the Southern Alps. Earth Mantle Workshop (Abstract), Toulouse France, 11-15 Sept., 2022.

Boscaini, A., Marzoli, A., Davies, J.F.H.L., Chiaradia, M., Bertrand, H., Zanetti, A., Visonà, D., De Min, A., Jourdan, F., 2020. Permian post-collisional basic magmatism from Corsica to the Southeastern Alps. Lithos 376–377. https://doi.org/10.1016/j.lithos.2020.105733.

Burg, J.P., Van Den Driessche, J., Brun, J.P., 1994. Syn- to post-thickening extension in the Variscan Belt of Western Europe: modes and structural consequences. Géol. Fr. 3, 33-51.

Cannaò, E., Tiepolo, M., Fumagalli, P., Grieco, G., Agostini, S., 2022. Metasomatism in the Finero Phlogopite Peridotite: New insights from C and N concentrations and δ13C-δ11B signatures. Chem. Geol. 614. https://doi.org/10.1016/j.chemgeo.2022.121181.

Casetta, F., Coltorti, M., Marocchino, E. 2018. Petrological evolution of the Middle Triassic Predazzo Intrusive Complex, Italian Alps. Inter. Geol. Rev. 60, 977–97. https://doi.org/10.1080/00206814.2017.1363676.

Casetta, F., Ickert, R.B., Mark, D.F., Bonadiman, C., Giacomoni, P.P., Ntaflos, T., Coltorti, M., 2019. The alkaline lamprophyres of the Dolomitic Area (Southern Alps, Italy): markers of the late Triassic change from orogenic-like to anorogenic magmatism. J. Petrol. 60, 1263–1298. https://doi.org/10.1093/petrology/egz031.

Casetta, F., Ickert, R.B., Mark, D.F., Giacomoni, P.P., Bonadiman, C., Ntaflos, T., Zanetti, A., Coltorti, M., 2021. The Variscan subduction inheritance in the Southern Alps Sub-Continental Lithospheric Mantle: Clues from the Middle Triassic shoshonitic magmatism of the Dolomites (NE Italy). Lithos 380-381. https://doi.org/10.1016/j.lithos.2020.105856.

Cassinis, G., Cortesogno, L., Gaggero, L., Perotti, C.R., Buzzi, L., 2008. Permian to Triassic geodynamic and magmatic evolution of the Brescian Prealps (Eastern Lombardy, Italy). Ital. J. Geosci. 127, 501–518.

Channell, J.E.T., Kozur, H.W., 1997. How many oceans? Meliata, Vardar and Pindos oceans in Mesozoic Alpine paleogeography. Geology 25, 183–186. https://doi.org/10.1130/0091-7613(1997)025<0183:HMOMVA>2.3.CO;2.

Chenin, P., Manatschal, G., Decarlis, A., Schmalholz, S.M., Duretz, T., Beltrando, M., 2019. Emersion of distal domains in advanced stages of continental rifting explained by asynchronous crust and mantle necking. Geochem. Geophys. Geosys. 20, 3821-3840.

https://doi.org/10.1029/2019GC008357.

Coltorti, M., Beccaluva, L., Bonadiman, C., Faccini, B., Ntaflos, T., Siena, F., 2004. Amphibole genesis via metasomatic reaction with clinopyroxene in mantle xenoliths from Victoria Land, Antarctica. Lithos 75, 115–139. https://doi.org/10.1016/j.lithos.2003.12.021.

Coltorti, M., Bonadiman, C., Faccini, B., Grégoire, M., O'Reilly, S.Y., Powell, W., 2007. Amphiboles from suprasubduction and intraplate lithospheric mantle. Lithos 99, 68–84. https://doi.org/10.1016/j.lithos.2007.05.009.

Conceição, R.V., Green, D.H., 2004. Derivation of potassic (shoshonitic) magmas by decompression melting of phlogopite+pargasite lherzolite. Lithos 72, 209–29. https://doi.org/10.1016/j.lithos.2003.09.003.

Corvò, S., Langone, A., Padrón-Navarta, J.A., Tommasi, A., Zanetti, A., 2020. Porphyroclasts: Source and Sink of Major and Trace Elements During Deformation-Induced Metasomatism (Finero, Ivrea-Verbano Zone, Italy). Geosci. 10, 196. https://doi.org/10.3390/geosciences10050196.

De Min, A., Velicogna, M., Ziberna, L., Chiaradia, M., Alberti, A., Marzoli, A., 2020. Triassic magmatism in the European Southern Alps as an early phase of Pangea break-up. Geol. Mag. 157, 1–23. https://doi.org/10.1017/S0016756820000084.

Decarlis, A., Beltrando, M., Manatschal, G., Ferrando, S., Carosi, R., 2017. Architecture of the Distal Piedmont-Ligurian Rifted Margin in NW Italy: Hints for a Flip of the Rift System Polarity. Tectonics 36. https://doi.org/10.1002/2017TC004561.

Decarlis, A., Manatschal, G., Haupert, I., Masini, E., 2015. The tectono-stratigraphic evolution of distal, hyper-extended magma-poor conjugate rifted margins: Examples from the Alpine Tethys and Newfoundland-Iberia. Mar. Pet. Geol. 68, 54-72. https://doi.org/10.1016/j.marpetgeo.2015.08.005.

Decarlis, A., Zanetti, A., Ogunyele, A.C., Ceriani, A., Tribuzio, R., 2023. The Ivrea-Verbano tectonic evolution: The role of the crust-mantle interactions in rifting localization. Earth-Sci. Rev. 238. https://doi.org/10.1016/j.earscirev.2023.104318.

Deng, H., Kusky, T., Bozurt, E., Chen, C., Wang, L., Dong, Z., Meng, J., 2023. Sr-Nd-Ca isotopic variations of Cenozoic calc-alkaline and alkaline volcanic rocks above a slab tear

in Western Anatolia, Turkey. GSA Bull. https://doi.org/10.1130/B36672.1.

Denyszyn, S.W., Fiorentini, M.L., Maas, R., Dering, G., 2018. A bigger tent for CAMP. Geology 46, 823–826. https://doi.org/10.1130/G45050.1.

Doglioni, C., 2007. Tectonics of the Dolomites. Bull. Ang. Geol. 12, 11–15.

Foley, S., 1990. A review and assessment of experiments on kimberlites, lamproites and lamprophyres as a guide to their origin. Proc. Indian Acad. Sci. 99, 57–80. https://doi.org/10.1007/BF02871896.

Galli, A., Grassi, D., Sartori, G., Gianola, O., Burg, J.P., Schmidt, M.W., 2019. Jurassic carbonatite and alkaline magmatism in the Ivrea zone (European Alps) related to the breakup of Pangea. Geology 47, 199-202. https://doi.org/10.1130/G45678.1.

Giovanardi, T., Morishita, T., Zanetti, A., Mazzucchelli, M., Vannucci, R., 2013. Igneous sapphirine as a product of melt-peridotite interactions in the Finero Phlogopite Peridotite Massif, Western Italian Alps. Eur. J. Miner. 25, 17–31. https://doi.org/10.1127/0935-1221/2013/0025-2251.

Giovanardi, T., Zanetti, A., Dallai, L., Morishita, T., Hémond, C., Mazzucchelli, M., 2020. Evidence of subduction-related components in sapphirine-bearing gabbroic dykes (Finero phlogopite–peridotite): Insights into the source of the Triassic–Jurassic magmatism at the Europe–Africa boundary. Lithos 356–357, 105366. https://doi.org/10.1016/j.lithos.2020.105366.

Gregoire, M., McInnes, B.I.A., O'Reilly, S.Y., 2001. Hydrous metasomatism of oceanic sub-arc mantle, Lihir, Papua New Guinea–Part 2. Trace element characteristics of slab-derived fluids. Lithos 59, 91–108. https://doi.org/10.1016/S0024-4937(01)00058-5.

Grieco, G., Ferrario, A., von Quadt, A., Köppel, V., Mathez, A., 2001. The zircon-bearing chromitites of the phlogopite peridotite of Finero (Ivrea Zone, Southern Alps): evidence and geochronology of a metasomatized mantle slab. J. Petrol. 42, 89–101. https://doi.org/10.1093/petrology/42.1.89.

Griffin, W.L., Powell, W.J., Pearson, N.J., O'Reilly, S.Y., 2008. GLITTER: data reduction software for laser ablation ICPMS. In: Sylvester, P. (Ed.), Laser Ablation ICP–MS in the Earth Sciences: Current Practices and Outstanding Issues. Mineral. Assoc. Canada Short

Course Series 40, pp. 308–311.

Handy, M. R., Schmid, S.M., Bousquet, R., Kissling, E., Bernoulli, D., 2010. Reconciling plate-tectonic reconstructions of Alpine Tethys with the geological-geophysical record of spreading and subduction in the Alps. Earth-Sci. Rev. 102, 121-158. https://doi.org/10.1016/j.earscirev.2010.06.002.

Handy, M., Franz, L., Heller, F., Janott, B., Zurbriggen, R., 1999. Multistage accretion, orogenic stacking, and exhumation of continental crust (Ivrea crustal section, Italy and Switzerland). Tectonics 18, 1154-1177.

Handy, M.R., Giese, J., Schmid, S.M., Pleuger, J., Spakman, W., Onuzi, K., Ustaszewski, K., 2019. Coupled crust-mantle response to slab tearing, bending, and rollback along the Dinaride-Hellenide orogen. Tectonics 38, 2803-2828. https://doi.org/10.1029/2019TC005524

Harangi, S., Downes, H., Thirlwall, M., Gméling, K., 2006. Geochemistry, petrogenesis and geodynamic relationships of Miocene calc-alkaline volcanic rocks in the Western Carpathian Arc, Eastern Central Europe. J. Petrol. 48, 2261–2287. https://doi.org/10.1093/petrology/egm059.

Hawthorne, F.C., Oberti, R., Harlow, G.E., Maresch, W.V., Martin, R.F., Schumacher, J.C., Welch, M.D., 2012. Nomenclature of the amphibole supergroup. Am. Mineral. 97, 2031–2048. https://doi.org/10.2138/am.2012.4276.

Holland, T., Blundy, J., 1994. Non-ideal interactions in calcic amphiboles and their bearing on amphibole-plagioclase thermometry. Contr. Mineral. Petrol. 116, 433–447. https://doi.org/10.1007/BF00310910.

Ishimaru, S., Arai, S., Ishida, Y., Shirasaka, M., Okrugin, M., 2007. Melting and multi-stage metasomatism in the mantle wedge beneath a frontal arc inferred from highly depleted peridotite xenoliths from the Avacha volcano, southern Kamchatka. J. Petrol. 48, 1–39. https://doi.org/10.1093/petrology/egl065.

Kretz, R., 1983. Symbols for rock-forming minerals. Am. Mineral. 68, 277–279.

Langone, A., José, A. P. N., Ji, W. Q., Zanetti, A., Mazzucchelli, M., Tiepolo, M., Giovanardi T., Bonazzi, M. (2017). Ductile–brittle deformation effects on crystal-chemistry and U–Pb

ages of magmatic and metasomatic zircons from a dyke of the Finero Mafic Complex (Ivrea–Verbano Zone, Italian Alps). Lithos, 284, 493-511. https://doi.org/10.1016/j.lithos.2017.04.020.

Langone, A., Zanetti, A., Daczko, N.R., Piazolo, S., Tiepolo, M., Mazzucchelli, M., 2018. Zircon U–Pb dating of a lower crustal shear zone: a case study from the northern sector of the Ivrea–Verbano Zone (Val Cannobina, Italy). Tectonics 37, 322–342.

Le Roux, V., Lee, C.-T.A., Turner, S.J. 2010. Zn/Fe systematics in mafic and ultramafic systems: Implications for detecting major element heterogeneities in the Earth's mantle. Geochim. Cosmochim. Acta 74, 2779-2796. https://doi.org/10.1016/j.gca.2010.02.004.

Lu, M., Hofmann, A.W., Mazzucchelli, M., Rivalenti, G., 1997. The mafic-ultramafic complex near Finero (Ivrea-Verbano Zone), I. Chemistry of MORB-like magmas. Chem. Geol. 140, 207–222. https://doi.org/10.1016/S0009-2541(97)00049-1.

Lustrino, M., Abbas, H., Agostini, S., Caggiati, M., Carminati, E., Gianolla, P., 2019. Origin of Triassic magmatism of the Southern Alps (Italy): Constraints from geochemistry and Sr-Nd-Pb isotopic ratios. Gondwana Res. 75, 218–238. https://doi.org/10.1016/j.gr.2019.04.011.

Lustrino, M., Anderson, D.L., 2015. The mantle isotopic printer: basic mantle plume geochemistry for seismologists and geodynamicists. Geol. Soc. Am. Spec. Paper 514, 257–279.

Lustrino, M., Duggen, S., Rosenberg, C.L., 2011. The Central-Western Mediterranean: anomalous igneous activity in an anomalous collisional tectonic setting. Earth-Sci. Rev. 104, 1–40. https://doi.org/10.1016/j.earscirev.2010.08.002.

Lustrino, M., Fedele, L., Melluso, L., Morra, V., Ronga, F., Geldmacher, J., Duggen, S., Agostini, S., Cucciniello, C., Franciosi, L., Meisel, T., 2013. Origin and evolution of Cenozoic magmatism of Sardinia (Italy). A combined isotopic (Sr–Nd–Pb–O–Hf–Os) and petrological view. Lithos 180–181, 138-158. https://doi.org/10.1016/j.lithos.2013.08.022.

Lyubetskaya, T., Korenaga, J., 2007. Chemical composition of Earth's primitive mantle and its variance: 1. Method and results. J. Geophys. Res. Solid Earth 112, B03211.

https://doi.org/10.1029/2005JB004223.

Marquez, A., Oyarzum, R., Doblas, M., Verma, S.P., 1999. Alkalic (ocean island basalt type) and calc-alkalic volcanism in Mexican volcanic belt: A case of plume-related magmatism and propagating rifting at an active margin? Geology 27, 51–54. https://doi.org/10.1130/0091-7613(1999)027<0051:AOIBTA>2.3.CO;2.

Mazzucchelli, M., Zanetti, A., Rivalenti, G., Vannucci, R., Correia, C.T., Tassinari, C.C.G., 2010. Age and geochemistry of mantle peridotites and diorite dykes from the Baldissero body: Insights into the Paleozoic-Mesozoic evolution of the Southern Alps. Lithos 119, 485–500. https://doi.org/10.1016/j.lithos.2010.08.002.

McDonough, W.F., Sun, S., 1995. The composition of the Earth. Chem. Geol. 120, 223–253. https://doi.org/10.1016/0009-2541(94)00140-4.

Moine, B.N., Gregoire, M., O'Reilly, S.Y., Sheppard, S.M.F., Cottin, J.-Y., 2001. High field strength element fractionation in the upper mantle: evidence from amphibole-rich composite mantle xenoliths from the Kerguelen Islands (Indian Ocean). J. Petrol. 42, 2145–2167. https://doi.org/10.1093/petrology/42.11.2145.

Morishita, T., Hattori, K.H., Terada, K., Matsumoto, T., Yamamoto, K., Takebe, M., Ishida, Y., Tamura, A., Arai, S., 2008. Geochemistry of apatite-rich layers in the Finero phlogopite–peridotite massif (Italian Western Alps) and ion microprobe dating of apatite. Chem. Geol. 251, 99–111. https://doi.org/10.1016/j.chemgeo.2008.02.018.

Nardini, N., Casetta, F., Ickert, R.B., Mark, D.F., Ntaflos, T., Zanetti, A., Coltorti, M., 2022. From the Middle Triassic Cima Pape complex (Dolomites; Southern Alps) to the feeding systems beneath active volcanoes: Clues from clinopyroxene textural and compositional zoning. J. Volcan. Geotherm. Res. 422. https://doi.org/10.1016/j.jvolgeores.2021.107459.

Obermiller, W.A., 1994. Chemical and Isotopic Variations in the Balmuccia, Baldissero and Finero Peridotite Massifs (Ivrea-Zone, N-Italy). Unpublished PhD thesis. Johannes-Gutenberg-Universität Mainz, p. 191.

Ogunyele, A.C., Giovanardi, T., Bonazzi, M., Mazzucchelli, M., Zanetti, A., 2021. Geochemistry and geochronology of alkaline dykes from the Finero Phlogopite Peridotite (Ivrea-Verbano Zone): insights into the Triassic-Jurassic tectono-magmatic events of the

Southern Alps. EGU Gen. Ass. Abstract (EGU21-10286). https://doi.org/10.5194/egusphere-egu21-10286.

Peressini, G., Quick, J.E., Sinigoi, S., Hofmann, A.W., Fanning, M., 2007. Duration of a large mafic intrusion and heat transfer in the lower crust: a SHRIMP U/Pb zircon study in the Ivrea–Verbano Zone (Western Alps, Italy). J. Petrol. 48, 1185-1218, https://doi.org/10.1093/petrology/egm014.

Petri, B., Wijbrans, J.R., Mohn, G., Manatschal, G., Beltrando, M., 2023. Thermal evolution of Permian post-orogenic extension and Jurassic rifting recorded in the Austroalpine basement (SE Switzerland, N Italy). Lithos 444–445. https://doi.org/10.1016/j.lithos.2023.107124.

Pin, C., Monchoux, P., Paquette, J-L., Azambre, B., Wang, R.C., Martin, R.F., 2006. Igneous albitite dikes in orogenic lherzolites, Western Pyrénées, France: A possible source for corundum and alkali feldspar xenocrysts in basaltic terranes. II. Geochemical and petrogenetic considerations. Can. Mineral. 44, 843–856. https://doi.org/10.2113/gscanmin.44.4.843

Plank, T., 2014. The chemical composition of subducting sediments, *in* Holland, H.D., eds., Treatise on Geochemistry, 2nd ed. Elsevier, Amsterdam, 607-629.

Ridolfi, F., Zanetti, A., Renzulli, A., Perugini, D., Holtz, F., Oberti, R., 2018. AMFORM, a new mass-based model for the calculation of the unit formula of amphiboles from electron microprobe analyses. Am. Miner. 103, 1112-1125. https://doi.org/10.2138/am-2018-6385.

Roeder, P., Gofton, E., Thornber, C., 2006. Cotectic proportions of olivine and spinel in olivine-tholeiitic basalt and evaluation of pre-eruptive processes. J. Petrol. 47, 883–900. https://doi.org/10.1093/petrology/egi099.

Roeder, P.L., Poustovetov, A., Oskarsson, N., 2001. Growth forms and composition of chromian spinel in MORB magma: diffusion-controlled crystallization of chromian spinel. Can. Mineral. 39, 397–416. https://doi.org/10.2113/gscanmin.39.2.397.

Salters, V.J.M., Stracke, A., 2004. Composition of the depleted mantle. Geochem. Geophys. Geosys. 5. https://doi.org/10.1029/2003GC000597.

Schaltegger, U., Ulianov, A., Müntener, O., Ovtcharova, M., Peytcheva, I., Vonlanthen, P., Vennemann, T., Antognini, M., & Girlanda, F. (2015). Megacrystic zircon with planar fractures in miaskite-type nepheline pegmatites formed at high pressures in the lower crust (Ivrea Zone, southern Alps, Switzerland). Am. Mineral. 100, 83-94. https://doi.org/10.2138/am-2015-4773.

Schettino, A., Turco, E., 2011. Tectonic history of the western Tethys since the Late Triassic. GSA Bull. 123, 89–105. https://doi.org/10.1130/B30064.1.

Schmid, S.M., 1993. Ivrea zone and adjacent southern Alpine basement, *in* von Raumer, J.F., and Neubauer, F., eds., Pre-Mesozoic Geology in the Alps. Springer–Verlag, Berlin, 567–583. https://doi.org/10.1007/978-3-642-84640-3_33.

Selverstone, J., Sharp, Z.D., 2011. Chlorine isotope evidence for multicomponent mantle metasomatism in the Ivrea Zone. Earth Planet. Sci. Lett. 310, 429–440. https://doi.org/10.1016/j.epsl.2011.08.034.

Siena, F., Coltorti, M., 1989. The petrogenesis of a hydrated mafic-ultramafic complex and the role of amphibole fractionation at Finero (Italian Western Alps). Neues Jahrbuch fur Mineralogie, Monatshefte 6, 255-274.

Søager, N., Portnyagin, M., Hoernle, K., Holm, P.M., Hauff, F., Garbe-Schönberg, D. 2015. Olivine major and trace element compositions in Southern Payenia basalts, Argentina: Evidence for pyroxenite–peridotite melt mixing in a back-arc setting. J. Petrol. 56, 1495–1518, https://doi.org/10.1093/petrology/egv043.

Soder, C.G., Romer, R.L., 2018. Post-collisional potassic-ultrapotassic magmatism of the Variscan orogen: Implications for mantle metasomatism during continental subduction. J. Petrol. 59, 1007-1034. https://doi.org/10.1093/petrology/egy053.

Stähle, V., Frenzel, G., Hess, J.C., Saupé, F., Schmidt, S.T., Schneider, W., 2001. Permian metabasalt and Triassic alkaline dykes in the Northern Ivrea Zone: clues to the post-Variscan geodynamic evolution of the Southern Alps. Schweizerische Mineralogische Petrographische Mitteillungen 81, 1–21.

Stälhe, V., Frenzel, G., Kober, B., Michard, A., Puchelt, H., Schneider, W., 1990. Zircon syenite pegmatites in the Finero peridotite (Ivrea Zone): evidence for a syenite from a mantle

source. Earth Planet. Sci. Lett. 101, 196–205. https://doi.org/10.1016/0012-821X(90)90153-O.

Stampfli, G., Kozur, H., 2006. Europe from the Variscan to the Alpine cycles. Geol. Soc. London Mem. 32, 57-82. https://doi.org/10.1144/GSL.MEM.2006.032.01.04.

Stampfli, G.M., Borel, G.D., 2002, A plate tectonic model for the Paleozoic and Mesozoic constrained by dynamic plate boundaries and restored synthetic oceanic isochrones. Earth Planet. Sci. Lett. 196, 17–33. https://doi.org/10.1016/S0012-821X(01)00588-X.

Stampfli, G.M., Borel, G.D., 2004. The TRANSMED transects in space and time: Constraints on the paleotectonic evolution of the Mediterranean domain, *in* Cavazza, W., Roure, F., Spakman, W., Stampfli, G. M., Ziegler, P., eds., The TRANSMED Atlas: the Mediterranean Region from crust to mantle. Springer-Verlag, 53-80.

Stampfli, G.M., Von Raumer, J.F., Borel, G.D., 2002. Paleozoic evolution of pre-Variscan terranes: from Gondwana to the Variscan collision, *in* Catalan, J.R.M., Hatcher, R.D., Arenas, R., Garcia, F.D., eds., Variscan-Appalachian dynamics: The building of the late Paleozoic basement. GSA Special Paper 364, 263–280. https://doi.org/10.1130/0-8137-2364-7.263.

Storck, J.-C., Brack, P., Wotzlaw, J.F., Ulmer, P. (2019). Timing and evolution of Middle Triassic magmatism in the Southern Alps (northern Italy). J. Geol. Soc. 176, 253-268. https://doi.org/10.1144/jgs2018-123.

Stracke, A., 2012. Earth's heterogeneous mantle: A product of convection-driven interaction between crust and mantle. Chem. Geol. 330–331, 274–299. https://doi.org/10.1016/j.chemgeo.2012.08.007.

Stracke, A., Bizimis, M., Salters, V.J., 2003. Recycling oceanic crust: quantitative constraints. Geochem. Geophys. Geosys. 4. https://doi.org/10.1029/2001GC000223.

Tappe, S., Foley, S.F., Jenner, G.A., Heaman, L.M., Kjarsgaard, B.A., Romer, R.L., Stracke, A., Joyce N., Hoefs, J., 2006. Genesis of ultramafic lamprophyres and carbonatites at Aillik Bay, Labrador: a consequence of incipient lithospheric thinning beneath the North Atlantic Craton. J. Petrol. 47, 1261–315. https://doi.org/10.1093/petrology/egl008.

Tiepolo, M., 1999. Determinazione sperimentale dei coefficient di distribuzione solido/liquid in

anfiboli di mantello: Ruolo del controllo cristallochimica. Unpubl. PhD thesis. Universita di Pavia, 314 p.

van Hinsbergen, D.J.J., Torsvik, T.H., Schmid, S.M., Maţenco, L.C., Maffione, M., Vissers, R.L.M., Gürer, D., Spakman, W., 2020. Orogenic architecture of the Mediterranean region and kinematic reconstruction of its tectonic evolution since the Triassic. Gondwana Res. 81, 79-229. https://doi.org/10.1016/j.gr.2019.07.009.

Velicogna, M., De Min, A., Prašek, M.K., Ziberna, L., Brombin, V., Jourdan, F., Renne, P.R., Balen, D., Grégoire, M., Marzoli, A., 2022. The Norian magmatic rocks of Jabuka, Brusnik and Vis Islands (Croatia) and their bearing on the evolution of Triassic magmatism in the Northern Mediterranean. Int. Geol. Rev. 65.

von Raumer, J.F., Bussy, F., Schaltegger, U., Schulz, B., Stampfli, G.M., 2013. Pre-Mesozoic Alpine basements – Their place in the European Paleozoic framework. GSA Bull. 125, 89–108. https://doi.org/10.1130/B30654.1.

Voshage, H., Hunziker, J.C., Hofmann, A.W., Zingg, A., 1987. A Nd and Sr isotopic study of the Ivrea zone, Southern Alps, N-Italy. Contrib. Mineral. Petrol. 97, 31–42. https://doi.org/10.1007/BF00375212.

Wang, J., Su, B.-X., Robinson, P.T., Xiao, Y., Bai, Y., Liu, X., Sakyi, P.A., Jing, J.-J., Chen, C., Liang, Z., Bao, Z.-A., 2021. Trace elements in olivine: Proxies for petrogenesis, mineralization and discrimination of mafic-ultramafic rocks. Lithos 388–389, https://doi.org/10.1016/j.lithos.2021.106085.

Witt-Eickschen, G., Seck, H.A., Mezger, K., Eggins, S.M., Altherr, R., 2003. Lithospheric mantle evolution beneath the Eifel (Germany): constraints from Sr–Nd–Pb isotopes and trace element abundances in spinel peridotite and pyroxenite xenoliths. J. Petrol. 44, 1077–1095. https://doi.org/10.1093/petrology/44.6.1077.

Woelki, D., Salters, V., Beier, C., Dick, H., Koepke, J., Romer, R., 2023. Shallow recycling of lower continental crust: The Mahoney Seamount at the Southwest Indian Ridge. Earth Planet. Sci. Lett. 602, 117968. https://doi.org/10.1016/j.epsl.2022.117968.

Zanetti, A., Giovanardi, T., Langone, A., Tiepolo, M., Wu, F.Y., Dallai, L., Mazzucchelli, M., 2016. Origin and age of zircon-bearing chromitite layers from the Finero phlogopite

peridotite (Ivrea–Verbano Zone, Western Alps) and geodynamic consequences. Lithos, 262, 58-74. https://doi.org/10.1016/j.lithos.2016.06.015.

Zanetti, A., Mazzucchelli, M., Rivalenti, G., Vannucci, R., 1999. The Finero phlogopite–peridotite massif: an example of subduction-related metasomatism. Contrib. Mineral. Petrol. 134, 107–122. https://doi.org/10.1007/s004100050472.

Zanetti, A., Mazzucchelli, M., Sinigoi, S., Giovanardi, T., Peressini, G., Fanning, M., 2013. SHRIMP U-Pb zircon Triassic intrusion age of the Finero mafic complex (Ivrea–Verbano Zone, Western Alps) and its geodynamic implications. J. Petrol. 54, 2235–2265. https://doi.org/10.1093/petrology/egt046.

Zheng, Y.-F., 2019. Subduction zone geochemistry. Geosci. Frontiers 10, 1223-1254. https://doi.org/10.1016/j.gsf.2019.02.003.

Zurbriggen, R., 1996. Crustal genesis and uplift history of the Strona-Ceneri zone (Southern Alps). Unpubl. PhD thesis, University of Bern, Switzerland.

CHAPTER 3

Timing, mantle source characteristics and geodynamic significance of Late Triassic to Early Jurassic alkaline magmatism in the Ivrea-Verbano Zone (western Southern Alps): Further evidences from zircon trace elements, U-Pb geochronology and Lu-Hf isotopes

Abimbola C. Ogunyele[1,2], Mattia Bonazzi[1], Alberto Zanetti[2], Tommaso Giovanardi[3], and Maurizio Mazzucchelli[1,3]

[1] Department of Earth and Environmental Sciences, University of Pavia, Via Ferrata 1, 27100 Pavia, Italy

[2] CNR – Istituto Geoscienze e Georisorse, Via Ferrata 1, 27100 Pavia, Italy

[3] Department of Chemical and Geological Sciences, University of Modena and Reggio Emilia, Via Campi 103, 41125 Modena, Italy

Declaration

This manuscript is submitted to **Lithos** for peer-review and possible publication. The study was conducted in collaboration with the co-authors cited above. The contribution of each author is given below.

ACO: Data curation, Formal analysis, Investigation, Methodology, Validation, Visualization, Writing - original draft, Writing - review & editing; **MB**: Data curation, Formal analysis, Investigation, Methodology, Writing - original draft, Writing - review & editing; **AZ**: Conceptualization, Funding acquisition, Methodology, Project administration, Resources, Supervision, Validation, Visualization, Writing - review & editing. **TG**: Data curation, Formal analysis, Investigation, Methodology, Validation, Visualization, Writing - review & editing; **MM**: Conceptualization, Funding acquisition, Supervision, Writing - review & editing.

Abstract

Zircon is a common accessory mineral in evolved magmatic rocks and its investigation can provide invaluable information on the geochemical nature, sources, timing and rate of magmatic processes. The Ivrea-Verbano Zone (IVZ) in western Southern Alps exposes deep continental to upper mantle sequences cross-cut by dyke swarms of variable geochemical affinities and ages. We here present new trace elements, U-Pb dating and Hf isotopic data of zircons from alkaline dykes which discordantly intrude the Finero Phlogopite Peridotite mantle unit in the northern IVZ to further constrain the age, mantle source characteristics and geodynamic significance of Late Triassic alkaline magmatism in the IVZ. The studied alkaline dykes are diorites and anorthosites mainly containing Nb-Ta-rich amphibole and phlogopite in association with albite and apatite. Zircon as well as monazite, ilmenite, titanite, Nb-rich oxides and carbonates are common accessories in the dykes. Zircons from the dyke samples are mostly anhedral, with textures varying from magmatic (oscillatory to sector zoning) to recrystallized (convoluted to homogeneous). Concordant U-Pb ages of the zircons range from 216 ± 9 Ma to 191 ± 10 Ma with most magmatic oscillatory zircons providing concordant ages around ca. 200 Ma. The zircons display a bimodal distribution of Hf isotopes with $\varepsilon Hf_{(t)}$ in zircons from the dioritic and anorthositic dykes ranging from +6.2 to +15.4 and –0.4 to +3.6, respectively. Our geochronological and Hf isotopic data in combination with those from literature indicate that the IVZ experienced an episodic protracted period (~50 Ma) of alkaline magmatism from the Late Triassic to Early Jurassic. The alkaline magmas were largely derived from an upwelling depleted asthenosphere containing and/or interacting with variable amounts of recycled enriched components. The IVZ Late Triassic alkaline magmatism and coeval alkaline magmatisms in the central and eastern sectors of the Southern Alps can thus be related to the same geodynamic

cycle involving upwelling of the asthenosphere in an intraplate environment. This tectono-magmatic event represents a precursor of the rifting stage that caused the opening of the Alpine Tethys in the western Mediterranean region.

3.1 Introduction

Alkaline to ultra-alkaline rocks, geochemically similar to ocean island basalts (OIBs) and characterized by enrichments in large-ion lithophile elements (LILEs) and light rare earth elements (LREEs), and enrichment or no depletion in high field strength elements (HFSEs, e.g., Nb and Ta) are consistent with derivation from a deep mantle source, sometimes requiring inputs from enriched components (Agostini et al., 2007; Casetta et al., 2019; Deng et al., 2023; Ogunyele et al., 2024). The chemical and isotopic compositions of these rocks can therefore encode information fundamental to unraveling the nature and geodynamics of the deep Earth. Additionally, the chemistry of mineral phases in alkaline rocks can be very useful as they may provide information that may not be easily decoded from bulk rock analysis (e.g., Schaltegger et al., 2015; Casetta et al., 2019; Galli et al., 2019; Bonazzi et al., 2020). Among the mineral phases commonly used to investigate the composition, sources, timing and evolution of alkaline magmatism, zircon is peculiar owing to its refractory nature and capacity to preserve a record of magmatic events and furnish this record through petrographic, trace elements and isotopic (e.g., Hf, Zr, O, Li, etc) analyses.

In the Ivrea-Verbano Zone (IVZ, western Southern Alps; Figure 3.1a), zircon-bearing alkaline and carbonatitic rocks occurring as pipes, veins, dykes, sills, and pods within upper mantle to lower crustal lithologies are well-documented in many localities (e.g., Stähle et al., 1990; 2001; Schaltegger et al., 2015; Galli et al., 2019; Bonazzi et al., 2020). Recent detailed

petrochemical and amphibole Nd-Sr-Hf-Pb isotopic study (Ogunyele et al., 2024; Chapter 2) of dyke swarms intruding the Finero Phlogopite Peridotite (FPP) in the northernmost part of the IVZ (Figure 3.1a-b) document a shift of the IVZ magmatism from orogenic-like to anorogenic/alkaline affinity during the Late Triassic, and provide a temporal correlation between the Early Mesozoic magmatisms in the IVZ and those from the eastern and central sectors of the Southern Alps. To further characterize the Late Triassic alkaline tectono-magmatic cycle in the Southern Alps, we here present new trace elements, U-Pb dating and Lu-Hf isotopic data of zircons from the alkaline dykes earlier investigated by Ogunyele et al. (2024). The information derived from the zircon investigations are used to decipher the timeframe, magmatic processes, and source compositions of alkaline magmatism in the IVZ and the Southern Alps at large, and provide a geodynamic scenario of the region during the Late Triassic to Early Jurassic.

3.2 Triassic tectono-magmatic cycles of the Southern Alps: A synopsis

Available geochemical, geochronological and isotopic data (e.g., Cassinis et al., 2008; Lustrino et al., 2019; Storck et al., 2019; 2020; Casetta et al., 2019, 2021; De Min et al., 2020; Bonazzi et al., 2020; Giovanardi et al., 2020; Nardini et al., 2022; Ogunyele et al., 2024) converge to discriminate Triassic magmatic events in the Southern Alps into two distinct tectono-magmatic cycles: (i) the Middle to early Late Triassic (~243-235 Ma) calc-alkaline to shoshonitic cycle, and (ii) the Late Triassic to Early Jurassic (~230-190 Ma) alkaline to transitional and tholeiitic magmatic cycle.

During the Middle to early Late Triassic (~243–235 Ma), a diffuse igneous activity developed throughout the Southern Alps (Lustrino et al., 2019). Remnants of lava flows, dykes and pyroclastic succession formed during this cycle crop out in the eastern (Dolomites,

Vicentinian Alps, Val di Non, and Julian Alps) and central (Brescian Prealps) sectors of the Southern Alps (Cassinis et al., 2008; Storck et al., 2019; 2020; Lustrino et al., 2019; Casetta et al., 2021; De Min et al., 2020; Nardini et al., 2022). The Monzoni, Predazzo and Cima di Pape plutonic complexes also belong to this tectono-magmatic cycle (Bonadiman et al., 1994; Casetta et al., 2018). Coeval magmatic products can be traced westward to the Ivrea-Verbano Zone (Giovanardi et al., 2013; 2020; Ogunyele et al., 2024) and eastward to Austria and the Dinarides (Pamic, 1984; Lustrino et al., 2019; De Min et al., 2020). The geochemical signature of volcano-plutonic rocks formed during this cycle vary mainly from high-K calc-alkaline to shoshonitic affinity, typical of magmas derived from subduction-modified lithospheric mantle sources with negligible crustal contamination during magma transport and/or emplacement (Lustrino et al., 2019; Casetta et al., 2021).

The geodynamic framework in which the Southern Alps Middle Triassic magmatism originated is still a subject of debate. A long list of geodynamic scenarios to explain the Middle Triassic tectonic and magmatic activity in the Dolomites and whole Southern Alps has been proposed in the literature (see Lustrino et al., 2019 and references therein). Some of these plausible models are: (1) aborted continental rifting – based on the association of extensional structures and mafic volcanism (Bechstadt et al., 1977); (2) sinistral strike-slip tectonics – based on the association of compressional and extensional structures with volcanic and plutonic intrusions (Blendinger, 1985; Doglioni, 1987, 1988); (3) heritage of ancient subduction events of Variscan age, coupled with assimilation of upper crustal rocks (Crisci et al., 1984; Sloman, 1989; Bonadiman et al., 1994; Beccaluva et al., 2005; De Min et al., 2020; Casetta et al., 2021; Nardini et al., 2022); (4) intra-Pangea dextral mega-shear system with lithosphere-scale extension enabling hybridization between mantle melts and lower crust lithologies (Brandner and Keim,

2011); (5) subduction of small Permian back-arc oceanic basins (Garzanti, 1985; Zanetti et al., 2013); (6) active arc/back-arc development following the NNW-directed subduction of the Paleotethys oceanic lithosphere beneath the south-eastern European paleo-margin (Cassinis et al., 2008); and (7) closure, by a subduction dipping beneath the Southalpine, of a Paleozoic rifted continental basin or a narrow oceanic basin, located between the Southalpine and Austroalpine continental blocks (Bianchini et al., 2018). Recent model by Ogunyele et al. (2024) suggest that the Middle Triassic magmatism in the IVZ may have been triggered by the Paleotethys subduction but the crustal components in the mantle sources were related to the Variscan orogenic cycle via subduction and/or crustal delamination.

From the Late Triassic to Early Jurassic (~230-190 Ma), a widespread alkaline to ultra-alkaline magmatism developed in the Southern Alps as a consequence of upwelling of the asthenosphere. This magmatism produced the ca. 219 Ma alkaline lamprophyre dykes in the Dolomites (Casetta et al., 2019; De Min et al., 2020) and the ca. 217 Ma transitional basaltic dykes in the Brescian Prealps (Cassinis et al., 2008). In the IVZ, evidence of this magmatism is well-documented as alkaline, carbonatitic and corundum-bearing rocks intruding the lower crust and upper mantle lithologies (e.g., Stähle et al., 1990; 2001; Mazzucchelli et al., 2010; Schaltegger et al., 2015; Langone et al., 2017; Galli et al., 2019; Bonazzi et al., 2020; Munnikhius, 2020; Ogunyele et al., 2024). Geochronological investigations of these rocks in the IVZ provide evidence for complex, multi-stage, short-lived intrusions which followed one another down to 190 Ma. Notably, one of these peaks at ca. 200 Ma, provided by U-Pb zircon dating on dunitic to pyroxenitic intrusions (Denyszyn et al., 2018) and internal Sm-Nd isochron ages of diorite dykes of transitional to tholeiitic affinity (Mazzucchelli et al., 2010), was interpreted to represent a distal and deep-seated expression of the Central Atlantic Magmatic

Province (CAMP) magmatism at lower crustal levels in the IVZ (Denyszyn et al., 2018). As a whole, the Southern Alps Late Triassic tectonomagmatic cycle is likely related to the onset of the opening of the Alpine Tethys and subsequently to the break-up of the Pangea Supercontinent (Cassinis et al., 2008; Casetta et al., 2019; Galli et al., 2019; De Min et al., 2020).

3.3 Geological settings and sample suite

The dykes investigated in this work discordantly intrude the phlogopite peridotite of Finero Complex in the northern part of the IVZ (Figure 3.1a-b). The IVZ is the westernmost sector of the Southern Alps and was part of the Mesozoic continental margin of the Adriatic Plate during the opening of the Alpine Tethys. Detailed descriptions of the geological settings of the IVZ and the Finero Complex are given in Section 2.2 of Chapter 2.

Four alkaline dyke samples comprising three diorites (i.e., FI1603, FI1604 and FI1605; see Figure 2.3a-c) and one anorthosite (FI19A01) were selected for the study. The studied dyke samples belong to the HFSE-rich group (see Section 2.3.1) composed by Nb-Ta-rich amphibole and phlogopite in association with albite and apatite. Zircon as well as monazite, ilmenite, titanite, Nb-rich oxides and carbonates are common accessories in the dykes. Detailed chemical analysis of amphiboles from these samples point to an "anorogenic" alkaline affinity, with amphiboles characterized by Al-poor (9-13 wt. % Al_2O_3) composition, enrichments in HFSE, LILE and LREE, low radiogenic $^{87}Sr/^{86}Sr_{(i)}$ (0.703761–0.704103) and high radiogenic Nd isotopes ($\varepsilon Nd_{(i)}$ from +3.4 to +5.4) (Ogunyele et al., 2024; see Chapter 2).

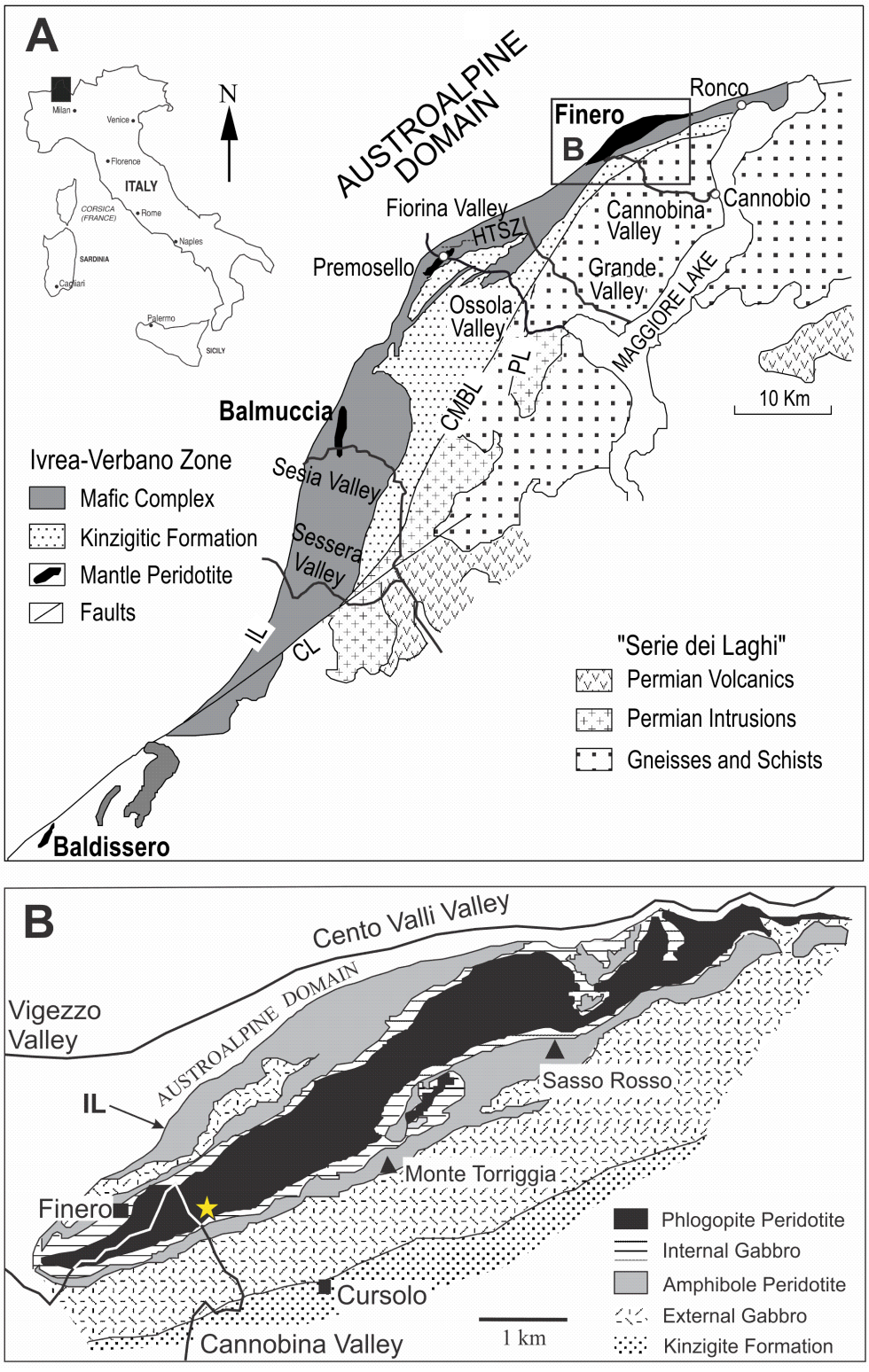

Figure 2.1: Geological maps of (a) the Ivrea-Verbano Zone and (b) the Finero Complex with sampling location (yellow star) of the studied dykes around Rio Creves. IL – Insubric Line, CMBL – Cossato-Mergozzo-Brissago Line, PL – Pogallo Line (after Zanetti et al., 1999).

3.4 Analytical methods

3.4.1 Zircon separation and cathodoluminiscence (CL) imaging

Zircon grains were separated from the dioritic and anorthosite dyke samples following the conventional procedure of grinding, hydrodynamic separation, magnetic separation by Frantz and density separation using heavy liquids (bromoform 2.84 g/cm^3). In all the dyke samples, zircons are only present in the leucocratic parts and not in the melanocratic parts. Separated zircon grains ranging in size from 125 to 250 μm and as free as possible from inclusions were mounted in epoxy resin, polished and characterized for their internal structures by cathodoluminiscence (CL) imaging using a scanning electron microscope (Philips SEM 505) housed at the CNR-IGG Pavia.

3.4.2 LA-ICP-MS zircon trace element measurement and U–Pb dating

Trace element contents of zircons were determined in-situ by LA-ICP-MS at the CNR-IGG Pavia. The LA-ICP-MS at the IGG-CNR Pavia comprises a 266 nm Nd:YAG laser ablation system (Quentel^{TM}) coupled to an Agilent 8900 QQQ-ICP-MS. The ICP-MS was tuned using NIST SRM 610 synthetic glass to optimize the signal intensity and stability and remove molecular interferences by monitoring ^{24}Mg, ^{115}In, ^{238}U and the ^{232}Th/^{248}ThO ratio. The laser was operated at a 10 Hz repetition rate, 10 J/cm^2 fluence and 50 μm spot size. Data reduction was done with the GLITTER software (Griffin et al., 2008). NIST SRM 610 was used as external standard and ^{29}Si was used as an internal standard for the zircons. The USGS reference sample BCR2g was repeatedly analyzed together with the unknowns to assess precision and accuracy at ± 5% and ± 10%, respectively. The zircon trace elements dataset is reported in Appendix 3.1.

In-situ U–Pb dating of zircon was conducted using a 193 nm ArF excimer laser microprobe (Geolas200Q-Microlas) coupled to an Agilent 8900 QQQ-ICP-MS. The laser was operated at a repetition rate of 5 Hz with a pulse-energy of about 12 J/cm^2; instrumental and laser-induced U/Pb fractionations were simultaneously corrected using the GJ-1 zircon as external standard (Jackson et al., 2004). The same integration interval and spot size (25 μm) were used on both the external standard and unknowns. During each analytical run, reference zircon 91500 (Wiedenbeck et al., 1995) and Plešovice (Sláma et al., 2008) were analyzed together with the unknowns for quality control. Data reduction was done with the GLITTER software (Griffin et al., 2008), setting the error of the external standard at 1%. During each analytical run, the reproducibility on the standards was propagated in all determinations according to the equation given by Horstwood et al. (2003). After this operation, analyses are considered accurate within the quoted errors. Concordant and weighted mean ages were calculated using the IsoplotR software (Vermeesch, 2008). The zircon U-Pb geochronological dataset is reported in Appendix 3.2. Errors are quoted at 2σ.

3.4.3 In-situ Lu-Hf isotopic analysis on zircon

In-situ Lu-Hf isotope analyses on zircons were performed at the Centro Interdipartimentale Grandi Strumenti (CIGS) of the University of Modena and Reggio Emilia (UNIMORE) using a double focusing MC-ICP-MS with a forward Nier–Johnson geometry (Thermo Fisher Scientific, Neptune™) coupled to a 213 nm Nd:YAG laser ablation system (New Wave Research™). All of the Hf isotopic analyses were performed near the U–Pb spots. During the analytical session, zircon reference materials 91500 (Wiedenbeck et al., 1995) and Plešovice (Sláma et al., 2008) were employed to check the accuracy and precision of the measurements.

Eight of nine Faraday detectors were used to collect the following masses: ^{171}Yb, ^{173}Yb, ^{175}Lu, ^{176}Hf + Lu + Yb, ^{177}Hf, ^{178}Hf, ^{179}Hf, and ^{180}Hf. Isotopic ratios were acquired in static mode with a block of 250 cycles (including laser warm-up, ~50–80 cycles of analysis and washout), an integration time of 0.5 s, laser spot of 55 μm and fluence of ~10 J/cm^2. A low laser frequency (~10 Hz) was used to achieve better signal stability (Vroon et al., 2008) with a He flux of ~0.5 L/min. Data reduction was performed with the Hf-INATOR excel spreadsheet (Giovanardi and Lugli, 2017). Reference material 91500 provides a ^{176}Hf/^{177}Hf value of 0.282101 ± 128 (n = 5, error as 2 standard deviation; Georem database values = 0.281663 – 0.28307) and Plešovice yields a value of 0.282436 ± 28 (n = 8; Georem database values = 0.282432 – 0.282553). The zircon Hf isotopic dataset is reported in Appendix 3.3.

3.5 Analytical results

3.5.1 Zircon internal structures

Zircon crystals are mostly anhedral and exhibit a variety of internal structures (Figures 3.2, 3.3). The zircons from the dioritic dykes are mainly characterized by recrystallized homogeneous to convolute textures with few crystals showing sector to oscillatory zoning. Thin bright rims are also noticeable in some crystals (Figure 3.2). Zircons from the anorthosite dyke are highly fractured and mainly characterized by primary magmatic oscillatory to sector zoning. Few crystals show recrystallized homogeneous texture (Figure 3.3).

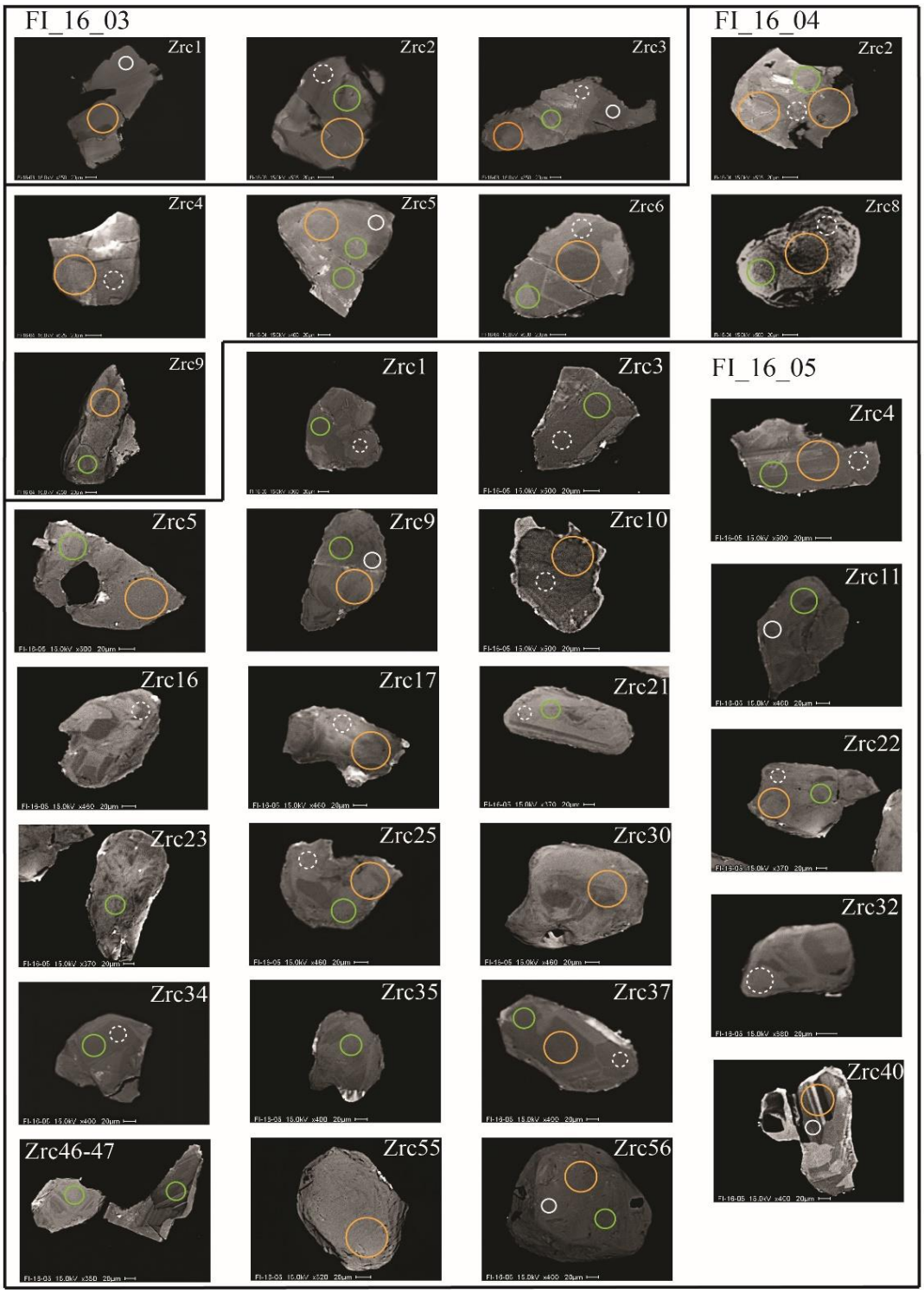

Figure 3.2: CL images showing the internal structures of zircons from the alkaline dioritic dyke samples (FI1603, FI1604 and FI1605) from Finero. Unbroken and broken white circles represent concordant and discordant U-Pb ages spots, respectively; green and orange colored circles are trace element and Hf isotopes analysis spots, respectively. The scale bar (in white) is 20 µm.

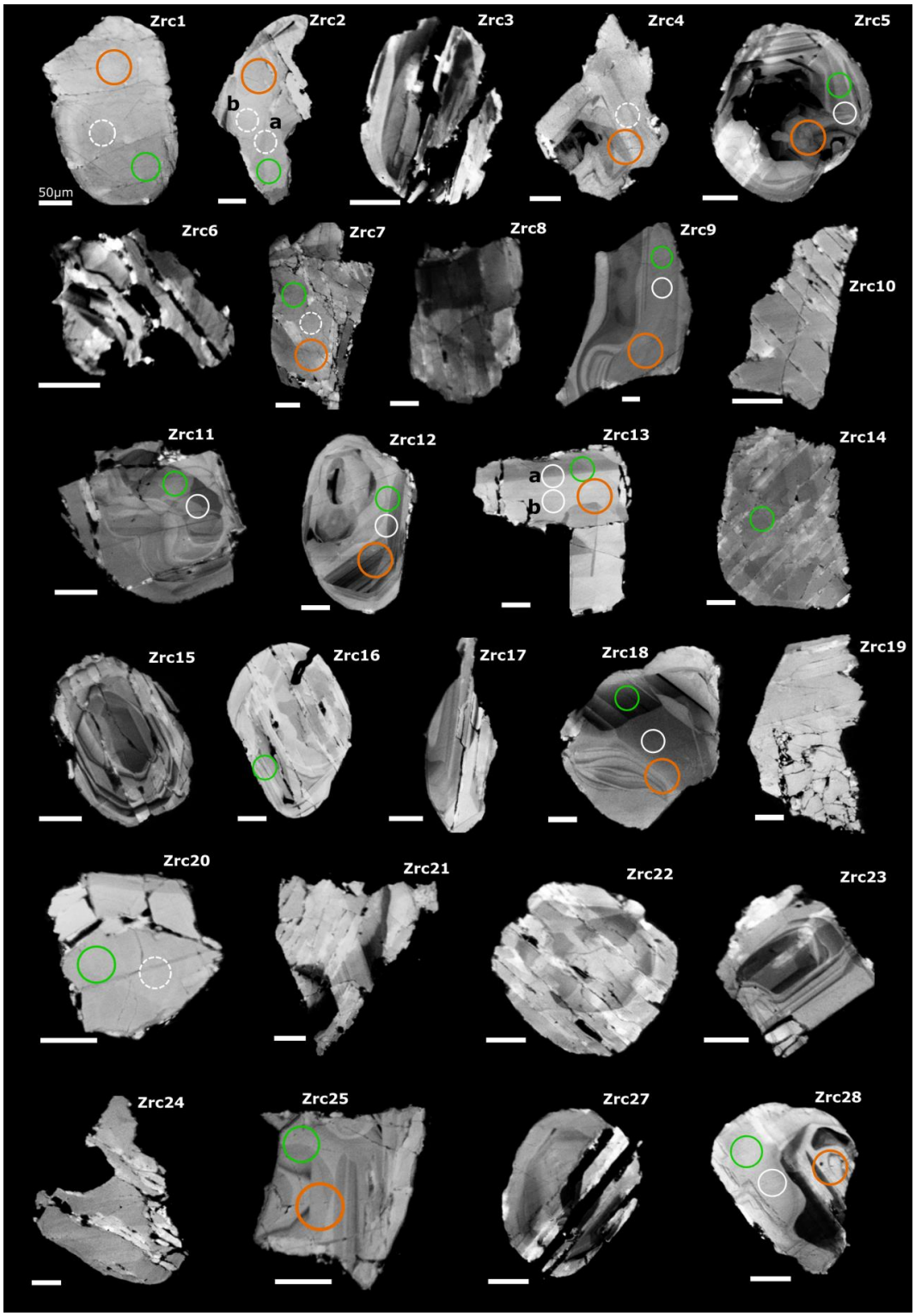

Figure 3.3: CL images showing the internal structures of zircons from the alkaline anorthosite dyke sample (FI19A01) from Finero. Circle colors are the same as in Figure 3.2. The scale bar (in white) is 50 µm.

3.5.2 Zircon trace element composition

Zircons from both dioritic and anorthosite dykes show similar trace element composition characterized by low U, Th, Nb, Ta, Pb and LREE contents. The bright domains show the lowest total trace element and Hf contents (e.g., Zrc 2 of FI1604; total = 5651 ppm, Hf = 3926 ppm). Excluding the bright domains and inherited cores, Hf and Ti contents of the zircon grains varies from 4395 ppm to 7785 ppm and 2.2 ppm to 5.3 ppm, respectively. Nb, Ta and Pb are commonly lower than 2 ppm. Th (16-115 ppm) and U (27-239 ppm) contents and Th/U (0.33-0.83) and U/Yb (0.40-3.37) ratios of the zircons are widely variable.

CI chondrite-normalized (values from Lyubetskaya and Korenaga, 2007) REE patterns of zircons from the studied dykes (Figure 3.4) are characterized by enrichment in HREE, depletion in LREE and positive Ce anomaly. HREE in the zircons are higher compared to the IVZ carbonatite zircons (Galli et al., 2019) but lower with respect to zircons from the corundum-bearing felsic dykes from central IVZ (Bonazzi et al., 2020) and the miaskitic pegmatites from the Finero Complex (Schaltegger et al., 2015).

On the Hf versus Y discrimination diagram (Figure 3.5), zircons from the studied dykes plot mainly in the field of carbonatites, similar to some IVZ carbonatite zircons (Galli et al., 2019). Two zircon grains plot in the field of alkaline rocks approaching the composition of the miaskitic pegmatites from the Finero Complex (Schaltegger et al., 2015).

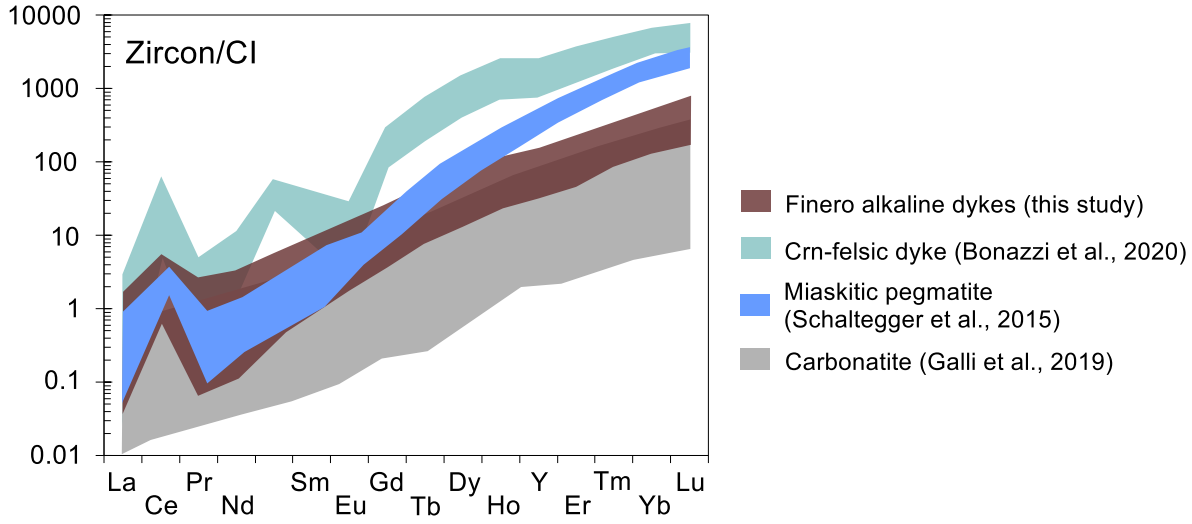

Figure 3.4: CI chondrite-normalized REE patterns of zircons from Finero alkaline dioritic and anorthosite dykes compared to zircons from corundum-bearing felsic dykes, central IVZ (Bonazzi et al., 2020), miaskitic pegmatites, Finero Complex (Schaltegger et al., 2015), and IVZ carbonatites (Galli et al., 2019). CI chondrite values are from Lyubetskaya and Korenaga (2007).

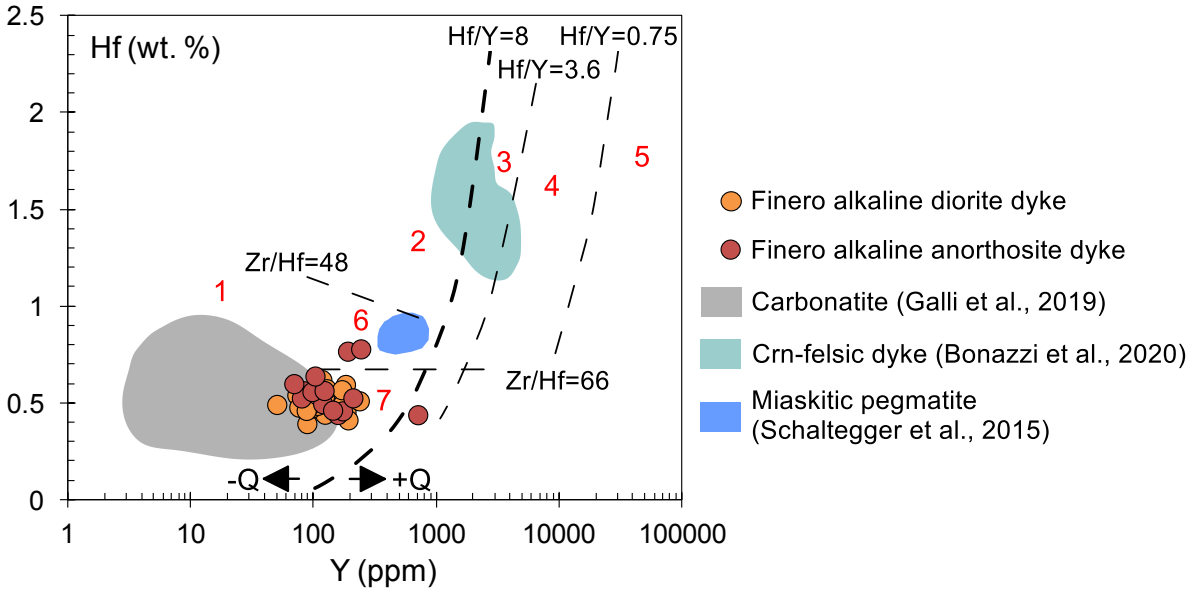

Figure 3.5: Hf (wt. %) versus Y (ppm) discrimination plot for zircons from Finero alkaline dioritic and anorthosite dyke samples compared to zircons from corundum-bearing felsic dykes, central IVZ (Bonazzi et al., 2020), miaskitic pegmatites, Finero Complex (Schaltegger et al., 2015), and IVZ carbonatites (Galli et al., 2019). The fields of zircon composition are defined by Shnukov et al. (1997). 1 – Kimberlites; 2 – Ultramafic, mafic and intermediate rocks; 3 – Quartz-

bearing intermediate and felsic rocks; 4 – Felsic rocks with 'high' SiO_2 content; 5 – Greisens; 6 – Alkaline rocks and alkaline metasomatites of alkaline complexes; 7 – Carbonatites.

3.5.3 Zircon U-Pb geochronology

U-Pb dating of zircons from the three dioritic dyke samples furnished mostly discordant ages with only seven analyses providing concordant ages varying from 216 ± 9 to 192 ± 8 Ma (Late Triassic to Early Jurassic). The other discordant analyses show $^{206}Pb/^{238}U$ ages (223 ± 5 to 184 ± 7 Ma) similar to the age interval defined by the concordant ages. However, owing to the sparse concordant age dataset, no meaningful concordia or weighted mean ages could be estimated for any of these samples.

Zircons from the anorthosite dyke sample provide seven concordant ages from fourteen analyses. The concordant ages vary from 203 ± 13 to 191 ± 10, with concordia and weighted mean age of 198.46 ± 3.30 Ma (Figure 3.6a, b). Notably, most magmatic oscillatory zoned zircons yield concordant ages around ca. 200 Ma. Analysis of an inherited zircon core (Zrc28) from this sample yielded a concordant age of 233 ± 13 Ma.

As a whole, the concordant ages provided by the studied zircons are comparable with previous U-Pb ages reported in the literature for other IVZ alkaline rocks and carbonatites, particularly from the corundum-bearing felsic dykes from central IVZ (224 ± 7 Ma; Bonazzi et al., 2020), nepheline-bearing syenite dykes from FPP (225 ± 13 Ma; Stähle et al., 1990), miaskitic pegmatites from the Finero Complex (212.5–190 Ma; Schaltegger et al., 2015), the IVZ carbonatites (187 ± 2.4 and 192 ± 2.5 Ma; Galli et al., 2019), and some plagioclase-rich dykes from the Finero Mafic Complex (246 ± 12 to 173 ± 6; Munnikhuis, 2020).

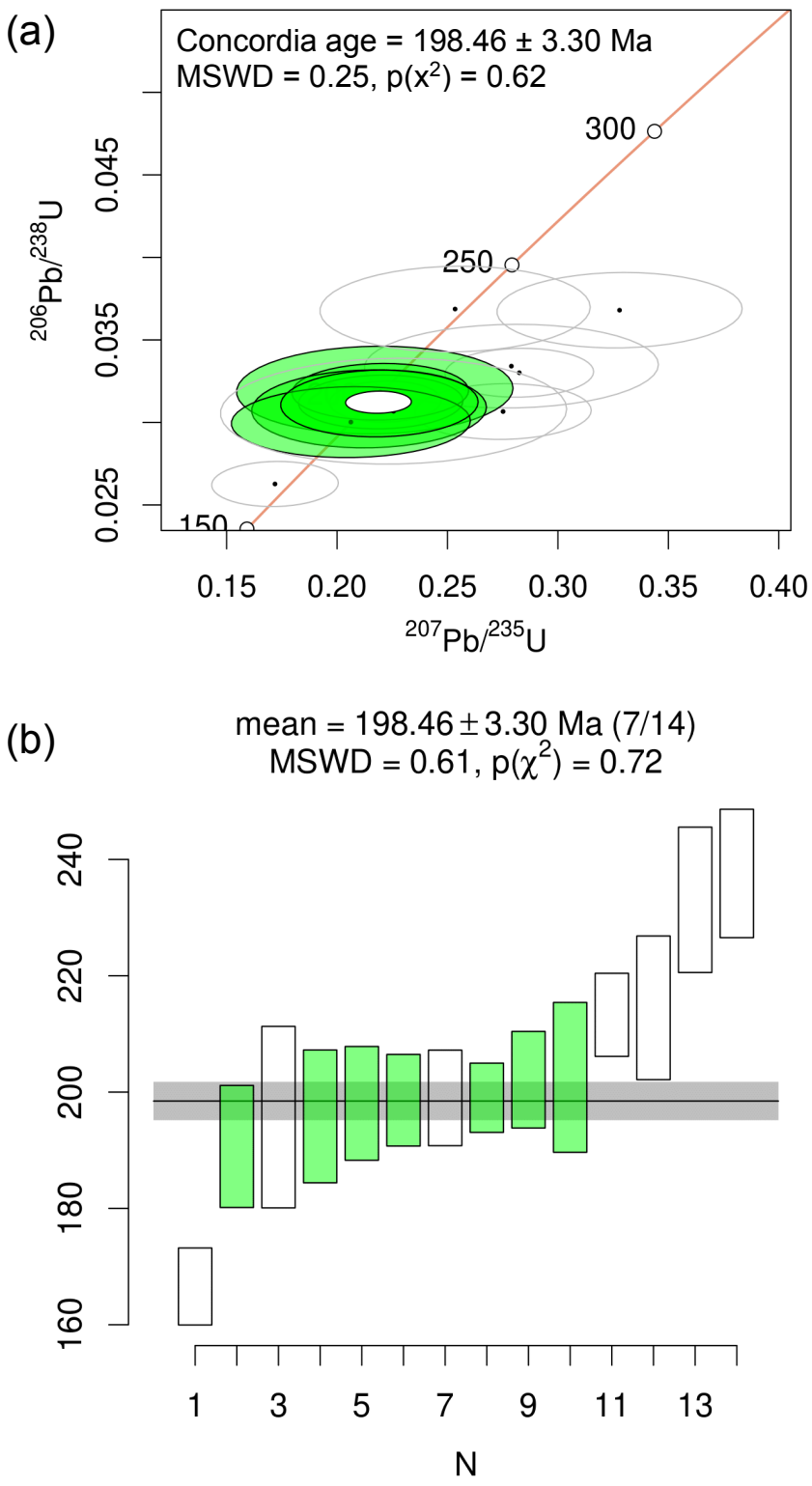

Figure 3.6: (a) Concordia diagram and (b) weighted mean age plot for zircons from Finero anorthosite dyke sample (FI19A01). The abscissa in (b) is in million years (Ma). Errors are quoted at 2σ.

3.5.4 Zircon Hf isotopic composition

The zircons display a bimodal distribution of Hf isotopes with $\varepsilon Hf_{(t)}$ in zircons from the dioritic and anorthositic dykes ranging from +6.2 to +15.4 and –0.4 to +3.6, respectively (Figure 3.7). A similar wide interval in $\varepsilon Hf_{(t)}$ of zircons is also reported for some plagioclase-rich dykes intruding the Finero Mafic Complex ($\varepsilon Hf_{(t)}$ = –0.21 to +8.55; Munnikhuis, 2020).

The high $\varepsilon Hf_{(t)}$ in zircons from the studied dioritic dykes is comparable to $\varepsilon Hf_{(t)}$ values in zircons from the corundum-bearing felsic dykes from central IVZ (+5.6 to +19.5; Bonazzi et al., 2020) and the miaskitic pegmatites from the Finero Complex (+6.4 to +9.8; Schaltegger et al., 2015) (Figure 3.7). Notably, co-existing amphiboles in the dioritic dykes also show comparable $\varepsilon Hf_{(t)}$ values (+5.3 to +7.6; Ogunyele et al., 2024).

On the other hand, the relatively low $\varepsilon Hf_{(t)}$ in zircons from the anorthosite dykes is very similar to the $\varepsilon Hf_{(t)}$ values in zircons from the IVZ carbonatites, particularly from the sample VF33 group 1 (–0.8 to +3.5; Galli et al., 2019) (Figure 3.7).

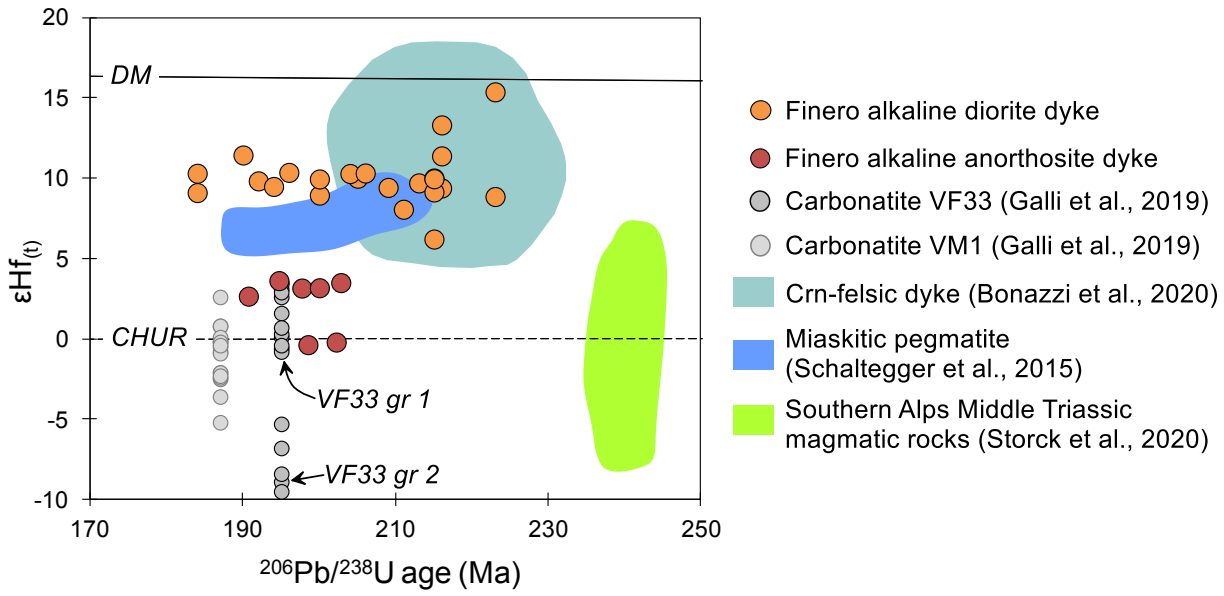

Figure 3.7: Plot of $\varepsilon Hf_{(t)}$ vs single-spot U-Pb ages of zircons from Finero alkaline dioritic and anorthosite dykes compared to zircons from corundum-bearing felsic dykes, central IVZ

(Bonazzi et al., 2020), miaskitic pegmatites, Finero Complex (Schaltegger et al., 2015), IVZ carbonatites (Galli et al., 2019) and the Southern Alps Middle Triassic magmatic and volcano-sedimentary rocks (Storck et al., 2020).

3.6 Discussion

3.6.1 Timeframe of alkaline magmatism in the Ivrea-Verbano Zone, Southern Alps

Zircons from the studied dykes, particularly from the dioritic dykes, provide a wide time interval for the alkaline magmatism of the IVZ ranging from 216 ± 9 to 191 ± 10 Ma (concordant U-Pb ages). This large time frame however does not allow for documenting specific emplacement ages for the alkaline dioritic dykes and may be related to zircon crystallization and recrystallization processes. The intrusion of the studied dykes into the Finero Phlogopite Peridotite (FPP) when it was still at subcontinental mantle levels (P = ~1 GPa, T = ~660-1000 °C; Zanetti et al., 2016; Giovanardi et al., 2020; Ogunyele et al., 2024), coupled with (i) the prolonged residence of the dykes at this high P-T conditions until the Jurassic (~187 Ma; Zanetti et al., 2016) when the FPP was exhumed, and (ii) the repeated injection of volatile-rich alkaline melts into the dykes' conduits (Ogunyele et al., 2024) are very likely to have caused the perturbation of the U–Pb zircon systems from the Late Triassic to Early Jurassic.

Zircons from the anorthosite dykes, on the other hand, provide a concordia age of 198 ± 3 Ma which can be ascribed to an episode of alkaline magmatism in the IVZ. Magmatic oscillatory zoned zircons from the anorthosite as well as from the dioritic dykes yield concordant ages around ca. 200 Ma supporting this assertion. The highly-fractured nature of zircons from the anorthosite dykes attest to the volatile-rich nature of the segregating melts which caused high-pressure brecciation of the dykes and their constituent minerals including zircons. This high-pressure brecciation is however not observed within the host peridotite.

Our U-Pb geochronological data in combination with those from other IVZ alkaline rocks and carbonatites, particularly from the corundum-bearing felsic dykes from central IVZ (224 ± 7 Ma; Bonazzi et al., 2020), nepheline-bearing syenite dykes from FPP (225 ± 13 Ma; Stähle et al., 1990), miaskitic pegmatites from the Finero Complex (212.5–190 Ma; Schaltegger et al., 2015), and the IVZ carbonatites (187 ± 2.4 and 192 ± 2.5 Ma; Galli et al., 2019) suggest the following: (i) the IVZ alkaline magmatism probably occurred over a protracted period of time from around ca. 230–180 Ma; (ii) the magmatism occurred in multiple episodes (see also section 3.6.2); and (iii) the closure of the U-Pb geochronological clocks of zircons from the IVZ alkaline and carbonatitic rocks around 180-190 Ma, similar to the peak age of zircons (~187 Ma; Zanetti et al., 2016) from mantle chromitites in the FPP, provides further evidence for the exhumation of the Finero mantle massif around this time.

The timeframe inferred for the alkaline magmatism in the IVZ (ca. 230–180 Ma) suggest that it is coeval with the alkaline magmatism which produced the alkaline lamprophyre dykes in the Dolomites (ca. 219 Ma; Casetta et al., 2019) and the transitional basaltic dykes in the Brescian Prealps (ca. 217 Ma; Cassinis et al., 2008).

3.6.2 Mantle source characteristics

The trace elements and Hf isotopic signatures of zircons point to mantle sources for the magmas which segregated the studied alkaline dykes. Notably, trace element discrimination of the zircons indicates a carbonatitic to alkaline affinity (Hf vs Y; Figure 3.5). This affinity is supported by the abundance of amphiboles with enrichments in LILEs, REEs and HFSEs in the dykes. Nb-Ta-rich phlogopites and oxides (e.g., columbite) and primary calcite also occur in the

dykes (Ogunyele et al., 2024). However, co-existing zircons show low Nb-Ta contents (< 2 ppm) possibly due to competition for these elements by the Nb-Ta-rich phases.

Hf isotopes in zircon offer important clues into the nature of the mantle sources of the dykes. The high $\varepsilon Hf_{(t)}$ in zircons from the Finero alkaline dioritic dykes (+6.2 to +15.4) coupled with their young T_{DM} ages (209–615 Ma, see Appendix 3.3) suggest a heterogeneous variably depleted asthenospheric mantle source. This is consistent with the depleted Nd, Sr and Hf isotopic composition of co-existing amphiboles in these dykes reported by Ogunyele et al. (2024). A similar depleted asthenospheric source was inferred for the alkaline magmas which segregated the 224 ± 7 Ma corundum-bearing felsic dykes from central IVZ with $\varepsilon Hf_{(t)}$ in zircons from +5.6 to +19.5 (Bonazzi et al., 2020).

The variability in $\varepsilon Hf_{(t)}$ of zircons from the Finero alkaline dioritic dykes may suggest that the upwelling asthenosphere contained and/or interacted with some enriched components. This enrichment is well observed in zircons from the anorthosite dykes which have relatively low $\varepsilon Hf_{(t)}$ (–0.4 to +3.6). The mantle melt(s) which segregated the anorthosites probably contained relatively larger amounts of enriched components compared to the magmas segregating the diorites. Because the mantle-derived melts which segregated the alkaline dykes intruded the host peridotite (FPP) when it was still at mantle levels (Zanetti et al., 2016; Decarlis et al., 2023), we suggest, in agreement with Ogunyele et al. (2024), that the enriched components may be related to recycled crustal components brought to mantle depths by subduction and/or delamination. The partial melting of these deep recycled crustal components and its interaction to different extents with the upwelling depleted asthenosphere can generate the geochemical and isotopic signatures of the Finero alkaline dykes. Another possibility is the interaction of the upwelling asthenosphere with metasomatized lithospheric mantle (Casetta et al., 2019).

The different ranges of $\varepsilon Hf_{(t)}$ recorded by zircons from the dioritic and anorthosite dykes also probably documents at least two episodes of alkaline magmatism in the IVZ: (i) an early episode which generated magmas with high $\varepsilon Hf_{(t)}$ in zircons, starting from around ca. 230 Ma, and (ii) a later episode which produced low $\varepsilon Hf_{(t)}$ in zircons at around ca. 200 Ma.

3.6.3 Geodynamic implications

Geochronological and Hf isotope data from the studied alkaline dykes within the phlogopite peridotite of Finero in combination with available literature data (e.g., Stähle et al., 1990, 2001; Mazzucchelli et al., 2010; Schaltegger et al., 2015; Zanetti et al., 2016; Galli et al., 2019; Bonazzi et al., 2020, Ogunyele et al., 2024) suggest that the IVZ witnessed a protracted period (from Late Triassic to Early Jurassic) during which alkaline magmas derived from upwelling asthenosphere and/or metasomatized deep lithospheric mantle sources were injected into the upper mantle and lower crust. This magmatism occurred in multiple episodes, releasing mantle magmas with variable amounts of recycled crustal components.

The question of when and how the crustal components were recycled into the subcontinental mantle beneath the IVZ and the whole Southern Alps has been extensively argued by several authors (e.g., Zanetti et al., 1999, 2016; Lustrino et al., 2019; Casetta et al., 2021; Bonazzi et al., 2020, De Min et al., 2020; Giovanardi et al., 2020; Ogunyele et al., 2024). In agreement with previous authors, subduction during the Variscan and/or older orogenic cycles coupled with subsequent delamination affecting the thickened orogen in the Variscan realm may have provided the enriched crustal components beneath the Southern Alps. This assertion is supported by the pervasive metasomatism of the FPP by hydrous crustal-contaminated melts starting from the end of the Variscan orogenic cycle (Voshage et al., 1987; Zanetti et al., 1999,

2016; Decarlis et al., 2023). Also, prior to the Late Triassic to Early Jurassic alkaline magmatism, orogenic-like magmatism containing significant amounts of recycled crustal components occurred in the IVZ and throughout the Southern Alps (Lustrino et al., 2019; Giovanardi et al., 2013, 2020; Casetta et al., 2021; De Min et al., 2020; Ogunyele et al., 2024). All these evidences point to the fact that the IVZ and Southern Alps subcontinental mantle contained crustal components over a prolonged period of time, probably since the Variscan or even older times.

Ogunyele et al. (2024) highlighted the importance of the subduction of the Paleotethys in triggering and remobilizing the Variscan-related crustal components in the Southern Alps subcontinental mantle during the Early Mesozoic. They suggest that the Paleotethys subduction may be regarded as the paleotectonic scenario in which the Middle Triassic orogenic-like magmatism which occurred throughout the Southern Alps may have developed. Subsequently, starting from the Late Triassic onwards when the Adriatic lithosphere underwent extreme extension and a profound reorganization of its thermal structure (Beltrando et al., 2015), alkaline magmatism, object of the present study, developed throughout the Southern Alps. This alkaline magmatic cycle occurred in an intraplate setting before the rifting that caused the opening of the Alpine Tethys in the western Mediterranean region (Stälhe et al., 2001; Mazzucchelli et al., 2010; Schaltegger et al., 2015; Galli et al., 2019; Casetta et al., 2019; Bonazzi et al., 2020; Giovanardi et al., 2020; De Min et al., 2020).

3.7 Concluding remarks

Trace elements, U-Pb geochronology and in-situ Hf isotopic study of zircons from alkaline dykes within the phlogopite peridotite of Finero indicate that alkaline magmatism occurred in the Ivrea-Verbano Zone over a prolonged period from the Late Triassic to Early Jurassic (ca. 230–180 Ma). This magmatism occurred in multiple episodes, releasing asthenospheric mantle-derived magmas with variable amounts of recycled crustal components. The IVZ alkaline magmatism is coeval to the Late Triassic alkaline magmatism which occurred in the central and eastern sectors of the Southern Alps and thus belongs to the same geodynamic cycle involving upwelling of the asthenosphere in an intraplate setting prior to the rifting that caused the opening of the Alpine Tethys.

References

Agostini, S., Doglioni, C., Innocenti, F., Manetti, P., Tonarini, S., Savaşçin, M.Y., 2007. The transition from subduction-related to intraplate Neogene magmatism in the Western Anatolia and Aegean area, *in* Beccaluva, L., Bianchini, G., and Wilson, M., eds., Cenozoic Volcanism in the Mediterranean Area. Geol. Soc. Am. Spec. Paper 418, 1–15. https://doi.org/10.1130/2007.2418(01).

Beccaluva, L., Coltorti, M., Saccani, E., Siena, F., Zeda, O., 2005. Triassic magmatism and Jurassic ophiolites at the margins of the Adria Plate, *in* Finetti, I.R., ed., CROP PROJECT: Deep Seismic Exploration of the Central Mediterranean and Italy. Elsevier, pp. 607–618.

Bechstadt, T., Brandner, R., Mostler, H., Schmidt, K., 1977. Aborted rifting in the Triassic of the Eastern and Southern Alps. N. Jb. Geol. Palaont. Abh. 156, 157–178.

Beltrando, M., Stockli, D.F., Decarlis, A., Manatschal, G., 2015. A crustal-scale view at rift localization along the fossil Adriatic margin of the Alpine Tethys preserved in NW Italy. Tectonics 34. https://doi.org/10.1002/2015TC003973.

Bianchini, G., Natali, C., Shibata, T., Yoshikawa, M., 2018. Basic dykes crosscutting the crystalline basement of Valsugana (Italy): new evidence of early Triassic volcanism in the Southern Alps. Tectonics 37.

Blendinger, W., 1985. Middle Triassic strike-slip tectonics and igneous activity of the Dolomites (Southern Alps). Tectonophysics 113, 105–121.

Bonadiman, C., Coltorti, M., Siena, F., 1994. Petrogenesis and T-fO_2 estimates of Mt. Monzoni complex (Central Dolomites, Southern Alps): a Triassic shoshonitic intrusion in a transcurrent geodynamic setting. Eur. J. Mineral. 6, 943–966.

Bonazzi, M., Langone, A., Tumiati, S., Dellarole, E., Mazzucchelli, M., Giovanardi, T., Zanetti, A., 2020. Mantle-derived corundum-bearing felsic dykes may survive only within the lower (refractory/inert) crust: Evidence from zircon geochemistry and geochronology (Ivrea–Verbano Zone, Southern Alps, Italy). Geosciences 10, 281. https://doi.org/10.3390/geosciences10080281.

Brandner, R., Keim, L., 2011. A 4-day geological field trip in the Western Dolomites. Geo. Alp. 8, 76–118.

Casetta, F., Coltorti, M., Marocchino, E. 2018. Petrological evolution of the Middle Triassic Predazzo Intrusive Complex, Italian Alps. Inter. Geol. Rev. 60, 977–97. https://doi.org/10.1080/00206814.2017.1363676.

Casetta, F., Ickert, R.B., Mark, D.F., Bonadiman, C., Giacomoni, P.P., Ntaflos, T., Coltorti, M., 2019. The alkaline lamprophyres of the Dolomitic Area (Southern Alps, Italy): markers of the late Triassic change from orogenic-like to anorogenic magmatism. J. Petrol. 60, 1263–1298. https://doi.org/10.1093/petrology/egz031.

Casetta, F., Ickert, R.B., Mark, D.F., Giacomoni, P.P., Bonadiman, C., Ntaflos, T., Zanetti, A., Coltorti, M., 2021. The Variscan subduction inheritance in the Southern Alps Sub-Continental Lithospheric Mantle: Clues from the Middle Triassic shoshonitic magmatism of the Dolomites (NE Italy). Lithos 380-381. https://doi.org/10.1016/j.lithos.2020.105856.

Cassinis, G., Cortesogno, L., Gaggero, L., Perotti, C.R., Buzzi, L., 2008. Permian to Triassic geodynamic and magmatic evolution of the Brescian Prealps (Eastern Lombardy, Italy).

Ital. J. Geosci. 127, 501–518.

Crisci, C.M., Ferrara, G., Mazzuoli, R., Rossi, P.M., 1984. Geochemical and geochronological data on Triassic volcanism of the Southern Alps of Lombardy (Italy): genetic implications. Geol. Rundsch. 73, 279–292.

De Min, A., Velicogna, M., Ziberna, L., Chiaradia, M., Alberti, A., Marzoli, A., 2020. Triassic magmatism in the European Southern Alps as an early phase of Pangea break-up. Geol. Mag. 157, 1–23. https://doi.org/10.1017/S0016756820000084.

Decarlis, A., Zanetti, A., Ogunyele, A.C., Ceriani, A., Tribuzio, R., 2023. The Ivrea-Verbano tectonic evolution: The role of the crust-mantle interactions in rifting localization. Earth-Sci. Rev. 238. https://doi.org/10.1016/j.earscirev.2023.104318.

Deng, H., Kusky, T., Bozurt, E., Chen, C., Wang, L., Dong, Z., Meng, J., 2023. Sr-Nd-Ca isotopic variations of Cenozoic calc-alkaline and alkaline volcanic rocks above a slab tear in Western Anatolia, Turkey. GSA Bull. https://doi.org/10.1130/B36672.1.

Denyszyn, S.W., Fiorentini, M.L., Maas, R., Dering, G., 2018. A bigger tent for CAMP. Geology 46, 823–826. https://doi.org/10.1130/G45050.1.

Doglioni, C., 1987. Tectonics of the Dolomites (Southern Alps, Northern Italy). J. Struct. Geol. 9, 181–193.

Doglioni, C., 1988. Examples of strike-slip tectonics on platform-basin margins. Tectonophysics 156, 293–302.

Galli, A., Grassi, D., Sartori, G., Gianola, O., Burg, J.P., Schmidt, M.W., 2019. Jurassic carbonatite and alkaline magmatism in the Ivrea zone (European Alps) related to the breakup of Pangea. Geology 47, 199-202. https://doi.org/10.1130/G45678.1.

Garzanti, E., 1985. The sandstone memory of the evolution of a Triassic volcanic arc in the Southern Alps, Italy. Sedimentology 32, 423–433.

Giovanardi, T. Lugli, F., 2017 The Hf-INATOR: A free data reduction spreadsheet for Lu/Hf isotope analysis. Earth Sci. Inform. 10, 517–523.

Giovanardi, T., Morishita, T., Zanetti, A., Mazzucchelli, M., Vannucci, R., 2013. Igneous sapphirine as a product of melt-peridotite interactions in the Finero Phlogopite Peridotite

Massif, Western Italian Alps. Eur. J. Miner. 25, 17–31. https://doi.org/10.1127/0935-1221/2013/0025-2251.

Giovanardi, T., Zanetti, A., Dallai, L., Morishita, T., Hémond, C., Mazzucchelli, M., 2020. Evidence of subduction-related components in sapphirine-bearing gabbroic dykes (Finero phlogopite–peridotite): Insights into the source of the Triassic–Jurassic magmatism at the Europe–Africa boundary. Lithos 356–357, 105366. https://doi.org/10.1016/j.lithos.2020.105366.

Grieco, G., Ferrario, A., von Quadt, A., Köppel, V., Mathez, A., 2001. The zircon-bearing chromitites of the phlogopite peridotite of Finero (Ivrea Zone, Southern Alps): evidence and geochronology of a metasomatized mantle slab. J. Petrol. 42, 89–101. https://doi.org/10.1093/petrology/42.1.89.

Griffin, W.L., Powell, W.J., Pearson, N.J., O'Reilly, S.Y., 2008. GLITTER: data reduction software for laser ablation ICPMS. In: Sylvester, P. (Ed.), Laser Ablation ICP–MS in the Earth Sciences: Current Practices and Outstanding Issues. Mineral. Assoc. Canada Short Course Series 40, pp. 308–311.

Handy, M., Franz, L., Heller, F., Janott, B., Zurbriggen, R., 1999. Multistage accretion, orogenic stacking, and exhumation of continental crust (Ivrea crustal section, Italy and Switzerland). Tectonics 18, 1154-1177.

Jackson, S.E., Pearson, N.J., Griffin, W.L., Belousova, E.A., 2004. The application of laser ablation-inductively coupled plasma-mass spectrometry to in situ U–Pb zircon geochronology. Chem. Geol. 211, 47-69. https://doi.org/10.1016/j.chemgeo.2004.06.017.

Langone, A., José, A. P. N., Ji, W. Q., Zanetti, A., Mazzucchelli, M., Tiepolo, M., Giovanardi T., Bonazzi, M. (2017). Ductile–brittle deformation effects on crystal-chemistry and U–Pb ages of magmatic and metasomatic zircons from a dyke of the Finero Mafic Complex (Ivrea–Verbano Zone, Italian Alps). Lithos, 284, 493-511. https://doi.org/10.1016/j.lithos.2017.04.020.

Lustrino, M., Abbas, H., Agostini, S., Caggiati, M., Carminati, E., Gianolla, P., 2019. Origin of Triassic magmatism of the Southern Alps (Italy): Constraints from geochemistry and Sr-Nd-Pb isotopic ratios. Gondwana Res. 75, 218–238.

https://doi.org/10.1016/j.gr.2019.04.011.

Lyubetskaya, T., Korenaga, J., 2007. Chemical composition of Earth's primitive mantle and its variance: 1. Method and results. J. Geophys. Res. Solid Earth 112, B03211. https://doi.org/10.1029/2005JB004223.

Mazzucchelli, M., Zanetti, A., Rivalenti, G., Vannucci, R., Correia, C.T., Tassinari, C.C.G., 2010. Age and geochemistry of mantle peridotites and diorite dykes from the Baldissero body: Insights into the Paleozoic-Mesozoic evolution of the Southern Alps. Lithos 119, 485–500. https://doi.org/10.1016/j.lithos.2010.08.002.

Munnikhuis, J.K., 2020. The metasomatic history of the Finero Mafic Complex, Ivrea-Verbano Zone, Italy: Melt migration, melt-rock interaction, and effects on geochronology. Unpubl. PhD thesis, Macquarie University. 189 p.

Nardini, N., Casetta, F., Ickert, R.B., Mark, D.F., Ntaflos, T., Zanetti, A., Coltorti, M., 2022. From the Middle Triassic Cima Pape complex (Dolomites; Southern Alps) to the feeding systems beneath active volcanoes: Clues from clinopyroxene textural and compositional zoning. J. Volcan. Geotherm. Res. 422. https://doi.org/10.1016/j.jvolgeores.2021.107459.

Ogunyele A.C., Bonazzi M., Giovanardi T., Mazzucchelli M., Salters V.J.M., Decarlis A., Sanfilippo A., Zanetti A., 2024. Transition from orogenic-like to anorogenic magmatism in the Southern Alps during the Early Mesozoic: Evidence from elemental and Nd-Sr-Hf-Pb isotope geochemistry of alkali-rich dykes from the Finero Phlogopite Peridotite, Ivrea–Verbano Zone. Gondwana Res. 129, 201-219.

Pamic, J.J., 1984. Triassic magmatism of the Dinarides in Yugoslavia. Tectonophysics 109, 273–307.

Peressini, G., Quick, J.E., Sinigoi, S., Hofmann, A.W., Fanning, M., 2007. Duration of a large mafic intrusion and heat transfer in the lower crust: a SHRIMP U/Pb zircon study in the Ivrea–Verbano Zone (Western Alps, Italy). J. Petrol. 48, 1185-1218, https://doi.org/10.1093/petrology/egm014.

Schaltegger, U., Ulianov, A., Müntener, O., Ovtcharova, M., Peytcheva, I., Vonlanthen, P., Vennemann, T., Antognini, M., & Girlanda, F. (2015). Megacrystic zircon with planar fractures in miaskite-type nepheline pegmatites formed at high pressures in the lower

crust (Ivrea Zone, southern Alps, Switzerland). Am. Mineral. 100, 83-94. https://doi.org/10.2138/am-2015-4773.

Schmid, S.M., 1993. Ivrea zone and adjacent southern Alpine basement, *in* von Raumer, J.F., and Neubauer, F., eds., Pre-Mesozoic Geology in the Alps. Springer–Verlag, Berlin, 567–583. https://doi.org/10.1007/978-3-642-84640-3_33.

Siena, F., Coltorti, M., 1989. The petrogenesis of a hydrated mafic-ultramafic complex and the role of amphibole fractionation at Finero (Italian Western Alps). Neues Jahrbuch fur Mineralogie, Monatshefte 6, 255-274.

Sláma, J., Košler, J., Condon, D.J., Crowley, J.L., Gerdes, A., Hanchar, J.M., Horstwood, M.S.A., Morris, G.A., Nasdala, L., Norberg, N., Schaltegger, U., Schoene, B., Tubrett, M.N., Whitehouse, M.J., 2008. Plešovice zircon — A new natural reference material for U–Pb and Hf isotopic microanalysis. Chem. Geol. 249, 1-35. https://doi.org/10.1016/j.chemgeo.2007.11.005.

Sloman, L.E., 1989. Triassic shoshonites from the dolomites, northern Italy: alkaline arc rocks in a strike-slip setting. J. Geophys. Res. 94, 4655-4666.

Stähle, V., Frenzel, G., Hess, J.C., Saupé, F., Schmidt, S.T., Schneider, W., 2001. Permian metabasalt and Triassic alkaline dykes in the Northern Ivrea Zone: clues to the post-Variscan geodynamic evolution of the Southern Alps. Schweizerische Mineralogische Petrographische Mitteillungen 81, 1-21.

Stälhe, V., Frenzel, G., Kober, B., Michard, A., Puchelt, H., Schneider, W., 1990. Zircon syenite pegmatites in the Finero peridotite (Ivrea Zone): evidence for a syenite from a mantle source. Earth Planet. Sci. Lett. 101, 196-205. https://doi.org/10.1016/0012-821X(90)90153-O.

Storck, J.-C., Brack, P., Wotzlaw, J.F., Ulmer, P. (2019). Timing and evolution of Middle Triassic magmatism in the Southern Alps (northern Italy). J. Geol. Soc. 176, 253-268. https://doi.org/10.1144/jgs2018-123.

Storck, J.C., Wotzlaw, J.F., Karakas, Ö., Brack, P., Gerdes, A., Ulmer, P., 2020. Hafnium isotopic record of mantle-crust interaction in an evolving continental magmatic system. Earth Planet. Sci. Lett. 535, 116100.

Voshage, H., Hunziker, J.C., Hofmann, A.W., Zingg, A., 1987. A Nd and Sr isotopic study of the Ivrea zone, Southern Alps, N-Italy. Contrib. Mineral. Petrol. 97, 31-42. https://doi.org/10.1007/BF00375212.

Wiedenbeck, M., Alle, P., Corfu, F., Griffin, W.L., Meier, M., Oberli, F., von Quadt, A., Roddick, J.C., Spiegel, W., 1995. Three natural zircon standards for U-Th-Pb, Lu–Hf, trace elements ad REE analyses. Geostandards Newsletter 19, 1-23.

Zanetti, A., Giovanardi, T., Langone, A., Tiepolo, M., Wu, F.Y., Dallai, L., Mazzucchelli, M., 2016. Origin and age of zircon-bearing chromitite layers from the Finero phlogopite peridotite (Ivrea–Verbano Zone, Western Alps) and geodynamic consequences. Lithos, 262, 58-74. https://doi.org/10.1016/j.lithos.2016.06.015.

Zanetti, A., Mazzucchelli, M., Rivalenti, G., Vannucci, R., 1999. The Finero phlogopite–peridotite massif: an example of subduction-related metasomatism. Contrib. Mineral. Petrol. 134, 107-122. https://doi.org/10.1007/s004100050472.

Zanetti, A., Mazzucchelli, M., Sinigoi, S., Giovanardi, T., Peressini, G., Fanning, M., 2013. SHRIMP U-Pb zircon Triassic intrusion age of the Finero mafic complex (Ivrea–Verbano Zone, Western Alps) and its geodynamic implications. J. Petrol. 54, 2235-2265. https://doi.org/10.1093/petrology/egt046.

CHAPTER 4

On the Middle Triassic high-K calc-alkaline to shoshonitic magmatism in the Dolomites, Southern Alps: Trace elements and Nd-Sr-Hf-Pb isotopic constraints on the nature of crustal components in the Southern Alps subcontinental lithospheric mantle

Abimbola C. Ogunyele[1,2], Alberto Zanetti[2], Mattia Bonazzi[2], Angelo De Min[3], Andrea Marzoli[4], Paolo Nimis[5], Guido Roghi[6], Alessio Sanfilippo[1,2], Vincent J.M. Salters[7]

[1] Department of Earth and Environmental Sciences, University of Pavia, Via Ferrata 1, 27100 Pavia, Italy

[2] CNR – Istituto Geoscienze e Georisorse, Via Ferrata 1, 27100 Pavia, Italy

[3] Department of Mathematics and Geosciences, University of Trieste, Via Weiss 8, 34128 Trieste, Italy

[4] Department of Land, Environment, Agriculture and Forestry, University of Padova, Viale Dell'Universita 16, 35020 Legnaro, Italy

[5] Department of Geosciences, University of Padova, Via Gradenigo 6, 35131 Padova, Italy

[6] CNR – Istituto Geoscienze e Georisorse, Via Gradenigo 6, 35131 Padova, Italy

[7] National High Magnetic Field Laboratory, Department of Earth, Ocean and Atmospheric Sciences, Florida State University, Tallahassee, FL 32310, USA

Declaration

This manuscript is in preparation for submission to a journal for peer-review and possible publication. The study was conducted in collaboration with the co-authors cited above. The contribution of each author is given below.

ACO: Data curation, Formal analysis, Investigation, Methodology, Validation, Visualization, Writing - original draft, Writing - review & editing; **AZ**: Conceptualization, Funding acquisition, Methodology, Project administration, Resources, Supervision, Validation, Visualization, Writing - review & editing; **MB**: Formal analysis, Investigation, Methodology; **AD**: Investigation, Resources; **AM**: Investigation, Resources; Visualization; **PN**: Investigation, Resources; **GR**: Investigation, Resources; **AS**: Supervision, Resources; Writing - review & editing; **VJMS**: Funding acquisition, Methodology, Investigation, Resources, Supervision.

Abstract

Some of the world's most classical outcrops of high-K calc-alkaline to shoshonitic magmatic and volcanic rocks are found in the Dolomitic area in the eastern sector of the Southern Alps. The timing of this magmatism in the Dolomites between the Variscan subduction and the opening of the Alpine Tethys makes it an important window into understanding lithospheric processes and crust-mantle geodynamics. We here present new mineral chemical, whole-rock trace elements and radiogenic isotopes (Nd-Sr-Hf-Pb) dataset on a suite of Middle Triassic high-K calc-alkaline to shoshonitic lavas and dykes from the western part of the Dolomites. We show that the "crust-like" isotopic and trace element signatures exhibited by the studied rocks is related to their magmas derivation from heterogeneous mantle sources containing variable amounts of recycled continental and oceanic crustal materials. Similar geochemical and isotopic signatures are shown by a suite of HFSE-poor calc-alkaline dykes from the Ivrea-Verbano Zone suggesting that the Middle Triassic magmatism in the Dolomites and the Ivrea-Verbano Zone are related. The enrichment of the subcontinental lithospheric mantle sources beneath the Dolomites and the whole Southern Alps is hypothesized to be related to the recycling of crustal materials brought down to mantle depths by the Variscan and/or older subduction events, as well as by delamination of the roots of the Variscan chain.

4.1 Introduction

From a geochemical perspective, magmatic and volcanic rocks with shoshonitic to high-K calc-alkaline affinities usually have "crust-like" radiogenic isotope and trace element signatures (Campbell et al., 2014; Plank, 2014; Lustrino et al., 2019; Casetta et al., 2021). The origin of these "crust-like" signatures and consequently the origin of shoshonitic to high-K calc-alkaline rocks are controversial (Peccerillo, 1992; Conticelli et al., 2009; Peccerillo and Frezzotti, 2015). One of the commonly accepted model of formation of these rocks is the partial melting of mantle sources that had been metasomatically modified by subduction-related fluids/melts (e.g., Foley and Peccerillo, 1992; Jiang et al., 2002; Williams et al., 2004; Plank, 2014; Lustrino et al., 2019; Casetta et al., 2021). The enrichment in large ion lithophile elements (LILEs), light rare earth elements (LREEs) and volatiles, which characterize these rocks, are assumed to have been introduced into their mantle source region by fluids/melts derived from the underlying subducted slab (Campbell et al., 2014). This metasomatic model is also consistent with experimental works (e.g., Wyllie and Sekine, 1982; Meen et al., 1987; Conceição and Green, 2004) which show that shoshonitic and potassic magmas can be formed by low-degree melting of hydrous (phlogopite- and pargasite-bearing) upper mantle lherzolites that had been metasomatically enriched in LILEs and LREEs.

The partial melting of the lower crust underplated by mantle-derived magmas (e.g., Jiang et al., 2002; Küster and Harms, 1998) and partial melting of subducted continental crust plus minimal interaction of the generated magma with the overlying mantle (e.g., Campbell et al., 2014) are other models that have been invoked to explain the genesis of shoshonitic rocks particular those of granitic compositions.

High-K calc-alkaline to shoshonitic magmatism occurred in the Dolomites, Southern Alps during the Middle Triassic. This magmatism has been shown to be derived from mantle sources previously modified by subduction-derived materials (e.g., Lustrino et al., 2019; De Min et al., 2020; Casetta et al., 2018, 2021; Nardini et al., 2022). In this study, we conduct a systematic mineral chemical, whole-rock trace elements and radiogenic isotopes (Nd-Sr-Hf-Pb) investigation on a new suite of high-K calc-alkaline to shoshonitic lavas and dykes from the western part of the Dolomites, Southern Alps. The Hf isotopes presented here constitute the first ever dataset reported for the Middle Triassic shoshonitic lavas and dykes from the Southern Alps. Our main objectives are: (i) to further unravel the geochemical signatures and origin of the Middle Triassic magmatism in the Southern Alps, (ii) to constrain the nature and sources of enriched crustal components in the mantle source of the lavas and dykes, and (iii) to correlate the Middle Triassic tectonomagmatic event in the Dolomites with that of the Ivrea-Verbano Zone in the westernmost part of the Southern Alps.

4.2 Middle Triassic magmatism in the Dolomites, Southern Alps

The Dolomites is in the eastern sector of the Southern Alps (Figure 4.1). The Southern Alps, located south of the Periadriatic Line, is part of the Adriatic Plate, a promontory of the African continent (Stampfli et al., 2002). The Southern Alps preserves a complex geological record of the evolution of the Gondwana–Laurussia boundary from the Variscan times when the Pangea supercontinent was assembled up to its break-up in the Late Triassic–Jurassic and subsequent events up to the Alpine collision. The tectono-magmatic events that occurred during the Late Paleozoic to Early Mesozoic period in the area now corresponding to the Southern Alps are particularly complicated. Even though there are abundant volcano-sedimentary sequences

and plutonic complexes formed during these period, their widespread alteration coupled with the ambiguous paleogeographic reconstruction and structural setting of the Southern Alps makes the deciphering of the geodynamic evolution of the region highly controversial and debated (e.g., Lustrino et al., 2019; De Min et al., 2020).

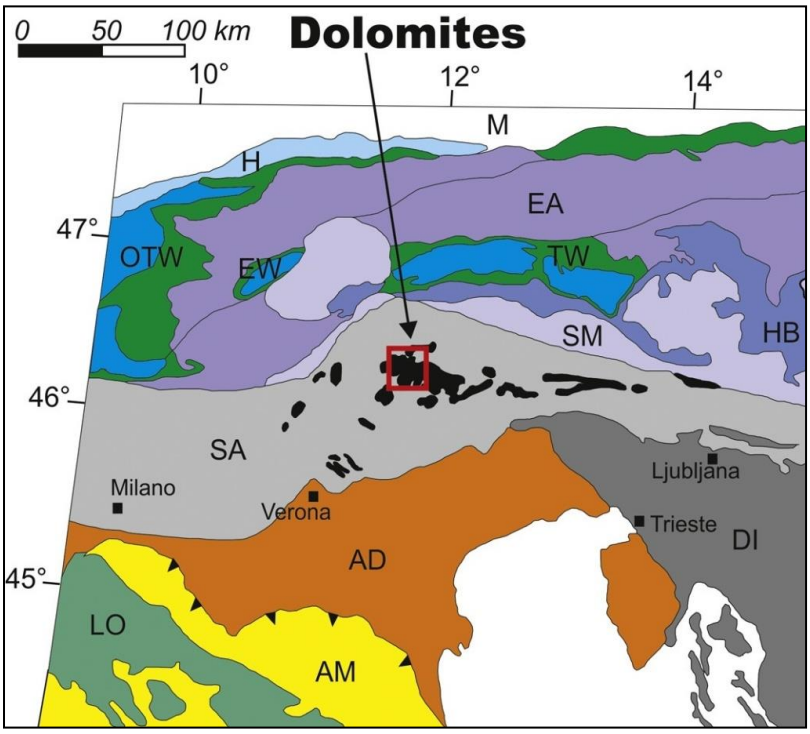

Figure 4.1: (a) Map of the tectonic units of the central to eastern sectors of the Alps showing the location of Dolomites (modified from Schmid et al., 2020; Casetta et al., 2021). SA: Southern Alps; AD: Adriatic Microplate; AM: deformed Adriatic margin; DI: Dinarides; SM: Southern margin of Meliata; LO: Ligurian Ophiolites; HB: Eoalpine High-Pressure Belt; TW: Tauern tectonic Window; EW: Engadine tectonic Window; OTW: Ossola-Tessin tectonic Window; EA: Eastern Austroalpine; H: Helvetic domain; M: Molasse foredeep. The Middle Triassic volcano-plutonic occurrences in the Southern Alps domain are shown in black.

In the Dolomitic area, Late Paleozoic (Early Permian, 300 ± 20 Ma; Massari and Neri, 1997; Brandner and Keim, 2011**)** volcanics and older basement rocks are unconformably overlain by sedimentary sequences of carbonates, evaporites and siliciclastics of Late Permian to

Late Ladinian age (see Lustrino et al., 2019). During the Middle Triassic (ca. 243–237 Ma), the Dolomites and neighboring areas (e.g., eastern Carnia, Karawanken, Julian Alps, Vicentinian Prealps, Dinarides) witnessed large magmatic and effusive events starting with the localized emplacement of small volumes of acid volcanics in the Anisian followed by widespread and voluminous volcanism and magmatism in the Ladinian (Lustrino et al., 2019; Storck et al., 2019, 2020; De Min et al., 2020; Casetta et al., 2021; Velicogna et al., 2022). The Ladinian magmatic event was short lived, lasting for ~5 Ma, from 242.653 ± 0.036 Ma to 237.579 ± 0.052 Ma and reached its peak from 239.04 ± 0.04 to 237.58 ± 0.04 (Mietto et al., 2012; Storck et al., 2019, 2020). The Predazzo and Monzoni intrusives are iconic magmatic complexes formed during the Ladinian (Casetta et al., 2018). Basaltic lavas and dykes coeval to these magmatic complexes are widespread throughout the Dolomitic area, some of which are the subject of the present study. Previous petrological, geochemical and geochronological studies of the Middle Triassic magmatism of the Dolomites area revealed that they are of high-K calc-alkaline to shoshonitic affinity, probably derived from subduction-modified mantle sources (e.g., Lustrino et al., 2019; De Min et al., 2020; Casetta et al., 2018, 2021; Nardini et al., 2022).

The timing of the Middle Triassic magmatism of the Dolomites between the Variscan subduction (~320 Ma) and the opening of the Alpine Tethys (~200–170 Ma) makes it an important window into understanding lithospheric processes and geodynamic evolution of the region (Sloman, 1989; Stampfli et al., 2013; Kroner and Romer, 2014; De Min et al., 2020; Casetta et al., 2018, 2021). Notwithstanding the increased interest and research into the Middle Triassic magmatism of the Dolomites, consensus on the geodynamic framework of the area is still lacking. Even though the geochemical signature of the Middle Triassic magmatism points to an orogenic-like/subduction-related affinity, structural geological studies (e.g., Doglioni, 1992,

2007; Gianolla et al., 1998; Abbas et al., 2018) points to dominantly strike-slip to extensional tectonic regime during this period. Several geodynamic models have therefore been put forward to reconcile these contrasting geological evidences and to possibly explain the tectonic framework of the region. These models include: (i) aborted continental rifting associated with Alpine Tethys opening **(**Bechstadt et al., 1977); (ii) inheritance of ancient subduction signatures, probably of Variscan age, coupled with assimilation of upper crustal rocks **(**Bonadiman et al., 1994; Lustrino et al., 2019; De Min et al., 2020; Casetta et al., 2018, 2021); (iii) sinistral strike-slip tectonics (Doglioni, 1987, 1988); (iv) Active arc/back-arc development following NNW subduction of Paleotethys oceanic lithosphere beneath the south-eastern European paleo-margin (Cassinis et al., 2008); **(**v) subduction of small Permian back-arc oceanic basins (Zanetti et al., 2013); (vi) subduction of a Paleozoic oceanic basin located between Austroalpine and Southern Alps (Bianchini et al., 2018); and (vii) Intra-Pangea dextral mega-shear system with lithosphere-scale extension enabling hybridization between mantle melts and lower crust lithologies (Brandner and Keim, 2011).

4.3 Analytical methods

Fresh and representative samples of basaltic lavas and dykes were collected from Val Giumela and Latemar in the western part of the Dolomites for detailed petrographic and geochemical characterization. Petrographic investigation was performed using polarized light microscope at the Department of Earth and Environmental Sciences, University of Pavia. The major element composition of mineral phases (i.e., clinopyroxene and plagioclase) in the samples were measured by electronprobe microanalysis using a JEOL JXA-8200 Superprobe equipped with five WDS spectrometers operating in wavelength dispersive mode at the Department of Earth Sciences, University of Milan following the methods described in Ogunyele

et al. (2024). The dataset of the major element composition of mineral phases from the investigated samples are reported in Appendix 4.1.

The trace element content of mineral phases was determined in thin sections at the CNR-IGG Pavia using an Agilent 8900 QQQ-ICP-MS coupled to a 266 nm Nd:YAG laser ablation system (Quentel^{TM}). The ICP-MS was tuned using NIST SRM 610 synthetic glass to optimize the signal intensity and stability, and remove molecular interferences by monitoring ^{24}Mg, ^{115}In, ^{238}U and ^{232}Th/^{248}ThO ratio. Operating condition of the laser are repetition rate of 10 Hz, fluence of 10 J/cm^2 and spot size of 50 μm. The data reduction was done with the GLITTER software (Griffin et al., 2008). NIST SRM 610 was used as an external standard; ^{44}Ca was used as an internal standard for clinopyroxene; and ^{29}Si for plagioclase. USGS reference sample BCR2g was repeatedly analyzed with the unknowns to assess precision and accuracy at ±5% and ±10%, respectively. The mineral trace elements dataset is reported in Appendix 4.2.

Trace element analysis of whole-rock samples was performed on glass prepared from pulverized rock powder mixed with lithium metaborate/tetraborate. The mixture was melted at ~900-1000 °C to make the glass using a perlatrice at the CNR-IGG Pavia. The analysis of the glasses for trace elements follow the method described above for mineral phases. NIST SRM 610 was used as an external standard and ^{29}Si was used as an internal standard. The SiO_2 contents (~50-55 wt. %) of similar basaltic lavas and dykes from the Dolomites (e.g., De Min et al., 2020) was used for the data reduction. Owing to the freshness of all studied samples, Loss on Ignition (LOI) was estimated to be less than 2 wt. %. The whole-rock trace elements dataset is reported in Appendix 4.3.

Whole-rock Nd, Sr, Hf and Pb isotopic measurements were performed at the National High Magnetic Field Laboratory, Florida State University. For each sample, about 100 mg of

pulverized rock powder was leached, dissolved and processed through ion exchange columns. The powder was leached in 5 ml 2.5N HCl and <30% H_2O_2 for 60 minutes at room temperature to remove any alteration products. The leached sample was rinsed several times with quartz sub-boiling distilled water. Subsequent dissolution and column chemistry was performed after procedures described by Stracke et al. (2003) and Woelki et al. (2023). Sr isotope compositions were measured by thermal ionization mass spectrometry (TIMS) using a Finnigan MAT 262 RPQ system. Measurements of the Eimer & Amend (E&A) $SrCO_3$ standard provided a $^{87}Sr/^{86}Sr$ ratio of 0.708010 ± 0.000010 (2σ, n = 3). The $^{87}Sr/^{86}Sr$ ratios are corrected for mass bias using a $^{88}Sr/^{86}Sr$ value of 0.1194 and reported relative to the E&A $SrCO_3$ standard value of $^{87}Sr/^{86}Sr$ = 0.708000. Blanks for Sr were less than 100 pg. Nd, Hf and Pb isotopes were measured using a ThermoFisher Neptune Multi-Collector ICP-MS system. Repeated measurements of the La Jolla standard yielded $^{143}Nd/^{144}Nd$ ratio of 0.511790 ± 0.000012 (2σ, n = 17). The $^{143}Nd/^{144}Nd$ ratios are corrected for mass bias using a $^{146}Nd/^{144}Nd$ ratio of 0.7219 and are reported relative to the La Jolla standard of 0.511850. Blanks for Nd were less than 10 pg. Measured value of the JMC-475 standard is $^{176}Hf/^{177}Hf$ = 0.282150 ± 0.000008 (2σ, n = 20). The $^{176}Hf/^{177}Hf$ ratios are corrected for mass bias using a $^{179}Hf/^{177}Hf$ ratio of 0.7325 and reported relative to JMC-475 value of $^{176}Hf/^{177}Hf$ = 0.282150. Blanks for Hf were less than 40 pg. Ten measurements of NBS 981 provided $^{206}Pb/^{204}Pb$, $^{207}Pb/^{204}Pb$, and $^{208}Pb/^{204}Pb$ ratios and 2σ of 16.9332 ± 0.0073, 15.4847 ± 0.0121, and 36.6744 ± 0.0434, respectively. The measured Pb isotopes were normalized to NBS 981 $^{206}Pb/^{204}Pb$, $^{207}Pb/^{204}Pb$, and $^{208}Pb/^{204}Pb$ ratios of 16.9356, 15.4891, and 36.7006, respectively. Blanks for Pb were less than 30 pg. $^{87}Rb/^{86}Sr$, $^{147}Sm/^{144}Nd$, $^{176}Lu/^{177}Hf$, $^{238}U/^{204}Pb$, $^{235}U/^{204}Pb$ and $^{232}Th/^{204}Pb$ ratios were calculated from the Rb, Sr, Sm, Nd, Lu, Hf, Pb, U and Th

concentrations measured on whole-rock samples by LA-ICP-MS. The isotopes dataset are reported in Appendix 4.4.

4.4 Analytical results

4.4.1 Petrography and mineral major element chemistry

Lavas occurring as flows, columns and pillows in Val Giumela and Latemar are some of the freshest volcanic products outcropping in the Dolomites (Figure 4.2a). They exhibit holocrystalline, porphyritic to glomerophyric textures and are composed of phenocrysts of clinopyroxene, plagioclase, olivine (usually altered) and subordinate oxides within a fine-grained, acicular groundmass of similar minerals (Figure 4.2c-d). The porphyricity index (PI) of the lavas is variable from 45 to 60%. Clinopyroxene, constituting about 30-40 vol. % of the lava samples, occurs as large euhedral prismatic phenocrysts (up to 5 mm in size), sometimes zoned, and often forming glomerophyric aggregates with plagioclase and oxides (Figure 4.2d, f). The clinopyroxenes are mainly augitic in composition (Figure 4.3a), except for a crystal preserving a diopsidic composition in the core (Figure 4.2f). Although they sometimes show core-to-rim zonation under the microscope, most clinopyroxene crystals show no significant systematic variation in major element contents from core to rim. Except for the crystal with a diopside core, the clinopyroxenes from Val Giumela and Latemar lava samples exhibit Mg# from 69.8 to 77.7, Al_2O_3 from 2.0 to 5.3 wt. % and TiO_2 between 0.3 and 1.2 wt. % (Figure 4.3b-c). This composition is similar to those reported for Middle Triassic lavas from other areas of the Dolomites (e.g., Lustrino et al., 2019; De Min et al., 2020; Casetta et al., 2021; Nardini et al., 2022). The composition of the crystal with diopside core show relatively higher Mg# (86.6) and lower Al_2O_3 (1.56 wt. %) and TiO_2 (0.19 wt. %), closely resembling those of clinopyroxenes

from the clinopyroxenite cumulates from Latemar (Figure 4.3a-c; Casetta et al., 2021). Plagioclase constitutes about 20–30 vol. % of the lava samples and is tabular, large-sized (up to 3 mm), strongly zoned, and bytownitic in composition (An_{76}–An_{90}; Figure 4.3d) without variation between core and rim. Olivine altered to iddingsite, and Fe-oxides (magnetite) occurring as inclusions within clinopyroxene constitute less abundant phenocrysts within the lava samples.

Dykes from Val Giumela and Latemar are similar in mineralogy, textures, porphyricity index and mineral chemistry to the lavas they crosscut (Figures 4.2b, 4.2e, 4.3a-d). Similar to the lavas, they are porphyritic in textures with large crystals of clinopyroxene, plagioclase, olivine (usually altered) and oxides embedded within a matrix of similar minerals. The major element composition of clinopyroxene (Mg#: 68.6–75.3) and plagioclase (An_{80}–An_{89}) from the dykes are also consistent with those from the lavas. However, compared to the diopsidic clinopyroxenes from the Late Triassic lamprophyres from Predazzo (ca. 219 Ma, Casetta et al., 2019), the investigated lavas and dykes show markedly lower Al_2O_3 and TiO_2 contents (Figure 4.3a-c).

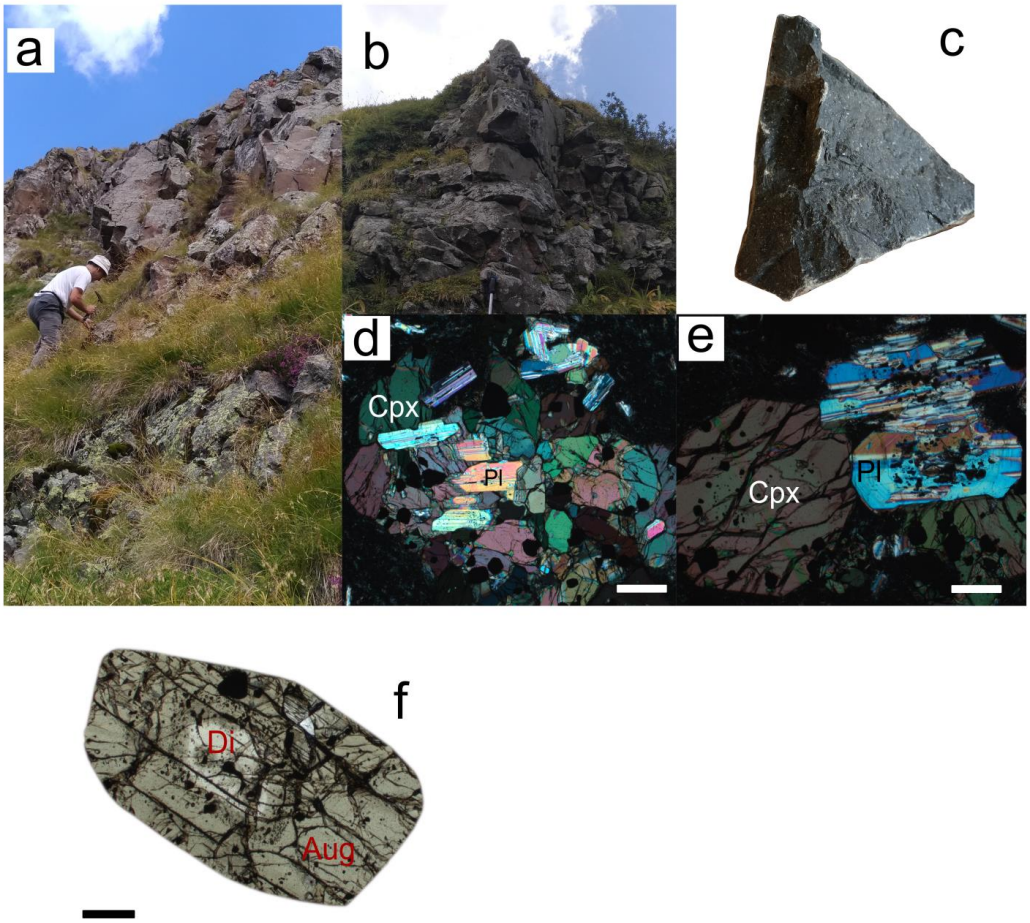

Figure 4.2: Outcrops of (a) basaltic lava flow and (b) basaltic dykes in Val Giumela, Dolomites. (c) Fresh hand specimen of basaltic lava with phenocrysts of clinopyroxene, plagioclase and olivine. Photomicrographs of (d) basaltic lava and (e) dyke samples showing porphyritic to glomerophyric textures comprising phenocrysts of clinopyroxene, plagioclase, altered olivine and oxides in a microlitic matrix of similar minerals; and (f) zoned clinopyroxene crystal with a diopside core and Al-rich augite rim from a basaltic lava. The bars in (d, e, f) represent 500 µm.

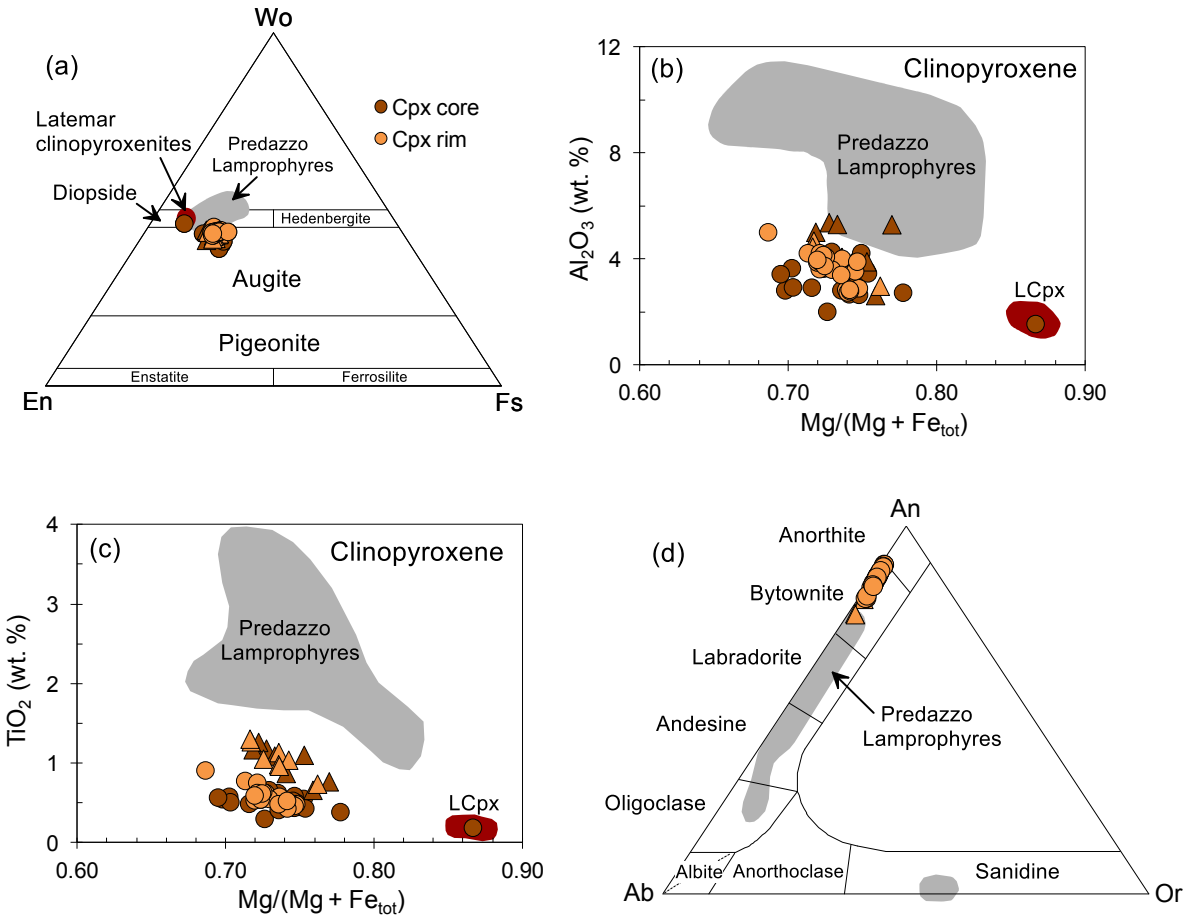

Figure 4.3: (a) Wollastonite (Wo) – Enstatite (En) – Ferrosilite (Fs) classification diagram (Morimoto, 1988); (b) Al_2O_3 (wt. %) vs Mg#; and (c) TiO_2 (wt. %) vs Mg# discrimination diagrams for clinopyroxene in Val Giumela (circle) and Latemar (triangle) lavas and dykes. In (a-c), the composition of clinopyroxenes from Latemar clinopyroxenite cumulates (LCpx; Casetta et al., 2021) and Predazzo lamprophyres (Casetta et al., 2019) are plotted for comparison. (d) Anorthite (An) – Albite (Ab) – Orthoclase (Or) classification diagram for plagioclase in the studied samples compared to feldspars from Predazzo lamprophyres (Casetta et al., 2019).

4.4.2 Mineral trace element chemistry

The trace element composition of clinopyroxene and plagioclase from the Val Giumela and Latemar lava and dyke samples are similar. The Primitive Mantle (PM)-normalized plot of clinopyroxene (Figure 4.4a) displays enrichment in REE, strong depletion in Ba, Nb, Ta, Cs, Rb, Th, U and Pb, and relatively weak negative anomaly in Zr, Hf and Ti. The REE show a convex-upward pattern in CI chondrite-normalized diagram characterized by MREE-enrichment relative to LREE (La_N/Sm_N=0.3–0.6) and HREE (Sm_N/Yb_N=2–4; La_N/Yb_N=0.6–1.7) and a weak negative Eu (Eu_N/Eu_N*=0.7–1) anomaly (Figure 4.4b). The PM- and CI chondrite-normalized patterns of the clinopyroxene from the studied lavas and dykes are similar to those of the Latemar clinopyroxenite cumulates and Predazzo lamprophyres, but different in absolute abundances with the latter having the highest contents (Figure 4.4a-b). Plagioclase from studied lavas and dykes show typical enrichment in L-MREE, depletion in HREE and positive Eu (Eu_N/Eu^*_N=5–29) anomaly.

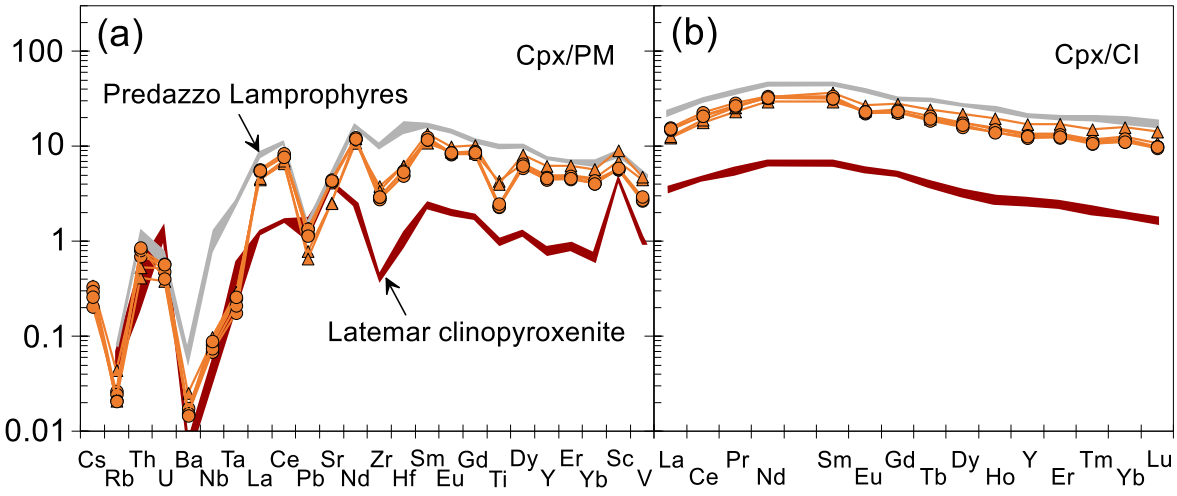

Figure 4.4: (a) PM-normalized incompatible trace elements and (b) CI chondrite-normalized REE patterns of clinopyroxene from Val Giumela (circle) and Latemar (triangle) lavas and dykes compared to clinopyroxenes from Latemar clinopyroxenite cumulates (Casetta et al., 2021) and

Predazzo lamprophyres (Casetta et al., 2019). PM and CI chondrite values are from McDonough and Sun (1995) and Lyubetskaya and Korenaga (2007), respectively.

4.4.3 Whole-rock trace element chemistry

Trace element discrimination of the lava and dyke samples from Val Giumela and Latemar indicates that they are basaltic rocks with calc-alkaline to shoshonitic affinity (Figure 4.5a-d). Consistently, in PM-normalized plot (Figure 4.6a), the lavas and dykes display enrichment in LILEs, strong negative anomalies in Nb-Ta, weak negative anomalies in Zr, Hf and Ti, and positive anomalies in Pb. The Latemar samples show slightly lower Th–U compared to the Val Giumela samples. Generally, all the samples show enrichments in LREE relative to M-HREE (La_N/Yb_N=7–13; La_N/Sm_N=2.7–3.5; Figure 4.6b). By comparison, the trace element patterns of the studied lava and dyke samples are similar to those of clinopyroxenite cumulates from Latemar (Casetta et al., 2021), however, the latter are characterized by significantly lower trace element contents except for Pb. The studied lava and dyke samples can also be differentiated from the Late Triassic lamprophyres from Predazzo on the basis of the absence of negative anomalies in the HFSEs (Nb, Ta, Zr, Hf and Ti) in the latter, but they both show similarities in Pb, Ba and REE contents (Figure 4.6a, b; Casetta et al., 2019).

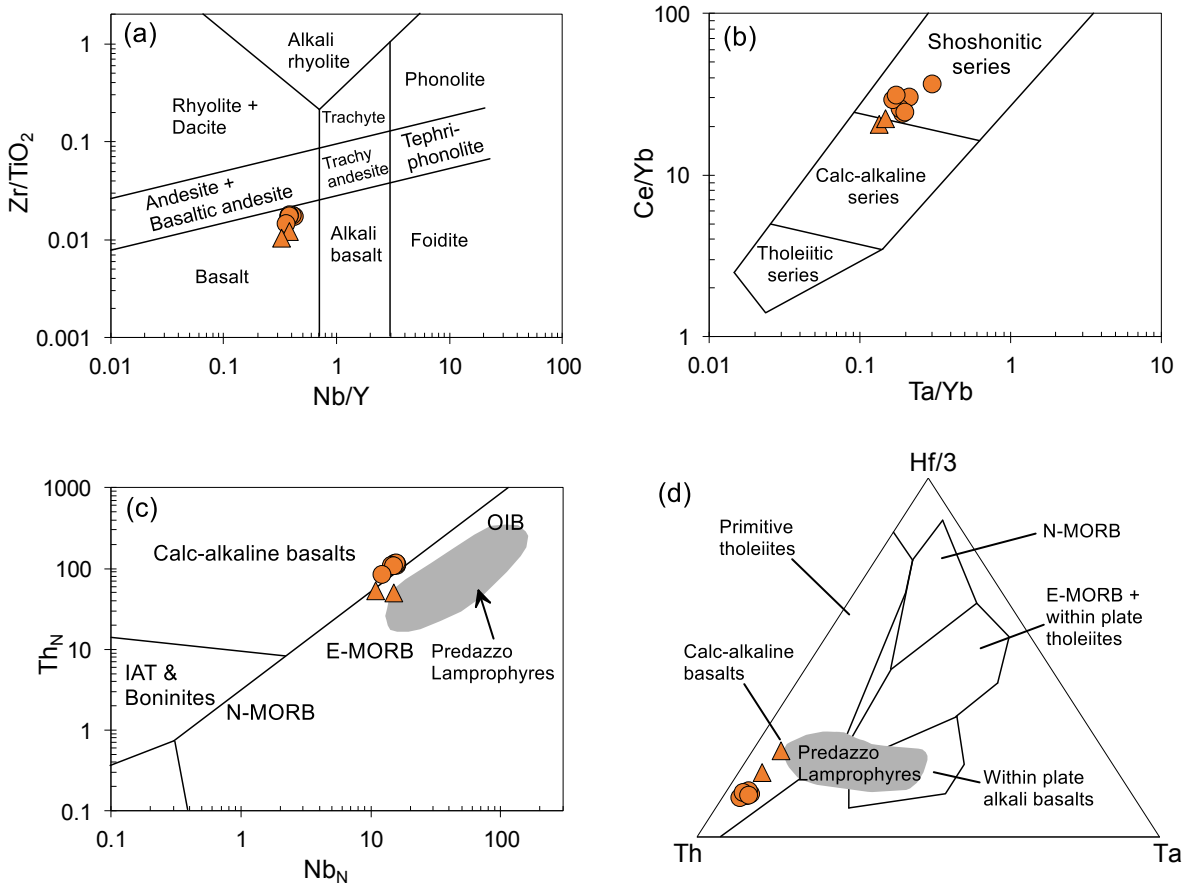

Figure 4.5: Trace element discrimination of the lavas and dykes from Val Giumela (circle) and Latemar (triangle) in comparison with the Late Triassic lamprophyres from Predazzo, Dolomites (Casetta et al., 2019). (a) Zr/TiO_2 vs Nb/Y (Pearce, 1996); (b) Ce/Yb vs Ta/Yb (Pearce, 1982) (c) Th_N vs Nb_N (Saccani, 2015); and (d) Th-Hf-Ta (Wood, 1980) diagrams.

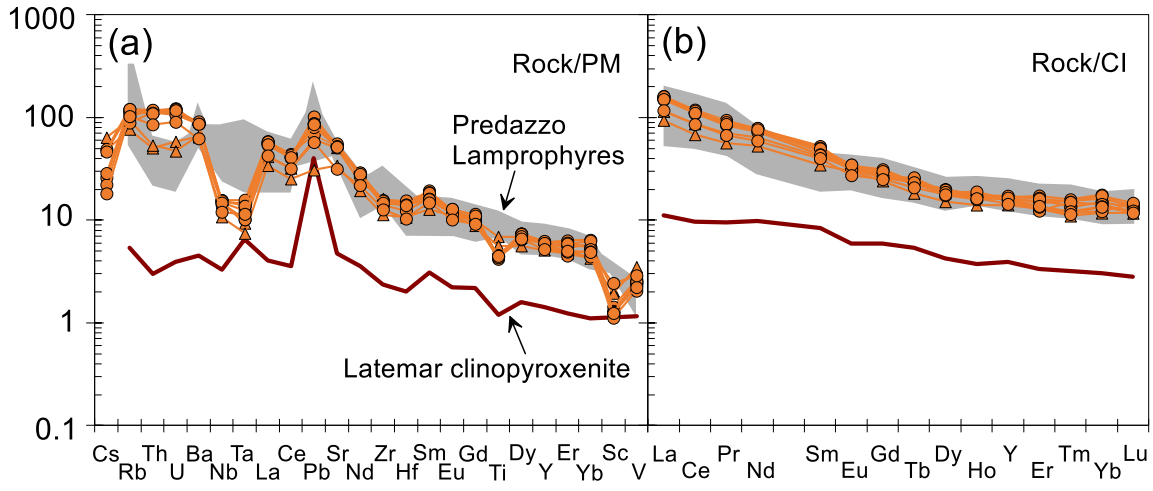

Figure 4.6: (a) PM-normalized incompatible trace elements and (b) CI chondrite-normalized REE patterns of Val Giumela (circle) and Latemar (triangle) lavas and dykes compared to Latemar clinopyroxenite cumulates (Casetta et al., 2021) and Predazzo lamprophyres (Casetta et al., 2019). PM and CI-chondrite values are from McDonough and Sun (1995) and Lyubetskaya and Korenaga (2007), respectively.

4.4.4 Whole-rock Nd-Sr-Hf-Pb isotopic composition

Measured Nd-Sr-Hf-Pb isotopic ratios were corrected to their initial compositions using an age of 238 Ma, based on the U-Pb datings of Storck et al. (2020). The Val Giumela and Latemar lavas and dykes have similar $^{143}Nd/^{144}Nd_{(i)}$ ranging from 0.512212 to 0.512375 ($\varepsilon Nd_{(i)}$: –2.2 to +1.0), clustering around the chondritic uniform reservoir (CHUR) at the same age. Val Giumela lavas and dykes show homogenous $^{87}Sr/^{86}Sr_{(i)}$ ratios (0.704540–0.704655; $\varepsilon Sr_{(i)}$: –0.8 to +0.8) which are in contrast to the Latemar lava (0.704082; $\varepsilon Sr_{(i)}$: –7.3) and dyke (0.706126; $\varepsilon Sr_{(i)}$: +21.7) samples. The samples from both areas also show minor variation in $^{176}Hf/^{177}Hf_{(i)}$ ratios with Val Giumela samples being less radiogenic ($\varepsilon Hf_{(i)}$: –2.1 to –2.8) relative to Latemar samples ($\varepsilon Hf_{(i)}$: +1.4 to +3.8). As a whole, the $\varepsilon Hf_{(i)}$ composition of the whole-rocks fall within the $\varepsilon Hf_{(i)}$ values of zircons (–6.9 to +6.2) from the Southern Alps Middle Triassic magmatic and volcano-sedimentary sequences investigated by Storck et al. (2020).

In terms of Pb isotopic composition, the Latemar dyke sample ($^{206}Pb/^{204}Pb_{(i)}$=18.52; $^{207}Pb/^{204}Pb_{(i)}$=15.65; $^{208}Pb/^{204}Pb_{(i)}$=38.61) is more radiogenic than the Val Giumela lavas and dykes ($^{206}Pb/^{204}Pb_{(i)}$=18.04–18.12; $^{207}Pb/^{204}Pb_{(i)}$=15.62–15.63; $^{208}Pb/^{204}Pb_{(i)}$=38.04–38.12) and the Latemar lava ($^{206}Pb/^{204}Pb_{(i)}$=17.63; $^{207}Pb/^{204}Pb_{(i)}$=15.58; $^{208}Pb/^{204}Pb_{(i)}$=37.28). The highly radiogenic $^{87}Sr/^{86}Sr_{(i)}$ and $^{208}Pb/^{204}Pb_{(i)}$ composition of the studied Latemar dyke is consistent with the ratios earlier reported by Lustrino et al. (2019) for a basaltic dyke from the same area ($^{87}Sr/^{86}Sr_{(i)}$: 0.7058, $\varepsilon Sr_{(230)}$: +22.5; $^{208}Pb/^{204}Pb_{(230)}$=38.89).

On the Nd-Sr isotopic diagram (Figure 4.7a), the Val Giumela and Latemar lavas and dykes plot within the field delimited for the Southern Alps Middle Triassic igneous rocks based on previous studies in the Dolomites area (e.g., Lustrino et al., 2019; De Min et al., 2020; Casetta et al., 2021; Nardini et al., 2022). With the exception of the Latemar dyke, they plot close to the HFSE-poor calc-alkaline dykes intruding the Finero phlogopite peridotite (FPP, Ivrea-Verbano Zone) (Giovanardi et al., 2020; Ogunyele et al., 2024) but far away from the Predazzo alkaline lamprophyres (Casetta et al., 2019) and HFSE-rich alkaline dykes in the FPP (Figure 4.7a; Stähle et al., 2001; Ogunyele et al., 2024). All the studied samples also plot at the end of the oceanic island basalt (OIB) field on the Nd-Hf and Nd-Pb isotopic plots (Figure 4.7b-c), typically clustering around the HFSE-poor calc-alkaline dykes in the FPP (Giovanardi et al., 2020; Ogunyele et al., 2024).

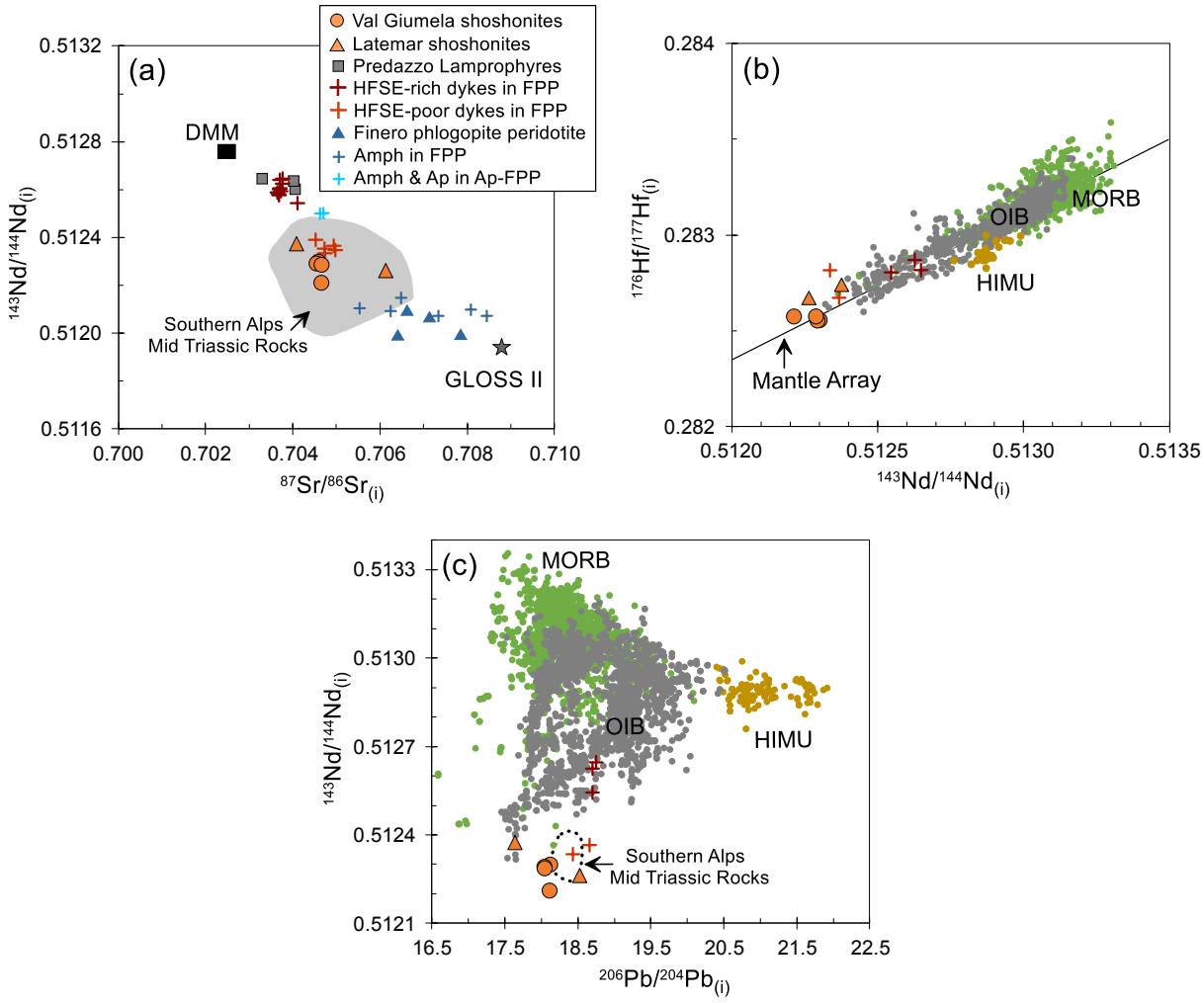

Figure 4.7: Diagrams of (a) $^{87}Sr/^{86}Sr$ vs. $^{143}Nd/^{144}Nd$, (b) $^{143}Nd/^{144}Nd$ vs. $^{176}Hf/^{177}Hf$, and (c) $^{206}Pb/^{204}Pb$ vs $^{143}Nd/^{144}Nd$ (corrected to 238 Ma) for the studied lavas and dyke samples from Val Giumela (circle) and Latemar (triangle) compared to the alkaline lamprophyres from Predazzo, Dolomites (219 Ma; Casetta et al., 2019), Southern Alps Mid-Triassic igneous rocks from Dolomites (230 Ma; Lustrino et al., 2019; De Min et al., 2020; Casetta et al., 2021); HFSE-rich and HFSE-poor dykes from FPP (200-225 Ma; Ogunyele et al., 2024; Giovanardi et al., 2020; Stähle et al., 2001), Finero phlogopite peridotite (FPP, 300 Ma; Voshage et al., 1987), metasomatic amphiboles in the FPP (300 Ma; Obermiller, 1994; Giovanardi et al., 2020), amphibole and apatite from apatite-bearing layers in the FPP (215 Ma; Morishita et al., 2008), modern MORB, OIB and HIMU (Stracke, 2012), DMM (Salters and Stracke, 2004; corrected to 238 Ma), GLOSS-II (average global subducting sediments II; Plank, 2014; corrected to 320 Ma).

4.5 Discussion

4.5.1 Parental melts composition

The high-K calc-alkaline to shoshonitic affinity of the Middle Triassic volcano-plutonic rocks from the Dolomites is well-known and points to derivation from volatile-rich, evolved mantle magmas containing significant amounts of crustal components (e.g., Lustrino et al., 2019; De Min et al., 2020; Casetta et al., 2018, 2021; Nardini et al., 2022). This inference is supported by the unradiogenic Nd–Hf and largely radiogenic Sr and Pb isotopic compositions of the studied lavas and dykes.

Thermobarometric and hygrometric modeling of lavas and dykes from the Dolomitic area using the composition of constituent clinopyroxene also provides some constraints on the nature and water contents of the crystallizing melts and the P-T conditions of crystallization. The modelling estimates of Nardini et al. (2022) for augitic clinopyroxenes with similar Mg# (70-75) to those from the studied lavas and dykes point to their crystallization from a slightly evolved, H_2O-rich (2.6–3.8 wt. %), basaltic trachyandesitic magmas (Mg# = 43–45) at temperatures of 1035–1075 °C and depths of 7–14 km.

4.5.2 Crustal contamination

In order to identify the mantle sources involved in the genesis of the Middle Triassic shoshonitic magmatism of the Dolomites, contamination of the mantle-derived magmas by pre-existing crust during ascent, storage and/or emplacement was evaluated as a preliminary possibility. This interaction or contamination process can result in modification of the elemental and isotopic compositions of the primary magmas. Hence, to test this hypothesis, the relationship between whole-rock elemental and isotopic ratios is useful.

In Figure 4.8, the Val Giumela and Latemar lavas and dykes show a lack of correlation between trace element ratios sensitive to crustal contamination (e.g., Th/Nb and Ce/Pb) and isotopic compositions (such as $^{143}Nd/^{144}Nd$). This feature is also true for samples of Middle Triassic lavas and dykes previously investigated by other authors (Lustrino et al., 2019; De Min et al., 2020; Casetta et al., 2021; Nardini et al., 2022). Instead, all samples define a wide spread in Th/Nb and Ce/Pb. A non-correlation is also observed between Nd-Sr-Pb isotopes versus major oxides and differentiation index (DI) (Lustrino et al., 2019; De Min et al., 2020). This non-correlation between isotopes and elements could therefore suggest that the isotopic variability and crustal signature observed in the Middle Triassic lavas and dykes from the Dolomites are largely related to mantle source heterogeneities rather than to post-melting interaction with upper crustal lithologies (Bianchini et al., 2018; Lustrino et al., 2019; De Min et al., 2020; Casetta et al., 2021).

The Latemar dyke sample with highly radiogenic $^{87}Sr/^{86}Sr_{(i)}$ and Pb isotopic composition may however provide some evidence for minimal post-melting interaction with upper crustal lithologies. The $^{87}Sr/^{86}Sr_{(i)}$ ratio (0.706126) of the dyke approaches the composition of Permian–Triassic carbonate sediments ($^{87}Sr/^{86}Sr_{(i)}$: 0.7072; Korte et al., 2003) which are typical crustal rocks in the Dolomitic area, suggesting a possible interaction between the mantle melts segregating the Latemar dykes and crustal sediments.

In conclusion, we infer, in agreement with previous studies, that crustal contamination by post-melting interaction was not significant enough to obscure the geochemical signatures of the mantle sources during the genesis of the Middle Triassic high-K calc-alkaline to shoshonitic magmatism of the Dolomites.

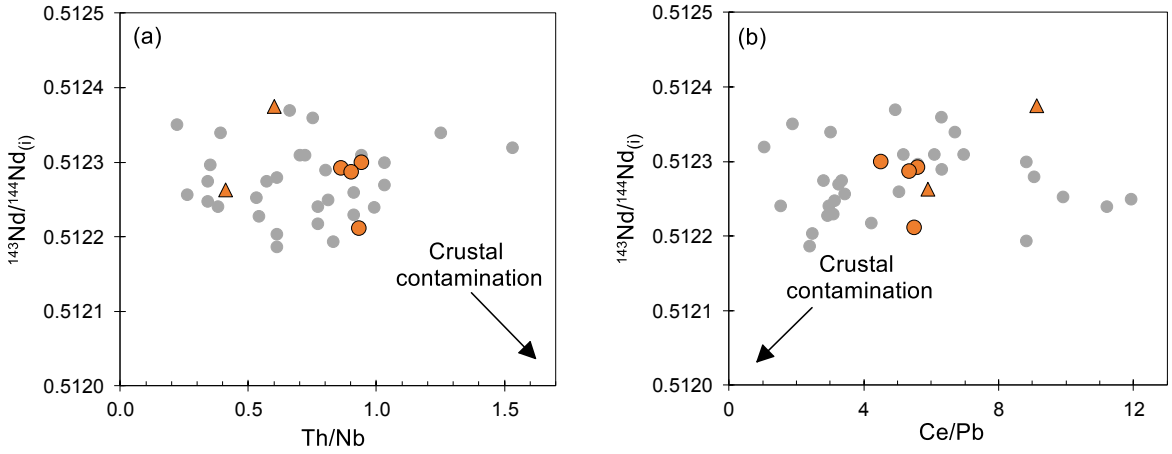

Figure 4.8: Diagrams of $^{143}Nd/^{144}Nd_{(i)}$ vs. (a) Th/Nb and (b) Ce/Pb for the studied lavas and dyke samples from Val Giumela (circle) and Latemar (triangle). The dataset from literature (Lustrino et al., 2019; De Min et al., 2020; Casetta et al., 2021; Nardini et al., 2022) for other Middle Triassic lava and dyke samples (grey circles) from the Dolomitic area are also plotted.

4.5.3 Crustal components in mantle source: oceanic versus continental materials

Trace element discrimination using the Nb/La vs La/Yb diagram (Smith et al., 1999; Figure 4.9a**)** show that the studied lava and dyke samples plot in the lithospheric mantle field. On the Th/Yb vs Ta/Yb diagram (Pearce, 1982; Pearce and Peate, 1995; Figure 4.9b**)**, the samples plot outside of the mantle array, clustering around the global subducting sediments (GLOSS) pointing to a subduction-related affinity. These discrimination plots coupled with the high-K calc-alkaline to shoshonitic affinity of the rocks, their enrichments in LILEs, LREEs, Th, U, and Pb, depletion in HFSEs and HREEs, and lack of significant post-melting contamination strongly indicates that their parental melts were most likely generated from volatile-rich, metasomatised lithospheric mantle sources containing slab-derived and/or delaminated crustal components. This is supported by the Nd, Sr, Hf and Pb isotopic compositions of the studied lavas and dykes distinctly far away from the Depleted Mantle (DM) composition, pointing to an enriched mantle source (Figure 4.7).

The question of whether the crustal materials in the lithospheric mantle source are related to the oceanic or continental crust is tricky. In general, available Nd and Sr isotopic data of all Middle Triassic basaltic lavas and dykes from previous and present study plot towards the EMI-like composition (Lustrino et al., 2019; De Min et al., 2020; Casetta et al., 2021; Nardini et al., 2022). On the other hand, the positive Pb anomaly of the basaltic lavas and dykes and their EMII-like Pb isotopic composition suggest an enrichment in continental or GLOSS components (Bianchini et al., 2018; De Min et al., 2020). Trace element ratios such as Ba/La (15-19.8), Ba/Nb (43.6-61.6) and Ba/Zr (2.5-3.9) of the studied samples similar to those of average continental crust (Ba/La: 22.8, Ba/Nb: 57, Ba/Zr: 3.5); Rudnick and Gao, 2004) lend further support to a mantle source significantly enriched in continental crustal components. These geochemical and isotopic messages are reconciled by relating the Middle Triassic magmatism of the Dolomitic and neighboring areas to heterogeneous mantle sources containing variable amounts of recycled continental and oceanic crustal materials.

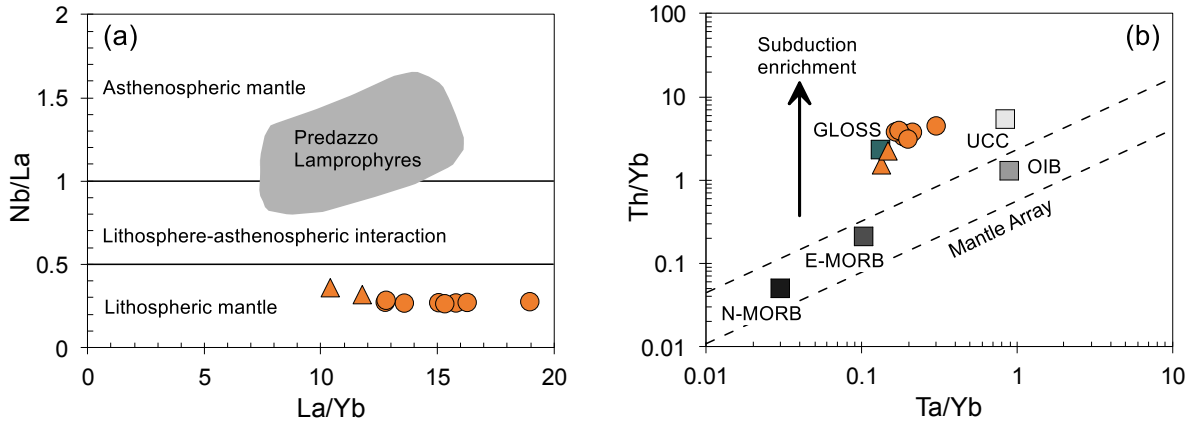

Figure 4.9: (a) Nb/La vs La/Yb (Smith et al., 1999) and (b) Th/Yb vs Ta/Yb (Pearce, 1982; Pearce and Peate, 1995) diagrams for deciphering the mantle source characteristics of the Middle Triassic magmatism of the Dolomitic area.

4.5.4 Possible correlation with Triassic magmatism in the Ivrea-Verbano Zone (western Southern Alps)

The Middle Triassic high-K calc-alkaline to shoshonitic magmatic and volcanic rocks of the Dolomites share similar Nd-Sr-Hf-Pb isotopic and trace elements composition with the HFSE-poor calc-alkaline dykes within the Finero phlogopite peridotite (FPP) in the Ivrea-Verbano Zone (IVZ) investigated by Giovanardi et al. (2013, 2020) and Ogunyele et al. (2024) (Figure 4.7). The absolute age of the Finero HFSE-poor calc-alkaline dykes is presently unknown (due to absence of zircons) but petrographic and geochemical observations suggest they are older than the alkaline dykes which intruded the FPP during the Late Triassic to Early Jurassic. These evidences suggest a possible correlation of the high-K calc-alkaline to shoshonitic rocks of the Dolomitic area with the HFSE-poor calc-alkaline dykes of the IVZ.

Similar to what is inferred for the Dolomitic Middle Triassic magmatism, isotopic composition and trace element modeling indicates that the parental mantle melts of the Finero HFSE-poor calc-alkaline dykes contained large amounts of crustal components. The possibility of contamination of the melts by crustal materials during transport and/or emplacement is also negligible because the dykes intruded the FPP at mantle depths (Ogunyele et al., 2024). This therefore indicates that the Middle Triassic magmatism in both sectors of the Southern Alps was produced by the same mantle sources, relatively enriched in crustal component.

The enrichment of the subcontinental lithospheric mantle sources beneath the Southern Alps is hypothesized to be related to the recycling of crustal materials brought down to mantle depths by the Variscan and/or older subduction events, as well as by delamination of the roots of the Variscan chain (Zanetti et al., 1999, 2013; Mazzucchelli et al., 2010; Giovanardi et al., 2013, 2020; Casetta et al., 2021; Decarlis et al., 2023; Ogunyele et al., 2024). In particular, the

widespread and lasting crustal contamination of the mantle sources beneath the Southern Alps is, as a matter of fact, well-documented by the pervasive metasomatism of the FPP and by the melts erupted in the region from Upper Carboniferous to Triassic (Zanetti et al., 1999, Giovanardi et al., 2020; Casetta et al., 2021; Decarlis et al., 2023).

4.6 Concluding remarks

Mineral chemical, whole-rock trace elements and radiogenic isotopes (Nd-Sr-Hf-Pb) investigation on a new suite of Middle Triassic high-K calc-alkaline to shoshonitic lavas and dykes from the western part of the Dolomites, Southern Alps provide important constraints on the nature and origin of the "crust-like" isotopic and trace element signatures exhibited by these rocks. The origin of the studied rocks is related to magmas derived from heterogeneous mantle sources incorporating variable amounts of different types (continental and oceanic) of recycled crustal materials. A possible correlation of the high-K calc-alkaline to shoshonitic rocks of the Dolomitic area with the HFSE-poor calc-alkaline dykes from the IVZ is also inferred based on similar geochemical and isotopic signatures.

References

Abbas, H., Michail, M., Cifelli, F., Mattei, M., Gianolla, P., Lustrino, M., Carminati, E., 2018. Emplacement modes of the Ladinian plutonic rocks of the Dolomites: insights from anisotropy of magnetic susceptibility. J. Struct. Geol. 113, 42–61.

Bechstadt, T., Brandner, R., Mostler, H., Schmidt, K., 1977. Aborted rifting in the Triassic of the Eastern and Southern Alps. N. Jb. Geol. Palaont. Abh. 156, 157–178.

Bianchini, G., Natali, C., Shibata, T., Yoshikawa, M., 2018. Basic dykes crosscutting the crystalline basement of Valsugana (Italy): new evidence of early Triassic volcanism in the Southern Alps. Tectonics 37.

Bonadiman, C., Coltorti, M., Siena, F., 1994. Petrogenesis and T-fO_2 estimates of Mt. Monzoni complex (Central Dolomites, Southern Alps): a Triassic shoshonitic intrusion in a transcurrent geodynamic setting. Eur. J. Mineral. 6, 943–966.

Brandner, R., Keim, L., 2011. A 4-day geological field trip in the Western Dolomites. Geo. Alp. 8, 76–118.

Campbell, I.H., Stepanov, A.S., Liang, H.-Y., Allen, C.M., Norman, M.D., Zhang, Y.-Q., Xie, Y.-W., 2014. The origin of shoshonites: new insights from the Tertiary high-potassium intrusions of eastern Tibet. Contrib. Mineral. Petrol. 167. https://doi.org/10.1007/s00410-014-0983-9.

Casetta, F., Coltorti, M., Marocchino, E. 2018. Petrological evolution of the Middle Triassic Predazzo Intrusive Complex, Italian Alps. Inter. Geol. Rev. 60, 977–97. https://doi.org/10.1080/00206814.2017.1363676.

Casetta, F., Ickert, R.B., Mark, D.F., Bonadiman, C., Giacomoni, P.P., Ntaflos, T., Coltorti, M., 2019. The alkaline lamprophyres of the Dolomitic Area (Southern Alps, Italy): markers of the late Triassic change from orogenic-like to anorogenic magmatism. J. Petrol. 60, 1263–1298. https://doi.org/10.1093/petrology/egz031.

Casetta, F., Ickert, R.B., Mark, D.F., Giacomoni, P.P., Bonadiman, C., Ntaflos, T., Zanetti, A., Coltorti, M., 2021. The Variscan subduction inheritance in the Southern Alps Sub-Continental Lithospheric Mantle: Clues from the Middle Triassic shoshonitic magmatism of the Dolomites (NE Italy). Lithos 380-381. https://doi.org/10.1016/j.lithos.2020.105856.

Cassinis, G., Cortesogno, L., Gaggero, L., Perotti, C.R., Buzzi, L., 2008. Permian to Triassic geodynamic and magmatic evolution of the Brescian Prealps (Eastern Lombardy, Italy). Ital. J. Geosci. 127, 501–518.

Conceição, R.V., Green, D.H., 2004. Derivation of potassic (shoshonitic) magmas by decompression melting of phlogopite+pargasite lherzolite. Lithos 72, 209–29. https://doi.org/10.1016/j.lithos.2003.09.003.

Conticelli, S., Guarnieri, L., Farinelli, A., Mattei, M., Avanzinelli, R., Bianchini, G., Venturelli, G., 2009. Trace elements and Sr–Nd–Pb isotopes of K-rich, shoshonitic, and calc-alkaline

magmatism of the Western Mediterranean Region: Genesis of ultrapotassic to calc-alkaline magmatic associations in a post-collisional geodynamic setting. Lithos 107, 68–92.

De Min, A., Velicogna, M., Ziberna, L., Chiaradia, M., Alberti, A., Marzoli, A., 2020. Triassic magmatism in the European Southern Alps as an early phase of Pangea break-up. Geol. Mag. 157, 1–23. https://doi.org/10.1017/S0016756820000084.

Doglioni, C., 1987. Tectonics of the Dolomites (Southern Alps, Northern Italy). J. Struct. Geol. 9, 181–193.

Doglioni, C., 1988. Examples of strike-slip tectonics on platform-basin margins. Tectonophysics 156, 293–302.

Foley, S.F., Peccerillo, A., 1992. Potassic and ultrapotassic magmas and their origin. Lithos 28, 181–185.

Gianolla, P., De Zanche, V., Mietto, P., 1998. Triassic Sequence Stratigraphy in the Southern Alps. Definition of sequences and basin evolution, *in* de Graciansky, P.C., Hardenbol, J., Jacquin, T., Vail, P.R., Ulmer-Scholle, D., eds., Mesozoic-Cenozoic Sequence Stratigraphy of European Basins, SEPM Special Publication 60, 723–751, Tulsa/Oklahoma.

Giovanardi, T., Morishita, T., Zanetti, A., Mazzucchelli, M., Vannucci, R., 2013. Igneous sapphirine as a product of melt-peridotite interactions in the Finero Phlogopite Peridotite Massif, Western Italian Alps. Eur. J. Miner. 25, 17–31. https://doi.org/10.1127/0935-1221/2013/0025-2251.

Giovanardi, T., Zanetti, A., Dallai, L., Morishita, T., Hémond, C., Mazzucchelli, M., 2020. Evidence of subduction-related components in sapphirine-bearing gabbroic dykes (Finero phlogopite–peridotite): Insights into the source of the Triassic–Jurassic magmatism at the Europe–Africa boundary. Lithos 356–357, 105366. https://doi.org/10.1016/j.lithos.2020.105366.

Griffin, W.L., Powell, W.J., Pearson, N.J., O'Reilly, S.Y., 2008. GLITTER: data reduction software for laser ablation ICPMS. In: Sylvester, P. (Ed.), Laser Ablation ICP–MS in the Earth Sciences: Current Practices and Outstanding Issues. Mineral. Assoc. Canada Short

Course Series 40, pp. 308–311.

Jiang, Y.H., Jiang, S.Y., Ling, H.F., Zhou, X.R., Rui, X.J., Yang, W.Z., 2002. Petrology and geochemistry of shoshonitic plutons from the western Kunlun orogenic belt, Xinjiang, northwestern China: implications for granitoid geneses. Lithos 63, 165–187.

Korte, C., Kozur, H.W., Bruckschen, P., Veizer, J., 2003. Strontium isotope evolution of Late Permian and Triassic seawater. Geochim. Cosmochim. Acta 67, 47–62.

Kroner, U., Romer, R.L., 2014. Anatomy of a diffuse cryptic suture zone: an example from the Bohemian Massif, European Variscides: comment. Geology 42.

Küster, D., Harms, U., 1998. Post-collisional potassic granitoids from the southern and northwestern parts of the Late Neoproterozoic East African Orogen: a review. Lithos 45, 177–195.

Lustrino, M., Abbas, H., Agostini, S., Caggiati, M., Carminati, E., Gianolla, P., 2019. Origin of Triassic magmatism of the Southern Alps (Italy): Constraints from geochemistry and Sr-Nd-Pb isotopic ratios. Gondwana Res. 75, 218–238. https://doi.org/10.1016/j.gr.2019.04.011.

Lyubetskaya, T., Korenaga, J., 2007. Chemical composition of Earth's primitive mantle and its variance: 1. Method and results. J. Geophys. Res. Solid Earth 112, B03211. https://doi.org/10.1029/2005JB004223.

McDonough, W.F., Sun, S., 1995. The composition of the Earth. Chem. Geol. 120, 223–253. https://doi.org/10.1016/0009-2541(94)00140-4.

Meen, J.K., 1987. Formation of shoshonites from calc-alkaline basalt magmas: geochemical and experimental constraints from the type locality. Contrib. Mineral. Petrol. 97, 333–351.

Morishita, T., Hattori, K.H., Terada, K., Matsumoto, T., Yamamoto, K., Takebe, M., Ishida, Y., Tamura, A., Arai, S., 2008. Geochemistry of apatite-rich layers in the Finero phlogopite–peridotite massif (Italian Western Alps) and ion microprobe dating of apatite. Chem. Geol. 251, 99–111. https://doi.org/10.1016/j.chemgeo.2008.02.018.

Nardini, N., Casetta, F., Ickert, R.B., Mark, D.F., Ntaflos, T., Zanetti, A., Coltorti, M., 2022. From the Middle Triassic Cima Pape complex (Dolomites; Southern Alps) to the feeding

systems beneath active volcanoes: Clues from clinopyroxene textural and compositional zoning. J. Volcan. Geotherm. Res. 422. https://doi.org/10.1016/j.jvolgeores.2021.107459.

Obermiller, W.A., 1994. Chemical and Isotopic Variations in the Balmuccia, Baldissero and Finero Peridotite Massifs (Ivrea-Zone, N-Italy). Unpublished PhD thesis. Johannes-Gutenberg-Universität Mainz, p. 191.

Ogunyele A.C., Bonazzi M., Giovanardi T., Mazzucchelli M., Salters V.J.M., Decarlis A., Sanfilippo A., Zanetti A., 2024. Transition from orogenic-like to anorogenic magmatism in the Southern Alps during the Early Mesozoic: Evidence from elemental and Nd-Sr-Hf-Pb isotope geochemistry of alkali-rich dykes from the Finero Phlogopite Peridotite, Ivrea–Verbano Zone. Gondwana Res. 129, 201-219.

Pearce, J.A., 1982. Trace element characteristics of lavas from destructive plate boundaries, *in* Thorpe R.S., ed., Andesites 8, 525–548, John Wiley & Sons.

Pearce, J.A., Peate, D.W., 1995. Tectonic implications of the composition of volcanic arc magmas. Annual Rev. Earth Planet. Sci. 23, 251–285.

Peccerillo, A., 1992. Potassic and ultrapotassic rocks: compositional characteristics, petrogenesis, and geologic significance. Episodes 15, 243–251.

Peccerillo, A., Frezzotti, M.L., 2015. Magmatism, mantle evolution and geodynamics at the converging plate margins of Italy. J. Geol. Soc. London 172 (4), 407–427.

Plank, T., 2014. The chemical composition of subducting sediments, *in* Holland, H.D., eds., Treatise on Geochemistry, 2nd ed. Elsevier, Amsterdam, 607-629.

Rudnick, R.L., Gao, S., 2004. Composition of the continental crust. Treatise on Geochemistry 3, 1-65.

Saccani, E., 2015. A new method of discriminating different types of post-Archean ophiolitic basalts and their tectonic significance using Th-Nb and Ce-Dy-Yb systematics. Geosci. Front. 6 , 481–501.

Saccani, E., 2015. A new method of discriminating different types of post-Archean ophiolitic basalts and their tectonic significance using Th-Nb and Ce-Dy-Yb systematics. Geosci. Front. 6, 481–501.

Salters, V.J.M., Stracke, A., 2004. Composition of the depleted mantle. Geochem. Geophys. Geosys. 5. https://doi.org/10.1029/2003GC000597.

Schmid, S.M., Fügenschuh, B., Kounov, A., Maţenco, L., Nievergelt, P., Oberhänsli, R., Ustaszewski, K., 2020. Tectonic units of the Alpine collision zone between Eastern Alps and western Turkey. Gondwana Res. 78, 308–374.

Sloman, L.E., 1989. Triassic shoshonites from the dolomites, northern Italy: alkaline arc rocks in a strike-slip setting. J. Geophys. Res. Solid Earth 94, 4655–4666.

Smith, E.I., Sanchez, A., Walker, J.D., Wang, K., 1999. Geochemistry of mafic magmas in the Hurricane Volcanic field, Utah: implications for small-and large-scale chemical variability of the lithospheric mantle. J. Geol. 107, 433–448.

Stähle, V., Frenzel, G., Hess, J.C., Saupé, F., Schmidt, S.T., Schneider, W., 2001. Permian metabasalt and Triassic alkaline dykes in the Northern Ivrea Zone: clues to the post-Variscan geodynamic evolution of the Southern Alps. Schweizerische Mineralogische Petrographische Mitteillungen 81, 1–21.

Stampfli, G.M., Hochard, C., Vérard, C., Wilhem, C., 2013. The formation of Pangea. Tectonophysics 593, 1–19.

Stampfli, G.M., Von Raumer, J.F., Borel, G.D., 2002. Paleozoic evolution of pre-Variscan terranes: from Gondwana to the Variscan collision, *in* Catalan, J.R.M., Hatcher, R.D., Arenas, R., Garcia, F.D., eds., Variscan-Appalachian dynamics: The building of the late Paleozoic basement. GSA Special Paper 364, 263–280. https://doi.org/10.1130/0-8137-2364-7.263.

Storck, J.-C., Brack, P., Wotzlaw, J.F., Ulmer, P. (2019). Timing and evolution of Middle Triassic magmatism in the Southern Alps (northern Italy). J. Geol. Soc. 176, 253-268. https://doi.org/10.1144/jgs2018-123.

Storck, J.C., Wotzlaw, J.F., Karakas, Ö., Brack, P., Gerdes, A., Ulmer, P., 2020. Hafnium isotopic record of mantle-crust interaction in an evolving continental magmatic system. Earth Planet. Sci. Lett. 535, 116100.

Stracke, A., 2012. Earth's heterogeneous mantle: A product of convection-driven interaction between crust and mantle. Chem. Geol. 330–331, 274–299.

https://doi.org/10.1016/j.chemgeo.2012.08.007.

Stracke, A., Bizimis, M., Salters, V.J., 2003. Recycling oceanic crust: quantitative constraints. Geochem. Geophys. Geosys. 4. https://doi.org/10.1029/2001GC000223.

Velicogna, M., De Min, A., Prašek, M.K., Ziberna, L., Brombin, V., Jourdan, F., Renne, P.R., Balen, D., Grégoire, M., Marzoli, A., 2022. The Norian magmatic rocks of Jabuka, Brusnik and Vis Islands (Croatia) and their bearing on the evolution of Triassic magmatism in the Northern Mediterranean. Int. Geol. Rev. 65.

Voshage, H., Hunziker, J.C., Hofmann, A.W., Zingg, A., 1987. A Nd and Sr isotopic study of the Ivrea zone, Southern Alps, N-Italy. Contrib. Mineral. Petrol. 97, 31–42. https://doi.org/10.1007/BF00375212.

Williams, H.M., Turner, S.P., Pearce, J.A., Kelley, S.P., Harris, N.B.W., 2004. Nature of the source regions for post-collisional, potassic magmatism in southern and northern Tibet from geochemical variations and inverse trace element modelling. J. Petrol. 45, 555–607.

Woelki, D., Salters, V., Beier, C., Dick, H., Koepke, J., Romer, R., 2023. Shallow recycling of lower continental crust: The Mahoney Seamount at the Southwest Indian Ridge. Earth Planet. Sci. Lett. 602, 117968. https://doi.org/10.1016/j.epsl.2022.117968.

Wood, D.A., 1980. The application of a Th-Hf-Ta diagram to problems of tectonomagmatic classification and to establishing the nature of crustal contamination of basaltic lavas of the British Tertiary Volcanic Province. Earth Planet. Sci. Lett. 50, 11–30.

Wyllie, P.J., Sekine, T., 1982. The formation of mantle phlogopite in subduction zone hybridization. Contrib. Mineral. Petrol. 79, 375–380.

Zanetti, A., Mazzucchelli, M., Rivalenti, G., Vannucci, R., 1999. The Finero phlogopite–peridotite massif: an example of subduction-related metasomatism. Contrib. Mineral. Petrol. 134, 107–122. https://doi.org/10.1007/s004100050472.

Zanetti, A., Mazzucchelli, M., Sinigoi, S., Giovanardi, T., Peressini, G., Fanning, M., 2013. SHRIMP U-Pb zircon Triassic intrusion age of the Finero mafic complex (Ivrea–Verbano Zone, Western Alps) and its geodynamic implications. J. Petrol. 54, 2235–2265. https://doi.org/10.1093/petrology/egt046.

PART 2

CHAPTER 5

Accretion of "young" Phanerozoic subcontinental lithospheric mantle triggered by back-arc extension: The case of the Ivrea-Verbano lherzolites

Abimbola C. Ogunyele[1,2], Alessio Sanfilippo[1,2], Vincent J.M. Salters[3], Mattia Bonazzi[2] and Alberto Zanetti[2]

[1] Department of Earth and Environmental Sciences, University of Pavia, Via Ferrata 1, 27100 Pavia, Italy

[2] CNR – Istituto Geoscienze e Georisorse, Via Ferrata 1, 27100 Pavia, Italy

[3] National High Magnetic Field Laboratory, Department of Earth, Ocean and Atmospheric Sciences, Florida State University, Tallahassee, FL 32310, USA

Declaration

This manuscript is submitted to **Scientific Reports** for peer-review and possible publication. The study was conducted in collaboration with the co-authors cited above. The contribution of each author is given below.

ACO: Data curation, Formal analysis, Investigation, Methodology, Validation, Visualization, Writing - original draft, Writing - review & editing; **AS**: Conceptualization, Supervision, Methodology, Validation, Visualization, Writing - original draft, Writing - review & editing; **VJMS**: Funding acquisition, Investigation, Methodology, Validation, Visualization, Supervision, Writing - review & editing; **MB**: Formal analysis, Investigation, Writing - review & editing; **AZ**: Conceptualization, Funding acquisition, Methodology, Project administration, Resources, Supervision, Validation, Visualization, Writing - review & editing.

Abstract

The subcontinental lithospheric mantle (SCLM) beneath Phanerozoic regions is mostly constituted by fertile lherzolites, which sharply contrast with cratonic mantle made of melt-depleted peridotites. The question of whether this chemical difference results from lower degrees of melting in Phanerozoic SCLM or from the refertilization of ancient depleted SCLM remains a subject of debate. Additionally, the timing and geodynamic environment of accretion of the fertile SCLM in many Phanerozoic regions are poorly constrained. We here document new geochemical and Nd-Hf isotopic data for orogenic lherzolite massifs from the Ivrea-Verbano Zone (IVZ), Southern Alps. Even though a few Proterozoic Re depletion ages are locally preserved in these mantle sequences, our data reveal that the IVZ lherzolitic massifs were "recently" accreted to the SCLM in the Upper Devonian (ca. 370 Ma) during Pangea amalgamation, with a petrochemical evolution characterized by low-degree (~5–12%) depletion and nearly contemporaneous pervasive to focused melt migration. The lithospheric accretion putatively took place through asthenospheric upwelling triggered by Variscan intra-continental extension in a back-arc setting related to the subduction of the Rheic Ocean. We thus conclude that the fertile sections of Phanerozoic SCLM can be accreted during "recent" events of back-arc continental extension, even where Os isotopes preserve memories of melting events in much older times.

5.1 Introduction

The subcontinental lithospheric mantle (SCLM) beneath Phanerozoic (off-craton) terrains is made largely of peridotites having fertile compositions, contrary to cratonic areas where the lithosphere is dominantly formed by highly depleted peridotites, more buoyant than the rest of the mantle and stable for billions of years (e.g., Ionov et al., 2020). This ancient history of depletion is revealed through high $^{176}Hf/^{177}Hf$ and $^{143}Nd/^{144}Nd$ of mantle xenoliths from basalts and kimberlites in Precambrian terrains and Archean cratons (Figure 5.1; Lee et al., 2011), which are often associated with unradiogenic $^{187}Os/^{188}Os$ preserving old Re depletion ages (Reisberg and Lorand, 1995; Shirey and Walker, 1998; Pearson et al., 2021). Still, extremely variable Nd-Hf isotopes characterize these cratonic peridotites, suggesting that the long-term preservation of depleted signatures can be overprinted by metasomatic episodes (Tilhac et al., 2022). Highly-depleted isotopic signatures are nearly absent in subcontinental Phanerozoic lherzolite massifs which, consistently, are more fertile (i.e., lower Mg#, higher Al_2O_3, CaO, and Na_2O) than the Archean peridotites (Lee et al., 2011). Nonetheless, these lherzolitic massifs locally show Proterozoic to Archean Re depletion ages, suggesting that records of ancient melting episodes may be ubiquitously preserved in the upper mantle (Wang et al., 2013; Pearson et al., 2021; Reisberg, 2021). Hence, whether the fertile character of the Phanerozoic mantle reflects secular decreases in the average degree of melting associated with the formation of continental mantle (Ionov et al., 2005; Ionov and Hofmann, 2007) or refertilization of ancient depleted SCLM portions (Reisberg et al., 1989; Le Roux et al., 2007, 2009; Griffin et al., 2009; McCoy-West et al., 2013) is still strongly debated (e.g., Wang, et al., 2013; Reisberg, 2021; Tilhac et al., 2022). Moreover, the timing and environment of accretion of the SCLM in many Phanerozoic regions are open questions.

We here show that coupled Nd-Hf isotopes on residual to melt-reacted peridotites and associated pyroxenites from the IVZ lherzolitic mantle massifs place fundamental constraints on the depletion signatures, timing, mechanism and geodynamic environment of accretion of Phanerozoic SCLM. Despite a few Re depletion ages extending up to 1.6 Ga (Wang et al., 2013), we show that the IVZ fertile mantle lithosphere was accreted in the Paleozoic at ca. 370 Ma, during a process of intra-continental extension in a back-arc setting where low-degree (~5–12%) melting, pervasive metasomatism and pyroxenites segregation occurred almost synchronously. Rather than being a piece of cratonic mantle reworked during more recent tectonic cycles, we here document that the fertile SCLM beneath many Phanerozoic regions can be produced in "recent" times.

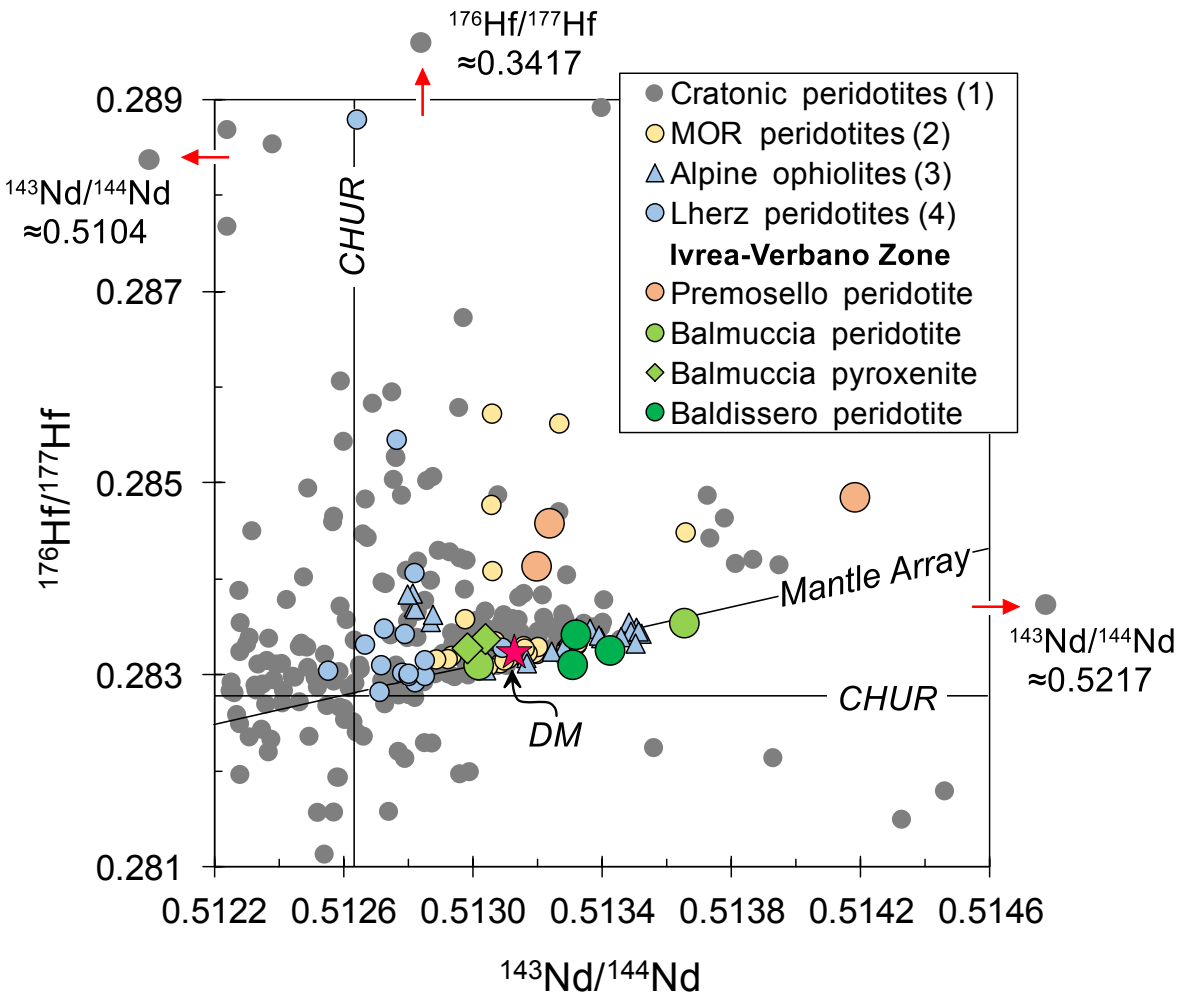

Figure 5.1: Present-day Nd–Hf diagram showing depletion signatures preserved in IVZ lherzolites and pyroxenites compared to (1) cratonic peridotites; (2) Mid-Ocean Ridge peridotites; (3) Alpine ophiolites; and (4) orogenic peridotites. DM – Depleted Mantle (Salters and Stracke, 2004); CHUR – Chondritic Uniform Reservoir (Bouvier et al., 2008). Plotted literature data are from the compilation of Tilhac et al. (2022).

5.2 Subcontinental Lithospheric Mantle in the Ivrea-Verbano Zone

The Ivrea-Verbano Zone (IVZ) is the westernmost sector of the Southern Alps and represents a continuously exposed section of lower to intermediate crust (Schmid, 1993). The IVZ consists of i) a Variscan poly-metamorphic amphibolite- to granulite-facies volcano-sedimentary sequence representing the crystalline basement of the Adriatic Plate (Ewing et al., 2013); ii) the Mafic Complex, an igneous complex formed by mantle-derived melts of Upper Carboniferous–Lower Permian age (314–282 Ma; Klötzli et al., 2014; Peressini et al., 2007); and iii) several lens-like peridotite bodies, which mostly have a mantle origin and differ in composition, degree of depletion and metasomatic overprint (Zanetti et al., 2016; Decarlis et al., 2023) (Figure 5.2).

Samples were selected from the largest spinel-facies lherzolite bodies, i.e., the Balmuccia, Baldissero and Premosello massifs, located in the central and southern sectors of IVZ (Figures 5.3-5.5). The Balmuccia and Baldissero massifs comprise mainly fresh spinel lherzolites (with ~10-15 vol. % clinopyroxene) and subordinate harzburgites and replacive dunites which, in Balmuccia, are cut by several generations of websterites, Cr-diopside and Al-augite pyroxenites (Figures 5.3-5.4; Rivalenti et al., 1995; Rivalenti and Mazzucchelli, 2000; Mazzucchelli et al., 2009, 2010; Wang et al., 2013; Wang and Becker, 2015). The poorly-known Premosello massif consists of clinopyroxene-poor (~5 vol. % cpx) spinel lherzolite and minor replacive dunites also cut by Cr-diopside and Al-diopside pyroxenites (Figure 5.5; Mazzucchelli et al., 1992). Previous geochemical data indicate that most IVZ lherzolites underwent variable extent of melt extraction and melt migration (Mazzucchelli et al., 1992, 2010; Wang et al., 2013; Decarlis et al., 2023 and references therein). Available Re depletion ages are predominantly Paleozoic with peak ages around 350–500 Ma, although a few Proterozoic depletion ages (up to 1.6 Ga) are locally

preserved (Mazzucchelli et al., 2010; Wang et al., 2013). Consistently, Sm-Nd pseudo-isochron obtained from clinopyroxene separates of Baldissero peridotite furnished 378 ± 48 Ma (Obermiller, 1994). Considering samples from both Baldissero and Balmuccia, Sm-Nd isotopes on clinopyroxene separates yield pseudo-isochron at 390 Ma (Obermiller et al., 1992).

The timing and mechanisms of emplacement of the IVZ mantle peridotites at lower crustal levels is still a matter of debate. Field and structural relationships suggest that some of the mantle peridotite bodies (e.g. the Balmuccia peridotite) were emplaced at crustal levels since the end of the Variscan orogeny (Rivalenti and Mazzucchelli, 2000; Mazzucchelli et al., 2010). Alternative hypotheses involve emplacement at crustal level at the onset of the Mesozoic extensional regime, or tectonic addition to accretionary wedges of Paleozoic subduction zones (Decarlis et al., 2023). Independently on the timing of crustal exhumation, recent gravimetric and seismic data converge to indicate that high-density rocks occur very close to the surface near the Insubric Line (Scarponi et al., 2020; Ryberg et al., 2023), thus supporting the possibility that some of the mantle peridotite bodies (e.g. the Balmuccia peridotite) may be a direct expression of the underlying SCLM.

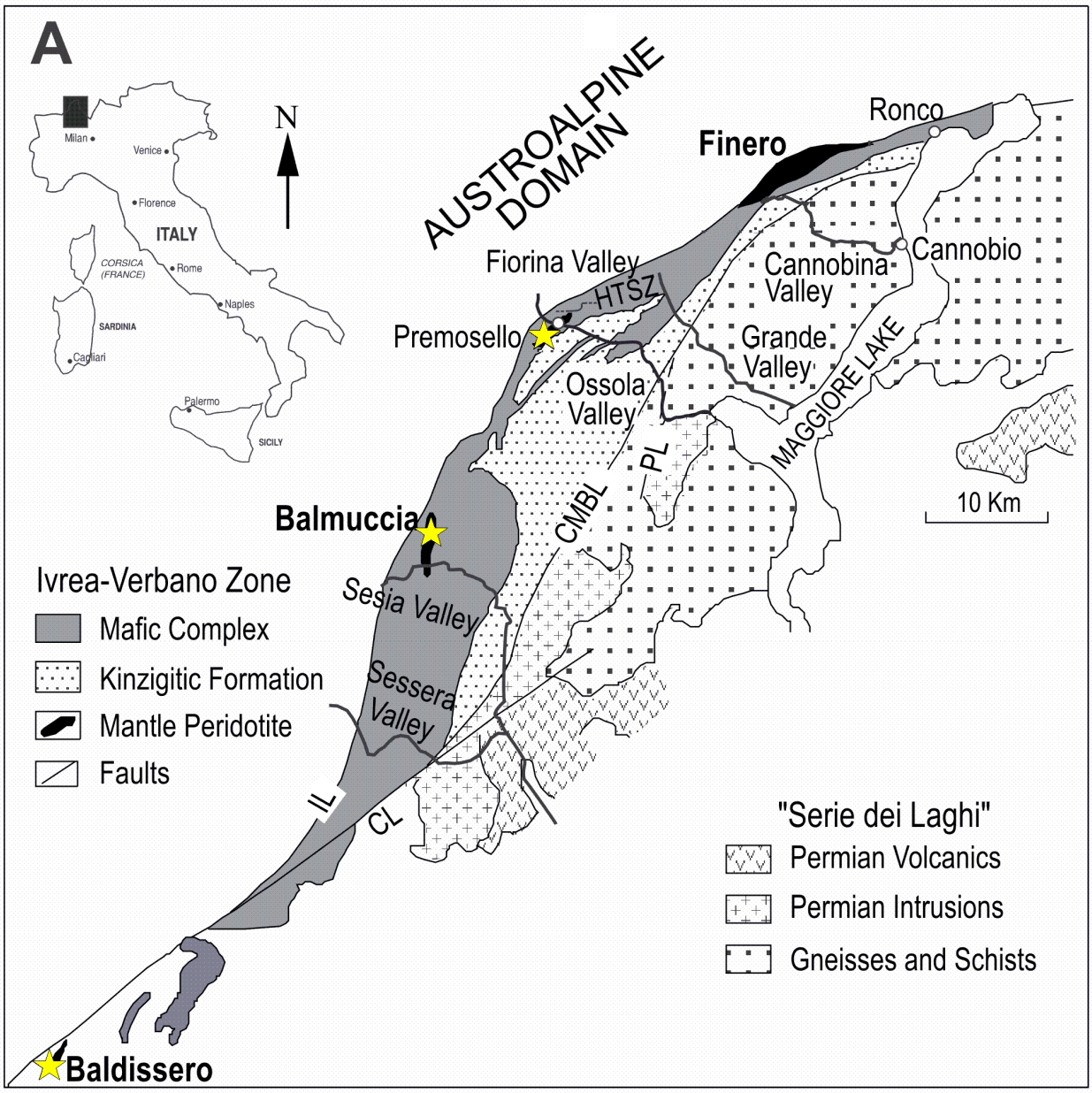

Figure 5.2: Geological setting of the Ivrea-Verbano Zone and the locations of studied orogenic peridotite massifs at Balmuccia (45.816853 N, 8.136250 E), Baldissero (45.42098 N, 7.75106 E) and Premosello (46.005298 N, 8.320076 E) (after Mazzucchelli et al., 2010).

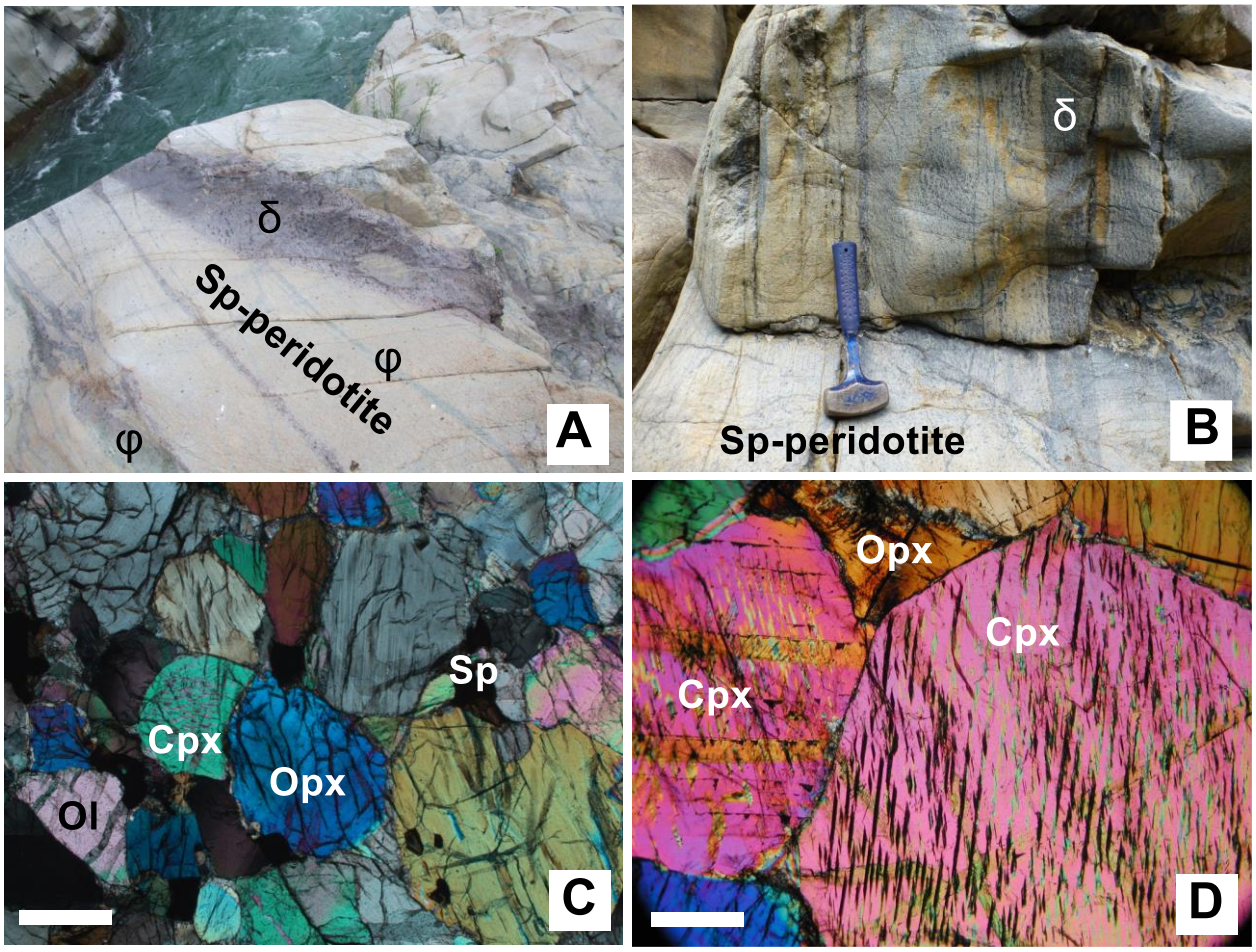

Figure 5.3: (a, b) Spinel lherzolite of the Balmuccia mantle massif cut by Cr-diopside clinopyroxenite (φ) and Al-augite pyroxenite (δ); (c) thick sections (60 μm, x-nicols) of Balmuccia lherzolite showing protogranular texture and (d) Cr-diopside websterite displaying granoblastic texture with 120° triple junctions. The white bars to the left of panels (c, d) represent 1 mm scale.

Figure 5.4: (a, b) Spinel lherzolite of the Baldissero mantle massif; (c) thick section (60 μm, x-nicols) of Baldissero lherzolite showing protogranular texture. The white bar to the left of panel (c) represents 1 mm scale.

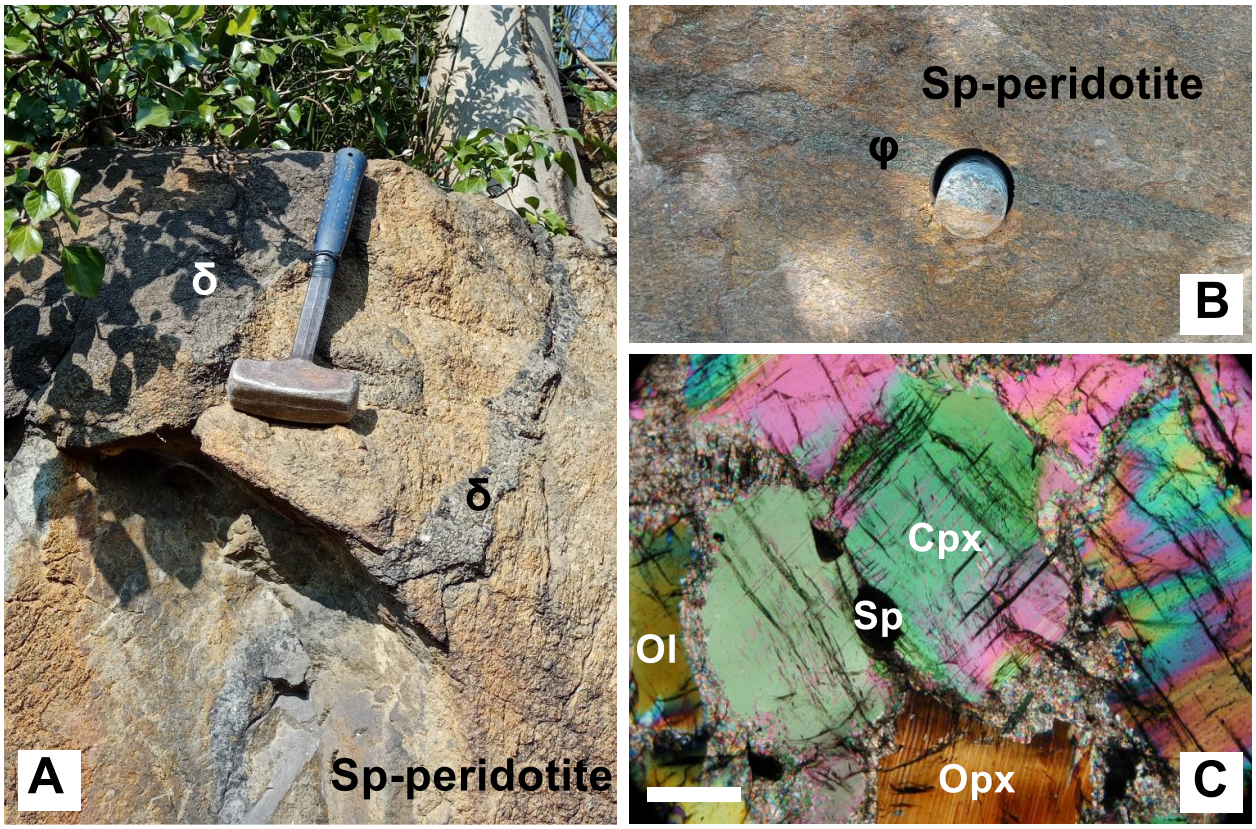

Figure 5.5: (a, b) Spinel lherzolite of the Premosello mantle massif cut by Cr-diopside clinopyroxenite (φ) and Al-rich diopside pyroxenite (δ); (c) thick section (60 μm, x-nicols) of Premosello lherzolite showing porphyroclastic texture. The white bar to the left of panel (c) represents 1 mm scale.

5.3 Analytical methods

5.3.1 New sample collection and petrography

We collected representative samples of spinel lherzolites from the Balmuccia, Baldissero and Premosello lherzolite massifs. Samples of the first generation of Cr-diopside pyroxenites were also collected from the Balmuccia massif. Where possible, lherzolites were collected far away (at least 50 cm) from other typologies of pyroxenites and gabbroic intrusives, although the pyroxenite trails along the tectonitic fabric in Premosello peridotite hampered the collection of samples far from Cr-diopside veins. Balmuccia and Baldissero peridotites show protogranular to weakly foliated textures (Figures 5.3-5.4), whereas Premosello peridotite has a porphyroclastic texture defined by large, kinked crystals of olivine, orthopyroxene and clinopyroxene embedded within relatively finer grained crystals of similar minerals and spinel (Figure 5.5). Accessory amounts of Ti-rich amphibole and sulphides occur in all the three peridotite bodies.

5.3.2 Mineral major and trace elements chemistry

The major element compositions of mineral phases (olivine, orthopyroxene, clinopyroxene and spinel) in the IVZ lherzolite and pyroxenite samples were measured by electronprobe microanalysis using a JEOL JXA-8230 Superprobe equipped with five WDS spectrometers operating in wavelength dispersive mode, housed at the Joint Laboratory of the Department of Earth Sciences, University of Florence and the CNR-IGG Florence. Operating conditions were 15 kV accelerating voltage, 20 nA beam current, 3 μm spot size, and a counting time of 15 s on the peaks and 7 s on the backgrounds. Natural minerals (olivine for Mg; albite for Si and Na; ilmenite for Fe and Ti; bustamite for Mn; sanidine for K; plagioclase for Al; diopside for Ca; metallic nickel for Ni; chromite for Cr) were used as standards. The results were

corrected for matrix effects using the conventional ZAF method provided by the JEOL software package. Results are considered to be accurate within 2–5%. The result of the major element composition of the mineral phases is reported in Appendix 5.1.

The trace element contents of clinopyroxenes were measured on thin sections and mineral separates using an Agilent 8900 QQQ-ICP-MS coupled to a 266 nm Nd:YAG laser ablation system at the CNR-IGG Pavia. The ICP-MS was tuned using NIST SRM 610 synthetic glass to optimize the signal intensity and stability and remove molecular interferences by monitoring ^{24}Mg, ^{115}In, ^{238}U and the $^{232}Th/^{248}ThO$ ratio. Data reduction was done with the GLITTER software (Griffin et al., 2008). The laser was operated at a repetition rate of 10 Hz, fluence of 10 J/cm^2 and 50-60 μm spot size. NIST SRM 610 was used as an external standard, whereas Ca was used as internal standard for the clinopyroxene. USGS reference sample BCR2g was repeatedly analyzed together with the unknowns to assess precision and accuracy at ± 5% and ± 10%, respectively. The trace element dataset of the clinopyroxenes is reported in Appendix 5.2.

5.3.3 Nd and Hf isotopic measurements

Nd and Hf isotope measurements on clinopyroxene separates from the samples were performed at the National High Magnetic Field Laboratory, Florida State University. For each sample, ~100-120 mg of clinopyroxene separates were leached, dissolved, processed through ion exchange columns and measured for Nd-Hf isotopes. The separates were leached in 5 ml 2.5N HCl and <30% H_2O_2 for 60 min at room temperature to remove any alteration products. The leached separates were rinsed several times with quartz sub-boiling distilled water. Subsequent dissolution and column chemistry was performed after procedures described by Stracke et al (2003a) and Woelki et al (2023). Nd and Hf isotopes were measured using a ThermoFisher

Neptune Multi-Collector ICP-MS system. Measurements of the La Jolla standard yielded $^{143}Nd/^{144}Nd$ ratio of 0.511790 ± 0.000012 (2σ, n = 17). The $^{143}Nd/^{144}Nd$ ratios were corrected for mass bias using a $^{146}Nd/^{144}Nd$ ratio of 0.7219 and are reported relative to the La Jolla standard of 0.511850. Blanks for Nd were less than 10 pg. Measured value of the JMC-475 standard is $^{176}Hf/^{177}Hf$ = 0.282150 ± 0.000008 (2σ, n = 20). The $^{176}Hf/^{177}Hf$ ratios were corrected for mass bias using a $^{179}Hf/^{177}Hf$ ratio of 0.7325 and reported relative to JMC-475 value of $^{176}Hf/^{177}Hf$ = 0.282150. Blanks for Hf were less than 40 pg. $^{147}Sm/^{144}Nd$ and $^{176}Lu/^{177}Hf$ ratios were calculated from the Sm, Nd, Lu and Hf concentrations measured on clinopyroxenes by LA-ICP-MS. The Nd-Hf isotopes dataset of the clinopyroxenes is reported in Appendix 5.3.

5.3.4 Partial melting modeling

Modeling of the degree of partial melting underwent by the IVZ lherzolites was performed following the dynamic melting model described in detail by Stracke et al (2003b). The dynamic melting model calculates the trace element and isotopic compositions of mantle residues using the average Depleted Mantle (DM) estimates of Salters and Stracke (2004) as the initial source composition. The choice of the DM end-member as the initial source composition is based on (i) the presumption that the composition of the Upper Mantle (UM) at 370 Ma (according to errorchron ages provided in this study, see Results section) could not have been Primitive, as the UM is expected to have previously experienced about 2-3% partial melting to produce the Continental Crust (CC) and a complementary DM reservoir (Salters and Stracke, 2004; Workman and Hart, 2005); (ii) the similarity of the initial εNd and εHf of the studied IVZ lherzolites to those of the average DM ($\varepsilon Nd_{(i)}$ = +8.0, $\varepsilon Hf_{(i)}$ = +15.6; Salters and Stracke, 2004); and (iii) the average lherzolitic modal composition of the DM.

In the modeling, residual porosity was fixed at 1% and percentage of melting per km at 0.15%. Partition coefficients are from Salters and Stracke (2004). Garnet melting is assumed to begin at 100 km (degree of melting, F = 0–5%) followed by further melting in the spinel stability field. Spinel melting starts at 75 km. Melting reactions are recalculated at 60 km, 48 km, 33 km, and 24 km following the phase relations from Longhi (2002). The present-day isotopic compositions of ancient residues are calculated as initial isotopes ratios plus radiogenic ingrowth after 370 Ma. Initial isotope ratios at the time of melting were calculated using a two-stage DM mantle evolution starting from primitive mantle at 3.5 Ga and present-day DM isotope ratios of $^{176}Hf/^{177}Hf = 0.28330$ and $^{143}Nd/^{144}Nd = 0.51311$ (Salters and Stracke, 2004). The results and starting compositions of the partial melting modeling are reported in Appendix 5.4.

5.3.5 Melt-rock reaction modeling

Melt-rock reaction modeling of the IVZ lherzolites was performed following Sani et al (2023). We opted for an assimilation-fractional crystallization (AFC) model based on equations 6a and 15a from DePaolo (1981). The model reproduces a melt migrating through a peridotite column, modified by partial assimilation of the peridotite and crystallization of new mineral phases at a constant melt mass during reaction and at a ratio of mass assimilated to mass crystallized of 0.99. The interaction forms a re-enriched peridotite gradually acquiring a lherzolitic composition by preferential dissolution of olivine and crystallization of clinopyroxene (partition coefficients as in the melting model). This approach follows natural examples of melt-rock reaction in SCLM (e.g., Le Roux et al., 2009; Bodinier and Godard, 2014). The incoming melt is assumed to crystallize in the matrix and its incompatible element content is redistributed in chemical equilibrium between melt and solid. The trace element composition of the solid is

calculated from the liquid following the equation $Cs = DC_L$, where D is the bulk partition coefficient for a given element. The trace element composition of the reacted peridotite is calculated at 1% increments, which indicate the mass fraction of peridotite equilibrated with the melt undergoing AFC (scaled from 0 to 100%). We performed several scenarios, using N-MORB and E-MORB starting melts compositions (Gale et al., 2013). The use of N- or E-MORB trace element compositions causes subtle differences in the melt-rock reaction trends. Since the Nd-Hf isotopic composition of clinopyroxene from the slightly LREE-depleted peridotite from Balmuccia is similar to the composition of E-MORB, we preferably used an E-MORB-like starting melt composition and mantle residues after 5 and 11 degrees of partial melting to reproduce the isotopic and trace elements compositions of the refertilized peridotites from Balmuccia-Baldissero (Appendix 5.5a) and Premosello (Appendix 5.5b), respectively. Present-day isotopic compositions are calculated adding the initial isotopic ratios, calculated from Eqn. 15a from DePaolo (1981), to the radiogenic Nd and Hf ingrowth for 370 Ma.

5.4 Analytical results

Mineral compositions distinguish the three peridotite bodies, with olivine, clinopyroxene (cpx) and orthopyroxene (opx) from the Premosello peridotite having the highest Mg# (see Appendix 5.1). Low Al_2O_3 and Na_2O in cpx and high Cr# in spinel also characterize the Premosello peridotite compared to those from Balmuccia and Baldissero (Figure 5.6a). In terms of trace elements (Appendix 5.2), cpx from Premosello peridotite show the lowest M-HREE and Hf contents, with REE pattern characterized by gradual decrease in chondrite-normalized concentrations from Lu to Sm, and positive inflections in Nd to La [$(Ce/Yb)_N$=0.03–0.12]. On the other hand, Balmuccia and Baldissero peridotites cpx are more variable, ranging from

samples having gradual decrease from Lu to La and marked LREE depletion [$(Ce/Yb)_N$=0.02] to samples only slightly LREE-depleted [$(Ce/Yb)_N$=0.4]. Cpx from the Balmuccia pyroxenites show REE patterns similar to cpx of the least depleted host peridotite, having slight depletions in LREE [$(Ce/Yb)_N$=0.4–0.7] and distinct negative Hf anomaly. Notably, the pyroxenite cpx has enrichments in MREE with respect to HREE [$(Sm/Yb)_N$=0.9–1.4], a feature not seen in the peridotites (Figure 5.6b-d).

The present-day Nd-Hf isotopic compositions of cpx further confirm the difference between the three peridotite bodies (Appendix 5.3). Balmuccia and Baldissero peridotites cpx display large variations in $^{143}Nd/^{144}Nd$ and $^{176}Hf/^{177}Hf$ and plot along the mantle Nd-Hf isotope array (Figure 5.1). On close inspection, the strongly LREE-depleted Balmuccia and Baldissero peridotites cpx show radiogenic $^{143}Nd/^{144}Nd$ compositions, whereas the Balmuccia sample having high LREE has $^{143}Nd/^{144}Nd$ lower than Depleted Mantle (DM) composition (Salters and Stracke, 2004). Premosello peridotite cpx, instead, exhibits wider range in Nd-Hf isotope ratios, with Nd ranging from DM-like values towards highly radiogenic $^{143}Nd/^{144}Nd$ (up to 0.514181), and coupled with highly radiogenic Hf isotope compositions ($^{176}Hf/^{177}Hf$ from 0.284139 to 0.284859) (Figure 5.1). All Premosello peridotites plot well above the mantle Nd-Hf isotope array, having Hf isotopes more radiogenic than most of the orogenic peridotites. They approach the compositions of some abyssal (Stracke et al., 2011; Sani et al., 2023) and Alpine ophiolite (Guarnieri et al., 2012; Sanfilippo et al., 2019) peridotites. Clinopyroxenes from the Balmuccia pyroxenites show Nd-Hf isotope ratios of 0.512982–0.513038 and 0.283284–0.283381, similar to the Balmuccia peridotite with high LREE contents but less depleted compared to the other peridotites (Figure 5.1).

Taken as a whole, the samples from the three mantle sections preserve well-defined correlations between present-day Nd-Hf isotope ratios and parent-daughter ratios, which are aligned along errorchrons different from those of the Alpine ophiolites. Considering some uncertainties in $^{147}Sm/^{144}Nd$ and $^{176}Lu/^{177}Hf$ mainly for the Premosello peridotites, these errorchrons return ages of 370 ± 20 Ma, exceptionally consistent for both Sm-Nd and Lu-Hf systematics (Figure 5.7a-b). This age is also consistent with Sm–Nd pseudo-isochrons previously reported for the Balmuccia and Baldissero lherzolites (378 ± 48 Ma, 390 Ma; Obermiller, 1994; Obermiller et al., 1992) and will be later discussed as the timing of the isotopic resetting for both Nd-Hf systematics. In addition, we emphasize that Paleozoic ages are commonly reported as Re depletion ages for both Balmuccia and Baldissero lherzolite massifs, having peaks in the Middle–Lower Paleozoic (350–500 Ma; Mazzucchelli et al., 2010; Wang et al., 2013).

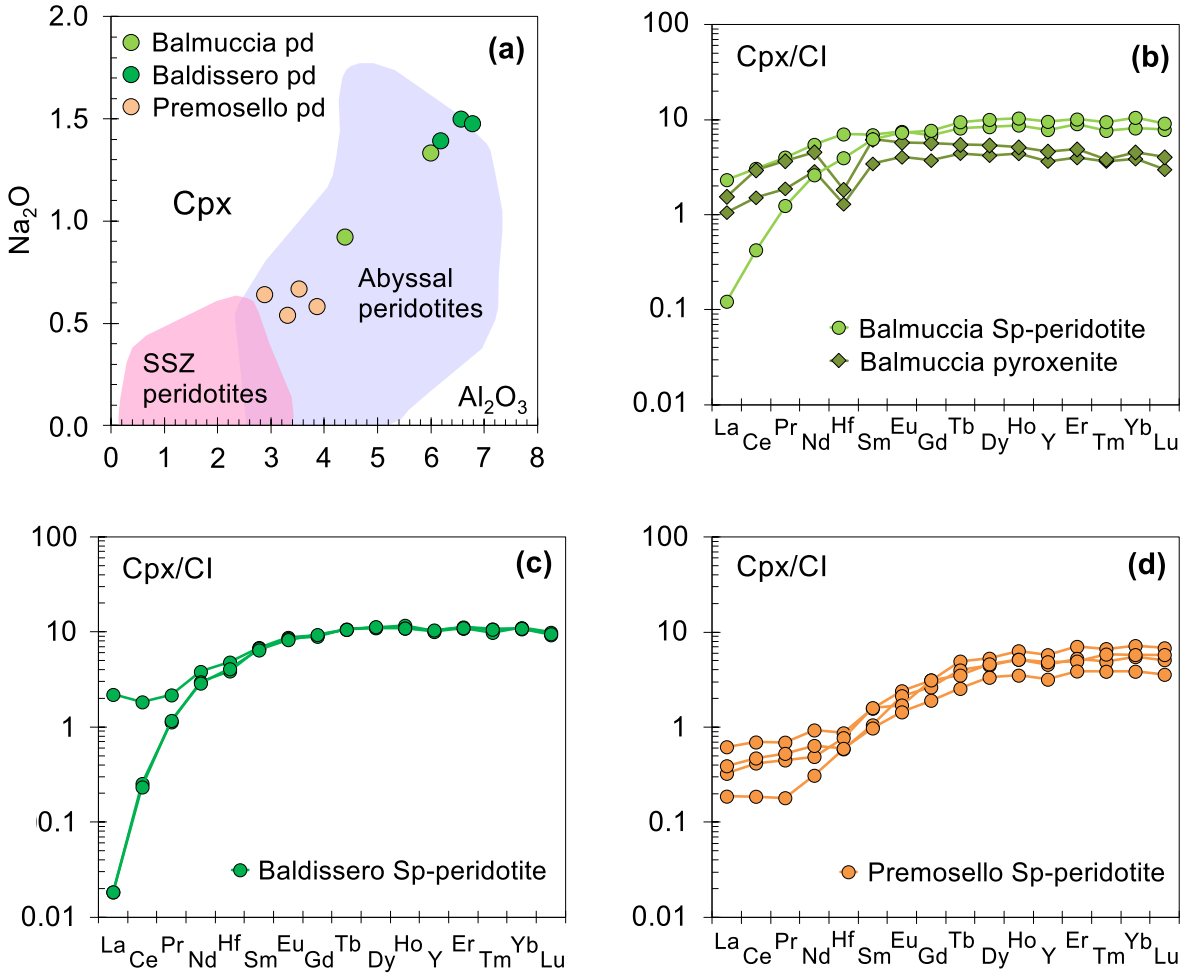

Figure 5.6: Plots of (a) Na_2O (wt. %) versus Al_2O_3 (wt. %) in clinopyroxenes, and (b-d) Chondrite-normalized REE–Hf patterns of clinopyroxenes from the studied IVZ peridotite and pyroxenite samples. pd – peridotite; SSZ – Suprasubduction Zone; OSMA – Olivine-Spinel Mantle Array defined from Arai (1994). Chondrite normalization values are from Lyubetskaya and Korenaga (2007).

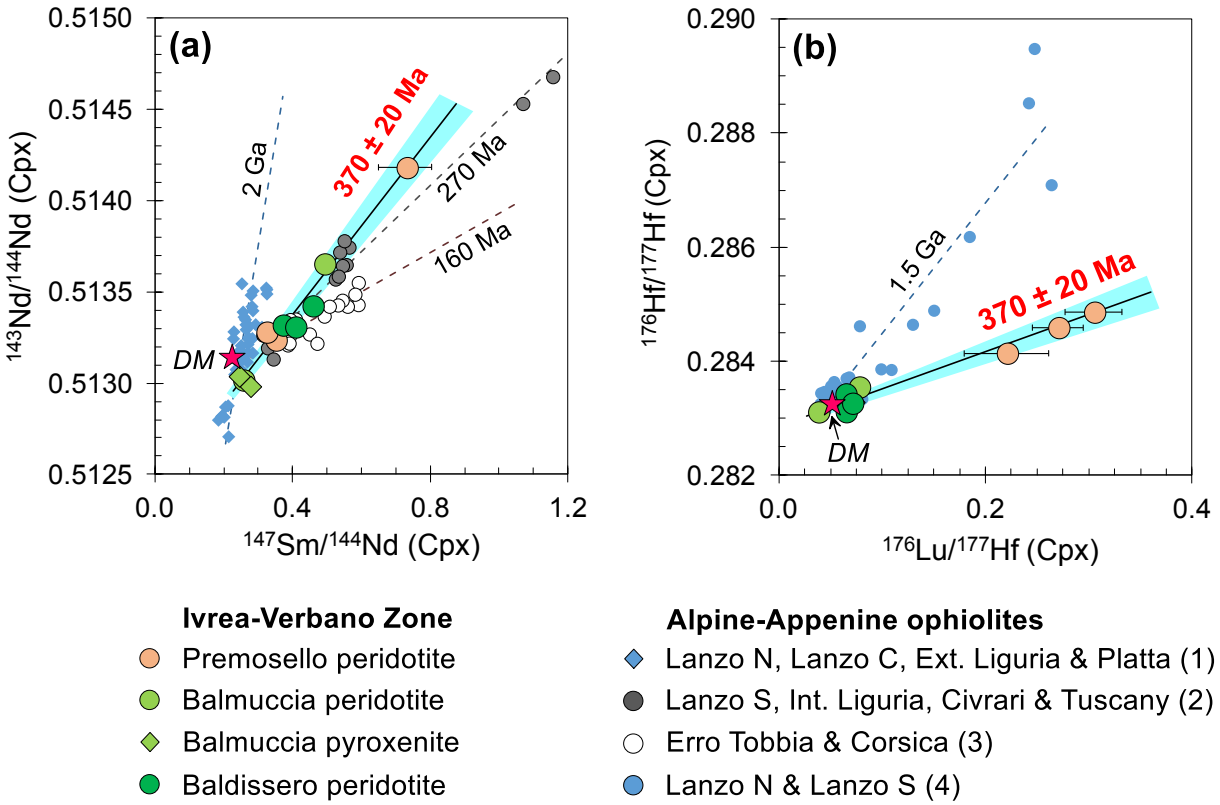

Figure 5.7: (a) Sm/Nd and (b) Lu/Hf errorchrons of IVZ lherzolites and pyroxenites (370 ± 20 Ma) compared to errorchrons of Alpine-Apennine ophiolites from (1) Lanzo North, Lanzo Central, External Liguria and Platta (Bodinier et al., 1991; Rampone et al., 1995; Müntener et al., 2004); (2) Lanzo South, Internal Liguria, Civrari and Tuscany (Bodinier et al., 1991; Sanfilippo et al., 2019; McCharty and Müntener, 2015; Rampone et al., 1996; Tribuzio et al., 2004); (3) Erro-Tobbio and Corsica (Rampone et al., 2005, 2009); and (4) Lanzo North and South (Guarnieri et al., 2012; Sanfilippo et al., 2019). $^{143}Nd/^{144}Nd$ and $^{176}Hf/^{177}Hf$ error bars are smaller than sample symbols.

5.5 Discussion

5.5.1 Isotopic response to Paleozoic mantle melting and chemical re-enrichment

Field, textural and geochemical evidence suggest that the IVZ lherzolites have a complex history of partial melting and melt migration. They show elemental compositions similar to abyssal peridotites (Figure 5.6a), and range from residual to melt-reacted. Specifically, cpx from three Balmuccia and Baldissero peridotite samples indicates that they have a strictly residual character, and their REE patterns can be reproduced by ~5% fractional melting of a DM-like source (Figure 5.8a). The other two samples, instead, have LREE too high requiring enrichment by melt addition. In Premosello samples, cpx have low M-HREE and Y reproducible by ~10–12% depletion of a DM source. However, all Premosello cpx have LREE too high for only fractional melting to be responsible, and require reaction with melts (Figure 5.8a).

Based on the exceptional preservation of Nd and Hf errorchrons giving similar ages, we infer that the resetting of Nd-Hf isotope systematics for all samples occurred at an age of circa 370 Ma (Figure 5.7). The two errorchrons do not provide precise age measurements but give temporal constraints to the event of isotopic resetting, which in the case of the IVZ peridotites likely occurred in the middle Paleozoic, specifically in the Upper Devonian. Coherently, Re-Os isotopes of the IVZ peridotites also suggest a major resetting event in the Paleozoic (Mazzucchelli et al., 2010; Wang et al., 2013).

As suggested by the local preservation of a few Proterozoic Re depletion ages (Wang et al., 2013), one hypothesis is that the present-day decoupled, highly radiogenic Nd-Hf isotope compositions of Premosello peridotites were generated by metasomatism at ca. 370 Ma, but the original peridotites were already depleted during an older Proterozoic melting event. Hence, the metasomatism affecting the IVZ peridotites could have been the result of a much younger (c.f.,

Paleozoic) secondary event in a Proterozoic SCLM (e.g., Wang et al., 2013; McCoy-West et al., 2016). If this was the case, however, the samples might not have preserved similar errorchrons in both Nd and Hf systematics, as the highly radiogenic Hf isotopic signature of Premosello cpx would have already existed prior to 370 Ma. There is also the high possibility that ancient mantle metasomatism would have affected ancient isotopically depleted peridotites, mitigating their isotopic and trace element depletion. On the other hand, when the Nd-Hf isotopes are corrected to 370 Ma, highly radiogenic signatures ascribable to any significant melting event in the Proterozoic was not found. Rather, Premosello peridotites exhibit initial Nd-Hf isotopes ($\varepsilon Nd_{(i)}$ = +4.3 to +6.4, $\varepsilon Hf_{(i)}$ = +2.3 to +7.1) similar to Balmuccia and Baldissero peridotites ($\varepsilon Nd_{(i)}$ = +2.9 to +5.8, $\varepsilon Hf_{(i)}$ = +5.5 to +16.4) suggesting that prior to ca. 370 Ma, the three mantle sections had similar isotopic and geochemical compositions. The few unradiogenic $^{187}Os/^{188}Os$ isotopes which yielded Proterozoic Re depletion ages in the IVZ lherzolites (Wang et al., 2013) may therefore be interpreted as ancient mantle lithosphere relics delaminated and entrapped in an upwelling asthenosphere. Hence, rather than portions of an ancient depleted (cratonic) SCLM refertilized in more 'recent' times, we prefer the possibility that the three sequences were in the asthenospheric mantle and evolved with a similar geochemical composition until ca. 370 Ma.

In line with the preceding statement and supported by isotopic and trace elements modeling (Figure 5.8b-d), we hypothesize that at ca. 370 Ma, an intrinsically homogenous asthenospheric mantle section suffered variable degrees of partial melting (i.e., up to 12% in Premosello, ~5% in Balmuccia and Baldissero) plus different extents of nearly contemporaneous refertilization which partly obscured the depletion signatures. The original Sm/Nd and Lu/Hf ratios were modified by melting and melt-rock reaction, thereafter the different sequences evolved by Nd-Hf radiogenic ingrowths along an isotopic evolution dictated by their Sm/Nd and

Lu/Hf ratios, in turn defined by both melting and melt-rock reaction processes (Figure 5.8b). Hence, the two errorchrons pointing to ca. 370 Ma may represent the age of depletion for both the residual and refertilized peridotites, also coinciding with the timing of the metasomatic event for the refertilized rocks. Notably, the ca. 370 Ma Nd-Hf errorchrons are preserved when the compositions of the pyroxenites are also considered (Figure 5.7a-b). Previous studies interpreted this first generation of pyroxenites as segregations of melts with MORB affinity (Mazzucchelli et al., 2009), which also caused refertilization of the host lherzolites (Wang and Becker, 2015). This is in agreement with the MORB-like REE signature of the cpx in our pyroxenite samples, along with their DM-like isotopic compositions. Although the Nd-Hf isotopic compositions of the pyroxenites and the host peridotites might have been rather similar at ca. 370 Ma, migration of such melts modified the parent/daughter ratios causing deviation in isotopic evolutions of the residual vs. the melt-reacted peridotites. This effect is well depicted by the Balmuccia peridotite sample having REE and present-day Nd-Hf isotopes nearly coinciding with the pyroxenites. This sample interacted extensively with the pyroxenite-forming melt, following a similar isotopic evolution.

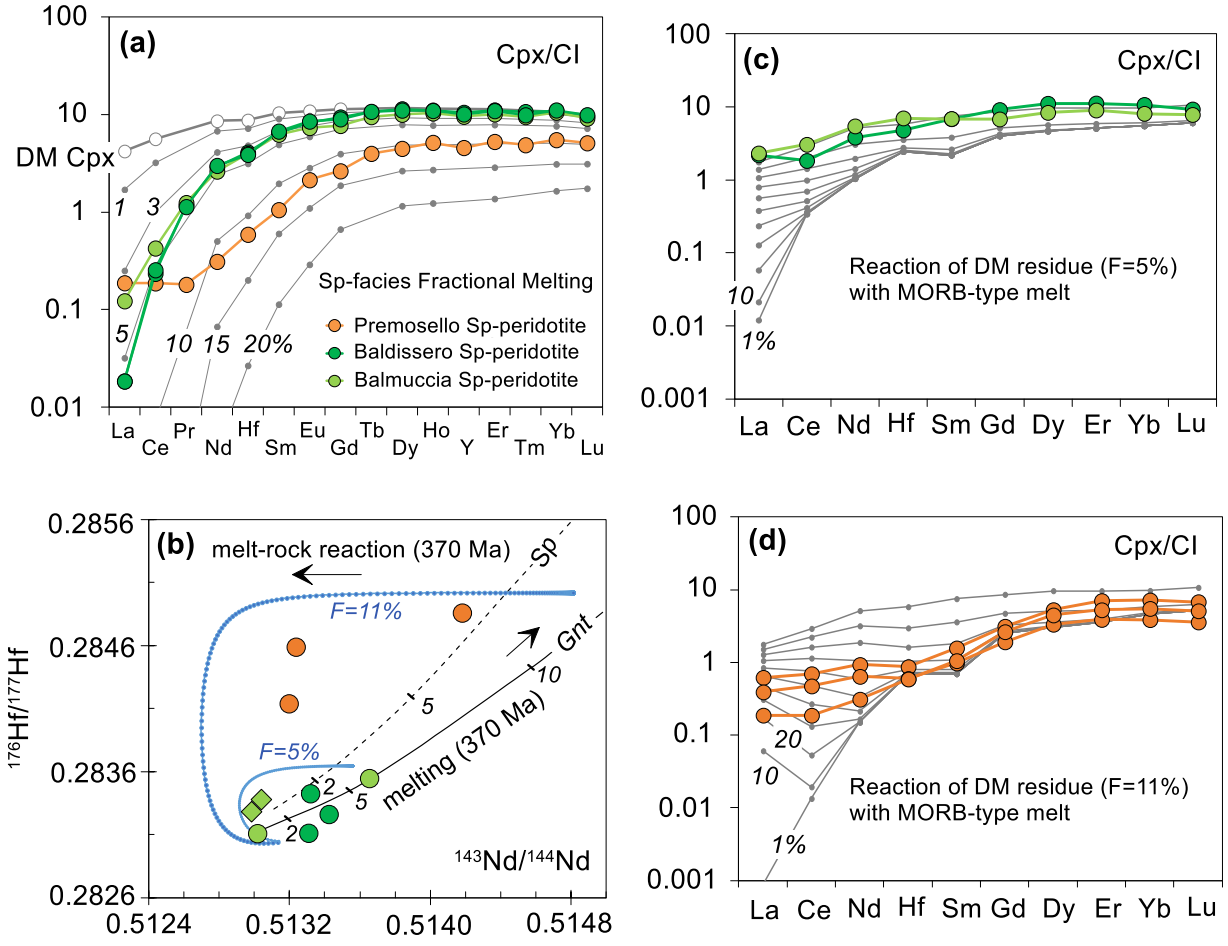

Figure 5.8: (a) Chondrite-normalized REE–Hf patterns of clinopyroxenes (cpx) from the most refractory IVZ lherzolites compared to cpx from DM residues after variable degrees of fractional melting; (b) $^{176}Hf/^{177}Hf$–$^{143}Nd/^{144}Nd$ isotopic evolution (at ca. 370 Ma) of DM residues (bulk rock) after 2, 5 and 10% of partial melting. Melting in the garnet and spinel facies conditions are denoted by unbroken and broken black lines. The isotopic evolution paths of DM residues (F=5, 11%) after interaction with MORB-type melt are indicated by blue lines; (c-d) REE–Hf patterns of cpx from DM residues (F=5, 11%) after variable degrees of interaction with MORB-type melt (between 1 and 100% re-equilibration, in 10% increments) compared to cpx from refertilized peridotites of this study. Details of the modeling can be found in the analytical methods section and Appendix 5.4–5.5.

5.5.2 Geodynamic implication and global significance

We here report unequivocal Sm-Nd and Lu-Hf isotopic evidence that combined with previous Sm-Nd and Re depletion ages (Obermiller et al., 1992; Obermiller, 1994; Mazzucchelli et al., 2010; Wang et al., 2013) constrain the accretion of the lherzolitic SCLM beneath the IVZ to the Upper Devonian. At that time, the Adriatic Plate was part of the Galatian terrane (Figure 5.9a), a continental ribbon detached from Gondwana and accreted to the margin of Laurussia shortly before the Late Carboniferous Variscan collision (Stampfli et al., 2002; von Raumer et al., 2013). At 370 Ma, the northern and western borders of the Galatian terrane were characterized by a long-lasting extension in a back-arc region caused by the subduction of the Rheic Ocean, whereas the southern and eastern ones were passive margins of the PaleoTethys. The lithospheric thinning led to the development of large basins associated with intrabasinal magmatism, starting from 370 Ma and well documented in both Southern Alps and Austroalpine units (Siegesmund et al., 2021). In this framework, we propose that the IVZ lherzolitic massifs were accreted to the SCLM through asthenospheric upwelling triggered by Variscan intra-continental extension in a back-arc setting related to the subduction of the Rheic Ocean (Figure 5.9b). This model of lithospheric accretion in a back-arc environment well explains (i) the low degrees of partial melting inferred for the IVZ peridotites, and the nearly contemporaneous migration of melts refertilizing the peridotites and crystallizing pyroxenites at deep lithospheric levels, (ii) the emplacement of young, fertile lithospheric mantle below older and thinned continental crust, as in the Variscan realm including the IVZ, and (iii) the exhumation of mantle peridotites to crustal levels during compressive regimes affecting thinned back-arc continental lithosphere.

Hence, rather than the product of recent processes of rejuvenation of old cratonic roots, we here suggest a model of formation of Phanerozoic SCLM in "recent" continental back-arc settings, where a combination of low-degree melting and nearly contemporaneous melt migration produce fertile mantle lithologies. Young mantle lithosphere thus exist off-craton, even if old Re depletion ages preserve memories of ancient melting events captured during lithospheric accretion.

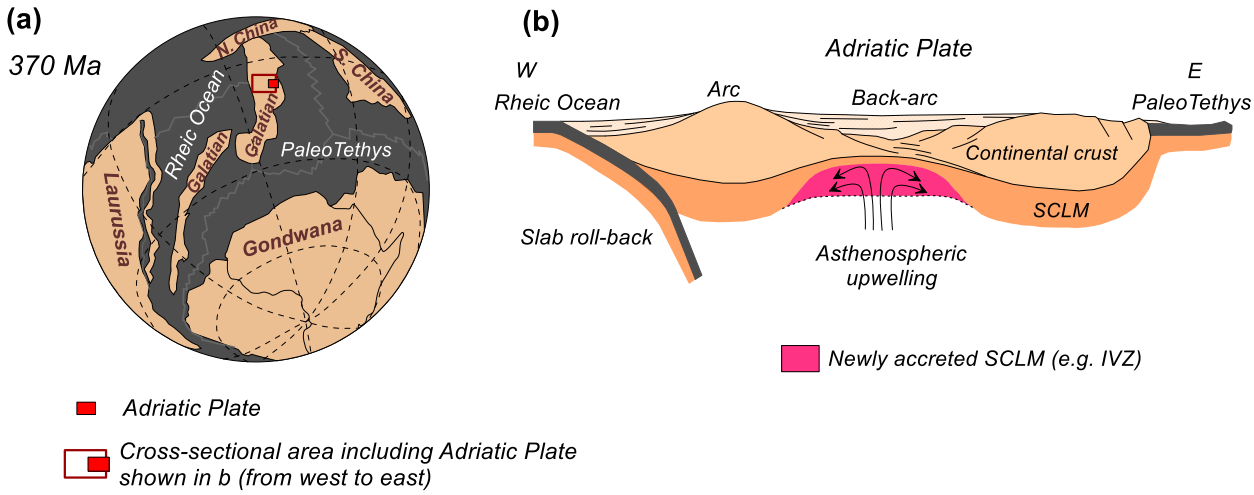

Figure 5.9: (a) Global reconstruction of the Devonian showing the location of Adria within the Galatian terrane (after von Raumer et al., 2014); (b) schematic model of accretion of the IVZ SCLM by asthenospheric upwelling in the Devonian (adapted from Siegesmund et al., 2021).

Acknowledgments

We acknowledge funding from NSF grant OCE-2126496 (to VJMS). Part of this work was performed at the National High Magnetic Field Laboratory, supported by NSF Cooperative Agreement No. DMR-1157490 and DMR-1644779 and the State of Florida. AS and AZ were supported by the Italian PRIN projects PRIN_2017KY5ZX8 and PRIN_20178LPCPW.

References

Bodinier, J.-L., Godard, M., 2014. Orogenic, ophiolitic and abyssal peridotites. In: Holland, H.D., Turekian, K.K., eds., Treatise on Geochemistry 2nd ed. Elsevier Oxford, 103-167. https://doi.org/10.1016/B978-0-08-095975-7.00204-7.

Bouvier, A., Vervoort, J.D., Patchett, P.J., 2008. The Lu–Hf and Sm–Nd isotopic composition of CHUR: constraints from unequilibrated chondrites and implications for the bulk composition of terrestrial planets. Earth Planet. Sci. Lett. 273, 48–57.

Decarlis, A., Zanetti, A., Ogunyele, A.C., Ceriani, A., Tribuzio, R., 2023. The Ivrea-Verbano tectonic evolution: The role of the crust-mantle interactions in rifting localization: Earth-Sci. Rev. 238. https://doi.org/10.1016/j.earscirev.2023.104318.

DePaolo, D.J., 1981. Trace element and isotopic effects of combined wallrock assimilation and fractional crystallization. Earth Planet. Sci. Lett. 53, 189-202. https://doi.org/10.1016/0012-821X(81)90153-9.

Ewing, T.A., Hermann, J., Rubatto, D., 2013. The robustness of the Zr-in-rutile and Ti-in-zircon thermometers during high-temperature metamorphism (Ivrea-Verbano Zone, Northern Italy). Contrib. Mineral. Petrol. 165, 757-779.

Gale, A., Dalton, C.A., Langmuir, C.H., Su, Y., Schilling, J.-G., 2013. The mean composition of ocean ridge basalts. Geochem. Geophys. Geosys. 14, 489-518.

Griffin, W.L., Powell, W.J., Pearson, N.J., O'Reilly, S.Y., 2008. GLITTER: data reduction software for laser ablation ICPMS: *in* Sylvester, P., ed., Laser Ablation ICP–MS in the Earth Sciences. Current Practices and Outstanding Issues. Mineralogical Association of Canada Short Course Series 40, 308–311.

Griffin, W.L., O'Reilly, S.Y., Afonso, J.C., Begg, G.C., 2009. The composition and evolution of lithospheric mantle: A re-evaluation and its tectonic implications. J. Petrol. 50, 1185–1204. https://doi.org/10.1093/petrology/egn033.

Guarnieri, L., Nakamura, E., Piccardo, G.B., Sakaguchi, C., Shimizu, N., Vannucci, R., Zanetti, A., 2012. Petrology, trace element and Sr, Nd, Hf isotope geochemistry of the North Lanzo Peridotite Massif (Western Alps, Italy). J. Petrol. 53, 2259-2306.

https://doi.org/10.1093/petrology/egs049.

Ionov, D.A., Ashchepkov, I., Jagoutz, E., 2005. The provenance of fertile off-craton lithospheric mantle: Sr–Nd isotope and chemical composition of garnet and spinel peridotite xenoliths from Vitim, Siberia. Chem. Geol. 217, 41-75. https://doi.org/10.1016/j.chemgeo.2004.12.001.

Ionov, D.A., Hofmann, A.W., 2007. Depth of formation of subcontinental off-craton peridotites. Earth Planet. Sci. Lett. 261, 620-634. https://doi.org/10.1016/j.epsl.2007.07.036.

Ionov, D.A., Liu, Z., Li, J., Golovin, A.V., Korsakov, A.V., Xu, Y., 2020. The age and origin of cratonic lithospheric mantle: Archean dunites vs. Paleoproterozoic harzburgites from the Udachnaya kimberlite, Siberian craton. Geochim. Cosmochim. Acta 281, 67-90. https://doi.org/10.1016/j.gca.2020.05.009.

Klötzli, U.S., Sinigoi, S., Quick, J.E., Demarchi, G., Tassinari, C.C.G., Sato, K., Günes, Z., 2014. Duration of igneous activity in the Sesia Magmatic System and implications for high-temperature metamorphism in the Ivrea–Verbano deep crust. Lithos 206-207, 19-33. https://doi.org/10.1016/j.lithos.2014.07.020.

Le Roux, V., Bodinier, J.-L., Alard, O., O'Reilly, S.Y., Griffin, W.L., 2009. Isotopic decoupling during porous melt flow: A case-study in the Lherz peridotite. Earth Planet. Sci. Lett. 279, 76-85. https://doi.org/10.1016/j.epsl.2008.12.033.

Le Roux, V., Bodinier, J.-L., Tommasi, A., Alard, O., Dautria, J.-M., Vauchez, A., Riches, A.J.V., 2007. The Lherz spinel lherzolite: refertilized rather than pristine mantle. Earth Planet. Sci. Lett. 259, 599–612. https://doi.org/10.1016/j.epsl.2007.05.026.

Lee, C.-T.A., Luffi, P., Chin, E.J., 2011. Building and destroying continental mantle. Annual Rev. Earth Planet. Sci. 39, 59-90. https://doi.org/10.1146/annurev-earth-040610-133505.

Longhi, J., 2002. Some phase equilibrium systematics of lherzolite melting: I. Geochem. Geophys. Geosys. 3, 1-33. https://doi.org/10.1029/2001GC000204.

Lyubetskaya, T., Korenaga, J., 2007. Chemical composition of Earth's primitive mantle and its variance: 1. Method and results. J. Geophys. Res. 112. https://doi.org/10.1029/2005JB004223.

Mazzucchelli, M., Rivalenti, G., Brunelli, D., Zanetti, A., Boari, E., 2009. Formation of highly refractory dunite by focused percolation of pyroxenite-derived melt in the Balmuccia Peridotite Massif (Italy). J. Petrol. 50, 1205-1233. https://doi.org/10.1093/petrology/egn053.

Mazzucchelli, M., Zanetti, A., Rivalenti, G., Vannucci, R., Correia, C.T., Tassinari, C.C.G., 2010. Age and geochemistry of mantle peridotites and diorite dykes from the Baldissero body: Insights into the Paleozoic-Mesozoic evolution of the Southern Alps. Lithos 119, 485-500. https://doi.org/10.1016/j.lithos.2010.08.002.

Mazzucchelli, M., Marchesi, S., Bottazzi, P., Ottolini, L., Vannucci, R., 1992. The Premosello Chiovenda peridotitic body in Ossola valley (Ivrea-Verbano Zone, Italy). Atti Ticinensi Sci. Terra 35, 75-82.

McCoy-West, A.J., Bennett, V.C., Amelin, Y., 2016. Rapid Cenozoic ingrowth of isotopic signatures simulating "HIMU" in ancient lithospheric mantle: Distinguishing source from process. Geochim. Cosmochim. Acta 187, 79-101.

McCoy-West, A.J., Bennett, V.C., Puchtel, I.S., Walker, R.J., 2013. Extreme persistence of cratonic lithosphere in the southwest Pacific: Paleoproterozoic Os isotopic signatures in Zealandia. Geology v. 41, 231-234. https://doi.org/10.1130/G33626.1.

Obermiller, W.A., 1994. Chemical and isotopic variations in the Balmuccia, Baldissero and Finero Peridotite Massifs (Ivrea-Zone, N-Italy). Unpubl. Ph.D. thesis, Johannes-Gutenberg-Universität Mainz.

Obermiller, W.A., Hoffmann, A.W., Mazzucchelli, M., Rivalenti, G., 1992. Sr and Nd isotope in Mantel-Peridotiten der Ivrea-Zone: Hinweise auf die Heterogenitat des oberen Mantels. European J. Mineral. 4, 209.

Pearson, D.G., Scott, J.M., Liu, J., Schaeffer, A., Wang, L.H., van Hunen, J., Szilas, K., Chacko, T., Kelemen, P.B., 2021. Deep continental roots and cratons. Nature 596, 199-210. https://doi.org/10.1038/s41586-021-03600-5.

Peressini, G., Quick, J.E., Sinigoi, S., Hofmann, A.W., Fanning, M, 2007. Duration of a large mafic intrusion and heat transfer in the lower crust: a SHRIMP U/Pb zircon study in the Ivrea–Verbano Zone (Western Alps, Italy): J. Petrol. 48, 1185-1218.

https://doi.org/10.1093/petrology/egm014.

Reisberg, L., 2021. Osmium isotope constraints on formation and refertilization of the non-cratonic continental mantle lithosphere. Chem. Geol. 574. https://doi.org/10.1016/j.chemgeo.2021.120245.

Reisberg, L., and Lorand, J.P., 1995, Longevity of sub-continental mantle lithosphere from osmium isotope systematics in orogenic peridotite massifs: Nature 376, 159-162. https://doi.org/10.1038/376159a0.

Reisberg, L., Zindler, A., and Jagoutz, E., 1989, Further Sr and Nd isotopic results from peridotites of the Ronda Ultramafic Complex: Earth and Planetary Science Letters 96, 161-180. https://doi.org/10.1016/0012-821X(89)90130-1.

Rivalenti, G., Mazzucchelli, M., 2000. Interaction of mantle-derived magmas and crust in the IVZ and the Ivrea mantle peridotite. In: Proceedings, International School of Earth and Planetary Sciences, Crust Mantle Interactions, 153-198.

Rivalenti, G., Mazzucchelli, M., Vannucci, R., Hofmann, A.W., Ottolini, L., Bottazzi, P., Obermiller, W., 1995. The relationship between websterite and peridotite in the Balmuccia peridotite massif (NW Italy) as revealed by trace element variations in clinopyroxene. Contrib. Mineral. Petrol. 121, 275-288. https://doi.org/10.1007/BF02688243.

Ryberg, T., Haberland, C., Wawerzinek, B., Stiller, M., Bauer, K., Zanetti, A., Ziberna, L., Hetényi, G., Müntener, O., Weber, M.M., Krawczyk, C.M., 2023. 3-D imaging of the Balmuccia peridotite body (Ivrea–Verbano zone, NW-Italy) using controlled source seismic data. Geophys. J. Inter. 234, 1985-1998, https://doi.org/10.1093/gji/ggad182.

Salters, V.J.M., Stracke, A., 2004. Composition of the depleted mantle. Geochem. Geophys. Geosys. 5. https://doi.org/10.1029/2003GC000597.

Sanfilippo, A., Salters, V., Tribuzio, R., Zanetti, A., 2019. Role of ancient, ultra-depleted mantle in Mid-Ocean-Ridge magmatism. Earth Planet. Sci. Lett. 511, 89-98. https://doi.org/10.1016/j.epsl.2019.01.018.

Sani, C., Sanfilippo, A., Peyve, A.A., Genske, F., Stracke, A., 2023. Earth mantle's isotopic record of progressive chemical depletion. AGU Advances 4.

https://doi.org/10.1029/2022AV000792.

Scarponi, M., Hetényi, G., Berthet, T., Baron, L., Manzotti, P., Petri, B., Pistone, M., Müntener, O., 2000. New gravity data and 3-D density model constraints on the Ivrea Geophysical Body (Western Alps). Geophys. J. Inter. 222, 1977-1991.

Schmid, S.M., 1993. Ivrea zone and adjacent southern Alpine basement, *in* von Raumer, J.F., and Neubauer, F., eds., Pre-Mesozoic Geology in the Alps. Springer–Verlag, Berlin, 567–583. https://doi.org/10.1007/978-3-642-84640-3_33.

Shirey, S.B., and Walker, R.J., 1998, The Re-Os isotope system in cosmochemistry and high-temperature geochemistry: Annual Review of Earth and Planetary Sciences, v. 26, p. 423-500. https://doi.org/10.1146/annurev.earth.26.1.423.

Siegesmund, S., Oriolo, S., Schulz, B., Heinrich, T., Basei, M.A.S., Lammerer, B., 2021. The birth of the Alps: Ediacaran to Paleozoic accretionary processes and crustal growth along the northern Gondwana margin. Inter. J. Earth Sci. 110, 1321–1348. https://doi.org/10.1007/s00531-021-02019-7.

Stampfli, G.M., Von Raumer, J.F., Borel, G.D., 2002. Paleozoic evolution of pre-Variscan terranes: from Gondwana to the Variscan collision. Geol. Soc. Am. Spec. Paper 364, 263–280. https://doi.org/10.1130/0-8137-2364-7.263.

Stracke, A., Bizimis, M., Salters, V.J., 2003a. Recycling oceanic crust: quantitative constraints. Geochem. Geophys. Geosys. 4. https://doi.org/10.1029/2001GC000223

Stracke, A., Snow, J.E., Hellebrand, E., von der Handt, A., Bourdon, B., Birbaum, K., Günther, D., 2011. Abyssal peridotite Hf isotopes identify extreme mantle depletion. Earth Planet. Sci. Lett. 308, 359-368. https://doi.org/10.1016/j.epsl.2011.06.012.

Stracke, A., Zindler, A., Salters, V. J. M., McKenzie, D., Groenvold, K., 2003b. The dynamics of melting beneath Theistareykir, northern Iceland. Geochem. Geophys. Geosys. 4. https://doi.org/10.1029/2002GC000347.

Tilhac, R., Begg, G.C., O'Reilly, S.Y., Griffin, W.L., 2022. A global review of Hf-Nd isotopes: new perspectives on the chicken-and-egg problem of ancient mantle signatures. Chem. Geol. 609, 1–25. https://doi.org/10.1016/j.chemgeo.2022.121039.

von Raumer, J.F., Bussy, F., Schaltegger, U., Schulz, B., Stampfli, G.M., 2013. Pre-Mesozoic Alpine basements–Their place in the European Paleozoic framework. GSA Bulletin 125, 89–108. https://doi.org/10.1130/B30654.1.

Wang, Z., Becker, H., 2015. Fractionation of highly siderophile and chalcogen elements during magma transport in the mantle: Constraints from pyroxenites of the Balmuccia peridotite massif. Geochim. Cosmochim. Acta 159, 244-263. https://doi.org/10.1016/j.gca.2015.03.036.

Wang, Z., Becker, H., Gawronski, T., 2013. Partial re-equilibration of highly siderophile elements and the chalcogens in the mantle: a case study on the Baldissero and Balmuccia peridotite massifs (Ivrea Zone, Italian Alps). Geochim. Cosmochim. Acta 108, 21–44. https://doi.org/10.1016/j.gca.2013.01.021.

Woelki, D., Salters, V., Beier, C., Dick, H., Koepke, J., Romer, R., 2023. Shallow recycling of lower continental crust: The Mahoney Seamount at the Southwest Indian Ridge. Earth Planet. Sci. Lett. 602. https://doi.org/10.1016/j.epsl.2022.117968.

Workman, R.K., Hart, S.R., 2005. Major and trace element composition of the depleted MORB mantle (DMM). Earth Planet. Sci. Lett. 231, 53–72.

Zanetti, A., Giovanardi, T., Langone, A., Tiepolo, M., Wu, F.Y., Dallai, L., Mazzucchelli, M., 2016. Origin and age of zircon-bearing chromitite layers from the Finero phlogopite peridotite (Ivrea–Verbano Zone, Western Alps) and geodynamic consequences. Lithos 262, 58-74. https://doi.org/10.1016/j.lithos.2016.06.015.

CHAPTER 6

Occurrence and origin of the DUPAL isotope anomaly in an orogenic peridotite massif: The Finero phlogopite peridotite example

Abimbola C. Ogunyele[1,2], Alessio Sanfilippo[1,2], Vincent J.M. Salters[3], Mattia Bonazzi[2] and Alberto Zanetti[2]

[1] Department of Earth and Environmental Sciences, University of Pavia, Via Ferrata 1, 27100 Pavia, Italy

[2] CNR – Istituto Geoscienze e Georisorse, Via Ferrata 1, 27100 Pavia, Italy

[3] National High Magnetic Field Laboratory, Department of Earth, Ocean and Atmospheric Sciences, Florida State University, Tallahassee, FL 32310, USA

Declaration

This manuscript is in preparation for submission to a journal for review and possible publication. The study was conducted in collaboration with the co-authors cited above. The contribution of each author is given below.

ACO: Data curation, Formal analysis, Investigation, Methodology, Validation, Visualization, Writing - original draft, Writing - review & editing; **AS**: Conceptualization, Supervision, Methodology, Validation, Visualization, Writing - original draft, Writing - review & editing; **VJMS**: Funding acquisition, Investigation, Methodology, Validation, Visualization, Supervision, Writing - review & editing; **MB**: Formal analysis, Investigation, Writing - review & editing; **AZ**: Conceptualization, Funding acquisition, Methodology, Project administration, Resources, Supervision, Validation, Visualization, Writing - review & editing.

Abstract

We report the occurrence of the DUPAL isotope anomaly in phlogopite- and amphibole-bearing peridotite and websterite from the orogenic peridotite massif of Finero, Ivrea-Verbano Zone (northwest Italy). Amphiboles from the peridotite and websterite are characterized by highly radiogenic $^{208}Pb/^{204}Pb$ and $^{207}Pb/^{204}Pb$ for a given $^{206}Pb/^{204}Pb$ deviating significantly from the Northern Hemisphere Reference Line with $\Delta 8/4$ and $\Delta 7/4$ ranging from 61.6–64.5 and 12.3–14.9, respectively. The amphiboles also exhibit elevated $^{87}Sr/^{86}Sr_{(i)}$ (0.706746–0.707632) coupled to unradiogenic $\varepsilon Nd_{(i)}$ (–1.9 to –3.2) and $\varepsilon Hf_{(i)}$ (+0.1 to –1.9). Similarly, whole-rocks of the peridotite show highly radiogenic Sr and unradiogenic Nd isotopes. We propose that the DUPAL isotope anomaly exhibited by the Finero phlogopite peridotite was the result of pervasive percolation and reaction of the mantle body with hydrous silica-saturated melts carrying DUPAL anomaly. These DUPAL-bearing metasomatizing melts were derived by partial melting of continental crust subducted and/or delaminated into the upper mantle. The lack of significant geochemical and isotopic variation between the peridotite and websterite is explained by the segregation of the latter from crystal mushes made of harzburgites and the hydrous silica-saturated melts carrying the DUPAL anomaly. The proposed model involving the recycling of subducted and/or delaminated continental crust components within the Finero mantle is consistent and well explains the occurrence of mantle-derived magmatism with continental crust components in the IVZ and throughout the Southern Alps during the Triassic–Jurassic period.

6.1 Introduction

The DUPAL isotope anomaly, first documented in mid-ocean ridge basalts (MORB) from the Indian Ocean by Dupré and Allègre (1983) is defined by Hart (1984, 1988) by elevated $^{87}Sr/^{86}Sr$ ratios (> 0.705 or $\Delta Sr > 50$) and deviations of $^{208}Pb/^{204}Pb$ and $^{207}Pb/^{204}Pb$ from the Northern Hemisphere Reference Line (NHRL) expressed as $\Delta 8/4$ (> 60) and $\Delta 7/4$ (> 10) (Xing, 1997; Mazzucchelli et al., 2016; Tian et al., 2022). Hart (1984) upon discovering that basalts from many other Southern Hemisphere localities also show this anomalous Sr and Pb isotopic characteristics, he delineated the occurrence of the DUPAL anomaly around the Southern Hemisphere between the Equator and 60° S. The finding of this anomaly established the existence of a vast mantle isotopic domain in the Southern Hemisphere, distinguishing this mantle source from that of the Pacific and north Atlantic in the Northern Hemisphere (Dupré and Allègre, 1983; Hart, 1984, 1988; Mahoney et al., 1998, 2002; Kempton et al., 2002; Escrig et al., 2004; Hanan et al., 2004; Meyzen et al., 2005). The origin of this isotopic anomaly has often been attributed to the contamination of the Southern Hemisphere upper mantle by one or more of the following materials: (i) lower continental crust delaminated from cratonic Gondwanan lithosphere (e.g., Arndt and Goldstein, 1989; Escrig et al., 2004; Hanan et al., 2004; Meyzen et al., 2005); (ii) subcontinental lithospheric mantle introduced prior to and/or during the breakup of Gondwana (e.g., Mahoney et al., 1992); (iii) convectively recycled subducted altered oceanic crust and/or sediment (e.g., Dupré and Allègre, 1983; Rehkämper and Hofmann, 1997); (iv) Indian ocean hot spot sources, especially from the large long-lived Kerguelen mantle plume (e.g., Storey et al., 1989); and (5) subduction-modified mantle (e.g., Kempton et al., 2002). With renewed interests in solving the origin of the DUPAL anomaly, Escrig et al. (2004) and Meyzen et al. (2005) using Os, Pb, Sr and Nd isotopic compositions of Indian MORB coupled with

isotopic and geodynamical modeling and arguments, have shown that the recycling of subcontinental lithospheric mantle, old subduction-modified mantle or sediments with oceanic crust cannot be responsible for the DUPAL isotopic signature of Indian MORB. The extreme signature of the Indian MORB also does not bear any isotopic affinities with recent products of the nearby Marion hot spot (Meyzen et al., 2005). Both studies concluded that delamination of the lower continental crust best explains the Indian upper-mantle isotopic anomaly.

Outside the Southern Hemisphere, the DUPAL isotope anomaly has also been found in basalts from some areas in the Northern Hemisphere particularly in Asia (Smith, 1998) and in the western Gakkel Ridge, Arctic (Goldstein et al., 2008). Smith (1998) asserted that the volcanism in Asia demonstrates that DUPAL signatures can be generated in the continental mantle. Mazzucchelli et al. (2016) proved the correctness of this assertion when they found, for the first time, the DUPAL anomaly in lithospheric mantle xenoliths from Tres Lagos in Patagonia, South America. They proposed that partial melting of deep-seated subducted DUPAL components (LCC and/or EMII) triggered by uprising hot asthenosphere produced melts which metasomatized the SCLM (with DMM and HIMU affinity) generating the hybrid DUPAL-bearing mantle sampled by the xenoliths.

So far, and as much as we are aware, no occurrence of the DUPAL isotope anomaly in orogenic peridotite massif in any part of the world has been reported. We here report, for the first time, the occurrence of the DUPAL isotope anomaly in phlogopite- and amphibole-bearing peridotite and websterite from an orogenic peridotite massif in Finero, Ivrea-Verbano Zone (northwest Italy). We argue that the DUPAL isotope anomaly was imparted to the Finero peridotite by pervasive and reactive migration of hydrous silica-saturated melts derived from the partial melting of continental crust subducted and/or delaminated into the upper mantle. The

websterites were formed from crystal mushes consisting of harzburgites and the hydrous silica-saturated melts carrying the DUPAL isotope anomaly. Recycling of subducted and/or delaminated continental crust materials within the Southern Alps upper mantle, as testified by the Finero peridotite massif, plausibly explains the development of magmatism derived from mantle sources containing continental crust components in the IVZ and throughout the Southern Alps during the Triassic–Jurassic period. We therefore reject the melting of residual oceanic slab and serpentinites as the source of the melts/fluids which metasomatized the Finero massif as proposed by Cannaò et al. (2022).

6.2 Orogenic peridotite massifs in the Ivrea-Verbano Zone

The Ivrea-Verbano Zone (IVZ) in the westernmost sector of the Southern Alps is a cross-section through the lowermost continental crust of the Adriatic Plate (Voshage et al., 1987; Schmid, 1993; Zanetti et al., 1999, 2013; Decarlis et al., 2023). The IVZ lower continental crust comprises Variscan-age amphibolite- to granulite-facies metasediments underplated by an igneous Mafic Complex during the Late Carboniferous–Early Permian (Klötzli et al., 2014; Peressini et al., 2007). Within the IVZ lower crustal sequence, tens of orogenic peridotite massifs of clear mantle origin are aligned parallel to the Insubric Line (Voshage et al., 1987; Hartman and Wedepohl, 1993; Rivalenti et al., 1995; Decarlis et al., 2023). The largest of the mantle massifs occur at Balmuccia, Baldissero, Premosello and Finero (Figure 6.1A). The first three massifs, outcropping in the southern to central IVZ, are predominantly lherzolitic in composition and show weak or no metasomatic overprinting (see Obermiller, 1994; Rivalenti et al., 1995; Mazzucchelli et al., 1992, 2010; Decarlis et al., 2023; Ogunyele et al., 2024a).

The Finero orogenic peridotite massif (object of the present study; Figure 6.1A-B) is the most north-easterly, most depleted and pervasively metasomatized lens of peridotite bodies occurring in the Ivrea-Verbano Zone (Voshage et al., 1987; Hartman and Wedepohl, 1993; Zanetti et al., 1999, 2016; Giovanardi et al., 2020; Decarlis et al., 2023). It is mainly formed by a lithologic association of phlogopite- and amphibole-bearing harzburgites and pyroxenites (mainly olivine-websterites, websterites and orthopyroxenites; Figure 6.2A-C) which do not show significant geochemical gradients among them (Zanetti et al., 1999; Giovanardi et al., 2020). Replacive dunites (Figure 6.2D) containing stratiform to podiform zircon-bearing chromitites also occur within the Finero phlogopite peridotite (FPP) (Grieco et al., 2001; Zaccarini et al., 2004; Zanetti et al., 2016). Hartmann and Wedepohl (1993), based on the depleted major element chemistry of the FPP estimated that the peridotite body experienced the extraction of about 18% MORB-like melt after which it was pervasively metasomatized. The pervasive metasomatism of the FPP occurred in multi-stages (Grieco et al., 2001; Morishita et al., 2008; Zanetti et al., 2016; Malitch et al., 2017; Selverstone and Sharp, 2017; Giovanardi et al., 2020; Decarlis et al., 2023) and probably started in the Late Carboniferous–Early Permian constrained by whole-rock Rb-Sr isochron (293 ± 13 Ma, Voshage et al., 1987) and U-Pb dating of zircons from chromitite veins within the FPP (~310 Ma, Malitch et al., 2017). The final stages of the metasomatism occurred around ~187 Ma and have been linked to the time of exhumation of the FPP (Zanetti et al., 2016; Malitch et al., 2017).

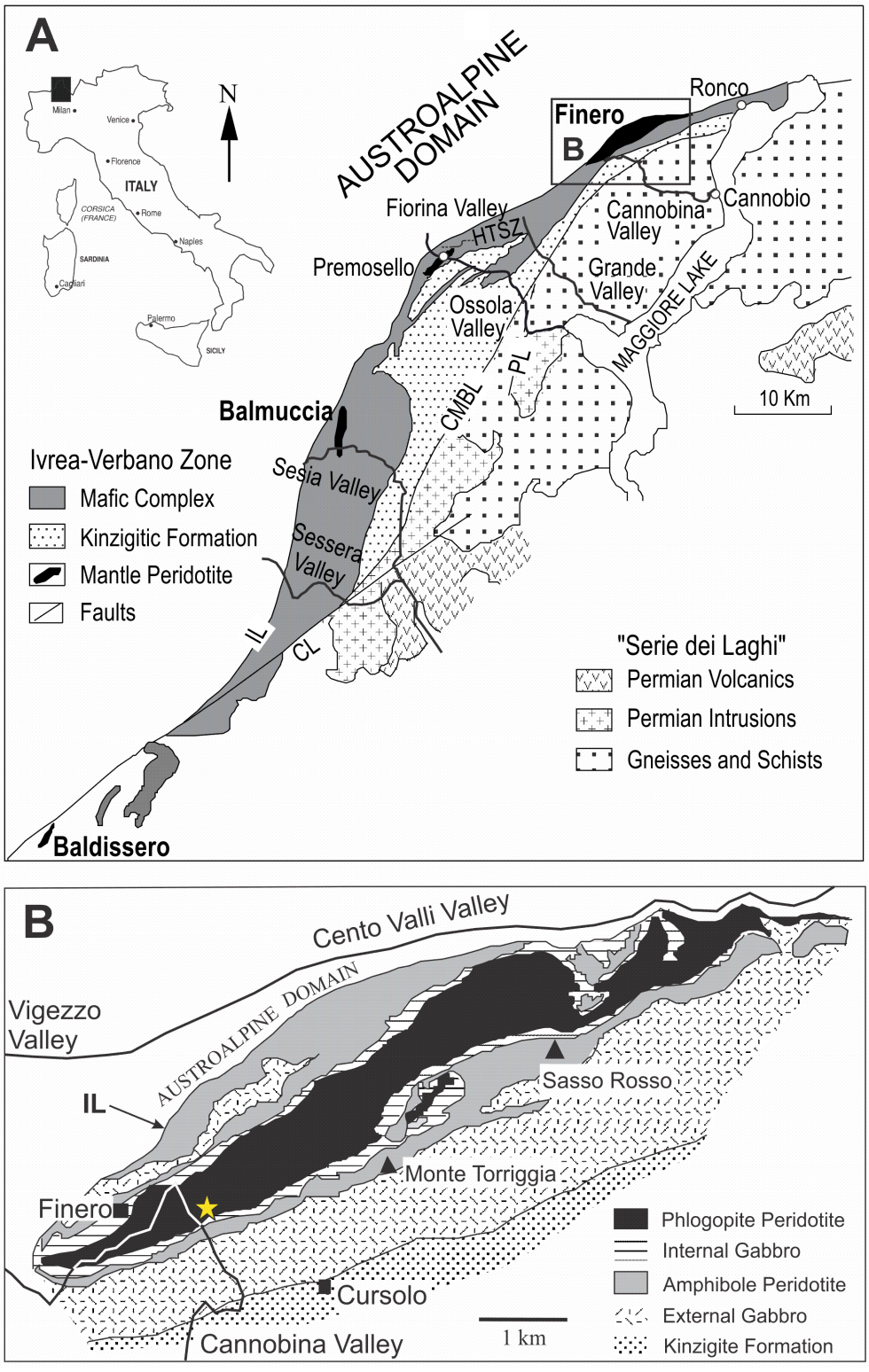

Figure 6.1: Geological maps of (a) the Ivrea-Verbano Zone and (b) the Finero Complex with location (yellow star) of the sampled peridotite and websterite around Rio Creves. IL – Insubric Line, CMBL – Cossato-Mergozzo-Brissago Line, PL – Pogallo Line (after Zanetti et al., 1999).

6.3 New sample suite and petrography

Two peridotite and one websterite samples were collected from the Finero mantle massif in the Rio Creves area (Figures 6.1, 6.2A-C). One of the phlogopite peridotite samples (FIN5, Figure 6.2B) is concordantly cut by phlogopite-bearing websterites, orthopyroxenites and amphibole veinlets. The phlogopite peridotite samples (FI2203 and FIN5; Figure 6.2A-B) are harzburgitic (~2-3 vol. % clinopyroxene) and contain abundant phlogopite and amphibole. Sample FI2203 shows the highest amounts of phlogopite (~6 vol. %) and amphibole (~15 vol. %) compared to sample FIN5 (~2 vol. % phlogopite and ~10 vol. % amphibole). They both exhibit weakly foliated to porphyroblastic textures with amphibole and phlogopite defining the foliation (Figures 6.2A-B, 6.3A-D). Porphyroblasts of olivine and sometimes orthopyroxene display kink banding. Olivine sometimes includes smaller grains of orthopyroxene (Figure 6.3D). Clinopyroxene is rare, undeformed and occurs in the interstitial spaces between other minerals (Figure 6.3A). Spinel occurs as small rounded crystals between mineral interstices (Figure 6.3A) and also within olivine porphyroblasts (Figure 6.3C).

The phlogopite-bearing websterite sample (FIN6, Figure 6.2C) is composed mainly by large crystals of clinopyroxene (40 vol. %), orthopyroxene (35 vol. %), amphibole (12 vol. %) and phlogopite (8 vol. %) (Figure 6.3E, F) and is veined by numerous orthopyroxenites. The contacts between the pyroxenites and the host peridotite are sharp with no evidence of reactions between both rocks (e.g., Figure 6.2B). The websterite is mainly characterized by coarse granoblastic texture (Figure 6.3E, F). Spinel (3 vol. %) and minor amount of olivine (~2 vol. %) with no kink banding also occur in the sample (Figure 6.3E). Amphibole and phlogopite, unlike in the peridotite samples, are modally less abundant than clinopyroxene.

Figure 6.2: Typical lithologies of the Finero mantle massif, Ivrea-Verbano Zone. (A) Weakly foliated harzburgite with foliation defined mainly by amphibole and subordinately by phlogopite. (B) Harzburgite veined of websterite (φ), orthopyroxenite (δ) and amphiboles (ϕ). (C) Phlogopite-rich websterite alternating with orthopyroxenite veins (δ). (D) Dunite composed largely of olivine with abundant metasomatic phlogopite and amphibole. In the bottom left part of the sample, an amphibole oikocryst encloses olivine chadacrysts.

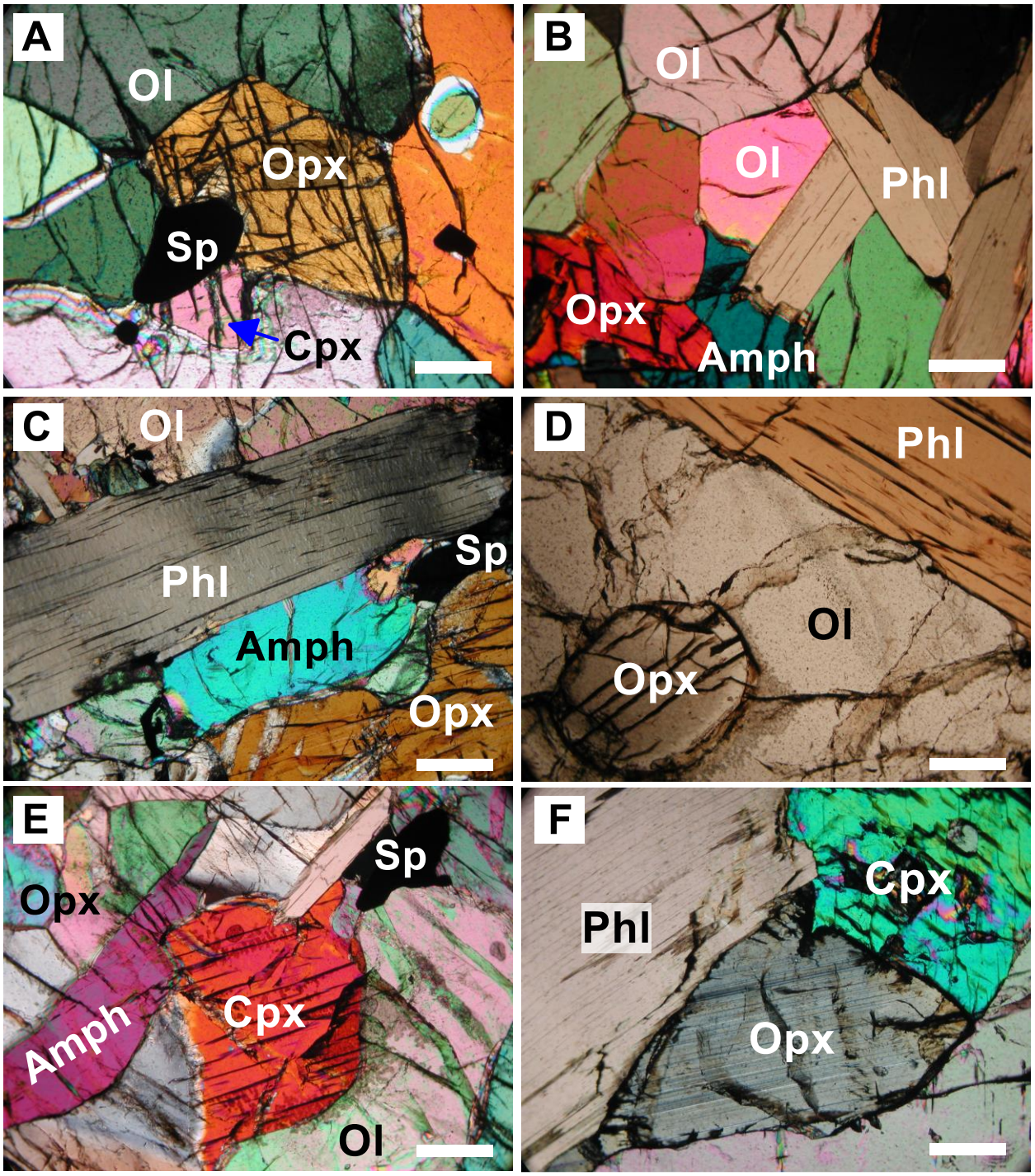

Figure 6.3: Photomicrographs of (A-D) phlogopite peridotite and (E-F) websterite from Finero, IVZ. (A) Small grains of clinopyroxene and spinel in the interstitial spaces between olivine and orthopyroxene porphyroblasts. Spinels also occur within olivine porphyroblasts. (B, C) Abundant phlogopite and amphibole associated with olivine, orthopyroxene and spinel in the FPP. (D) Orthopyroxene inclusions within olivine porphyroblast in the FPP. (E, F) Finero

websterite showing granoblastic texture composed of large clinopyroxene, orthopyroxene, phlogopite and amphibole. Spinel and olivine occur as accessories. Sections are thicker than normal (80 μm). White bars to the right of panels represent 1 mm scale.

6.4 Analytical methods

Major element compositions of mineral phases (olivine, orthopyroxene, spinel, amphibole and phlogopite) in the peridotite sample FI2203 were measured by electronprobe microanalysis using a JEOL JXA-8230 Superprobe at the Joint Laboratory of the Department of Earth Sciences, University of Florence and the CNR-IGG Florence. Detailed analytical procedures and operating conditions can be found in Section 5.3.2 of Chapter 5. For samples FIN5 and FIN6, mineral major element dataset were compiled from Zanetti et al. (1999). The combined mineral major element dataset is reported in Appendix 6.1.

Trace element contents of mineral phases (olivine, orthopyroxene, clinopyroxene, spinel, amphibole and phlogopite) in the peridotites and websterite were measured on thin sections and mineral separates using an Agilent 8900 QQQ-ICP-MS coupled to a 266 nm Nd:YAG laser ablation system at the CNR-IGG Pavia. The analytical procedures and operating conditions are detailed in Section 5.3.2 of Chapter 5. The trace element dataset is reported in Appendix 6.2.

Amphiboles were separated from the peridotite and websterite samples for Sr, Pb, Nd and Hf isotopes measurements. The sample processing and isotopic measurements were performed at the National High Magnetic Field Laboratory, Florida State University. For each sample, 100 mg of amphibole separates were leached, dissolved and processed through ion exchange columns in ultraclean lab. The separates were leached in 5 ml 2.5N HCl and <30% H_2O_2 for 60 min at room temperature to remove any alteration products. The leached separates were rinsed several times with quartz sub-boiling distilled water. Subsequent dissolution and column chemistry was

performed after procedures described by Stracke et al. (2003) and Woelki et al. (2023). Sr isotope compositions were measured by thermal ionization mass spectrometry (TIMS) using a Finnigan MAT 262 RPQ system. Measurements of the Eimer & Amend (E&A) $SrCO_3$ standard provided a $^{87}Sr/^{86}Sr$ ratio of 0.708010 ± 0.000010 (2σ, n = 3). The $^{87}Sr/^{86}Sr$ ratios are corrected for mass bias using a $^{88}Sr/^{86}Sr$ value of 0.1194 and reported relative to the E&A $SrCO_3$ standard value of $^{87}Sr/^{86}Sr$ = 0.708000. Blanks for Sr were less than 100 pg. Nd, Hf and Pb isotopes were measured using a ThermoFisher Neptune Multi-Collector ICP-MS system. Repeated measurements of the La Jolla standard yielded $^{143}Nd/^{144}Nd$ ratio of 0.511790 ± 0.000012 (2σ, n = 17). The $^{143}Nd/^{144}Nd$ ratios are corrected for mass bias using a $^{146}Nd/^{144}Nd$ ratio of 0.7219 and are reported relative to the La Jolla standard of 0.511850. Blanks for Nd were less than 10 pg. Measured value of the JMC-475 standard is $^{176}Hf/^{177}Hf$ = 0.282150 ± 0.000008 (2σ, n = 20). The $^{176}Hf/^{177}Hf$ ratios are corrected for mass bias using a $^{179}Hf/^{177}Hf$ ratio of 0.7325 and reported relative to JMC-475 value of $^{176}Hf/^{177}Hf$ = 0.282150. Blanks for Hf were less than 40 pg. Ten measurements of NBS 981 provided $^{206}Pb/^{204}Pb$, $^{207}Pb/^{204}Pb$, and $^{208}Pb/^{204}Pb$ ratios and 2σ of 16.9332 ± 0.0073, 15.4847 ± 0.0121, and 36.6744 ± 0.0434, respectively. The measured Pb isotopes were normalized to NBS 981 $^{206}Pb/^{204}Pb$, $^{207}Pb/^{204}Pb$, and $^{208}Pb/^{204}Pb$ ratios of 16.9356, 15.4891, and 36.7006, respectively. Blanks for Pb were less than 30 pg. $^{87}Rb/^{86}Sr$, $^{147}Sm/^{144}Nd$, and $^{176}Lu/^{177}Hf$ ratios were calculated from the Rb, Sr, Sm, Nd, Lu and Hf concentrations measured on the amphibole samples by LA-ICP-MS. The Sr, Pb, Nd and Hf isotopes dataset of the amphiboles is reported in Appendix 6.3.

6.5 Analytical results

6.5.1 Mineral major element chemistry

Olivine, orthopyroxene, clinopyroxene and spinel from the Finero phlogopite peridotite show the most depleted and unfertile major element compositions compared to other IVZ peridotites (i.e., the Premosello, Balmuccia and Baldissero lherzolites). They have compositions geochemically similar to Suprasubduction Zone (SSZ) peridotites (Figure 6.4A-D). Olivine exhibits forsterite contents **(**Fo = molar [Mg/(Mg + Fe_t)]∗100**)** ranging from 90.6 to 91.0. Orthopyroxene and clinopyroxene (Cr-diopside) are characterized by magnesium numbers (Mg# = molar [Mg/(Mg + Fe_t)] ∗ 100) of 90.7-91.4 and 94.9, respectively. Both phases also show low contents of Al_2O_3 (0.84-1.14 wt. %). Spinels are the richest in chromium numbers (Cr# = molar $Cr_2O_3/[Cr_2O_3+Al_2O_3]$ ∗ 100) varying between 59.9 and 60.3 (Figure 6.4A-D). Amphiboles in the peridotite are pargasites and characterized by 90.4-91.4 Mg#, ~ 1 wt. % K_2O, ~ 0.6 wt. % TiO_2 and ~ 11 wt. % Al_2O_3. Phlogopites are richer in K_2O (8.2-8.9 wt. %) and TiO_2 (~ 1 wt. %) and show high Mg# (~ 93.4). In the websterite sample (FIN6), Mg# values of clinopyroxene (94.1), orthopyroxene (91.7), amphibole (90.5) and phlogopite (93.2), and Cr# value of spinel (59.4) are very similar to those from the peridotite.

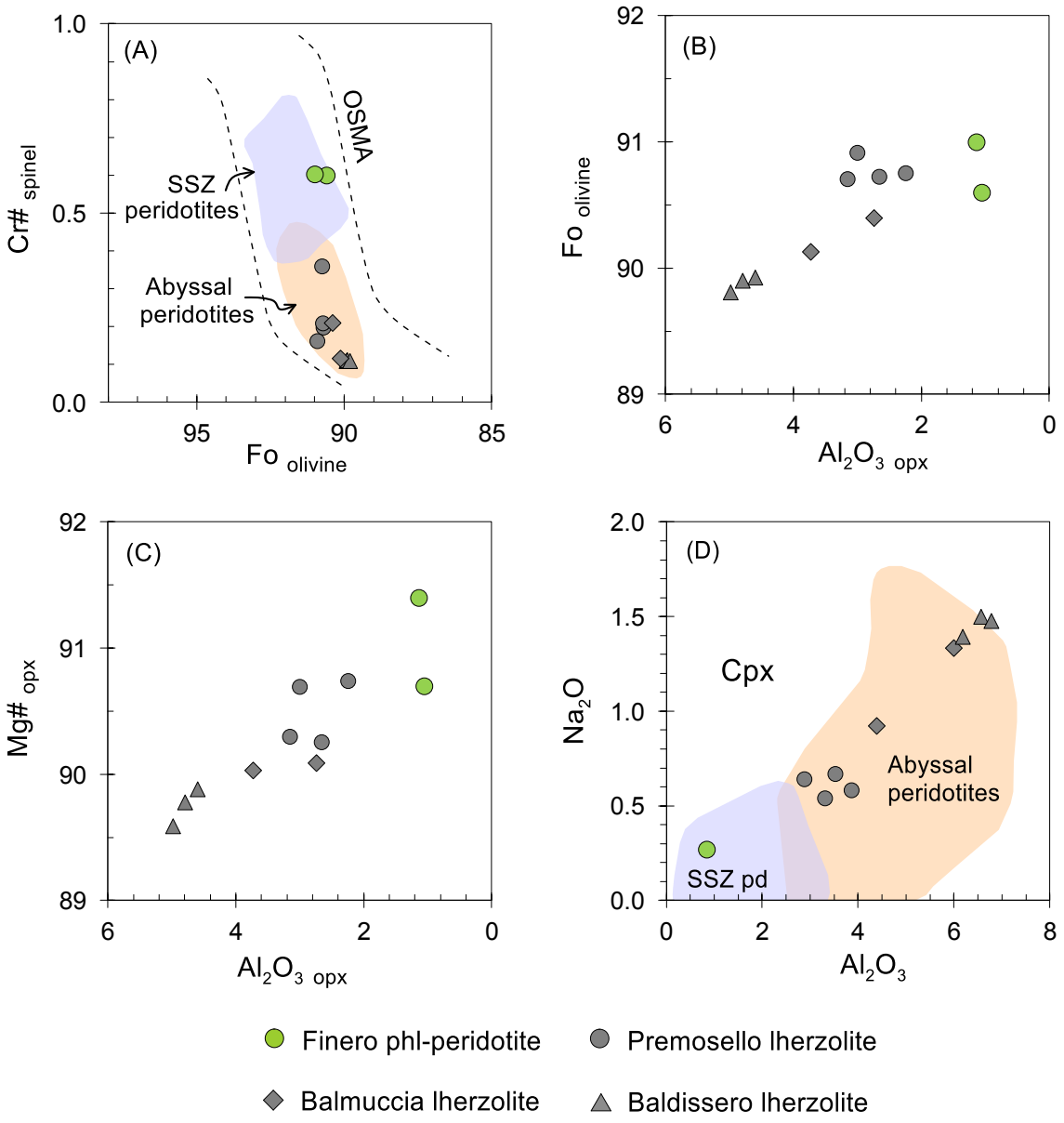

Figure 6.4: Plots of (A) forsterite content (Fo) of olivine versus chromium number (Cr#) of spinel; (B) forsterite content (Fo) of olivine versus Al_2O_3 (wt. %) content of orthopyroxenes; (C) Mg# versus Al_2O_3 (wt. %) content of orthopyroxenes; and (D) Na_2O (wt. %) content versus Al_2O_3 (wt. %) content of clinopyroxenes for the studied Finero phlogopite peridotite samples compared to lherzolites from Premosello, Balmuccia and Baldissero (Ogunyele et al., 2024a). SSZ pd – Suprasubduction Zone peridotites; OSMA – Olivine-Spinel Mantle Array defined from Arai (1994).

6.5.2 Mineral trace element chemistry

In terms of trace element composition, similar to what is observed for the major elements and also reported by Zanetti et al. (1999), we find no large chemical difference between the phlogopite peridotite and websterite. Clinopyroxenes from the Finero phlogopite peridotite and websterite are highly enriched in LREE and depleted in HREE with strong fractionation in the MREE (Figure 6.5A). This REE signature is in contrast to those of refractory lherzolites and Cr-diopside websterites from Balmuccia and Baldissero (Figure 6.5A; Ogunyele et al., 2024a). Amphiboles from the Finero peridotite and websterite also show REE patterns similar to those of co-existing clinopyroxenes, differing only in the absolute contents (Figure 6.5B). In both clinopyroxene and amphibole, the websterite sample shows a slightly higher enrichment in LREE compared to the peridotite samples (Figure 6.5A-B). This results in higher Ce/Yb_N in the websterite (Cpx = 29.5; Amph = 30.1) compared to the peridotite samples (Ce/Yb_N Cpx = 18.2; Amph = 15.5-18.6). Amphiboles from the peridotite and websterite samples show enrichments in Rb, Ba, Sr and Pb, strong depletion in Cs, Nb, Ta, Zr and Hf, and slightly weak depletion in Ti. In the websterite amphibole, Pb defines a weak negative anomaly (Figure 6.5C). Amphibole from one peridotite sample (FIN5) shows enrichments in Th-U, whereas amphiboles from the other peridotite and websterite samples are depleted in these elements (Figure 6.5C). Coexisting clinopyroxenes in the peridotite and websterite have significantly lower Rb, Th, U, Ba, Nb, Ta, Zr, Hf and Ti concentrations than amphiboles due to crystallochemical constraints (Figure 6.5C). Sr and Pb (although defining a negative anomaly) are high in the clinopyroxenes. Phlogopites are depleted in REE, Th, U, Nb, Ta, Zr and Hf but enriched in Cs, Rb, Ba, Sr, Pb, Ti and other transition elements. Olivine, orthopyroxene and spinel are depleted in the LILE and REE. Olivine contains higher Ni, and lower Cr, V, and Ti relative to orthopyroxene and spinel.

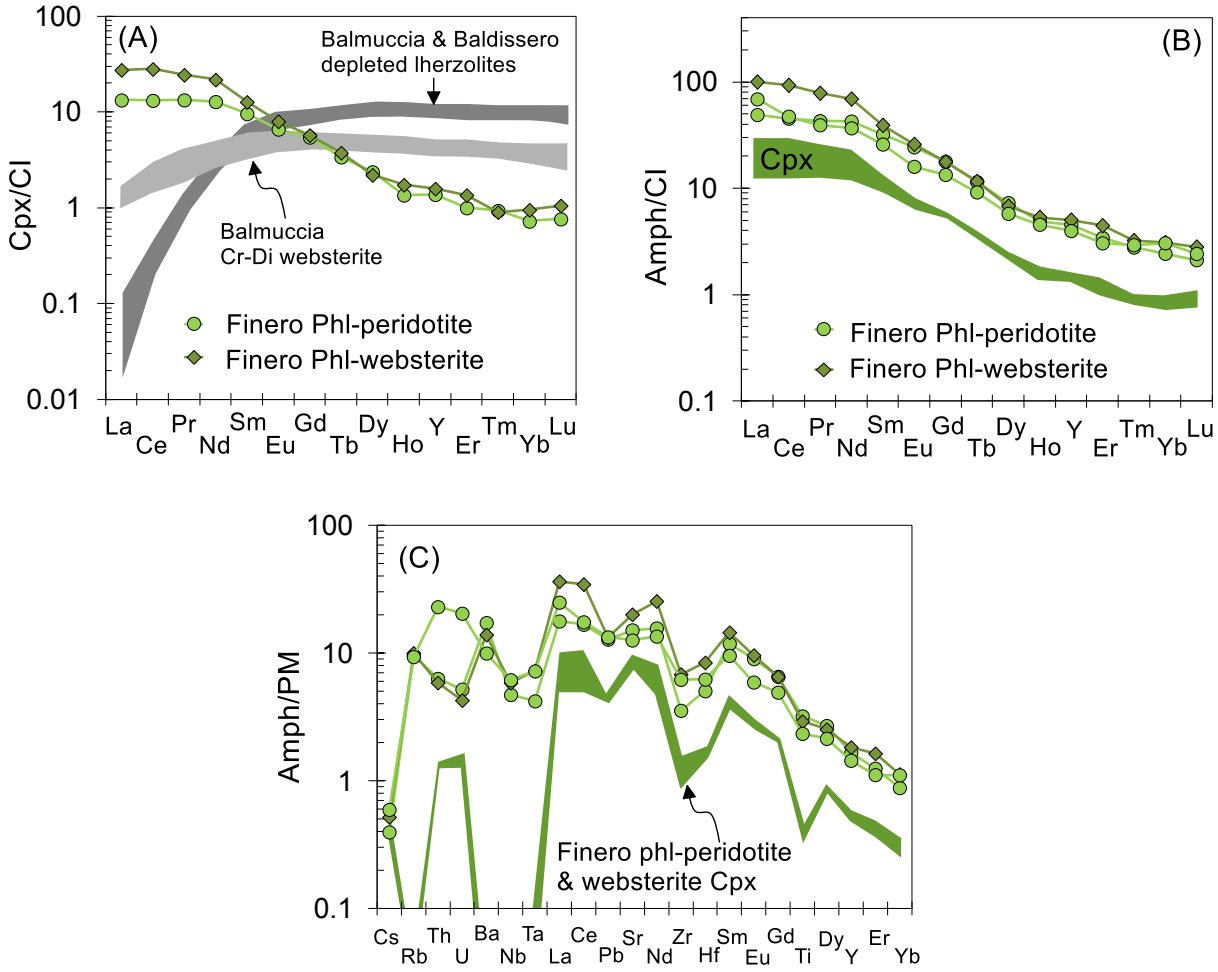

Figure 6.5: CI chondrite-normalized REE patterns of (A) clinopyroxenes and (B) amphiboles from the studied Finero phlogopite peridotite and websterite samples compared to refractory lherzolites and Cr-diopside websterites from Balmuccia and Baldissero (Ogunyele et al., 2024a). (C) Primitive Mantle (PM)-normalized incompatible trace element patterns of clinopyroxenes and amphiboles from the Finero phlogopite peridotite and websterite samples. CI chondrite and PM compositions are from Lyubetskaya and Korenaga (2007) and McDonough and Sun (1995), respectively.

6.5.3 Amphibole Sr, Pb, Nd and Hf isotopic composition

The measured Sr, Nd and Hf isotopic ratios of amphiboles from the Finero phlogopite peridotite and websterite samples were corrected to 300 Ma in accordance with the age of pervasive metasomatism which produced amphiboles in the mantle massif (Voshage et al., 1987; Zanetti et al., 2016; Malitch et al., 2017).

Amphiboles from the Finero phlogopite peridotites and websterite exhibit similar Sr-Nd-Hf isotopic ratios. They are characterized by radiogenic $^{87}Sr/^{86}Sr_{(i)}$ composition (peridotite = 0.706785–0.707632; websterite = 0.706746) coupled to unradiogenic $^{143}Nd/^{144}Nd_{(i)}$ (peridotite $\varepsilon Nd_{(i)}$ = –1.9 to –3.2; websterite $\varepsilon Nd_{(i)}$ = –2.8) and $^{176}Hf/^{177}Hf_{(i)}$ (peridotite $\varepsilon Hf_{(i)}$ = +0.1 to –1.9; websterite $\varepsilon Hf_{(i)}$ = –0.8). In the Sr-Nd isotope space (Figure 6.6A), amphiboles from the Finero phlogopite peridotites and websterite, as well as bulk-rocks of the phlogopite peridotite (Voshage et al., 1987) show composition similar to the post-collisional (Groups 1 & 2) K-rich lamprophyre dykes formed across the European Variscides during a period of 50 Myr, following the peak of the Variscan orogeny at 340 Ma (Soder and Romer, 2018). The Sr-Nd and Hf isotopic signatures of the Finero phlogopite peridotite and websterite are clearly more enriched than the signatures of the Middle Triassic calc-alkaline magmatism and the Late Triassic–Early Jurassic alkaline magmatism which occurred in the IVZ and throughout the Southern Alps (Figure 6.6A, B; Giovanardi et al., 2020; Ogunyele et al., 2024b; see Chapter 2).

The Pb isotopic compositions of amphiboles from the Finero phlogopite peridotites and websterite also show close similarity to the post-collisional K-rich lamprophyre dykes from the European Variscides. The amphiboles exhibit typical crustal and radiogenic $^{207}Pb/^{204}Pb$ (15.64-15.67), $^{208}Pb/^{204}Pb$ (38.56-39.19) and $^{206}Pb/^{204}Pb$ (18.46-18.95) plotting around the Pb evolution curves for orogen (Figure 6.6C, D; Zartman and Doe, 1981). The deviations of $^{208}Pb/^{204}Pb$ and

$^{207}Pb/^{204}Pb$ from the NHRL expressed as Δ8/4 and Δ7/4 for our amphibole samples range from 61.6 to 64.5 and 12.3 to 14.9, plotting in the field of DUPAL-bearing samples (Figure 6.6E, F).

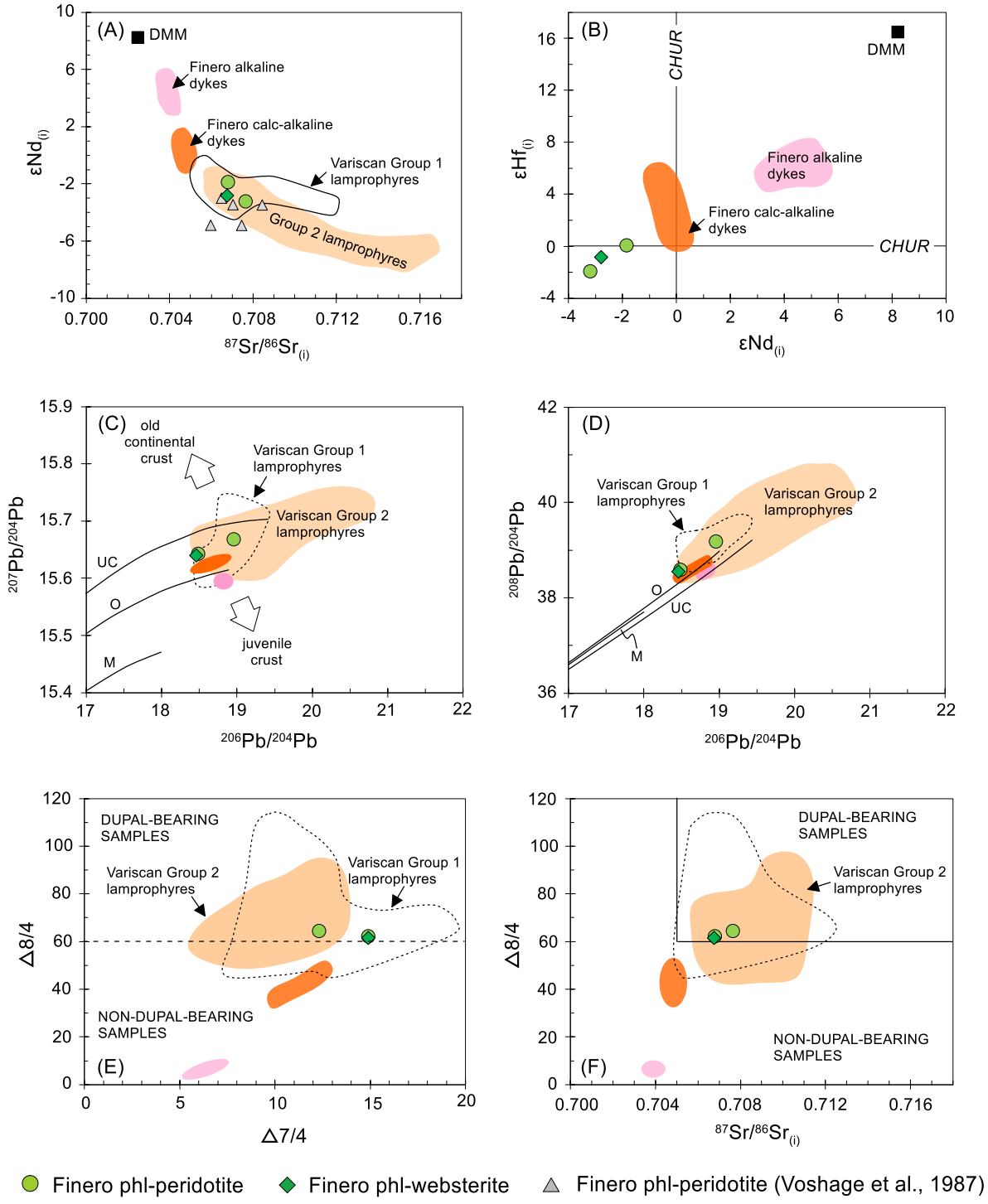

Figure 6.6: (A) $^{87}Sr/^{86}Sr_{(i)}$–$εNd_{(i)}$; (B) $εNd_{(i)}$–$εHf_{(i)}$; (C) $^{206}Pb/^{204}Pb$–$^{207}Pb/^{204}Pb$; (D) $^{206}Pb/^{204}Pb$–$^{208}Pb/^{204}Pb$; (E) Δ7/4–Δ8/4; and (F) $^{87}Sr/^{86}Sr_{(i)}$–Δ8/4 isotopic compositions of amphiboles from

studied Finero phlogopite peridotites and websterite. The isotopic compositions of the Finero phlogopite peridotite bulk-rocks (corrected to 300 Ma, Voshage et al., 1987), post-collisional (Groups 1 and 2) K-rich lamprophyre dykes from the European Variscides (Soder and Romer, 2018), Middle Triassic calc-alkaline dykes and Late Triassic alkaline dykes within the FPP (Giovanardi et al., 2020; Ogunyele et al., 2024b) are also plotted for comparison. In (E) and (F), only lamprophyre dykes showing the DUPAL isotope anomaly are plotted. Pb evolution curves for mantle (M), orogen (O) and upper crust (UC) are from Zartman and Doe (1981).

6.6 Discussion

6.6.1 DUPAL isotope signatures of Finero phlogopite peridotite and websterite

Amphiboles from the Finero phlogopite peridotite and websterite are characterized by highly radiogenic $^{208}Pb/^{204}Pb$ and $^{207}Pb/^{204}Pb$ for a given $^{206}Pb/^{204}Pb$ deviating significantly from the NHRL. The studied amphiboles clearly exhibit the DUPAL isotope anomaly with Δ8/4 (61.6-64.5), Δ7/4 (12.3-14.9) and $^{87}Sr/^{86}Sr_{(i)}$ (0.706746–0.707632) well above the designated values for DUPAL-bearing rocks (Δ8/4 > 60; Δ7/4 > 10; $^{87}Sr/^{86}Sr > 0.705$; Hart 1984, 1988; Meyzen et al., 2005; Mazzucchelli et al., 2016; Tian et al., 2022). In addition, the amphiboles show unradiogenic $^{143}Nd/^{144}Nd_{(i)}$ and $^{176}Hf/^{177}Hf_{(i)}$ which are typical of rocks with the DUPAL isotope anomaly (Escrig et al., 2004; Meyzen et al., 2005; Tian et al., 2022). The radiogenic $^{87}Sr/^{86}Sr_{(i)}$ and unradiogenic $^{143}Nd/^{144}Nd_{(i)}$ signature is not only peculiar to amphiboles from the mantle massif but is also exhibited by the whole-rock of the peridotite (Voshage et al., 1987; Figure 6.6A) indicating that the anomaly is pervasive.

6.6.2 Origin of the DUPAL anomaly

Voshage et al. (1987), Zanetti et al. (1999, 2016), and Malitch et al. (2017) have shown that the pervasive metasomatism which produced amphibole, phlogopite and secondary clinopyroxene in the FPP probably started at the end of the Variscan orogenic cycle (Late Carboniferous to Early Permian, ~310 Ma) in post-collisional settings. The trace element composition of the metasomatic amphiboles characterized by depletion in HFSE (Nb, Ta, Zr, Hf) and HREE, and enrichment in LILE, LREE, Sr and Pb coupled with their crust-like Sr, Nd, Pb and Hf isotopic signatures (Figures 6.5, 6.6) point to derivation from hydrous, silica-saturated melts with crustal affinity. Due to the fact that most radiogenic ^{207}Pb were formed early in Earth's history (Zartman and Doe, 1981; Soder and Romer, 2018), the high $^{207}Pb/^{204}Pb$ ratios at a given $^{206}Pb/^{204}Pb$ of amphiboles from the Finero phlogopite peridotites and websterite very likely indicates that the Pb in these rocks was derived from old continental crust (Figure 6.6C).

Notably, in the timeframe when the Finero mantle massif was undergoing metasomatism by hydrous silica-saturated melts of continental crust origin, there was the concomitant development of potassic to ultrapotassic magmatism which produced lamprophyre dykes throughout the European Variscides. This magmatism occurred during a period of 50 Myr, following the peak of the Variscan orogeny at 340 Ma and was derived from mantle sources modified by subducted continental crust materials (i.e., granulites, orthogneisses and granitoids; Soder and Romer, 2018). These post-collisional lamprophyre dykes share similar isotopic signatures to the amphiboles produced from the metasomatizing melts of the FPP (Figure 6.6). This leads us to suggest that there is a possibility that subducted continental crust from the Variscan subduction zone (far to the North of the Southern Alps) made its way to the Finero upper mantle. These subducted continental crust components were then partially melted to

produce hydrous, silica-saturated melts carrying the DUPAL isotope anomaly. Pervasive and reactive migration of these hydrous, silica-saturated melts imparted the DUPAL anomaly to the already depleted Finero harzburgitic mantle body.

Another possibility, proposed in Decarlis et al. (2023) and Ogunyele et al. (2024b), is the delamination of the lower continental crust into the upper mantle beneath the Southern Alps. These authors suggested that, after the Variscan collision and formation of the Variscan orogen, delamination associated with orogenic collapse led to the detachment of wide slabs from the root of the orogen (and neighbouring areas) that sunk into the mantle favouring the mixing of the mantle with continental melts. This model is supported by the plot of amphiboles from the Finero phlogopite peridotite and websterite around the Pb evolution curves for orogen (Figure 6C, D; Zartman and Doe, 1981).

The absence of significant differences in mineral major, trace and isotopic composition between the Finero phlogopite peridotite and websterite can be explained by segregation of the websterites from crystal mushes consisting of harzburgites and the hydrous silica-saturated melts carrying the DUPAL isotope anomaly. This model is consistent with the hypothesis of Zanetti et al. (1999). Had the websterites been solely segregated from the continental-derived, hydrous, silica-saturated melts carrying the DUPAL isotope anomaly, they would have been characterized by more enriched isotopic signatures compared to the peridotites.

The finding of the DUPAL isotope anomaly in the Finero phlogopite peridotite and websterite and the proposed model of origin of this anomaly involving subducted and/or delaminated continental crust components sharply contrasts and strongly refutes the model involving the melting of residual oceanic slab and serpentinites as the source of the melts/fluids which metasomatized the Finero massif as proposed by Cannaò et al. (2022).

6.6.3 Geodynamic significance

The origin of the DUPAL isotope anomaly in the Finero orogenic peridotite massif can explain the following geodynamic scenarios:

(1) Our working model involving the contamination of the upper mantle by continental crust components sourced from a distal subduction zone provides evidence that subducted materials can possibly travel a great distance before melting and interacting with the local mantle reservoir.

(2) If the continental crust components were introduced into the upper mantle by delamination, it can explain how a thickened unstable orogen such as the Variscan orogen can be destroyed, recycled and stabilized within a short period of time. In the case of the Variscan orogen, the collapse and stabilization probably occurred in few tens of millions of years.

(3) The polycyclic nature of the metasomatism of the Finero orogenic peridotite massif (from ~310 Ma to 187 Ma; Voshage et al., 1987; Zanetti et al., 2016; Malitch et al., 2017) also suggest that subducted and/or delaminated continental crustal materials can reside at mantle depths over a prolonged period of time.

(4) Lastly, the recycling of continental crust components within the Finero mantle is consistent and well explains the occurrence of mantle-derived magmatism with continental crust components in the IVZ and throughout the Southern Alps during the Triassic–Jurassic period (see Chapter 2). A synthesis of the isotopic and trace element features of the Finero mantle massif and the calc-alkaline to alkaline dykes within the mantle body (Figure 6.6A) indicates that there was the continuous release of continental crustal components from the upper mantle from the Early Permian to Early Jurassic over a time interval of ~120 Myr. Notably, the mantle sources progressively became depleted over this time frame (Figure 6.6A).

References

Arai, S., 1994. Characterization of spinel peridotites by olivine-spinel compositional relationships: Review and interpretation. Chem. Geol. 113, 191–204. https://doi.org/10.1016/0009-2541(94)90066-3.

Arndt, N.T., Goldstein, S.L., 1989. An open boundary between lower continental crust and mantle: Its role in crust formation and crustal recycling. Tectonophysics 161, 201–212.

Cannaò, E., Tiepolo, M., Fumagalli, P., Grieco, G., Agostini, S., 2022. Metasomatism in the Finero Phlogopite Peridotite: New insights from C and N concentrations and δ13C-δ11B signatures. Chem. Geol. 614. https://doi.org/10.1016/j.chemgeo.2022.121181.

Decarlis, A., Zanetti, A., Ogunyele, A.C., Ceriani, A., Tribuzio, R., 2023. The Ivrea-Verbano tectonic evolution: The role of the crust-mantle interactions in rifting localization. Earth-Sci. Rev. 238. https://doi.org/10.1016/j.earscirev.2023.104318.

Dupré, B., Allègre, C.J., 1983. Pb–Sr isotope variation in Indian Ocean basalts and mixing phenomena. Nature 303, 142–146.

Escrig, S., Capmas, F., Dupre´, B., Allègre, C.J., 2004. Osmium isotopic constraints on the nature of the DUPAL anomaly from Indian mid-ocean-ridge basalts. Nature 431, 59–63.

Giovanardi, T., Zanetti, A., Dallai, L., Morishita, T., Hémond, C., Mazzucchelli, M., 2020. Evidence of subduction-related components in sapphirine-bearing gabbroic dykes (Finero phlogopite–peridotite): Insights into the source of the Triassic–Jurassic magmatism at the Europe–Africa boundary. Lithos 356–357, 105366. https://doi.org/10.1016/j.lithos.2020.105366.

Goldstein, S.L., Soffer, G., Langmuir, C.H., Lehnert, K., Graham, D.W., Michael, P.J., 2008. Origin of a ‘Southern Hemisphere’ geochemical signature in the Arctic upper mantle. Nature 453, 89–93.

Grieco, G., Ferrario, A., von Quadt, A., Köppel, V., Mathez, A., 2001. The zircon-bearing chromitites of the phlogopite peridotite of Finero (Ivrea Zone, Southern Alps): evidence and geochronology of a metasomatized mantle slab. J. Petrol. 42, 89–101. https://doi.org/10.1093/petrology/42.1.89.

Hanan, B.B., Blichert-Toft, J., Pyle, D.G., Christie, D.M., 2004. Contrasting origins of the upper mantle revealed by hafnium and lead isotopes from the Southeast Indian Ridge. Nature 432, 91–94.

Hart, S.R., 1984. A large scale isotope anomaly in the southern hemisphere mantle. Nature 309, 753–757.

Hart, S.R., 1988. Heterogeneous mantle domains: signatures, genesis and mixing chronologies. Earth and Planetary Science Letters 90, 273–296.

Hartmann, G., Wedepohl, K.H., 1993. The composition of peridotite tectonites from the Ivrea complex, northern Italy: residues from melt extraction. Geochim. Cosmochim. Acta 57, 1761–1782.

Kempton, P.D., Pearce, J.A., Barry, T.L., Fitton, J.G., Langmuir, C., Christie, D.M., 2002. Sr-Nd-Pb-Hf isotope results from ODP Leg 187: Evidence for mantle dynamics of the Australian-Antarctic Discordance and origin of the Indian MORB source. Geochem. Geophys. Geosyst. 3. https://doi.org/10.1029/2002GC000320.

Klötzli, U.S., Sinigoi, S., Quick, J.E., Demarchi, G., Tassinari, C.C.G., Sato, K., Günes, Z., 2014. Duration of igneous activity in the Sesia Magmatic System and implications for high-temperature metamorphism in the Ivrea–Verbano deep crust. Lithos 206–207, 19-33. https://doi.org/10.1016/j.lithos.2014.07.020.

Lyubetskaya, T., Korenaga, J., 2007. Chemical composition of Earth's primitive mantle and its variance: 1. Method and results. J. Geophys. Res. Solid Earth 112, B03211. https://doi.org/10.1029/2005JB004223.

Mahoney, J., LeRoex, A.P., Peng, Z., Fisher, R.L., Natland, J.H., 1992. Southwestern limits of Indian ocean ridge mantle and origin of low $^{206}Pb/^{204}Pb$ mid-ocean ridge basalt: Isotope systematics of the Central Southwest Indian Ridge (17–50E). J. Geophys. Res., 97, 19,771–19,790.

Mahoney, J.J., Frei, R., Tejada, M.L.G., Nägler, T.F. 1998. Tracing the Indian Ocean mantle domain through time: Isotopic results from old west Indian, East Thetyan, and South Pacific seafloor. J. Petrol. 39, 1285–1306.

Mahoney, J.J., Graham, D.W. Christie, D.M., Johnson, K.T.M., Hall, L.S., Vonderhaar, L., 2002.

Between a hotspot and a cold Spot: Isotopic variations in the Southeast Indian Ridge asthenosphere, 86E-118E. J. Petrol. 43, 1155–1176.

Malitch, K.N., Belousova, E.A., Griffin, W.L., Badanina, I.Y., Knauf, V.V., O'Reilly, S.Y., Pearson, N.J., 2017. Laurite and zircon from the Finero chromitites (Italy): New insights into evolution of the subcontinental mantle. Ore Geol. Rev. 90, 210-225. https://doi.org/10.1016/j.oregeorev.2017.06.027.

Mazzucchelli, M., Cipriani, A., Hémond, C., Zanetti, A., Bertotto, G.W., Cingolani, C.A., 2016. Origin of the DUPAL anomaly in mantle xenoliths of Patagonia (Argentina) and geodynamic consequences. Lithos 248–251, 257-271. https://doi.org/10.1016/j.lithos.2016.01.010.

Mazzucchelli, M., Zanetti, A., Rivalenti, G., Vannucci, R., Correia, C.T., Tassinari, C.C.G., 2010. Age and geochemistry of mantle peridotites and diorite dykes from the Baldissero body: Insights into the Paleozoic-Mesozoic evolution of the Southern Alps. Lithos 119, 485–500. https://doi.org/10.1016/j.lithos.2010.08.002.

Mazzucchelli, M., Marchesi, S., Bottazzi, P., Ottolini, L., Vannucci, R., 1992. The Premosello Chiovenda peridotitic body in Ossola valley (Ivrea-Verbano Zone, Italy). Atti Ticinensi Sci. Terra 35, 75-82.

McDonough, W.F., Sun, S., 1995. The composition of the Earth. Chem. Geol. 120, 223–253. https://doi.org/10.1016/0009-2541(94)00140-4.

Meyzen, C.M., Ludden, J.N., Humler, E., Luais, B., Toplis, M.J., Mével, C., Storey, M., 2005. New insights into the origin and distribution of the DUPAL isotope anomaly in the Indian Ocean mantle from MORB of the Southwest Indian Ridge. Geochem. Geophys. Geosyst., 6. https://doi.org/10.1029/2005GC000979.

Morishita, T., Hattori, K.H., Terada, K., Matsumoto, T., Yamamoto, K., Takebe, M., Ishida, Y., Tamura, A., Arai, S., 2008. Geochemistry of apatite-rich layers in the Finero phlogopite–peridotite massif (Italian Western Alps) and ion microprobe dating of apatite. Chem. Geol. 251, 99–111. https://doi.org/10.1016/j.chemgeo.2008.02.018.

Obermiller, W.A., 1994. Chemical and Isotopic Variations in the Balmuccia, Baldissero and Finero Peridotite Massifs (Ivrea-Zone, N-Italy). Unpublished PhD thesis. Johannes-

Gutenberg-Universität Mainz, p. 191.

Ogunyele A.C., Bonazzi M., Giovanardi T., Mazzucchelli M., Salters V.J.M., Decarlis A., Sanfilippo A., Zanetti A., 2024b. Transition from orogenic-like to anorogenic magmatism in the Southern Alps during the Early Mesozoic: Evidence from elemental and Nd-Sr-Hf-Pb isotope geochemistry of alkali-rich dykes from the Finero Phlogopite Peridotite, Ivrea–Verbano Zone. Gondwana Res. 129, 201-219.

Ogunyele A.C., Sanfilippo A., Salters V.J.M., Bonazzi M., Zanetti A., 2024a. Accretion of "young" Phanerozoic subcontinental lithospheric mantle triggered by back-arc extension. Sci. Rep. (under review).

Peressini, G., Quick, J.E., Sinigoi, S., Hofmann, A.W., Fanning, M., 2007. Duration of a large mafic intrusion and heat transfer in the lower crust: a SHRIMP U/Pb zircon study in the Ivrea–Verbano Zone (Western Alps, Italy). J. Petrol. 48, 1185-1218, https://doi.org/10.1093/petrology/egm014.

Rehkämper, M., Hofmann, A.W., 1997. Recycled ocean crust and sediment in Indian Ocean MORB, Earth Planet. Sci. Lett., 147, 93–106.

Rivalenti, G., Mazzucchelli, M., Vannucci, R., Hofmann, A.W., Ottolini, L., Bottazzi, P., Obermiller, W., 1995. The relationship between websterite and peridotite in the Balmuccia peridotite massif (NW Italy) as revealed by trace element variations in clinopyroxene. Contrib. Mineral. Petrol. 121, 275–288. https://doi.org/10.1007/BF02688243.

Salters, V.J.M., Stracke, A., 2004. Composition of the depleted mantle. Geochem. Geophys. Geosys. 5. https://doi.org/10.1029/2003GC000597.

Schmid, S.M., 1993. Ivrea zone and adjacent southern Alpine basement, *in* von Raumer, J.F., and Neubauer, F., eds., Pre-Mesozoic Geology in the Alps. Springer–Verlag, Berlin, 567–583. https://doi.org/10.1007/978-3-642-84640-3_33.

Selverstone, J., Sharp, Z.D., 2011. Chlorine isotope evidence for multicomponent mantle metasomatism in the Ivrea Zone. Earth Planet. Sci. Lett. 310, 429–440. https://doi.org/10.1016/j.epsl.2011.08.034.

Smith, A.D., 1998. The geodynamic significance of the DUPAL anomaly in Asia, *in* Martin

Flower, M.F.J., Chung, S.-L., Lo, C.-H., Lee, T.-Y., eds., Mantle Dynamics and Plate Interactions in East Asia. Geophysical Monograph 27, American Geophysical Union, Washington, D.C., 89–105.

Soder, C.G., Romer, R.L., 2018. Post-collisional potassic-ultrapotassic magmatism of the Variscan orogen: Implications for mantle metasomatism during continental subduction. J. Petrol. 59, 1007-1034. https://doi.org/10.1093/petrology/egy053.

Storey, M., Saunders, A.D., Tarney, J., Gibson, I.L., Norry, M.J., Thirlwall, M.F., Leat, P., Thompson, R.N., Menzies, M.A., 1989. Contamination of Indian Ocean asthenosphere by the Kerguelen Heard mantle plume. Nature 338, 574–576.

Stracke, A., Bizimis, M., Salters, V.J., 2003. Recycling oceanic crust: quantitative constraints. Geochem. Geophys. Geosys. 4. https://doi.org/10.1029/2001GC000223.

Tian, Y., Xu, J., Liu, X., 2022. Dupal anomaly and identification using Nd-Hf isotopes. Acta Geol. Sinica 96, 416–429. https://doi.org/10.1111/1755-6724.14934.

von Raumer, J.F., Bussy, F., Schaltegger, U., Schulz, B., Stampfli, G.M., 2013. Pre-Mesozoic Alpine basements – Their place in the European Paleozoic framework. GSA Bull. 125, 89–108. https://doi.org/10.1130/B30654.1.

Voshage, H., Hunziker, J.C., Hofmann, A.W., Zingg, A., 1987. A Nd and Sr isotopic study of the Ivrea zone, Southern Alps, N-Italy. Contrib. Mineral. Petrol. 97, 31–42. https://doi.org/10.1007/BF00375212.

Woelki, D., Salters, V., Beier, C., Dick, H., Koepke, J., Romer, R., 2023. Shallow recycling of lower continental crust: The Mahoney Seamount at the Southwest Indian Ridge. Earth Planet. Sci. Lett. 602, 117968. https://doi.org/10.1016/j.epsl.2022.117968.

Xing, G.F., 1997. Concept, genesis and geological significance of Dupal isotopic anomaly. Volcan. Miner. Res. 18, 281–291.

Zaccarini, F., Stumpfl, E.F., Garuti, G., 2004. Zirconolite and Zr–Th–U minerals in chromitites of the Finero complex, Western Alps, Italy: evidence for carbonatite-type metasomatism in a subcontinental mantle plume. Can. Mineral. 42, 1825–1845.

Zanetti, A., Giovanardi, T., Langone, A., Tiepolo, M., Wu, F.Y., Dallai, L., Mazzucchelli, M.,

2016. Origin and age of zircon-bearing chromitite layers from the Finero phlogopite peridotite (Ivrea–Verbano Zone, Western Alps) and geodynamic consequences. Lithos, 262, 58-74. https://doi.org/10.1016/j.lithos.2016.06.015.

Zanetti, A., Mazzucchelli, M., Rivalenti, G., Vannucci, R., 1999. The Finero phlogopite–peridotite massif: an example of subduction-related metasomatism. Contrib. Mineral. Petrol. 134, 107–122. https://doi.org/10.1007/s004100050472.

Zanetti, A., Mazzucchelli, M., Sinigoi, S., Giovanardi, T., Peressini, G., Fanning, M., 2013. SHRIMP U-Pb zircon Triassic intrusion age of the Finero mafic complex (Ivrea–Verbano Zone, Western Alps) and its geodynamic implications. J. Petrol. 54, 2235–2265. https://doi.org/10.1093/petrology/egt046.

Zartman, R. E., Doe, B. R., 1981. Plumbotectonics – the model. Tectonophysics 75, 135–162.

CHAPTER 7

Conclusions and future prospects

7.1 Concluding remarks

This thesis unravels the complex tectono-magmatic evolution of the Southern Alps during the Triassic with special focus on the westernmost (Ivrea-Verbano Zone, IVZ) and eastern (Dolomites) sectors of the region. The Southern Alps is part of the continental margin of the Adriatic Plate located between Gondwana and Laurasia during and after the Variscan orogenic cycle and can therefore provide important insights into the geodynamic evolution of the boundary between these two megacontinents shortly before the breakup of the Pangea Supercontinent in the Late Triassic–Early Jurassic.

To achieve our goal of understanding the geodynamic evolution of the Gondwana–Laurasia boundary in Triassic times, we applied a multidisciplinary approach including detailed petrography, geochemistry, geochemical modeling, geochronology and radiogenic isotope systematics on Triassic to Early Jurassic magmatic and volcanic rocks outcropping in the Southern Alps. Further constraints were provided from the perspective of the lherzolitic to harzburgitic mantle massifs outcropping in the IVZ. The possibility of these massifs representing analogues of the mantle sources from which the Triassic to Early Jurassic magmatic and volcanic rocks were derived was tested. The IVZ mantle massifs also provided unique insights into the geodynamic environment of the Adriatic Plate in Paleozoic times before the assembly of Pangea.

In Chapter 2, we report detailed petrochemical and amphibole Nd-Sr-Hf-Pb isotopic data for Early Mesozoic (Middle Triassic–Early Jurassic) alkali-rich dyke swarms which intruded the Finero Phlogopite Peridotite in the northernmost part of the IVZ, western Southern Alps. We show that these dykes record a shift of the IVZ magmatism from orogenic-like to anorogenic

alkaline affinity during the Late Triassic, and provide a temporal correlation between the Early Mesozoic magmatisms in the IVZ and those from the eastern and central sectors of the Southern Alps. The sources of the orogenic-like (calc-alkaline) magmatism are metasomatized lithospheric mantle containing relatively large amount of subducted and/or delaminated continental crust components. A change of the mantle sources to predominantly depleted asthenosphere was identified for the subsequent anorogenic alkaline magmatism. We related both the orogenic-like and alkaline anorogenic magmatisms in the Southern Alps to a period of protracted extension in the Early Mesozoic that started at ca. 245 Ma and ended around ca. 170-160 Ma (Schettino and Turco, 2011; Denyszyn et al., 2018). With additional evidence from zircon trace elements, U-Pb geochronology and in-situ Hf isotopes (Chapter 3), the alkaline magmatism was related to a rift-related asthenospheric upwelling event that occurred at the Gondwana–Laurasia boundary in a typical intraplate geodynamic setting, probably representing a precursor of the rifting stage that caused the opening of the Alpine Tethys in the western Mediterranean region and subsequently the break-up of the Pangea.

In Chapter 4, we further established a correlation between the Middle Triassic high-K calc-alkaline to shoshonitic magmatism in the Dolomites (eastern Southern Alps) and the possibly coeval orogenic-like, calc-alkaline magmatism in the IVZ (western Southern Alps). We report the first ever whole-rock Hf isotope dataset on the Dolomitic high-K calc-alkaline to shoshonitic lavas and dykes. Nd-Sr-Pb isotopes and trace elements of these rocks were also analyzed. The goal was to provide further constraints on the nature of crustal components (continental or oceanic) in the subcontinental mantle beneath the Southern Alps generating the Triassic magmatisms. The lavas and dykes exhibit “crust-like” isotopic and trace element signatures, similar to the IVZ orogenic-like dykes. We conclude that the Dolomitic high-K calc-

alkaline to shoshonitic magmatism were derived from heterogeneous mantle sources containing variable amounts of recycled continental and oceanic crustal materials. The similarity of the isotopic and trace element signatures of the Middle Triassic magmatism in the Dolomites and the orogenic-like magmatism in the IVZ strongly suggest that they are coeval. To summarize our findings in Chapters 2–4, we proposed a model in which the Southern Alps Middle Triassic and Late Triassic–Early Jurassic magmatisms were triggered by Paleotethys subduction but the recycled continental (and oceanic?) crust materials in the mantle sources of these magmatisms are related to crustal materials brought down to mantle depths by the Variscan and/or older subduction events, as well as by delamination of the roots of the Variscan chain.

In the second section of the thesis focusing on the mantle massifs in the IVZ, we report geochemical and coupled Nd-Hf isotopes on residual to melt-reacted lherzolites and associated pyroxenites from the lherzolitic mantle massifs from Premosello, Balmuccia and Baldissero to place fundamental constraints on the depletion signatures, timing, mechanism and geodynamic environment of accretion of the subcontinental lithospheric mantle (SCLM) beneath the Phanerozoic IVZ area (Chapter 5). Our data reveal that the IVZ in the Adriatic Plate was in back-arc setting in the Upper Devonian (ca. 370 Ma) during Pangea amalgamation. It was in this timeframe and setting that the IVZ lherzolites were accreted to the Adriatic SCLM through asthenospheric upwelling triggered by Variscan intra-continental extension.

Lastly, we performed new trace elements and Sr, Nd, Pb and Hf isotopic study on the Finero harzburgitic mantle massif in the IVZ (Chapter 6). We show, for the first time, that this massif exhibits the DUPAL isotope anomaly. We argue that the DUPAL isotope anomaly was imparted to the highly depleted Finero peridotite by pervasive and reactive migration of hydrous silica-saturated melts derived from the partial melting of continental crust subducted and/or

delaminated into the upper mantle. Websterites within the peridotite massif represent the cooled and crystallized products of crystal mushes consisting of harzburgites and the hydrous silica-saturated melts carrying the DUPAL isotope anomaly. We conclude that the recycling of subducted and/or delaminated continental crust materials within the Southern Alps upper mantle, as testified by the Finero peridotite massif, plausibly explains the development of magmatism derived from mantle sources containing continental crust components in the IVZ and throughout the Southern Alps during the Triassic–Jurassic period.

7.2 Future prospects

The research findings presented in this thesis suggest that additional investigation could further enhance our knowledge of the geodynamic evolution of the Gondwana–Laurasia boundary in the Southern Alps region. Specifically, two key lines of investigation are recommended:

(1) Geochronological investigation to determine the age of the orogenic-like magmatism which occurred in the Ivrea-Verbano Zone. Zircon is absent in the orogenic-like calc-alkaline dykes, however apatite which can be dated by Lu-Hf geochronology is present. The whole-rock and/or amphiboles may also provide useful ages if dated by Ar-Ar or K-Ar methods. This investigation is important to provide additional evidence for a definite correlation of this magmatism to the Middle Triassic magmatism of the Dolomites.

(2) Detailed mineral chemical, geochronological (e.g., U-Pb, Ar-Ar) and radiogenic isotopes (e.g., Sr, Nd, Pb and Hf) study of the Triassic magmatic events which occurred in the central part of the Southern Alps. Only a few dataset on the Triassic magmatism of this sector is

available and reported in Cassinis et al. (2008). With new dataset from this sector, a more complete view of the Southern Alps can emerge.

References

Cassinis, G., Cortesogno, L., Gaggero, L., Perotti, C.R., Buzzi, L., 2008. Permian to Triassic geodynamic and magmatic evolution of the Brescian Prealps (Eastern Lombardy, Italy). Ital. J. Geosci. 127, 501–518.

Denyszyn, S.W., Fiorentini, M.L., Maas, R., Dering, G., 2018. A bigger tent for CAMP. Geology 46, 823–826. https://doi.org/10.1130/G45050.1.

Schettino, A., Turco, E., 2011. Tectonic history of the western Tethys since the Late Triassic. GSA Bull. 123, 89–105. https://doi.org/10.1130/B30064.1.

Appendices

Chapter 2

Appendix 2.1: Major and minor elements composition of mineral phases from Finero dykes

Appendix 2.2: Trace element composition of mineral phases from Finero dykes

Appendix 2.3: Nd-Sr-Hf-Pb isotopic composition of amphiboles from selected Finero dykes

Chapter 3

Appendix 3.1: Trace elements composition of zircons from Finero alkaline dykes

Appendix 3.2: U-Pb geochronology dataset of zircons from Finero alkaline dykes

Appendix 3.3: In-situ Hf isotope composition of zircons from Finero alkaline dykes

Chapter 4

Appendix 4.1: Major and minor elements composition of mineral phases in shoshonites from Dolomites, Southern Alps

Appendix 4.2: Trace element composition of mineral phases in shoshonites from Dolomites

Appendix 4.3: Whole-rock trace elements composition of shoshonites from Dolomites

Appendix 4.4: Whole-rock Nd-Hf-Sr-Pb isotopic composition of shoshonites from Dolomites

Chapter 5

Appendix 5.1: Average major and minor elements composition of mineral phases from studied IVZ lherzolites and pyroxenites

Appendix 5.2: Average trace element composition of clinopyroxenes from studied IVZ lherzolites and pyroxenites

Appendix 5.3: Present-day Nd-Hf isotopic composition of clinopyroxenes from studied IVZ lherzolites and pyroxenites

Appendix 5.4: Results of partial melting modeling of the Depleted Mantle (DM) at 370 Ma using the dynamic melting model of Stracke et al. (2003)

Appendix 5.5: Initial compositions and results of melt-rock reaction modeling of DM residues and MORB melt at 370 Ma

Chapter 6

Appendix 6.1: Average major and minor elements composition of mineral phases from selected Finero phlogopite peridotite and websterite

Appendix 6.2: Average trace element composition of mineral phases from selected Finero phlogopite peridotite and websterite

Appendix 6.3: Nd-Hf-Sr-Pb isotopic composition of amphiboles from selected Finero phlogopite peridotite and websterite

Appendix 2.1: Major and minor elements composition of mineral phases from Finero dykes

Grouping	HFSE-rich dyke											
Rock type	Dioritic dyke											
Sample	FI1603	FI1603	FI1603	FI1603	FI1603	FI1603	FI1603	FI1603	FI1603	FI1603	FI1603	FI1603
Thin section	FI1603B	FI1603B	FI1603B	FI1603B	FI1603B	FI1603B	FI1603B	FI1603B	FI1603B	FI1603B	FI1603B	FI1603B
Phase	Plag	Plag	Plag	Plag	Plag	Plag	Plag	Plag	Plag	Plag	Plag	Plag
Spot No.	1	1	7	8	8	11	11	15	15	16	16	20
Analysis No.	1	2	27a	29	30	35	36	42	43	44	45	48
SiO_2	65.94	65.21	64.52	65.59	65.10	65.04	65.18	65.51	65.48	66.01	65.65	66.11
TiO_2	0.00	0.00	0.00	0.00	0.00	0.00	0.00	0.00	0.00	0.00	0.00	0.00
Al_2O_3	21.83	22.87	22.74	22.00	22.51	22.90	22.05	22.11	22.32	21.70	21.96	21.65
Cr_2O_3	0.00	0.00	0.00	0.00	0.00	0.00	0.00	0.00	0.00	0.00	0.00	0.00
FeO_T	0.00	0.00	0.00	0.00	0.00	0.00	0.00	0.00	0.00	0.00	0.00	0.00
MnO	0.00	0.00	0.00	0.00	0.00	0.00	0.00	0.00	0.00	0.00	0.00	0.00
NiO	0.00	0.00	0.00	0.00	0.00	0.00	0.00	0.00	0.00	0.00	0.00	0.00
MgO	0.00	0.00	0.00	0.00	0.00	0.00	0.00	0.00	0.00	0.00	0.00	0.00
CaO	1.85	1.72	2.07	1.82	1.90	2.22	2.01	1.83	1.92	1.72	1.65	1.77
Na_2O	10.61	10.45	10.23	10.54	10.40	10.27	10.40	10.52	10.48	10.66	10.60	10.67
K_2O	0.00	0.00	0.00	0.00	0.00	0.00	0.00	0.00	0.00	0.00	0.00	0.00
P_2O_5												
Cl												
Total	100.23	100.25	99.56	99.95	99.91	100.43	99.64	99.97	100.20	100.09	99.86	100.20
An	8.8	8.3	10.1	8.7	9.2	10.7	9.6	8.8	9.2	8.2	7.9	8.4
Ab	91.2	91.7	89.9	91.3	90.8	89.3	90.4	91.2	90.8	91.8	92.1	91.6
Or	0.0	0.0	0.0	0.0	0.0	0.0	0.0	0.0	0.0	0.0	0.0	0.0

Appendix 2.1: Major and minor elements composition of mineral phases from Finero dykes (contd.)

Grouping	HFSE-rich dyke											
Rock type	Dioritic dyke											
Sample	FI1603	FI1603	FI1603	FI1603	FI1603	FI1603	FI1603	FI1603	FI1603	FI1604	FI1604	FI1604
Thin section	FI1603B	FI1603C	FI1603C	FI1603C	FI1603C	FI1603C	FI1603C	FI1603C	FI1603C	FI1604C	FI1604C	FI1604C
Phase	Plag	Plag	Plag	Plag	Plag	Plag	Plag	Plag	Plag	Plag	Plag	Plag
Spot No.	20	1	1	5	7	7	7	11	11	9	11	12
Analysis No.	49	1	3	15	22	23	24	35	36	1	4	1
SiO_2	66.05	64.90	65.04	64.61	65.11	65.19	65.56	65.39	65.47	65.63	65.91	66.17
TiO_2	0.00	0.00	0.00	0.00	0.00	0.00	0.00	0.00	0.00	0.06	0.00	0.02
Al_2O_3	21.70	22.60	22.36	22.81	22.43	22.16	22.48	22.21	22.12	21.04	20.93	20.57
Cr_2O_3	0.00	0.00	0.00	0.00	0.00	0.00	0.00	0.00	0.00	0.03	0.00	0.01
FeO_T	0.00	0.00	0.00	0.00	0.00	0.00	0.00	0.00	0.00	0.02	0.16	0.06
MnO	0.00	0.00	0.00	0.00	0.00	0.00	0.00	0.00	0.00	0.00	0.04	0.04
NiO	0.00	0.00	0.00	0.00	0.00	0.00	0.00	0.00	0.00	0.00	0.00	0.01
MgO	0.00	0.00	0.00	0.00	0.00	0.00	0.00	0.00	0.00	0.01	0.00	0.00
CaO	1.61	2.21	2.27	2.09	1.70	1.72	1.73	1.75	1.87	1.62	1.78	1.56
Na_2O	10.71	10.08	10.28	10.23	10.45	10.48	10.53	10.50	10.49	10.04	10.05	10.00
K_2O	0.00	0.27	0.00	0.00	0.00	0.00	0.00	0.00	0.00	0.11	0.03	0.21
P_2O_5										0.00	0.00	0.03
Cl										0.00	0.02	0.00
Total	100.07	100.06	99.95	99.74	99.69	99.55	100.30	99.85	99.95	98.57	98.92	98.69
An	7.7	10.6	10.9	10.1	8.2	8.3	8.3	8.4	9.0	8.1	8.9	7.8
Ab	92.3	87.8	89.1	89.9	91.8	91.7	91.7	91.6	91.0	91.2	90.9	90.9
Or	0.0	1.5	0.0	0.0	0.0	0.0	0.0	0.0	0.0	0.7	0.2	1.2

Appendix 2.1: Major and minor elements composition of mineral phases from Finero dykes (contd.)

Grouping	HFSE-rich dyke										
Rock type	Dioritic dyke										
Sample	FI1604	FI1604	FI1605	FI1605	FI1605	FI1605	FI1605	FI1605	FI1605	FI1605	FI1605
Thin section	FI1604C	FI1604C	FI1605A	FI1605A	FI1605A	FI1605A	FI1605A	FI1605A	FI1605A2	FI1605A2	FI1605A2
Phase	Plag	Plag	Plag	Plag	Plag	Plag	Plag	Plag	Plag	Plag	Plag
Spot No.	13	19	2	4	6	6	7	7	1	1	2
Analysis No.	2	3	8	14	15	16	17	18	3	5	4
SiO_2	65.36	65.28	64.80	64.87	65.27	65.33	65.61	65.02	65.55	65.85	65.65
TiO_2	0.00	0.00	0.00	0.00	0.00	0.00	0.00	0.00	0.00	0.03	0.00
Al_2O_3	20.98	21.39	22.88	22.74	22.69	22.12	22.14	22.48	20.68	20.83	21.43
Cr_2O_3	0.00	0.00	0.00	0.00	0.00	0.00	0.00	0.00	0.02	0.01	0.00
FeO_T	0.15	0.25	0.00	0.00	0.00	0.00	0.00	0.00	0.04	0.06	0.07
MnO	0.03	0.00	0.00	0.00	0.00	0.00	0.00	0.00	0.00	0.03	0.02
NiO	0.02	0.00	0.00	0.00	0.00	0.00	0.00	0.00	0.00	0.02	0.00
MgO	0.02	0.02	0.00	0.00	0.00	0.00	0.00	0.00	0.00	0.02	0.02
CaO	1.84	1.77	2.16	2.21	1.94	2.01	1.81	1.86	1.88	1.67	1.93
Na_2O	9.82	9.89	10.24	10.25	10.40	10.43	10.38	10.39	10.05	10.16	9.99
K_2O	0.05	0.02	0.00	0.00	0.00	0.00	0.23	0.00	0.04	0.06	0.04
P_2O_5	0.00	0.00							0.05	0.04	0.06
Cl	0.01	0.02							0.00	0.01	0.00
Total	98.29	98.64	100.08	100.07	100.30	99.89	100.17	99.75	98.32	98.78	99.21
An	9.4	9.0	10.4	10.6	9.3	9.6	8.7	9.0	9.3	8.3	9.6
Ab	90.3	90.9	89.6	89.4	90.7	90.4	90.0	91.0	90.4	91.4	90.2
Or	0.3	0.2	0.0	0.0	0.0	0.0	1.3	0.0	0.3	0.3	0.2

Appendix 2.1: Major and minor elements composition of mineral phases from Finero dykes (contd.)

Grouping	HFSE-rich dyke									
Rock type	Dioritic dyke									
Sample	FI1605	FI1605	FI1605	FI1605	FI1605	FI1605	FI1605	FI1605	FI2102	FI2103
Thin section	FI1605A2	FI1605A2	FI1605A2	FI1605A2	FI1605A2	FI1605A2	FI1605A2	FI1605A2	FI2102C	FI2103C
Phase	Plag	Plag	Plag	Plag	Plag	Plag	Plag	Plag	Plag	Plag
Spot No.	3	4	5	6	7	8	9	10	1	3
Analysis No.	4	3	3	1	3	1	1	5	1a	2
SiO_2	64.90	64.89	64.87	65.83	64.96	65.75	66.04	65.41	66.86	65.57
TiO_2	0.00	0.03	0.00	0.00	0.00	0.00	0.00	0.00	0.02	0.00
Al_2O_3	21.26	21.66	21.46	20.43	21.71	21.10	20.71	21.28	20.96	20.92
Cr_2O_3	0.04	0.00	0.00	0.03	0.00	0.00	0.03	0.00	0.00	0.06
FeO_T	0.06	0.06	0.04	0.10	0.09	0.01	0.10	0.09	0.08	0.09
MnO	0.06	0.03	0.00	0.00	0.00	0.02	0.00	0.00	0.00	0.00
NiO	0.00	0.00	0.01	0.02	0.01	0.02	0.00	0.00	0.00	0.03
MgO	0.01	0.00	0.03	0.00	0.00	0.00	0.00	0.00	0.00	0.02
CaO	1.87	1.86	1.81	1.53	1.84	1.75	1.45	1.82	1.36	1.70
Na_2O	10.13	9.86	9.92	10.10	9.90	10.36	10.20	10.05	10.35	9.95
K_2O	0.03	0.05	0.04	0.14	0.03	0.14	0.02	0.03	0.29	0.03
P_2O_5	0.03	0.01	0.00	0.03	0.03	0.03	0.03	0.04	0.04	0.03
Cl	0.01	0.00	0.00	0.00	0.01	0.02	0.00	0.01	0.00	0.01
Total	98.39	98.45	98.19	98.21	98.58	99.20	98.58	98.73	99.97	98.41
An	9.2	9.4	9.1	7.7	9.3	8.5	7.3	9.1	6.7	8.6
Ab	90.6	90.3	90.6	91.5	90.5	90.7	92.6	90.7	91.6	91.2
Or	0.2	0.3	0.3	0.9	0.2	0.8	0.1	0.2	1.7	0.2

Appendix 2.1: Major and minor elements composition of mineral phases from Finero dykes (contd.)

Grouping	HFSE-rich dyke											
Rock type	Dioritic dyke											
Sample	FI2103	FI2103	FI2103	FI2104	FI2104	FI2104	FI2104	FI2104	FI2104	FI2104	FI2104	FI2104
Thin section	FI2103C	FI2103C	FI2103C	FI2104B	FI2104B	FI2104B	FI2104B	FI2104B	FI2104C	FI2104C	FI2104C	FI2104C
Phase	Plag	Plag	Plag	Plag	Plag	Plag	Plag	Plag	Plag	Plag	Plag	Plag
Spot No.	4	5	6	1	2	3	6	8	1	5	7	8
Analysis No.	1a	1	2	1a	2a	3a	10	17	1	2	2	1
SiO_2	66.44	66.09	66.52	66.35	66.27	66.23	65.76	66.05	66.17	66.03	66.49	65.86
TiO_2	0.01	0.00	0.00	0.00	0.00	0.08	0.03	0.00	0.00	0.00	0.02	0.00
Al_2O_3	20.29	20.53	20.83	20.90	20.88	20.97	21.11	21.38	19.77	20.88	20.85	20.74
Cr_2O_3	0.03	0.00	0.00	0.02	0.00	0.00	0.00	0.00	0.04	0.02	0.03	0.00
FeO_T	0.00	0.10	0.08	0.06	0.07	0.07	0.05	0.09	0.08	0.04	0.06	0.01
MnO	0.00	0.00	0.00	0.00	0.00	0.00	0.00	0.00	0.02	0.00	0.00	0.02
NiO	0.04	0.06	0.00	0.01	0.05	0.02	0.00	0.00	0.00	0.03	0.05	0.01
MgO	0.00	0.01	0.01	0.00	0.00	0.02	0.02	0.00	0.00	0.00	0.01	0.00
CaO	1.36	1.41	1.40	1.42	1.38	1.51	1.54	1.69	1.29	1.74	1.74	1.77
Na_2O	10.12	10.07	9.91	10.26	10.26	10.64	10.38	10.07	10.33	10.00	9.48	10.27
K_2O	0.22	0.11	0.03	0.24	0.36	0.29	0.08	0.09	0.16	0.13	0.03	0.20
P_2O_5	0.01	0.04	0.01	0.02	0.01	0.01	0.00	0.04	0.00	0.03	0.00	0.01
Cl	0.00	0.00	0.01	0.00	0.00	0.02	0.00	0.00	0.02	0.00	0.01	0.00
Total	98.53	98.43	98.81	99.27	99.28	99.86	98.96	99.41	97.89	98.90	98.76	98.89
An	6.8	7.1	7.2	7.0	6.8	7.2	7.5	8.4	6.4	8.7	9.2	8.6
Ab	91.8	92.2	92.6	91.6	91.1	91.2	92.0	91.0	92.6	90.5	90.6	90.2
Or	1.3	0.7	0.2	1.4	2.1	1.7	0.4	0.5	1.0	0.8	0.2	1.2

Appendix 2.1: Major and minor elements composition of mineral phases from Finero dykes (contd.)

Grouping	HFSE-rich dyke		HFSE-rich dyke							
Rock type	Dioritic dyke		Albite-dominated anorthosite dyke							
Sample	FI2104	FI2104	FI19A02	FI19A02	FI19A02	FI19A02	FI19A02	FI19A02	FI19A02	FI19A04
Thin section	FI2104C	FI2104C	FI19A02B	FI19A02B	FI19A02B	FI19A02B	FI19A02B	FI19A02B	FI19A02B	FI19A04A
Phase	Plag	Plag	Plag	Plag	Plag	Plag	Plag	Plag	Plag	Plag
Spot No.	9	11	3	4	4	5	5	6	9	2
Analysis No.	2	1	7	8	9	10a	10b	12	22	5
SiO_2	65.68	65.83	64.58	62.63	65.22	64.92	64.68	65.16	64.35	66.59
TiO_2	0.00	0.00	0.00	0.02	0.00	0.02	0.03	0.05	0.04	0.00
Al_2O_3	20.33	20.64	22.19	21.65	22.41	22.47	22.42	22.52	22.40	21.99
Cr_2O_3	0.00	0.08	0.02	0.03	0.00	0.01	0.03	0.02	0.01	0.00
FeO_T	0.09	0.02	0.12	0.06	0.11	0.00	0.09	0.05	0.16	0.14
MnO	0.00	0.00	0.00	0.01	0.00	0.00	0.00	0.01	0.00	0.00
NiO	0.00	0.02	0.03	0.01	0.02	0.02	0.00	0.03	0.00	0.03
MgO	0.02	0.00	0.00	0.00	0.01	0.00	0.01	0.02	0.01	0.00
CaO	1.80	1.74	2.36	2.26	2.47	2.47	2.44	2.58	2.70	1.99
Na_2O	9.91	9.80	10.16	9.71	9.98	9.76	10.19	9.90	9.65	10.04
K_2O	0.02	0.07	0.09	0.04	0.05	0.21	0.06	0.10	0.06	0.06
P_2O_5	0.03	0.00	0.03	0.04	0.09	0.03	0.01	0.02	0.01	0.00
Cl	0.00	0.01	0.00	0.00	0.02	0.00	0.00	0.00	0.01	0.00
Total	97.88	98.21	99.58	96.46	100.38	99.91	99.95	100.47	99.42	100.84
An	9.1	8.9	11.3	11.4	12.0	12.1	11.6	12.5	13.3	9.8
Ab	90.8	90.7	88.2	88.4	87.7	86.7	88.0	86.9	86.3	89.8
Or	0.1	0.4	0.5	0.2	0.3	1.2	0.3	0.6	0.4	0.3

Appendix 2.1: Major and minor elements composition of mineral phases from Finero dykes (contd.)

Grouping	HFSE-rich dyke										
Rock type	Albite-dominated anorthosite dyke										
Sample	FI19A04	FI19A04	FI19A04	FI19A04	FI19A04	FI19A04	FI19A04	FI19A04	FI19A04	FI19A04	FI19A04
Thin section	FI19A04A	FI19A04A	FI19A04A	FI19A04A	FI19A04A	FI19A04A	FI19A04A	FI19A04B	FI19A04B	FI19A04B	FI19A04B
Phase	Plag	Plag	Plag	Plag	Plag	Plag	Plag	Plag	Plag	Plag	Plag
Spot No.	5	6	7	8	9	10	11	1	2	5	7
Analysis No.	15	18	21	22	23	24	25	1a	3	9	13
SiO_2	65.38	65.75	66.03	65.72	66.05	65.61	66.53	66.04	66.67	66.15	66.25
TiO_2	0.00	0.06	0.02	0.01	0.00	0.04	0.00	0.03	0.00	0.00	0.10
Al_2O_3	21.82	21.47	21.69	21.94	22.06	21.50	21.58	21.71	22.14	22.09	22.28
Cr_2O_3	0.00	0.03	0.01	0.00	0.00	0.01	0.00	0.00	0.00	0.02	0.00
FeO_T	0.00	0.02	0.05	0.07	0.00	0.06	0.07	0.07	0.12	0.13	0.11
MnO	0.04	0.02	0.07	0.00	0.04	0.04	0.00	0.05	0.00	0.00	0.01
NiO	0.00	0.01	0.04	0.00	0.00	0.03	0.00	0.00	0.00	0.02	0.11
MgO	0.00	0.00	0.02	0.00	0.01	0.01	0.00	0.01	0.00	0.00	0.04
CaO	1.98	1.90	1.84	2.07	1.98	1.94	1.85	1.81	1.72	1.98	2.03
Na_2O	10.28	10.31	10.44	10.03	10.39	10.41	10.04	10.24	10.42	10.21	10.16
K_2O	0.00	0.04	0.06	0.11	0.04	0.11	0.04	0.03	0.06	0.01	0.09
P_2O_5	0.02	0.01	0.03	0.02	0.06	0.10	0.06	0.02	0.01	0.01	0.05
Cl	0.00	0.00	0.00	0.00	0.00	0.02	0.01	0.01	0.02	0.00	0.00
Total	99.53	99.61	100.30	99.96	100.64	99.88	100.18	100.01	101.16	100.62	101.24
An	9.6	9.2	8.8	10.2	9.5	9.3	9.2	8.9	8.3	9.7	9.9
Ab	90.4	90.6	90.8	89.2	90.3	90.1	90.5	90.9	91.3	90.3	89.6
Or	0.0	0.2	0.3	0.6	0.2	0.6	0.2	0.2	0.3	0.0	0.5

Appendix 2.1: Major and minor elements composition of mineral phases from Finero dykes (contd.)

Grouping	HFSE-poor dyke				Composite HFSE-poor and -rich dyke					
Rock type	Gabbroic dyke bordered by orthopyroxenite				Dioritic dyke					
Sample	FI2101	FI2101	FI2101	FI2101	FI2106	FI2106	FI2106	FI2106	FI2106	FI2106
Thin section	FI2101A	FI2101A	FI2101A	FI2101A	FI2106A	FI2106A	FI2106A	FI2106A	FI2106A	FI2106A
Phase	Plag	Plag	Plag	Plag	Plag	Plag	Plag	Plag	Plag	Plag
Spot No.	3	4	4	10	3	3	6	7	8	9
Analysis No.	1a	1	2	1	7	8	12	13	14	18
SiO_2	50.86	46.30	46.92	49.91	61.49	61.62	61.06	62.69	62.06	61.85
TiO_2	0.04	0.00	0.00	0.01	0.00	0.02	0.00	0.01	0.00	0.00
Al_2O_3	30.94	33.42	33.23	31.16	24.74	24.87	24.23	24.28	24.52	24.43
Cr_2O_3	0.00	0.05	0.04	0.00	0.00	0.02	0.04	0.00	0.02	0.01
FeO_T	0.02	0.04	0.03	0.00	0.05	0.02	0.12	0.05	0.08	0.06
MnO	0.00	0.00	0.02	0.00	0.01	0.00	0.00	0.02	0.01	0.00
NiO	0.00	0.00	0.03	0.02	0.00	0.02	0.00	0.00	0.01	0.00
MgO	0.00	0.00	0.00	0.00	0.01	0.02	0.00	0.00	0.01	0.02
CaO	14.03	17.41	17.62	14.85	6.00	6.22	5.68	4.61	5.80	5.97
Na_2O	3.37	1.50	1.52	3.00	8.30	8.12	8.09	8.34	8.28	8.26
K_2O	0.04	0.00	0.00	0.05	0.13	0.10	0.15	0.21	0.15	0.08
P_2O_5	0.10	0.18	0.14	0.14	0.05	0.01	0.06	0.11	0.08	0.09
Cl	0.00	0.01	0.01	0.00	0.01	0.00	0.02	0.00	0.03	0.00
Total	99.41	98.91	99.57	99.15	100.78	101.02	99.44	100.32	101.05	100.77
An	69.5	86.5	86.5	73.0	28.3	29.6	27.7	23.1	27.7	28.4
Ab	30.2	13.5	13.5	26.7	70.9	69.9	71.4	75.6	71.5	71.1
Or	0.2	0.0	0.0	0.3	0.7	0.5	0.9	1.3	0.8	0.4

Appendix 2.1: Major and minor elements composition of mineral phases from Finero dykes (contd.)

Grouping	HFSE-rich dyke											
Rock type	Dioritic dyke											
Sample	FI1603	FI1603	FI1603	FI1603	FI1603	FI1603	FI1603	FI1603	FI1603	FI1603	FI1603	FI1603
Thin section	FI1603A	FI1603A	FI1603A	FI1603A	FI1603A	FI1603A	FI1603A	FI1603A	FI1603A	FI1603A	FI1603A	FI1603A
Phase	Amph	Amph	Amph	Amph	Amph	Amph	Amph	Amph	Amph	Amph	Amph	Amph
Spot No.	1	1	1	5ext	10	10	12	12	13	16	16	20
Analysis No.	1	2	5	18	42	43	44	45	48	65	66	67
SiO_2	48.71	48.00	47.65	48.64	48.02	46.07	48.12	46.73	46.06	48.21	47.78	48.15
TiO_2	0.59	0.74	0.68	0.61	0.60	0.59	0.88	0.70	0.66	0.88	0.52	0.80
Al_2O_3	9.45	9.56	9.91	9.40	9.19	9.87	10.08	9.85	10.65	9.40	9.46	10.34
Cr_2O_3	0.12	0.06	0.11	0.03	0.13	0.11	0.00	0.05	0.00	0.07	0.05	0.15
FeO_T	6.98	6.88	7.15	6.38	6.82	7.35	7.02	7.37	7.92	6.70	7.21	7.40
MnO	0.07	0.17	0.19	0.21	0.28	0.11	0.00	0.04	0.08	0.00	0.17	0.36
NiO	0.00	0.00	0.00	0.00	0.00	0.00	0.00	0.00	0.00	0.00	0.00	0.00
MgO	16.88	17.24	17.39	17.66	17.04	17.33	16.37	17.17	16.44	17.01	17.09	15.97
CaO	10.89	10.83	9.98	10.41	11.23	11.63	10.90	11.68	11.55	11.07	11.20	10.16
Na_2O	3.31	3.55	3.23	3.56	3.62	3.78	3.48	3.28	3.66	3.48	3.55	3.66
K_2O	0.63	0.62	1.40	0.73	0.69	0.75	0.80	0.74	0.59	0.84	0.57	0.71
P_2O_5												
Cl												
Total	97.63	97.64	97.69	97.64	97.62	97.58	97.66	97.62	97.60	97.65	97.59	97.70
Mg#	81.2	81.7	81.2	83.1	81.6	80.8	80.6	80.6	78.7	81.9	80.8	79.4

Appendix 2.1: Major and minor elements composition of mineral phases from Finero dykes (contd.)

Grouping	HFSE-rich dyke											
Rock type	Dioritic dyke											
Sample	FI1603	FI1603	FI1603	FI1603	FI1603	FI1603	FI1603	FI1603	FI1603	FI1603	FI1603	FI1603
Thin section	FI1603A	FI1603A	FI1603A	FI1603B	FI1603B	FI1603B	FI1603B	FI1603B	FI1603B	FI1603B	FI1603B	FI1603B
Phase	Amph	Amph	Amph	Amph	Amph	Amph	Amph	Amph	Amph	Amph	Amph	Amph
Spot No.	20	24	24	2	2	5	6	6	9	10	10	12
Analysis No.	68	69	70	3	4a	17	19	20	31	33	34	39
SiO_2	45.88	48.09	48.00	48.25	46.81	48.11	47.12	47.14	47.53	46.78	47.63	46.42
TiO_2	1.10	0.84	0.68	1.09	1.10	0.98	1.52	1.37	1.46	1.51	1.32	1.42
Al_2O_3	10.61	9.20	9.61	9.28	10.03	9.23	9.67	9.44	10.12	10.16	9.81	11.04
Cr_2O_3	0.11	0.07	0.07	0.07	0.00	0.03	0.09	0.00	0.06	0.01	0.03	0.05
FeO_T	7.91	7.58	7.42	7.54	8.56	7.20	7.83	7.63	7.21	7.82	7.38	7.33
MnO	0.00	0.17	0.16	0.13	0.17	0.16	0.14	0.07	0.09	0.10	0.12	0.10
NiO	0.00	0.00	0.00	0.00	0.00	0.00	0.00	0.00	0.00	0.00	0.00	0.00
MgO	17.38	16.97	16.62	16.61	15.81	16.96	16.13	16.57	16.36	16.04	16.67	15.88
CaO	10.50	10.87	10.89	10.98	11.11	11.42	10.94	11.52	10.84	10.65	10.49	10.49
Na_2O	2.88	3.26	3.53	3.15	3.44	3.08	3.65	3.30	3.44	3.93	3.59	4.16
K_2O	1.42	0.62	0.66	0.61	0.66	0.53	0.67	0.67	0.65	0.73	0.69	0.84
P_2O_5												
Cl												
Total	97.78	97.66	97.63	97.71	97.69	97.68	97.74	97.71	97.76	97.73	97.73	97.73
Mg#	79.6	79.9	80.0	79.7	76.7	80.7	78.6	79.5	80.2	78.5	80.1	79.4

Appendix 2.1: Major and minor elements composition of mineral phases from Finero dykes (contd.)

Grouping	HFSE-rich dyke											
Rock type	Dioritic dyke											
Sample	FI1603	FI1603	FI1603	FI1603	FI1603	FI1603	FI1603	FI1603	FI1603	FI1603	FI1604	FI1604
Thin section	FI1603B	FI1603B	FI1603C	FI1603C	FI1603C	FI1603C	FI1603C	FI1603C	FI1603C	FI1603C	FI1604C	FI1604C
Phase	Amph	Amph	Amph	Amph	Amph	Amph	Amph	Amph	Amph	Amph	Amph	Amph
Spot No.	13	13	3	3	5	8	8	9	9	10	9	11
Analysis No.	40	41	8	9	12	29	30	31	32	33	2	1b
SiO_2	46.50	46.72	47.35	46.64	46.82	47.43	47.36	47.44	47.14	47.19	46.82	46.26
TiO_2	1.43	1.51	1.06	1.13	0.79	1.19	1.46	1.24	0.90	1.35	0.35	0.50
Al_2O_3	10.78	10.41	9.96	10.04	10.94	9.95	10.18	9.77	9.23	10.08	9.66	9.89
Cr_2O_3	0.00	0.00	0.00	0.00	0.00	0.00	0.01	0.02	0.02	0.03	0.05	0.01
FeO_T	7.62	7.53	7.65	7.47	8.60	7.48	8.03	7.62	8.05	7.58	7.73	7.94
MnO	0.19	0.25	0.16	0.17	0.19	0.20	0.22	0.16	0.16	0.16	0.17	0.15
NiO	0.00	0.00	0.00	0.00	0.00	0.00	0.00	0.00	0.00	0.00	0.09	0.04
MgO	16.30	16.33	16.29	16.67	15.48	16.42	16.51	16.16	16.43	16.17	17.51	17.60
CaO	10.47	10.52	10.91	11.79	11.40	10.98	10.24	11.09	12.04	11.02	10.83	10.58
Na_2O	3.66	3.54	3.57	3.24	2.91	3.38	3.18	3.53	3.27	3.47	3.71	3.64
K_2O	0.81	0.96	0.74	0.54	0.56	0.68	0.62	0.68	0.40	0.68	0.53	0.62
P_2O_5											0.08	0.10
Cl											0.10	0.11
Total	97.76	97.78	97.68	97.69	97.68	97.72	97.80	97.71	97.63	97.73	97.63	97.43
Mg#	79.2	79.4	79.1	79.9	76.2	79.6	78.5	79.1	78.4	79.2	80.1	79.8

Appendix 2.1: Major and minor elements composition of mineral phases from Finero dykes (contd.)

Grouping	HFSE-rich dyke											
Rock type	Dioritic dyke											
Sample	FI1604	FI1604	FI1604	FI1604	FI1604	FI1604	FI1605	FI1605	FI1605	FI1605	FI1605	FI1605
Thin section	FI1604C	FI1604C	FI1604C	FI1604C	FI1604C	FI1604C	FI1605A	FI1605A	FI1605A	FI1605A	FI1605A	FI1605A
Phase	Amph	Amph	Amph	Amph	Amph	Amph	Amph	Amph	Amph	Amph	Amph	Amph
Spot No.	14	15	16	17	18	19	1	1	2	2	3	3
Analysis No.	1	1	1	4	1	1	1	2	6	7	10	11
SiO_2	46.61	45.81	46.30	46.43	46.54	46.59	47.95	47.93	48.19	47.62	47.75	47.85
TiO_2	0.63	0.61	0.43	0.68	0.42	0.51	0.64	0.64	0.73	0.65	0.71	0.69
Al_2O_3	10.01	10.18	10.21	10.52	10.31	9.69	9.62	9.28	9.14	9.57	9.47	10.03
Cr_2O_3	0.01	0.07	0.00	0.06	0.05	0.04	0.18	0.20	0.18	0.13	0.17	0.04
FeO_T	7.70	7.82	7.57	7.61	7.52	7.61	7.18	7.39	6.91	7.37	7.08	6.98
MnO	0.12	0.11	0.11	0.12	0.13	0.16	0.20	0.13	0.14	0.06	0.26	0.16
NiO	0.14	0.10	0.09	0.09	0.03	0.06	0.00	0.00	0.00	0.00	0.00	0.00
MgO	17.32	17.65	17.39	17.49	17.41	17.86	16.77	16.77	17.08	16.86	16.99	16.67
CaO	10.32	10.41	10.44	10.34	10.14	10.35	11.27	11.31	11.25	11.21	11.28	11.25
Na_2O	3.73	3.67	3.86	3.71	3.81	3.74	3.34	3.41	3.32	3.48	3.30	3.35
K_2O	0.75	0.69	0.66	0.73	0.84	0.70	0.51	0.57	0.71	0.67	0.63	0.63
P_2O_5	0.11	0.11	0.05	0.06	0.08	0.10						
Cl	0.09	0.08	0.09	0.10	0.10	0.09						
Total	97.56	97.31	97.20	97.93	97.40	97.50	97.64	97.63	97.65	97.62	97.66	97.64
Mg#	80.0	80.1	80.4	80.4	80.5	80.7	80.6	80.2	81.5	80.3	81.0	81.0

Appendix 2.1: Major and minor elements composition of mineral phases from Finero dykes (contd.)

Grouping	HFSE-rich dyke										
Rock type	Dioritic dyke										
Sample	FI1605	FI1605	FI1605	FI1605	FI1605	FI1605	FI1605	FI1605	FI1605	FI1605	FI1605
Thin section	FI1605A	FI1605A	FI1605A	FI1605A	FI1605A2	FI1605A2	FI1605A2	FI1605A2	FI1605A2	FI1605A2	FI1605A2
Phase	Amph	Amph	Amph	Amph	Amph	Amph	Amph	Amph	Amph	Amph	Amph
Spot No.	4	4	9	9	1	2	2	3	3	4	5
Analysis No.	12	13	21	22	1	1	2	1	2	1	1
SiO_2	48.04	48.21	48.08	47.44	46.46	46.06	46.41	46.42	46.68	45.79	46.41
TiO_2	0.77	0.64	0.52	0.58	0.70	0.70	0.73	0.71	0.70	0.86	0.77
Al_2O_3	9.47	8.95	9.40	9.76	10.13	10.08	10.15	10.12	9.76	10.73	10.27
Cr_2O_3	0.13	0.10	0.06	0.06	0.05	0.10	0.04	0.07	0.08	0.07	0.00
FeO_T	7.03	7.17	7.25	7.53	7.31	7.28	7.40	7.31	7.36	7.32	7.31
MnO	0.11	0.15	0.10	0.18	0.20	0.18	0.17	0.18	0.13	0.16	0.12
NiO	0.00	0.00	0.00	0.00	0.04	0.15	0.05	0.05	0.09	0.02	0.13
MgO	17.00	17.31	17.18	16.85	17.38	17.71	17.72	17.57	17.62	17.38	17.76
CaO	11.01	11.13	11.08	11.37	10.46	10.40	10.91	10.27	10.68	10.19	10.53
Na_2O	3.22	3.28	3.26	3.39	3.81	3.84	3.68	4.00	3.77	3.69	3.66
K_2O	0.88	0.69	0.68	0.48	0.64	0.70	0.61	0.73	0.61	0.75	0.70
P_2O_5					0.08	0.11	0.08	0.08	0.06	0.08	0.13
Cl					0.08	0.08	0.09	0.07	0.08	0.05	0.06
Total	97.66	97.63	97.61	97.61	97.33	97.40	98.04	97.58	97.62	97.09	97.84
Mg#	81.2	81.1	80.8	79.9	80.9	81.2	81.0	81.1	81.0	80.9	81.2

Appendix 2.1: Major and minor elements composition of mineral phases from Finero dykes (contd.)

Grouping	HFSE-rich dyke										
Rock type	Dioritic dyke										
Sample	FI1605	FI1605	FI1605	FI1605	FI1605	FI2102	FI2102	FI2102	FI2102	FI2102	FI2102
Thin section	FI1605A2	FI1605A2	FI1605A2	FI1605A2	FI1605A2	FI2102C	FI2102C	FI2102C	FI2102C	FI2102C	FI2102C
Phase	Amph	Amph	Amph	Amph	Amph	Amph	Amph	Amph	Amph	Amph	Amph
Spot No.	7	9	10	10	11	2	3	4	5	6	7
Analysis No.	1	2	2	3	1	2b	5a	10	11a	16	17
SiO_2	46.27	46.40	45.94	46.23	46.06	46.85	46.84	46.46	46.65	46.19	46.16
TiO_2	1.03	0.89	0.93	0.91	0.77	0.20	0.28	0.20	0.17	0.27	0.46
Al_2O_3	10.48	10.06	10.59	10.05	10.41	10.29	10.20	10.06	10.18	10.32	10.03
Cr_2O_3	0.08	0.06	0.05	0.12	0.00	0.00	0.17	0.00	0.00	0.02	0.18
FeO_T	7.42	7.70	7.43	7.52	7.22	6.35	6.43	6.73	6.44	6.63	6.48
MnO	0.21	0.14	0.16	0.12	0.18	0.12	0.09	0.16	0.11	0.13	0.13
NiO	0.06	0.08	0.08	0.10	0.05	0.05	0.08	0.02	0.05	0.00	0.08
MgO	17.41	17.60	17.61	17.44	17.37	18.31	18.05	18.41	18.28	18.20	17.88
CaO	10.41	10.48	10.17	10.48	10.31	10.50	10.34	10.83	10.65	10.79	10.55
Na_2O	3.81	3.82	3.72	3.78	3.77	3.99	3.99	3.93	4.16	3.89	3.91
K_2O	0.67	0.61	0.81	0.69	0.71	0.68	0.71	0.59	0.67	0.62	0.67
P_2O_5	0.14	0.11	0.14	0.09	0.09	0.09	0.11	0.13	0.12	0.07	0.10
Cl	0.12	0.07	0.09	0.10	0.11	0.10	0.05	0.06	0.08	0.05	0.08
Total	98.12	98.01	97.72	97.63	97.04	97.54	97.34	97.58	97.56	97.17	96.70
Mg#	80.7	80.3	80.8	80.5	81.1	83.7	83.3	83.0	83.5	83.0	83.1

Appendix 2.1: Major and minor elements composition of mineral phases from Finero dykes (contd.)

Grouping	HFSE-rich dyke											
Rock type	Dioritic dyke											
Sample	FI2103	FI2103	FI2103	FI2103	FI2103	FI2103	FI2103	FI2103	FI2104	FI2104	FI2104	FI2104
Thin section	FI2103C	FI2103C	FI2103C	FI2103C	FI2103C	FI2103C	FI2103C	FI2103C	FI2104B	FI2104B	FI2104B	FI2104B
Phase	Amph	Amph	Amph	Amph	Amph	Amph	Amph	Amph	Amph	Amph	Amph	Amph
Spot No.	1	6	7	8	8	9	10	11	4	5	5	6
Analysis No.	1a	1	1a	1a	2	1	1	1	5a	7	8b	11
SiO_2	47.20	47.12	47.31	47.81	47.06	47.96	47.42	47.52	46.56	47.57	47.47	47.11
TiO_2	0.68	0.54	0.59	0.42	0.59	0.51	0.46	0.50	0.63	0.61	0.59	0.53
Al_2O_3	9.34	9.68	9.56	9.34	9.41	9.34	9.28	9.51	10.23	10.14	10.02	9.96
Cr_2O_3	0.03	0.00	0.09	0.15	0.14	0.23	0.11	0.16	0.00	0.03	0.06	0.03
FeO_T	6.54	6.25	6.65	6.40	6.50	6.50	6.45	6.36	7.11	6.59	6.68	6.96
MnO	0.10	0.16	0.16	0.04	0.09	0.15	0.16	0.14	0.09	0.13	0.09	0.17
NiO	0.02	0.08	0.05	0.03	0.05	0.09	0.01	0.03	0.06	0.08	0.12	0.10
MgO	17.79	17.93	18.25	18.33	18.22	18.64	17.93	18.38	17.70	18.06	17.74	17.98
CaO	9.87	10.21	10.28	10.08	10.40	10.15	10.25	9.84	10.75	10.16	10.43	10.81
Na_2O	4.09	3.86	3.79	3.87	3.79	3.91	4.02	4.00	4.13	4.12	4.02	3.95
K_2O	0.69	0.67	0.63	0.66	0.59	0.69	0.63	0.76	0.60	0.73	0.68	0.61
P_2O_5	0.10	0.12	0.12	0.09	0.13	0.08	0.07	0.05	0.10	0.15	0.07	0.10
Cl	0.07	0.07	0.10	0.06	0.10	0.05	0.07	0.07	0.08	0.07	0.05	0.07
Total	96.51	96.69	97.58	97.29	97.07	98.30	96.86	97.31	98.03	98.44	98.04	98.37
Mg#	82.9	83.6	83.0	83.6	83.3	83.6	83.2	83.7	81.6	83.0	82.5	82.1

Appendix 2.1: Major and minor elements composition of mineral phases from Finero dykes (contd.)

Grouping	HFSE-rich dyke											
Rock type	Dioritic dyke											
Sample	FI2104	FI2104	FI2104	FI2104	FI2104	FI2104	FI2104	FI2104	FI2104	FI2104	FI2104	FI2104
Thin section	FI2104B	FI2104B	FI2104B	FI2104B	FI2104B	FI2104B	FI2104B	FI2104B	FI2104C	FI2104C	FI2104C	FI2104C
Phase	Amph	Amph	Amph	Amph	Amph	Amph	Amph	Amph	Amph	Amph	Amph	Amph
Spot No.	7	8	10	11	12	13	14	15	2	3	4	4
Analysis No.	15	16	22	24	26	27	30	33	1a	1a	1	2
SiO_2	45.92	47.23	47.14	47.45	47.46	47.41	47.21	47.30	46.26	46.40	46.92	46.30
TiO_2	0.59	0.66	0.53	0.64	0.52	0.54	0.49	0.56	0.64	0.79	0.78	0.82
Al_2O_3	10.03	9.99	10.11	9.90	9.78	9.88	10.01	10.09	10.03	10.09	10.26	10.57
Cr_2O_3	0.01	0.11	0.07	0.01	0.02	0.08	0.06	0.17	0.05	0.01	0.00	0.00
FeO_T	7.08	6.89	6.67	6.87	6.72	6.83	6.94	6.86	9.10	7.00	7.21	6.96
MnO	0.15	0.12	0.18	0.13	0.17	0.14	0.17	0.20	0.15	0.14	0.15	0.19
NiO	0.04	0.06	0.10	0.03	0.02	0.10	0.06	0.06	0.05	0.03	0.11	0.08
MgO	17.60	17.63	18.02	17.77	17.90	17.98	17.95	17.89	16.22	17.43	17.63	17.52
CaO	10.41	10.25	10.26	10.38	10.65	10.60	10.56	10.44	11.43	10.11	10.29	10.20
Na_2O	4.04	4.24	4.29	4.03	4.05	4.05	3.94	4.02	3.26	4.17	4.08	4.08
K_2O	0.68	0.72	0.75	0.68	0.63	0.63	0.68	0.66	0.23	0.81	0.60	0.72
P_2O_5	0.04	0.09	0.11	0.09	0.11	0.12	0.09	0.07	0.11	0.11	0.09	0.07
Cl	0.05	0.06	0.06	0.08	0.07	0.03	0.05	0.08	0.02	0.07	0.08	0.10
Total	96.64	98.07	98.30	98.04	98.10	98.40	98.21	98.41	97.55	97.16	98.22	97.61
Mg#	81.6	82.0	82.8	82.2	82.6	82.4	82.2	82.3	76.0	81.6	81.3	81.8

Appendix 2.1: Major and minor elements composition of mineral phases from Finero dykes (contd.)

Grouping	HFSE-rich dyke											
Rock type	Dioritic dyke											
Sample	FI2104	FI2104	FI2104	FI2104	FI2104	FI2105	FI2105	FI2105	FI2105	FI2105	FI2105	FI2105
Thin section	FI2104C	FI2104C	FI2104C	FI2104C	FI2104C	FI2105B	FI2105B	FI2105B	FI2105B	FI2105B	FI2105B	FI2105B
Phase	Amph	Amph	Amph	Amph	Amph	Amph	Amph	Amph	Amph	Amph	Amph	Amph
Spot No.	6	7	9	11	12	9	10	11	12	13	14	15
Analysis No.	2	1a	1	3	1	21a	23	25	26	27	28	29
SiO_2	46.19	45.16	46.41	46.68	46.20	45.21	45.48	45.79	45.24	45.12	44.81	45.01
TiO_2	0.80	0.93	0.74	0.92	0.87	1.34	1.35	1.19	1.27	1.11	1.23	1.23
Al_2O_3	10.00	11.14	9.75	10.33	10.36	11.50	11.58	11.28	11.52	10.94	11.36	11.22
Cr_2O_3	0.02	0.01	0.00	0.03	0.01	0.07	0.08	0.08	0.05	0.38	0.30	0.22
FeO_T	7.44	7.34	6.88	6.97	7.06	6.20	5.98	5.84	5.82	7.25	7.07	6.86
MnO	0.20	0.13	0.14	0.14	0.17	0.06	0.13	0.09	0.12	0.15	0.10	0.06
NiO	0.10	0.07	0.07	0.03	0.00	0.07	0.07	0.09	0.11	0.06	0.11	0.15
MgO	17.45	17.20	17.99	17.50	17.60	17.63	17.76	18.09	17.62	17.06	16.70	17.00
CaO	10.82	10.88	10.70	10.18	10.33	11.93	11.61	11.88	11.70	11.34	11.32	11.46
Na_2O	3.93	3.64	3.97	3.95	3.92	3.44	3.40	3.06	3.34	3.40	3.35	3.43
K_2O	0.56	0.61	0.59	0.71	0.66	0.67	0.76	0.78	0.75	0.68	0.74	0.72
P_2O_5	0.03	0.07	0.09	0.11	0.15	0.14	0.09	0.16	0.10	0.12	0.10	0.10
Cl	0.08	0.08	0.07	0.07	0.08	0.08	0.07	0.06	0.07	0.04	0.09	0.08
Total	97.62	97.26	97.39	97.62	97.40	98.33	98.37	98.39	97.72	97.65	97.30	97.54
Mg#	80.7	80.7	82.3	81.7	81.6	83.5	84.1	84.7	84.4	80.7	80.8	81.5

Appendix 2.1: Major and minor elements composition of mineral phases from Finero dykes (contd.)

Grouping	HFSE-rich dyke									
Rock type	Dioritic dyke			Clinopyroxenite cumulate in HFSE-rich dioritic dyke						
Sample	FI2105	FI2105	FI2105	FI1604	FI1604	FI1604	FI1604	FI1604	FI1604	FI1604
Thin section	FI2105B	FI2105B	FI2105B	FI1604C*	FI1604C*	FI1604C*	FI1604C*	FI1604C*	FI1604C*	FI1604C*
Phase	Amph	Amph	Amph	Amph	Amph	Amph	Amph	Amph	Amph	Amph
Spot No.	16	17	18	1	2	3	4	4	5	7
Analysis No.	30	32	33	1	3	2	1a	1b	1	1
SiO_2	44.34	45.28	45.12	47.16	46.31	47.47	47.28	47.29	47.56	47.59
TiO_2	1.33	1.43	1.29	0.54	0.54	0.59	0.51	0.57	0.68	0.51
Al_2O_3	12.01	11.57	11.19	9.70	9.70	9.68	9.62	9.15	9.35	8.88
Cr_2O_3	0.00	0.03	0.06	0.20	0.12	0.28	0.33	0.29	0.28	0.25
FeO_T	6.56	6.35	6.06	7.57	7.82	7.04	7.14	7.29	7.51	7.08
MnO	0.15	0.09	0.07	0.21	0.17	0.15	0.18	0.14	0.11	0.17
NiO	0.04	0.04	0.04	0.03	0.03	0.13	0.01	0.11	0.00	0.10
MgO	16.97	17.27	17.70	17.48	17.16	17.65	17.50	17.71	17.55	17.86
CaO	11.28	11.80	11.77	10.43	10.61	10.30	10.50	10.36	10.47	10.37
Na_2O	3.35	3.20	3.29	3.73	3.77	3.81	3.75	3.72	3.74	3.58
K_2O	1.05	0.78	0.70	0.67	0.56	0.59	0.61	0.68	0.64	0.65
P_2O_5	0.11	0.09	0.09	0.12	0.05	0.07	0.11	0.05	0.10	0.10
Cl	0.06	0.08	0.08	0.07	0.09	0.07	0.09	0.09	0.09	0.09
Total	97.24	98.01	97.46	97.91	96.92	97.82	97.62	97.46	98.07	97.22
Mg#	82.2	82.9	83.9	80.4	79.6	81.7	81.4	81.2	80.6	81.8

Appendix 2.1: Major and minor elements composition of mineral phases from Finero dykes (contd.)

Grouping	HFSE-rich dyke									
Rock type	Clinopyroxenite cumulate in HFSE-rich dioritic dyke					Hornblendite dyke with olivine layer (Amph near Ol)				
Sample	FI1604	FI1604	FI2105	FI2105	FI2105	FI1501	FI1501	FI1501	FI1501	FI1501
Thin section	FI1604C*	FI1604C*	FI2105B*	FI2105B*	FI2105B*	FI1501B	FI1501B	FI1501B	FI1501B	FI1501B
Phase	Amph	Amph	Amph	Amph	Amph	Amph	Amph	Amph	Amph	Amph
Spot No.	8	10	3	4	8	1	2	3	4	5
Analysis No.	1	1	7a	10	20	1	4	6	9	10
SiO_2	47.45	46.56	46.69	46.32	47.73	44.76	46.49	46.22	45.38	45.13
TiO_2	0.63	0.64	0.71	0.67	0.55	1.66	1.59	1.53	1.52	1.53
Al_2O_3	8.73	9.42	9.73	9.88	9.02	10.06	9.05	9.31	9.35	9.67
Cr_2O_3	0.35	0.28	0.66	0.64	0.60	0.41	0.37	0.35	0.40	0.35
FeO_T	7.38	7.31	6.62	6.51	6.58	7.51	6.23	6.64	6.72	6.67
MnO	0.11	0.20	0.09	0.13	0.12	0.12	0.11	0.08	0.12	0.12
NiO	0.09	0.06	0.10	0.07	0.14	0.07	0.04	0.07	0.02	0.06
MgO	17.90	17.34	18.04	17.51	18.11	16.99	18.16	17.89	17.71	17.81
CaO	10.43	10.37	11.61	11.69	11.16	10.91	10.92	11.32	11.17	11.21
Na_2O	3.73	3.71	3.18	3.13	3.45	3.53	3.54	3.31	3.38	3.56
K_2O	0.64	0.72	0.59	0.57	0.67	0.62	0.50	0.50	0.54	0.54
P_2O_5	0.05	0.04	0.10	0.15	0.10	0.06	0.14	0.08	0.09	0.11
Cl	0.09	0.11	0.07	0.06	0.06	0.04	0.04	0.06	0.05	0.05
Total	97.58	96.76	98.19	97.33	98.29	96.74	97.18	97.37	96.46	96.82
Mg#	81.2	80.9	82.9	82.7	83.1	80.1	83.8	82.8	82.4	82.6

Appendix 2.1: Major and minor elements composition of mineral phases from Finero dykes (contd.)

Grouping	HFSE-rich dyke										
Rock type	Hornblendite dyke with olivine layer (Amph far from Ol)					Hornblendite dyke					
Sample	FI1501	FI1501	FI1501	FI1501	FI1501	FI1612	FI1612	FI1612	FI1612	FI1612	FI1612
Thin section	FI1501B	FI1501B	FI1501B	FI1501B	FI1501B	FI1612A	FI1612A	FI1612A	FI1612A	FI1612A	FI1612A
Phase	Amph	Amph	Amph	Amph	Amph	Amph	Amph	Amph	Amph	Amph	Amph
Spot No.	6	7	7	8	9	1	2	2	2	3	4
Analysis No.	11	13	14	16b	19	1	1	2	3	3	2
SiO_2	43.63	43.52	42.79	43.81	45.09	43.37	43.55	43.11	43.09	43.57	43.60
TiO_2	2.03	1.94	1.99	1.80	2.09	1.76	1.86	1.93	1.83	1.79	1.90
Al_2O_3	12.79	13.05	12.89	11.80	12.37	11.91	12.27	12.27	12.50	11.98	12.55
Cr_2O_3	0.02	0.03	0.15	0.01	0.03	0.08	0.02	0.08	0.03	0.05	0.01
FeO_T	6.28	6.03	5.84	6.68	6.21	8.37	8.76	8.53	8.68	8.70	8.49
MnO	0.08	0.09	0.12	0.07	0.15	0.14	0.15	0.13	0.16	0.10	0.15
NiO	0.02	0.02	0.07	0.02	0.08	0.02	0.06	0.03	0.04	0.07	0.00
MgO	16.77	16.62	16.80	16.63	16.71	15.87	15.44	15.64	15.23	15.76	15.44
CaO	11.51	11.65	11.69	11.68	11.45	11.07	11.02	10.95	11.14	10.94	10.94
Na_2O	3.75	3.67	3.70	3.73	3.75	3.60	3.57	3.77	3.43	3.62	3.60
K_2O	0.58	0.53	0.59	0.39	0.55	0.63	0.63	0.70	0.57	0.63	0.74
P_2O_5	0.14	0.07	0.09	0.12	0.09	0.15	0.10	0.08	0.14	0.15	0.11
Cl	0.07	0.04	0.05	0.04	0.08	0.08	0.06	0.09	0.09	0.11	0.06
Total	97.67	97.26	96.77	96.78	98.65	97.05	97.50	97.31	96.93	97.46	97.60
Mg#	82.6	83.1	83.7	81.6	82.7	77.2	75.8	76.6	75.8	76.3	76.4

Appendix 2.1: Major and minor elements composition of mineral phases from Finero dykes (contd.)

Grouping	HFSE-rich dyke									
Rock type	Hornblendite dyke				Albite-dominated anorthosite dyke					
Sample	FI1612	FI1612	FI1612	FI1612	FI19A04	FI19A04	FI19A04	FI19A04	FI19A04	FI19A04
Thin section	FI1612A	FI1612A	FI1612A	FI1612A	FI19A04A	FI19A04A	FI19A04A	FI19A04A	FI19A04A	FI19A04A
Phase	Amph	Amph	Amph	Amph	Amph	Amph	Amph	Amph	Amph	Amph
Spot No.	6	7	8	10	1	1	2	2	2	1
Analysis No.	1	2	2	1	1a	1b	4a	7c	7a	1a
SiO_2	43.63	43.76	42.97	43.05	44.63	44.61	45.17	44.91	44.95	44.63
TiO_2	1.98	1.96	1.82	2.05	1.17	1.32	1.00	1.11	1.12	1.17
Al_2O_3	12.51	12.63	12.88	12.67	11.16	10.90	11.26	11.34	11.06	11.16
Cr_2O_3	0.07	0.04	0.11	0.05	0.03	0.00	0.04	0.05	0.00	0.03
FeO_T	8.72	8.63	8.63	8.87	10.33	10.18	10.00	9.93	10.09	10.33
MnO	0.11	0.16	0.12	0.09	0.22	0.15	0.17	0.20	0.21	0.22
NiO	0.01	0.06	0.01	0.00	0.00	0.10	0.09	0.08	0.06	0.00
MgO	15.59	15.58	15.71	15.51	15.92	15.61	15.80	15.73	15.45	15.92
CaO	10.61	10.67	10.76	10.91	10.53	10.48	10.46	10.53	10.44	10.53
Na_2O	3.90	3.62	3.77	3.60	4.07	4.09	3.91	3.95	4.03	4.07
K_2O	0.72	0.68	0.73	0.61	0.82	0.81	0.87	0.86	0.81	0.82
P_2O_5	0.12	0.07	0.11	0.10	0.10	0.11	0.11	0.06	0.06	0.10
Cl	0.07	0.05	0.09	0.04	0.07	0.07	0.06	0.06	0.08	0.07
Total	98.04	97.89	97.71	97.56	99.06	98.45	98.96	98.80	98.36	99.06
Mg#	76.1	76.3	76.4	75.7	73.3	73.2	73.8	73.8	73.2	73.3

Appendix 2.1: Major and minor elements composition of mineral phases from Finero dykes (contd.)

Grouping	HFSE-poor dyke										
Rock type	Hornblendite dyke						Gabbroic dyke bordered by orthopyroxenite				
Sample	FI1608	FI1608	FI1608	FI1608	FI1608	FI1608	FI2101	FI2101	FI2101	FI2101	FI2101
Thin section	FI1608B	FI1608B	FI1608B	FI1608B	FI1608B	FI1608B	FI2101A	FI2101A	FI2101A	FI2101A	FI2101A
Phase	Amph	Amph	Amph	Amph	Amph	Amph	Amph	Amph	Amph	Amph	Amph
Spot No.	1	2	3	4	6	7	1	2	5	5	7
Analysis No.	1a	2b	3	4	7a	8	1a	1b	1b	2	2
SiO_2	42.06	41.37	39.71	41.14	42.33	41.33	42.99	41.60	43.42	42.87	45.55
TiO_2	2.15	2.48	2.53	2.56	2.49	2.51	1.92	2.04	1.45	1.56	1.28
Al_2O_3	14.64	14.64	14.56	14.63	13.05	13.38	15.54	16.25	14.91	16.08	12.45
Cr_2O_3	0.10	0.02	0.11	0.08	0.12	0.07	0.03	0.07	0.04	0.01	0.37
FeO_T	10.16	11.99	12.48	11.88	11.54	11.94	7.22	8.55	5.71	6.07	4.50
MnO	0.13	0.13	0.18	0.10	0.19	0.15	0.08	0.16	0.11	0.09	0.09
NiO	0.03	0.08	0.03	0.00	0.00	0.01	0.11	0.04	0.04	0.03	0.09
MgO	13.83	12.52	12.05	12.54	12.99	12.97	15.57	14.04	16.52	16.25	18.08
CaO	11.52	11.39	11.48	11.40	11.06	11.22	11.25	11.14	11.68	11.56	12.12
Na_2O	3.60	3.64	3.82	3.64	3.90	3.78	2.53	2.66	2.62	2.81	2.48
K_2O	0.56	0.50	0.49	0.52	0.47	0.56	0.68	0.67	0.54	0.64	0.15
P_2O_5	0.08	0.11	0.11	0.10	0.07	0.08	0.12	0.08	0.13	0.12	0.13
Cl	0.04	0.03	0.06	0.05	0.04	0.06	0.04	0.09	0.08	0.09	0.08
Total	98.90	98.91	97.61	98.64	98.25	98.06	98.09	97.40	97.24	98.18	97.37
Mg#	70.8	65.0	63.2	65.3	66.7	65.9	79.3	74.5	83.7	82.7	87.7

Appendix 2.1: Major and minor elements composition of mineral phases from Finero dykes (contd.)

Grouping	Composite HFSE-poor and -rich dyke											
Rock type	Dioritic dyke											
Sample	FI2106	FI2106	FI2106	FI2106	FI2106	FI2106	FI2106	FI2106	FI2106	FI2106	FI2106	FI2106
Thin section	FI2106A	FI2106A	FI2106A	FI2106A	FI2106A	FI2106A	FI2106A	FI2106A	FI2106A	FI2106A	FI2106A	FI2106A
Phase	Amph	Amph	Amph	Amph	Amph	Amph	Amph	Amph	Amph	Amph	Amph	Amph
Spot No.	1	2	2	4	5	9	9	9	10	11	12	12
Analysis No.	1	3	4	9	10	15	16	17	19	21	22	23
SiO_2	41.24	41.42	41.29	41.35	40.97	40.77	41.11	40.70	41.09	40.36	41.10	41.32
TiO_2	2.23	2.20	2.30	2.21	2.24	2.23	2.35	2.17	2.20	2.22	2.17	2.29
Al_2O_3	14.71	14.55	14.73	14.71	14.58	15.07	14.72	14.84	15.19	14.56	14.72	14.69
Cr_2O_3	0.04	0.04	0.01	0.08	0.02	0.15	0.11	0.07	0.02	0.08	0.11	0.05
FeO_T	13.55	13.06	13.02	13.67	13.17	13.77	13.14	13.58	12.86	13.95	13.01	13.41
MnO	0.20	0.19	0.14	0.21	0.23	0.22	0.26	0.22	0.21	0.21	0.17	0.17
NiO	0.00	0.04	0.00	0.00	0.03	0.00	0.00	0.00	0.03	0.03	0.03	0.02
MgO	12.13	12.19	12.22	11.89	12.05	11.75	12.12	12.02	11.98	11.76	12.11	12.35
CaO	10.53	10.86	10.97	10.65	10.62	10.57	10.88	10.50	10.74	10.43	10.87	10.60
Na_2O	3.30	3.39	3.30	3.21	3.31	3.57	3.37	3.41	3.38	3.35	3.34	3.35
K_2O	0.71	0.66	0.54	0.70	0.68	0.72	0.61	0.74	0.53	0.71	0.54	0.61
P_2O_5	0.05	0.13	0.13	0.16	0.11	0.05	0.14	0.10	0.13	0.16	0.11	0.09
Cl	0.10	0.13	0.11	0.08	0.10	0.13	0.11	0.10	0.10	0.12	0.09	0.10
Total	98.79	98.86	98.77	98.92	98.12	99.01	98.92	98.45	98.47	97.94	98.37	99.06
Mg#	61.5	62.4	62.6	60.8	62.0	60.3	62.2	61.2	62.4	60.0	62.4	62.1

Appendix 2.1: Major and minor elements composition of mineral phases from Finero dykes (contd.)

Grouping	Composite HFSE-poor and -rich dyke											
Rock type	Dioritic dyke						Hornblendite dyke with cumulus peridotite					
Sample	FI2106	FI2106	FI2106	FI2106	FI2106	FI2106	FI1607	FI1607	FI1607	FI1607	FI1607	FI1607
Thin section	FI2106A	FI2106A	FI2106A	FI2106A	FI2106A	FI2106A	FI1607A	FI1607A	FI1607A	FI1607A	FI1607A	FI1607A
Phase	Amph	Amph	Amph	Amph	Amph	Amph	Amph	Amph	Amph	Amph	Amph	Amph
Spot No.	12	13	14	15	16	16	1	1	2	3	3	10
Analysis No.	24	26	27	28	29	30	1	2	3	4	5	9
SiO_2	41.18	40.56	41.23	40.59	41.39	41.19	42.75	42.73	42.44	42.51	42.10	42.43
TiO_2	2.31	2.52	2.49	2.49	2.39	2.43	2.50	2.59	2.45	2.33	2.34	2.36
Al_2O_3	15.08	15.04	14.83	15.19	14.98	15.21	13.75	13.75	14.22	13.43	14.28	13.63
Cr_2O_3	0.00	0.00	0.03	0.06	0.12	0.06	0.08	0.04	0.02	0.21	0.24	0.28
FeO_T	13.47	13.69	13.23	13.01	12.48	12.50	11.64	11.46	12.65	12.74	12.73	13.23
MnO	0.23	0.18	0.14	0.17	0.18	0.17	0.11	0.18	0.20	0.25	0.06	0.19
NiO	0.00	0.01	0.00	0.01	0.02	0.03	0.00	0.00	0.00	0.00	0.00	0.00
MgO	11.89	11.57	11.62	11.55	12.31	12.16	12.29	12.43	11.21	11.67	11.31	11.26
CaO	10.63	10.63	10.72	10.97	11.05	11.14	11.31	11.32	11.26	11.35	11.32	11.31
Na_2O	3.29	3.31	3.46	3.16	3.27	3.51	3.05	3.08	3.02	2.92	3.15	2.86
K_2O	0.63	0.68	0.69	0.73	0.69	0.51	0.56	0.48	0.57	0.61	0.49	0.48
P_2O_5	0.10	0.12	0.13	0.10	0.06	0.05						
Cl	0.11	0.04	0.07	0.08	0.06	0.07						
Total	98.92	98.35	98.65	98.10	98.99	99.02	98.04	98.05	98.03	98.02	98.02	98.04
Mg#	61.1	60.1	61.0	61.3	63.7	63.4	65.3	65.9	61.2	62.0	61.3	60.2

Appendix 2.1: Major and minor elements composition of mineral phases from Finero dykes (contd.)

Grouping	Composite HFSE-poor and -rich dyke											
Rock type	Hornblendite dyke with cumulus peridotite											
Sample	FI1607	FI1607	FI1607	FI1607	FI1607	FI1607	FI1607	FI1607	FI1607	FI1607	FI1607	FI1607
Thin section	FI1607A	FI1607A	FI1607A	FI1607A	FI1607A	FI1607B	FI1607B	FI1607B	FI1607B	FI1607B	FI1607B	FI1607B
Phase	Amph	Amph	Amph	Amph	Amph	Amph	Amph	Amph	Amph	Amph	Amph	Amph
Spot No.	10	15	15	16	16	1	2	2	6	6	7	7
Analysis No.	10	14	15	16	17	2	5	6	16	17	19	20
SiO_2	42.27	42.86	41.65	43.18	42.22	42.19	42.40	42.36	42.20	42.30	41.98	42.00
TiO_2	2.21	2.35	2.54	2.15	2.20	2.61	2.26	2.47	2.53	2.53	2.54	2.61
Al_2O_3	13.93	13.78	14.56	12.99	13.78	13.95	13.78	13.63	13.82	13.79	14.03	14.00
Cr_2O_3	0.25	0.08	0.06	0.26	0.13	0.11	0.04	0.04	0.09	0.07	0.10	0.06
FeO_T	13.23	13.25	13.47	13.14	13.33	13.52	13.20	13.24	12.82	13.14	13.37	13.58
MnO	0.26	0.13	0.18	0.21	0.27	0.24	0.20	0.25	0.22	0.20	0.22	0.21
NiO	0.00	0.00	0.00	0.00	0.00	0.00	0.00	0.00	0.00	0.00	0.00	0.00
MgO	11.29	11.18	10.82	11.40	11.20	10.98	11.49	11.00	11.40	11.06	10.69	10.84
CaO	11.42	11.39	11.54	11.35	11.33	11.44	11.66	11.98	11.93	11.80	11.67	11.58
Na_2O	2.69	2.54	2.68	2.81	2.96	2.57	2.44	2.47	2.55	2.66	2.91	2.69
K_2O	0.47	0.49	0.59	0.49	0.58	0.50	0.56	0.61	0.52	0.51	0.54	0.50
P_2O_5												
Cl												
Total	98.02	98.04	98.08	97.98	97.99	98.09	98.03	98.04	98.06	98.05	98.04	98.07
Mg#	60.3	60.0	58.9	60.7	59.9	59.1	60.8	59.7	61.3	60.0	58.7	58.7

Appendix 2.1: Major and minor elements composition of mineral phases from Finero dykes (contd.)

Grouping	Composite HFSE-poor and -rich dyke											
Rock type	Hornblendite dyke with cumulus peridotite											
Sample	FI1607	FI1607	FI1607	FI1607	FI1607	FI1607	FI1607	FI1607	FI1607	FI1607	FI1607	FI1607
Thin section	FI1607B	FI1607B	FI1607B	FI1607B	FI1607C	FI1607C	FI1607C	FI1607C	FI1607C	FI1607C	FI1607C	FI1607C
Phase	Amph	Amph	Amph	Amph	Amph	Amph	Amph	Amph	Amph	Amph	Amph	Amph
Spot No.	9	9	15	15	1	1	2	2	4	4	5	5
Analysis No.	21	22	23	24	1	2	3	4	7	9	10	11
SiO_2	41.88	42.69	41.89	42.09	42.17	43.17	41.81	42.60	42.55	42.31	42.44	42.84
TiO_2	2.53	2.43	2.72	2.55	2.49	2.52	2.60	2.35	2.61	2.51	2.73	2.45
Al_2O_3	14.47	13.62	14.03	13.35	13.86	13.10	14.20	14.06	14.13	14.26	14.11	14.11
Cr_2O_3	0.05	0.02	0.06	0.00	0.01	0.00	0.01	0.00	0.05	0.09	0.05	0.04
FeO_T	13.53	13.30	13.19	13.51	12.70	12.19	13.09	12.08	11.56	11.93	10.43	10.44
MnO	0.18	0.20	0.23	0.41	0.30	0.23	0.19	0.11	0.27	0.19	0.20	0.13
NiO	0.00	0.00	0.00	0.00	0.00	0.00	0.00	0.00	0.00	0.00	0.00	0.00
MgO	10.64	10.98	11.00	11.22	11.56	11.99	11.19	12.09	12.13	11.99	13.11	13.05
CaO	11.60	11.57	11.64	11.32	11.25	11.13	11.27	11.20	10.83	11.09	11.51	11.21
Na_2O	2.60	2.75	2.86	3.00	3.06	3.17	3.07	3.10	3.29	3.08	3.08	3.27
K_2O	0.60	0.46	0.46	0.58	0.64	0.51	0.65	0.42	0.65	0.62	0.44	0.48
P_2O_5												
Cl												
Total	98.08	98.02	98.08	98.03	98.03	98.01	98.05	98.01	98.07	98.06	98.09	98.03
Mg#	58.3	59.5	59.8	59.7	61.9	63.7	60.3	64.1	65.1	64.2	69.1	69.0

Appendix 2.1: Major and minor elements composition of mineral phases from Finero dykes (contd.)

Grouping	Composite HFSE-poor and -rich dyke			
Rock type	Hornblendite dyke with cumulus peridotite			
Sample	FI1607	FI1607	FI1607	FI1607
Thin section	FI1607C	FI1607C	FI1607C	FI1607C
Phase	Amph	Amph	Amph	Amph
Spot No.	6	6	10	10
Analysis No.	12	13	14	15
SiO_2	42.77	43.28	42.96	43.50
TiO_2	2.60	2.48	2.22	2.12
Al_2O_3	14.27	13.69	13.97	13.61
Cr_2O_3	0.09	0.00	0.05	0.17
FeO_T	10.80	10.93	9.59	9.33
MnO	0.07	0.16	0.14	0.23
NiO	0.00	0.00	0.00	0.00
MgO	12.56	12.47	14.03	14.11
CaO	11.19	11.08	11.49	11.33
Na_2O	3.08	3.42	3.03	3.06
K_2O	0.65	0.50	0.53	0.54
P_2O_5				
Cl				
Total	98.08	98.00	98.01	97.99
Mg#	67.4	67.0	72.3	72.9

Appendix 2.1: Major and minor elements composition of mineral phases from Finero dykes (contd.)

Grouping	HFSE-rich dyke											
Rock type	Dioritic dyke											
Sample	FI1603	FI1603	FI1603	FI1603	FI1603	FI1603	FI1603	FI1603	FI1603	FI1603	FI1603	FI1603
Thin section	FI1603A	FI1603A	FI1603A	FI1603A	FI1603A	FI1603A	FI1603A	FI1603A	FI1603A	FI1603A	FI1603A	FI1603A
Phase	Phl	Phl	Phl	Phl	Phl	Phl	Phl	Phl	Phl	Phl	Phl	Phl
Spot No.	3	3	4	4	5	5	7	7	8	8	8	14
Analysis No.	10	11	12	13	14	15	37	38	39	40	41	61
SiO_2	40.44	40.21	40.18	39.61	39.76	40.42	39.64	40.35	40.82	39.09	39.09	39.83
TiO_2	1.10	1.15	1.09	1.24	1.09	1.01	1.26	1.15	1.18	1.12	1.51	1.18
Al_2O_3	15.03	14.45	14.62	14.68	14.95	14.74	15.29	15.47	14.67	15.13	14.85	15.00
Cr_2O_3	0.00	0.00	0.00	0.00	0.00	0.00	0.00	0.00	0.00	0.00	0.00	0.00
FeO_T	6.40	6.63	6.65	6.47	6.21	6.44	5.90	6.02	6.12	7.04	6.47	6.69
MnO	0.00	0.00	0.00	0.00	0.00	0.00	0.00	0.00	0.00	0.00	0.00	0.00
NiO	0.00	0.00	0.00	0.00	0.00	0.00	0.00	0.00	0.00	0.00	0.00	0.00
MgO	22.86	23.10	23.30	22.95	23.36	22.89	24.07	24.60	23.23	23.01	23.93	23.05
CaO	0.00	0.00	0.00	0.00	0.00	0.00	0.00	0.00	0.00	0.00	0.00	0.00
Na_2O	1.58	1.40	1.16	0.99	1.60	1.83	1.86	3.46	1.84	0.95	0.00	0.85
K_2O	9.45	9.37	9.61	9.82	8.83	8.96	8.21	5.87	9.14	9.43	10.69	10.07
P_2O_5												
Cl												
Total	96.86	96.31	96.61	95.76	95.79	96.29	96.24	96.92	97.00	95.78	96.54	96.67
Mg#	86.4	86.1	86.2	86.3	87.0	86.4	87.9	87.9	87.1	85.3	86.8	86.0

Appendix 2.1: Major and minor elements composition of mineral phases from Finero dykes (contd.)

Grouping	HFSE-rich dyke											
Rock type	Dioritic dyke											
Sample	FI1603	FI1603	FI1603	FI1603	FI1603	FI1603	FI1603	FI1603	FI1603	FI1603	FI1603	FI1603
Thin section	FI1603B	FI1603B	FI1603B	FI1603B	FI1603B	FI1603B	FI1603B	FI1603B	FI1603B	FI1603C	FI1603C	FI1603C
Phase	Phl	Phl	Phl	Phl	Phl	Phl	Phl	Phl	Phl	Phl	Phl	Phl
Spot No.	4	5	5	5	12	12	9	3	3	6	16	16
Analysis No.	14	15	16	18	37	38	32	7	8	18	41	42
SiO_2	39.52	39.71	39.76	38.61	39.33	39.35	39.14	40.07	39.49	38.94	39.23	39.22
TiO_2	1.19	1.77	1.60	1.27	2.09	1.97	1.58	1.48	1.58	1.74	2.06	2.36
Al_2O_3	14.57	14.45	13.95	14.71	14.56	14.00	14.31	13.20	13.86	14.06	14.15	14.38
Cr_2O_3	0.00	0.00	0.00	0.00	0.00	0.00	0.00	0.00	0.00	0.00	0.00	0.00
FeO_T	9.89	7.10	7.02	10.11	7.15	7.55	8.72	8.48	8.58	8.63	7.47	7.42
MnO	0.00	0.00	0.00	0.00	0.00	0.00	0.00	0.00	0.00	0.00	0.00	0.00
NiO	0.00	0.00	0.00	0.00	0.00	0.00	0.00	0.00	0.00	0.00	0.00	0.00
MgO	21.10	22.21	22.35	20.85	22.61	22.83	21.38	21.59	21.28	21.26	21.91	21.78
CaO	0.00	0.00	0.00	0.00	0.00	0.00	0.00	0.00	0.00	0.00	0.00	0.00
Na_2O	0.98	1.08	0.93	1.15	0.97	0.85	1.52	0.81	0.88	0.91	1.08	0.89
K_2O	9.71	10.13	10.22	9.07	10.02	9.87	9.02	10.39	10.21	9.96	9.98	10.50
P_2O_5												
Cl												
Total	96.96	96.46	95.83	95.78	96.74	96.43	95.67	96.02	95.87	95.50	95.89	96.55
Mg#	79.2	84.8	85.0	78.6	84.9	84.3	81.4	81.9	81.5	81.4	83.9	83.9

Appendix 2.1: Major and minor elements composition of mineral phases from Finero dykes (contd.)

Grouping	HFSE-rich dyke										
Rock type	Dioritic dyke										
Sample	FI1603	FI1603	FI1603	FI1603	FI1603	FI1603	FI1604	FI1604	FI1604	FI1604	FI1604
Thin section	FI1603C	FI1603C	FI1603C	FI1603C	FI1603C	FI1603C	FI1604C	FI1604C	FI1604C	FI1604C	FI1604C
Phase	Phl	Phl	Phl	Phl	Phl	Phl	Phl	Phl	Phl	Phl	Phl
Spot No.	17	17	19	19	20	20	9	11	13	14	15
Analysis No.	43	44	45	46	47	16	3	3	1	2	2
SiO_2	39.53	39.64	39.50	39.32	39.91	39.88	39.87	40.24	39.37	39.19	39.65
TiO_2	2.06	1.91	1.85	1.95	1.73	1.53	0.80	0.72	1.13	0.97	1.01
Al_2O_3	14.61	14.27	14.63	14.53	14.50	14.25	14.42	14.42	14.67	14.74	14.62
Cr_2O_3	0.00	0.00	0.00	0.00	0.00	0.00	0.05	0.04	0.00	0.07	0.03
FeO_T	7.47	7.88	7.36	7.44	7.16	7.20	7.05	7.07	7.32	7.07	7.13
MnO	0.00	0.00	0.00	0.00	0.00	0.00	0.05	0.05	0.01	0.02	0.01
NiO	0.00	0.00	0.00	0.00	0.00	0.00	0.23	0.17	0.14	0.13	0.15
MgO	21.93	21.84	22.35	22.34	22.23	22.56	22.46	22.16	22.24	22.20	22.33
CaO	0.00	0.00	0.00	0.00	0.00	0.00	0.00	0.00	0.00	0.03	0.03
Na_2O	1.17	1.11	1.05	1.15	1.21	1.12	0.96	0.98	1.09	1.11	1.15
K_2O	10.08	10.06	9.99	9.74	10.02	9.85	9.08	8.74	8.82	8.72	8.64
P_2O_5							0.00	0.02	0.00	0.05	0.00
Cl							0.07	0.09	0.08	0.10	0.09
Total	96.85	96.71	96.73	96.47	96.75	96.39	95.05	94.71	94.87	94.41	94.85
Mg#	83.9	83.2	84.4	84.2	84.7	84.8	85.0	84.8	84.4	84.8	84.8

Appendix 2.1: Major and minor elements composition of mineral phases from Finero dykes (contd.)

Grouping	HFSE-rich dyke										
Rock type	Dioritic dyke										
Sample	FI1604	FI1604	FI1604	FI1604	FI1604	FI1604	FI1604	FI1605	FI1605	FI1605	FI1605
Thin section	FI1604C	FI1604C	FI1604C	FI1604C	FI1604C	FI1604C	FI1604C	FI1605A	FI1605A	FI1605A	FI1605A
Phase	Phl	Phl	Phl	Phl	Phl	Phl	Phl	Phl	Phl	Phl	Phl
Spot No.	15	16	17	17	17	18	19	1	1	2	9
Analysis No.	3	2	1	2	3	3	2	3	4	9	19
SiO_2	39.57	39.58	39.32	40.18	39.72	39.92	39.60	40.09	40.16	39.49	40.08
TiO_2	1.00	0.73	1.05	0.82	1.06	0.83	1.00	1.36	1.19	1.16	1.21
Al_2O_3	14.51	14.58	14.72	14.40	14.81	14.39	14.34	14.73	13.91	14.66	14.84
Cr_2O_3	0.06	0.04	0.06	0.06	0.05	0.01	0.00	0.00	0.00	0.00	0.00
FeO_T	7.33	7.08	7.23	7.10	7.28	7.37	6.79	6.99	6.87	6.89	6.52
MnO	0.07	0.07	0.09	0.04	0.02	0.02	0.05	0.00	0.00	0.00	0.00
NiO	0.24	0.15	0.19	0.16	0.21	0.16	0.20	0.00	0.00	0.00	0.00
MgO	22.55	22.78	22.33	22.38	22.55	22.32	22.25	22.79	22.48	22.81	22.66
CaO	0.00	0.01	0.00	0.00	0.02	0.01	0.02	0.00	0.00	0.00	0.00
Na_2O	1.08	1.20	1.11	1.06	1.14	1.20	1.05	1.22	1.14	0.96	1.14
K_2O	8.67	8.72	8.58	8.55	8.65	8.81	8.68	9.74	9.92	9.73	10.01
P_2O_5	0.02	0.01	0.03	0.08	0.01	0.05	0.08				
Cl	0.13	0.13	0.10	0.08	0.11	0.11	0.10				
Total	95.23	95.08	94.81	94.91	95.63	95.21	94.15	96.92	95.68	95.70	96.45
Mg#	84.6	85.1	84.6	84.9	84.7	84.4	85.4	85.3	85.3	85.5	86.1

Appendix 2.1: Major and minor elements composition of mineral phases from Finero dykes (contd.)

Grouping	HFSE-rich dyke										
Rock type	Dioritic dyke										
Sample	FI1605	FI1605	FI1605	FI1605	FI1605	FI1605	FI1605	FI1605	FI1605	FI1605	FI1605
Thin section	FI1605A	FI1605A2	FI1605A2	FI1605A2	FI1605A2	FI1605A2	FI1605A2	FI1605A2	FI1605A2	FI1605A2	FI1605A2
Phase	Phl	Phl	Phl	Phl	Phl	Phl	Phl	Phl	Phl	Phl	Phl
Spot No.	9	1	2	3	4	5	7	9	10	11	12
Analysis No.	20	2	3	3	2	2	2	3	1	2	1
SiO_2	40.29	39.73	40.04	39.53	38.99	39.56	39.25	39.53	39.79	39.14	39.48
TiO_2	1.11	1.31	1.16	1.10	1.43	1.32	1.04	1.53	1.53	1.28	1.16
Al_2O_3	14.29	14.72	14.37	14.66	14.77	14.94	15.10	14.92	14.44	14.88	14.75
Cr_2O_3	0.00	0.11	0.07	0.04	0.00	0.00	0.00	0.00	0.07	0.06	0.12
FeO_T	6.68	6.99	6.63	6.53	6.71	6.57	6.81	6.84	6.67	6.73	6.80
MnO	0.00	0.05	0.05	0.01	0.04	0.05	0.06	0.02	0.00	0.02	0.04
NiO	0.00	0.09	0.14	0.13	0.17	0.12	0.08	0.16	0.18	0.17	0.21
MgO	22.70	22.58	22.51	23.12	22.58	22.58	22.17	21.97	22.56	22.81	22.74
CaO	0.00	0.01	0.00	0.00	0.01	0.04	0.00	0.00	0.03	0.00	0.00
Na_2O	1.35	1.21	1.16	1.06	1.27	1.12	1.11	1.01	1.17	1.02	1.18
K_2O	9.63	8.59	8.71	8.74	8.55	8.69	8.73	8.82	8.52	8.74	8.68
P_2O_5		0.03	0.00	0.00	0.00	0.03	0.05	0.00	0.04	0.00	0.00
Cl		0.06	0.08	0.07	0.10	0.11	0.09	0.10	0.12	0.10	0.08
Total	96.05	95.47	94.92	94.98	94.61	95.15	94.49	94.91	95.12	94.93	95.24
Mg#	85.8	85.2	85.8	86.3	85.7	86.0	85.3	85.1	85.8	85.8	85.6

Appendix 2.1: Major and minor elements composition of mineral phases from Finero dykes (contd.)

Grouping	HFSE-rich dyke										
Rock type	Dioritic dyke										
Sample	FI2102	FI2102	FI2102	FI2102	FI2102	FI2102	FI2102	FI2102	FI2102	FI2103	FI2103
Thin section	FI2102C	FI2102C	FI2102C	FI2102C	FI2102C	FI2102C	FI2102C	FI2102C	FI2102C	FI2103C	FI2103C
Phase	Phl	Phl	Phl	Phl	Phl	Phl	Phl	Phl	Phl	Phl	Phl
Spot No.	2	3	3	4	5	6	7	8	9	1	2
Analysis No.	3	6	7	9	12	15	18	20b	22a	2	1
SiO_2	40.59	39.80	40.76	40.25	40.20	38.89	39.26	40.33	40.13	39.91	40.06
TiO_2	0.25	0.79	0.45	0.37	0.30	0.45	0.81	0.87	1.00	0.89	0.97
Al_2O_3	15.02	14.99	15.21	15.22	15.02	15.06	15.16	15.08	15.21	14.26	14.40
Cr_2O_3	0.00	0.09	0.02	0.04	0.02	0.01	0.08	0.12	0.06	0.01	0.00
FeO_T	5.42	5.77	5.71	5.79	5.67	5.59	6.21	6.21	6.11	6.37	6.11
MnO	0.00	0.00	0.04	0.07	0.00	0.05	0.03	0.04	0.07	0.04	0.09
NiO	0.08	0.11	0.17	0.13	0.08	0.10	0.10	0.13	0.16	0.14	0.17
MgO	23.63	23.26	23.82	23.69	23.48	23.29	23.11	22.98	22.89	22.89	23.15
CaO	0.01	0.02	0.01	0.02	0.00	0.01	0.02	0.01	0.00	0.02	0.00
Na_2O	1.45	1.30	1.37	1.37	1.36	1.39	1.16	1.21	1.39	0.98	1.27
K_2O	8.83	8.82	8.81	8.78	8.76	8.69	8.85	8.98	8.78	8.79	8.48
P_2O_5	0.04	0.03	0.03	0.02	0.04	0.01	0.02	0.00	0.01	0.05	0.00
Cl	0.09	0.07	0.12	0.06	0.05	0.04	0.05	0.04	0.04	0.07	0.06
Total	95.41	95.06	96.52	95.81	94.99	93.58	94.86	95.99	95.85	94.41	94.76
Mg#	88.6	87.8	88.1	87.9	88.1	88.1	86.9	86.8	87.0	86.5	87.1

Appendix 2.1: Major and minor elements composition of mineral phases from Finero dykes (contd.)

Grouping	HFSE-rich dyke										
Rock type	Dioritic dyke										
Sample	FI2103	FI2103	FI2103	FI2103	FI2103	FI2103	FI2104	FI2104	FI2104	FI2104	FI2104
Thin section	FI2103C	FI2103C	FI2103C	FI2103C	FI2103C	FI2103C	FI2104B	FI2104B	FI2104B	FI2104B	FI2104B
Phase	Phl	Phl	Phl	Phl	Phl	Phl	Phl	Phl	Phl	Phl	Phl
Spot No.	2	3	6	7	9	11	3	4	5	6	7
Analysis No.	2	1	4	2	2	2	4	6	9	12	13
SiO_2	39.92	40.24	40.30	40.52	40.81	40.55	38.58	40.04	39.51	39.74	40.15
TiO_2	0.97	0.98	0.95	0.84	0.74	0.83	3.11	0.96	1.01	0.92	0.93
Al_2O_3	14.18	14.22	14.31	14.08	14.42	14.30	14.18	14.50	14.80	15.05	14.88
Cr_2O_3	0.05	0.00	0.00	0.03	0.12	0.12	0.04	0.00	0.01	0.00	0.04
FeO_T	6.28	5.97	5.67	6.38	6.35	6.05	7.85	6.28	5.81	6.09	6.36
MnO	0.04	0.07	0.00	0.00	0.03	0.02	0.04	0.02	0.07	0.05	0.03
NiO	0.14	0.07	0.16	0.13	0.05	0.12	0.02	0.06	0.12	0.09	0.14
MgO	22.82	23.00	23.02	23.18	23.14	23.39	19.95	22.54	22.89	22.64	22.93
CaO	0.00	0.00	0.00	0.00	0.00	0.00	0.01	0.01	0.00	0.00	0.01
Na_2O	1.24	1.00	1.18	1.15	1.20	1.17	0.09	1.25	1.23	1.20	1.24
K_2O	8.44	8.63	8.56	8.64	8.45	8.64	10.50	9.00	9.11	9.26	9.05
P_2O_5	0.01	0.01	0.00	0.00	0.00	0.00	0.00	0.00	0.00	0.00	0.00
Cl	0.08	0.09	0.10	0.04	0.08	0.10	0.09	0.08	0.06	0.08	0.08
Total	94.16	94.27	94.25	94.98	95.40	95.27	94.46	94.74	94.61	95.12	95.85
Mg#	86.6	87.3	87.8	86.6	86.6	87.3	81.9	86.5	87.5	86.9	86.5

Appendix 2.1: Major and minor elements composition of mineral phases from Finero dykes (contd.)

Grouping	HFSE-rich dyke											
Rock type	Dioritic dyke											
Sample	FI2104	FI2104	FI2104	FI2104	FI2104	FI2104	FI2104	FI2104	FI2104	FI2104	FI2104	FI2104
Thin section	FI2104B	FI2104B	FI2104B	FI2104B	FI2104B	FI2104B	FI2104B	FI2104B	FI2104C	FI2104C	FI2104C	FI2104C
Phase	Phl	Phl	Phl	Phl	Phl	Phl	Phl	Phl	Phl	Phl	Phl	Phl
Spot No.	7	8	9	9	9	10	14	15	6	10	10	12
Analysis No.	14	18	19	20	21a	23b	32	34	1	1	2	2
SiO_2	39.52	39.96	40.21	40.01	40.51	39.73	39.62	40.33	40.34	39.59	39.92	39.93
TiO_2	0.87	0.87	0.92	0.92	0.89	0.85	0.80	0.87	1.18	1.32	1.18	1.19
Al_2O_3	15.07	15.22	15.20	15.05	15.02	14.87	14.87	14.73	14.57	13.76	14.22	13.76
Cr_2O_3	0.01	0.07	0.08	0.00	0.08	0.03	0.07	0.20	0.00	0.02	0.01	0.05
FeO_T	5.95	6.40	6.37	6.25	6.28	6.33	6.51	6.28	7.11	7.04	7.42	7.22
MnO	0.01	0.05	0.06	0.03	0.05	0.06	0.01	0.01	0.00	0.04	0.06	0.05
NiO	0.07	0.09	0.06	0.07	0.09	0.17	0.11	0.22	0.09	0.10	0.11	0.12
MgO	22.51	22.71	22.76	22.72	22.74	22.82	22.81	22.49	22.25	22.23	22.36	22.44
CaO	0.00	0.01	0.00	0.00	0.02	0.01	0.00	0.05	0.00	0.00	0.00	0.00
Na_2O	1.40	1.28	1.19	1.12	1.24	1.17	1.01	1.00	0.85	0.85	0.92	0.84
K_2O	8.99	8.96	9.05	9.02	8.96	8.97	9.16	8.92	8.89	8.73	8.97	9.15
P_2O_5	0.01	0.03	0.00	0.04	0.00	0.00	0.01	0.02	0.00	0.02	0.01	0.01
Cl	0.08	0.08	0.06	0.05	0.08	0.09	0.07	0.02	0.06	0.02	0.05	0.03
Total	94.49	95.74	95.96	95.29	95.96	95.11	95.06	95.13	95.34	93.74	95.23	94.79
Mg#	87.1	86.3	86.4	86.6	86.6	86.5	86.2	86.4	84.8	84.9	84.3	84.7

Appendix 2.1: Major and minor elements composition of mineral phases from Finero dykes (contd.)

Grouping	HFSE-rich dyke										
Rock type	Clinopyroxenite cumulate in HFSE-rich dioritic dyke										
Sample	FI1604	FI1604	FI1604	FI1604	FI2105	FI2105	FI2105	FI2105	FI2105	FI2105	FI2105
Thin section	FI1604C*	FI1604C*	FI1604C*	FI1604C*	FI2105B*	FI2105B*	FI2105B*	FI2105B*	FI2105B*	FI2105B*	FI2105B*
Phase	Phl	Phl	Phl	Phl	Phl	Phl	Phl	Phl	Phl	Phl	Phl
Spot No.	1	2	8	10	1	3	5	7	10	16	18
Analysis No.	2	2	2	3	1	5	15	18	24	31	34
SiO_2	39.63	39.93	40.18	40.10	40.15	40.47	41.59	40.35	40.92	39.84	40.04
TiO_2	0.85	0.74	0.94	1.00	1.12	1.15	1.17	1.17	1.84	1.91	1.86
Al_2O_3	14.59	14.63	13.92	13.98	14.52	14.36	15.05	15.11	15.32	15.26	15.14
Cr_2O_3	0.02	0.07	0.13	0.20	0.66	0.46	0.42	0.25	0.05	0.11	0.05
FeO_T	6.98	6.98	6.76	7.05	5.79	5.96	5.76	6.22	5.21	6.21	5.53
MnO	0.00	0.09	0.02	0.00	0.03	0.02	0.00	0.01	0.00	0.06	0.00
NiO	0.19	0.13	0.17	0.24	0.20	0.21	0.23	0.20	0.03	0.10	0.12
MgO	22.30	22.30	22.16	22.32	22.65	22.91	22.92	22.34	22.76	21.81	22.46
CaO	0.01	0.00	0.00	0.00	0.03	0.02	0.00	0.01	0.02	0.04	0.00
Na_2O	1.13	1.03	0.88	1.04	1.12	1.06	1.27	1.02	1.22	1.04	1.06
K_2O	8.82	8.89	9.09	8.81	8.97	9.02	8.92	9.24	8.79	9.08	9.09
P_2O_5	0.06	0.00	0.00	0.02	0.02	0.04	0.00	0.01	0.03	0.02	0.02
Cl	0.09	0.10	0.10	0.11	0.03	0.05	0.03	0.08	0.05	0.05	0.06
Total	94.67	94.89	94.34	94.88	95.30	95.73	97.36	96.01	96.25	95.54	95.44
Mg#	85.1	85.1	85.4	84.9	87.4	87.3	87.6	86.5	88.6	86.2	87.9

Appendix 2.1: Major and minor elements composition of mineral phases from Finero dykes (contd.)

Grouping	HFSE-rich dyke										
Rock type	Hornblendite dyke with olivine layer			Hornblendite dyke							
Sample	FI1501	FI1501	FI1501	FI1612	FI1612	FI1612	FI1612	FI1612	FI1612	FI1612	FI1612
Thin section	FI1501B	FI1501B	FI1501B	FI1612A	FI1612A	FI1612A	FI1612A	FI1612A	FI1612A	FI1612A	FI1612A
Phase	Phl	Phl	Phl	Phl	Phl	Phl	Phl	Phl	Phl	Phl	Phl
Spot No.	2	6	7	1	2	3	4	5	6	7	9
Analysis No.	3	12	15b	3	4	2	3	2	2	1	2
SiO_2	39.18	39.11	38.77	38.43	38.56	38.41	37.95	38.23	38.56	38.86	37.88
TiO_2	2.14	2.79	2.76	2.88	2.87	2.44	2.51	2.72	3.01	2.61	2.90
Al_2O_3	15.51	16.08	15.88	15.63	15.34	14.58	15.29	15.49	15.44	15.37	15.94
Cr_2O_3	0.44	0.04	0.05	0.09	0.06	0.04	0.04	0.03	0.03	0.02	0.09
FeO_T	5.43	5.45	5.35	7.81	8.18	9.54	8.14	7.69	8.40	7.89	8.38
MnO	0.03	0.04	0.08	0.03	0.05	0.02	0.06	0.03	0.09	0.01	0.06
NiO	0.14	0.02	0.11	0.06	0.03	0.10	0.04	0.02	0.02	0.09	0.00
MgO	22.73	21.86	21.47	20.49	20.48	20.35	20.91	20.89	20.16	20.95	20.12
CaO	0.03	0.01	0.02	0.02	0.01	0.06	0.02	0.00	0.07	0.00	0.01
Na_2O	1.55	1.89	1.86	1.25	1.14	1.38	1.45	1.21	1.47	1.32	1.35
K_2O	8.65	8.03	8.29	8.27	8.39	8.37	8.29	8.54	7.95	8.50	8.33
P_2O_5	0.00	0.03	0.00	0.02	0.02	0.03	0.05	0.04	0.00	0.04	0.00
Cl	0.06	0.05	0.01	0.04	0.05	0.07	0.07	0.04	0.08	0.09	0.06
Total	95.88	95.40	94.65	95.03	95.18	95.39	94.81	94.92	95.28	95.75	95.12
Mg#	88.2	87.7	87.7	82.4	81.7	79.2	82.1	82.9	81.0	82.5	81.0

Appendix 2.1: Major and minor elements composition of mineral phases from Finero dykes (contd.)

Grouping	HFSE-rich dyke										
Rock type	Albite-dominated anorthosite dyke										
Sample	FI19A02	FI19A02	FI19A02	FI19A02	FI19A02	FI19A02	FI19A02	FI19A02	FI19A02	FI19A02	FI19A02
Thin section	FI19A02B	FI19A02B	FI19A02B	FI19A02B	FI19A02B	FI19A02B	FI19A02B	FI19A02B	FI19A02B	FI19A02B	FI19A02B
Phase	Phl	Phl	Phl	Phl	Phl	Phl	Phl	Phl	Phl	Phl	Phl
Spot No.	1	1	2	2	2	7	7	7	8	8	9
Analysis No.	1	2	4	5	6	14	15	16	18	19	23
SiO_2	35.70	37.26	36.80	35.54	36.88	36.21	36.23	35.24	36.31	35.41	38.14
TiO_2	2.44	2.47	2.61	2.22	2.30	2.36	2.38	2.46	2.89	2.35	2.29
Al_2O_3	14.61	15.15	15.08	14.56	15.25	15.30	15.54	14.78	15.30	14.86	16.16
Cr_2O_3	0.00	0.00	0.01	0.04	0.00	0.04	0.01	0.06	0.06	0.05	0.04
FeO_T	10.06	10.47	10.83	9.61	10.81	10.83	10.73	10.48	10.92	10.23	10.94
MnO	0.02	0.08	0.09	0.13	0.11	0.05	0.14	0.08	0.09	0.12	0.12
NiO	0.10	0.08	0.05	0.09	0.13	0.05	0.04	0.10	0.09	0.08	0.09
MgO	21.39	21.26	21.82	22.36	19.59	21.36	21.24	20.61	20.19	22.09	20.46
CaO	0.05	0.06	0.18	0.12	0.11	0.04	0.06	0.15	0.08	0.09	0.14
Na_2O	0.03	0.29	0.00	0.08	0.26	0.24	0.25	0.08	0.51	0.23	0.40
K_2O	0.03	3.78	0.11	0.05	4.32	3.35	3.06	0.18	4.45	0.02	3.96
P_2O_5	0.00	0.00	0.01	0.00	0.00	0.06	0.01	0.01	0.04	0.02	0.02
Cl	0.04	0.04	0.05	0.04	0.03	0.04	0.02	0.04	0.06	0.03	0.03
Total	84.48	90.96	87.64	84.84	89.79	89.94	89.72	84.28	90.98	85.58	92.78
Mg#	79.1	78.3	78.2	80.6	76.3	77.8	77.9	77.8	76.7	79.4	76.9

Appendix 2.1: Major and minor elements composition of mineral phases from Finero dykes (contd.)

Grouping	HFSE-rich dyke									
Rock type	Albite-dominated anorthosite dyke									
Sample	FI19A04	FI19A04	FI19A04	FI19A04	FI19A04	FI19A04	FI19A04	FI19A04	FI19A04	FI19A04
Thin section	FI19A04A	FI19A04A	FI19A04A	FI19A04A	FI19A04A	FI19A04A	FI19A04A	FI19A04B	FI19A04B	FI19A04B
Phase	Phl	Phl	Phl	Phl	Phl	Phl	Phl	Phl	Phl	Phl
Spot No.	1	2	2	2	3	4	6	1	3	4
Analysis No.	3	6	9	10	11	12	19	2	4	7
SiO_2	39.25	36.76	38.86	37.82	37.76	37.81	37.95	39.25	38.52	37.08
TiO_2	1.75	1.78	1.83	1.81	1.70	1.87	2.00	1.95	2.01	1.89
Al_2O_3	14.77	14.28	14.89	14.58	14.93	14.70	14.78	14.99	14.55	14.49
Cr_2O_3	0.02	0.00	0.02	0.00	0.07	0.04	0.01	0.04	0.02	0.00
FeO_T	10.49	9.76	10.25	10.14	8.98	9.39	9.90	10.15	9.35	9.18
MnO	0.04	0.10	0.10	0.06	0.05	0.06	0.08	0.12	0.05	0.07
NiO	0.10	0.05	0.10	0.09	0.11	0.14	0.02	0.13	0.10	0.08
MgO	23.02	22.05	23.23	24.34	21.95	23.50	23.53	21.31	20.20	20.20
CaO	0.16	0.05	0.17	0.25	0.03	0.08	0.19	0.19	0.02	0.04
Na_2O	0.10	0.00	0.03	0.04	0.00	0.04	0.02	0.02	0.01	0.03
K_2O	0.35	0.13	0.07	0.14	0.03	0.07	0.13	0.10	0.02	0.21
P_2O_5	0.02	0.03	0.00	0.03	0.00	0.00	0.02	0.00	0.00	0.00
Cl	0.08	0.08	0.05	0.05	0.07	0.08	0.04	0.06	0.09	0.03
Total	90.15	85.06	89.61	89.36	85.67	87.77	88.67	88.31	84.95	83.31
Mg#	79.6	80.1	80.1	81.0	81.3	81.7	80.9	78.9	79.4	79.7

Appendix 2.1: Major and minor elements composition of mineral phases from Finero dykes (contd.)

Grouping	Composite HFSE-poor and -rich dyke											
Rock type	Dioritic dyke		Hornblendite dyke with cumulus peridotite									
Sample	FI2106	FI2106	FI1607	FI1607	FI1607	FI1607	FI1607	FI1607	FI1607	FI1607	FI1607	FI1607
Thin section	FI2106A	FI2106A	FI1607C	FI1607C	FI1607C	FI1607C	FI1607C	FI1607C	FI1607C	FI1607C	FI1607C	FI1607C
Phase	Phl	Phl	Phl	Phl	Phl	Phl	Phl	Phl	Phl	Phl	Phl	Phl
Spot No.	2	5	11	11	11	13	13	14	14	15	15	16
Analysis No.	6	11	17	18	19	20	21	22	23	24	25	29
SiO_2	37.55	36.60	36.64	36.70	36.64	35.70	35.42	35.73	36.49	39.11	39.14	38.42
TiO_2	4.36	3.49	3.41	3.56	3.55	4.36	3.93	3.89	3.48	2.28	2.40	3.25
Al_2O_3	17.26	16.80	16.35	16.11	16.21	16.61	17.10	17.34	16.82	15.01	14.96	15.63
Cr_2O_3	0.00	0.00	0.00	0.00	0.00	0.00	0.00	0.00	0.00	0.37	0.38	0.39
FeO_T	11.80	11.41	8.60	8.76	9.02	9.81	9.21	9.28	9.42	6.21	6.11	5.81
MnO	0.06	0.04	0.00	0.00	0.00	0.00	0.00	0.00	0.00	0.00	0.00	0.00
NiO	0.04	0.00	0.00	0.00	0.00	0.00	0.00	0.00	0.00	0.00	0.00	0.00
MgO	16.27	17.37	20.40	20.29	20.25	19.75	19.84	19.95	19.65	22.95	23.40	23.57
CaO	0.06	0.01	0.00	0.00	0.00	0.00	0.00	0.00	0.00	0.00	0.00	0.00
Na_2O	1.16	1.31	1.58	1.60	1.60	1.47	1.76	2.44	1.58	1.79	1.91	3.26
K_2O	8.81	8.76	9.07	9.13	9.05	9.14	8.56	7.64	9.23	8.93	8.59	6.60
P_2O_5	0.04	0.00										
Cl	0.08	0.09										
Total	97.47	95.88	96.06	96.14	96.33	96.85	95.81	96.25	96.68	96.65	96.89	96.93
Mg#	71.1	73.1	80.8	80.5	80.0	78.2	79.3	79.3	78.8	86.8	87.2	87.8

Appendix 2.1: Major and minor elements composition of mineral phases from Finero dykes (contd.)

Grouping	HFSE-rich dyke										
Rock type	Clinopyroxenite cumulate in dioritic dyke										
Sample	FI1604	FI1604	FI1604	FI1604	FI1604	FI2105	FI2105	FI2105	FI2105	FI2105	FI2105
Thin section	FI1604C*	FI1604C*	FI1604C*	FI1604C*	FI1604C*	FI2105B*	FI2105B*	FI2105B*	FI2105B*	FI2105B*	FI2105B*
Phase	Cpx	Cpx	Cpx	Cpx	Cpx	Cpx	Cpx	Cpx	Cpx	Cpx	Cpx
Spot No.	3	4	6	7	8	1	2	3	3	3	4
Analysis No.	1	4	1	2	3	2	3	4	6	8	9
SiO_2	54.89	55.07	55.09	54.85	55.11	54.04	54.74	53.85	54.03	54.46	54.73
TiO_2	0.09	0.03	0.00	0.08	0.05	0.01	0.04	0.05	0.02	0.09	0.02
Al_2O_3	2.05	2.05	1.94	1.89	2.16	0.91	1.65	1.70	1.68	1.63	1.61
Cr_2O_3	0.38	0.31	0.29	0.21	0.27	0.34	0.49	0.43	0.42	0.36	0.53
FeO_T	4.77	4.88	4.73	4.70	4.96	3.71	4.20	4.35	4.43	4.25	4.15
MnO	0.25	0.22	0.20	0.20	0.22	0.11	0.19	0.22	0.22	0.19	0.16
NiO	0.02	0.09	0.00	0.03	0.02	0.08	0.04	0.01	0.05	0.09	0.00
MgO	15.13	15.03	15.31	15.18	15.12	16.16	15.86	15.42	15.71	15.67	15.54
CaO	21.39	21.32	21.53	21.64	21.26	23.56	22.52	22.37	22.34	22.47	22.48
Na_2O	1.65	1.80	1.59	1.65	1.70	0.89	1.29	1.39	1.32	1.22	1.29
K_2O	0.00	0.01	0.01	0.01	0.00	0.00	0.00	0.00	0.02	0.00	0.00
P_2O_5	0.18	0.13	0.17	0.22	0.15	0.19	0.14	0.14	0.14	0.19	0.20
Cl	0.00	0.03	0.00	0.00	0.01	0.00	0.00	0.02	0.00	0.00	0.00
Total	100.80	100.96	100.87	100.66	101.03	100.00	101.14	99.96	100.39	100.61	100.71
Mg#	85.0	84.6	85.2	85.2	84.5	88.6	87.1	86.3	86.3	86.8	87.0
Wo	46.1	46.1	46.1	46.4	45.9	48.1	46.9	47.2	46.7	47.1	47.4
En	45.4	45.2	45.6	45.3	45.4	45.9	46.0	45.3	45.7	45.7	45.5
Fe	8.5	8.6	8.3	8.2	8.7	6.1	7.1	7.5	7.6	7.3	7.1

Appendix 2.1: Major and minor elements composition of mineral phases from Finero dykes (contd.)

Grouping	HFSE-rich dyke					
Rock type	Clinopyroxenite cumulate in dioritic dyke					
Sample	FI2105	FI2105	FI2105	FI2105	FI2105	FI2105
Thin section	FI2105B*	FI2105B*	FI2105B*	FI2105B*	FI2105B*	FI2105B*
Phase	Cpx	Cpx	Cpx	Cpx	Cpx	Cpx
Spot No.	5	5	5	6	7	8
Analysis No.	11	12	13	16	17	19
SiO_2	54.16	55.03	54.95	54.49	54.46	54.56
TiO_2	0.03	0.01	0.01	0.07	0.06	0.07
Al_2O_3	1.77	1.50	1.58	1.60	1.63	1.68
Cr_2O_3	0.52	0.43	0.29	0.53	0.53	0.34
FeO_T	4.28	4.34	4.27	4.28	4.06	4.29
MnO	0.16	0.16	0.12	0.13	0.10	0.21
NiO	0.00	0.03	0.05	0.10	0.13	0.08
MgO	15.57	15.86	15.62	15.48	15.63	15.74
CaO	22.31	22.66	22.59	22.52	22.57	22.56
Na_2O	1.33	1.27	1.29	1.29	1.16	1.15
K_2O	0.01	0.00	0.00	0.00	0.00	0.00
P_2O_5	0.13	0.13	0.13	0.16	0.14	0.15
Cl	0.00	0.00	0.01	0.01	0.00	0.00
Total	100.27	101.41	100.92	100.65	100.47	100.84
Mg#	86.6	86.7	86.7	86.6	87.3	86.7
Wo	47.0	47.0	47.3	47.4	47.4	47.0
En	45.7	45.7	45.5	45.3	45.7	45.6
Fe	7.3	7.3	7.2	7.2	6.8	7.3

Appendix 2.1: Major and minor elements composition of mineral phases from Finero dykes (contd.)

Grouping	HFSE-rich dyke	HFSE-poor dyke				Composite HFSE-poor and -rich dyke				
Rock type	Hornblendite dyke with olivine layer	Orthopyroxenite layers bordering gabbroic dyke				Hornblendite dyke with cumulus peridotite				
Sample	FI1501	FI2101	FI2101	FI2101	FI2101	FI1607	FI1607	FI1607	FI1607	FI1607
Thin section	FI1501B	FI2101A	FI2101A	FI2101A	FI2101A	FI1607B	FI1607B	FI1607B	FI1607B	FI1607B
Phase	Opx	Opx	Opx	Opx	Opx	Opx	Opx	Opx	Opx	Opx
Spot No.	4	6	7	8	9	1	4	4	4	6
Analysis No.	8	1	1a	1a	1	4	7	8	9	18
SiO_2	56.14	56.13	56.13	55.85	56.24	51.76	51.82	52.05	51.32	52.31
TiO_2	0.06	0.15	0.10	0.11	0.10	0.00	0.00	0.00	0.00	0.00
Al_2O_3	0.18	3.10	3.10	3.03	2.59	2.97	2.80	2.89	3.84	2.16
Cr_2O_3	0.02	0.11	0.20	0.20	0.31	0.00	0.00	0.00	0.00	0.00
FeO_T	11.68	8.30	7.75	7.65	7.75	22.23	22.25	21.99	22.70	22.20
MnO	0.41	0.16	0.17	0.22	0.16	0.56	0.53	0.72	0.63	0.83
NiO	0.01	0.11	0.05	0.06	0.03	0.00	0.00	0.00	0.00	0.00
MgO	31.23	33.17	33.00	33.14	33.23	21.58	21.62	21.82	20.99	22.16
CaO	0.20	0.28	0.18	0.29	0.29	0.50	0.52	0.51	0.49	0.00
Na_2O	0.00	0.01	0.00	0.03	0.00	0.00	0.00	0.00	0.00	0.00
K_2O	0.00	0.00	0.00	0.00	0.00	0.00	0.00	0.00	0.00	0.00
P_2O_5	0.00	0.01	0.00	0.05	0.00					
Cl	0.00	0.01	0.00	0.00	0.00					
Total	99.94	101.54	100.68	100.63	100.70	99.60	99.54	99.98	99.97	99.66
Mg#	82.7	87.7	88.4	88.5	88.4	63.4	63.4	63.9	62.2	64.0
Wo	0.4	0.5	0.3	0.6	0.6	1.0	1.1	1.0	1.0	0.0
En	81.8	87.0	87.8	87.7	87.7	62.1	62.2	62.5	61.0	63.2
Fe	17.8	12.5	11.8	11.7	11.7	36.8	36.8	36.5	38.0	36.8

Appendix 2.1: Major and minor elements composition of mineral phases from Finero dykes (contd.)

Grouping	HFSE-rich dyke			Composite HFSE-poor and -rich dyke							
Rock type	Olivine layer in hornblendite dyke			Cumulus peridotite bordering hornblendite dyke							
Sample	FI1501	FI1501	FI1501	FI1607	FI1607	FI1607	FI1607	FI1607	FI1607	FI1607	FI1607
Thin section	FI1501B	FI1501B	FI1501B	FI1607C	FI1607C	FI1607C	FI1607C	FI1607C	FI1607C	FI1607C	FI1607C
Phase	Ol	Ol	Ol	Ol	Ol	Ol	Ol	Ol	Ol	Ol	Ol
Spot No.	2	3	4	15ext	15ext	15ext	19	19	20ext	20ext	21
Analysis No.	2	5	7	25	26	27	30	31	32	33	34
SiO_2	39.32	38.78	38.63	38.97	39.00	38.76	39.17	38.93	39.10	38.78	38.95
TiO_2	0.02	0.00	0.00	0.00	0.00	0.00	0.00	0.00	0.00	0.00	0.00
Al_2O_3	0.00	0.01	0.00	0.00	0.00	0.00	0.00	0.00	0.00	0.00	0.00
Cr_2O_3	0.00	0.00	0.00	0.00	0.00	0.00	0.00	0.00	0.00	0.00	0.00
FeO_T	17.62	17.07	17.36	18.48	18.84	19.88	19.17	19.54	20.05	19.78	19.08
MnO	0.32	0.25	0.33	0.43	0.37	0.00	0.00	0.00	0.00	0.36	0.37
NiO	0.24	0.09	0.12	0.00	0.00	0.00	0.00	0.54	0.00	0.00	0.32
MgO	43.36	44.05	43.79	41.64	41.52	40.90	41.79	40.97	41.24	40.76	41.21
CaO	0.01	0.01	0.02	0.00	0.00	0.00	0.00	0.00	0.00	0.00	0.00
Na_2O	0.00	0.02	0.00	0.00	0.00	0.00	0.00	0.00	0.00	0.00	0.00
K_2O	0.00	0.00	0.00	0.00	0.00	0.00	0.00	0.00	0.00	0.00	0.00
P_2O_5	0.00	0.02	0.02								
Cl	0.01	0.00	0.02								
Total	100.90	100.30	100.29	99.52	99.73	99.54	100.13	99.98	100.39	99.68	99.93
Mg#	81.4	82.1	81.8	80.1	79.7	78.6	79.5	78.9	78.6	78.6	79.4

Appendix 2.1: Major and minor elements composition of mineral phases from Finero dykes (contd.)

Grouping	Composite HFSE-poor and -rich dyke						
Rock type	Cumulus peridotite bordering hornblendite dyke						
Sample	FI1607	FI1607	FI1607	FI1607	FI1607	FI1607	FI1607
Thin section	FI1607C	FI1607C	FI1607C	FI1607C	FI1607C	FI1607C	FI1607C
Phase	Ol	Ol	Ol	Ol	Ol	Ol	Ol
Spot No.	21	22	22	25	25	25	25
Analysis No.	35	36	37	38	39	40	41
SiO_2	38.97	38.81	38.51	38.84	39.07	38.89	39.07
TiO_2	0.00	0.00	0.00	0.00	0.00	0.00	0.00
Al_2O_3	0.00	0.00	0.00	0.00	0.00	0.00	0.00
Cr_2O_3	0.00	0.00	0.00	0.00	0.00	0.00	0.00
FeO_T	19.74	19.69	20.99	19.15	19.34	19.48	20.26
MnO	0.41	0.00	0.39	0.32	0.00	0.40	0.00
NiO	0.00	0.00	0.00	0.33	0.33	0.33	0.00
MgO	41.02	41.05	39.69	41.00	41.40	40.88	41.03
CaO	0.00	0.00	0.00	0.00	0.00	0.00	0.00
Na_2O	0.00	0.00	0.00	0.00	0.00	0.00	0.00
K_2O	0.00	0.00	0.00	0.00	0.00	0.00	0.00
P_2O_5							
Cl							
Total	100.14	99.55	99.58	99.64	100.14	99.98	100.36
Mg#	78.7	78.8	77.1	79.2	79.2	78.9	78.3

Appendix 2.1: Major and minor elements composition of mineral phases from Finero dykes (contd.)

Grouping	HFSE-rich dyke									
Rock type	Dioritic dyke									
Sample	FI1604	FI1604	FI1604	FI1604	FI1604	FI1605	FI1605	FI1605	FI1605	FI1605
Thin section	FI1604C	FI1604C	FI1604C	FI1604C	FI1604C	FI1605A	FI1605A2	FI1605A2	FI1605A2	FI1605A2
Phase	Ap	Ap	Ap	Ap	Ap	Ap	Ap	Ap	Ap	Ap
Spot No.	11	15	16	18	19	1	1	5	9	10
Analysis No.	2	4	3	2	4	5	4	4	4	4
SiO_2	0.09	0.08	0.04	0.11	0.09	0.00	0.15	0.06	0.06	0.04
TiO_2	0.00	0.00	0.00	0.01	0.00	0.00	0.00	0.00	0.03	0.06
Al_2O_3	0.00	0.00	0.01	0.01	0.01	0.00	0.02	0.00	0.02	0.00
Cr_2O_3	0.00	0.00	0.01	0.00	0.00	0.00	0.04	0.00	0.00	0.00
FeO_T	0.30	0.37	0.33	0.23	0.31	0.42	0.26	0.34	0.22	0.20
MnO	0.10	0.15	0.12	0.14	0.20	0.00	0.08	0.16	0.14	0.06
NiO	0.02	0.03	0.00	0.03	0.00	0.00	0.04	0.00	0.01	0.02
MgO	0.19	0.16	0.13	0.15	0.18	0.00	0.13	0.19	0.13	0.11
CaO	52.15	51.80	51.92	52.34	51.40	49.48	52.13	52.52	52.19	52.60
Na_2O	0.45	0.42	0.42	0.38	0.47	0.00	0.50	0.50	0.51	0.50
K_2O	0.00	0.02	0.00	0.01	0.00	0.00	0.03	0.00	0.01	0.00
P_2O_5	40.18	39.93	40.10	39.68	39.77	47.23	39.46	40.19	39.78	40.12
Cl	2.52	2.59	2.62	2.61	2.58	2.66	2.23	2.61	2.66	2.73
Total	95.99	95.55	95.70	95.69	95.01	99.79	95.06	96.56	95.77	96.44

Appendix 2.1: Major and minor elements composition of mineral phases from Finero dykes (contd.)

Grouping	HFSE-rich dyke										
Rock type	Dioritic dyke										
Sample	FI2102	FI2102	FI2102	FI2102	FI2102	FI2103	FI2103	FI2104	FI2104	FI2104	FI2104
Thin section	FI2102C	FI2102C	FI2102C	FI2102C	FI2102C	FI2103C	FI2103C	FI2104B	FI2104B	FI2104B	FI2104B
Phase	Ap	Ap	Ap	Ap	Ap	Ap	Ap	Ap	Ap	Ap	Ap
Spot No.	3	4	5	6	8	6	10	11	13	13	14
Analysis No.	4	8	13	14	21	3	2	25	28	29	31
SiO_2	0.03	0.05	0.05	0.09	0.10	0.06	0.05	0.07	0.09	0.06	0.09
TiO_2	0.00	0.00	0.07	0.00	0.00	0.00	0.00	0.00	0.01	0.00	0.03
Al_2O_3	0.00	0.00	0.02	0.00	0.02	0.00	0.00	0.00	0.00	0.00	0.01
Cr_2O_3	0.00	0.08	0.00	0.04	0.00	0.00	0.00	0.00	0.00	0.02	0.00
FeO_T	0.28	0.05	0.08	0.14	0.20	0.08	0.09	0.21	0.25	0.15	0.26
MnO	0.10	0.16	0.06	0.12	0.09	0.03	0.15	0.06	0.06	0.06	0.04
NiO	0.00	0.00	0.04	0.00	0.03	0.00	0.01	0.03	0.00	0.00	0.00
MgO	0.13	0.07	0.10	0.12	0.05	0.14	0.11	0.11	0.12	0.09	0.08
CaO	54.53	53.88	53.89	53.44	54.03	51.46	52.93	52.68	52.75	53.74	54.36
Na_2O	2.65	0.46	0.60	0.49	0.43	0.56	0.57	0.78	0.50	0.53	0.64
K_2O	0.00	0.02	0.01	0.00	0.00	0.00	0.00	0.00	0.01	0.01	0.02
P_2O_5	37.54	38.93	37.62	37.72	38.49	39.00	39.95	38.66	38.89	39.46	38.50
Cl	3.50	2.11	2.38	2.25	1.85	2.35	2.11	2.23	2.13	1.53	1.89
Total	98.76	95.81	94.91	94.39	95.30	93.68	95.97	94.82	94.82	95.65	95.91

Appendix 2.1: Major and minor elements composition of mineral phases from Finero dykes (contd.)

Grouping	HFSE-rich dyke										
Rock type	Clinopyroxenite cumulate in HFSE-rich dioritic dyke					Hornblendite dyke					
Sample	FI1604	FI1604	FI1604	FI1604	FI1604	FI1612	FI1612	FI1612	FI1612	FI1612	FI1612
Thin section	FI1604C*	FI1604C*	FI1604C*	FI1604C*	FI1604C*	FI1612A	FI1612A	FI1612A	FI1612A	FI1612A	FI1612A
Phase	Ap	Ap	Ap	Ap	Ap	Ap	Ap	Ap	Ap	Ap	Ap
Spot No.	1	2	4	4	10	1	3	4	5	8	9
Analysis No.	3	1	3	5	2	2	1	1a	1	1	1
SiO_2	0.05	0.05	0.06	0.07	0.08	0.07	0.08	0.05	0.07	0.00	0.05
TiO_2	0.00	0.00	0.02	0.05	0.00	0.00	0.00	0.00	0.00	0.00	0.00
Al_2O_3	0.00	0.01	0.00	0.00	0.00	0.00	0.00	0.00	0.00	0.00	0.02
Cr_2O_3	0.03	0.00	0.00	0.00	0.00	0.03	0.01	0.01	0.00	0.00	0.00
FeO_T	0.29	0.24	0.25	0.19	0.29	0.09	0.22	0.18	0.14	0.20	0.11
MnO	0.16	0.12	0.17	0.12	0.07	0.06	0.08	0.06	0.10	0.06	0.15
NiO	0.04	0.00	0.00	0.02	0.11	0.01	0.00	0.01	0.02	0.00	0.00
MgO	0.20	0.19	0.20	0.10	0.23	0.10	0.07	0.08	0.07	0.11	0.12
CaO	51.62	51.67	52.36	51.93	51.38	53.33	52.85	52.99	52.78	52.83	52.91
Na_2O	0.52	0.42	0.39	0.44	0.53	0.37	0.33	0.36	0.34	0.34	0.29
K_2O	0.00	0.00	0.01	0.00	0.00	0.01	0.00	0.00	0.00	0.01	0.00
P_2O_5	39.54	39.79	40.27	39.88	40.01	40.51	40.36	40.16	40.03	40.49	40.46
Cl	2.57	2.54	2.43	2.60	2.34	1.98	2.01	1.99	1.95	1.80	1.80
Total	95.02	95.02	96.17	95.41	95.05	96.56	96.02	95.89	95.49	95.85	95.91

Appendix 2.1: Major and minor elements composition of mineral phases from Finero dykes (contd.)

Grouping	HFSE-rich dyke									
Rock type	Albite-dominated anorthosite dyke									
Sample	FI19A02	FI19A02	FI19A04	FI19A04	FI19A04	FI19A04	FI19A04	FI19A04	FI19A04	FI19A04
Thin section	FI19A02B	FI19A02B	FI19A04A	FI19A04A	FI19A04A	FI19A04A	FI19A04A	FI19A04B	FI19A04B	FI19A04B
Phase	Ap	Ap	Ap	Ap	Ap	Ap	Ap	Ap	Ap	Ap
Spot No.	2	9	5	5	5	6	7	4	5	6
Analysis No.	3b	21	13	14	16	17	20	6	8	11
SiO_2	0.05	0.11	0.07	0.10	0.09	0.09	0.07	0.08	0.05	0.09
TiO_2	0.00	0.00	0.00	0.00	0.06	0.01	0.00	0.00	0.03	0.02
Al_2O_3	0.00	0.00	0.01	0.00	0.00	0.00	0.01	0.02	0.00	0.00
Cr_2O_3	0.00	0.00	0.02	0.00	0.00	0.00	0.00	0.00	0.01	0.00
FeO_T	0.28	0.38	0.19	0.26	0.20	0.21	0.17	0.35	0.22	0.24
MnO	0.14	0.13	0.07	0.12	0.10	0.13	0.08	0.16	0.18	0.14
NiO	0.01	0.00	0.01	0.00	0.04	0.05	0.01	0.04	0.04	0.00
MgO	0.10	0.14	0.16	0.15	0.11	0.14	0.18	0.16	0.14	0.12
CaO	55.46	54.64	54.87	54.31	54.90	54.58	54.55	55.54	56.26	54.94
Na_2O	0.44	0.58	0.53	0.68	0.51	0.51	0.52	0.60	0.51	0.58
K_2O	0.00	0.00	0.00	0.02	0.00	0.01	0.00	0.01	0.00	0.00
P_2O_5	39.45	40.61	40.75	39.48	40.50	40.76	39.95	40.93	39.62	39.38
Cl	1.22	1.32	1.46	1.65	1.47	1.47	1.45	1.21	0.97	1.35
Total	97.16	97.91	98.13	96.77	97.99	97.95	96.99	99.09	98.03	96.86

Appendix 2.1: Major and minor elements composition of mineral phases from Finero dykes (contd.)

Grouping	HFSE-poor dyke		Composite HFSE-poor and -rich dyke			
Rock type	Hornblendite dyke		Dioritic dyke			
Sample	FI1608	FI1608	FI2106	FI2106	FI2106	FI2106
Thin section	FI1608B	FI1608B	FI2106A	FI2106A	FI2106A	FI2106A
Phase	Ap	Ap	Ap	Ap	Ap	Ap
Spot No.	5	5	1	2	10	12
Analysis No.	5	6	2	5	20	25
SiO_2	0.03	0.04	0.07	0.05	0.04	0.04
TiO_2	0.02	0.00	0.05	0.00	0.04	0.00
Al_2O_3	0.00	0.00	0.07	0.00	0.00	0.00
Cr_2O_3	0.00	0.00	0.00	0.01	0.00	0.00
FeO_T	0.31	0.28	0.32	0.26	0.20	0.30
MnO	0.07	0.01	0.09	0.13	0.16	0.07
NiO	0.02	0.00	0.00	0.00	0.00	0.00
MgO	0.10	0.10	0.09	0.06	0.05	0.09
CaO	55.85	55.89	56.92	56.41	56.53	56.41
Na_2O	0.21	0.18	0.19	0.12	0.21	0.16
K_2O	0.00	0.00	0.01	0.00	0.00	0.02
P_2O_5	40.83	40.93	41.14	39.41	39.74	39.47
Cl	0.62	0.61	1.52	1.86	1.50	1.50
Total	98.06	98.04	100.48	98.31	98.46	98.06

Appendix 2.1: Major and minor elements composition of mineral phases from Finero dykes (contd.)

Grouping	HFSE-rich dyke											
Rock type	Dioritic dyke											
Sample	FI1603	FI1603	FI1603	FI1603	FI1603	FI1603	FI1603	FI1603	FI1603	FI1603	FI1603	FI1603
Thin section	FI1603A	FI1603A	FI1603A	FI1603A	FI1603A	FI1603A	FI1603A	FI1603A	FI1603A	FI1603A	FI1603A	FI1603A
Phase	Ap	Ap	Ap	Ap	Ap	Ap	Ap	Ap	Ap	Ap	Ap	Ap
Spot	5ext	5ext	5ext	6	6	6a	13	13	13ext	13ext	13ext	13ext
Analysis No.	16	17	21	24	25	27	46	47	50	51	52	53
SiO_2	0.00	0.00	0.00	0.00	0.00	0.00	0.00	0.00	0.00	0.00	0.00	0.00
TiO_2	0.00	0.00	0.00	0.00	0.00	0.00	0.00	0.00	0.00	0.00	0.00	0.00
Al_2O_3	0.00	0.00	0.00	0.00	0.00	0.00	0.00	0.00	0.00	0.00	0.00	0.00
Cr_2O_3	0.00	0.00	0.00	0.00	0.00	0.00	0.00	0.00	0.00	0.00	0.00	0.00
FeO_T	0.00	0.00	0.00	0.00	0.00	0.00	0.00	0.00	0.00	0.00	0.00	0.00
MnO	0.00	0.00	0.00	0.00	0.00	0.00	0.00	0.00	0.00	0.00	0.00	0.00
NiO	0.00	0.00	0.00	0.00	0.00	0.00	0.00	0.00	0.00	0.00	0.00	0.00
MgO	0.00	0.00	0.00	0.00	0.00	0.00	0.00	0.00	0.00	0.00	0.00	0.00
CaO	47.83	47.86	47.94	49.81	47.71	46.42	45.62	47.22	30.29	39.35	47.22	47.23
Na_2O	0.00	0.00	0.56	0.00	0.00	0.65	0.81	0.00	0.00	0.00	0.00	0.00
K_2O	0.00	0.00	0.00	0.00	0.00	0.00	0.00	0.00	0.00	0.00	0.00	0.00
P_2O_5	47.20	48.50	44.71	47.06	46.57	47.86	49.05	48.17	32.67	36.03	47.89	47.98
Cl	2.40	1.15	1.12	2.81	2.79	2.38	1.31	1.23	0.93	1.00	1.44	1.31
F	0.00	0.00	2.57	0.00	0.00	0.00	0.00	0.00	0.00	2.01	0.00	0.00
La_2O_3	0.00	0.00	0.00	0.00	0.00	0.00	0.00	0.00	14.39	8.25	0.00	0.00
Ce_2O_3	0.00	0.00	0.00	0.00	0.00	0.00	0.00	0.00	19.10	11.82	0.00	0.00
SrO	3.04	2.60	2.68	0.00	2.96	3.03	3.37	3.35	0.00	0.00	3.30	3.19
Nd_2O_3	0.00	0.00	0.00	0.00	0.00	0.00	0.00	0.00	2.51	1.86	0.00	0.00
Total	100.47	100.11	99.58	99.68	100.03	100.34	100.16	99.97	99.89	100.32	99.85	99.71

Appendix 2.1: Major and minor elements composition of mineral phases from Finero dykes (contd.)

Grouping	HFSE-rich dyke											
Rock type	Dioritic dyke											
Sample	FI1603	FI1603	FI1603	FI1603	FI1603	FI1603	FI1603	FI1603	FI1603	FI1603	FI1603	FI1603
Thin section	FI1603A	FI1603A	FI1603A	FI1603A	FI1603B	FI1603B	FI1603B	FI1603B	FI1603B	FI1603B	FI1603B	FI1603B
Phase	Ap	Ap	Ap	Ap	Ap	Ap	Ap	Ap	Ap	Ap	Ap	Ap
Spot	14	14	15	15	2	2	3	4	4	6	7	7
Analysis No.	58	60	63	64	5	6	9	12	13	23	24	25
SiO_2	0.00	0.00	0.00	0.00	0.00	0.00	0.00	0.00	0.00	0.00	0.00	0.00
TiO_2	0.00	0.00	0.00	0.00	0.00	0.00	0.00	0.00	0.00	0.00	0.00	0.00
Al_2O_3	0.00	0.00	0.00	0.00	0.00	0.00	0.00	0.00	0.00	0.00	0.00	0.00
Cr_2O_3	0.00	0.00	0.00	0.00	0.00	0.00	0.00	0.00	0.00	0.00	0.00	0.00
FeO_T	0.00	0.00	0.00	0.00	0.00	0.00	0.00	0.00	0.00	0.00	0.00	0.00
MnO	0.00	0.00	0.00	0.00	0.00	0.00	0.00	0.00	0.00	0.00	0.00	0.00
NiO	0.00	0.00	0.00	0.00	0.00	0.00	0.00	0.00	0.00	0.00	0.00	0.00
MgO	0.00	0.00	0.00	0.00	0.00	0.00	0.00	0.00	0.00	0.00	0.00	0.00
CaO	47.98	49.51	50.00	49.49	49.88	49.66	51.52	47.59	49.21	50.58	51.36	49.01
Na_2O	0.00	0.00	0.00	0.00	0.00	0.00	0.00	0.00	0.00	0.00	0.00	0.00
K_2O	0.00	0.00	0.00	0.00	0.00	0.00	0.00	0.00	0.00	0.00	0.00	0.00
P_2O_5	46.82	44.05	47.88	42.13	48.23	45.02	44.83	49.21	46.12	45.71	44.38	45.42
Cl	2.70	1.51	2.28	2.51	1.89	0.43	0.32	0.64	0.34	1.73	2.01	1.21
F	0.00	2.52	0.00	2.85	0.00	2.68	3.10	0.00	2.27	1.53	2.33	1.79
La_2O_3	0.00	0.00	0.00	0.00	0.00	0.00	0.00	0.00	0.00	0.00	0.00	0.00
Ce_2O_3	0.00	0.00	0.00	0.00	0.00	0.00	0.00	0.00	0.00	0.00	0.00	0.00
SrO	2.70	2.54	0.00	2.59	0.00	2.32	0.00	2.23	2.22	0.00	0.00	2.33
Nd_2O_3	0.00	0.00	0.00	0.00	0.00	0.00	0.00	0.00	0.00	0.00	0.00	0.00
Total	100.20	100.13	100.16	99.57	100.00	100.11	99.77	99.67	100.16	99.55	100.08	99.76

Appendix 2.1: Major and minor elements composition of mineral phases from Finero dykes (contd.)

Grouping	HFSE-rich dyke						Composite HFSE-poor and -rich dyke				
Rock type	Dioritic dyke						Hornblendite dyke with cumulus peridotite				
Sample	FI1603	FI1603	FI1603	FI1603	FI1603	FI1603	FI1607	FI1607	FI1607	FI1607	FI1607
Thin section	FI1603B	FI1603C	FI1603C	FI1603C	FI1603C	FI1603C	FI1607A	FI1607A	FI1607B	FI1607C	FI1607C
Phase	Ap	Ap	Ap	Ap	Ap	Ap	Ap	Ap	Ap	Ap	Ap
Spot	7	3	3	3	3	6	4	4	5	2	4
Analysis No.	26	6	7	10	11	17	7	8	26	5	8
SiO_2	0.00	2.49	0.00	0.00	0.00	0.00	0.00	0.00	0.00	0.00	0.00
TiO_2	0.00	0.00	0.00	0.00	0.00	0.00	0.00	0.00	0.00	0.00	0.00
Al_2O_3	0.00	0.75	0.00	0.00	0.00	0.00	0.00	0.00	0.00	0.00	0.00
Cr_2O_3	0.00	0.00	0.00	0.00	0.00	0.00	0.00	0.00	0.00	0.00	0.00
FeO_T	0.00	0.00	0.00	0.00	0.00	0.00	0.28	0.33	0.00	0.41	0.00
MnO	0.00	0.00	0.00	0.00	0.00	0.00	0.00	0.00	0.00	0.00	0.00
NiO	0.00	0.00	0.00	0.00	0.00	0.00	0.00	0.00	0.00	0.00	0.00
MgO	0.00	1.69	0.00	0.00	0.00	0.00	0.00	0.00	0.00	0.00	0.00
CaO	47.80	46.52	50.12	49.71	51.63	48.55	50.35	50.57	50.78	50.71	48.07
Na_2O	0.00	0.00	0.00	0.79	0.00	0.00	0.00	0.00	0.00	0.00	0.00
K_2O	0.00	0.12	0.00	0.00	0.00	0.00	0.00	0.00	0.00	0.00	0.00
P_2O_5	47.01	45.60	46.60	46.36	44.80	45.13	46.63	46.84	46.36	46.76	47.93
Cl	2.44	0.44	0.86	1.40	1.53	1.42	0.82	0.90	0.76	0.48	1.70
F	0.00	2.79	1.42	2.15	2.51	1.71	1.60	1.58	1.85	1.93	0.00
La_2O_3	0.00	0.00	0.00	0.00	0.00	0.00	0.00	0.00	0.00	0.00	0.00
Ce_2O_3	0.00	0.00	0.86	0.00	0.00	0.00	0.00	0.00	0.00	0.00	0.00
SrO	2.82	0.00	0.00	0.00	0.00	2.74	0.00	0.00	0.00	0.00	2.38
Nd_2O_3	0.00	0.00	0.00	0.00	0.00	0.00	0.00	0.00	0.00	0.00	0.00
Total	100.07	100.40	99.86	100.41	100.47	99.55	99.68	100.22	99.75	100.29	100.08

Appendix 2.1: Major and minor elements composition of mineral phases from Finero dykes (contd.)

Grouping	HFSE-rich dyke							
Rock type	Dioritic dyke							
Sample	FI1603	FI1603	FI1603	FI1603	FI1603	FI1603	FI1603	FI1603
Thin section	FI1603A	FI1603A	FI1603A	FI1603A	FI1603A	FI1603A	FI1603A	FI1603A
Phase	Tnt	Tnt	Tnt	Ilm	Ilm	Ilm	Ilm	Ilm
Spot No.	6b	6b	6b	6b	6b	6b	13	13
Analysis No.	33	35	36	30	31	34	54	55
SiO_2	33.05	32.90	33.70	0.00	0.00	0.00	1.24	1.81
TiO_2	37.66	37.56	36.79	52.71	53.26	52.66	51.37	51.46
Al_2O_3	1.01	1.26	1.20	0.00	0.00	0.00	0.95	0.00
Cr_2O_3	0.00	0.00	0.00	0.00	0.00	0.00	0.00	0.00
FeO_T	0.00	0.00	0.00	43.44	42.46	43.25	40.48	40.02
MnO	0.00	0.00	0.00	3.99	3.56	3.70	4.63	4.26
NiO	0.00	0.00	0.00	0.00	0.00	0.00	0.00	0.00
MgO	0.00	0.00	0.00	0.00	1.06	0.00	1.00	1.70
CaO	28.35	28.21	28.28	0.00	0.00	0.30	0.61	0.80
Na_2O	0.00	0.00	0.00	0.00	0.00	0.00	0.00	0.00
K_2O	0.00	0.00	0.00	0.00	0.00	0.00	0.00	0.00
P_2O_5								
Cl								
Total	100.07	99.93	99.97	100.14	100.34	99.91	100.28	100.05

Appendix 2.2: Trace element composition of mineral phases from Finero dykes

Grouping	HFSE-rich dyke												
Rock type	Dioritic dyke												
Sample	FI1603	FI1603	FI1603	FI1603	FI1603	FI1603	FI1603	FI1603	FI1603	FI1603	FI1603	FI1603	FI1603
Thin section	FI1603B	FI1603B	FI1603B	FI1603B	FI1603B	FI1603B	FI1603B	FI1603B	FI1603B	FI1603B	FI1603C	FI1603C	FI1603C
Phase	Plag	Plag	Plag	Plag	Plag	Plag	Plag	Plag	Plag	Plag	Plag	Plag	Plag
Spot No.	1	1	7	7	11	11	15	15	16	16	1	1	7
Analysis No.	1	2	27a	27b	35	36	42	43	44	45	1	2	22
Sc	4.71	4.37	3.99	4.00	4.00	3.96	3.90	4.07	4.03	3.59	3.85	3.78	3.71
Ti	43.7	38.8	29.2	36.0	39.4	31.1	39.2	32.8	68.4	59.8	51.5	40.7	70.7
V	0.04	bdl.	0.05	0.10	bdl.	0.03	0.10	0.01	bdl.	0.08	bdl.	bdl.	0.06
Cr	0.49	0.55	0.91	0.93	0.37	0.51	1.70	0.34	0.34	0.48	0.49	0.47	0.28
Co	bdl.	bdl.	bdl.	0.09	bdl.	0.02	0.03	0.01	bdl.	0.01	0.01	0.52	0.02
Ni	0.25	bdl.	0.62	1.02	bdl.	0.03	0.58	0.12	0.06	0.29	bdl.	bdl.	0.22
Zn	0.33	2.83	1.15	0.71	0.13	0.48	0.49	2.41	0.22	1.23	0.34	1.87	1.34
Rb	0.59	0.53	0.05	0.21	0.25	0.12	0.54	0.39	0.52	0.35	0.51	0.26	0.17
Sr	4592	4197	6114	5967	6526	6373	5891	6263	4761	5119	6739	6727	5208
Y	0.04	0.04	0.04	0.03	0.03	0.02	0.04	0.03	0.02	0.04	0.06	0.04	0.04
Zr	0.04	0.00	0.07	0.19	0.00	0.01	0.03	0.02	0.00	0.05	0.00	0.01	0.03
Nb	0.01	0.02	0.07	0.18	0.01	0.01	0.02	0.00	0.02	0.02	0.01	0.04	0.05
Cs	bdl.	bdl.	bdl.	bdl.	bdl.	bdl.	0.02	bdl.	0.01	bdl.	0.01	bdl.	0.01
Ba	1758	1643	923	996	1084	914	1083	1094	1592	1654	1125	982	851
La	2.04	1.69	1.68	1.71	1.94	1.78	1.75	1.78	1.07	1.12	2.82	2.28	1.89
Ce	2.23	1.98	1.63	1.57	1.95	1.75	1.63	1.80	1.17	1.21	2.71	2.17	1.82
Pr	0.13	0.12	0.09	0.09	0.13	0.09	0.08	0.10	0.05	0.07	0.16	0.14	0.12
Nd	0.29	0.25	0.23	0.21	0.27	0.23	0.19	0.22	0.16	0.14	0.32	0.27	0.24
Sm	0.03	0.04	0.02	0.01	0.02	0.01	0.00	0.01	0.03	0.02	0.06	0.01	0.04
Eu	0.37	0.30	0.27	0.30	0.30	0.31	0.26	0.32	0.27	0.25	0.29	0.29	0.26
Gd	0.02	0.02	0.01	0.00	0.01	0.01	0.02	0.02	0.01	bdl.	0.04	0.02	0.02
Tb	bdl.	bdl.	bdl.	bdl.	bdl.	bdl.	bdl.	bdl.	bdl.	bdl.	0.01	bdl.	bdl.
Dy	bdl.	bdl.	bdl.	bdl.	bdl.	bdl.	bdl.	bdl.	bdl.	bdl.	bdl.	bdl.	bdl.
Ho	bdl.	bdl.	bdl.	bdl.	bdl.	bdl.	bdl.	bdl.	bdl.	bdl.	bdl.	bdl.	bdl.
Er	bdl.	bdl.	bdl.	bdl.	bdl.	bdl.	bdl.	bdl.	bdl.	bdl.	bdl.	bdl.	bdl.
Tm	bdl.	bdl.	bdl.	bdl.	bdl.	bdl.	bdl.	bdl.	bdl.	bdl.	bdl.	bdl.	bdl.
Yb	bdl.	bdl.	bdl.	bdl.	bdl.	bdl.	bdl.	bdl.	bdl.	bdl.	bdl.	bdl.	bdl.
Lu	bdl.	bdl.	bdl.	bdl.	bdl.	bdl.	bdl.	bdl.	bdl.	bdl.	bdl.	bdl.	bdl.
Hf	bdl.	bdl.	bdl.	bdl.	bdl.	bdl.	bdl.	bdl.	bdl.	bdl.	bdl.	bdl.	bdl.
Ta	bdl.	bdl.	bdl.	bdl.	bdl.	bdl.	bdl.	bdl.	bdl.	bdl.	bdl.	bdl.	bdl.
Pb	n.d.	n.d.	n.d.	n.d.	n.d.	n.d.	n.d.	n.d.	n.d.	n.d.	n.d.	n.d.	n.d.
Th	bdl.	bdl.	bdl.	bdl.	bdl.	bdl.	bdl.	bdl.	bdl.	bdl.	bdl.	bdl.	bdl.
U	bdl.	bdl.	bdl.	bdl.	bdl.	bdl.	bdl.	bdl.	bdl.	bdl.	bdl.	bdl.	bdl.

bdl. – below detection limit; n.d. – not determined

Appendix 2.2: Trace element composition of mineral phases from Finero dykes (contd.)

Grouping	HFSE-rich dyke									
Rock type	Dioritic dyke									
Sample	FI1603	FI1603	FI1604	FI1605	FI1605	FI1605	FI2102	FI2102	FI2103	FI2103
Thin section	FI1603C	FI1603C	FI1604C	FI1605A2	FI1605A2	FI1605A2	FI2102C	FI2102C	FI2103C	FI2103C
Phase	Plag	Plag	Plag	Plag	Plag	Plag	Plag	Plag	Plag	Plag
Spot No.	7	11	7	1	6	8	1	1	4	4
Analysis No.	23	36	1a	5	1	1	1a	1b	1a	1b
Sc	3.80	3.59	7.70	5.77	4.58	5.89	5.51	5.83	4.99	4.53
Ti	35.0	48.9	15.9	4.2	16.5	23.7	83.4	101.8	29.6	27.6
V	0.03	0.05	0.23	0.06	0.17	0.15	0.147	0.2	bdl.	bdl.
Cr	0.82	0.30	0.80	1.41	2.27	1.59	1.77	2.95	bdl.	bdl.
Co	0.09	0.01	0.04	0.04	0.07	0.07	0.07	0.15	0.16	0.24
Ni	1.00	0.24	1.72	0.24	0.50	1.59	bdl.	0.76	0.55	0.94
Zn	4.53	0.36	0.83	0.85	2.26	0.43	1.05	0.99	0.85	1.61
Rb	0.33	0.16	0.27	0.33	0.33	0.41	0.90	0.71	0.46	0.75
Sr	7753	5461	8645	8769	6596	6376	6707	6834	6695	7038
Y	0.07	0.02	0.01	0.12	0.05	0.03	0.03	0.04	0.05	0.05
Zr	0.09	0.00	0.03	0.07	0.07	0.06	0.06	0.10	0.10	0.53
Nb	0.20	0.00	0.06	0.02	0.05	0.02	0.03	0.05	0.05	0.07
Cs	bdl.	bdl.	0.01	0.01	0.02	0.01	0.02	0.04	0.04	0.03
Ba	790	996	657	684	682	660	1630	1672	954	957
La	1.53	1.63	1.51	1.46	1.45	1.96	1.52	1.34	1.36	1.60
Ce	1.37	1.46	1.44	1.50	1.52	1.90	1.69	1.65	1.31	1.41
Pr	0.08	0.07	0.10	0.08	0.07	0.09	0.12	0.15	0.10	0.08
Nd	0.18	0.17	0.45	0.06	0.10	0.14	0.26	bdl.	0.13	0.55
Sm	0.04	0.01	0.04	0.18	0.00	0.14	bdl.	bdl.	bdl.	bdl.
Eu	0.25	0.25	0.23	0.12	0.30	0.24	0.37	0.13	0.19	0.44
Gd	0.02	0.01	0.06	0.08	0.10	0.11	0.13	bdl.	bdl.	0.63
Tb	bdl.	bdl.	bdl.	bdl.	bdl.	bdl.	bdl.	bdl.	bdl.	bdl.
Dy	bdl.	bdl.	bdl.	bdl.	bdl.	bdl.	bdl.	bdl.	bdl.	bdl.
Ho	bdl.	bdl.	bdl.	bdl.	bdl.	bdl.	bdl.	bdl.	bdl.	bdl.
Er	bdl.	bdl.	bdl.	bdl.	bdl.	bdl.	bdl.	bdl.	bdl.	bdl.
Tm	bdl.	bdl.	bdl.	bdl.	bdl.	bdl.	bdl.	bdl.	bdl.	bdl.
Yb	bdl.	bdl.	bdl.	bdl.	bdl.	bdl.	bdl.	bdl.	bdl.	bdl.
Lu	bdl.	bdl.	bdl.	bdl.	bdl.	bdl.	bdl.	bdl.	bdl.	bdl.
Hf	bdl.	bdl.	bdl.	bdl.	bdl.	bdl.	bdl.	bdl.	bdl.	bdl.
Ta	bdl.	bdl.	bdl.	bdl.	bdl.	bdl.	bdl.	bdl.	bdl.	bdl.
Pb	n.d.	n.d.	16.08	14.30	14.81	13.10	6.12	6.30	7.15	8.16
Th	bdl.	bdl.	bdl.	bdl.	bdl.	bdl.	bdl.	bdl.	bdl.	0.07
U	bdl.	bdl.	bdl.	bdl.	bdl.	bdl.	bdl.	bdl.	bdl.	0.07

Appendix 2.2: Trace element composition of mineral phases from Finero dykes (contd.)

Grouping	HFSE-rich dyke												
Rock type	Dioritic dyke												
Sample	FI2103	FI2103	FI2103	FI2104	FI2104	FI2104	FI2104	FI2104	FI2104	FI2104	FI2104	FI2104	
Thin section	FI2103C	FI2103C	FI2103C	FI2104B	FI2104B	FI2104B	FI2104B	FI2104B	FI2104B	FI2104B	FI2104B	FI2104C	
Phase	Plag	Plag	Plag	Plag	Plag	Plag	Plag	Plag	Plag	Plag	Plag	Plag	
Spot No.	4	5	6	1	1	1	2	2	3	3	6	1	
Analysis No.	1c	1	2	1a	1b	1c	2a	2b	3a	3b	10	1	
Sc	3.17	4.1	5.48	10.56	10.56	9.84	10.27	9.42	8.69	8.41	7.19	6.19	
Ti	24.0	19.0	11.9	61.6	50.5	42.8	62.6	62.8	49.1	69.9	10.5	50.6	
V	0.28	bdl.	bdl.	0.12	0.12	0.14	0.15	0.12	0.16	0.15	0.13	0.13	
Cr	bdl.	bdl.	bdl.	bdl.	bdl.	bdl.	bdl.	bdl.	bdl.	bdl.	bdl.	bdl.	
Co	0.20	0.21	0.17	0.07	0.05	0.06	0.06	0.07	0.07	0.06	0.06	0.06	
Ni	0.97	0.95	1.14	0.27	0.52	0.32	0.42	0.25	0.32	0.29	0.26	0.24	
Zn	1.08	1.5	1.74	1.97	1.02	0.87	0.69	1.56	bdl.	0.85	bdl.	bdl.	
Rb	1.13	0.36	0.47	0.53	0.49	0.27	0.70	0.59	0.54	0.60	0.21	0.37	
Sr	6821	7419	8810	7262	7277	7216	6225	6632	5768	5979	8826	6984	
Y	0.07	0.10	0.16	bdl.	0.03	bdl.	0.02	0.07	0.11	0.03	bdl.	0.09	
Zr	0.14	0.19	0.18	bdl.	bdl.	bdl.	bdl.	bdl.	bdl.	bdl.	bdl.	bdl.	
Nb	0.03	0.15	0.06	0.04	bdl.	bdl.	bdl.	bdl.	bdl.	bdl.	bdl.	bdl.	
Cs	0.04	0.05	0.07	bdl.	bdl.	bdl.	bdl.	bdl.	bdl.	bdl.	bdl.	bdl.	
Ba	788	898	843	1287	1232	1134	1439	1401	1454	1538	749	1104	
La	1.62	1.78	1.94	2.02	1.78	1.89	1.65	1.51	2.82	2.12	1.68	1.43	
Ce	1.40	1.68	1.79	1.68	1.49	1.25	1.68	1.63	2.92	2.33	1.41	1.42	
Pr	0.03	0.13	0.19	0.08	0.10	0.12	0.09	0.13	0.16	0.15	0.09	0.09	
Nd	bdl.	0.32	0.26	0.34	0.24	0.28	0.22	0.33	0.68	0.42	0.14	0.38	
Sm	bdl.	bdl.	bdl.	bdl.	bdl.	bdl.	bdl.	0.04	bdl.	bdl.	bdl.	bdl.	
Eu	0.36	0.18	0.29	0.31	0.35	0.40	0.41	0.28	0.28	0.50	0.31	0.26	
Gd	bdl.	0.15	0.30	bdl.	bdl.	bdl.	bdl.	bdl.	bdl.	bdl.	bdl.	bdl.	
Tb	bdl.	bdl.	bdl.	bdl.	bdl.	bdl.	bdl.	bdl.	bdl.	bdl.	bdl.	bdl.	
Dy	bdl.	bdl.	bdl.	bdl.	bdl.	bdl.	bdl.	bdl.	bdl.	bdl.	bdl.	bdl.	
Ho	bdl.	bdl.	bdl.	bdl.	bdl.	bdl.	bdl.	bdl.	bdl.	bdl.	bdl.	bdl.	
Er	bdl.	bdl.	bdl.	bdl.	bdl.	bdl.	bdl.	bdl.	bdl.	bdl.	bdl.	bdl.	
Tm	bdl.	bdl.	bdl.	bdl.	bdl.	bdl.	bdl.	bdl.	bdl.	bdl.	bdl.	bdl.	
Yb	bdl.	bdl.	bdl.	bdl.	bdl.	bdl.	bdl.	bdl.	bdl.	bdl.	bdl.	bdl.	
Lu	bdl.	bdl.	bdl.	bdl.	bdl.	bdl.	bdl.	bdl.	bdl.	bdl.	bdl.	bdl.	
Hf	bdl.	bdl.	bdl.	bdl.	bdl.	bdl.	bdl.	bdl.	bdl.	bdl.	bdl.	bdl.	
Ta	bdl.	bdl.	bdl.	0.02	bdl.	bdl.	0.03	bdl.	bdl.	0.02	0.01	0.01	
Pb	6.78	7.02	9.07	8.48	7.72	7.32	6.90	7.23	7.80	7.73	8.02	6.62	
Th	bdl.	bdl.	0.04	0.01	0.01	bdl.	0.01	0.02	0.04	0.01	0.01	bdl.	
U	bdl.	bdl.	bdl.	bdl.	bdl.	bdl.	bdl.	bdl.	bdl.	bdl.	bdl.	bdl.	

Appendix 2.2: Trace element composition of mineral phases from Finero dykes (contd.)

Grouping	HFSE-rich dyke												
Rock type	Dioritic dyke			Albite-dominated anorthosite dyke									
Sample	FI2104	FI2104	FI2104	FI19A01	FI19A01	FI19A01	FI19A01	FI19A01	FI19A01	FI19A01	FI19A01	FI19A01	FI19A01
Thin section	FI2104C	FI2104C	FI2104C	MS	MS	MS	MS	MS	MS	MS	MS	MS	MS
Phase	Plag	Plag	Plag	Plag	Plag	Plag	Plag	Plag	Plag	Plag	Plag	Plag	Plag
Spot No.	5	8	11										
Analysis No.	2	1	1	1	2	3	4	5	6	7	8	9	10
Sc	5.09	5.18	3.93	0.58	0.70	0.54	0.66	0.88	0.58	0.58	0.61	0.57	0.64
Ti	18.3	29.7	20.9	55.8	24.7	42.2	37.2	49.7	47.0	16.0	46.0	31.9	33.5
V	0.07	0.10	0.16	0.09	0.04	0.10	0.03	0.04	0.04	0.03	0.05	0.04	0.05
Cr	bdl.	bdl.	bdl.	bdl.	bdl.	bdl.	bdl.	bdl.	bdl.	bdl.	bdl.	bdl.	bdl.
Co	0.04	0.06	0.07	0.019	bdl.	bdl.	bdl.	0.035	bdl.	0.016	bdl.	bdl.	0.024
Ni	0.51	0.25	0.32	3.14	0.374	2.45	0.15	0.74	4.1	0.165	0.442	0.305	2.81
Zn	bdl.	0.79	bdl.	3.85	0.51	bdl.	bdl.	1.73	1.15	1.07	bdl.	0.39	2.43
Rb	0.19	0.44	0.33	0.42	0.09	0.39	0.13	0.28	0.19	bdl.	0.07	0.10	0.21
Sr	9977	9144	9698	4811	5890	5805	6473	5705	5607	6529	5276	5237	3240
Y	1.11	0.05	0.06	0.08	0.03	0.12	0.04	0.08	0.15	0.03	0.06	0.04	0.08
Zr	bdl.	bdl.	bdl.	0.20	0.01	0.13	0.02	0.03	0.05	0.03	0.03	0.02	0.07
Nb	bdl.	bdl.	bdl.	0.11	0.04	0.12	0.02	0.06	0.16	0.01	0.03	0.02	0.08
Cs	bdl.	bdl.	bdl.	0.11	0.01	0.13	0.04	0.02	0.07	bdl.	0.02	0.02	0.18
Ba	720	1009	734	707	684	752	771	988	869	653	795	851	491
La	7.20	1.97	2.13	2.12	3.10	2.86	2.55	2.87	3.38	3.21	2.51	1.77	1.89
Ce	9.55	1.93	1.56	1.93	2.15	2.69	2.10	3.28	4.04	2.62	2.56	1.73	2.02
Pr	1.24	0.12	0.15	0.17	0.08	0.15	0.11	0.24	0.30	0.13	0.16	0.08	0.11
Nd	3.10	0.25	0.23	0.32	0.21	0.49	0.47	0.63	0.78	0.40	0.40	0.22	0.22
Sm	0.60	bdl.	bdl.	0.04	0.04	0.03	0.01	bdl.	bdl.	bdl.	0.02	0.02	0.02
Eu	0.57	0.29	0.31	0.31	0.22	0.33	0.36	0.53	0.25	0.21	0.35	0.19	0.25
Gd	0.35	bdl.	bdl.	0.02	0.02	0.01	0.02	bdl.	0.08	bdl.	0.02	bdl.	0.02
Tb	0.04	bdl.	bdl.	bdl.	bdl.	0.01	0.00	bdl.	bdl.	bdl.	bdl.	bdl.	0.00
Dy	0.23	bdl.	bdl.	bdl.	bdl.	bdl.	0.01	bdl.	bdl.	bdl.	bdl.	0.01	0.01
Ho	0.05	bdl.	bdl.	0.00	bdl.	0.00	bdl.	bdl.	0.02	0.00	bdl.	bdl.	bdl.
Er	0.16	bdl.	bdl.	bdl.	bdl.	bdl.	bdl.	bdl.	bdl.	bdl.	bdl.	bdl.	0.01
Tm	0.02	bdl.	bdl.	bdl.	bdl.	0.00	bdl.	bdl.	bdl.	bdl.	bdl.	bdl.	bdl.
Yb	0.08	bdl.	bdl.	bdl.	bdl.	0.01	bdl.	bdl.	bdl.	bdl.	bdl.	bdl.	bdl.
Lu	bdl.	bdl.	bdl.	bdl.	bdl.	bdl.	0.00	bdl.	bdl.	bdl.	bdl.	bdl.	bdl.
Hf	0.03	bdl.	bdl.	bdl.	bdl.	bdl.	bdl.	bdl.	bdl.	bdl.	0.38	bdl.	0.02
Ta	0.01	bdl.	0.04	0.00	bdl.	bdl.	0.00	bdl.	bdl.	bdl.	0.01	bdl.	bdl.
Pb	8.41	7.87	9.47	5.90	5.09	7.99	6.13	9.04	6.69	6.79	6.64	4.35	6.24
Th	0.33	bdl.	bdl.	0.01	bdl.	0.01	bdl.	bdl.	0.06	0.02	bdl.	0.00	0.01
U	0.09	bdl.	bdl.	bdl.	bdl.	bdl.	bdl.	bdl.	bdl.	bdl.	bdl.	bdl.	bdl.

MS – Mineral Separate

Appendix 2.2: Trace element composition of mineral phases from Finero dykes (contd.)

Grouping	HFSE-rich dyke										
Rock type	Albite-dominated anorthosite dyke										
Sample	FI19A02	FI19A02	FI19A02	FI19A02	FI19A02	FI19A04	FI19A04	FI19A04	FI19A04	FI19A04	FI19A04
Thin section	FI19A02B	FI19A02B	FI19A02B	FI19A02B	FI19A02B	FI19A04A	FI19A04A	FI19A04B	FI19A04B	FI19A04B	FI19A04B
Phase	Plag	Plag	Plag	Plag	Plag	Plag	Plag	Plag	Plag	Plag	Plag
Spot No.	3	5	6	4	4	10	8	1	1	2	7
Analysis No.	7	10a	12	8	9	24	22	1a	1b	3	13
Sc	4.66	5.65	5.66	5.37	5.21	4.07	4.48	4.23	3.93	3.97	5.21
Ti	26.9	46.8	30.9	36.5	28.2	23.2	18.8	19.5	20.3	26.6	30.2
V	bdl.	bdl.	bdl.	bdl.	bdl.	bdl.	bdl.	bdl.	bdl.	bdl.	0.104
Cr	bdl.	bdl.	2.04	1.65	1.25	5.01	bdl.	2.07	bdl.	bdl.	1.69
Co	bdl.	1.006	0.249	0.117	bdl.	bdl.	0.14	0.08	0.12	bdl.	0.54
Ni	1.17	6.79	3.95	3.16	1.16	0.6	2.71	0.89	2.41	2.61	1.69
Zn	1.22	1.19	24.94	3.72	1.28	bdl.	1.85	bdl.	bdl.	bdl.	bdl.
Rb	bdl.	0.23	0.48	0.47	0.34	0.58	0.57	0.37	0.75	0.63	0.66
Sr	2886	3229	2103	2888	2479	3397	2277	2850	3259	2977	2035
Y	bdl.	bdl.	0.03	0.07	0.05	bdl.	0.04	0.03	0.03	bdl.	0.04
Zr	0.05	0.03	0.09	0.27	0.26	bdl.	0.04	0.21	0.07	0.07	0.08
Nb	0.04	bdl.	0.06	0.05	bdl.	bdl.	0.18	bdl.	bdl.	bdl.	bdl.
Cs	0.03	bdl.	bdl.	0.01	bdl.	bdl.	0.08	bdl.	bdl.	bdl.	bdl.
Ba	336	370	264	350	306	393	285	314	357	332	254
La	0.97	1.07	0.79	0.87	0.88	0.65	4.75	0.64	0.70	0.82	5.37
Ce	4.43	1.85	1.59	1.53	1.26	23.88	8.56	0.96	1.24	1.03	1.04
Pr	0.07	0.14	0.07	0.10	0.05	0.13	0.09	0.07	0.05	0.06	0.04
Nd	0.03	0.17	0.08	0.13	bdl.	0.07	1.26	0.14	0.48	0.21	0.07
Sm	bdl.	bdl.	bdl.	bdl.	0.15	bdl.	0.14	bdl.	bdl.	bdl.	bdl.
Eu	0.13	0.23	0.18	0.10	0.16	0.29	0.14	0.14	0.17	0.12	0.08
Gd	0.08	bdl.	bdl.	0.08	bdl.	bdl.	bdl.	bdl.	bdl.	bdl.	bdl.
Tb	bdl.	bdl.	bdl.	0.02	bdl.	bdl.	bdl.	bdl.	bdl.	bdl.	bdl.
Dy	bdl.	bdl.	bdl.	bdl.	bdl.	bdl.	bdl.	bdl.	bdl.	bdl.	bdl.
Ho	bdl.	bdl.	bdl.	bdl.	bdl.	bdl.	bdl.	bdl.	bdl.	bdl.	bdl.
Er	bdl.	bdl.	bdl.	0.11	0.10	bdl.	bdl.	bdl.	bdl.	bdl.	bdl.
Tm	bdl.	bdl.	bdl.	bdl.	bdl.	bdl.	bdl.	bdl.	bdl.	bdl.	bdl.
Yb	bdl.	bdl.	bdl.	bdl.	bdl.	bdl.	bdl.	bdl.	bdl.	bdl.	bdl.
Lu	bdl.	bdl.	bdl.	bdl.	bdl.	bdl.	bdl.	bdl.	bdl.	bdl.	bdl.
Hf	0.05	0.08	12.46	bdl.	0.07	bdl.	bdl.	bdl.	bdl.	bdl.	bdl.
Ta	0.03	bdl.	bdl.	0.01	0.03	bdl.	bdl.	bdl.	bdl.	bdl.	bdl.
Pb	7.10	7.94	11.69	8.17	7.67	7.76	6.75	5.55	7.41	7.75	10.13
Th	0.03	bdl.	0.01	bdl.	0.01	bdl.	bdl.	bdl.	bdl.	bdl.	bdl.
U	0.04	bdl.	0.02	0.03	0.01	bdl.	bdl.	bdl.	bdl.	bdl.	bdl.

Appendix 2.2: Trace element composition of mineral phases from Finero dykes (contd.)

Grouping	HFSE-poor dyke					Composite HFSE-poor and -rich dyke							
Rock type	Gabbroic dyke bordered by orthopyroxenite					Dioritic dyke							
Sample	FI2101	FI2101	FI2101	FI2101	FI2101	FI2106	FI2106	FI2106	FI2106	FI2106	FI2106	FI2106	FI2106
Thin section	FI2101A	FI2101A	FI2101A	FI2101A	FI2101A	FI2106A	FI2106A	FI2106A	FI2106A	FI2106A	FI2106A	FI2106A	FI2106A
Phase	Plag	Plag	Plag	Plag	Plag	Plag	Plag	Plag	Plag	Plag	Plag	Plag	Plag
Spot No.	3	3	4	4	10	3	3	6	7	8	T1	T1	T1
Analysis No.	1a	1b	1	2	1	7	8	12	13	14			
Sc	5.67	5.16	4.75	5.42	4.41	3.31	3.32	3.26	3.35	3.37	1.20	1.24	1.72
Ti	12.7	13.3	6.6	4.6	33.2	54.2	49.9	66.7	64.6	56.5	41.1	35.2	46.9
V	bdl.	bdl.	bdl.	bdl.	bdl.	0.087	bdl.	0.234	0.169	0.135	0.249	0.194	0.33
Cr	bdl.	bdl.	1.17	bdl.	bdl.	1.28	bdl.	bdl.	2.42	2.2	bdl.	2.15	bdl.
Co	bdl.	bdl.	0.08	bdl.	bdl.	bdl.	bdl.	bdl.	0.093	0.12	bdl.	bdl.	bdl.
Ni	bdl.	0.36	bdl.	0.36	bdl.	0.4	0.83	bdl.	bdl.	0.7	bdl.	bdl.	bdl.
Zn	bdl.	0.82	bdl.	bdl.	bdl.	bdl.	bdl.	bdl.	0.99	0.98	bdl.	bdl.	bdl.
Rb	0.06	0.35	0.05	0.07	bdl.	0.09	bdl.	0.10	bdl.	0.11	1.11	1.50	1.01
Sr	2803	2762	2920	2899	2350	3540	3457	3716	3815	3720	3573	4096	3733
Y	bdl.	0.02	0.05	bdl.	0.06	bdl.	0.12	0.07	0.14	0.11	0.04	0.09	bdl.
Zr	bdl.	0.10	0.04	0.10	0.18	bdl.	bdl.	bdl.	bdl.	bdl.	bdl.	bdl.	bdl.
Nb	bdl.	bdl.	bdl.	bdl.	bdl.	bdl.	bdl.	bdl.	bdl.	bdl.	bdl.	bdl.	bdl.
Cs	bdl.	bdl.	bdl.	bdl.	bdl.	bdl.	bdl.	bdl.	bdl.	bdl.	bdl.	bdl.	bdl.
Ba	116	131	36	52	112	185	171	217	215	199	163	195	175
La	6.13	6.45	7.78	7.57	5.83	7.20	7.51	7.76	7.79	7.79	7.78	8.04	7.73
Ce	7.66	7.00	9.03	9.54	7.97	7.33	6.94	6.64	7.60	7.57	6.01	6.85	6.61
Pr	0.49	0.56	0.55	0.58	0.59	0.41	0.42	0.41	0.33	0.38	0.31	0.42	0.33
Nd	1.15	1.39	1.11	1.73	2.08	0.90	1.36	0.96	1.11	1.04	0.96	1.29	0.63
Sm	0.16	0.17	bdl.	0.23	0.10	bdl.	bdl.	bdl.	bdl.	bdl.	bdl.	0.16	bdl.
Eu	0.42	0.44	0.22	0.36	0.54	0.36	0.33	0.44	0.53	0.47	0.42	0.46	0.52
Gd	0.08	0.13	bdl.	bdl.	bdl.	0.11	0.13	0.18	0.17	bdl.	bdl.	bdl.	bdl.
Tb	bdl.	bdl.	bdl.	bdl.	bdl.	bdl.	bdl.	bdl.	bdl.	bdl.	0.01	bdl.	bdl.
Dy	0.05	0.10	bdl.	bdl.	bdl.	0.04	bdl.	bdl.	bdl.	bdl.	bdl.	bdl.	bdl.
Ho	bdl.	bdl.	bdl.	bdl.	bdl.	0.03	bdl.	0.03	bdl.	bdl.	0.02	bdl.	0.03
Er	bdl.	bdl.	bdl.	bdl.	bdl.	0.05	bdl.	bdl.	0.12	bdl.	bdl.	bdl.	bdl.
Tm	bdl.	bdl.	bdl.	bdl.	bdl.	bdl.	bdl.	bdl.	bdl.	bdl.	0.02	bdl.	bdl.
Yb	bdl.	bdl.	bdl.	bdl.	bdl.	0.08	bdl.	bdl.	bdl.	bdl.	bdl.	bdl.	bdl.
Lu	bdl.	bdl.	bdl.	bdl.	bdl.	bdl.	bdl.	bdl.	bdl.	0.03	bdl.	bdl.	bdl.
Hf	bdl.	bdl.	bdl.	bdl.	bdl.	0.13	bdl.	bdl.	bdl.	bdl.	bdl.	bdl.	bdl.
Ta	bdl.	bdl.	bdl.	bdl.	bdl.	bdl.	bdl.	bdl.	bdl.	bdl.	bdl.	bdl.	bdl.
Pb	3.68	3.66	3.55	3.57	3.51	11.44	12.15	11.97	13.44	12.46	11.16	11.91	10.97
Th	bdl.	bdl.	bdl.	bdl.	bdl.	bdl.	bdl.	bdl.	0.04	0.03	bdl.	bdl.	0.02
U	bdl.	bdl.	bdl.	bdl.	bdl.	bdl.	bdl.	bdl.	bdl.	bdl.	bdl.	bdl.	bdl.

T1 – Traverse 1

Appendix 2.2: Trace element composition of mineral phases from Finero dykes (contd.)

Grouping	HFSE-rich dyke												
Rock type	Dioritic dyke												
Sample	FI1603	FI1603	FI1603	FI1603	FI1603	FI1603	FI1603	FI1603	FI1603	FI1603	FI1603	FI1603	FI1603
Thin section	FI1603A	FI1603A	FI1603A	FI1603A	FI1603A	FI1603A	FI1603A	FI1603A	FI1603A	FI1603A	FI1603B	FI1603B	FI1603B
Phase	Amph	Amph	Amph	Amph	Amph	Amph	Amph	Amph	Amph	Amph	Amph	Amph	Amph
Spot No.	10	10	11	11	16	16	20	20	24	24	2	2	2
Analysis No.	42	43	44a	44b	65	66	67	68	69	70	3	4a	4b
Sc	14.1	14.0	13.5	12.1	13.6	13.2	10.3	10.8	11.4	11.6	11.2	11.1	10.6
Ti	3259	3217	3473	3371	3334	3249	4208	4272	4219	3950	5839	6291	5911
V	86.4	86.3	85.4	81.6	83.3	87.0	67.3	67.5	79.5	75.4	79.4	77.8	74.0
Cr	689	698	417	407	722	741	424	402	431	361	200	186	156
Co	34.6	33.8	37.7	35.7	35.0	34.6	32.7	33.9	35.2	35.4	40.6	38.0	35.9
Ni	428	424	446	417	415	399	373	378	404	402	450	427	416
Zn	45.0	46.1	52.6	49.0	46.8	47.9	50.3	58.3	53.4	55.3	67.4	58.9	53.6
Rb	6.73	3.39	9.49	11.65	6.78	7.10	4.02	18.55	9.76	17.69	22.08	6.07	3.86
Sr	644	656	634	606	665	642	648	604	594	558	632	684	728
Y	30.6	31.1	27.0	26.8	29.7	30.5	27.1	26.2	25.5	26.5	33.2	33.1	34.5
Zr	365	377	336	349	368	347	403	371	369	365	559	549	596
Nb	209	213	227	218	216	214	200	193	206	202	222	218	218
Cs	0.12	0.22	0.12	0.25	0.17	0.36	0.04	0.44	0.28	0.48	0.55	0.09	0.07
Ba	130	96	150	145	125	120	115	209	149	210	328	197	192
La	17.7	18.1	16.9	17.0	17.5	18.3	16.6	15.0	17.0	17.8	17.9	18.4	32.8
Ce	47.2	48.8	51.2	50.7	48.3	49.5	46.8	43.6	52.5	50.0	55.9	54.4	77.4
Pr	6.73	6.89	7.06	6.97	6.89	6.97	6.50	6.24	7.12	6.90	7.96	7.75	9.86
Nd	34.2	35.2	33.9	34.4	34.2	35.3	32.5	31.0	33.0	32.8	40.9	38.0	44.6
Sm	8.63	8.98	8.51	8.35	8.40	8.55	7.70	7.46	8.14	7.93	10.19	9.42	10.62
Eu	3.01	3.10	3.02	3.15	3.03	3.25	2.86	2.82	2.93	3.22	3.69	3.39	3.78
Gd	7.36	7.45	6.65	6.57	7.22	7.36	6.10	6.78	6.47	6.38	8.14	7.50	8.12
Tb	1.16	1.08	1.01	1.07	1.10	1.14	0.99	1.03	1.00	0.95	1.27	1.25	1.31
Dy	6.55	6.48	5.92	5.92	6.26	6.35	6.14	5.90	5.82	5.68	7.49	7.07	7.68
Ho	1.26	1.33	1.13	1.15	1.31	1.30	1.20	1.20	1.07	1.14	1.41	1.35	1.41
Er	3.58	3.55	2.96	3.10	3.30	3.24	3.47	2.97	3.25	3.03	3.98	3.84	4.25
Tm	0.48	0.51	0.44	0.42	0.43	0.47	0.48	0.41	0.44	0.44	0.50	0.52	0.55
Yb	3.35	3.59	3.07	3.07	3.34	3.31	3.04	2.95	2.95	2.65	3.44	3.77	3.70
Lu	0.46	0.47	0.40	0.43	0.44	0.50	0.43	0.39	0.35	0.46	0.48	0.49	0.50
Hf	5.76	6.67	5.87	6.36	6.75	6.37	9.40	9.20	8.25	7.59	14.91	13.00	14.28
Ta	8.87	9.34	7.95	7.39	9.93	9.50	8.64	8.38	8.12	8.17	10.25	9.79	10.91
Pb	n.d.	n.d.	n.d.	n.d.	n.d.	n.d.	n.d.	n.d.	n.d.	n.d.	n.d.	n.d.	n.d.
Th	0.34	0.39	0.33	0.36	0.41	0.39	0.31	0.38	0.33	0.38	0.44	0.45	1.16
U	0.06	0.05	0.08	0.07	0.06	0.06	0.10	0.10	0.08	0.06	0.10	0.09	0.49

Appendix 2.2: Trace element composition of mineral phases from Finero dykes (contd.)

Grouping	HFSE-rich dyke												
Rock type	Dioritic dyke												
Sample	FI1603	FI1603	FI1603	FI1603	FI1603	FI1603	FI1603	FI1603	FI1603	FI1603	FI1603	FI1603	FI1603
Thin section	FI1603B	FI1603B	FI1603B	FI1603B	FI1603B	FI1603B	FI1603B	FI1603C	FI1603C	FI1603C	FI1603C	FI1603C	FI1603C
Phase	Amph	Amph	Amph	Amph	Amph	Amph	Amph	Amph	Amph	Amph	Amph	Amph	Amph
Spot No.	3	3	6	6	10	10	13	3	8	8	9	9	12
Analysis No.	7	8	19	20	33	34	40	8	29	30	31	32	35a
Sc	8.3	8.1	12.1	12.0	11.2	11.2	10.6	11.6	11.4	11.4	11.9	13.1	10.7
Ti	4271	4145	8237	7640	6206	7701	7029	6561	7489	6098	6804	7243	7193
V	55.7	57.1	70.9	69.9	80.2	75.5	69.6	75.3	72.3	67.9	73.8	81.8	80.2
Cr	245	232	188	169	203	202	170	156	157	135	133	156	138
Co	27.8	27.5	35.2	34.8	39.2	38.5	34.6	35.1	36.0	33.3	33.0	36.2	36.2
Ni	307	299	394	379	406	370	360	432	402	357	344	364	400
Zn	44.0	39.3	52.6	55.1	61.6	58.8	54.1	54.6	63.6	48.5	53.0	54.0	61.6
Rb	16.59	3.49	12.73	4.77	9.84	5.68	3.04	11.80	7.57	13.79	2.58	3.74	9.49
Sr	432	437	610	600	580	608	672	708	763	554	644	674	901
Y	22.7	21.5	47.4	44.2	35.9	34.1	36.8	33.6	41.3	46.3	35.4	38.4	33.4
Zr	424	389	794	758	466	631	689	612	740	774	656	690	498
Nb	148	159	240	250	235	227	241	223	228	206	212	237	223
Cs	0.47	0.06	0.23	0.05	0.21	0.10	0.02	0.36	0.21	0.51	0.01	0.06	0.19
Ba	209	102	310	214	190	218	225	230	232	204	167	170	384
La	12.9	12.4	22.4	21.2	17.9	17.8	19.8	18.2	20.6	18.6	18.0	19.5	18.5
Ce	38.7	37.1	60.7	60.3	59.8	60.8	58.1	52.8	55.1	51.1	50.7	57.2	56.7
Pr	5.29	5.00	8.98	8.59	8.18	7.79	8.33	7.38	7.90	7.28	7.10	7.94	7.75
Nd	25.5	25.1	45.2	43.5	39.4	37.5	40.8	37.3	40.9	38.3	36.4	39.0	38.6
Sm	6.17	6.31	11.33	11.44	10.58	9.92	10.62	9.19	10.62	10.35	9.08	9.42	9.24
Eu	2.29	2.31	3.94	4.09	3.73	3.52	3.63	3.32	3.47	3.59	3.36	3.66	3.26
Gd	5.15	5.16	10.74	9.99	8.11	7.44	8.30	7.98	9.07	8.66	7.37	8.08	7.34
Tb	0.81	0.86	1.58	1.56	1.25	1.26	1.34	1.19	1.39	1.46	1.17	1.32	1.18
Dy	4.87	4.75	9.47	9.49	7.64	7.21	7.75	7.41	7.93	8.68	6.90	7.67	6.88
Ho	0.95	0.89	1.94	1.89	1.44	1.42	1.48	1.42	1.65	1.71	1.42	1.54	1.43
Er	2.59	2.51	5.55	5.12	3.98	3.90	3.95	3.92	4.57	5.30	3.98	4.42	3.82
Tm	0.38	0.32	0.78	0.73	0.59	0.52	0.61	0.53	0.65	0.71	0.58	0.54	0.59
Yb	2.62	2.54	5.35	4.88	3.86	4.10	4.40	3.82	4.52	4.80	4.10	4.54	3.96
Lu	0.30	0.31	0.72	0.62	0.53	0.53	0.53	0.51	0.65	0.67	0.54	0.57	0.53
Hf	11.03	10.61	19.25	19.86	13.61	17.44	17.52	15.48	17.71	18.76	13.94	14.57	7.72
Ta	7.00	7.32	12.55	12.22	11.18	11.11	11.98	10.73	11.77	10.97	10.54	10.90	8.70
Pb	n.d.	n.d.	n.d.	n.d.	n.d.	n.d.	n.d.	n.d.	n.d.	n.d.	n.d.	n.d.	n.d.
Th	0.69	0.30	0.61	0.53	0.34	0.46	0.40	0.42	0.60	0.91	0.40	0.40	0.42
U	0.22	0.07	0.09	0.09	0.11	0.16	0.08	0.10	0.17	0.22	0.08	0.08	0.12

Appendix 2.2: Trace element composition of mineral phases from Finero dykes (contd.)

Grouping	HFSE-rich dyke											
Rock type	Dioritic dyke											
Sample	FI1604	FI1604	FI1604	FI1604	FI1604	FI1604	FI1605	FI1605	FI1605	FI1605	FI1605	FI1605
Thin section	FI1604C	FI1604C	FI1604C	FI1604C	FI1604C	FI1604C	FI1605A2	FI1605A2	FI1605A2	FI1605A2	FI1605A2	FI1605A2
Phase	Amph	Amph	Amph	Amph	Amph	Amph	Amph	Amph	Amph	Amph	Amph	Amph
Spot No.	11	11	19	18	17	14	1	2	2	2	3	3
Analysis No.	1a	1b	1	1	4	1	1	1	2	3	1	2
Sc	14.5	13.9	13.2	11.9	12.8	12.6	11.1	12.2	12.4	11.3	11.6	12.0
Ti	2755	2536	2982	2431	3712	3147	4115	3831	4186	4110	3814	3968
V	69.9	63.4	63.7	59.7	65.8	66.4	67.2	64.0	67.1	67.6	63.0	67.1
Cr	84	74	183	205	162	401	374	460	316	407	416	406
Co	38.2	37.2	36.3	35.6	37.3	35.6	33.7	33.9	33.7	36.3	35.2	36.6
Ni	595	585	567	550	559	557	522	502	504	515	487	525
Zn	66.0	63.8	59.3	65.1	65.4	62.8	59.0	56.1	56.7	61.9	60.4	62.7
Rb	2.14	2.25	2.44	2.85	2.10	2.57	2.27	2.14	1.94	5.40	2.63	2.06
Sr	600	587	581	618	600	594	570	580	583	567	610	562
Y	26.0	26.3	23.5	26.2	26.0	25.8	25.5	24.8	28.2	22.4	25.2	23.5
Zr	273	268	309	260	423	314	337	349	372	327	360	325
Nb	152	147	175	177	189	177	173	180	183	174	189	176
Cs	0.00	0.01	0.00	0.01	0.01	0.01	0.02	0.01	0.02	0.02	0.02	0.01
Ba	69	79	73	88	81	84	75	79	77	105	88	78
La	13.4	13.8	12.3	13.9	13.7	14.0	14.9	13.9	15.4	12.8	14.4	14.1
Ce	42.2	41.5	38.9	39.9	42.3	42.2	42.3	41.7	45.1	43.2	42.6	46.1
Pr	6.11	6.01	5.68	5.95	6.19	5.81	6.23	6.05	6.54	6.14	6.28	6.26
Nd	28.7	29.7	26.8	27.1	28.0	27.9	31.4	28.3	29.2	27.2	28.2	28.6
Sm	6.59	7.19	5.90	6.88	6.50	6.61	7.33	6.66	7.19	6.48	6.81	7.04
Eu	2.78	2.64	2.34	2.62	2.58	2.26	2.40	2.41	2.47	2.34	2.41	2.62
Gd	5.65	5.79	5.35	6.10	5.85	5.40	5.04	5.86	6.25	5.89	5.72	5.45
Tb	0.97	0.98	0.86	0.91	0.92	0.99	0.92	0.84	1.00	0.94	0.84	0.82
Dy	5.60	5.63	4.84	5.87	5.95	5.62	5.52	5.33	5.65	4.84	5.11	5.05
Ho	1.08	1.00	0.95	0.99	1.05	1.02	0.97	1.02	1.14	1.06	1.07	0.96
Er	2.65	2.80	2.40	2.57	2.85	3.04	2.78	2.66	2.71	2.29	2.38	2.55
Tm	0.39	0.41	0.29	0.34	0.35	0.34	0.34	0.35	0.41	0.31	0.40	0.31
Yb	2.45	2.37	2.30	2.53	2.70	2.98	2.65	2.36	2.97	2.12	2.37	2.47
Lu	0.34	0.37	0.28	0.38	0.45	0.29	0.44	0.34	0.41	0.38	0.36	0.30
Hf	4.49	4.86	7.87	3.93	9.25	6.12	7.56	7.38	8.06	7.89	7.20	7.45
Ta	4.41	4.31	6.20	4.23	8.72	6.40	6.29	6.11	6.48	6.01	6.51	5.84
Pb	2.03	1.85	2.16	2.00	2.03	1.91	1.94	2.19	2.46	2.01	2.65	2.29
Th	0.32	0.31	0.27	0.36	0.29	0.32	0.43	0.40	0.45	0.35	0.37	0.37
U	0.09	0.08	0.06	0.12	0.07	0.05	0.06	0.06	0.07	0.10	0.09	0.08

Appendix 2.2: Trace element composition of mineral phases from Finero dykes (contd.)

Grouping	HFSE-rich dyke											
Rock type	Dioritic dyke											
Sample	FI1605	FI1605	FI1605	FI1605	FI1605	FI2102	FI2102	FI2102	FI2102	FI2102	FI2102	FI2102
Thin section	FI1605A2	FI1605A2	FI1605A2	FI1605A2	FI1605A2	FI2102C	FI2102C	FI2102C	FI2102C	FI2102C	FI2102C	FI2102C
Phase	Amph	Amph	Amph	Amph	Amph	Amph	Amph	Amph	Amph	Amph	Amph	Amph
Spot No.	4	9	10	10	11	2	2	3	5	5	7	8
Analysis No.	1	2	2	3	1	2a	2b	5a	11a	11b	17	19
Sc	11.7	12.9	10.6	12.2	10.9	10.1	9.5	11.8	9.6	10.2	12.3	12.2
Ti	5149	4684	4659	4788	4230	980	1006	1602	1147	1096	2713	3148
V	63.5	64.3	64.9	69.8	66.7	76.3	74.2	77.5	77.6	76.9	84.6	83.6
Cr	305	390	229	255	195	40	51	571	61	55	923	849
Co	35.4	32.6	33.9	36.8	36.4	32.6	30.6	31.9	32.7	30.4	32.0	31.2
Ni	495	441	502	514	517	340	354	363	365	335	380	357
Zn	59.8	52.5	56.2	60.7	61.0	39.7	35.5	40.5	38.1	36.3	36.0	38.6
Rb	2.45	2.03	2.34	2.45	2.44	2.03	2.23	2.17	2.56	1.54	1.99	1.68
Sr	652	551	625	614	600	751	732	721	707	584	748	733
Y	29.3	29.5	29.1	28.5	24.8	27.0	26.1	24.9	24.3	26.4	28.0	31.8
Zr	809	340	573	542	466	135	136	156	130	135	235	286
Nb	212	177	203	201	190	150	150	207	174	155	177	173
Cs	0.01	0.01	0.01	0.01	0.00	0.01	0.01	0.01	0.03	0.01	0.01	0.01
Ba	100	81	102	94	95	53.8	58.5	58.3	63.6	42.4	59.8	57.8
La	14.9	14.5	13.7	14.5	13.8	13.8	13.6	13.2	15.8	14.8	13.8	14.6
Ce	43.0	43.8	42.9	44.4	43.9	41.3	39.9	37.8	44.3	42.8	40.5	43.1
Pr	6.39	6.25	6.31	6.41	6.33	6.06	5.63	5.54	6.24	6.23	6.26	6.59
Nd	30.9	31.5	30.3	30.6	27.9	28.1	28.4	24.8	28.9	28.3	29.2	33.0
Sm	7.63	7.49	7.36	7.45	6.68	6.74	6.98	6.43	6.15	5.73	7.23	7.78
Eu	2.52	2.73	2.85	2.70	2.81	2.28	2.34	2.31	2.41	2.67	2.74	2.88
Gd	7.00	7.22	6.38	6.47	6.14	5.97	5.23	5.66	6.32	5.95	6.17	6.65
Tb	1.02	1.16	1.12	1.04	0.92	0.84	0.90	0.86	0.79	0.98	0.94	1.14
Dy	6.39	6.22	6.23	6.58	5.37	6.09	5.49	5.00	4.76	5.13	5.72	6.14
Ho	1.28	1.07	1.06	1.28	1.09	1.04	1.03	0.87	0.87	0.98	1.13	1.32
Er	3.10	2.82	3.50	2.87	2.67	2.84	2.69	2.97	2.69	2.40	2.73	2.71
Tm	0.41	0.49	0.38	0.44	0.39	0.28	0.39	0.35	0.34	0.33	0.49	0.46
Yb	2.81	3.69	2.87	2.50	2.52	2.54	3.06	2.49	1.89	2.41	2.92	3.58
Lu	0.38	0.43	0.52	0.33	0.35	0.39	0.40	0.37	0.33	0.37	0.42	0.37
Hf	21.40	13.83	14.36	14.65	11.05	1.18	1.40	1.73	1.09	1.33	3.53	5.68
Ta	12.38	9.27	9.94	9.80	9.24	2.67	2.79	5.90	3.20	2.94	5.19	6.35
Pb	2.27	2.21	2.19	2.44	2.36	1.67	1.47	1.66	1.51	1.39	1.63	1.43
Th	0.37	0.42	0.43	0.37	0.39	0.35	0.31	0.28	0.34	0.41	0.37	0.36
U	0.09	0.07	0.14	0.08	0.09	0.08	0.10	0.07	0.13	0.04	0.07	0.07

Appendix 2.2: Trace element composition of mineral phases from Finero dykes (contd.)

Grouping	HFSE-rich dyke										
Rock type	Dioritic dyke										
Sample	FI2103	FI2103	FI2103	FI2103	FI2103	FI2103	FI2103	FI2103	FI2103	FI2103	FI2103
Thin section	FI2103C	FI2103C	FI2103C	FI2103C	FI2103C	FI2103C	FI2103C	FI2103C	FI2103C	FI2103C	FI2103C
Phase	Amph	Amph	Amph	Amph	Amph	Amph	Amph	Amph	Amph	Amph	Amph
Spot No.	1	1	6	7	7	8	8	8	9	10	11
Analysis No.	1a	1b	1	1a	1b	1a	1b	2	1	1	1
Sc	9.6	10.1	9.9	11.2	11.3	11.0	10.5	10.9	11.9	12.3	11.5
Ti	3281	3274	2957	3281	3162	2528	2560	2781	2693	2598	2608
V	64.0	66.4	66.2	67.3	68.9	65.0	67.2	66.9	70.0	70.6	72.0
Cr	154	148	46	181	244	800	811	879	1498	787	1073
Co	32.9	32.9	33.0	34.5	32.0	31.2	32.6	31.2	33.5	31.9	32.1
Ni	385	375	378	403	386	372	393	390	409	402	403
Zn	40.3	39.9	44.1	40.9	38.6	34.2	40.6	37.0	38.0	40.4	36.6
Rb	1.70	1.93	2.38	1.99	1.74	1.82	2.09	1.85	2.18	1.70	2.16
Sr	615	643	699	659	603	584	626	629	670	670	725
Y	28.3	27.6	29.8	29.0	30.4	26.1	25.7	29.7	27.2	29.0	27.4
Zr	315	330	297	364	345	259	249	281	250	225	261
Nb	182	190	199	174	177	158	162	165	157	145	152
Cs	0.01	0.02	0.01	0.01	0.02	0.01	0.01	0.01	0.01	0.01	0.01
Ba	76.4	78.7	80.8	77.4	68.8	56.8	61.2	62.9	71.2	63.2	74.2
La	16.8	16.6	16.0	16.2	16.8	15.8	15.6	16.4	16.2	17.0	16.9
Ce	50.0	49.3	47.2	48.7	50.3	47.1	47.5	50.8	50.4	51.0	50.1
Pr	7.22	7.16	6.69	7.10	7.13	6.41	6.61	7.06	7.06	7.13	7.10
Nd	33.3	33.5	31.2	31.6	33.1	30.7	29.3	32.3	32.1	33.5	34.1
Sm	7.20	7.66	8.36	7.03	7.71	7.79	6.74	6.95	6.12	8.34	7.76
Eu	2.81	2.77	2.51	2.66	2.89	2.77	2.50	3.06	2.54	2.54	2.64
Gd	5.64	5.11	5.74	6.74	6.30	5.60	5.59	6.71	5.55	5.99	6.60
Tb	0.76	0.97	0.97	1.00	1.07	0.91	0.92	1.08	0.90	0.98	1.03
Dy	6.22	6.22	5.66	4.99	5.95	4.97	4.99	6.35	5.37	5.83	5.67
Ho	1.19	1.04	1.22	1.12	1.27	0.97	1.07	1.22	1.17	1.11	0.93
Er	3.11	3.10	2.94	3.41	2.94	3.08	2.58	3.00	2.89	2.93	3.07
Tm	0.38	0.43	0.53	0.52	0.47	0.31	0.44	0.44	0.45	0.45	0.38
Yb	2.85	3.72	2.99	2.95	3.17	3.15	2.42	3.90	2.47	2.54	2.96
Lu	0.42	0.40	0.45	0.49	0.39	0.40	0.36	0.41	0.47	0.47	0.34
Hf	6.05	7.30	5.67	9.47	9.06	3.49	3.84	4.69	5.06	3.63	6.63
Ta	6.49	6.00	7.65	7.40	6.50	6.23	5.76	6.01	7.32	3.97	6.11
Pb	1.35	1.12	1.44	1.40	1.36	1.26	1.36	1.06	1.22	1.49	1.17
Th	0.30	0.43	0.26	0.28	0.26	0.40	0.24	0.28	0.25	0.27	0.28
U	0.06	0.03	0.05	0.07	0.10	0.10	0.05	0.06	0.05	0.06	0.05

Appendix 2.2: Trace element composition of mineral phases from Finero dykes (contd.)

Grouping	HFSE-rich dyke												
Rock type	Dioritic dyke												
Sample	FI2104	FI2104	FI2104	FI2104	FI2104	FI2104	FI2104	FI2104	FI2104	FI2104	FI2104	FI2104	FI2104
Thin section	FI2104B	FI2104B	FI2104B	FI2104B	FI2104B	FI2104B	FI2104B	FI2104B	FI2104B	FI2104B	FI2104B	FI2104B	FI2104C
Phase	Amph	Amph	Amph	Amph	Amph	Amph	Amph	Amph	Amph	Amph	Amph	Amph	Amph
Spot No.	4	4	5	5	7	8	10	11	12	13	14	15	2
Analysis No.	5a	5b	8a	8b	15	16	22	24	26	27	30	33	1a
Sc	15.2	14.8	15.8	15.0	13.4	13.5	13.8	13.3	13.8	14.7	14.3	13.4	10.2
Ti	3531	3429	3407	3545	3246	3205	3174	3167	3225	3126	2958	2881	5162
V	69.8	69.6	66.2	66.0	67.0	64.8	68.1	64.7	67.8	67.8	69.2	65.8	68.5
Cr	165	169	174	150	242	422	272	355	334	401	349	1007	34
Co	33.3	33.0	32.6	31.5	32.8	32.8	31.5	29.9	32.8	32.5	29.7	32.2	33.8
Ni	384	381	362	364	366	375	370	357	375	389	376	381	364
Zn	44.3	45.1	46.4	45.3	44.7	43.4	43.6	42.9	45.7	43.7	42.2	41.2	50.0
Rb	2.17	2.28	2.07	2.45	2.07	2.23	2.85	1.55	1.74	2.12	1.73	2.01	2.77
Sr	690	680	697	711	715	693	750	620	670	686	606	646	714
Y	35.0	33.3	32.7	34.5	33.8	32.2	32.7	38.2	34.1	35.5	37.7	34.3	39.8
Zr	363	364	337	373	353	331	349	346	347	356	339	322	507
Nb	185	197	175	192	177	181	191	175	175	187	177	176	254
Cs	0.01	0.01	0.01	0.01	0.01	0.00	0.01	0.01	0.01	0.01	0.01	0.01	0.02
Ba	85.6	90.7	74.6	88.9	79.0	72.4	84.2	62.7	70.4	74.5	67.8	62.5	114
La	18.2	17.9	16.9	17.5	17.5	16.8	18.1	17.8	17.3	17.4	17.2	17.2	17.2
Ce	51.3	52.0	47.5	48.9	49.0	48.4	48.3	51.2	50.0	49.4	52.1	48.9	51.4
Pr	7.66	7.57	7.05	7.42	7.12	6.97	6.98	7.77	7.42	7.18	7.87	7.17	7.64
Nd	35.7	35.4	38.0	33.1	35.2	32.9	32.4	35.7	35.2	34.8	36.0	34.1	36.7
Sm	7.78	8.46	8.29	8.35	7.91	7.62	7.24	7.60	7.92	7.62	8.87	7.98	9.04
Eu	3.07	3.00	2.77	2.79	2.69	2.76	2.91	3.19	2.67	2.76	3.28	2.61	3.15
Gd	7.15	7.01	6.50	6.84	7.82	7.19	6.14	7.77	7.18	6.62	7.89	6.45	7.52
Tb	1.08	1.13	1.18	1.10	1.18	1.03	1.07	1.27	1.17	1.14	1.13	1.18	1.28
Dy	6.67	6.63	5.81	6.79	6.26	6.53	6.52	6.91	6.85	6.72	7.15	6.11	7.44
Ho	1.36	1.23	1.34	1.30	1.41	1.19	1.16	1.45	1.41	1.42	1.47	1.26	1.49
Er	3.27	3.29	3.53	3.23	3.57	3.31	3.31	3.32	3.21	3.68	3.81	3.49	3.76
Tm	0.54	0.48	0.46	0.49	0.54	0.35	0.46	0.52	0.55	0.50	0.51	0.48	0.61
Yb	3.66	3.36	3.12	3.13	3.17	3.10	3.39	3.23	3.43	3.47	3.89	3.01	3.86
Lu	0.53	0.49	0.45	0.50	0.48	0.44	0.58	0.42	0.48	0.49	0.51	0.43	0.57
Hf	7.49	9.26	7.86	7.69	7.32	6.75	6.92	7.41	6.69	5.69	6.87	5.04	8.26
Ta	7.39	7.62	7.08	7.76	7.51	7.72	8.00	7.11	6.90	6.82	6.62	6.40	8.85
Pb	1.50	1.33	1.36	1.60	1.58	1.51	1.37	1.43	1.44	1.36	1.42	1.27	1.76
Th	0.35	0.33	0.29	0.32	0.31	0.36	0.33	0.37	0.33	0.28	0.35	0.27	0.32
U	0.10	0.06	0.10	0.07	0.05	0.06	0.06	0.04	0.04	0.08	0.04	0.04	0.08

Appendix 2.2: Trace element composition of mineral phases from Finero dykes (contd.)

Grouping	HFSE-rich dyke										
Rock type	Dioritic dyke										
Sample	FI2104	FI2104	FI2104	FI2104	FI2104	FI2104	FI2104	FI2104	FI2104	FI2105	FI2105
Thin section	FI2104C	FI2104C	FI2104C	FI2104C	FI2104C	FI2104C	FI2104C	FI2104C	FI2104C	FI2105B	FI2105B
Phase	Amph	Amph	Amph	Amph	Amph	Amph	Amph	Amph	Amph	Amph	Amph
Spot No.	2	3	3	4	4	7	7	9	12	9	9
Analysis No.	1b	1a	1b	1	2	1a	1b	1	1	21a	21b
Sc	9.5	9.1	8.8	8.9	8.8	9.5	9.7	9.2	7.6	9.4	9.4
Ti	5098	4459	4535	4511	4570	5381	5474	4304	4690	7428	7203
V	68.9	61.0	62.0	59.5	60.8	61.7	64.7	62.7	62.6	76.3	76.2
Cr	26	28	27	24	29	28	30	27	20	442	363
Co	34.6	30.6	30.0	29.7	30.5	32.9	32.4	27.0	31.0	33.3	34.2
Ni	375	332	331	331	332	342	368	280	345	347	354
Zn	51.2	44.3	44.9	42.1	43.0	41.8	44.4	37.6	41.0	26.5	27.7
Rb	1.71	2.13	1.87	2.00	1.94	2.77	2.82	1.47	2.15	2.22	2.39
Sr	715	630	633	575	658	668	694	484	606	688	731
Y	41.5	35.9	35.2	34.0	35.4	38.2	40.0	42.0	33.2	33.3	32.7
Zr	533	474	470	462	462	473	468	379	455	377	386
Nb	259	218	213	229	223	237	249	236	225	217	223
Cs	0.01	0.01	0.01	0.01	0.02	0.01	0.01	0.01	0.02	0.01	0.01
Ba	91.6	111	90.2	88.4	90.6	120	135	64.4	103	89.5	91.3
La	17.0	14.7	14.4	14.9	15.2	15.7	16.7	15.4	15.1	20.7	20.2
Ce	50.2	43.5	43.2	44.6	44.0	47.2	49.2	48.2	47.4	60.8	59.0
Pr	7.51	6.52	6.64	6.90	6.98	7.06	7.39	7.82	7.21	8.25	8.59
Nd	38.6	32.7	31.0	32.2	32.1	35.8	37.7	35.4	32.7	39.2	38.9
Sm	9.72	7.40	7.79	7.86	8.02	8.14	9.37	9.50	8.22	9.07	8.84
Eu	3.27	2.71	2.87	2.80	2.84	2.86	3.02	3.28	3.06	3.12	3.55
Gd	7.94	7.51	6.75	6.82	6.99	8.12	8.60	8.72	7.83	7.92	7.58
Tb	1.28	1.25	1.18	1.21	1.20	1.34	1.31	1.36	1.11	1.24	1.27
Dy	8.26	7.64	7.37	7.16	7.07	7.59	8.42	8.34	7.19	7.57	7.93
Ho	1.59	1.41	1.38	1.33	1.36	1.62	1.63	1.82	1.42	1.28	1.33
Er	3.97	3.73	3.95	3.54	3.56	4.03	4.33	4.45	3.46	2.97	3.51
Tm	0.58	0.46	0.56	0.52	0.43	0.54	0.56	0.56	0.48	0.57	0.48
Yb	3.81	3.56	3.36	3.38	3.69	3.93	3.84	4.81	3.39	2.96	3.21
Lu	0.53	0.53	0.42	0.52	0.51	0.54	0.54	0.61	0.50	0.48	0.50
Hf	8.41	7.72	7.96	7.26	7.77	6.39	6.99	7.58	6.61	11.76	12.87
Ta	9.45	8.25	8.18	8.43	8.67	8.47	8.09	9.07	7.67	8.65	8.90
Pb	1.63	1.33	1.57	1.34	1.50	1.41	1.72	1.25	1.56	2.04	2.07
Th	0.31	0.34	0.36	0.34	0.33	0.32	0.41	0.32	0.32	0.52	0.55
U	0.06	0.06	0.06	0.08	0.07	0.07	0.09	0.04	0.05	0.07	0.13

Appendix 2.2: Trace element composition of mineral phases from Finero dykes (contd.)

Grouping	HFSE-rich dyke												
Rock type	Dioritic dyke									Cpxnite cumulate in HFSE-rich dioritic dyke			
Sample	FI2105	FI2105	FI2105	FI2105	FI2105	FI2105	FI2105	FI2105	FI2105	FI1604	FI1604	FI2105	FI2105
Thin section	FI2105B	FI2105B	FI2105B	FI2105B	FI2105B	FI2105B	FI2105B	FI2105B	FI2105B	FI1604C*	FI1604C*	FI2105B*	FI2105B*
Phase	Amph	Amph	Amph	Amph	Amph	Amph	Amph	Amph	Amph	Amph	Amph	Amph	Amph
Spot No.	10	11	12	13	14	15	16	17	18	4	4	3	3
Analysis No.	23	25	26	27	28	29	30	32	33	1a	1b	7a	7b
Sc	9.1	12.1	11.0	11.6	11.8	11.7	8.1	9.7	10.6	17.9	17.0	22.3	20.1
Ti	7182	6758	6958	6493	6876	6806	7217	7225	6941	3280	3292	3702	3897
V	73.2	89.6	76.9	76.4	80.3	81.3	65.2	69.6	74.9	78.2	76.9	143	134
Cr	578	416	357	1983	1698	1362	238	261	477	1820	2012	3784	3801
Co	32.1	31.2	31.8	33.2	34.3	33.1	30.0	32.4	30.5	35.9	36.2	32.2	28.4
Ni	401	436	411	489	498	443	316	306	322	651	642	696	667
Zn	29.3	26.2	28.8	35.5	34.1	32.4	26.1	28.4	26.8	71.0	71.3	41.7	32.7
Rb	2.21	2.11	1.81	2.12	2.43	1.97	2.37	2.29	1.99	2.20	1.89	1.94	1.39
Sr	743	683	729	719	749	718	716	728	714	594	533	600	590
Y	31.9	37.7	33.0	27.5	29.9	28.9	31.1	32.1	33.1	20.8	21.9	30.2	30.9
Zr	449	378	459	319	379	403	497	494	469	244	213	262	258
Nb	217	235	222	197	218	218	211	225	221	207	159	123	125
Cs	0.02	0.02	0.02	0.01	0.02	0.01	0.01	0.01	0.01	0.01	0.00	0.02	0.01
Ba	90.1	80.4	93.9	78.2	94.9	94.7	102.9	90.4	89.3	64.5	60.1	52.0	52.0
La	19.6	22.6	19.9	16.9	17.5	17.6	20.4	19.6	19.1	11.4	11.6	16.0	14.8
Ce	55.2	63.7	53.8	45.2	48.0	45.9	54.1	56.1	57.1	34.4	36.7	45.0	43.7
Pr	8.11	9.07	7.43	6.73	7.00	6.75	7.67	8.14	7.89	5.17	5.11	7.47	6.61
Nd	38.4	44.6	37.4	31.4	34.9	31.9	37.7	38.8	41.2	23.3	24.1	32.1	31.5
Sm	8.96	10.00	8.28	6.59	8.15	6.52	8.05	9.06	10.15	5.96	6.44	8.40	8.07
Eu	2.93	3.62	3.10	2.83	2.78	2.80	3.00	3.06	3.43	2.00	2.21	3.34	3.22
Gd	7.74	9.73	8.23	6.65	6.86	5.82	6.58	7.58	7.74	5.11	4.16	7.70	6.61
Tb	1.23	1.40	1.09	1.08	1.00	1.11	1.27	1.09	1.22	0.76	0.82	1.31	1.09
Dy	6.92	8.20	6.95	6.31	6.33	6.40	6.43	6.84	7.37	4.60	4.52	7.56	6.38
Ho	1.35	1.58	1.54	1.15	1.25	1.15	1.30	1.42	1.47	0.85	0.90	1.24	1.22
Er	3.11	4.00	3.75	3.30	3.44	2.68	3.48	3.45	3.39	2.26	2.51	2.43	3.06
Tm	0.48	0.60	0.49	0.44	0.52	0.40	0.46	0.46	0.56	0.29	0.33	0.43	0.41
Yb	3.78	3.59	3.73	2.89	3.14	2.84	3.92	3.59	3.23	1.80	2.12	2.81	2.89
Lu	0.44	0.48	0.55	0.38	0.38	0.37	0.51	0.42	0.45	0.27	0.27	0.44	0.36
Hf	10.43	10.28	11.49	5.91	6.03	7.72	12.67	11.83	11.54	4.49	4.03	6.10	4.63
Ta	8.18	9.74	9.01	7.34	7.79	8.33	9.08	9.21	8.50	7.06	5.55	3.83	3.90
Pb	1.91	1.68	2.27	2.02	2.24	2.09	1.81	1.74	1.91	2.26	2.07	1.92	1.50
Th	0.59	0.63	0.73	0.43	0.52	0.41	0.59	0.54	0.65	0.27	0.25	0.23	0.23
U	0.13	0.10	0.15	0.07	0.10	0.11	0.13	0.07	0.09	0.06	0.05	0.04	0.03

Appendix 2.2: Trace element composition of mineral phases from Finero dykes (contd.)

Grouping	HFSE-rich dyke											
Rock type	Hornblendite dyke with olivine layer (Amph close to Ol)					Hornblendite dyke with olivine layer (Amph far from Ol)						
Sample	FI1501	FI1501	FI1501	FI1501	FI1501	FI1501	FI1501	FI1501	FI1501	FI1501	FI1501	FI1501
Thin section	FI1501B	FI1501B	FI1501B	FI1501B	FI1501B	FI1501B	FI1501B	FI1501B	FI1501B	FI1501B	FI1501B	FI1501B
Phase	Amph	Amph	Amph	Amph	Amph	Amph	Amph	Amph	Amph	Amph	Amph	Amph
Spot No.	1	2	3	4	5	6	7	7	8	8	8	9
Analysis No.	1	4	6	9	10	11	14	13	16a	16b	16c	19
Sc	38.4	33.9	34.9	33.7	35.6	43.5	51.0	43.6	41.7	39.7	39.4	37.7
Ti	8925	8287	8054	8225	8903	11424	10382	11016	11008	11448	11077	11100
V	238	215	231	230	247	350	403	372	342	350	336	325
Cr	2358	1858	2109	2285	2114	326	424	676	313	337	273	370
Co	36.1	34.7	34.7	32.3	38.2	34.2	34.0	37.7	37.7	37.3	36.6	33.8
Ni	415	387	402	365	415	281	260	283	298	284	295	285
Zn	54.4	45.3	44.2	42.2	55.7	42.1	37.6	39.8	43.5	40.1	40.1	42.5
Rb	1.65	0.97	0.58	1.36	1.14	2.64	1.85	1.69	1.71	1.45	1.35	1.29
Sr	459	447	422	450	469	601	608	608	612	629	623	591
Y	22.5	20.1	20.0	19.7	21.4	32.2	36.4	34.2	31.6	30.9	31.1	30.0
Zr	131	113	113	112	128	90	85	81	99	93	94	87
Nb	162	147	148	150	151	84	70	73	97	94	95	95
Cs	0.01	0.02	0.02	0.01	0.02	0.02	0.02	0.02	0.02	0.01	0.02	0.02
Ba	54.3	29.0	25.8	46.5	40.4	103	92.3	85.5	87.4	78.9	80.3	76.6
La	10.7	9.9	9.6	10.6	11.1	14.5	14.3	14.0	14.1	14.2	13.8	13.8
Ce	31.9	28.7	29.9	32.3	31.8	42.1	42.4	43.2	42.8	43.6	41.5	41.6
Pr	4.74	4.19	4.35	4.64	4.68	6.53	6.80	6.62	6.33	6.04	6.10	6.06
Nd	22.9	22.3	20.4	22.9	23.6	31.8	33.0	31.3	30.2	30.8	29.8	27.8
Sm	5.47	6.04	5.04	5.67	6.00	8.39	9.07	8.17	8.14	8.59	7.87	8.49
Eu	1.99	1.66	1.97	1.90	2.07	2.90	3.03	2.83	2.88	2.65	2.97	2.56
Gd	5.70	4.63	4.73	4.44	6.24	7.72	8.31	7.94	7.28	7.86	6.62	6.76
Tb	0.88	0.95	0.70	0.85	0.87	1.19	1.41	1.18	0.97	1.22	1.16	1.19
Dy	5.66	4.72	4.02	4.32	4.62	6.44	8.30	7.80	6.35	6.83	6.72	6.42
Ho	0.97	0.92	0.97	0.77	0.94	1.31	1.56	1.41	1.22	1.25	1.26	0.96
Er	2.43	2.37	1.89	2.02	2.38	3.46	3.88	3.37	3.16	3.19	2.97	2.97
Tm	0.29	0.31	0.28	0.32	0.31	0.51	0.51	0.55	0.47	0.44	0.43	0.32
Yb	2.82	1.54	1.75	2.21	2.11	2.51	3.56	3.19	3.19	3.07	2.73	2.57
Lu	0.29	0.26	0.26	0.24	0.25	0.41	0.46	0.47	0.40	0.42	0.43	0.35
Hf	2.44	2.26	2.37	1.95	2.08	2.15	2.76	2.35	1.92	1.76	2.33	1.99
Ta	4.97	4.06	4.15	4.11	4.05	1.36	1.10	1.39	2.04	1.85	1.99	1.93
Pb	2.52	1.67	1.35	1.34	1.41	1.82	1.94	1.46	2.04	1.66	2.10	1.73
Th	0.22	0.20	0.15	0.18	0.21	0.46	0.54	0.52	0.32	0.40	0.37	0.41
U	0.04	0.06	0.03	0.03	0.04	0.03	0.11	0.09	0.12	0.12	0.06	0.06

Appendix 2.2: Trace element composition of mineral phases from Finero dykes (contd.)

Grouping	HFSE-rich dyke											
Rock type	Hornblendite dyke									Albite-dominated anorthosite dyke		
Sample	FI1612	FI1612	FI1612	FI1612	FI1612	FI1612	FI1612	FI1612	FI1612	FI19A02	FI19A02	FI19A04
Thin section	FI1612A	FI1612A	FI1612A	FI1612A	FI1612A	FI1612A	FI1612A	FI1612A	FI1612A	FI19A02B	FI19A02B	FI19A04A
Phase	Amph	Amph	Amph	Amph	Amph	Amph	Amph	Amph	Amph	Amph	Amph	Amph
Spot No.	1	2	2	2	3	6	7	8	10	9	9	2
Analysis No.	1	1	2	3	3	1	2	2	1	20a	20b	7a
Sc	9.4	8.3	7.7	8.8	8.8	7.8	8.7	8.1	8.9	22.5	22.1	15.9
Ti	9900	10118	10494	10820	9993	10336	9701	10491	10654	8754	8681	6610
V	78.2	67.5	67.6	75.0	70.8	65.0	65.5	66.2	65.9	111	108	83.0
Cr	414	470	444	441	438	390	402	381	409	150	156	142
Co	29.6	32.1	30.8	28.5	33.7	32.2	30.8	33.0	32.3	33.1	33.5	37.8
Ni	249	230	215	206	240	204	210	214	194	276	273	328
Zn	53.6	54.2	58.8	52.3	58.1	52.4	49.2	51.4	62.0	81.1	77.2	79.6
Rb	1.98	1.87	9.10	1.53	2.48	1.47	1.85	2.06	1.82	2.87	3.42	1.85
Sr	704	679	689	673	749	766	637	768	746	446	461	442
Y	35.6	29.6	27.1	29.5	32.3	27.4	29.4	28.3	30.4	40.9	35.1	29.8
Zr	572	504	440	452	533	463	490	480	476	1101	877	667
Nb	241	227	224	236	235	219	227	224	226	270	263	237
Cs	0.01	0.02	0.37	0.01	0.03	0.01	0.01	0.01	0.01	0.01	0.01	0.01
Ba	99.9	114	127	77.4	148	107	99	134	108	127	129	75.7
La	17.1	14.6	14.5	14.2	14.6	14.7	13.7	14.9	14.2	11.2	11.1	12.1
Ce	55.0	46.3	50.1	47.1	50.5	45.9	45.4	47.7	44.9	41.4	39.6	37.5
Pr	8.34	7.05	7.25	7.58	7.15	6.97	6.61	7.14	6.90	6.18	6.02	6.06
Nd	41.6	32.8	31.9	32.8	34.1	31.0	32.0	32.1	32.3	31.6	29.8	27.9
Sm	10.19	7.76	8.03	8.88	9.24	6.95	7.52	8.59	7.20	9.07	7.38	7.74
Eu	3.42	2.94	3.27	3.69	3.29	2.92	2.88	2.61	2.92	3.20	2.92	2.45
Gd	7.90	7.10	6.15	6.38	8.00	6.71	7.13	6.69	7.32	8.29	6.67	5.54
Tb	1.31	1.05	1.13	1.21	1.27	1.07	1.12	1.18	1.11	1.21	1.18	1.01
Dy	8.43	6.70	6.39	6.93	7.17	6.27	6.78	6.33	6.47	8.90	7.06	5.34
Ho	1.31	1.14	0.94	1.23	1.24	1.21	1.14	1.12	1.18	1.64	1.34	1.07
Er	3.54	3.45	1.95	3.18	3.58	3.44	3.04	3.00	3.28	4.47	3.79	3.45
Tm	0.55	0.50	0.48	0.53	0.41	0.39	0.43	0.43	0.34	0.73	0.70	0.37
Yb	3.30	2.43	3.01	3.40	3.28	3.18	3.20	2.78	2.49	5.29	4.64	3.14
Lu	0.49	0.48	0.49	0.46	0.42	0.40	0.38	0.39	0.46	0.70	0.72	0.46
Hf	14.73	12.16	9.40	11.37	12.70	11.59	12.31	11.70	11.30	28.99	18.17	18.21
Ta	10.19	9.29	9.07	10.07	10.03	8.46	9.30	9.23	9.57	12.73	11.93	9.92
Pb	1.86	1.83	2.00	2.13	2.33	2.06	1.78	1.73	1.76	1.08	1.27	0.73
Th	0.46	0.39	0.31	0.36	0.44	0.40	0.37	0.40	0.23	0.22	0.24	0.28
U	0.13	0.06	0.10	0.08	0.07	0.06	0.06	0.05	0.07	0.02	0.06	0.05

Appendix 2.2: Trace element composition of mineral phases from Finero dykes (contd.)

Grouping	HFSE-rich dyke					HFSE-poor dyke					
Rock type	Albite-dominated anorthosite dyke					Hornblendite dyke					
Sample	FI19A04	FI19A04	FI19A04	FI19A04	FI19A04	FI1608	FI1608	FI1608	FI1608	FI1608	FI1608
Thin section	FI19A04A	FI19A04A	FI19A04A	FI19A04A	FI19A04A	FI1608B	FI1608B	FI1608B	FI1608B	FI1608B	FI1608B
Phase	Amph	Amph	Amph	Amph	Amph	Amph	Amph	Amph	Amph	Amph	Amph
Spot No.	2	2	2	2	1	1	1	2	2	3	4
Analysis No.	7b	7c	4a	4b	1a	1a	1b	2a	2b	3	4a
Sc	17.0	15.1	13.7	16.0	16.7	40.1	40.4	44.8	44.7	44.5	44.1
Ti	6826	6580	6369	6590	6654	13223	12710	13489	14219	15092	13664
V	82.0	83.4	81.0	82.6	82.9	445	432	400	443	463	433
Cr	138	146	124	153	162	209	217	557	329	317	352
Co	35.6	37.9	36.3	35.6	35.3	48.4	43.2	51.9	52.8	52.4	54.0
Ni	357	356	323	342	333	58.8	49.4	72.9	76.7	97.0	76.3
Zn	79.4	80.6	82.3	79.7	90.9	79.8	72.1	99.1	96.6	106	101
Rb	2.28	1.93	2.93	2.82	2.83	5.44	4.81	5.88	5.17	5.51	5.73
Sr	445	406	410	450	436	463	475	348	364	311	347
Y	32.7	31.7	26.5	26.6	29.3	21.6	22.4	21.3	21.3	21.8	21.2
Zr	755	676	577	624	610	45.8	48.4	37.6	40.1	36.5	37.2
Nb	254	245	229	246	245	5.39	4.89	3.78	3.81	3.24	4.2
Cs	0.02	0.01	0.01	0.01	0.01	0.03	0.01	0.01	0.01	0.01	0.01
Ba	81.4	73.3	77.1	94.4	77.1	96.7	83.7	72.9	67.6	60.1	59.1
La	12.4	12.2	11.5	11.1	10.5	5.51	6.15	3.72	3.88	3.05	3.49
Ce	39.8	40.9	35.9	38.1	35.0	14.5	16.0	11.0	10.7	10.4	10.7
Pr	6.08	6.22	5.14	5.42	5.16	2.19	2.40	2.11	2.08	1.92	2.10
Nd	29.8	28.1	25.0	25.0	26.4	14.9	16.0	12.8	12.8	12.3	13.1
Sm	7.52	6.86	6.86	6.80	6.52	6.38	5.19	4.38	4.45	4.66	5.27
Eu	2.74	2.95	2.69	2.45	2.74	1.88	1.71	1.74	1.92	1.74	1.74
Gd	6.61	6.87	5.43	6.23	5.81	4.85	5.02	5.01	5.20	5.05	5.38
Tb	1.21	1.17	0.76	1.15	0.76	0.81	0.70	0.84	0.79	0.81	0.81
Dy	6.33	6.61	4.74	6.14	5.57	4.43	4.64	4.81	4.27	4.19	4.51
Ho	1.50	1.21	0.99	0.91	1.35	0.92	0.87	0.83	0.84	0.90	0.91
Er	3.14	3.96	3.08	2.76	2.71	2.33	2.23	2.44	2.10	2.24	2.01
Tm	0.45	0.56	0.48	0.40	0.41	0.27	0.37	0.33	0.29	0.32	0.29
Yb	2.58	3.86	3.32	2.76	2.69	2.12	2.15	1.77	1.75	2.03	2.21
Lu	0.53	0.52	0.31	0.38	0.57	0.28	0.31	0.26	0.22	0.26	0.28
Hf	18.44	16.03	14.61	24.01	14.20	1.58	1.83	1.35	1.45	1.44	1.35
Ta	10.15	9.27	9.24	11.00	8.89	0.21	0.21	0.13	0.14	0.14	0.13
Pb	1.24	1.12	1.00	1.10	0.95	3.21	2.48	2.53	3.05	2.53	2.88
Th	0.21	0.25	0.20	0.18	0.14	0.34	0.39	0.31	0.33	0.27	0.26
U	0.08	0.02	0.05	0.07	0.06	0.10	0.11	0.13	0.10	0.05	0.06

Appendix 2.2: Trace element composition of mineral phases from Finero dykes (contd.)

Grouping	HFSE-poor dyke									
Rock type	Hornblendite dyke									
Sample	FI1608	FI1608	FI1608	FI1608	FI1608	FI1608	FI1608	FI1608	FI1608	FI1608
Thin section	FI1608B	FI1608B	FI1608B	FI1608B	FI1608B	FI1608B	FI1608B	FI1608B	FI1608B	FI1608B
Phase	Amph	Amph	Amph	Amph	Amph	Amph	Amph	Amph	Amph	Amph
Spot No.	4	5	6	6	6	7	8	8	9	9
Analysis No.	4b	5	7a	7b	7c	8	9a	9b	10a	10b
Sc	43.2	44.0	42.7	45.9	46.8	44.8	43.8	45.0	45.1	43.4
Ti	14670	12628	14043	14856	14526	14271	14627	14896	15205	15122
V	446	459	465	500	485	489	483	494	502	502
Cr	374	552	337	367	360	476	426	503	455	493
Co	52.4	57.5	54.0	58.4	58.1	54.1	50.1	53.4	52.2	50.7
Ni	77.1	166	112	131	121	100	97.2	95.1	100	96.2
Zn	96.4	118	104	114	113	104	104	106	106	106
Rb	5.80	5.67	4.42	5.24	3.97	2.62	4.54	3.58	4.20	4.68
Sr	379	244	324	313	356	402	411	433	420	389
Y	23.8	19.1	18.9	19.5	20.0	19.3	20.3	21.0	17.9	20.1
Zr	40.6	47.1	32.8	33.8	33.4	33.5	31.8	34.1	32.1	32.7
Nb	3.63	6.41	2.88	3.52	3.34	6.47	7.33	7.77	4.17	4.23
Cs	0.02	0.03	0.01	0.01	0.12	0.02	0.02	0.01	0.01	0.02
Ba	83.2	55.8	60.9	60.6	63.8	70.5	89.3	99.1	88.2	91.8
La	3.53	2.91	3.59	3.42	4.32	5.90	6.45	6.80	6.32	5.60
Ce	11.7	10.4	11.4	11.2	12.7	17.3	18.9	19.4	16.7	16.9
Pr	2.11	1.89	1.88	1.82	2.12	2.84	3.20	3.08	2.35	2.46
Nd	14.8	11.5	10.1	10.7	11.6	13.9	13.6	14.7	12.2	15.5
Sm	5.93	4.41	3.51	4.73	4.54	5.43	4.96	4.75	4.68	5.23
Eu	1.61	1.48	1.25	1.71	1.51	1.46	1.82	1.63	1.46	1.11
Gd	4.83	4.21	3.91	4.83	4.44	4.43	5.36	5.40	5.25	4.40
Tb	0.92	0.68	0.76	0.78	0.84	0.70	0.83	0.65	0.84	0.82
Dy	5.21	4.38	3.82	4.05	4.54	4.43	5.41	4.22	3.96	4.25
Ho	0.88	0.71	0.83	0.71	0.84	0.81	1.03	0.87	0.79	0.65
Er	2.96	2.35	1.92	1.97	1.80	1.88	2.12	2.45	1.50	1.65
Tm	0.29	0.26	0.22	0.19	0.30	0.24	0.24	0.36	0.33	0.22
Yb	3.34	1.21	1.31	1.87	1.95	1.79	1.77	1.76	1.19	2.16
Lu	0.28	0.23	0.27	0.18	0.27	0.23	0.21	0.24	0.27	0.24
Hf	1.32	1.31	1.33	0.77	1.49	1.05	1.19	1.25	1.01	1.41
Ta	0.12	0.32	0.09	0.11	0.16	0.10	0.09	0.15	0.07	0.11
Pb	2.87	1.69	1.92	2.22	2.19	2.22	1.77	2.00	2.62	2.19
Th	0.31	0.10	0.14	0.19	0.16	0.13	0.21	0.26	0.32	0.21
U	0.12	0.02	0.05	0.04	0.05	0.06	0.09	0.02	0.05	0.08

Appendix 2.2: Trace element composition of mineral phases from Finero dykes (contd.)

Grouping	HFSE-poor dyke						Composite HFSE-poor and -rich dyke					
Rock type	Gabbroic dyke bordered by orthopyroxenite						Dioritic dyke					
Sample	FI2101	FI2101	FI2101	FI2101	FI2101	FI2101	FI2106	FI2106	FI2106	FI2106	FI2106	FI2106
Thin section	FI2101A	FI2101A	FI2101A	FI2101A	FI2101A	FI2101A	FI2106A	FI2106A	FI2106A	FI2106A	FI2106A	FI2106A
Phase	Amph	Amph	Amph	Amph	Amph	Amph	Amph	Amph	Amph	Amph	Amph	Amph
Spot No.	1	1	2	2	5	5	1	2	2	4	5	9
Analysis No.	1a	1b	1a	1b	1a	1b	1	3	4	9	10	15
Sc	28.4	28.3	27.9	26.1	25.1	24.7	37.4	42.0	37.4	37.4	34.6	35.6
Ti	10304	10349	11526	11338	8165	8331	12662	13942	12923	12902	12185	12324
V	182	182	232	233	158	160	333	366	334	331	335	341
Cr	47	42	41	47	64	62	261	286	273	251	267	229
Co	31.0	30.1	31.7	30.2	36.6	36.0	46.1	41.8	42.2	48.6	45.8	47.8
Ni	150	151	108	97	323	300	61.4	52.3	58.2	62.1	57.8	59.3
Zn	38.3	42.6	52.3	49.1	29.8	28.3	96.9	98.4	96.0	113	107	101
Rb	8.79	7.68	8.79	8.90	6.50	4.83	3.94	2.36	2.18	5.67	4.48	4.08
Sr	270	279	277	255	249	254	318	293	274	333	306	311
Y	25.3	26.8	26.9	25.4	24.0	23.8	38.1	41.4	40.7	42.9	38.8	40.8
Zr	60.7	63.6	61.4	61.4	61.8	62.1	194	205	191	224	198	203
Nb	8.28	8.65	8.56	8.49	7.93	8.05	56.9	62.6	62.6	67.0	61.8	63.7
Cs	0.06	0.02	0.03	0.03	0.01	0.02	0.01	0.01	0.01	0.01	0.02	0.01
Ba	110	106	152	146	95.3	87.6	109	84.5	78.4	125	107	120
La	5.93	5.67	4.83	4.87	6.58	6.47	15.69	15.61	15.72	15.95	15.19	15.15
Ce	22.7	22.3	19.2	19.8	22.3	23.0	44.8	46.3	43.9	44.9	43.7	41.7
Pr	4.20	4.56	3.69	3.82	4.04	4.05	6.18	6.61	6.40	6.41	5.92	6.21
Nd	25.6	27.1	22.8	22.7	21.7	22.3	29.2	33.0	29.8	32.1	28.6	30.3
Sm	7.32	7.46	7.03	7.55	6.49	6.02	7.33	8.68	7.45	8.99	7.33	7.49
Eu	2.45	2.35	2.46	2.32	2.17	1.98	2.40	2.75	2.52	2.46	2.49	2.48
Gd	5.98	6.61	6.95	6.70	5.10	5.55	7.29	7.76	8.26	7.70	7.24	7.90
Tb	1.02	1.03	1.07	1.01	0.87	0.86	1.23	1.38	1.45	1.28	1.18	1.33
Dy	5.79	5.97	5.85	5.54	4.81	4.65	7.19	8.04	7.67	8.35	7.48	7.86
Ho	1.04	0.98	1.05	1.00	0.93	0.91	1.49	1.60	1.75	1.71	1.42	1.54
Er	2.35	2.28	2.32	2.18	2.46	2.21	4.38	4.21	3.97	4.46	3.79	4.02
Tm	0.32	0.29	0.31	0.29	0.29	0.27	0.60	0.64	0.59	0.57	0.52	0.53
Yb	2.12	1.99	1.62	1.76	1.59	1.81	4.42	3.95	3.24	4.32	3.74	4.00
Lu	0.33	0.24	0.27	0.23	0.29	0.29	0.63	0.65	0.65	0.63	0.47	0.54
Hf	2.66	2.50	2.28	2.21	2.36	2.34	5.56	5.59	5.30	7.34	5.47	6.37
Ta	0.30	0.29	0.27	0.24	0.26	0.29	3.01	4.37	4.32	4.95	4.24	4.61
Pb	1.00	0.93	0.96	0.85	0.55	0.56	3.35	2.97	2.50	2.90	2.55	3.01
Th	0.26	0.20	0.23	0.28	0.24	0.30	1.05	1.18	1.01	1.00	1.01	0.92
U	0.04	0.05	0.04	0.07	0.12	0.09	0.24	0.28	0.19	0.22	0.25	0.22

Appendix 2.2: Trace element composition of mineral phases from Finero dykes (contd.)

Grouping	Composite HFSE-poor and -rich dyke												
Rock type	Dioritic dyke												
Sample	FI2106	FI2106	FI2106	FI2106	FI2106	FI2106	FI2106	FI2106	FI2106	FI2106	FI2106	FI2106	FI2106
Thin section	FI2106A	FI2106A	FI2106A	FI2106A	FI2106A	FI2106A	FI2106A	FI2106A	FI2106A	FI2106A	FI2106A	FI2106A	FI2106A
Phase	Amph	Amph	Amph	Amph	Amph	Amph	Amph	Amph	Amph	Amph	Amph	Amph	Amph
Spot No.	9	9	10	11	12	12	12	13	14	15	16	17	17
Analysis No.	16	17	19	21	22	23	24	26	27	28	29	30	31
Sc	35.0	40.4	35.1	33.3	35.1	33.1	35.8	36.6	40.0	41.6	40.3	35.4	38.8
Ti	12331	13853	11946	12028	12455	11994	12235	12984	14073	14157	13779	13613	14093
V	340	381	332	334	340	324	342	362	395	398	391	370	391
Cr	238	306	247	209	248	233	259	265	428	431	454	162	257
Co	48.3	45.9	47.2	48.8	44.8	44.0	45.2	49.2	48.7	48.5	45.4	49.3	52.6
Ni	63.2	51.5	57.5	65.4	53.5	51.3	55.3	59.2	62.3	60.5	61.7	56.0	63.6
Zn	111	106	95.5	108	109	100	102	108	103	110	88.4	128	130
Rb	6.18	5.34	1.80	5.80	2.04	3.49	5.31	3.69	5.41	5.27	5.85	4.08	2.62
Sr	341	311	301	304	311	288	328	326	351	361	350	303	324
Y	42.8	43.5	48.0	41.7	42.8	40.0	40.9	35.9	25.8	27.7	25.3	38.1	41.1
Zr	214	212	188	217	198	184	189	165	80	86	71	194	223
Nb	64.3	64.9	54.8	64.5	55.9	56.0	53.7	42.9	10.6	12.2	5.95	66.0	66.9
Cs	0.02	0.02	0.02	0.02	0.01	0.01	0.01	0.02	0.02	0.01	0.02	0.20	0.02
Ba	143	127	61	117	79	94	117	103	112	115	106	111	121
La	16.07	15.03	16.88	14.66	14.79	13.81	13.78	13.39	8.58	8.97	6.48	15.04	15.18
Ce	44.7	43.9	48.4	43.0	44.6	39.7	41.4	38.5	22.1	25.2	17.7	48.5	46.2
Pr	6.78	6.53	7.24	6.36	6.56	6.13	6.25	5.65	3.27	3.62	2.73	6.81	6.63
Nd	33.0	33.1	36.0	31.5	33.9	29.9	30.9	27.9	18.5	18.9	15.4	31.1	33.6
Sm	8.59	9.46	9.48	7.73	8.72	8.57	7.86	7.28	4.57	5.72	6.09	7.23	9.00
Eu	2.64	2.48	2.97	2.47	2.89	2.37	2.36	2.14	1.82	1.99	1.89	2.59	2.78
Gd	8.41	8.49	9.22	8.08	9.49	7.96	7.49	7.79	5.44	5.94	5.74	7.10	7.71
Tb	1.47	1.40	1.55	1.35	1.43	1.28	1.26	1.30	0.92	0.94	0.90	1.20	1.41
Dy	7.85	8.66	9.34	8.78	8.68	7.88	7.73	7.60	5.08	6.15	5.84	7.04	8.70
Ho	1.59	1.59	1.92	1.70	1.66	1.51	1.62	1.38	0.92	1.07	1.01	1.32	1.47
Er	4.24	4.83	4.72	3.92	3.95	4.36	4.46	3.38	2.77	2.76	2.58	4.01	3.94
Tm	0.65	0.66	0.70	0.58	0.60	0.58	0.58	0.55	0.31	0.37	0.37	0.62	0.58
Yb	3.95	4.29	5.07	4.04	5.29	3.64	3.92	3.31	2.00	3.33	2.61	4.79	4.74
Lu	0.47	0.52	0.59	0.61	0.61	0.49	0.55	0.55	0.35	0.38	0.34	0.49	0.64
Hf	6.68	7.50	6.07	7.76	6.28	5.93	6.04	4.95	2.57	2.51	2.20	5.85	7.40
Ta	4.66	4.68	4.06	5.00	4.11	4.08	3.77	2.68	0.36	0.37	0.20	4.15	4.66
Pb	2.92	3.17	2.88	2.98	2.93	3.02	3.16	3.13	3.09	3.16	3.29	3.58	3.51
Th	0.96	0.95	0.89	0.82	1.04	0.70	0.69	0.76	0.61	0.58	0.65	0.86	0.94
U	0.20	0.23	0.26	0.17	0.15	0.12	0.14	0.12	0.10	0.12	0.10	0.16	0.19

Appendix 2.2: Trace element composition of mineral phases from Finero dykes (contd.)

Grouping	Composite HFSE-poor and -rich dyke											
Rock type	Dioritic dyke											
Sample	FI2106	FI2106	FI2106	FI2106	FI2106	FI2106	FI2106	FI2106	FI2106	FI2106	FI2106	FI2106
Thin section	FI2106A	FI2106A	FI2106A	FI2106A	FI2106A	FI2106A	FI2106A	FI2106A	FI2106A	FI2106A	FI2106A	FI2106A
Phase	Amph	Amph	Amph	Amph	Amph	Amph	Amph	Amph	Amph	Amph	Amph	Amph
Spot No.	17	T1	T1	T1	T1	T1	T1	T1	T1	T1	T1	T1
Analysis No.	32	1	2	3	4	5	6	7	8	9	10	11
Sc	36.5	41.7	42.6	40.1	40.1	41.2	43.5	43.8	43.5	40.7	40.0	36.1
Ti	13158	12207	11882	12213	13054	12872	13699	14034	14650	13886	13481	13054
V	375	386	381	384	384	367	409	411	415	398	376	341
Cr	180	411	403	376	490	371	401	427	421	407	319	276
Co	49.3	45.6	46.8	43.4	48.6	47.3	48.7	49.7	49.0	49.0	47.5	47.6
Ni	53.7	67.1	62.3	53.8	62.2	60.7	66.4	64.8	65.4	65.1	64.5	57.1
Zn	136	83.7	75.4	83.1	89.9	96.4	104	110	108	117	109	113
Rb	1.58	5.21	5.68	2.48	2.02	4.75	6.09	6.12	2.49	5.90	2.49	3.33
Sr	310	330	306	340	325	328	342	347	368	340	306	303
Y	39.5	26.8	26.5	29.4	27.2	28.3	29.2	27.4	29.5	27.3	32.5	40.5
Zr	207	72.8	74.2	77.2	67.7	74.0	79.5	81.4	82.1	95.3	106.0	170.8
Nb	64.4	4.99	4.99	5.21	5.42	5.39	6.19	6.89	8.90	15.0	21.5	43.6
Cs	0.04	0.01	0.01	0.02	0.02	0.01	0.01	0.02	0.01	0.02	0.01	0.02
Ba	120	86.8	92.4	71.4	51.3	92.9	108	107	73.4	105	73.9	91.4
La	15.36	5.56	5.03	5.50	5.22	5.68	6.55	6.82	8.32	8.99	10.45	14.10
Ce	47.8	15.5	14.6	15.7	15.5	15.8	17.3	18.1	21.6	24.6	29.1	39.2
Pr	7.34	2.70	2.57	2.79	2.59	2.64	2.64	2.78	3.22	3.77	4.46	6.01
Nd	32.9	14.6	15.2	17.5	15.1	16.3	15.1	17.0	17.8	20.2	22.9	30.4
Sm	9.12	5.25	4.04	5.40	4.61	6.03	5.64	4.86	5.73	5.61	6.20	8.54
Eu	2.84	1.83	1.80	2.09	1.91	1.70	1.77	1.88	1.83	1.90	2.20	2.36
Gd	7.20	5.96	5.51	6.05	6.28	6.03	6.12	6.45	6.14	5.72	6.76	8.81
Tb	1.33	0.96	0.83	1.02	0.98	0.89	1.02	0.91	1.04	0.96	1.09	1.35
Dy	7.72	5.42	5.57	6.25	5.95	5.31	5.42	5.45	6.21	5.44	6.18	8.06
Ho	1.48	1.08	1.04	1.02	1.00	1.22	1.05	1.09	1.29	1.03	1.44	1.64
Er	4.23	2.84	2.48	2.70	2.69	2.78	2.99	2.90	2.94	2.70	3.11	4.43
Tm	0.52	0.36	0.44	0.34	0.39	0.38	0.42	0.49	0.44	0.33	0.43	0.51
Yb	3.95	2.34	2.58	2.38	2.63	2.86	2.51	2.12	2.70	2.66	3.09	3.94
Lu	0.57	0.33	0.33	0.35	0.35	0.33	0.38	0.34	0.38	0.40	0.43	0.61
Hf	6.46	2.08	2.78	2.70	2.39	2.38	2.64	2.40	3.08	2.63	2.87	4.97
Ta	4.09	0.22	0.26	0.19	0.17	0.20	0.23	0.21	0.27	0.60	1.07	2.95
Pb	2.95	3.34	3.16	3.30	2.81	3.03	3.34	3.39	3.49	3.33	2.86	2.85
Th	0.98	0.75	0.44	0.54	0.37	0.46	0.42	0.54	0.57	0.54	0.61	0.78
U	0.18	0.09	0.14	0.15	0.08	0.11	0.10	0.13	0.11	0.11	0.10	0.12

T1 – Traverse 1

Appendix 2.2: Trace element composition of mineral phases from Finero dykes (contd.)

Grouping	Composite HFSE-poor and -rich dyke												
Rock type	Hornblendite dyke									Amphibole veinlets		Hornblendite dyke	
Sample	FI1607	FI1607	FI1607	FI1607	FI1607	FI1607	FI1607	FI1607	FI1607	FI1607	FI1607	FI1607	FI1607
Thin section	FI1607C	FI1607C	FI1607C	FI1607C	FI1607C	FI1607C	FI1607C	FI1607C	FI1607C	FI1607C	FI1607C	FI1607B2	FI1607B2
Phase	Amph	Amph	Amph	Amph	Amph	Amph	Amph	Amph	Amph	Amph	Amph	Amph	Amph
Spot No.	1	1	2	2	4	4	10	10	12	18	18	T1	T1
Analysis No.	1	2	3	4	7	9	14	15	16	20a	20b	3	4
Sc	39.7	40.5	39.1	39.4	40.6	41.2	43.2	41.0	30.5	34.8	34.6	45.9	44.1
Ti	13560	14010	13910	13770	14630	14680	12660	11570	10550	10750	10530	14648	14800
V	427	439	427	422	416	430	423	385	312	301	304	420	412
Cr	87	94	104	103	84	91	163	169	113	3240	3187	107	112
Co	51.6	52.8	51.8	51.7	47.9	49.0	39.4	37.7	32.5	34.1	33.8	48.4	48.2
Ni	55.2	57.3	55.4	54.9	56.2	61.7	175	196	167	519	509	53.7	55.1
Zn	116	120	126	125	98.1	96.3	74.6	68.7	70.6	57.2	53.0	104	100
Rb	6.55	6.53	6.09	6.12	6.13	5.49	3.20	2.31	5.00	2.02	1.81	2.08	4.48
Sr	432	421	359	350	520	510	570	451	389	521	494	517	543
Y	24.5	23.1	21.2	22.5	24.3	25.6	28.4	27.6	20.5	25.4	24.7	29.1	30.1
Zr	52.0	51.5	47.4	49.1	45.9	45.9	51.3	46.5	36.9	53.2	52.1	52.5	53.4
Nb	6.83	6.68	5.69	5.58	8.86	9.82	8.63	8.16	6.97	48.6	46.5	12.7	12.1
Cs	0.01	0.02	0.02	0.05	0.02	0.02	0.01	0.05	0.02	0.00	0.00	0.01	0.01
Ba	204	182	127	138	344	377	216	125	140	139	110	117	205
La	7.16	6.99	4.77	4.81	8.97	9.14	11.92	9.89	8.08	14.22	13.09	7.72	8.78
Ce	21.7	20.8	15.0	15.1	25.3	25.0	31.4	28.2	22.4	37.2	34.6	23.4	23.5
Pr	3.25	3.43	2.52	2.60	3.60	3.73	4.38	4.17	3.19	5.14	4.94	3.70	3.66
Nd	20.1	19.8	16.4	16.5	19.8	21.1	24.6	22.4	16.5	26.8	25.9	19.6	20.1
Sm	5.96	6.68	5.66	5.81	6.45	6.31	6.74	7.07	5.29	7.31	6.84	6.20	5.88
Eu	2.06	2.00	1.81	1.78	2.14	2.27	2.37	2.24	1.64	2.59	2.18	2.07	2.18
Gd	6.00	5.71	5.36	5.41	5.71	5.97	6.66	6.91	5.02	6.37	6.25	6.63	6.48
Tb	0.97	0.84	0.83	0.84	0.86	0.91	1.02	1.04	0.70	1.01	0.96	1.12	1.04
Dy	5.40	4.78	4.65	4.74	5.10	5.24	6.00	5.71	4.24	5.64	5.28	6.50	5.93
Ho	0.99	0.95	0.89	0.87	1.02	1.07	1.23	1.19	0.85	1.11	0.99	1.13	1.11
Er	2.47	2.37	2.12	2.20	2.75	2.86	3.23	3.03	2.13	2.86	2.57	3.32	3.05
Tm	0.35	0.35	0.31	0.32	0.36	0.35	0.44	0.38	0.27	0.43	0.37	0.46	0.42
Yb	2.39	2.31	2.15	1.92	2.33	2.31	2.73	2.60	1.88	2.56	2.54	2.56	2.19
Lu	0.30	0.27	0.27	0.25	0.31	0.30	0.35	0.31	0.25	0.32	0.32	0.41	0.33
Hf	2.03	1.96	1.91	1.96	1.80	1.75	1.99	1.82	1.45	1.44	1.38	2.19	2.09
Ta	0.23	0.24	0.18	0.20	0.19	0.27	0.22	0.21	0.15	0.87	0.83	0.23	0.22
Pb	n.d.	n.d.	n.d.	n.d.	n.d.	n.d.	n.d.	n.d.	n.d.	n.d.	n.d.	1.94	1.97
Th	0.25	0.17	0.13	0.11	0.30	0.25	0.55	0.34	0.35	0.43	0.42	0.35	0.44
U	0.06	0.04	0.05	0.04	0.09	0.07	0.13	0.05	0.09	0.09	0.09	0.07	0.06

Appendix 2.2: Trace element composition of mineral phases from Finero dykes (contd.)

Grouping	Composite HFSE-poor and -rich dyke											
Rock type	Hornblendite dyke				Amphibole veinlets (in peridotite)							
Sample	FI1607	FI1607	FI1607	FI1607	FI1607	FI1607	FI1607	FI1607	FI1607	FI1607	FI1607	FI1607
Thin section	FI1607B2	FI1607B2	FI1607B2	FI1607B2	FI1607B2	FI1607B2	FI1607B2	FI1607B2	FI1607B2	FI1607B2	FI1607B2	FI1607B2
Phase	Amph	Amph	Amph	Amph	Amph	Amph	Amph	Amph	Amph	Amph	Amph	Amph
Spot No.	T1	T1	T1	T1	T1	T1	T1	T1	T1	T1	T1	T1
Analysis No.	5	6	7	8	10	11	12	13	14	15	16	17
Sc	46.7	43.3	44.4	42.3	39.8	37.6	29.2	36.9	34.6	35.9	35.9	36.3
Ti	15161	14076	13770	13297	11827	10585	7717	8864	8781	8684	9798	9868
V	428	402	412	401	358	321	241	286	290	284	294	294
Cr	105	68	114	111	94	507	9392	2873	1972	3058	2183	1908
Co	51.3	46.9	44.8	44.7	39.4	36.4	34.1	34.3	32.7	35.1	34.8	34.8
Ni	56.8	62.9	91.6	114	288	402	558	584	551	581	560	552
Zn	107	103	99.4	95.8	79.5	70.3	62.9	71.1	64.7	61.2	65.6	60.0
Rb	5.83	4.77	2.78	2.11	1.75	1.21	1.42	2.53	0.70	2.97	1.25	1.19
Sr	561	536	569	588	523	454	404	454	447	454	487	522
Y	31.0	30.5	32.8	32.2	31.3	28.2	23.2	29.1	29.2	29.8	28.4	29.7
Zr	57.6	54.0	57.7	57.8	53.1	46.7	34.5	53.6	53.8	54.2	60.4	63.4
Nb	10.5	11.9	12.3	12.1	10.5	18.2	33.3	53.6	56.2	54.2	61.9	62.5
Cs	0.01	0.01	0.01	0.01	0.02	0.01	0.01	0.01	0.01	0.02	0.01	0.01
Ba	207	241	159	122	74.0	54.6	45.4	65.8	36.1	91.6	52.8	63.9
La	8.71	7.87	8.74	10.47	10.66	11.38	11.08	12.56	12.31	13.24	11.39	12.65
Ce	24.2	23.8	25.0	27.3	29.7	29.9	30.7	33.8	34.3	35.7	32.7	35.9
Pr	3.65	3.74	3.86	4.26	4.47	4.55	4.45	4.95	5.21	5.58	5.05	5.30
Nd	19.0	21.2	21.7	22.5	23.1	22.4	21.9	25.6	26.4	27.0	25.3	26.5
Sm	6.65	6.52	6.59	6.65	6.91	5.89	5.94	7.28	7.09	7.66	6.85	7.25
Eu	2.01	2.19	2.29	2.59	2.69	2.03	1.88	2.33	2.15	2.47	2.05	2.60
Gd	7.37	7.06	6.50	6.58	6.39	6.13	5.06	6.30	6.77	6.26	6.10	7.14
Tb	1.03	0.99	1.12	1.12	1.11	0.94	0.89	1.02	1.06	1.12	1.03	1.10
Dy	6.42	6.30	7.02	7.07	5.91	6.22	5.24	6.30	5.88	6.23	5.50	5.87
Ho	1.21	1.22	1.27	1.23	1.21	1.10	0.88	1.23	1.06	1.21	1.12	1.17
Er	3.39	3.28	3.50	3.26	3.20	3.15	2.24	2.88	2.84	3.07	2.79	3.20
Tm	0.39	0.42	0.40	0.51	0.43	0.40	0.34	0.37	0.30	0.39	0.42	0.43
Yb	2.86	3.19	2.83	2.86	3.42	2.73	2.24	2.64	2.73	2.64	2.92	2.55
Lu	0.41	0.40	0.37	0.41	0.34	0.38	0.23	0.38	0.38	0.36	0.36	0.36
Hf	2.22	2.20	2.13	1.99	2.29	1.79	1.26	1.58	1.64	1.59	1.74	1.86
Ta	0.22	0.23	0.24	0.25	0.14	0.22	0.35	0.63	0.56	0.62	0.69	0.89
Pb	2.23	2.00	2.20	2.03	1.36	1.37	1.21	1.17	1.08	1.32	1.45	1.39
Th	0.38	0.36	0.47	0.52	0.39	0.40	0.24	0.28	0.28	0.36	0.28	0.38
U	0.09	0.06	0.15	0.09	0.06	0.06	0.04	0.06	0.04	0.04	0.11	0.09

Appendix 2.2: Trace element composition of mineral phases from Finero dykes (contd.)

Grouping	Composite HFSE-poor and -rich dyke											
Rock type	Hornblendite dyke											
Sample	FI1607	FI1607	FI1607	FI1607	FI1607	FI1607	FI1607	FI1607	FI1607	FI1607	FI1607	FI1607
Thin section	FI1607B2	FI1607D	FI1607D	FI1607D	FI1607D	FI1607D	FI1607D	FI1607D	FI1607D	FI1607D	FI1607D	FI1607D
Phase	Amph	Amph	Amph	Amph	Amph	Amph	Amph	Amph	Amph	Amph	Amph	Amph
Spot No.	2	1	1	1	1	1	2	2	2	3	3	3
Analysis No.	23	3	4	5	6	7	8	9	10	11	12	13
Sc	43.5	45.2	42.8	43.6	41.3	43.7	45.0	44.7	44.1	41.9	42.2	42.7
Ti	13434	13279	13269	12793	13239	13219	13667	13034	12982	13659	13342	13180
V	407	410	394	374	399	374	421	363	373	394	377	367
Cr	82	214	224	237	170	288	132	102	152	109	110	107
Co	44.0	51.6	52.4	49.4	51.6	50.9	203.1	51.5	49.9	50.2	50.2	47.8
Ni	71.7	56.5	58.3	55.7	50.8	56.5	415.2	56.8	52.2	55.0	57.5	60.0
Zn	87.6	135	133	122	140	124	144	118	116	127	124	116
Rb	1.89	5.91	5.27	5.15	5.41	5.21	6.03	5.46	6.12	4.97	5.48	5.12
Sr	562	316	274	258	288	254	320	277	292	275	266	180
Y	33.9	26.5	25.5	25.1	26.4	26.1	28.9	25.7	28.6	27.1	26.7	27.7
Zr	56.9	47.5	41.6	43.7	43.2	44.2	51.2	46.0	48.7	45.3	44.8	46.4
Nb	11.4	3.54	3.54	3.53	3.59	3.63	3.38	3.47	3.41	3.73	3.42	3.75
Cs	0.01	0.01	0.02	0.01	0.01	0.01	0.02	0.02	0.02	0.01	0.01	0.01
Ba	112.0	62.9	53.4	49.6	56.5	54.3	58.2	54.6	63.8	53.2	51.0	46.0
La	10.33	3.13	2.91	2.71	2.84	2.89	3.04	2.84	2.84	2.60	2.53	2.47
Ce	27.0	11.8	10.9	10.1	11.6	10.8	11.3	11.3	11.8	10.1	10.3	10.1
Pr	4.32	2.53	2.34	2.02	2.11	2.04	2.30	2.32	2.43	2.18	2.23	2.30
Nd	24.3	14.8	14.0	12.9	14.9	14.0	14.7	15.4	15.3	14.0	14.4	15.0
Sm	6.60	5.84	5.43	5.13	5.12	5.27	5.99	4.72	5.88	4.78	5.42	5.38
Eu	2.29	1.80	1.67	1.63	1.53	1.50	2.00	1.67	1.90	1.68	1.81	1.96
Gd	7.23	6.25	5.81	5.51	5.27	4.86	6.67	5.41	6.81	5.91	4.64	6.30
Tb	1.33	0.90	1.01	0.79	0.85	0.91	0.98	1.03	0.95	0.83	0.89	0.85
Dy	7.47	5.80	5.68	4.88	5.58	5.70	6.20	5.60	5.94	5.53	5.54	5.51
Ho	1.44	0.92	0.91	1.04	0.96	1.11	1.15	1.03	0.97	1.20	1.02	0.99
Er	3.53	2.62	2.49	2.37	2.52	2.93	2.73	2.47	2.82	2.43	2.30	2.48
Tm	0.48	0.39	0.21	0.28	0.36	0.33	0.47	0.32	0.40	0.38	0.29	0.30
Yb	2.88	2.62	2.07	2.48	2.48	2.00	2.78	2.03	2.16	2.76	2.10	2.47
Lu	0.41	0.21	0.29	0.24	0.26	0.30	0.33	0.26	0.31	0.35	0.34	0.37
Hf	2.23	1.86	1.84	1.84	1.38	1.96	1.79	1.82	2.30	1.80	1.87	2.17
Ta	0.22	0.11	0.14	0.09	0.12	0.12	0.14	0.21	0.10	0.11	0.14	0.17
Pb	1.80	1.31	1.06	0.95	1.12	1.01	1.52	1.02	1.10	0.83	0.88	0.80
Th	0.59	0.07	0.08	0.04	0.05	0.04	0.10	0.06	0.11	0.08	0.07	0.06
U	0.13	0.03	0.01	0.02	0.02	0.01	0.02	0.01	0.03	0.02	0.01	0.01

Appendix 2.2: Trace element composition of mineral phases from Finero dykes (contd.)

Grouping	Composite HFSE-poor and -rich dyke						
Rock type	Hornblendite dyke						
Sample	FI1607	FI1607	FI1607	FI1607	FI1607	FI1607	FI1607
Thin section	FI1607D	FI1607D	FI1607D	FI1607D	FI1607D	FI1607D	FI1607D
Phase	Amph	Amph	Amph	Amph	Amph	Amph	Amph
Spot No.	4	5	6	6	7	7	8
Analysis No.	15	17	21	22	29	30	31
Sc	43.7	43.8	44.4	45.0	41.5	40.0	40.9
Ti	13789	13616	13605	13944	12809	12745	13269
V	390	419	412	401	358	376	384
Cr	90	102	169	139	193	213	101
Co	50.8	53.3	49.7	50.5	48.1	51.3	50.3
Ni	65.5	74.9	73.3	74.0	84.6	81.9	70.0
Zn	98	109	94.4	90.7	93.7	102.7	82.0
Rb	5.31	5.60	5.06	4.77	5.06	5.33	5.40
Sr	284	275	266	258	265	249	271
Y	26.3	27.1	26.9	26.9	26.0	25.1	26.5
Zr	47.0	48.7	47.2	45.3	44.5	42.5	45.6
Nb	3.53	3.71	3.20	3.75	3.59	3.45	3.63
Cs	0.05	0.02	0.01	0.03	0.01	0.01	0.02
Ba	59.0	53.1	54.8	53.6	55.4	51.8	50.2
La	2.86	2.78	2.90	2.61	2.69	2.61	2.71
Ce	11.4	10.6	9.9	9.9	10.2	10.1	10.9
Pr	2.50	2.22	2.19	2.17	2.18	2.49	2.35
Nd	13.9	14.3	14.1	13.0	15.2	13.3	15.0
Sm	5.77	5.85	5.26	4.72	4.47	5.28	5.57
Eu	2.11	1.78	1.65	1.66	1.61	1.49	1.82
Gd	5.63	5.50	6.25	6.45	6.22	5.04	5.98
Tb	1.01	1.02	0.82	1.03	0.98	0.97	0.89
Dy	4.96	5.25	5.33	5.29	5.61	5.61	5.57
Ho	0.98	1.10	1.05	1.06	0.98	0.98	1.07
Er	2.54	2.38	3.07	2.73	2.37	2.58	2.60
Tm	0.37	0.28	0.31	0.34	0.36	0.38	0.37
Yb	2.73	2.21	1.99	2.02	2.40	2.13	2.06
Lu	0.32	0.29	0.32	0.26	0.33	0.28	0.32
Hf	2.07	1.70	2.01	1.99	1.90	1.72	1.23
Ta	0.13	0.10	0.15	0.16	0.13	0.12	0.09
Pb	0.82	0.93	0.96	0.92	0.77	0.81	0.64
Th	0.02	0.03	0.08	0.09	0.10	0.06	0.06
U	0.02	0.02	0.01	0.02	0.02	0.01	0.03

Appendix 2.2: Trace element composition of mineral phases from Finero dykes (contd.)

Grouping	HFSE-rich dyke												
Rock type	Dioritic dyke												
Sample	FI1603	FI1603	FI1603	FI1603	FI1603	FI1603	FI1603	FI1603	FI1603	FI1603	FI1603	FI1603	FI1603
Thin section	FI1603A	FI1603A	FI1603A	FI1603A	FI1603A	FI1603A	FI1603A	FI1603B	FI1603B	FI1603B	FI1603C	FI1603C	FI1603C
Phase	Phl	Phl	Phl	Phl	Phl	Phl	Phl	Phl	Phl	Phl	Phl	Phl	Phl
Spot No.	3	4	4	5	5	11	11	5	5	12	16	16	17
Analysis No.	11	12	13	14	15	20a	20b	15	16	37	41	42	43
Sc	4.09	4.08	4.29	4.02	4.27	3.90	4.24	3.08	3.00	2.69	2.75	2.81	2.65
Ti	4582	5014	5526	4546	4619	4754	4879	7340	6893	8328	9812	9411	9419
V	58.9	59.3	62.0	58.6	54.9	45.9	46.4	42.5	40.9	39.5	42.8	44.3	44.1
Cr	931	973	993	1274	1389	263	261	109	105	111	106	102	102
Co	51.7	51.8	53.2	52.7	51.6	52.9	53.1	50.9	48.7	49.4	50.6	48.8	49.4
Ni	872	905	894	919	894	801	797	705	674	679	697	690	714
Zn	70.4	72.4	74.1	74.7	73.9	71.4	72.7	78.3	76.1	81.7	75.3	72.5	80.1
Rb	277	280	282	283	281	295	289	292	274	264	268	270	272
Sr	38.8	39.7	40.5	54.5	42.2	15.3	15.2	14.6	15.4	21.1	23.8	26.4	19.4
Y	0.14	0.11	0.12	0.46	0.28	0.01	0.02	0.08	0.10	1.22	0.03	0.01	bdl.
Zr	5.42	5.56	6.78	9.77	8.98	7.50	6.82	5.49	5.73	5.35	15.3	14.5	14.4
Nb	94.4	94.6	95.0	93.6	96.4	110	109	113	108	111	114	112	116
Cs	5.12	5.16	5.30	5.40	5.16	4.78	4.75	4.98	4.77	3.70	4.11	4.06	3.98
Ba	3329	3575	3535	3643	3510	3278	3286	3823	3750	4185	4466	4494	4469
La	0.43	0.55	0.53	1.22	1.01	0.05	0.04	0.12	0.32	0.55	0.04	0.03	0.03
Ce	0.77	1.00	1.05	2.29	1.88	0.01	0.01	0.26	0.40	0.71	0.10	0.02	0.05
Pr	0.06	0.07	0.09	0.21	0.14	0.00	0.00	0.03	0.02	0.07	0.01	0.01	0.01
Nd	0.28	0.25	0.24	0.61	0.63	0.01	bdl.	0.07	0.13	0.53	bdl.	0.03	0.01
Sm	0.05	0.02	0.02	0.11	0.13	bdl.	bdl.	0.02	0.04	0.26	bdl.	bdl.	0.01
Eu	0.08	0.10	0.09	0.11	0.10	0.03	0.03	0.03	0.04	0.09	0.01	0.01	0.02
Gd	0.04	0.05	0.04	0.11	0.10	0.00	bdl.	0.01	0.01	0.15	0.03	bdl.	bdl.
Tb	0.01	0.00	0.01	0.01	0.01	bdl.	0.00	bdl.	0.00	0.02	bdl.	bdl.	0.00
Dy	0.01	0.03	0.01	0.09	0.06	bdl.	bdl.	0.00	0.01	0.16	0.00	bdl.	0.00
Ho	0.01	0.01	0.01	0.01	0.01	bdl.	bdl.	bdl.	0.01	0.01	0.00	0.00	bdl.
Er	0.01	0.02	0.02	0.04	0.03	bdl.	0.00	0.01	0.01	0.02	bdl.	0.01	bdl.
Tm	0.00	0.01	0.01	0.01	0.01	0.00	0.00	0.00	0.00	0.01	0.00	bdl.	bdl.
Yb	0.01	0.01	0.01	0.05	0.01	bdl.	0.00	0.01	0.02	0.03	0.01	0.01	0.01
Lu	0.00	0.01	0.00	0.01	bdl.	bdl.	bdl.	0.00	0.01	0.02	bdl.	0.00	0.00
Hf	0.06	0.09	0.09	0.14	0.13	0.11	0.07	0.09	0.19	0.09	0.27	0.24	0.27
Ta	3.54	3.89	3.81	3.88	3.59	3.80	3.58	4.41	4.46	4.59	5.00	5.04	4.70
Pb	n.d.	n.d.	n.d.	n.d.	n.d.	n.d.	n.d.	n.d.	n.d.	n.d.	n.d.	n.d.	n.d.
Th	0.11	0.15	0.15	0.17	0.14	0.01	0.01	0.03	0.05	0.04	0.02	0.01	0.02
U	0.07	0.12	0.10	0.12	0.08	0.02	0.02	0.03	0.03	0.09	0.02	0.02	0.01

Appendix 2.2: Trace element composition of mineral phases from Finero dykes (contd.)

Grouping	HFSE-rich dyke											
Rock type	Dioritic dyke											
Sample	FI1604	FI1604	FI1604	FI1604	FI1604	FI1604	FI1605	FI1605	FI1605	FI1605	FI1605	FI1605
Thin section	FI1604C	FI1604C	FI1604C	FI1604C	FI1604C	FI1604C	FI1605A2	FI1605A2	FI1605A2	FI1605A2	FI1605A2	FI1605A2
Phase	Phl	Phl	Phl	Phl	Phl	Phl	Phl	Phl	Phl	Phl	Phl	Phl
Spot No.	1	19	17	17	17	14	2	3	4	10	11	12
Analysis No.	1a	2	1	2	3	2	2a	3	2	1	2	1
Sc	6.42	5.24	5.00	5.26	4.71	4.57	4.41	4.00	3.89	3.34	3.59	3.47
Ti	3626	5544	5589	5378	5536	5853	6994	6912	7881	8698	8103	7667
V	42.8	42.4	43.2	42.3	41.0	40.1	46.7	43.2	42.9	45.0	48.6	51.1
Cr	48	156	271	308	332	285	342	369	264	202	215	483
Co	66.4	62.5	62.5	61.3	60.8	62.7	66.2	67.7	66.5	67.7	63.4	69.3
Ni	1341	1290	1218	1258	1222	1238	1243	1207	1174	1277	1203	1333
Zn	131	110	103	105	108	114	111	111	105	103	89.3	100
Rb	317	287	292	279	282	281	287	306	281	292	285	299
Sr	5.23	12.0	24.5	22.6	29.5	16.0	21.2	14.4	16.5	25.9	18.1	13.9
Y	0.01	0.07	0.04	0.01	0.08	0.02	0.36	0.37	0.04	0.06	0.06	0.06
Zr	5.18	3.52	5.37	5.07	5.55	3.32	11.36	6.46	9.80	10.70	10.18	7.33
Nb	83.2	85.3	95.4	92.9	88.5	97.5	104	106	103	116	116	105
Cs	5.22	4.83	4.30	4.21	4.16	4.79	4.53	5.41	4.66	4.43	4.50	5.02
Ba	2489	2678	2897	2882	2833	2960	3182	3202	3365	3466	3405	3380
La	0.01	0.06	0.02	0.02	0.02	0.02	0.44	0.62	0.02	0.16	0.03	0.03
Ce	0.02	0.10	0.50	0.01	0.01	0.02	1.00	0.34	0.21	0.11	0.02	0.05
Pr	0.01	0.01	0.01	0.02	0.01	0.01	0.12	0.08	0.02	0.06	0.02	0.04
Nd	0.05	0.05	0.05	0.06	0.03	0.06	0.58	0.17	0.10	0.36	0.10	0.11
Sm	0.05	0.06	0.08	0.11	0.05	0.08	0.22	0.12	0.11	0.20	0.00	0.14
Eu	0.11	0.09	0.03	0.08	0.05	0.07	0.14	0.11	0.09	0.05	0.07	0.06
Gd	0.04	0.04	0.03	0.05	0.07	0.10	0.18	0.10	0.16	0.14	0.08	0.40
Tb	0.01	0.01	0.01	0.02	0.02	0.01	0.04	0.02	0.01	0.02	0.02	0.02
Dy	0.02	0.02	0.03	0.03	0.05	0.07	0.11	0.04	0.04	0.11	0.05	0.13
Ho	0.00	0.01	0.01	0.02	0.01	0.01	0.03	0.03	0.03	0.02	0.02	0.04
Er	0.03	0.06	0.03	0.06	0.04	0.11	0.05	0.06	0.05	0.04	0.10	0.17
Tm	0.01	0.01	0.00	0.01	0.01	0.01	0.01	0.01	0.01	0.02	0.02	0.02
Yb	0.04	0.03	0.07	0.08	0.06	0.05	0.05	0.13	0.05	0.11	0.16	0.17
Lu	0.01	0.01	0.01	0.01	0.01	0.02	0.01	0.01	0.01	0.01	0.02	0.00
Hf	0.04	0.05	0.11	0.06	0.19	0.15	0.26	0.21	0.17	0.58	0.21	0.00
Ta	2.14	2.62	3.71	3.67	3.28	3.19	3.51	3.62	4.38	5.16	4.86	3.63
Pb	1.00	1.19	1.24	1.18	1.14	1.17	1.20	1.45	1.55	1.68	1.38	1.25
Th	0.03	0.10	0.01	0.02	0.01	0.04	0.11	0.06	0.02	0.03	0.02	0.04
U	0.02	0.02	0.02	0.02	0.01	0.05	0.03	0.08	0.02	0.02	0.04	0.07

Appendix 2.2: Trace element composition of mineral phases from Finero dykes (contd.)

Grouping	HFSE-rich dyke												
Rock type	Dioritic dyke												
Sample	FI2102	FI2102	FI2102	FI2102	FI2102	FI2102	FI2102	FI2102	FI2102	FI2102	FI2103	FI2103	FI2103
Thin section	FI2102C	FI2102C	FI2102C	FI2102C	FI2102C	FI2102C	FI2102C	FI2102C	FI2102C	FI2102C	FI2103C	FI2103C	FI2103C
Phase	Phl	Phl	Phl	Phl	Phl	Phl	Phl	Phl	Phl	Phl	Phl	Phl	Phl
Spot No.	3	3	3	4	5	6	8	8	9	9	2	2	3
Analysis No.	5a	7	6	9	12	15	20a	20b	22a	22b	1	2	1
Sc	3.48	2.74	2.84	2.5	3.16	2.97	2.45	2.97	2.51	2.64	2.98	2.43	3.32
Ti	3733	2856	4096	2060	1892	2322	4755	4813	5464	5426	5966	5906	6319
V	50.4	51.8	52.5	49.4	50.0	49.4	53.5	50.6	54.0	53.0	45.3	44.5	43.7
Cr	414	344	499	130	71	123	644	734	411	433	104	91	85
Co	54.6	59.1	58.4	59.4	57.7	58.6	59.9	59.7	59.9	59.9	63.3	59.3	57.6
Ni	841	880	851	843	809	816	854	867	871	841	972	949	875
Zn	64.7	74.7	61.7	68.6	68.3	65.1	68.8	71.0	68.3	70.0	76.1	71.4	80.1
Rb	256	265	270	275	271	263	273	270	281	276	262	266	259
Sr	19.3	42.9	21.0	23.5	13.7	24.2	19.6	19.7	31.9	29.4	20.0	19.0	12.3
Y	0.12	0.70	0.05	bdl.	0.07	0.05	bdl.	0.04	0.04	bdl.	0.04	0.04	0.04
Zr	7.20	8.95	4.48	3.38	2.77	3.65	4.05	5.33	6.50	6.73	7.02	8.11	5.22
Nb	98.5	105	101	93.4	94.1	92.7	94.7	96.3	101	98.6	102	104	112
Cs	3.83	4.06	3.81	3.74	3.88	3.59	3.91	3.8	3.81	3.76	2.95	3.62	3.23
Ba	2278	2350	2412	2222	2208	2185	2469	2457	2561	2620	3007	2950	3026
La	0.10	0.39	0.01	0.01	0.57	0.22	0.02	0.02	0.03	0.01	0.02	0.03	0.02
Ce	0.43	1.11	0.02	0.02	0.64	0.27	0.02	0.02	0.03	0.01	0.02	0.02	0.02
Pr	0.06	0.16	0.03	0.02	0.06	0.05	0.02	0.01	0.01	0.01	0.03	0.02	0.04
Nd	0.18	0.62	0.09	0.05	0.49	0.12	0.14	0.09	0.12	0.09	0.10	0.07	0.12
Sm	0.06	0.19	0.10	0.10	0.14	0.15	0.12	0.09	0.10	0.08	0.10	0.11	0.15
Eu	0.04	0.10	0.03	0.12	0.03	0.06	0.04	0.07	0.12	0.05	0.04	0.04	0.05
Gd	0.05	0.09	0.13	0.09	0.16	0.15	0.09	0.08	0.10	0.11	0.11	0.12	0.12
Tb	0.01	0.03	0.02	0.01	0.01	0.01	0.02	0.02	0.02	0.01	0.01	0.02	0.02
Dy	0.06	0.25	0.03	0.06	0.06	0.07	0.06	0.05	0.12	0.07	0.07	0.08	0.08
Ho	0.01	0.03	0.01	0.02	0.03	0.02	0.02	0.02	0.01	0.01	0.02	0.01	0.01
Er	0.06	0.04	0.05	0.08	0.06	0.08	0.09	0.07	0.07	0.06	0.04	0.06	0.04
Tm	0.01	0.01	0.01	0.01	0.02	0.01	0.02	0.01	0.02	0.02	0.03	0.02	0.02
Yb	0.05	0.11	0.08	0.11	0.08	0.12	0.09	0.14	0.14	0.11	0.11	0.00	0.16
Lu	0.01	0.01	0.02	0.02	0.01	0.02	0.01	0.02	0.02	0.02	0.02	0.02	0.02
Hf	0.07	0.13	0.06	0.05	0.13	0.10	0.00	0.11	0.21	0.14	0.31	0.10	0.09
Ta	2.36	2.09	2.80	1.76	1.84	1.83	2.85	2.90	2.98	3.21	4.22	4.31	4.88
Pb	0.84	1.12	0.97	0.98	0.78	0.88	0.76	0.96	1.16	1.08	1.14	0.80	0.51
Th	0.01	0.01	0.02	0.02	0.10	0.02	0.02	0.02	0.00	0.01	0.01	0.03	0.03
U	0.02	0.05	0.03	0.03	0.06	0.04	0.04	0.03	0.01	0.04	0.02	0.02	0.02

Appendix 2.2: Trace element composition of mineral phases from Finero dykes (contd.)

Grouping	HFSE-rich dyke												
Rock type	Dioritic dyke												
Sample	FI2104	FI2104	FI2104	FI2104	FI2104	FI2104	FI2104	FI2104	FI2104	FI2104	FI2104	FI2104	FI2104
Thin section	FI2104B	FI2104B	FI2104B	FI2104B	FI2104B	FI2104B	FI2104B	FI2104B	FI2104B	FI2104B	FI2104C	FI2104C	FI2104C
Phase	Phl	Phl	Phl	Phl	Phl	Phl	Phl	Phl	Phl	Phl	Phl	Phl	Phl
Spot No.	7	7	8	9	9	9	9	10	10	15	6	10	10
Analysis No.	13	14	18	19	20	21a	21b	23a	23b	34	1	1	2
Sc	5	5.09	4.61	4.89	4.73	4.83	3.98	4.32	4.44	3.78	3.29	3.98	3.01
Ti	5362	5603	5339	5566	5427	5329	5300	5209	5132	4855	6166	7361	6305
V	43.5	48.9	43.6	44.6	45.9	46.6	44.3	44.4	47.4	45.0	39.4	39.5	41.1
Cr	163	220	358	367	364	351	382	221	238	650	22	18	19
Co	58.6	58.3	60.0	60.2	56.9	58.4	60.4	58.3	57.3	56.7	45.7	48.6	50.1
Ni	853	874	895	866	873	888	883	852	866	883	664	648	724
Zn	83.8	81.6	89.4	88.5	90.6	93.1	85.0	88.1	85.6	80.2	66.6	71.9	70.6
Rb	265	272	263	277	268	278	267	262	270	258	227	235	226
Sr	29.4	26.4	14.7	19.5	16.9	17.3	25.4	16.8	20.3	19.3	7.3	16.4	10.6
Y	0.03	0.02	0.05	0.03	0.02	0.02	0.14	0.03	0.03	0.44	0.02	0.08	0.03
Zr	8.92	9.86	7.23	8.95	9.15	8.11	9.45	10.88	11.17	7.75	5.03	3.46	5.44
Nb	103	107	102	103	104	100	101	108	105	103	121	128	111
Cs	3.23	3.61	3.64	3.44	3.38	3.47	3.24	3.17	3.55	3.17	2.87	3.1	2.96
Ba	2969	3100	2979	3011	3041	2943	2942	2950	2876	2867	2521	3022	2639
La	0.01	0.01	0.01	0.01	0.01	0.01	0.07	0.02	0.02	0.20	0.02	0.03	0.02
Ce	0.01	0.01	0.01	0.01	0.01	0.04	0.26	0.00	0.01	0.40	0.02	0.01	0.01
Pr	0.01	0.01	0.01	0.01	0.00	0.01	0.04	0.01	0.01	0.08	0.01	0.01	0.02
Nd	0.08	0.04	0.07	0.08	0.08	0.04	0.23	0.07	0.08	0.27	0.05	0.04	0.05
Sm	0.12	0.14	0.03	0.09	0.06	0.08	0.11	0.14	0.07	0.13	0.07	0.08	0.14
Eu	0.04	0.08	0.03	0.04	0.04	0.01	0.04	0.10	0.03	0.10	0.07	0.06	0.05
Gd	0.08	0.09	0.06	0.00	0.04	0.04	0.12	0.04	0.08	0.11	0.06	0.04	0.03
Tb	0.01	0.01	0.01	0.01	0.01	0.01	0.01	0.01	0.01	0.01	0.01	0.01	0.02
Dy	0.07	0.06	0.03	0.04	0.03	0.05	0.08	0.10	0.04	0.05	0.06	0.02	0.05
Ho	0.01	0.01	0.01	0.01	0.01	0.01	0.01	0.01	0.01	0.02	0.00	0.01	0.02
Er	0.04	0.04	0.04	0.05	0.04	0.05	0.06	0.06	0.03	0.03	0.06	0.04	0.10
Tm	0.02	0.01	0.01	0.01	0.01	0.01	0.01	0.02	0.01	0.01	0.01	0.01	0.01
Yb	0.05	0.09	0.06	0.05	0.03	0.08	0.08	0.07	0.09	0.05	0.07	0.03	0.03
Lu	0.01	0.01	0.01	0.01	0.01	0.01	0.01	0.01	0.02	0.01	0.01	0.01	0.01
Hf	0.15	0.09	0.04	0.07	0.10	0.03	0.22	0.07	0.27	0.06	0.05	0.03	0.10
Ta	3.86	4.02	3.54	3.42	3.64	3.62	3.39	3.72	3.16	3.49	4.25	4.21	3.72
Pb	0.95	0.96	0.73	0.85	0.88	0.90	0.79	0.85	0.74	0.56	0.49	0.74	0.38
Th	0.01	0.01	0.02	0.01	0.04	0.01	0.02	0.01	0.02	0.08	0.07	0.01	0.01
U	0.01	0.01	0.01	0.01	0.02	0.03	0.01	0.01	0.03	0.04	0.02	0.02	0.01

Appendix 2.2: Trace element composition of mineral phases from Finero dykes (contd.)

Grouping	HFSE-rich dyke									
Rock type	Dioritic dyke		Hornblendite dyke with olivine layer					Hornblendite dyke		
Sample	FI2105	FI2105	FI1501	FI1501	FI1501	FI1501	FI1501	FI1612	FI1612	FI1612
Thin section	FI2105B	FI2105B	FI1501B	FI1501B	FI1501B	FI1501B	FI1501B	FI1612A	FI1612A	FI1612A
Phase	Phl	Phl	Phl	Phl	Phl	Phl	Phl	Phl	Phl	Phl
Spot No.	10	11	6	7	7	8	8	2	7	9
Analysis No.	1a	2a	12	15a	15b	17a	17b	4	1	2
Sc	2.54	2.57	5.57	6.03	6.69	5.93	6.04	3.5	2.59	2.84
Ti	11673	11020	13586	12971	14215	14198	14114	16394	15904	17153
V	54.1	55.4	195	215	224	202	205	48.4	52.5	50.4
Cr	437	389	197	357	264	201	206	431	333	343
Co	58.2	48.7	48.9	51.4	50.6	53.8	52.9	55.4	49.7	52.9
Ni	875	808	522	535	511	588	565	510	453	471
Zn	52.4	53.6	68.8	63.6	60.7	69.6	72.3	95.1	80.4	94.9
Rb	323	325	169	182	157	182	181	228	225	233
Sr	48.4	61.4	128	145	143	149	119	59.1	58.6	79.1
Y	0.28	0.56	0.05	0.02	0.10	0.06	0.19	0.44	0.42	0.06
Zr	6.93	13.96	1.06	1.02	2.12	1.42	2.18	11.50	17.03	11.45
Nb	132	136	42.5	39.3	38.9	53.2	51.0	131	144	141
Cs	6.56	7.69	3.05	3.79	3.14	3.74	3.72	3.69	3.07	3.8
Ba	3926	3660	2865	3115	3069	3143	3019	3208	3070	3669
La	0.26	0.39	0.01	0.00	0.07	0.04	0.14	0.25	0.20	0.03
Ce	0.48	1.01	0.02	0.01	0.14	0.08	0.38	0.92	1.02	0.01
Pr	0.05	0.13	0.01	0.01	0.02	0.01	0.06	0.15	0.11	0.01
Nd	0.40	0.87	0.04	0.05	0.12	0.04	0.04	0.47	0.55	0.06
Sm	0.09	0.13	0.00	0.04	0.05	0.07	0.06	0.36	0.17	0.04
Eu	0.09	0.09	0.05	0.07	0.04	0.04	0.07	0.18	0.13	0.05
Gd	0.05	0.11	0.07	0.04	0.13	0.03	0.11	0.21	0.09	0.06
Tb	0.01	0.02	0.01	0.01	0.00	0.01	0.01	0.01	0.05	0.01
Dy	0.20	0.06	0.04	0.04	0.04	0.03	0.04	0.05	0.36	0.04
Ho	0.02	0.02	0.01	0.00	0.01	0.01	0.00	0.09	0.01	0.01
Er	0.11	0.09	0.06	0.02	0.03	0.03	0.03	0.10	0.04	0.02
Tm	0.01	0.02	0.01	0.00	0.00	0.01	0.01	0.13	0.02	0.01
Yb	0.05	0.17	0.05	0.06	0.04	0.03	0.06	0.09	0.06	0.07
Lu	0.01	0.01	0.01	0.01	0.01	0.01	0.01	0.02	0.02	0.01
Hf	0.25	0.23	0.15	0.04	0.08	0.05	0.15	0.10	0.18	0.28
Ta	4.74	5.00	0.81	0.66	0.63	1.08	1.06	4.94	5.81	5.48
Pb	1.94	2.22	3.25	3.60	3.27	3.74	3.14	1.83	1.92	2.57
Th	0.10	0.05	0.04	0.01	0.01	0.03	0.08	0.01	0.03	0.01
U	0.03	0.02	0.02	0.01	0.01	0.01	0.02	0.03	0.02	0.01

Appendix 2.2: Trace element composition of mineral phases from Finero dykes (contd.)

Grouping	HFSE-rich dyke										
Rock type	Albite-dominated anorthosite dyke										
Sample	FI19A02	FI19A02	FI19A02	FI19A02	FI19A02	FI19A02	FI19A04	FI19A04	FI19A04	FI19A04	FI19A04
Thin section	FI19A02B	FI19A02B	FI19A02B	FI19A02B	FI19A02B	FI19A02B	FI19A04A	FI19A04A	FI19A04A	FI19A04B	FI19A04B
Phase	Phl	Phl	Phl	Phl	Phl	Phl	Phl	Phl	Phl	Phl	Phl
Spot No.	7	7	7	8	8	1	2	4	3	4	3
Analysis No.	14	15	16	18	19	1	10	12	11	7	4
Sc	2.93	3.55	2.82	2.78	2.92	2.91	2.35	2.45	2.15	2.86	1.98
Ti	16152	13841	14050	14731	14527	14023	10415	10370	9613	10443	11527
V	55.5	58.3	55.3	60.0	65.1	55.1	47.1	46.4	48.3	46.3	47.6
Cr	143	144	151	117	119	67	116	108	125	74	188
Co	51.7	52.7	52.6	54.9	52.1	54.5	59.4	59.4	58.7	59.1	54.8
Ni	674	680	696	844	619	604	737	720	712	745	722
Zn	104	126	129	128	125	117	146	120	123	88.6	116
Rb	65.4	91.1	81	13.6	7.16	6.47	5.93	3.00	3.33	25.15	5.21
Sr	19.2	32.4	17.4	22.4	20.1	19.5	11.7	6.89	5.83	11.4	5.63
Y	0.09	0.07	0.10	0.04	0.06	0.04	0.10	0.03	0.04	0.16	0.01
Zr	30.11	29.58	26.33	37.83	39.40	28.01	18.41	23.85	22.59	12.89	22.12
Nb	195	172	175	180	177	166	151	150	141	126	143
Cs	0.94	3.19	4.24	1.41	0.44	0.51	0.90	0.39	0.32	bdl.	0.49
Ba	1225	1383	1160	311	333	225	83.1	55.2	35.0	211	61.2
La	0.02	0.09	0.08	0.05	0.03	0.03	0.06	0.03	0.02	0.08	0.04
Ce	0.01	0.04	0.12	0.04	0.01	0.03	0.03	0.01	0.00	0.11	0.00
Pr	0.02	0.02	0.02	0.01	0.00	0.01	0.01	0.01	0.00	0.03	0.01
Nd	0.05	0.08	0.06	0.03	0.04	0.02	0.05	0.03	0.04	0.15	0.04
Sm	0.06	0.05	0.07	0.04	0.02	0.05	0.06	0.05	0.03	0.06	0.04
Eu	0.08	0.03	0.05	0.05	0.01	0.01	0.02	0.01	0.02	0.01	0.01
Gd	0.09	0.03	0.03	0.04	0.04	0.05	0.05	0.02	0.04	0.07	0.03
Tb	0.01	0.01	0.01	0.00	0.00	0.01	0.01	0.00	0.01	0.01	0.01
Dy	0.06	0.02	0.05	0.03	0.02	0.02	0.02	0.02	0.01	0.02	0.02
Ho	0.00	0.01	0.01	0.00	0.00	0.02	0.01	0.01	0.01	0.01	0.01
Er	0.04	0.03	0.03	0.00	0.02	0.05	0.03	0.02	0.02	0.06	0.02
Tm	0.01	0.00	0.00	0.01	0.00	0.01	0.00	0.01	0.01	0.00	0.00
Yb	0.11	0.04	0.03	0.02	0.02	0.02	0.04	0.07	0.02	0.05	0.04
Lu	0.02	0.01	0.00	0.01	0.01	0.00	0.02	0.01	0.01	0.01	0.01
Hf	0.90	1.03	0.76	1.01	0.88	0.51	0.32	0.47	0.48	0.19	0.43
Ta	8.39	7.82	7.85	7.72	7.54	7.30	5.28	4.92	4.68	5.24	5.60
Pb	0.49	0.74	0.83	0.42	0.45	0.37	0.82	0.29	0.26	0.35	0.31
Th	0.01	0.01	0.01	0.00	0.01	0.01	0.01	0.01	0.01	0.02	0.01
U	0.00	0.01	0.01	0.01	0.01	0.01	0.01	0.06	0.00	0.01	0.00

Appendix 2.2: Trace element composition of mineral phases from Finero dykes (contd.)

Grouping	Composite HFSE-poor and -rich dyke		
Rock type	Hornblendite dyke with cumulus peridotite		
Sample	FI1607	FI1607	FI1607
Thin section	FI1607C	FI1607C	FI1607B2
Phase	Phl	Phl	Phl
Spot No.	11	11	3
Analysis No.	18	19	24
Sc	5.57	5.00	5.31
Ti	13090	13870	24742
V	239	229	323
Cr	95	104	60
Co	36.4	38.6	69.5
Ni	363	375	118
Zn	103	99	170
Rb	246	244	262
Sr	32.5	38.8	185
Y	0.19	0.23	1.28
Zr	1.66	1.47	3.13
Nb	4.49	4.25	10.7
Cs	6.96	6.60	6.6
Ba	4000	4481	6699
La	0.12	0.06	0.61
Ce	0.16	0.08	0.71
Pr	0.02	0.02	0.04
Nd	0.05	0.07	0.41
Sm	0.02	0.01	0.08
Eu	0.03	0.02	0.04
Gd	0.03	0.06	0.33
Tb	0.01	0.01	0.12
Dy	0.01	0.03	0.22
Ho	0.00	0.01	0.08
Er	0.02	0.04	0.19
Tm	0.00	bdl.	0.01
Yb	0.04	0.03	bdl.
Lu	0.00	0.00	bdl.
Hf	0.09	0.04	0.08
Ta	0.08	0.08	0.22
Pb	n.d.	n.d.	6.88
Th	0.06	0.03	0.19
U	0.04	0.05	0.03

Appendix 2.2: Trace element composition of mineral phases from Finero dykes (contd.)

Grouping	HFSE-rich dyke											
Rock type	Dioritic dyke											Hbdite
Sample	FI1603	FI1603	FI1603	FI1604	FI1604	FI1604	FI2102	FI2102	FI2102	FI2104	FI2104	FI1501
Thin section	FI1603A	FI1603B	FI1603C	FI1604C	FI1604C	FI1604C	FI2102C	FI2102C	FI2102C	FI2104C	FI2104C	FI1501B
Phase	Ap	Ap	Ap	Ap	Ap	Ap	Ap	Ap	Ap	Ap	Ap	Ap
Spot No.	15	2	3	2	2	18	4	5	6	5	5	9
Analysis No.	63	5	6	2a	2b	2	8	13	14	1a	1b	18
Sc	0.80	0.63	0.44	0.63	0.37	0.29	0.28	0.28	0.35	0.23	0.23	0.51
Ti	bdl.	bdl.	bdl.	2.00	1.81	2.38	1.53	1.84	1.85	1.54	1.34	bdl.
V	1.85	1.58	0.78	1.05	0.76	0.19	0.99	0.72	1.13	0.78	0.83	2.21
Cr	9.39	1.93	0.71	13.1	1.81	1.85	1.71	1.44	1.9	1.11	1.09	1.83
Co	0.87	3.37	0.50	0.60	0.34	0.39	0.16	0.41	0.29	0.29	0.09	0.49
Ni	9.49		4.11	5.01	0.86	0.66	1.24	1.04	1.09	0.3	1.31	2.45
Zn	3.75	2.25	1.48	5.13	4.27	3.37	2.47	1.97	4.21	0.46	1.2	2.1
Rb	0.37	0.37	0.37	0.32	0.37	0.38	0.50	0.58	0.36	0.23	0.43	0.29
Sr	13940	9316	10600	22560	22273	20555	26938	25792	25211	19607	20308	20110
Y	259	322	355	242	252	268	341	330	339	461	442	166
Zr	1.00	1.00	1.69	1.00	1.02	1.13	0.50	0.51	0.48	2.1	2.12	0.31
Nb	0.05	0.05	0.05	0.05	0.02	0.09	0.06	0.02	0.03	0.05	0.05	0.10
Cs	0.02	0.02	0.02	0.02	0.01	0.02	0.02	0.02	0.02	0.02	0.01	0.01
Ba	68.7	99.9	74.8	25.8	27.0	30.8	33.3	30.5	26.9	33.0	29.7	17.6
La	2611	2603	2364	2228	2188	2280	2553	2550	2513	2730	2715	1423
Ce	4440	4299	4091	3773	3810	4435	5295	5074	4725	5468	5498	2448
Pr	383	392	386	328	330	352	427	433	412	455	464	210
Nd	1247	1418	1408	1106	1080	1158	1423	1383	1377	1549	1536	709
Sm	171	195	197	146	146	160	193	182	181	215	215	95
Eu	44.1	50.3	51.7	42.4	41.3	45.8	51.7	53.3	54.4	61.7	59.7	26.3
Gd	110	125	131	101	102	111	129	124	124	160	155	63.7
Tb	12.4	14.8	15.4	11.9	12.6	12.6	15.1	14.7	15.1	19.5	19.5	7.25
Dy	58.9	73.7	77.0	54.5	56.8	59.5	71.6	72.9	72.7	97.8	95.4	35.2
Ho	10.5	12.7	13.7	9.54	9.84	10.7	13.0	13.0	12.8	17.7	17.5	6.60
Er	24.3	30.8	34.3	21.6	23.8	23.7	30.1	31.3	32.0	41.0	39.7	14.0
Tm	2.97	3.68	4.01	2.59	2.96	2.95	3.44	3.67	3.29	4.94	4.77	1.67
Yb	16.2	22.1	22.8	15.5	16.6	15.0	21.7	19.3	21.1	30.1	26.6	10.2
Lu	2.12	2.73	2.85	1.99	2.07	2.02	2.64	2.57	2.64	3.79	3.26	1.43
Hf	0.05	0.05	0.05	0.05	0.05	0.06	0.07	0.08	0.08	0.06	0.05	0.07
Ta	0.01	0.01	0.01	0.01	0.01	0.01	0.02	0.03	0.01	0.01	0.01	0.02
Pb	n.d.	n.d.	n.d.	41.2	37.8	35.3	32.2	29.4	29.9	22.7	21.1	15.6
Th	139	160	153	163	172	177	174	173	166	179	171	83.4
U	34.2	39.4	36.5	49.2	53.3	54.1	51.5	47.6	48.3	48.7	47.6	33.9

Hbdite – Hornblendite with olivine layer

Appendix 2.2: Trace element composition of mineral phases from Finero dykes (contd.)

Grouping	HFSE-rich dyke										
Rock type	Hornblendite dyke							Albite-dominated anorthosite dyke			
Sample	FI1612	FI1612	FI1612	FI1612	FI1612	FI1612	FI1612	FI19A02	FI19A04	FI19A04	FI19A04
Thin section	FI1612A	FI1612A	FI1612A	FI1612A	FI1612A	FI1612A	FI1612A	FI19A02B	FI19A04A	FI19A04A	FI19A04A
Phase	Ap	Ap	Ap	Ap	Ap	Ap	Ap	Ap	Ap	Ap	Ap
Spot No.	1	3	4	4	5	8	9	2	7	6	5
Analysis No.	2	1	1a	1b	1	1	1	3b	20	17	16
Sc	0.38	0.27	0.34	0.28	0.19	0.16	0.25	0.30	0.09	0.11	0.14
Ti	1.41	4.23	2.77	2.54	2.27	1.44	2.05	3.02	0.75	1.85	0.97
V	0.40	0.51	0.23	0.31	0.91	0.71	0.77	0.73	0.67	0.56	0.67
Cr	1.58	1.89	4.45	1.49	1.34	1.56	1.91	0.48	0.46	0.78	0.86
Co	0.23	0.13	0.16	0.09	0.34	0.35	0.42	1.34	0.33	0.50	0.30
Ni	0.91	0.28	0.44	0.99	0.66	0.75	0.38	1.44	1.46	1.36	1.25
Zn	2.18	0.7	2.78	1.59	1.05	1.16	2.55	8.38	6.17	8.73	7.63
Rb	0.17	0.22	0.21	0.16	0.36	0.21	0.28	0.12	0.23	0.19	0.18
Sr	16631	11637	15885	16116	20428	16686	16263	6846	8381	7689	8380
Y	244	233	264	243	266	227	230	226	214	212	240
Zr	3.19	0.452	2.79	1.17	1.83	1.43	3.10	4.54	4.52	4.35	4.38
Nb	0.10	0.19	0.07	0.16	0.17	0.09	0.25	0.03	0.02	0.09	0.09
Cs	0.02	0.02	0.02	0.02	0.02	0.01	0.01	0.01	0.01	0.01	0.01
Ba	13.3	15.5	13.5	12.5	19.6	14.2	23.5	19.8	22.0	21.8	21.2
La	1538	1593	1657	1525	1624	1577	1556	930	970	1050	1052
Ce	2576	2885	2914	2771	3730	3206	3389	3720	3399	3695	3814
Pr	258	268	294	265	307	282	279	272	241	272	273
Nd	947	941	1030	936	1046	945	933	708	700	703	764
Sm	136	136	146	134	151	133	133	105	101	103	111
Eu	33.3	35.8	39.0	35.3	39.9	33.0	37.8	35.9	37.0	39.0	40.3
Gd	93.2	90.0	104.4	95.2	110.6	89.4	92.7	75.3	73.9	71.2	82.0
Tb	12.1	11.3	12.7	11.2	12.6	10.7	11.0	9.41	8.82	9.15	10.1
Dy	56.8	52.3	57.8	55.7	61.2	51.6	54.5	48.9	44.8	47.7	49.3
Ho	9.88	9.19	10.2	9.81	11.1	9.06	9.41	9.21	8.03	8.82	9.17
Er	21.8	21.0	21.7	20.8	24.6	22.2	22.4	21.6	19.4	19.9	23.2
Tm	2.5	2.6	2.57	2.93	2.95	2.2	2.36	2.61	2.3	2.51	2.85
Yb	16.6	15.2	20.2	16.7	18.7	13.4	15.6	17.0	14.3	15.0	17.5
Lu	2.18	1.96	2.20	2.21	2.47	2.05	2.10	1.98	1.83	2.02	2.27
Hf	0.05	0.10	0.09	0.05	0.04	0.05	0.05	0.00	0.09	0.03	0.07
Ta	0.01	0.02	0.02	0.04	0.01	0.01	0.02	0.01	0.00	0.00	0.01
Pb	15.8	21.7	15.9	17.6	23.6	16.4	19.1	10.4	11.4	11.3	11.2
Th	111	96	118	105	111	112	107	41.6	46.9	49.1	53.6
U	30.0	26.2	31.8	29.8	38.8	32.2	36.5	29.6	26.6	28.3	28.2

Appendix 2.2: Trace element composition of mineral phases from Finero dykes (contd.)

Grouping	HFSE-rich dyke			HFSE-poor dyke	Composite HFSE-poor and -rich dyke				
Rock type	Albite-dominated anorthosite dyke			Hornblendite dyke	Dioritic dyke	Hornblendite dyke with cumulus peridotite			
Sample	FI19A04	FI19A04	FI19A04	FI1608	FI2106	FI1607	FI1607	FI1607	FI1607
Thin section	FI19A04A	FI19A04B	FI19A04B	FI1608B	FI2106A	FI1607B2	FI1607B2	FI1607D	FI1607D
Phase	Ap	Ap	Ap	Ap	Ap	Ap	Ap	Ap	Ap
Spot No.	5	9	10	5	10	1	1	3	4
Analysis No.	13	15	16	5	20	21	22	14	16
Sc	0.24	0.23	0.18	0.66	0.18	0.21	0.23	0.18	1.01
Ti	0.62	1.85	4.03	bdl.	1.25	1.05	bdl.	bdl.	bdl.
V	0.90	0.84	0.80	6.16	1.14	2.00	1.94	1.93	4.06
Cr	2.05	0.67	0.85	4.45	1.09	2.07	1.32	1.43	1.08
Co	0.25	0.54	0.50	0.99	0.37	0.29	0.47	0.14	0.38
Ni	1.72	0.97	1.69	1.08	0.88	0.21	0.38	0.51	0.25
Zn	9.46	8.01	9.3	4.88	1.94	3.58	3.64	3.25	2.72
Rb	0.23	0.10	0.44	0.16	0.15	0.22	0.18	0.04	0.16
Sr	8135	8254	8870	3717	3926	8516	8778	1864	1255
Y	230	218	234	110	237	153	153	127	108
Zr	4.76	3.89	5.9	0.93	2.46	0.60	0.87	2.85	5.72
Nb	0.10	0.05	0.23	0.04	0.02	0.03	0.05	0.02	0.01
Cs	0.02	0.01	0.10	0.02	0.01	0.01	0.01	0.02	0.02
Ba	26.6	29.2	39.2	4.38	10.6	6.71	6.24	2.34	2.67
La	1094	932	980	193	1594	735	749	162	144
Ce	3505	3528	3910	383	2871	1109	1109	389	309
Pr	267	279	282	48	241	112	111	51.2	44.6
Nd	754	700	738	216	820	444	442	237	200
Sm	107	100	106	44.3	120	73.3	74.5	48.5	45.0
Eu	40.9	37.1	38.5	13.3	25.7	18.2	19.0	12.1	11.4
Gd	79.1	72.7	80.9	40.7	88.1	57.8	58.3	43.5	36.5
Tb	9.88	9.31	9.74	5.21	10.4	6.92	7.01	5.10	4.40
Dy	48.1	47.3	51.6	22.2	52.3	34.9	33.5	26.9	22.4
Ho	9.11	8.52	8.98	4.25	8.95	5.49	5.90	4.50	4.89
Er	23.5	20.9	22.6	9.0	22.3	13.1	13.2	11.0	8.3
Tm	2.68	2.57	2.72	1.01	2.62	1.63	1.36	1.26	1.00
Yb	16.2	15.8	16.0	6.00	14.3	8.41	8.92	7.63	5.29
Lu	2.01	1.90	2.07	0.89	1.82	1.14	1.11	0.94	0.85
Hf	0.02	0.02	0.07	0.04	0.05	0.05	0.20	0.06	0.06
Ta	0.01	0.01	0.01	0.01	0.01	0.01	0.02	0.01	0.02
Pb	11.6	13.0	16.9	6.34	10.3	10.0	8.18	1.77	1.01
Th	52.1	45.8	60.7	32.3	128	57.8	57.2	11.9	11.4
U	29.6	29.1	30.8	16.0	41.4	18.2	19.1	4.64	3.74

Appendix 2.2: Trace element composition of mineral phases from Finero dykes (contd.)

Grouping	HFSE-rich dyke											
Rock type	Clinopyroxenite cumulate in dioritic dyke											
Sample	FI1604	FI2105	FI2105	FI2105	FI2105	FI2105	FI2105	FI2105	FI2105	FI2105	FI2105	FI2105
Thin section	FI1604C*	FI2105B	FI2105B	FI2105B	FI2105B	FI2105B	FI2105B	FI2105B	FI2105B	FI2105B	FI2105B	FI2105B
Phase	Cpx	Cpx	Cpx	Cpx	Cpx	Cpx	Cpx	Cpx	Cpx	Cpx	Cpx	Cpx
Spot No.	8	2	3	3	3	4	5	5	5	6	7	8
Analysis No.	3	3	4	6	8	9	11	12	13	16	17	19
Sc	26.3	32.2	36.6	34.1	33.3	34.1	32.3	34.2	35.2	32.2	34.5	32.0
Ti	276	328	307	234	247	276	261	217	276	216	232	261
V	63.7	98.1	115	95.4	95.4	98.8	96.5	93.1	103	95.1	103	99.1
Cr	2634	2819	2335	2835	2788	2980	2869	2917	3062	2622	3554	2830
Co	18.9	17.7	17.0	16.2	17.6	17.6	16.7	17.9	18.3	16.6	16.0	16.5
Ni	220	339	300	271	289	317	296	320	312	292	275	293
Zn	36.2	19.6	19.2	20.6	19.6	20.8	19.9	20.3	20.8	19.0	18.6	17.8
Rb	0.14	0.02	0.03	0.09	0.03	0.04	0.03	0.07	0.03	0.03	0.03	0.04
Sr	656	549	567	576	579	577	604	580	527	588	608	589
Y	25.2	32.0	28.1	27.6	27.7	30.6	27.6	27.3	29.0	27.2	26.5	27.2
Zr	203	181	166	149	145	185	168	148	177	148	159	181
Nb	0.18	0.19	0.14	0.11	0.15	0.19	0.07	0.16	0.22	0.15	0.06	0.16
Cs	0.02	0.01	0.01	0.01	0.01	0.02	0.01	0.01	0.01	0.01	0.02	0.01
Ba	0.19	0.18	0.12	0.09	0.10	0.09	0.14	0.17	0.15	0.09	0.12	0.17
La	9.33	9.22	8.81	8.80	9.20	9.39	9.17	8.92	9.75	8.87	8.54	9.18
Ce	30.0	32.4	30.7	28.8	29.6	30.9	30.1	29.0	31.7	30.2	28.1	30.5
Pr	4.92	5.39	4.9	4.79	4.84	5.15	5.27	4.67	5.14	4.73	4.54	4.91
Nd	23.1	27.23	24.57	23.86	24.62	26.06	23.92	23.93	25.73	24.54	23.67	24.32
Sm	6.79	7.29	7.03	6.3	5.99	7.47	6.56	6.11	6.59	6.83	6.26	6
Eu	2.39	2.57	2.46	2.37	2.183	2.55	2.34	2.31	2.54	2.42	2.41	2.3
Gd	4.57	7.17	7.05	6.21	5.92	6.7	5.87	6.41	6.8	5.99	5.98	6.22
Tb	0.99	1.14	1.03	1.09	0.96	1.02	1.18	0.99	1.09	1.04	1.05	1.17
Dy	5.18	6.59	5.92	5.89	5.60	7.19	5.77	5.96	6.01	6.11	6.56	6.05
Ho	1.15	1.34	1.15	1.09	1.02	1.21	1.11	1.13	1.17	1.16	1.07	1.10
Er	3.03	3.18	2.93	3.07	2.74	3.61	3.30	2.77	2.57	3.00	2.56	2.64
Tm	0.26	0.42	0.45	0.35	0.41	0.40	0.47	0.41	0.40	0.36	0.38	0.47
Yb	2.83	3.04	2.32	2.63	2.98	2.97	2.79	2.90	2.70	2.38	2.74	2.73
Lu	0.40	0.49	0.38	0.41	0.38	0.40	0.41	0.42	0.38	0.38	0.32	0.48
Hf	5.13	3.93	4.16	3.83	3.71	4.27	3.85	3.56	4.03	3.74	4.24	5.20
Ta	0.03	0.03	0.03	0.02	0.02	0.03	0.02	0.02	0.02	0.04	0.02	0.02
Pb	1.81	1.08	0.93	1.06	1.00	0.91	0.99	0.72	0.99	0.91	0.97	0.95
Th	0.22	0.13	0.11	0.09	0.08	0.16	0.12	0.11	0.11	0.09	0.24	0.15
U	0.06	0.03	0.03	0.02	0.05	0.02	0.03	0.02	0.03	0.02	0.02	0.05

Appendix 2.2: Trace element composition of mineral phases from Finero dykes (contd.)

Grouping	Composite HFSE-poor and -rich dyke			HFSE-poor dyke						Composite HFSE-rich and -poor dyke		
Rock type	Hornblendite dyke			Orthopyroxenite layers bordering gabbroic dyke						Hornblendite dyke with cumulus peridotite		
Sample	FI1607	FI1607	FI1607	FI2101	FI2101	FI2101	FI2101	FI2101	FI2101	FI1607	FI1607	FI1607
Thin section	FI1607D	FI1607D	FI1607D	FI2101A	FI2101A	FI2101A	FI2101A	FI2101A	FI2101A	FI1607D	FI1607D	FI1607D
Phase	Cpx	Cpx	Cpx	Opx	Opx	Opx	Opx	Opx	Opx	Opx	Opx	Opx
Spot No.	7	7	7	6	7	7	8	8	9	6	6	6
Analysis No.	26	27	28	1	1a	1b	1a	1b	1	18	19	20
Sc	48.0	47.3	48.0	12.3	13.8	13.1	13.2	13.8	13.4	15.1	19.2	15.9
Ti	3561	3424	3076	435	611	546	515	591	584	513	524	466
V	252	253	250	37.7	45.0	47.5	42.6	50.6	48.8	115	123	110
Cr	150	138	151	800	1218	1319	1543	1635	1944	85.0	63.4	66.2
Co	23.3	22.8	25.6	56.2	58.7	56.5	56.0	55.6	56.4	68.3	70.5	69.7
Ni	30.4	29.0	27.2	506	651	602	601	577	603	56.4	53.0	53.2
Zn	41.7	47.9	52.3	66.6	58.3	56.6	51.4	55.6	55.5	232	245	246
Rb	0.03	0.02	0.04	0.04	0.04	0.04	0.04	0.04	0.03	0.03	0.07	0.13
Sr	40.3	39.1	45.8	0.05	0.03	0.03	0.10	0.06	0.02	0.56	1.25	0.72
Y	11.2	10.5	12.0	0.24	0.17	0.13	0.17	0.24	0.27	0.59	0.88	0.71
Zr	58.6	57.2	48.3	1.16	1.46	1.12	1.26	1.92	1.93	2.56	3.14	2.52
Nb	0.03	0.02	0.03	0.02	0.02	0.01	0.02	0.01	0.02	0.03	0.04	0.01
Cs	0.01	0.01	0.01	0.02	0.02	0.01	0.02	0.01	0.01	0.01	0.02	0.01
Ba	0.24	0.16	1.31	0.02	0.02	0.01	0.01	0.01	0.01	0.96	1.38	2.22
La	1.30	1.19	1.12	0.01	0.02	0.02	0.01	0.01	0.01	0.00	0.00	0.01
Ce	5.37	5.22	5.14	0.01	0.01	0.01	0.04	0.01	0.01	0.03	0.09	0.08
Pr	1.169	1.043	1.002	0.01	0.01	0.01	0.01	0.01	0.01	0.01	0.02	0.02
Nd	7.12	6.66	6.25	0.09	0.08	0.05	0.08	0.04	0.05	0.08	0.08	0.06
Sm	2.2	2.55	2.09	0.08	0.05	0.08	0.08	0.08	0.09	0.00	0.13	0.07
Eu	0.78	0.83	0.99	0.03	0.02	0.03	0.01	0.03	0.01	0.03	0.02	0.02
Gd	2.74	2.75	2.78	0.07	0.04	0.00	0.08	0.04	0.06	0.07	0.17	0.08
Tb	0.46	0.44	0.46	0.02	0.02	0.01	0.01	0.01	0.01	0.02	0.02	0.03
Dy	2.38	2.32	2.46	0.06	0.05	0.04	0.03	0.05	0.04	0.04	0.21	0.08
Ho	0.40	0.49	0.48	0.01	0.01	0.01	0.01	0.01	0.01	0.05	0.05	0.03
Er	1.13	1.38	0.90	0.05	0.09	0.08	0.05	0.07	0.08	0.12	0.17	0.17
Tm	0.12	0.14	0.16	0.01	0.01	0.01	0.01	0.01	0.02	0.03	0.03	0.01
Yb	0.84	0.84	1.00	0.09	0.11	0.10	0.06	0.15	0.06	0.16	0.09	0.22
Lu	0.10	0.14	0.11	0.01	0.01	0.01	0.02	0.02	0.01	0.01	0.04	0.03
Hf	2.17	2.30	2.53	0.13	0.11	0.07	0.06	0.11	0.18	0.17	0.09	0.08
Ta	0.01	0.02	0.02	0.01	0.01	0.01	0.01	0.01	0.01	0.01	0.01	0.01
Pb	0.13	0.15	0.12	0.02	0.02	0.02	0.02	0.02	0.02	0.03	0.03	0.07
Th	0.07	0.06	0.03	0.01	0.01	0.01	0.02	0.01	0.01	0.01	0.01	0.02
U	0.01	0.01	0.01	0.01	0.01	0.01	0.01	0.01	0.01	0.01	0.01	0.01

Appendix 2.2: Trace element composition of mineral phases from Finero dykes (contd.)

Grouping	HFSE-rich dyke			Composite dyke	
Rock type	Olivine layer in hornblendite dyke			Cumulus peridotite	
Sample	FI1501	FI1501	FI1501	FI1607	FI1607
Thin section	FI1501B	FI1501B	FI1501B	FI1607C	FI1607C
Phase	Ol	Ol	Ol	Ol	Ol
Spot No.	2	3	4	22	22
Analysis No.	2	5	7	36	37
Sc	6.24	6.06	5.01	2.33	2.21
Ti	2.91	4.10		6.85	6.90
V	0.23	0.10	0.47	0.16	0.11
Cr	5.37	7.58	9.99	2.80	2.18
Mn	2091	1921	2074		
Co	145	133	107	135	137
Ni	1440	1297	941	2076	2013
Cu	0.09	0.11	0.10		
Zn	175	168	165	188	177
Rb	0.02	0.03	0.04	0.01	
Sr	0.07	0.05	1.26	0.13	0.10
Y	0.01	0.02	0.02	0.02	0.01
Zr	0.03	0.08	0.24	0.01	0.01
Nb	0.05	0.02	0.46	0.00	0.01
Cs	0.01	0.01	0.01	0.02	0.02
Ba	0.01	0.13	0.14	1.18	0.04
La	0.03	0.01	0.04	0.01	0.04
Ce	0.01	0.00	0.14	0.01	0.01
Pr	0.01	0.00	0.01		
Nd	0.08	0.05	0.07	0.01	0.03
Sm	0.04	0.11	0.04		
Eu	0.01	0.02	0.01		
Gd	0.05	0.08	0.08	0.01	
Tb	0.01	0.01	0.01	0.00	0.00
Dy	0.03	0.03	0.02	0.01	0.00
Ho	0.01	0.01	0.00		
Er	0.04	0.05	0.04		
Tm	0.00	0.00	0.01	0.00	0.00
Yb	0.04	0.05	0.04	0.01	0.01
Lu	0.01	0.01	0.01	0.00	0.00
Hf	0.06	0.06	0.02		
Ta	0.01	0.01	0.01	0.00	0.00
Pb	0.03	0.03	0.02	n.d.	n.d.
Th	0.01	0.01	0.01	0.01	0.02
U	0.00	0.01	0.01	0.01	0.01

Appendix 2.3: Nd-Sr-Hf-Pb isotopic composition of amphiboles from selected Finero dykes

Sample ID	FI1603	FI2103	FI1501	FI1607	FI2101
Lithology	HR diorite	HR diorite	HR hornblendite	HP hornblendite	HP Spr-gabbro
Phase	Amph	Amph	Amph	Amph	Amph
$^{147}Sm/^{144}Nd$	0.1580	0.1452	0.1624	0.2327	0.1802
$^{143}Nd/^{144}Nd$	0.512833	0.512838	0.512758	0.512640	0.512603
$^{143}Nd/^{144}Nd_{(200)}$	0.512626	0.512648	0.512545	0.512336	0.512367
±2σ	0.000005	0.000004	0.000004	0.000003	0.000003
$\varepsilon Nd_{(200)}$	4.9	5.4	3.4	-0.7	-0.1
$^{87}Rb/^{86}Sr$	0.0400	0.0085	0.0074	0.0559	0.0853
$^{87}Sr/^{86}Sr$	0.703875	0.703787	0.704124	0.704891	0.705177
$^{87}Sr/^{86}Sr_{(200)}$	0.703761	0.703763	0.704103	0.704732	0.704934
±2σ	0.000007	0.000011	0.000008	0.000009	0.000015
$\varepsilon Sr_{(200)}$	-12.1	-12.1	-7.2	1.7	4.6
$^{176}Lu/^{177}Hf$	0.0058	0.0099	0.0215	0.0225	0.0153
$^{176}Hf/^{177}Hf$	0.282894	0.282857	0.282888	0.282903	0.282733
$^{176}Hf/^{177}Hf_{(200)}$	0.282873	0.282820	0.282808	0.282819	0.282675
±2σ	0.000022	0.000016	0.000005	0.000006	0.000006
$\varepsilon Hf_{(200)}$	7.6	5.7	5.3	5.7	0.6
$^{238}U/^{204}Pb$	4.9641	3.4000	2.4957	1.2769	5.5536
$^{206}Pb/^{204}Pb$	18.8512	18.8517	18.7734	18.4666	18.8295
$^{206}Pb/^{204}Pb_{(200)}$	18.6948	18.7445	18.6948	18.4263	18.6545
±2σ	0.0004	0.0004	0.0005	0.0004	0.0005
$^{235}U/^{204}Pb$	0.0360	0.0247	0.0181	0.0093	0.0403
$^{207}Pb/^{204}Pb$	15.5983	15.5920	15.5948	15.6185	15.6321
$^{207}Pb/^{204}Pb_{(200)}$	15.5905	15.5867	15.5909	15.6165	15.6233
±2σ	0.0004	0.0004	0.0005	0.0004	0.0005
$^{232}Th/^{204}Pb$	20.3324	16.3353	12.6451	4.8365	20.6230
$^{208}Pb/^{204}Pb$	38.6045	38.5724	38.5114	38.4373	38.7533
$^{208}Pb/^{204}Pb_{(200)}$	38.4023	38.4099	38.3856	38.3892	38.5483
±2σ	0.0012	0.0014	0.0016	0.0009	0.0015

Normalized to LaJolla $^{143}Nd/^{144}Nd = 0.51185$

Normalized to JMC475 $^{176}Hf/^{177}Hf = 0.282150$

Normalized to NBS 981 6/4 = 16.9356, 7/4 = 15.4891, 8/4 = 36.7006

HR – HFSE-rich; HP – HFSE-poor

Subscript represents correction to 200 Ma

Appendix 3.1: Trace elements composition of zircons from Finero alkaline dykes

Rock type	Dioritic dyke											
Sample No.	FI1603	FI1603	FI1604	FI1604	FI1604	FI1604	FI1604	FI1604	FI1605	FI1605	FI1605	FI1605
Zircon No.	Zrc2	Zrc3	Zrc2	Zrc5a	Zrc5b	Zrc6	Zrc8	Zrc9	Zrc1	Zrc4	Zrc3	Zrc5
Position	Core	Core	Rim	Core	Core	Rim	Rim	Rim	Rim	Core	Core	Core
Texture	Sector	Sector	Sector	Homog.	Homog.	Sector	Homog.	Sector	Sector	Oscil.	Sector	Homog.
Li	7.7	1.9	2.5	2.8	2.9	4.4	3.5	6.2	7.2	3.3	5.6	5.3
Sc	238	258	260	267	260	269	254	269	245	242	267	265
Ti	n.d.	n.d.	n.d.	n.d.	n.d.	n.d.	n.d.	n.d.	n.d.	n.d.	n.d.	n.d.
Rb	<0.08	<0.09	0.06	<0.07	<0.05	<0.06	0.05	0.04	<0.06	<0.06	<0.05	<0.03
Sr	0.06	2.08	0.65	0.08	0.12	0.11	<0.62	1.08	0.12	0.09	0.06	1.32
Y	172	122	88	116	106	181	91	116	123	169	127	96
Nb	0.67	1.67	0.75	0.57	0.54	0.75	0.51	1.39	0.82	0.34	0.24	1.60
Ba	<0.00	0.31	0.19	0.02	0.01	<0.00	<0.03	0.82	0.03	<0.00	<0.00	0.32
La	<0.00	0.44	<0.059	<0.00	<0.00	<0.00	<0.29	0.28	<0.00	<0.00	<0.00	0.35
Ce	1.25	3.29	0.95	1.25	1.27	2.61	<0.38	2.43	1.93	1.34	1.51	2.49
Pr	0.02	0.25	<0.04	0.01	0.01	0.01	<0.08	0.13	0.0202	<0.00	0.0121	0.038
Nd	0.58	1.61	0.10	0.21	0.25	0.10	<0.48	1.11	0.12	0.27	0.07	0.45
Sm	0.52	0.77	0.37	0.61	0.34	0.65	0.52	0.60	0.48	0.22	0.10	0.76
Eu	0.31	1.27	0.29	0.20	0.18	0.27	0.15	0.40	0.29	0.54	0.17	0.18
Gd	1.69	2.68	1.40	2.07	1.47	3.46	1.55	2.56	1.88	3.17	1.76	1.06
Tb	1.00	1.10	0.53	0.66	0.63	1.05	0.53	0.57	1.13	1.16	0.81	0.60
Dy	11.9	8.4	7.8	8.7	9.1	14.2	7.3	8.8	10.3	14.5	9.9	8.6
Ho	4.8	3.8	2.8	3.5	3.2	5.9	2.8	3.4	3.5	5.6	4.3	3.4
Er	26.6	18.2	13.7	18.2	17.2	29.7	14.4	17.5	17.6	27.0	19.6	16.7
Tm	6.4	5.0	3.5	4.8	3.7	7.0	3.5	4.6	4.3	6.6	4.6	3.5
Yb	82	52	35	45	38	70	35	45	51	72	58	42
Lu	18.1	11.9	7.5	9.4	8.2	15.9	8.3	10.4	9.0	14.2	11.7	8.3
Hf	4960	5351	3926	5846	5821	5948	4690	6195	4409	5676	5726	4729
Ta	0.57	0.42	0.81	0.64	0.43	0.40	0.58	1.30	0.38	0.16	0.21	0.30
Pb	1.48	0.50	0.63	0.49	0.42	0.93	0.40	0.81	1.42	1.16	1.08	0.75
Th	59	26	21	30	26	48	24	36	63	66	49	41
U	111	61	48	58	56	110	57	88	123	135	127	89
Th/U	0.53	0.43	0.43	0.52	0.47	0.44	0.41	0.41	0.51	0.49	0.38	0.46
U/Yb	1.36	1.17	1.37	1.28	1.48	1.57	1.61	1.93	2.41	1.87	2.20	2.14

Homog. – Homogeneous; Oscil – Oscillatory; n.d. – not determined

Appendix 3.1: Trace elements composition of zircons from Finero alkaline dykes (contd.)

Rock type	Dioritic dyke											
Sample No.	FI1605	FI1605	FI1605	FI1605	FI1605	FI1605	FI1605	FI1605	FI1605	FI1605	FI1605	FI1605
Zircon No.	Zrc9	Zrc11	Zrc16	Zrc17	Zrc21	Zrc22	Zrc25	Zrc32	Zrc34	Zrc37	Zrc40	Zrc56
Position	Core	Core	Core	Core	Core	Core	Rim	Core	Core	Core	Core	Core
Texture	Homog.	Homog.	Sector	Convol.	Convol.	Homog.	Convol.	Sector	Sector	Sector	Oscil.	Homog
Li	2.5	4.8	3.3	4.5	3.8	4.0	5.0	4.6	3.6	4.4	9.2	5.9
Sc	258	232	250	259	266	257	258	255	252	260	247	245
Ti	n.d.	n.d.	n.d.	n.d.	n.d.	n.d.	n.d.	n.d.	n.d.	n.d.	n.d.	n.d.
Rb	0.05	<0.05	0.04	<0.04	<0.03	<0.06	<0.05	<0.04	<0.04	0.05	0.09	<0.05
Sr	0.09	0.09	0.16	0.05	0.11	0.14	0.11	0.08	0.16	0.11	0.08	0.07
Y	107	50	73	88	90	183	92	89	235	76	190	87
Nb	0.65	0.47	0.39	0.55	0.61	0.55	0.35	0.43	0.56	0.31	0.65	0.56
Ba	0.04	<0.00	0.01	<0.00	0.02	<0.00	0.04	0.01	<0.00	0.02	0.03	<0.00
La	0.01	<0.00	0.01	<0.00	<0.00	<0.00	<0.00	<0.00	0.01	<0.00	0.01	<0.00
Ce	1.512	1.106	1.481	1.442	1.199	2.04	1.291	1.353	1.84	1.559	2.75	1.439
Pr	0.0076	<0.00	0.0302	0.0181	<0.0177	0.047	0.0083	<0.00	<0.00	<0.00	0.0371	<0.00
Nd	0.18	0.06	0.14	0.11	0.19	0.28	0.25	0.11	0.65	<0.00	0.67	0.05
Sm	0.36	<0.00	0.12	0.29	0.17	0.46	0.2	0.51	1.39	0.28	0.78	0.59
Eu	0.39	0.23	0.13	0.26	0.18	0.58	0.10	0.19	0.97	0.22	0.62	0.27
Gd	2.09	0.75	1.20	1.57	1.26	4.33	1.21	1.06	4.98	1.50	3.50	1.23
Tb	0.65	0.29	0.38	0.36	0.61	1.37	0.63	0.44	1.74	0.39	1.31	0.46
Dy	8.4	3.4	5.6	6.6	7.4	14.8	6.4	7.9	20.0	7.0	16.5	6.1
Ho	3.7	1.5	2.5	2.9	2.7	5.8	3.1	3.0	8.6	2.1	6.2	2.9
Er	17.4	7.5	11.3	13.4	14.6	25.6	14.8	14.3	35.4	11.5	31.8	16.1
Tm	3.8	2.3	2.7	3.4	3.7	6.1	3.8	3.8	8.7	3.1	7.3	3.4
Yb	39	23	33	37	36	65	42	41	86	33	71	37
Lu	9.0	4.7	6.7	7.8	7.9	13.7	8.2	8.2	17.0	7.7	16.3	8.3
Hf	4867	4914	5400	5046	5077	4513	4857	4936	5102	4774	4117	4606
Ta	0.36	0.32	0.22	0.38	0.39	0.37	0.15	0.38	0.32	0.15	0.36	0.57
Pb	1.77	0.83	0.63	0.85	1.25	1.72	0.70	0.71	2.50	0.90	2.14	0.46
Th	37	27	30	37	35	76	38	33	105	35	115	37
U	84	81	86	103	93	146	101	96	181	94	239	98
Th/U	0.44	0.33	0.34	0.36	0.38	0.52	0.38	0.34	0.58	0.37	0.48	0.38
U/Yb	2.13	3.49	2.61	2.82	2.60	2.25	2.42	2.33	2.11	2.82	3.37	2.65

Convol. – Convoluted

Appendix 3.1: Trace elements composition of zircons from Finero alkaline dykes (contd.)

Rock type	Anorthosite dyke											
Sample No.	FI19A01	FI19A01	FI19A01	FI19A01	FI19A01	FI19A01	FI19A01	FI19A01	FI19A01	FI19A01	FI19A01	FI19A01
Zircon No.	Zrc1	Zrc2	Zrc5	Zrc9	Zrc11	Zrc13	Zrc14	Zrc16	Zrc18	Zrc20	Zrc25	Zrc28
Position	Rim	Rim	Rim	Core	Core	Core	Core	Rim	Core	Core	Rim	Rim
Texture	Homog. inherited	Sector, inherited	Oscil.	Sector/ Oscil.	Sector/ Oscil.	Sector	Sector	Oscil.	Sector	Sector	Oscil.	Oscil. inherited
Li	4.2	3.1	3.6	3.3	4.7	7.2	9.5	7.2	10.9	2.1	3.9	4.5
Sc	185	178	179	183	179	186	189	182	191	178	178	172
Ti	4.1	5.0	2.8	4.2	3.2	2.2	3.3	3.4	4.0	5.3	4.1	2.7
Rb	<0.02	0.02	0.02	0.01	0.03	0.03	0.04	0.05	0.11	0.04	<0.02	0.02
Sr	0.31	0.26	<0.06	0.36	0.22	0.17	0.42	0.20	0.68	0.64	0.27	0.09
Y	83	157	79	69	172	189	241	208	704	142	121	102
Nb	0.52	0.81	0.67	0.48	1.07	0.90	1.37	1.25	4.54	1.07	1.03	0.48
Ba	0.19	0.11	0.01	0.12	0.06	0.03	0.09	0.08	0.07	0.38	0.14	<0.00
La	0.13	0.04	0.03	0.13	0.13	0.03	0.09	0.26	0.11	0.59	0.26	<0.00
Ce	0.96	1.25	0.85	1.11	1.66	0.92	1.32	2.05	2.42	2.47	4.15	1.23
Pr	0.0192	0.056	<0.0125	0.04	0.08	0.01	0.05	0.13	0.05	0.25	0.09	<0.00
Nd	0.165	0.33	0.084	0.10	0.46	0.08	0.70	0.79	0.99	1.36	0.53	0.21
Sm	0.28	0.39	0.09	0.33	0.59	0.42	1.13	1.22	1.44	0.73	0.32	0.22
Eu	0.29	0.34	0.17	0.20	0.42	0.45	0.86	0.62	0.78	0.48	0.38	0.24
Gd	0.98	2.52	1.09	0.95	2.78	2.60	4.92	4.70	7.39	2.55	1.96	1.29
Tb	0.54	0.97	0.46	0.32	1.14	1.11	1.86	1.43	3.48	0.88	0.77	0.61
Dy	6.7	12.6	5.6	5.2	13.9	14.3	21.6	18.7	51.9	12.8	10.4	8.0
Ho	2.5	5.1	2.6	1.9	5.6	6.1	8.1	7.0	23.0	4.5	4.0	3.6
Er	14.4	24.1	12.7	10.1	28.5	30.1	37.6	33.3	116.4	22.6	19.6	16.9
Tm	3.4	6.9	3.5	3.0	7.5	7.5	8.9	8.8	30.5	6.1	5.0	4.6
Yb	41	75	40	31	85	85	100	95	337	73	60	59
Lu	8.0	13.8	7.8	5.9	17.1	15.8	17.3	17.4	62.8	13.6	11.6	11.2
Hf	5620	4395	5249	5990	4582	7667	7785	5254	4384	4619	5635	6382
Ta	0.50	0.60	0.53	0.30	0.63	0.73	0.86	0.98	1.95	0.52	1.01	0.75
Pb	0.32	0.34	0.33	0.38	0.67	1.02	1.52	1.03	2.24	0.49	0.58	0.77
Th	18	21	16	16	31	46	83	49	101	18	35	33
U	37	33	30	27	41	78	106	64	153	29	42	35
Th/U	0.49	0.63	0.53	0.60	0.75	0.58	0.78	0.76	0.66	0.60	0.83	0.95
U/Yb	0.90	0.45	0.74	0.85	0.48	0.92	1.05	0.67	0.46	0.40	0.69	0.59

Appendix 3.2: U-Pb geochronology dataset of zircons from Finero alkaline dykes

					Ratio						
Rock type	Sample No.	Zrc No.	Spot Position	Zoning	$^{207}Pb/^{206}Pb$	2σ abs	$^{207}Pb/^{235}U$	2σ abs	$^{206}Pb/^{238}U$	2σ abs	Rho
Dioritic dyke	FI1603	Zrc1	Core	Sector	0.05017	0.01014	0.20853	0.04126	0.03015	0.00131	0.031689
	FI1603	Zrc2	Rim	Sector	0.05560	0.00881	0.22912	0.03546	0.02989	0.00111	0.031320
	FI1603	Zrc3a	Rim	Dark grey sector	0.06708	0.01124	0.27564	0.04495	0.02980	0.00124	0.027546
	FI1603	Zrc3b	Core	Light grey sector	0.05973	0.01209	0.25160	0.04970	0.03055	0.00142	0.028504
Dioritic dyke	FI1604	Zrc2	Rim	Sector	0.05363	0.00462	0.26043	0.02183	0.03522	0.00078	0.035781
	FI1604	Zrc4	Core	Homogeneous	0.05720	0.01357	0.25450	0.05903	0.03227	0.00171	0.028891
	FI1604	Zrc5	Rim	Homogeneous	0.05106	0.01336	0.23665	0.06063	0.03361	0.00188	0.030928
	FI1604	Zrc6	Rim	Sector	0.05578	0.00918	0.22280	0.03588	0.02897	0.00108	0.030094
	FI1604	Zrc8	Rim	Homogenous	0.05001	0.01152	0.23497	0.05325	0.03408	0.00152	0.028532
Dioritic dyke	FI1605	Zrc1	Rim	Sector	0.04647	0.00608	0.19715	0.02524	0.03078	0.00088	0.034845
	FI1605	Zrc3	Core	Sector	0.05278	0.00720	0.21094	0.02804	0.02899	0.00091	0.032336
	FI1605	Zrc4	Rim	Oscillatory	0.05370	0.00808	0.21385	0.03141	0.02888	0.00099	0.031371
	FI1605	Zrc9	Rim	Homogeneous	0.05131	0.01306	0.23565	0.05881	0.03331	0.00176	0.029949
	FI1605	Zrc10	Core	Homogeneous	0.04740	0.00568	0.20194	0.02365	0.03090	0.00080	0.033901
	FI1605	Zrc11	Core	Homogeneous	0.05117	0.00852	0.22686	0.03696	0.03216	0.00115	0.031018
	FI1605	Zrc16	Rim	Sector	0.05243	0.00975	0.22086	0.04022	0.03056	0.00120	0.029935
	FI1605	Zrc17	Rim	Bright	0.05630	0.00873	0.25016	0.03788	0.03223	0.00115	0.030259
	FI1605	Zrc21	Core	Homogeneous	0.05814	0.00966	0.25310	0.04106	0.03158	0.00120	0.029104
	FI1605	Zrc22	Rim	Homogeneous	0.05340	0.00834	0.24293	0.03707	0.03300	0.00116	0.031209
	FI1605	Zrc25	Rim	Sector	0.05339	0.01089	0.23879	0.04765	0.03244	0.00141	0.029663
	FI1605	Zrc32	Rim	Sector	0.04871	0.00836	0.21009	0.03530	0.03129	0.00114	0.032168
	FI1605	Zrc34	Core	Homogeneous	0.05289	0.00948	0.22676	0.03973	0.03110	0.00123	0.031061
	FI1605	Zrc37	Rim	Sector	0.04743	0.00873	0.20565	0.03707	0.03146	0.00120	0.032503
	FI1605	Zrc40	Core	Oscillatory	0.04995	0.00562	0.21683	0.02380	0.03149	0.00082	0.034541
	FI1605	Zrc56	Core	Homogeneous	0.05051	0.00880	0.23647	0.04031	0.03396	0.00128	0.031666
Anorthosite dyke	FI19A01	Zrc1	Core	Homogeneous, inherited	0.06211	0.00635	0.28250	0.02708	0.03301	0.00119	0.043921
	FI19A01	Zrc2a	Core	Sector, inherited	0.06466	0.00929	0.32789	0.04467	0.03680	0.00184	0.041149
	FI19A01	Zrc2b	Core	Sector, inherited	0.06057	0.01206	0.27891	0.05358	0.03341	0.00204	0.038129
	FI19A01	Zrc4	Core	Oscillatory	0.04750	0.00666	0.17189	0.02307	0.02627	0.00110	0.047574
	FI19A01	Zrc5	Rim	Oscillatory	0.05149	0.00500	0.22182	0.02031	0.03127	0.00100	0.049117
	FI19A01	Zrc7	Core	Sector	0.06515	0.00809	0.27515	0.03212	0.03066	0.00136	0.042446
	FI19A01	Zrc9	Core	Sector	0.04927	0.01179	0.21707	0.05037	0.03196	0.00214	0.042535
	FI19A01	Zrc11	Core	Sector	0.05104	0.00719	0.21976	0.02995	0.03124	0.00131	0.043863
	FI19A01	Zrc12	Rim	Oscillatory	0.04999	0.00756	0.21956	0.03218	0.03186	0.00138	0.043005
	FI19A01	Zrc13a	Core	Dark sector	0.05052	0.01043	0.21448	0.04277	0.03082	0.00190	0.044482
	FI19A01	Zrc13b	Core	Light sector	0.04984	0.01082	0.20624	0.04355	0.03002	0.00173	0.039787
	FI19A01	Zrc18	Core	Sector	0.05108	0.00870	0.21916	0.03597	0.03115	0.00163	0.045400
	FI19A01	Zrc20	Core	Sector	0.05344	0.01544	0.22557	0.06307	0.03068	0.00258	0.040936
	FI19A01	Zrc28	Rim	Oscillatory, inherited	0.04985	0.00997	0.25343	0.04924	0.03687	0.00209	0.042511

Appendix 3.2: U-Pb geochronology dataset of zircons from Finero alkaline dykes (contd.)

			Ages								
Rock type	Sample No.	Zrc No.	$^{207}Pb/^{206}Pb$	2σ abs	$^{207}Pb/^{235}U$	2σ abs	$^{206}Pb/^{238}U$	2σ abs	% disc.	Conc. age	2σ abs
Dioritic dyke	FI1603	Zrc1	203	41	192	38	191	8	0.4	192	8
	FI1603	Zrc2	436	69	209	32	190	7	9.4		
	FI1603	Zrc3a	840	141	247	40	189	8	23.4		
	FI1603	Zrc3b	594	120	228	45	194	9	14.9		
Dioritic dyke	FI1604	Zrc2	356	31	235	20	223	5	5.1		
	FI1604	Zrc4	499	118	230	53	205	11	11.1		
	FI1604	Zrc5	244	64	216	55	213	12	1.2	213	11
	FI1604	Zrc6	444	73	204	33	184	7	9.9		
	FI1604	Zrc8	195	45	214	49	216	10	-0.8	216	9
Dioritic dyke	FI1605	Zrc1	22	3	183	23	195	6	-7.0		
	FI1605	Zrc3	319	44	194	26	184	6	5.2		
	FI1605	Zrc4	358	54	197	29	184	6	6.7		
	FI1605	Zrc9	255	65	215	54	211	11	1.7	211	11
	FI1605	Zrc10	69	8	187	22	196	5	-5.0		
	FI1605	Zrc11	248	41	208	34	204	7	1.7	204	7
	FI1605	Zrc16	304	57	203	37	194	8	4.2		
	FI1605	Zrc17	464	72	227	34	204	7	9.8		
	FI1605	Zrc21	535	89	229	37	200	8	12.5		
	FI1605	Zrc22	346	54	221	34	209	7	5.2		
	FI1605	Zrc25	345	70	217	43	206	9	5.3		
	FI1605	Zrc32	134	23	194	33	199	7	-2.6		
	FI1605	Zrc34	324	58	208	36	197	8	4.9		
	FI1605	Zrc37	71	13	190	34	200	8	-5.2		
	FI1605	Zrc40	193	22	199	22	200	5	-0.3	200	5
	FI1605	Zrc56	219	38	216	37	215	8	0.1	215	8
Anorthosite	FI19A01	Zrc1	678	69	253	24	209	8	17.1		
dyke	FI19A01	Zrc2a	763	110	288	39	233	12	19.1		
	FI19A01	Zrc2b	624	124	250	48	212	13	15.2		
	FI19A01	Zrc4	74	10	161	22	167	7	-3.8		
	FI19A01	Zrc5	263	26	203	19	198	6	2.0	199	6
	FI19A01	Zrc7	779	97	247	29	195	9	21.1		
	FI19A01	Zrc9	161	38	199	46	203	14	-1.7	203	13
	FI19A01	Zrc11	243	34	202	27	198	8	1.7	199	8
	FI19A01	Zrc12	195	29	202	30	202	9	-0.3	202	8
	FI19A01	Zrc13a	219	45	197	39	196	12	0.8	196	11
	FI19A01	Zrc13b	188	41	190	40	191	11	-0.1	191	10
	FI19A01	Zrc18	244	42	201	33	198	10	1.7	198	10
	FI19A01	Zrc20	348	100	207	58	195	16	5.7		
	FI19A01	Zrc28	188	38	229	45	233	13	-1.8	233	13

*Concordant ages are calculated for only zircons with U-Pb discordance within ±2%

Appendix 3.3: In-situ Hf isotope composition of zircons from Finero alkaline dykes

Rock type	Sample	Zircon	Spot	Age	$^{176}Yb/^{177}Hf$	2σ	$^{176}Lu/^{177}Hf$	2σ	$^{176}Hf/^{177}Hf$	2σ	$^{176}Hf/^{177}Hf_{(t)}$	$\varepsilon Hf_{(t)}$	T_{DM}	T_{DM}^{C}
Diorite dyke	FI1603	Zrc1	Core	192	0.015236	0.000301	0.000332	0.000050	0.282932	0.000050	0.282931	9.8	443	724
	FI1603	Zrc2	Core	190	0.022035	0.000070	0.000480	0.000049	0.282979	0.000049	0.282977	11.4	358	584
	FI1603	Zrc3	Core	194	0.020904	0.000107	0.000433	0.000059	0.282921	0.000059	0.282919	9.5	463	756
Diorite dyke	FI1604	Zrc2a	Core	223	0.013628	0.000039	0.000288	0.000049	0.282885	0.000049	0.282884	8.9	515	841
	FI1604	Zrc2b	Rim	223	0.131718	0.001912	0.002298	0.000215	0.283077	0.000215	0.283068	15.4	209	341
	FI1604	Zrc4	Core	205	0.014233	0.000850	0.000310	0.000028	0.282928	0.000028	0.282927	10.0	443	723
	FI1604	Zrc5	Core	213	0.008445	0.000130	0.000183	0.000026	0.282915	0.000026	0.282914	9.7	469	766
	FI1604	Zrc6	Core	184	0.031817	0.000416	0.000719	0.000040	0.282951	0.000040	0.282949	10.3	421	687
	FI1604	Zrc7	Core	216	0.023479	0.001238	0.000475	0.000037	0.283016	0.000037	0.283014	13.3	318	519
	FI1604	Zrc8	Core	216	0.010457	0.000033	0.000231	0.000033	0.282904	0.000033	0.282903	9.4	475	776
	FI1604	Zrc9	Core	216	0.015750	0.000172	0.000358	0.000049	0.282961	0.000049	0.282960	11.4	391	639
Diorite dyke	FI1605	Zrc4	Core	184	0.012022	0.000024	0.000296	0.000033	0.282916	0.000033	0.282915	9.1	473	773
	FI1605	Zrc5	Core	215	0.019941	0.000094	0.000473	0.000046	0.282899	0.000046	0.282897	9.1	507	828
	FI1605	Zrc9	Core	211	0.011295	0.000110	0.000260	0.000036	0.282870	0.000036	0.282869	8.1	527	861
	FI1605	Zrc10	Core	196	0.029429	0.000034	0.000673	0.000047	0.282945	0.000047	0.282943	10.4	439	717
	FI1605	Zrc17	Core	204	0.020906	0.000689	0.000556	0.000060	0.282938	0.000060	0.282936	10.3	435	711
	FI1605	Zrc22	Core	209	0.011154	0.000255	0.000272	0.000038	0.282910	0.000038	0.282908	9.4	474	775
	FI1605	Zrc25	Core	206	0.017888	0.000186	0.000426	0.000036	0.282937	0.000036	0.282936	10.3	456	745
	FI1605	Zrc30	Core	215	0.020446	0.000216	0.000496	0.000041	0.282923	0.000041	0.282921	10.0	462	755
	FI1605	Zrc37	Core	200	0.017425	0.000224	0.000425	0.000036	0.282902	0.000036	0.282901	8.9	502	821
	FI1605	Zrc40	Core	200	0.023510	0.000186	0.000583	0.000043	0.282931	0.000043	0.282929	9.9	443	723
	FI1605	Zrc55	Core	215	0.010087	0.000033	0.000257	0.000032	0.282815	0.000032	0.282814	6.2	615	1004
	FI1605	Zrc56	Core	215	0.011562	0.000108	0.000295	0.000036	0.282921	0.000036	0.282920	10.0	459	750
Anorthosite dyke	FI19A01	Zrc1	Inh. c	209	0.020486	0.000939	0.000452	0.000029	0.282764	0.000029	0.282762	4.3	680	1111
	FI19A01	Zrc2	Inh. c	212	0.019263	0.000343	0.000440	0.000030	0.282703	0.000030	0.282701	2.1	765	1249
	FI19A01	Zrc4	Core	167	0.017323	0.000081	0.000401	0.000032	0.282708	0.000032	0.282706	1.4	754	1232
	FI19A01	Zrc5	Core	199	0.028861	0.000180	0.000670	0.000036	0.282641	0.000036	0.282638	-0.4	856	1399
	FI19A01	Zrc7	Core	195	0.016529	0.000117	0.000378	0.000025	0.282755	0.000025	0.282753	3.6	689	1126
	FI19A01	Zrc9	Core	203	0.011460	0.000081	0.000267	0.000021	0.282746	0.000021	0.282745	3.5	707	1155
	FI19A01	Zrc12	Rim	202	0.032358	0.000109	0.000770	0.000046	0.282643	0.000046	0.282641	-0.2	860	1405
	FI19A01	Zrc13	Core	191	0.008596	0.000017	0.000204	0.000022	0.282729	0.000022	0.282729	2.7	731	1195
	FI19A01	Zrc18	Core	198	0.012138	0.000065	0.000294	0.000024	0.282740	0.000024	0.282738	3.2	713	1165
	FI19A01	Zrc25	Core	200	0.023013	0.000151	0.000554	0.000039	0.282740	0.000039	0.282737	3.2	737	1204
	FI19A01	Zrc28	Inh. c	233	0.032733	0.000660	0.000757	0.000035	0.282758	0.000035	0.282754	4.5	703	1148

Inh. c – inherited core

Appendix 4.1: Major and minor elements composition of mineral phases in shoshonites from Dolomites, Southern Alps

Location	Val Giumela									
Rock type	Shoshonite (Basaltic Lava Flow)									
Sample ID	GIU01A	GIU01A	GIU01A	GIU01A	GIU01A	GIU01A	GIU01A	GIU01A	GIU01A	GIU01A
Phase	Cpx	Cpx	Cpx	Cpx	Cpx	Cpx	Cpx	Cpx	Cpx	Cpx
Spot	1	1	3	3	6	6	8	8	16	16
Analysis No.	1	2	9	10	12	13	16	17	30B	31
Comments	Core	Rim	Core	Rim	Core	Rim	Core	Rim	Core	Rim
SiO_2	50.06	51.06	50.22	49.85	50.16	50.17	49.25	50.12	50.00	51.17
TiO_2	0.45	0.51	0.55	0.63	0.55	0.62	0.58	0.63	0.59	0.49
Al_2O_3	4.23	2.85	3.59	3.72	2.83	3.72	3.67	3.79	3.61	2.91
Cr_2O_3	0.01	0.01	0.01	0.00	0.01	0.00	0.01	0.02	0.00	0.01
FeO_T	8.62	9.21	8.51	9.42	11.01	9.36	10.24	9.35	8.70	8.79
MnO	0.22	0.29	0.22	0.27	0.34	0.27	0.28	0.27	0.24	0.25
NiO										
MgO	14.42	14.61	14.50	13.98	14.25	13.95	13.55	13.94	14.35	14.58
CaO	21.28	20.77	21.68	21.05	19.37	21.12	20.02	21.17	21.39	21.16
Na_2O	0.27	0.31	0.26	0.31	0.24	0.28	0.33	0.29	0.26	0.28
K_2O	0.00	0.00	0.00	0.00	0.01	0.00	0.00	0.00	0.00	0.00
P_2O_5										
Cl										
Total	99.56	99.61	99.54	99.22	98.76	99.49	97.92	99.58	99.13	99.62
Mg#	74.9	73.9	75.2	72.6	69.8	72.7	70.2	72.7	74.6	74.7
Wo	44.1	42.8	44.5	43.8	40.3	44.0	42.5	44.0	44.2	43.6
En	41.6	41.9	41.5	40.5	41.3	40.4	40.0	40.3	41.3	41.8
Fe	14.3	15.3	14.0	15.7	18.4	15.6	17.4	15.6	14.5	14.5

Appendix 4.1: Major and minor elements composition of mineral phases in shoshonites from Dolomites, Southern Alps (contd.)

Location	Val Giumela											
Rock type	Shoshonite (Basaltic Pillow Lava)											
Sample ID	GIU02A	GIU02A	GIU02A	GIU02A	GIU02A	GIU02A	GIU02A	GIU02A	GIU02A	GIU02A	GIU02A	GIU02A
Phase	Cpx	Cpx	Cpx	Cpx	Cpx	Cpx	Cpx	Cpx	Cpx	Cpx	Cpx	Cpx
Spot	1	1	2	2	4	4	5	5	6	7	7	8
Analysis No.	1	2	7	8	10	11a	12	13	15	17	18	20
Comments	Core	Rim	Rim	Core	Rim	Core	Core	Rim	Rim	Core	Rim	Core
SiO_2	51.15	50.22	49.74	51.22	50.58	51.51	53.07	50.25	50.26	51.17	49.71	51.34
TiO_2	0.46	0.69	0.58	0.48	0.48	0.39	0.19	0.55	0.47	0.49	0.78	0.44
Al_2O_3	2.68	3.63	4.02	2.97	3.55	2.74	1.56	3.61	3.91	2.93	4.23	2.78
Cr_2O_3	0.00	0.04	0.00	0.00	0.01	0.13	0.21	0.01	0.09	0.03	0.00	0.00
FeO_T	9.20	9.67	9.17	8.87	8.65	7.93	4.61	9.49	8.90	10.02	9.90	9.07
MnO	0.27	0.30	0.26	0.28	0.21	0.16	0.07	0.27	0.22	0.37	0.20	0.28
NiO	0.00	0.01	0.01	0.04	0.01	0.00	0.02	0.01	0.09	0.10	0.01	0.00
MgO	14.75	14.01	14.34	14.47	14.16	15.51	16.78	14.33	14.68	14.14	13.79	14.94
CaO	21.29	21.52	21.45	21.69	22.00	21.35	23.19	21.51	21.42	20.93	21.56	21.58
Na_2O	0.23	0.34	0.30	0.30	0.20	0.23	0.21	0.28	0.34	0.30	0.31	0.27
K_2O	0.00	0.00	0.00	0.00	0.00	0.00	0.00	0.00	0.00	0.00	0.00	0.02
P_2O_5	0.20	0.16	0.11	0.14	0.23	0.15	0.14	0.14	0.13	0.19	0.15	0.11
Cl	0.00	0.00	0.02	0.00	0.00	0.00	0.00	0.01	0.00	0.00	0.00	0.00
Total	100.23	100.59	100.00	100.46	100.08	100.11	100.04	100.47	100.50	100.67	100.64	100.83
Mg#	74.1	72.1	73.6	74.4	74.5	77.7	86.6	72.9	74.6	71.6	71.3	74.6
Wo	43.3	44.1	44.0	44.3	45.2	43.4	46.2	43.8	43.7	43.0	44.3	43.4
En	41.7	39.9	40.9	41.1	40.5	43.8	46.5	40.6	41.7	40.4	39.5	41.9
Fe	15.0	16.0	15.1	14.6	14.2	12.8	7.3	15.5	14.5	16.6	16.2	14.7

Appendix 4.1: Major and minor elements composition of mineral phases in shoshonites from Dolomites, Southern Alps (contd.)

Location	Val Giumela									
Rock type	Shoshonite (Columnar Basalt)									
Sample ID	GIU03A	GIU03A	GIU03A	GIU03A	GIU03A	GIU03A	GIU03A	GIU03A	GIU03A	GIU03A
Phase	Cpx	Cpx	Cpx	Cpx	Cpx	Cpx	Cpx	Cpx	Cpx	Cpx
Spot	1	1	3	4	4	6	6	8	11	14
Analysis No.	1	2	4a	7	8	11	12	13	15a	17
Comments	Core	Rim	Core	Core	Rim	Rim	Core	Core	Core	Core
SiO_2	50.64	51.22	50.57	51.68	50.12	50.12	51.47	51.27	50.82	50.24
TiO_2	0.52	0.43	0.54	0.30	0.54	0.64	0.50	0.53	0.54	0.63
Al_2O_3	3.64	2.80	3.55	2.02	3.88	4.09	2.66	3.19	3.65	3.76
Cr_2O_3	0.00	0.03	0.00	0.02	0.00	0.00	0.00	0.01	0.02	0.05
FeO_T	8.77	9.20	9.10	9.83	9.69	9.60	8.85	8.96	9.60	9.12
MnO	0.21	0.26	0.26	0.40	0.25	0.32	0.27	0.28	0.27	0.28
NiO	0.00	0.06	0.00	0.02	0.00	0.02	0.04	0.02	0.00	0.01
MgO	14.12	14.79	14.32	14.61	13.93	14.20	14.69	14.69	14.09	14.19
CaO	21.64	20.95	21.74	20.94	21.07	21.44	21.65	21.60	20.54	21.74
Na_2O	0.30	0.26	0.23	0.23	0.33	0.34	0.28	0.22	0.30	0.30
K_2O	0.00	0.00	0.01	0.00	0.00	0.00	0.00	0.00	0.02	0.01
P_2O_5	0.16	0.13	0.20	0.12	0.17	0.15	0.13	0.11	0.12	0.18
Cl	0.00	0.01	0.00	0.00	0.01	0.01	0.00	0.03	0.00	0.00
Total	100.00	100.14	100.51	100.18	99.99	100.94	100.55	100.90	99.98	100.50
Mg#	74.2	74.1	73.7	72.6	71.9	72.5	74.7	74.5	72.3	73.5
Wo	44.8	42.8	44.4	42.5	43.7	43.8	44.0	43.9	42.9	44.5
En	40.7	42.1	40.7	41.3	40.2	40.4	41.5	41.5	41.0	40.4
Fe	14.5	15.1	14.9	16.2	16.1	15.8	14.5	14.6	16.1	15.0

Appendix 4.1: Major and minor elements composition of mineral phases in shoshonites from Dolomites, Southern Alps (contd.)

Location	Val Giumela										
Rock type	Shoshonite (Basaltic Dyke)										
Sample ID	GIU03DK	GIU03DK	GIU03DK	GIU03DK	GIU03DK	GIU03DK	GIU03DK	GIU03DK	GIU03DK	GIU03DK	GIU03DK
Phase	Cpx	Cpx	Cpx	Cpx	Cpx	Cpx	Cpx	Cpx	Cpx	Cpx	Cpx
Spot	1	2	2	3	3	5	5	6	6	8	8
Analysis No.	3	5	6	7	8	16	17	21	22	27	28
Comments	Rim	Core	Rim	Core	Rim	Core	Rim	Core	Rim	Core	Rim
SiO_2	49.39	50.52	50.51	49.45	50.71	50.18	50.22	51.38	48.59	50.67	51.24
TiO_2	0.76	0.43	0.63	0.66	0.49	0.53	0.62	0.41	0.91	0.57	0.53
Al_2O_3	4.23	3.47	3.91	4.28	3.41	3.67	3.75	2.83	5.02	3.44	2.85
Cr_2O_3	0.00	0.07	0.01	0.02	0.04	0.00	0.02	0.02	0.00	0.07	0.00
FeO_T	9.65	8.85	9.63	9.37	9.16	9.06	9.47	9.27	10.66	11.02	9.18
MnO	0.25	0.27	0.24	0.26	0.30	0.24	0.31	0.18	0.36	0.33	0.24
NiO	0.02	0.00	0.01	0.00	0.00	0.00	0.00	0.00	0.00	0.01	0.01
MgO	13.99	15.17	13.96	14.14	14.28	14.20	13.95	14.46	13.07	14.06	14.74
CaO	21.33	21.25	21.04	21.19	21.40	21.63	21.25	20.95	20.92	19.89	21.35
Na_2O	0.27	0.25	0.28	0.28	0.28	0.24	0.27	0.27	0.31	0.25	0.29
K_2O	0.00	0.00	0.00	0.00	0.00	0.01	0.00	0.01	0.00	0.02	0.00
P_2O_5	0.12	0.10	0.17	0.16	0.12	0.15	0.15	0.14	0.15	0.11	0.15
Cl	0.00	0.01	0.00	0.01	0.00	0.02	0.01	0.00	0.00	0.02	0.00
Total	100.00	100.39	100.39	99.82	100.19	99.93	100.02	99.93	100.00	100.46	100.59
Mg#	72.1	75.3	72.1	72.9	73.5	73.6	72.4	73.5	68.6	69.5	74.1
Wo	44.0	42.9	43.7	43.8	44.0	44.5	44.0	43.2	43.8	41.2	43.4
En	40.1	42.7	40.3	40.7	40.8	40.6	40.2	41.5	38.1	40.5	41.7
Fe	15.9	14.4	16.0	15.5	15.2	14.9	15.8	15.2	18.0	18.3	15.0

Appendix 4.1: Major and minor elements composition of mineral phases in shoshonites from Dolomites, Southern Alps (contd.)

Location	Latemar							
Rock type	Shoshonite (Basaltic Dyke)							
Sample ID	LAT01DK	LAT01DK	LAT01DK	LAT01DK	LAT01DK	LAT01DK	LAT01DK	LAT01DK
Phase	Cpx	Cpx	Cpx	Cpx	Cpx	Cpx	Cpx	Cpx
Spot	1	1	7	7	8	8	9	9
Analysis No.	1	2	10	11	12	13	14A	14B
Comments	Core	Rim	Core	Rim	Core	Rim	Core	Rim
SiO_2	49.71	49.62	48.73	48.99	50.64	50.15	49.38	49.20
TiO_2	1.10	1.14	1.18	1.27	0.87	1.04	1.26	1.31
Al_2O_3	3.91	4.06	5.38	4.69	2.94	3.85	4.11	4.46
Cr_2O_3	0.09	0.02	0.04	0.02	0.07	0.01	0.00	0.00
FeO_T	8.35	9.22	9.38	9.41	9.15	8.82	9.61	9.70
MnO	0.21	0.27	0.23	0.23	0.25	0.22	0.25	0.26
NiO								
MgO	14.25	14.38	14.03	13.37	14.66	14.25	14.01	13.72
CaO	21.27	20.50	20.24	20.55	20.24	20.92	20.78	20.52
Na_2O	0.38	0.35	0.42	0.45	0.32	0.36	0.32	0.32
K_2O	0.02	0.00	0.00	0.00	0.00	0.00	0.00	0.00
P_2O_5								
Cl								
Total	99.27	99.56	99.63	98.98	99.14	99.62	99.72	99.50
Mg#	75.3	73.6	72.7	71.7	74.1	74.2	72.2	71.6
Wo	44.5	42.8	42.8	44.0	42.2	43.8	43.3	43.3
En	41.5	41.8	41.3	39.8	42.5	41.5	40.6	40.3
Fe	14.0	15.5	15.9	16.1	15.3	14.8	16.1	16.4

Appendix 4.1: Major and minor elements composition of mineral phases in shoshonites from Dolomites, Southern Alps (contd.)

Location	Latemar							
Rock type	Shoshonite (Basaltic Lava Flow)							
Sample ID	LAT02A	LAT02A	LAT02A	LAT02A	LAT02A	LAT02A	LAT02A	LAT02A
Phase	Cpx	Cpx	Cpx	Cpx	Cpx	Cpx	Cpx	Cpx
Spot	1	1	3	3	4	4	5	5
Analysis No.	1	2	3	4	5	6	9	10
Comments	Core	Rim	Core	Rim	Core	Rim	Core	Rim
SiO_2	48.76	49.62	51.44	49.93	49.50	50.82	48.72	49.70
TiO_2	1.09	1.05	0.66	0.98	0.77	0.74	1.17	0.96
Al_2O_3	5.32	4.01	2.63	3.87	5.30	2.99	5.02	4.07
Cr_2O_3	0.01	0.00	0.01	0.01	0.12	0.01	0.00	0.01
FeO_T	9.01	9.63	8.76	9.17	7.74	8.26	9.59	9.39
MnO	0.21	0.31	0.31	0.28	0.19	0.24	0.28	0.30
NiO								
MgO	13.86	14.26	15.44	14.31	14.50	14.82	13.71	14.68
CaO	20.70	20.01	20.22	20.22	20.98	21.21	20.27	20.14
Na_2O	0.37	0.34	0.27	0.31	0.29	0.26	0.38	0.41
K_2O	0.01	0.00	0.00	0.00	0.00	0.00	0.00	0.00
P_2O_5								
Cl								
Total	99.34	99.24	99.74	99.08	99.39	99.35	99.15	99.67
Mg#	73.3	72.5	75.9	73.5	77.0	76.2	71.8	73.6
Wo	43.9	42.0	41.5	42.6	44.3	43.8	43.1	41.8
En	40.9	41.7	44.0	41.9	42.6	42.5	40.5	42.4
Fe	15.3	16.3	14.5	15.5	13.1	13.7	16.4	15.7

Appendix 4.1: Major and minor elements composition of mineral phases in shoshonites from Dolomites, Southern Alps (contd.)

Location	Val Giumela							
Rock type	Shoshonite (Basaltic Lava Flow)							
Sample ID	GIU01A	GIU01A	GIU01A	GIU01A	GIU01A	GIU01A	GIU01A	GIU01A
Phase	Plag	Plag	Plag	Plag	Plag	Plag	Plag	Plag
Spot	1	1	9	9	15	15	16	16
Analysis No.	3	4A	18	19	28	29	33	32
Comments	Core	Rim	Core	Rim	Core	Rim	Core	Rim
SiO_2	45.37	46.45	46.84	47.73	46.16	46.80	45.51	45.77
TiO_2	0.04	0.02	0.03	0.05	0.07	0.04	0.05	0.05
Al_2O_3	34.45	33.67	33.44	32.78	33.97	33.44	34.15	33.81
Cr_2O_3								
FeO_T	0.77	0.84	0.78	0.90	0.76	0.85	0.78	0.84
MnO	0.02	0.00	0.00	0.00	0.01	0.01	0.00	0.02
NiO								
MgO	0.06	0.08	0.09	0.09	0.07	0.08	0.10	0.09
CaO	17.85	16.81	16.73	16.06	17.24	16.78	17.58	17.40
Na_2O	1.07	1.59	1.54	1.97	1.34	1.63	1.05	1.36
K_2O	0.10	0.19	0.17	0.27	0.14	0.19	0.11	0.14
P_2O_5								
Cl								
Total	99.73	99.65	99.63	99.85	99.75	99.82	99.33	99.48
An	89.7	84.5	84.8	80.5	86.9	84.1	89.6	86.9
Ab	9.7	14.4	14.1	17.9	12.2	14.8	9.7	12.3
Or	0.6	1.1	1.1	1.6	0.8	1.1	0.7	0.9

Appendix 4.1: Major and minor elements composition of mineral phases in shoshonites from Dolomites, Southern Alps (contd.)

Location	Val Giumela						Val Giumela				
Rock type	Shoshonite (Basaltic Pillow Lava)						Shoshonite (Columnar Basalt)				
Sample ID	GIU02A	GIU02A	GIU02A	GIU02A	GIU02A	GIU02A	GIU03A	GIU03A	GIU03A	GIU03A	GIU03A
Phase	Plag	Plag	Plag	Plag	Plag	Plag	Plag	Plag	Plag	Plag	Plag
Spot	1	1	2	3	6	7	3	3	6	6	14
Analysis No.	3	4	6	9	16	19a	5	6	9	10	16
Comments	Core	Rim	Rim	Core	Core	Core	Core	Rim	Core	Rim	Core
SiO_2	45.86	46.77	46.41	46.24	46.59	46.24	46.71	46.02	46.18	46.11	46.01
TiO_2	0.00	0.08	0.00	0.12	0.00	0.00	0.00	0.01	0.03	0.04	0.01
Al_2O_3	33.99	33.21	33.40	33.99	33.70	33.33	33.61	33.17	33.38	33.58	34.18
Cr_2O_3	0.03	0.00	0.00	0.00	0.00	0.00	0.00	0.00	0.05	0.00	0.00
FeO_T	0.82	0.91	0.87	0.79	0.81	0.76	0.76	0.77	0.86	0.83	0.77
MnO	0.03	0.03	0.01	0.00	0.04	0.00	0.01	0.00	0.00	0.04	0.00
NiO	0.03	0.00	0.02	0.02	0.00	0.00	0.01	0.00	0.00	0.00	0.00
MgO	0.09	0.07	0.09	0.08	0.10	0.07	0.12	0.06	0.06	0.06	0.09
CaO	17.50	17.07	17.50	17.71	17.27	17.57	17.62	17.43	17.27	17.65	17.93
Na_2O	1.39	1.59	1.45	1.28	1.63	1.42	1.50	1.37	1.51	1.45	1.13
K_2O	0.14	0.19	0.15	0.13	0.15	0.14	0.15	0.14	0.16	0.15	0.11
P_2O_5	0.06	0.10	0.15	0.14	0.13	0.12	0.14	0.12	0.15	0.17	0.11
Cl	0.01	0.02	0.00	0.01	0.00	0.01	0.00	0.00	0.00	0.01	0.00
Total	99.96	100.04	100.05	100.53	100.42	99.66	100.62	99.10	99.64	100.09	100.35
An	86.7	84.6	86.2	87.8	84.6	86.5	85.9	86.8	85.5	86.3	89.2
Ab	12.5	14.3	12.9	11.5	14.5	12.7	13.2	12.3	13.5	12.8	10.2
Or	0.8	1.1	0.9	0.7	0.9	0.8	0.8	0.8	0.9	0.9	0.7

Appendix 4.1: Major and minor elements composition of mineral phases in shoshonites from Dolomites, Southern Alps (contd.)

Location	Val Giumela									
Rock type	Shoshonite (Basaltic Dyke)									
Sample ID	GIU03DK	GIU03DK	GIU03DK	GIU03DK	GIU03DK	GIU03DK	GIU03DK	GIU03DK	GIU03DK	GIU03DK
Phase	Plag	Plag	Plag	Plag	Plag	Plag	Plag	Plag	Plag	Plag
Spot	1	3	3	3	4	4	6	6	7	7
Analysis No.	1	9	10	11	12	13	18	19	23	24
Comments	Core	Core	Core	Rim	Core	Rim	Core	Rim	Core	Rim
SiO_2	45.12	46.15	45.88	47.76	46.65	46.42	46.30	46.96	45.63	47.96
TiO_2	0.05	0.04	0.07	0.01	0.05	0.02	0.02	0.00	0.00	0.08
Al_2O_3	32.51	33.15	33.11	32.53	33.56	33.58	33.87	33.29	33.77	32.73
Cr_2O_3	0.00	0.00	0.00	0.00	0.00	0.00	0.00	0.02	0.02	0.00
FeO_T	0.76	1.13	0.81	0.93	0.89	0.87	0.88	0.89	0.75	0.90
MnO	0.05	0.00	0.03	0.03	0.07	0.02	0.00	0.04	0.00	0.00
NiO	0.01	0.06	0.02	0.02	0.02	0.00	0.01	0.00	0.08	0.00
MgO	0.07	0.24	0.11	0.09	0.08	0.09	0.08	0.10	0.10	0.09
CaO	17.61	17.06	17.47	16.29	17.19	17.38	17.51	16.86	17.86	16.53
Na_2O	1.33	1.37	1.47	2.03	1.55	1.45	1.37	1.73	1.13	1.97
K_2O	0.14	0.14	0.17	0.23	0.18	0.15	0.15	0.18	0.13	0.23
P_2O_5	0.13	0.11	0.14	0.13	0.10	0.11	0.12	0.11	0.10	0.13
Cl	0.00	0.00	0.00	0.00	0.00	0.01	0.01	0.00	0.00	0.00
Total	97.77	99.46	99.28	100.05	100.33	100.10	100.34	100.18	99.58	100.62
An	87.3	86.6	85.9	80.5	85.1	86.1	86.8	83.4	89.0	81.2
Ab	11.9	12.6	13.1	18.2	13.9	13.0	12.3	15.5	10.2	17.5
Or	0.8	0.9	1.0	1.3	1.0	0.9	0.9	1.1	0.8	1.3

Appendix 4.1: Major and minor elements composition of mineral phases in shoshonites from Dolomites, Southern Alps (contd.)

Location	Val Giumela					Latemar	Latemar		
Rock type	Shoshonite (Basaltic Dyke)					Shoshonite	Shoshonite (Basaltic Lava Flow)		
Sample ID	GIU03DK	GIU03DK	GIU03DK	GIU03DK	GIU03DK	LAT01DK	LAT02A	LAT02A	LAT02A
Phase	Plag	Plag	Plag	Plag	Plag	Plag	Plag	Plag	Plag
Spot	7	7	8	9	9	1	2	2	8
Analysis No.	25	26	29	30	31	17	12	13	14
Comments	Rim	Core	Core	Core	Rim	Core	Core	Rim	Core
SiO_2	46.18	45.88	46.43	46.57	46.82	47.61	48.03	48.78	48.33
TiO_2	0.01	0.00	0.02	0.00	0.01	0.07	0.06	0.05	0.08
Al_2O_3	32.99	33.64	33.86	33.37	32.71	32.93	32.93	32.25	32.37
Cr_2O_3	0.01	0.00	0.02	0.01	0.01				
FeO_T	0.83	0.70	0.86	0.83	0.91	0.71	0.71	0.70	0.75
MnO	0.01	0.00	0.02	0.00	0.05	0.01	0.02	0.01	0.00
NiO	0.01	0.04	0.00	0.00	0.02				
MgO	0.08	0.05	0.09	0.09	0.07	0.08	0.08	0.10	0.09
CaO	17.38	17.59	17.35	16.83	16.89	15.85	15.98	15.28	15.29
Na_2O	1.40	1.25	1.44	1.64	1.66	2.04	2.05	2.48	2.49
K_2O	0.17	0.12	0.15	0.17	0.23	0.16	0.20	0.21	0.26
P_2O_5	0.14	0.15	0.15	0.13	0.14				
Cl	0.01	0.00	0.01	0.01	0.00				
Total	99.21	99.43	100.41	99.67	99.52	99.47	100.06	99.87	99.65
An	86.4	88.0	86.2	84.1	83.8	80.3	80.2	76.3	76.0
Ab	12.6	11.3	12.9	14.8	14.9	18.7	18.6	22.4	22.4
Or	1.0	0.7	0.9	1.0	1.3	1.0	1.2	1.3	1.5

Appendix 4.2: Trace element composition of mineral phases in shoshonites from Dolomites, Southern Alps

Location	Val Giumela												
Rock type	Shoshonite (Basaltic Lava Flow)												
Sample ID	GIU01A	GIU01A	GIU01A	GIU01A	GIU01A	GIU01A	GIU01A	GIU01A	GIU01A	GIU01A	GIU01A	GIU01A	GIU01A
Phase	Cpx	Cpx	Cpx	Cpx	Cpx	Cpx	Cpx	Cpx	Cpx	Cpx	Cpx	Cpx	Cpx
Spot	1	1	2	2	3	3	6	6	8	8	16	16	17
Analysis No.	1	2	5	6	9	10	12	13	16	17	31	30B	34
Comments	Core	Rim	Core	Rim	Core	Rim	Core	Rim	Core	Rim	Rim	Core	Core
Li	5.15	7.96	5.73	7.97	3.48	5.88	5.57	9.38	9.33	6.47	5.25	4.41	5.27
Be	0.093	0.173	0.154	0.047	0.14	0.19	0.27	0.153	0.37	0.135	0.083	0.27	0.19
B	17.89	15.97	16.48	12.8	17.23	14.64	18.1	17	13.32	13.91	13.48	11.05	15.57
Sc	86.5	87.8	90.8	94.3	90.7	90.4	98.8	89.2	105.0	91.5	95.4	90.7	92.5
Ti	2631	2707	3196	2921	2630	2836	3134	2545	3521	3041	2875	2622	2571
V	237	228	261	232	198	237	247	212	289	241	228	223	210
Cr	8.21	13.78	34.47	16.7	151.59	16.45	56.31	16.26	64.43	142.12	18.14	13.89	8.24
Mn	2421	2358	2438	2239	1414	2375	2137	2312	2735	2056	2013	2121	2006
Co	54.06	53.45	56.5	53.72	49.3	54.9	53.02	55.5	62.94	53.61	49.17	52.68	50.15
Ni	24.69	25.72	26.06	24.24	51.85	27.19	29.3	27.82	38.78	39.24	26.07	26.62	26.75
Cu	2.33	3.04	2.81	2.72	2.1	2.75	2.61	4.08	3.84	2.6	2.38	2.19	2.68
Zn	77.28	72.67	74.96	67.45	46.64	71.19	65.24	67.4	85.55	59.59	55.63	59.16	55.67
Rb	<0.01	0.03	0.03	<0.01	<0.02	<0.01	<0.01	0.02	<0.01	<0.01	<0.01	0.02	<0.01
Sr	88.12	85.87	97.74	92.75	85.88	89.12	93.35	88.88	90.68	89.98	85.46	82.19	84.75
Y	19.84	19.57	23.85	19.28	12.98	19.72	22.09	17.81	29.01	19.06	17.78	17.73	16.03
Zr	26.98	28.18	34.32	28	21.21	27.9	32.98	27.06	46.83	30.8	28.08	26.04	24.71
Nb	0.044	0.0293	0.061	0.053	0.044	0.0441	0.044	0.109	0.092	0.0468	0.0431	0.051	0.0442
Mo	0.098	0.102	0.133	0.181	0.093	0.1	0.188	0.078	0.199	0.078	0.076	<0.058	0.104
Cs	<0.00	<0.00	<0.00	<0.01	<0.00	<0.01	<0.00	0.01	<0.01	<0.00	0.01	<0.01	<0.01
Ba	0.089	0.173	0.157	0.1	0.053	0.075	0.079	0.1	0.116	0.099	0.143	0.084	0.239
La	3.49	3.43	4.29	3.64	2.08	3.46	3.8	3.08	5.58	3.33	3.3	3.25	3.03
Ce	13.24	13.38	15.35	13.36	8.38	13.43	13.98	12.25	20.27	12.45	12.11	12.29	11.2
Pr	2.46	2.46	3.02	2.49	1.806	2.48	2.81	2.27	3.51	2.5	2.29	2.22	2.17
Nd	14.32	14.98	17.41	15.19	10.07	15.38	15.85	13.98	21.28	14.41	14.5	13.65	12.77
Sm	4.91	4.63	5.87	4.95	3.6	4.99	5.4	4.77	6.85	4.73	4.59	4.3	4.25
Eu	1.272	1.409	1.51	1.289	0.885	1.285	1.308	1.171	1.72	1.136	1.16	1.3	1.05
Gd	4.61	4.7	4.94	4.61	3	4.68	4.99	4.16	6.49	4.71	3.88	4.18	4.05
Tb	0.717	0.804	0.8	0.724	0.428	0.685	0.801	0.719	1.098	0.709	0.67	0.634	0.575
Dy	3.94	4.45	5.02	4.15	2.67	4.33	4.65	3.69	6.2	3.93	3.8	3.67	3.26
Ho	0.789	0.744	1.018	0.736	0.536	0.752	0.828	0.771	1.186	0.79	0.771	0.749	0.659
Er	2.15	2.22	2.38	2.09	1.26	2.03	2.31	2.04	2.87	1.94	2.11	1.8	1.52
Tm	0.267	0.297	0.335	0.293	0.203	0.249	0.325	0.266	0.433	0.269	0.24	0.253	0.221
Yb	1.64	2.11	2.41	1.98	1.1	1.42	1.99	1.79	2.75	1.74	1.55	1.66	1.4
Lu	0.24	0.26	0.295	0.195	0.177	0.286	0.306	0.219	0.348	0.287	0.206	0.236	0.19
Hf	1.55	1.19	1.64	1.45	0.97	1.21	1.61	1.34	2.42	1.29	1.26	1.03	1.39
Ta	0.0073	0.0119	0.0163	0.0074	0.0056	0.0057	0.0088	0.0123	0.0168	0.0108	0.0034	0.0065	0.0076
Pb	0.217	0.243	0.168	0.204	0.097	0.166	0.08	0.13	0.274	0.216	0.149	0.218	0.171
Th	0.05	0.071	0.073	0.07	0.037	0.058	0.071	0.097	0.128	0.065	0.03	0.054	0.033
U	0.008	0.007	0.0042	0.0076	0.0058	0.0196	0.0181	0.0127	0.0174	0.0075	0.0071	0.009	0.004

Appendix 4.2: Trace element composition of mineral phases in shoshonites from Dolomites, Southern Alps (contd.)

Location	Val Giumela												
Rock type	Shoshonite (Basaltic Pillow Lava)												
Sample ID	GIU02A	GIU02A	GIU02A	GIU02A	GIU02A	GIU02A	GIU02A	GIU02A	GIU02A	GIU02A	GIU02A	GIU02A	GIU02A
Phase	Cpx	Cpx	Cpx	Cpx	Cpx	Cpx	Cpx	Cpx	Cpx	Cpx	Cpx	Cpx	Cpx
Spot	1	1	2	4	4	5	5	6	6	7	7	8	8
Analysis No.	1	2	8	11B	10	12	13	14	15	17	18	20	21
Comments	Core	Rim	Core	Rim	Core	Core	Rim	Core	Rim	Core	Rim	Core	Rim
Li	3.59	4.52	3.86	6.56	3.51	3.81	4.18	6.04	5.8	6.32	4.75	3.68	3.42
Be	0.21	0.29	<0.00	0.4	0.19	0.58	0.161	0.22	0.08	0.42	<0.00	<0.00	<0.00
B	16.81	13.38	10.7	6.13	9.49	12.25	10.89	11.17	14.88	10.01	11.93	9.77	11.27
Sc	89.78	97.23	86.41	87.24	99.15	94.19	102.63	90.11	91.26	87.2	102.47	92.55	85.59
Ti	2440.93	3276.92	2416.62	3146.37	3269.35	2744.64	3230.15	2351.04	2247.84	2659.13	3221.76	2562.71	2473.73
V	202.7	256.31	186.51	235.28	236.12	226.89	256.06	205.5	173.25	220.89	259.66	203.07	201.95
Cr	12.56	26.83	3.27	142.49	17.12	19.67	14.78	31.84	678.08	24.45	22.63	11.67	17.71
Mn	2037.73	2188.83	1781.57	1865.4	1837.94	2086.08	2111.72	2597.16	1614.15	2580.36	2238.79	2017.72	2101.86
Co	47.92	50.72	46.39	46.58	47.22	52.88	48.4	57.58	49.1	52.15	50.33	49.07	46.76
Ni	24.08	25.89	28.14	32.47	27.65	30.45	23.43	36.77	59.55	24.99	23.8	23.7	26.35
Cu	2.32	2.63	1.77	2.55	2.27	2.44	2.3	3.34	2.45	3.31	2.41	2.1	3.6
Zn	53.93	60.24	50.2	45.87	49.06	58.6	57.35	81	49.72	81.47	61.16	61.48	60.85
Rb	<0.0136	<0.0073	<0.0128	<0.0093	0.0133	0.041	<0.0103	0.024	<0.0119	<0.0102	0.0155	<0.0112	<0.0118
Sr	79.51	89.68	79.46	87.7	87.51	87.61	88.42	60.61	73.11	80.85	95.11	88.76	83.04
Y	16.12	22.73	14.43	18.1	17.97	17.56	21.61	22.75	15.48	25.28	23.35	16.73	17.09
Zr	23.34	37.56	22.55	32.67	31.62	28.06	33.73	28.45	22.87	32.97	35.9	24.29	25.49
Nb	0.031	0.06	0.0238	0.061	0.055	0.0356	0.048	0.063	0.0152	0.091	0.048	0.027	0.031
Cs	<0.0063	<0.00	<0.0084	<0.0033	<0.0064	<0.0091	<0.0052	<0.0077	<0.0107	<0.0091	<0.0094	0.0069	<0.0087
Ba	<0.031	0.115	0.065	0.0081	0.089	0.248	0.078	0.18	0.056	0.144	0.106	0.073	0.105
La	2.85	4.04	2.76	3.45	3.54	3.3	4.03	3.92	2.66	5.08	4.48	3.38	3.03
Ce	10.9	14.92	10.03	12.29	13.03	12.02	14.91	14.94	9.58	17.73	16.03	11.24	11.6
Pr	2.042	2.85	1.928	2.56	2.36	2.13	2.77	2.71	1.9	3.3	2.81	2.24	2.33
Nd	12.45	17.22	12.35	13.47	15.33	13.78	17.39	16.49	11.23	18.14	17.93	14.09	13.3
Sm	4.02	5.29	3.96	4.47	4.29	4.63	5.7	4.94	3.88	5.78	5.73	4.6	4.68
Eu	1.08	1.65	0.948	1.296	1.296	1.351	1.429	1.351	1.035	1.447	1.52	1.11	1.3
Gd	3.88	5	3.54	4.3	4.64	3.97	4.91	5.04	3.64	5.36	5.5	4.77	4.24
Tb	0.622	0.901	0.533	0.698	0.641	0.593	0.692	0.838	0.536	0.778	0.831	0.624	0.689
Dy	2.87	5.32	2.93	3.81	3.58	3.46	4.43	4.75	3.32	5.17	5.24	3.7	3.28
Ho	0.67	0.911	0.587	0.833	0.786	0.74	0.92	0.911	0.556	1.067	0.953	0.692	0.721
Er	1.53	2.2	1.46	1.86	1.8	1.65	2.26	2.81	1.66	2.54	2.57	1.73	1.64
Tm	0.223	0.31	0.194	0.247	0.251	0.215	0.287	0.315	0.214	0.354	0.378	0.237	0.238
Yb	1.38	2.1	1.25	1.94	1.86	1.57	2.23	2.24	1.23	2.6	2.2	1.44	1.23
Lu	0.172	0.285	0.176	0.198	0.249	0.224	0.299	0.274	0.195	0.313	0.269	0.226	0.239
Hf	0.85	1.66	1.39	1.59	1.62	1.23	1.48	1.23	1.14	1.48	1.78	1.38	1.24
Ta	0.0061	0.0064	0.0034	0.0069	0.0106	0.0083	<0.00	0.0064	0.0034	0.003	0.0161	0.0092	0.0053
Pb	0.064	0.217	0.209	0.122	0.165	0.169	0.108	0.28	0.176	0.263	0.256	0.376	0.265
Th	0.042	0.05	0.034	0.074	0.021	0.049	0.05	0.088	0.047	0.154	0.064	0.028	0.021
U	<0.0124	0.0067	0.022	0.022	0.0056	0.0059	0.0097	0.0068	0.0072	0.038	0.0069	0.0098	<0.00

Appendix 4.2: Trace element composition of mineral phases in shoshonites from Dolomites, Southern Alps (contd.)

Location	Val Giumela											
Rock type	Shoshonite (Columnar Basalt)											
Sample ID	GIU03A	GIU03A	GIU03A	GIU03A	GIU03A	GIU03A	GIU03A	GIU03A	GIU03A	GIU03A	GIU03A	GIU03A
Phase	Cpx	Cpx	Cpx	Cpx	Cpx	Cpx	Cpx	Cpx	Cpx	Cpx	Cpx	Cpx
Spot	1	1	3	3	4	4	6	6	8	11	11	14
Analysis No.	1	2	4A	4B	7	8	11	12	13	15A	15B	17
Comments	Core	Rim	Core	Rim	Core	Rim	Rim	Core	Core	Core	Rim	Core
Li	3.85	8.94	8.14	6.67	3.3	4.52	5.14	4.63	4.7	3.86	6.86	8.05
Be	0.22	0.3	0.12	0.18	0.142	0.151	0.16	0.32	0.34	<0.00	0.044	0.105
B	11.85	12.66	10.13	10.62	9.14	12.05	10.75	8.88	8.4	7.32	12.82	9.33
Sc	89.27	86.74	100.26	90.04	110.08	93.77	92.64	87.31	103.86	84.85	99.03	98.05
Ti	2761.77	2537.82	3225.08	2713.65	1811.27	3058.92	3049.79	2479.68	3225.4	2643	3100.69	3237.47
V	218.72	219.39	259.79	224.06	154.19	249.28	237.16	207.97	253.93	203.51	247.65	225.87
Cr	23.57	12.75	15.04	12.9	16.7	25.15	14.01	11.81	158.76	45.07	17.07	3.9
Mn	1836.64	2191.97	2196.8	2253.44	2793.23	2111.03	1918.87	2070.25	1828.56	1782.11	2080.96	1710.92
Co	47.1	51.18	49.37	51.57	51.66	49.8	45.31	48.61	49.47	45.29	47.59	46.95
Ni	28.04	23.93	24.01	24.63	17.54	24.59	24.34	25.05	34.13	32.4	22.06	26.04
Cu	2.43	2.82	3.62	3.01	2.23	2.4	2.47	2.56	2.5	2.27	2.78	2.96
Zn	53.46	63.65	59.7	62.58	77.83	56.19	57.94	55.08	48.56	48.84	54.76	46.73
Rb	<0.0178	<0.0176	<0.0126	<0.0103	<0.0068	<0.0115	0.011	<0.0148	<0.0123	<0.0099	<0.0172	<0.0105
Sr	82.84	82.66	90.63	85.94	76.99	95.1	95.45	79.9	89.33	81.74	86.78	85.93
Y	17.59	17.57	22.93	19.03	34.34	21.74	19.79	16.44	20.41	16.52	20.8	17.72
Zr	27.45	26.35	34.77	27.53	35.66	34.21	32.77	24.01	37.11	25.46	32.77	32.79
Nb	0.041	0.052	0.054	0.044	0.063	0.05	0.063	0.0341	0.056	0.0506	0.0469	0.0356
Mo	<0.073	0.064	0.174	0.143	0.077	0.115	0.032	0.159	0.125	0.103	0.082	0.06
Cs	0.0083	<0.0056	<0.0042	<0.0083	<0.0067	<0.0061	0.009	<0.0097	<0.0070	<0.0050	<0.0052	<0.00
Ba	0.064	0.075	0.069	0.064	0.088	0.083	0.155	0.102	0.125	0.055	0.08	0.265
La	3.04	3.41	3.9	3.44	5.59	4.19	4.06	2.8	3.76	3.04	3.88	3.32
Ce	11.84	11.96	15.71	12.69	22.78	15.67	14.39	10.93	14.35	11.92	14.87	12.53
Pr	2.17	2.28	2.94	2.55	4.14	2.92	2.8	2.111	2.82	2.34	2.84	2.44
Nd	12.81	14.11	16.71	14.34	25.65	17.27	15.88	11.99	15.38	12.86	15.78	13.69
Sm	4.05	4.21	5.44	5.16	8.23	5.04	5.3	4.29	4.95	4.31	5.48	4.5
Eu	1.216	1.184	1.49	1.239	1.82	1.478	1.37	1.129	1.507	1.098	1.296	1.16
Gd	3.98	4.46	5.62	4.39	8.14	5.05	4.56	3.91	4.72	3.88	4.92	4.5
Tb	0.635	0.621	0.826	0.692	1.258	0.864	0.899	0.628	0.771	0.623	0.819	0.659
Dy	3.75	3.9	4.69	4.2	7.2	4.72	4.45	3.29	4.78	3.62	4.47	3.96
Ho	0.69	0.783	0.96	0.739	1.344	0.959	0.877	0.749	0.799	0.728	0.816	0.679
Er	1.7	1.88	2.34	2.04	3.86	2.31	2.01	1.59	1.89	1.74	2.17	2.11
Tm	0.241	0.288	0.313	0.277	0.455	0.27	0.272	0.233	0.285	0.228	0.257	0.284
Yb	1.95	1.87	2.02	1.71	3.11	1.92	1.97	1.4	2	1.48	2.06	1.66
Lu	0.192	0.189	0.259	0.26	0.439	0.249	0.226	0.215	0.204	0.232	0.268	0.259
Hf	1.35	1.4	1.65	1.41	1.65	1.78	1.47	1.41	2	1.32	1.64	1.74
Ta	0.0047	0.0103	0.0077	0.005	0.0061	0.0065	0.0069	0.0113	0.0096	0.0052	0.0074	0.0132
Pb	0.12	0.249	0.258	0.159	0.303	0.156	0.242	0.148	0.246	0.26	0.136	0.158
Th	0.055	0.056	0.082	0.065	0.053	0.078	0.097	0.059	0.068	0.052	0.071	0.036
U	0.0196	0.022	0.0162	0.0105	0.026	0.0091	0.015	0.0096	<0.00	0.0037	0.0079	<0.00

Appendix 4.2: Trace element composition of mineral phases in shoshonites from Dolomites, Southern Alps (contd.)

Location	Val Giumela												
Rock type	Shoshonite (Basaltic Dyke)												
Sample ID	GIU03DK	GIU03DK	GIU03DK	GIU03DK	GIU03DK	GIU03DK	GIU03DK	GIU03DK	GIU03DK	GIU03DK	GIU03DK	GIU03DK	GIU03DK
Phase	Cpx	Cpx	Cpx	Cpx	Cpx	Cpx	Cpx	Cpx	Cpx	Cpx	Cpx	Cpx	Cpx
Spot	1	2	2	3	3	4	4	5	5	6	6	6	8
Analysis No.	3	5	6	7	8	14	15	16	17	20	21	22	27
Comments	Core	Core	Rim	Core	Rim	Core	Rim	Core	Rim	Rim	Core	Rim	Core
Li	11.12	5.49	11.62	5.93	6.64	1.52	9.34	4.1	5.08	8.22	3.35	8.01	4.16
Be	0.13	0.145	0.078	0.113	0.2	0.218	0.25	0.3	0.078	0.167	0.037	0.148	0.28
B	22.51	19.94	18.88	20.25	22.1	20.05	20.42	17.33	17.61	17.81	16.62	16.18	12.26
Sc	89.93	92.25	91.11	101.72	96.22	89.74	93.63	107.97	106.33	97.45	88.85	95.32	101.46
Ti	2672.19	2589.15	2699.16	3289.64	2891.15	3055.98	3243.35	3260.74	3482.15	3368.45	2527.25	3331.36	2955.77
V	211.9	208.74	224.9	254.42	247.87	237.99	264.09	258.96	284.97	274.12	212.54	258.13	241.08
Cr	3.85	15.47	11.78	16.47	10.09	31.18	23.27	18.58	20.96	22.88	13.43	30.01	51.86
Mn	1738.63	2021	2283.83	1981.11	2375.29	1936.36	2202.18	2092.36	2331.87	2347.23	2178.35	2180.28	1977.47
Co	52.48	51.34	55.22	52.84	55.46	52.98	55.81	53.91	55.99	54.81	53.37	53.33	54.41
Ni	29.56	27.72	25.51	28.01	26.7	33.92	31.08	28.75	28.31	28.71	26.02	30.25	35.23
Cu	3.82	2.55	3.86	2.89	2.83	1.79	3.47	2.83	2.86	3.15	2.39	3.02	2.43
Zn	58	62.45	68.8	63.03	70.48	59.34	64.18	64.17	68.19	69.28	63.47	64.03	69.44
Rb	<0.0166	0.0282	<0.0091	<0.0095	<0.0139	<0.0117	<0.0097	<0.0078	<0.0126	0.0119	<0.0124	<0.0092	<0.0124
Sr	81.55	83.25	82.68	91.31	87.99	91.9	93.67	92.03	93.36	92.48	80.91	88.12	71.44
Y	15.34	16.09	18.89	21.22	20.55	17.82	22.77	20.59	23.84	23.03	17.32	21.89	21.51
Zr	23.56	25.85	26.97	34.61	28.5	28.83	33.78	34.46	38.65	37.78	24.6	36.1	34
Nb	0.027	0.129	0.0447	0.0596	0.0466	0.0385	0.0533	0.065	0.085	0.053	0.0288	0.058	0.074
Mo	<0.071	0.139	0.168	0.087	0.088	0.06	<0.062	<0.059	0.127	0.141	0.122	0.141	0.1
Cs	<0.0039	<0.0070	<0.0050	<0.00	<0.0072	0.0021	<0.0048	<0.0050	<0.0065	<0.0093	<0.0040	<0.0089	0.0082
Ba	0.089	0.082	0.092	0.092	0.086	0.064	0.1	0.095	0.139	0.169	0.093	0.077	0.097
La	2.79	3.03	3.38	3.9	3.54	3.12	4.1	3.95	4.4	4.08	3	3.76	4.24
Ce	10.64	10.75	12.12	13.73	12.67	11.63	14.33	14.01	15.42	14.18	11.37	14.02	14.91
Pr	2.063	2.041	2.292	2.66	2.53	2.246	2.75	2.81	3.03	2.87	2.22	2.69	2.75
Nd	11.54	12.7	14.18	15.88	15.13	13.52	16.81	15.88	18.14	17.11	12.65	15.54	17.36
Sm	3.87	3.88	4.32	4.79	4.71	4.42	5.47	5.51	5.71	5.5	3.93	5.2	4.93
Eu	1.047	1.19	1.247	1.412	1.344	1.194	1.505	1.438	1.59	1.53	1.255	1.395	1.275
Gd	3.66	3.87	4.65	4.84	5.09	4.26	5.33	5.23	5.69	5.15	4.22	5.01	4.75
Tb	0.528	0.596	0.706	0.776	0.746	0.67	0.791	0.745	0.882	0.815	0.668	0.743	0.805
Dy	2.9	3.58	4.01	4.39	4.32	3.95	4.58	4.56	5.09	4.78	3.45	4.9	4.79
Ho	0.62	0.665	0.753	0.82	0.87	0.672	0.866	0.811	0.945	0.857	0.671	0.852	0.895
Er	1.62	1.55	1.87	2.14	2.03	2.03	2.22	2	2.63	2.47	1.63	2.21	1.93
Tm	0.196	0.248	0.25	0.257	0.276	0.239	0.278	0.255	0.331	0.352	0.219	0.282	0.321
Yb	1.36	1.43	1.81	1.84	1.82	1.43	2.11	1.87	1.93	2.14	1.61	2.08	1.88
Lu	0.184	0.222	0.213	0.261	0.233	0.209	0.258	0.267	0.314	0.296	0.224	0.265	0.294
Hf	1.32	1.113	1.3	1.83	1.3	1.31	1.7	1.73	1.77	1.89	1.1	1.91	1.69
Ta	0.0047	0.0084	0.0043	0.0083	0.0075	0.0163	0.0084	0.0129	0.0149	<0.0075	0.0087	0.0087	0.0132
Pb	0.145	0.196	0.155	0.202	0.13	0.153	0.179	0.15	0.174	0.171	0.119	0.195	0.276
Th	0.0339	0.0441	0.043	0.065	0.063	0.053	0.065	0.071	0.091	0.103	0.077	0.098	0.101
U	0.0085	0.0173	0.0131	0.0051	0.0055	0.0109	0.0067	0.0027	0.0112	0.0062	0.0111	0.0028	0.011

Appendix 4.2: Trace element composition of mineral phases in shoshonites from Dolomites, Southern Alps (contd.)

Location	Latemar										
Rock type	Shoshonite (Basaltic Dyke)										
Sample ID	LAT01DK	LAT01DK	LAT01DK	LAT01DK	LAT01DK	LAT01DK	LAT01DK	LAT01DK	LAT01DK	LAT01DK	LAT01DK
Phase	Cpx	Cpx	Cpx	Cpx	Cpx	Cpx	Cpx	Cpx	Cpx	Cpx	Cpx
Spot	1	1	2	2	7	7	8	8	9	9	9
Analysis No.	1	2	3	4	10	11	12	13	14A	14B	15
Comments	Core	Rim	Core	Rim	Core	Rim	Core	Rim	Core	Core	Rim
Li	5.07	6.2	5.66	7.04	5.01	8.06	2.57	4.58	3.16	4.21	6.73
Be	0.19	0.126	<0.00	0.19	0.26	0.29	0.145	0.21	0.24	0.26	0.128
B	15.7	17.08	10.84	11.94	11.97	13.32	10.45	14.09	12.82	15.98	14.87
Sc	114.85	112.19	118.5	118.8	98.08	127.09	98.13	100.66	109.76	123.67	115.29
Ti	4992.75	4679.7	5243.39	5023.02	4858.16	5599.35	4577.22	4766.61	5901.47	6604.7	5072.05
V	349.4	341.59	351.29	350.06	374.81	383.13	274.72	357.36	458.48	436.6	363.92
Cr	126.41	74.12	507.26	135.7	91.57	127.98	1149.7	46.21	1376.45	331.06	97.52
Mn	1706.07	2173.22	1383.04	1831.34	2192.49	1975.01	1279.18	2372.78	1365.95	1582.65	2178.05
Co	36.66	40.28	34.46	37.71	43.45	38.7	33.76	43.25	35.14	39.13	40.61
Ni	50.49	46.56	52.24	48.92	61.79	45.68	90.54	54.57	97.67	61.31	48.63
Cu	1.85	2.25	2.04	2.29	3.18	2.39	1.435	2.81	2.3	1.99	2.14
Zn	48.89	61.15	41.6	47.88	54.82	58.78	42.95	65.49	46.67	50.93	61.65
Rb	<0.0134	<0.0109	0.0267	0.0137	<0.0084	<0.0115	<0.0091	<0.0088	0.0107	<0.0129	<0.0124
Sr	50.65	46.95	53.73	47.12	45.69	49.73	55.48	50.81	60.82	53.75	44.35
Y	19.85	22.34	17.24	20.04	21.53	23.73	17.98	22.39	23.13	23.71	22.14
Zr	36.81	35.44	35.62	38.59	35.42	43.89	34.96	36.09	52.68	51.91	39.07
Nb	0.04	0.048	0.059	0.056	0.063	0.064	0.0588	0.067	0.104	0.101	0.0514
Mo	0.099	0.142	0.119	0.089	0.073	0.148	0.076	0.145	0.046	0.092	0.123
Cs	0.0091	<0.0050	<0.0087	0.0128	0.0045	<0.0058	<0.0072	<0.0057	<0.0062	<0.0046	<0.0040
Ba	0.056	0.1	0.407	0.099	0.052	0.067	0.055	0.073	0.108	0.107	0.044
La	2.81	2.97	2.43	2.71	2.51	3.36	2.44	2.88	3.61	3.32	2.87
Ce	10.49	11.03	9.32	10.47	9.8	12.6	9.42	11.47	13.13	12.71	11.51
Pr	2.205	2.2	1.8	2.036	1.978	2.5	1.856	2.217	2.66	2.41	2.188
Nd	13.67	13.9	11.53	12.66	11.86	15.66	11.48	13.89	15.29	15.52	13.83
Sm	4.28	4.76	3.53	4.19	4.24	5.08	3.57	4.33	5.09	5.29	4.34
Eu	1.304	1.424	1.112	1.167	1.481	1.634	1.168	1.32	1.458	1.523	1.236
Gd	4.48	4.68	3.72	4.36	4.41	5.2	4.09	5.2	4.94	5.11	4.91
Tb	0.686	0.805	0.594	0.662	0.759	0.804	0.585	0.72	0.775	0.794	0.749
Dy	4.24	4.52	3.82	4.12	4.18	5.25	3.86	4.45	4.58	5.02	4.76
Ho	0.786	0.93	0.706	0.811	0.969	0.953	0.764	0.917	0.919	0.939	0.944
Er	2.08	2.24	1.76	2.04	2.09	2.58	1.84	2.27	2.19	2.47	2.32
Tm	0.299	0.307	0.201	0.268	0.314	0.327	0.268	0.308	0.315	0.319	0.305
Yb	1.71	2.08	1.57	1.82	2.12	2.29	1.72	2.05	2.41	2.43	2.06
Lu	0.245	0.325	0.244	0.255	0.288	0.287	0.256	0.244	0.281	0.298	0.271
Hf	1.48	1.6	1.48	1.94	1.51	1.96	1.44	1.5	2.5	2.46	1.69
Ta	<0.0094	0.0051	0.012	0.0187	0.0053	0.0118	0.0118	0.0069	0.0099	0.021	0.0052
Pb	0.086	0.134	0.102	0.142	0.09	0.216	0.079	0.113	0.113	0.119	0.11
Th	0.044	<0.0072	0.038	0.04	0.034	0.0178	0.042	0.0275	0.035	0.056	0.0217
U	0.0112	<0.00	<0.0080	0.0072	<0.00	0.0066	0.0202	0.0101	0.0039	0.0148	0.0034

Appendix 4.2: Trace element composition of mineral phases in shoshonites from Dolomites, Southern Alps (contd.)

Location	Latemar							
Rock type	Shoshonite (Basaltic Lava Flow)							
Sample ID	LAT02A	LAT02A	LAT02A	LAT02A	LAT02A	LAT02A	LAT02A	LAT02A
Phase	Cpx	Cpx	Cpx	Cpx	Cpx	Cpx	Cpx	Cpx
Spot	1	1	3	3	4	4	4	9
Analysis No.	1	2	3	4	6	7	8	11
Comments	Rim	Core	Core	Rim	Rim	Rim	Rim	Rim
Li	5.08	4.32	34.23	5.5	3.78	4.02	4.91	4.7
Be	0.34	0.11	0.58	0.28	0.108	0.15	0.17	0.16
B	14.42	6.63	13.08	14.56	15.51	11.81	15.26	13.81
Sc	148.18	118.24	151.1	144.96	157.07	168.26	136.42	127.02
Ti	5475.95	3669.56	5634.13	4918.48	5303.45	5806.33	3787.64	3725.84
V	437.85	314.77	514.6	393.34	418.61	460.79	331.02	315.86
Cr	44.96	111.87	35.43	24.01	135.1	78.11	48.87	24.31
Mn	2405.27	1983.07	4126.6	2545.4	1675.08	1777.4	2296.48	2669.6
Co	35.91	35.24	89.02	36.03	34.08	33.14	37.81	38.49
Ni	38.82	52.25	71.63	34.66	45.25	37.93	41.6	37.06
Cu	4.46	3.91	5.08	5.16	3.28	3.52	4.02	3.99
Zn	67.37	50.9	179.14	66.01	44.64	44.8	55.85	70.25
Rb	0.094	0.125	0.587	<0.0116	<0.0097	0.0217	<0.0137	<0.0078
Sr	51.66	50.08	59.65	48.76	56.5	55.19	43.84	44.57
Y	30.4	17.13	33.66	31.06	24.09	29.65	19.9	25.21
Zr	41.82	21.55	46.12	39.61	37.41	45	24.6	26.02
Nb	0.081	0.074	0.107	0.05	0.058	0.091	0.0349	0.0288
Mo	0.096	0.087	0.43	0.145	<0.041	0.102	0.091	0.128
Cs	<0.0051	0.0077		<0.0054	<0.0072	<0.0053	<0.0102	<0.0100
Ba	0.532	1.227	1.95	0.136	0.072	0.14	0.043	0.08
La	3.79	1.94	4.05	3.34	3.07	3.31	1.887	2.61
Ce	14.05	7.93	15.17	13.8	11.69	13.5	7.55	10.37
Pr	2.89	1.595	2.92	2.82	2.28	2.77	1.579	2.13
Nd	17.8	10.41	17.95	17.36	14.78	17.91	9.97	12.87
Sm	5.99	3.51	5.55	6.57	5.02	6.37	4.11	5.09
Eu	1.65	1.11	1.89	1.78	1.448	1.9	1.072	1.369
Gd	6.64	3.7	6.86	6.03	5.27	6.48	3.75	5.41
Tb	1.147	0.535	1.179	0.951	0.884	1.043	0.612	0.802
Dy	6.39	3.2	6.52	6.3	4.9	6.03	4.22	5.2
Ho	1.221	0.815	1.42	1.276	1.011	1.239	0.774	1.122
Er	2.91	1.87	3.95	3.14	2.58	3.13	2.13	2.64
Tm	0.44	0.243	0.452	0.447	0.319	0.46	0.272	0.332
Yb	2.91	1.59	3.55	2.65	2.17	3.11	2	2.4
Lu	0.443	0.257	0.452	0.386	0.328	0.354	0.282	0.347
Hf	2.08	1.04	2.06	2.09	1.78	2.17	1.08	1.36
Ta	0.0114	0.0086	0.0047	0.0159	0.0109	0.0203	0.0046	0.0022
Pb	0.065	0.035	1.73	0.108	0.099	0.133	0.06	0.127
Th	0.067	0.023	0.184	0.057	0.0236	0.062	0.0207	0.0237
U	0.0139	<0.00	0.028	0.0092	0.0089	0.0083	0.0142	0.009

Appendix 4.2: Trace element composition of mineral phases in shoshonites from Dolomites, Southern Alps (contd.)

Location	Val Giumela									
Rock type	Shoshonite (Basaltic Lava Flow)									
Sample ID	GIU01A	GIU01A	GIU01A	GIU01A	GIU01A	GIU01A	GIU01A	GIU01A	GIU01A	GIU01A
Phase	Plag	Plag	Plag	Plag	Plag	Plag	Plag	Plag	Plag	Plag
Spot	1	1	1	3	9	9	15	16	16	17
Analysis No.	3	4A	4B	11A	18	19	29	32	33	35
Comments	Core	Rim	Rim	Core	Core	Rim	Rim	Rim	Core	Rim
Li	4.16	8.19	9.98	11.51	11.29	13.79	15.09	11.93	7.81	8.26
Be	0.15	1.66	0.3	0.36	0.59	0.84	0.63	0.11	0.34	0.35
B	17.39	23.91	22.77	19.64	14.43	13.54	14.77	22.97	8.75	26.02
Sc	1.52	1.52	1.77	1.019	1.3	1.26	1.24	3.07	2.54	1.35
Ti	90.38	116.24	114.77	116.97	102.25	100.98	111.98	172.52	149.89	107.07
V	1.288	1.89	1.74	2.61	1.03	1.26	1.28	6.89	5.13	1.77
Cr	<0.94	2.15	<1.42	<1.05	<1.45	<1.40	<1.27	<1.42	1.34	<1.46
Mn	51.5	58.63	58.9	57.94	54.03	55.07	53.31	103.08	83.85	52.07
Co	0.53	0.566	0.763	0.726	0.629	0.682	0.819	2.03	<1.11	0.736
Ni	0.093	0.27	0.171	0.094	<0.088	<0.113	<0.082	0.65	0.44	0.061
Cu	0.797	1.32	1.2	1.04	1.42	1.4	1.42	1.37	1.03	2.84
Zn	4.52	5.53	6.69	7.16	4.3	5.12	6.66	7.07	5.09	4.46
Rb	0.245	0.374	0.319	0.367	0.277	0.42	0.38	0.336	0.227	0.432
Sr	2239.42	2161.06	2239.25	2338.79	2386.56	2279.34	2297.34	2128.12	2101.7	2064.36
Y	0.141	0.295	0.27	0.23	0.206	0.246	0.194	0.427	0.444	0.176
Zr	0.013	0.249	0.295	0.531	<0.00	0.109	0.182	0.676	0.704	0.187
Nb	<0.00	<0.00	<0.00	0.057	<0.00	0.0088	<0.00	0.009	<0.00	<0.0104
Mo	<0.051	<0.118	<0.103	0.022	<0.057	<0.052	<0.107	<0.116	<0.093	<0.136
Cs	<0.0074	0.021	<0.0151	<0.0145	0.014	<0.0133	<0.0177	<0.0150	<0.0080	<0.0156
Ba	84.85	99.77	103.07	99.71	96.53	102.38	122.87	97.9	92.56	95.53
La	2.54	2.68	2.79	2.62	2.8	3.06	3.2	2.81	3.06	2.61
Ce	3.69	4.32	4.55	4.47	4.47	4.28	4.57	4.47	4.54	4.08
Pr	0.367	0.413	0.476	0.431	0.514	0.441	0.446	0.505	0.489	0.382
Nd	1.24	1.3	1.23	1.57	1.27	1.45	1.92	2.17	1.56	1.88
Sm	0.191	<0.00	0.235	0.191	0.186	0.225	0.074	0.341	0.326	0.166
Eu	0.357	0.533	0.537	0.466	0.7	0.574	0.587	0.447	0.429	0.488
Gd	0.112	0.05	0.108	0.077	0.042	0.068	0.164	0.26	0.147	0.1
Tb	0.0112	0.0088	0.0113	0.0169	<0.00	0.0079	0.019	0.025	0.03	0.0217
Dy	0.078	0.071	0.06	<0.00	0.03	0.063	0.057	0.215	0.12	0.07
Ho	0.0085	0.009	0.0115	0.0103	<0.00	0.0122	<0.0148	0.0127	<0.00	0.009
Er	0.012	0.039	0.017	0.015	<0.00	<0.00	<0.00	0.018	<0.00	0.019
Tm	<0.00	<0.00	0.0038	<0.00	<0.00	<0.00	<0.00	<0.00	<0.00	<0.00
Yb	<0.00	<0.00	<0.00	0.022	<0.00	<0.00	<0.00	<0.00	<0.00	<0.00
Lu	0.003	<0.00	<0.00	<0.00	<0.00	<0.00	<0.00	0.0045	<0.00	<0.00
Hf	<0.00	<0.00	0.023	0.084	<0.00	<0.00	<0.00	<0.00	0.079	<0.00
Ta	<0.00	<0.00	0.004	0.0036	<0.00	<0.00	<0.00	<0.00	<0.00	<0.00
Pb	1.48	1.97	1.89	1.67	1.42	2.1	1.86	1.79	1.79	1.99
Th	<0.00	<0.00	<0.00	0.027	<0.00	<0.00	<0.0172	0.0085	<0.00	<0.00
U	<0.00	<0.00	<0.00	0.0075	<0.00	<0.00	<0.00	<0.00	<0.00	<0.00

Appendix 4.2: Trace element composition of mineral phases in shoshonites from Dolomites, Southern Alps (contd.)

Location	Val Giumela						Val Giumela				
Rock type	Shoshonite (Basaltic Pillow Lava)						Shoshonite (Columnar Basalt)				
Sample ID	GIU02A	GIU02A	GIU02A	GIU02A	GIU02A	GIU02A	GIU03A	GIU03A	GIU03A	GIU03A	GIU03A
Phase	Plag	Plag	Plag	Plag	Plag	Plag	Plag	Plag	Plag	Plag	Plag
Spot	1	1	2	3	6	7	3	3	6	6	14
Analysis No.	3	4	5	9	16	19B	5	6	9	10	16
Comments	Core	Rim	Rim	Core	Rim	Rim	Core	Rim	Core	Rim	Rim
Li	3.83	11.36	6.72	<1.45	10.04	8.65	9.14	20.55	9.9	12.32	8.45
Be	0.55	<0.00	0.78	0.2	0.32	0.99	0.14	0.33	0.44	0.71	0.16
B	18.08	<8.01	<9.45	10.28	17.03	14.57	11.79	17.13	<9.16	18.13	<8.16
Sc	1.19	1.23	0.88	1.38	1.71	0.99	1.01	0.97	1.02	0.98	0.9
Ti	103.75	112.59	114.66	100.97	141.23	103.46	102.66	139.26	103.86	109.23	110.18
V	1.2	1.38	1.46	1.46	3.34	1.24	1.11	1.43	1.15	2.14	1.25
Cr	<1.50	<1.48	<1.51	<1.58	2.98	<1.63	<1.59	<1.46	1.73	<1.20	<1.52
Mn	58.52	53.13	57.04	55.63	67.43	56.65	54.48	52.45	59.03	54.56	56.72
Co	0.71	0.561	0.601	0.593	1.35	0.52	0.57	0.768	0.721	0.56	0.538
Ni	0.2	0.24	0.14	0.138	1	<0.00	0.09	0.045	<0.074	0.19	<0.065
Cu	1.84	1.67	1.04	0.95	1.39	1.18	0.58	1.06	0.74	1.2	0.73
Zn	7.53	6.62	5.66	5.69	8.32	3.95	5.63	6.2	4.91	5.3	3.48
Rb	0.81	0.697	0.384	0.427	0.381	0.242	0.309	0.436	0.309	0.307	0.348
Sr	2325.45	2381.37	2517.53	2282.67	2449.53	2378.4	2367.31	2463.89	2361.39	2259.05	2320.69
Y	0.263	0.208	0.267	0.158	0.307	0.228	0.202	0.231	0.209	0.235	0.19
Zr	0.241	0.97	0.04	0.198	0.341	0.15	<0.021	<0.00	0.18	0.3	<0.00
Nb	0.024	<0.0095	<0.00	<0.0118	0.0135	<0.0217	<0.00	<0.00	<0.0116	0.03	<0.00
Mo	<0.10	<0.111	0.064	<0.118	<0.130	0.2	<0.067	<0.078	<0.116	<0.093	<0.084
Cs	0.08	0.062	<0.00	<0.023	<0.0237	<0.0195	0.022	<0.00	0.016	<0.0144	<0.0092
Ba	109.07	114.67	121.46	94.28	120.28	115.99	105.39	138.32	103.09	103.09	100.38
La	3.46	3.08	3.51	2.73	3.18	3.37	3.35	3.47	2.8	3.19	2.81
Ce	4.5	4.63	5.13	3.9	4.89	4.93	5.18	4.86	4.47	4.78	4.49
Pr	0.356	0.429	0.509	0.424	0.484	0.431	0.464	0.574	0.394	0.46	0.347
Nd	1.62	1.44	2.27	1.42	1.64	1.21	1.58	1.8	1.41	1.96	1.51
Sm	0.28	0.173	0.46	0.35	0.16	0.12	0.211	0.167	0.3	0.36	0.205
Eu	0.72	0.608	0.7	0.66	0.62	0.32	0.659	0.759	0.653	0.52	0.616
Gd	0.063	0.087	0.06	0.09	0.22	<0.00	0.096	0.038	0.101	0.25	0.15
Tb	<0.00	0.015	0.01	<0.00	0.019	0.02	0.0169	<0.00	0.018	<0.00	<0.00
Dy	0.044	<0.00	0.042	<0.00	0.103	<0.00	<0.00	0.054	<0.00	0.116	<0.00
Ho	<0.0117	<0.00	<0.00	<0.00	0.0132	0.02	<0.00	<0.00	<0.00	<0.0091	<0.00
Er	<0.00	<0.00	<0.00	<0.00	<0.00	<0.00	<0.00	0.059	<0.00	<0.00	<0.00
Tm	<0.00	<0.00	<0.00	<0.00	<0.0096	<0.00	<0.00	<0.0130	<0.00	<0.00	<0.00
Yb	0.074	<0.00	<0.00	<0.00	<0.00	<0.00	<0.00	0.045	<0.00	<0.00	<0.00
Lu	<0.00	<0.0099	<0.00	<0.00	<0.00	<0.00	<0.00	<0.00	<0.00	<0.00	<0.00
Hf	<0.00	<0.00	<0.00	<0.00	<0.00	<0.00	<0.00	<0.00	<0.00	<0.00	<0.00
Ta	<0.00	<0.00	<0.00	<0.00	<0.00	<0.00	<0.00	<0.00	<0.00	<0.00	<0.00
Pb	2.18	1.92	1.92	1.82	1.82	2.21	1.73	2.16	1.66	1.71	1.62
Th	<0.00	<0.00	<0.00	0.05	<0.00	<0.00	<0.00	<0.00	0.013	<0.00	<0.00
U	<0.00	<0.00	<0.00	<0.00	<0.00	<0.00	<0.00	<0.00	<0.00	<0.00	<0.00

Appendix 4.2: Trace element composition of mineral phases in shoshonites from Dolomites, Southern Alps (contd.)

Location	Val Giumela								
Rock type	Shoshonite (Basaltic Dyke)								
Sample ID	GIU03DK	GIU03DK	GIU03DK	GIU03DK	GIU03DK	GIU03DK	GIU03DK	GIU03DK	GIU03DK
Phase	Plag	Plag	Plag	Plag	Plag	Plag	Plag	Plag	Plag
Spot	1	1	4	4	6	7	7	7	7
Analysis No.	1	2	12	13	19	23	24	25	26
Comments	Core	Rim	Core	Rim	Rim	Core	Rim	Rim	Core
Li	12.78	12.23	12.59	14.65	12.97	16.15	15.3	13.92	10.95
Be	0.58	0.32	0.37	<0.00	0.5	0.29	0.39	0.59	0.22
B	30.13	23.35	28.8	20.09	10.49	22.63	28.76	17.13	15.65
Sc	3.2	2.52	2.23	1.74	1.69	1.52	1.71	1.33	1.37
Ti	101.43	99.6	136.75	113.97	95.49	108.26	107.12	99.24	89.77
V	1.08	1.29	1.77	1.29	0.99	1.03	1.26	1.3	1.14
Cr	<2.23	<1.56	<1.72	<1.55	<1.72	<1.50	<1.71	<1.32	<1.46
Mn	52.72	53.11	60.72	73.58	52.57	52.9	54.07	52.56	50.96
Co	0.586	0.746	1.06	2.21	0.746	0.716	0.779	0.679	0.554
Ni	0.091	0.128	0.25	0.37	<0.120	<0.066	0.151	0.076	0.149
Cu	0.79	1.07	2.75	0.73	0.93	0.78	1.18	0.79	0.75
Zn	5.3	4.89	4.1	4.81	4.97	5.21	5.86	4.2	4.04
Rb	0.394	0.338	0.496	0.404	0.384	0.361	0.548	0.293	0.216
Sr	2231.88	2098.07	2075.4	2341.4	2092.16	2150.55	2250.8	2127.65	2042.49
Y	0.196	0.194	0.155	0.146	0.221	0.179	0.207	0.162	0.177
Zr	0.133	0.367	1.08		<0.00	0.044	0.337	0.154	0.0082
Nb	<0.00	0.025	0.117	0.156	<0.022	<0.00	0.016	0.0041	<0.00
Mo	<0.165	<0.123	<0.110	<0.091	<0.111	<0.121	<0.153	<0.114	<0.084
Cs	<0.00	<0.0112	<0.0160	0.024	<0.0249	<0.0126	<0.0160	<0.0107	<0.0124
Ba	99.4	94.97	99.54	109.08	99.8	94.8	114.12	93.53	84.46
La	2.8	2.86	3.61	3.19	2.58	2.71	3	2.89	2.42
Ce	4.14	3.75	4.69	4.88	4.1	4.09	4.11	4.09	3.65
Pr	0.462	0.396	0.501	0.451	0.376	0.355	0.458	0.323	0.349
Nd	1.55	1.54	1.46	1.71	1.52	1.35	1.48	1.24	1.25
Sm	0.27	0.252	0.18	0.28	0.252	0.112	0.3	0.226	0.224
Eu	0.556	0.528	0.56	0.39	0.483	0.572	0.609	0.393	0.422
Gd	0.078	0.088	0.077	0.083	0.083	0.164	0.22	0.088	0.123
Tb	0.013	0.0073	0.013	<0.00	0.0184	0.0109	0.015	0.0111	<0.00
Dy	<0.00	<0.00	<0.00	<0.00	<0.00	0.045	0.06	0.045	<0.00
Ho	<0.0094	<0.00	0.014	<0.00	<0.0185	0.0058	<0.00	<0.00	<0.00
Er	<0.00	0.032	<0.00	<0.00	<0.00	<0.00	0.032	<0.00	0.036
Tm	0.0127	<0.00	<0.00	<0.00	0.0045	<0.00	<0.00	0.0072	<0.00
Yb	<0.00	<0.00	<0.00	0.086	<0.00	0.034	0.046	<0.00	<0.00
Lu	<0.0093	0.0039	<0.00	<0.00	<0.0212	<0.00	<0.00	<0.00	0.0043
Hf	<0.00	<0.00	0.074	0.08	<0.058	<0.00	<0.057	<0.00	<0.00
Ta	<0.00	<0.00	<0.00	0.029	<0.0107	0.0058	<0.00	<0.00	<0.00
Pb	1.78	1.88	2.28	2.14	2.06	1.58	1.89	1.73	1.69
Th	<0.00	<0.00	0.023	<0.00	<0.00	<0.00	<0.00	<0.00	<0.00
U	<0.0170	<0.00	<0.00	<0.00	<0.0289	<0.00	<0.00	<0.00	<0.00

Appendix 4.2: Trace element composition of mineral phases in shoshonites from Dolomites, Southern Alps (contd.)

Location	Latemar			Latemar	
Rock type	Shoshonite (Basaltic Dyke)			Shoshonite	
Sample ID	LAT01DK	LAT01DK	LAT01DK	LAT02A	LAT02A
Phase	Plag	Plag	Plag	Plag	Plag
Spot	3	3	10	2	8
Analysis No.	8A	8B	16	12	14
Comments	Rim	Rim	Core	Core	Rim
Li	3.92	10.22	24.27	0.78	2.31
Be	0.23	0.55	0.68	0.51	0.15
B	18.81	16.21	35.54	12.55	17.48
Sc	1.24	1.35	1.05	1.15	0.86
Ti	407.47	362.2	242.1	234.62	281.29
V	4.11	3.87	3.27	3.53	2.34
Cr	<1.22	<1.36	1.99	<1.09	<1.33
Mn	52.5	55	76.39	59.75	50.74
Co	0.492	2.2	0.495	0.854	0.65
Ni	0.25	0.85	0.17	0.67	0.44
Cu	1.64	2.56	6.48	8.14	2.07
Zn	6.76	10.04	6.35	8.25	7.15
Rb		3.07	1.85	0.974	1.3
Sr	1141.32	1252.27	1219.5	1360.41	1375.98
Y	0.272	0.242	0.257	0.344	0.244
Zr		0.252	0.078	0.655	<0.00
Nb	0.164	0.0173	0.064	0.035	<0.00
Mo	<0.00	<0.086	<0.088	<0.040	<0.076
Cs	0.44	0.17	0.091	0.047	0.767
Ba	143.63	146.57	80.08	118.74	176.53
La	2.97	2.95	2.32	2.76	3.17
Ce	4.29	4.33	3.88	4.65	4.33
Pr	0.538	0.404	0.396	0.473	0.558
Nd	1.53	1.43	1.44	1.46	1.33
Sm	<0.00	0.208	0.26	0.42	0.3
Eu	0.527	0.693	0.577	0.528	0.7
Gd	0.21	0.216	0.192	0.112	0.136
Tb	0.017	0.0155	0.0129	0.0112	<0.00
Dy	0.105	<0.00	<0.00	0.077	0.047
Ho	0.018	0.0107	<0.00	<0.00	0.024
Er	0.076	<0.00	<0.00	0.033	0.025
Tm	<0.00	0.005	<0.00	<0.00	<0.00
Yb	0.054	0.032	<0.00	<0.00	<0.00
Lu	<0.00	<0.00	<0.00	0.004	0.0061
Hf	0.102	0.03	<0.00	<0.00	<0.00
Ta	0.019	<0.00	<0.00	0.0041	<0.00
Pb	1.88	1.35	1.08	1.44	1.77
Th	0.066	<0.00	0.012	0.022	<0.00
U	0.018	<0.00	<0.00	0.017	<0.00

Appendix 4.3: Whole-rock trace elements composition of shoshonites from Dolomites

Location	Giumela	Giumela	Giumela	Giumela	Giumela	Giumela	Giumela	Giumela	Latemar	Latemar
Rock type	Shoshonite	Shoshonite	Shoshonite	Shoshonite	Shoshonite	Shoshonite	Shoshonite	Shoshonite	Shoshonite	Shoshonite
Mode of occurrence	BLF	BLF	BPL	BPL	CB	CB	BDK	BDK	BDK	BLF
Sample ID	GIU01A	GIU01B	GIU02A	GIU02B	GIU03A	GIU03B	GIU03DK	GIU04DK	LAT01DK	LAT02B
Be	2.55	2.51	1.43	1.11	2.91	2.76	2.14	1.86	1.52	1.27
Sc	23.21	21.13	20.67	20.71	20.10	18.14	20.17	39.51	33.03	31.47
Ti	5367.73	5349.48	5416.57	5499.30	5342.92	5052.43	5232.95	5403.85	8346.04	6792.09
V	216.32	204.90	193.10	200.45	207.62	168.33	182.58	237.48	267.19	288.06
Cr	23.56	25.92	25.78	26.68	24.35	34.19	20.23	456.65	85.15	96.09
Mn	1541.63	1629.78	1203.88	1507.85	1648.04	1749.04	1563.28	2019.59	1214.27	1661.96
Co	39.43	38.05	35.47	35.08	37.18	35.82	37.04	39.38	41.68	32.24
Ni	30.58	20.44	37.62	18.99	31.59	26.65	32.76	106.04	68.23	71.10
Cu	149.36	150.87	144.99	142.66	150.96	159.03	143.63	83.56	63.83	71.03
Zn	86.39	88.46	76.77	103.00	85.67	88.26	88.75	66.05	46.42	76.16
Ga	19.24	18.85	19.35	19.62	19.31	18.91	18.68	15.47	19.82	18.69
Rb	70.91	67.04	53.40	61.71	72.55	67.15	72.49	61.79	46.15	56.99
Sr	1059.87	1044.83	1016.07	1055.09	1111.13	1048.89	1030.34	629.15	1012.39	678.79
Y	26.18	26.45	24.64	25.74	26.95	24.94	25.78	22.43	25.88	21.99
Zr	155.45	157.60	158.03	164.84	162.12	148.25	154.72	133.30	170.58	118.77
Nb	9.95	9.86	10.30	10.32	10.19	9.37	9.73	7.93	9.78	7.09
Cs	0.55	0.47	bdl	bdl	1.03	0.98	0.60	0.38	1.02	1.35
Ba	574.30	575.72	572.20	583.08	603.81	571.82	572.49	413.07	426.76	436.98
La	36.10	36.15	36.95	38.07	37.68	35.17	35.46	27.59	26.98	22.09
Ce	68.70	70.74	71.96	73.86	72.04	67.79	68.67	53.35	53.86	42.23
Pr	8.37	8.46	8.30	8.89	8.46	7.94	8.12	6.34	6.66	5.31
Nd	35.82	35.59	35.66	36.23	36.40	33.40	35.17	27.38	29.43	24.27
Sm	6.99	7.41	7.90	7.59	7.49	6.57	6.48	6.02	6.26	5.17
Eu	1.91	1.75	1.83	1.98	1.88	1.75	1.98	1.56	1.82	1.70
Gd	6.26	5.21	5.77	5.17	5.68	5.29	6.00	5.01	5.51	4.83
Tb	0.88	0.92	0.83	0.85	0.88	0.97	0.87	0.77	0.84	0.68
Dy	5.00	4.80	4.97	4.96	4.95	4.70	4.37	4.45	4.62	3.79
Ho	1.00	0.92	0.97	0.97	0.98	1.06	0.89	0.91	0.96	0.79
Er	2.77	2.64	2.13	2.46	2.59	1.98	2.16	2.20	2.36	2.08
Tm	0.40	0.33	0.30	0.34	0.38	0.38	0.30	0.29	0.39	0.27
Yb	2.83	2.40	1.95	2.41	2.78	2.30	2.18	2.16	2.60	1.88
Lu	0.32	0.33	0.36	0.33	0.37	0.30	0.31	0.30	0.35	0.29
Hf	3.97	4.06	3.95	4.39	4.02	3.49	3.95	2.93	4.19	3.03
Ta	0.54	0.46	0.58	0.51	0.51	0.38	0.38	0.43	0.35	0.28
Pb	15.31	13.17	12.90	10.23	13.14	12.08	12.89	8.63	9.15	4.63
Th	9.34	8.82	8.84	9.18	9.43	8.83	8.72	6.80	4.01	4.27
U	2.49	2.43	2.22	2.45	2.34	2.16	2.39	1.84	1.19	0.96

BLF – Basaltic Lava Flow; BPL – Basaltic Pillow Lava; CB – Columnar Basalt; BDK – Basaltic Dyke

Appendix 4.4: Whole-rock Nd-Hf-Sr-Pb isotopic composition of shoshonites from Dolomites

Sample ID	GIU01A	GIU02A	GIU03A	GIU03DK	LAT01DK	LAT02B
Lithology	Shoshonite	Shoshonite	Shoshonite	Shoshonite	Shoshonite	Shoshonite
$^{147}Sm/^{144}Nd$	0.1230	0.1396	0.1297	0.1161	0.1341	0.1344
$^{143}Nd/^{144}Nd$	0.512492	0.512510	0.512414	0.512469	0.512472	0.512585
$^{143}Nd/^{144}Nd_{(238)}$	0.512301	0.512293	0.512212	0.512288	0.512263	0.512375
±2σ	0.000003	0.000005	0.000006	0.000005	0.000005	0.000005
$\varepsilon Nd_{(238)}$	-0.5	-0.6	-2.2	-0.7	-1.2	1.0
$^{176}Lu/^{177}Hf$	0.0112	0.0127	0.0128	0.0109	0.0117	0.0135
$^{176}Hf/^{177}Hf$	0.282609	0.282613	0.282634	0.282626	0.282727	0.282803
$^{176}Hf/^{177}Hf_{(238)}$	0.282559	0.282556	0.282578	0.282578	0.282675	0.282743
±2σ	0.000005	0.000006	0.000011	0.000006	0.000006	0.000008
$\varepsilon Hf_{(238)}$	-2.7	-2.8	-2.1	-2.1	1.4	3.8
$^{87}Rb/^{86}Sr$	0.1888	0.1484	0.1843	0.1986	0.1287	0.2370
$^{87}Sr/^{86}Sr$	0.705220	0.705042	0.705274	0.705327	0.706562	0.704884
$^{87}Sr/^{86}Sr_{(238)}$	0.704581	0.704540	0.704650	0.704655	0.706126	0.704082
±2σ	0.000007	0.000014	0.000008	0.000008	0.000008	0.000007
$\varepsilon Sr_{(238)}$	-0.2	-0.8	0.8	0.8	21.7	-7.3
$^{238}U/^{204}Pb$	11.5477	12.1998	12.6419	13.1177	9.1831	14.6377
$^{206}Pb/^{204}Pb$	18.5494	18.4946	18.5825	18.5326	18.8649	18.1829
$^{206}Pb/^{204}Pb_{(238)}$	18.1151	18.0357	18.1070	18.0392	18.5195	17.6323
±2σ	0.0005	0.0005	0.0005	0.0005	0.0008	0.0005
$^{235}U/^{204}Pb$	0.0838	0.0885	0.0917	0.0951	0.0666	0.1062
$^{207}Pb/^{204}Pb$	15.6485	15.6491	15.6538	15.6486	15.6630	15.6090
$^{207}Pb/^{204}Pb_{(238)}$	15.6264	15.6257	15.6296	15.6235	15.6454	15.5810
±2σ	0.0006	0.0005	0.0006	0.0005	0.0008	0.0005
$^{232}Th/^{204}Pb$	43.5843	48.9019	51.2578	48.3149	31.3130	65.7702
$^{208}Pb/^{204}Pb$	38.6393	38.6198	38.7044	38.6373	38.9836	38.0634
$^{208}Pb/^{204}Pb_{(238)}$	38.1231	38.0406	38.0973	38.0651	38.6127	37.2844
±2σ	0.0019	0.0016	0.0019	0.0013	0.0020	0.0015

Normalized to LaJolla $^{143}Nd/^{144}Nd = 0.51185$

Normalized to JMC475 $^{176}Hf/^{177}Hf = 0.282150$

Normalized to NBS 981 6/4 = 16.9356, 7/4 = 15.4891, 8/4 = 36.7006

Subscript represents correction to 238 Ma

Appendix 5.1: Average major and minor elements composition of mineral phases from studied IVZ lherzolites and pyroxenites

Location	Premosello				Balmuccia				Baldissero		
Rock type	Sp-Lhz.	Sp-Lhz.	Sp-Lhz.	Sp-Lhz.	Sp-Lhz.	Sp-Lhz.	Cr-Di pyx.	Websterite	Sp-Lhz.	Sp-Lhz.	Sp-Lhz.
Sample ID	PR22S01A	PR22S02A	PR22S09	PR22S16	BAL02A	BAL05	BAL01	BAL18	BAD01	BAD02	BAD05
Phase	Cpx	Cpx	Cpx	Cpx	Cpx	Cpx	Cpx	Cpx	Cpx	Cpx	Cpx
No. of analysis	5	3	3	3	9	3	5	6	6	4	4
SiO_2	53.35	53.09	52.77	53.18	51.97	52.42	52.82	52.47	52.00	51.83	52.07
TiO_2	0.19	0.18	0.18	0.12	0.40	0.41	0.21	0.21	0.45	0.45	0.44
Al_2O_3	3.52	3.30	3.86	2.87	5.99	4.38	3.75	4.09	6.56	6.77	6.18
Cr_2O_3	0.66	0.61	0.70	0.88	0.83	0.92	0.77	0.32	0.81	0.85	0.68
FeO_T	2.40	2.36	2.33	2.30	2.44	2.32	2.72	3.33	2.20	2.34	2.41
MnO	0.07	0.08	0.07	0.08	0.06	0.07	0.10	0.11	0.08	0.08	0.08
NiO	0.04	0.00	0.00	0.00	0.05	0.00	0.00	0.00	0.00	0.00	0.00
MgO	16.16	16.14	15.82	16.27	14.79	15.18	16.07	16.01	14.72	14.65	14.46
CaO	23.53	23.43	23.32	23.06	22.22	22.90	23.27	23.06	21.84	21.62	21.92
Na_2O	0.67	0.54	0.58	0.64	1.34	0.92	0.48	0.52	1.50	1.48	1.39
K_2O	0.01	0.00	0.00	0.00	0.01	0.00	0.00	0.00	0.00	0.00	0.01
Total	100.60	99.73	99.63	99.40	100.10	99.54	100.20	100.12	100.15	100.07	99.64
Mg#	92.3	92.4	92.4	92.7	91.5	92.1	91.3	89.5	92.3	91.8	91.4
Cr#	11.2	11.0	10.9	17.1	8.5	12.4	12.2	5.0	7.7	7.8	6.9
Fs	4.0	4.0	4.0	3.9	4.4	4.1	4.6	5.6	4.0	4.3	4.4
En	46.9	47.0	46.6	47.6	46.0	46.0	46.7	46.4	46.4	46.4	45.7
Wo	49.1	49.0	49.4	48.5	49.7	49.9	48.6	48.0	49.5	49.3	49.8

Sp-Lhz. – Spinel-lherzolite; Cr-Di pyx – Cr-diopside pyroxenite

Appendix 5.1: Average major and minor elements composition of mineral phases from studied IVZ lherzolites and pyroxenites (contd.)

Location	Premosello				Balmuccia				Baldissero		
Rock type	Sp-Lhz.	Sp-Lhz.	Sp-Lhz.	Sp-Lhz.	Sp-Lhz.	Sp-Lhz.	Cr-Di pyx.	Websterite	Sp-Lhz.	Sp-Lhz.	Sp-Lhz.
Sample ID	PR22S01A	PR22S02A	PR22S09	PR22S16	BAL02A	BAL05	BAL01	BAL18	BAD01	BAD02	BAD05
Phase	Opx	Opx	Opx	Opx	Opx	Opx	Opx	Opx	Opx	Opx	Opx
No. of analysis	5	3	4	2	9	4	5	5	4	3	3
SiO_2	56.23	55.97	55.89	56.25	55.68	55.95	55.07	54.90	55.03	54.68	54.73
TiO_2	0.06	0.07	0.07	0.05	0.07	0.11	0.05	0.07	0.10	0.14	0.11
Al_2O_3	3.16	2.66	3.00	2.25	3.73	2.74	3.34	3.81	4.60	4.80	4.99
Cr_2O_3	0.37	0.29	0.34	0.39	0.35	0.34	0.48	0.19	0.38	0.42	0.38
FeO_T	6.50	6.45	6.14	6.13	6.60	6.54	8.44	9.04	6.73	6.52	6.68
MnO	0.14	0.14	0.14	0.14	0.16	0.15	0.20	0.21	0.15	0.15	0.14
NiO	0.09	0.00	0.00	0.00	0.08	0.00	0.00	0.00	0.00	0.00	0.00
MgO	33.93	33.52	33.58	33.72	33.44	33.34	32.46	32.05	33.53	32.14	32.26
CaO	0.43	0.31	0.34	0.39	0.39	0.29	0.32	0.36	0.35	0.78	0.45
Na_2O	0.02	0.01	0.01	0.01	0.04	0.02	0.01	0.01	0.03	0.05	0.04
K_2O	0.01	0.00	0.00	0.01	0.00	0.00	0.00	0.00	0.00	0.00	0.00
Total	100.94	99.43	99.52	99.34	100.56	99.50	100.37	100.64	100.90	99.68	99.78
Mg#	90.3	90.3	90.7	90.7	90.0	90.1	87.3	86.3	89.9	89.8	89.6
Cr#	7.3	6.9	7.0	10.3	6.0	7.8	8.7	3.3	5.2	5.5	4.9
Fs	9.8	9.9	9.4	9.4	10.1	10.1	12.9	13.8	10.3	10.3	10.5
En	89.4	89.5	89.9	89.9	89.1	89.4	86.5	85.5	89.1	88.2	88.6
Wo	0.8	0.6	0.7	0.7	0.8	0.6	0.6	0.7	0.7	1.5	0.9

Appendix 5.1: Average major and minor elements composition of mineral phases from studied IVZ lherzolites and pyroxenites (contd.)

Location	Premosello				Balmuccia			Baldissero		
Rock type	Sp-Lhz.	Sp-Lhz.	Sp-Lhz.	Sp-Lhz.	Sp-Lhz.	Sp-Lhz.	Websterite	Sp-Lhz.	Sp-Lhz.	Sp-Lhz.
Sample ID	PR22S01A	PR22S02A	PR22S09	PR22S16	BAL02A	BAL05	BAL18	BAD01	BAD02	BAD05
Phase	Olivine	Olivine	Olivine	Olivine	Olivine	Olivine	Olivine	Olivine	Olivine	Olivine
No. of analysis	4	3	2	4	9	3	3	3	3	3
SiO_2	40.37	40.82	40.82	40.65	40.72	40.73	40.07	40.67	40.73	40.71
TiO_2	0.03	0.02	0.03	0.03	0.01	0.03	0.03	0.03	0.02	0.03
Al_2O_3	0.04	0.00	0.00	0.00	0.01	0.00	0.01	0.00	0.01	0.00
Cr_2O_3	0.03	0.02	0.01	0.02	0.01	0.01	0.02	0.00	0.00	0.00
FeO_T	9.41	9.17	8.98	9.07	9.75	9.46	13.26	9.89	9.95	10.00
MnO	0.14	0.13	0.14	0.14	0.14	0.14	0.20	0.13	0.14	0.14
NiO	0.42	0.41	0.38	0.42	0.39	0.38	0.32	0.37	0.37	0.37
MgO	51.55	50.33	50.43	49.97	49.98	49.99	46.64	49.54	49.70	49.45
CaO	0.02	0.01	0.02	0.02	0.01	0.02	0.02	0.02	0.02	0.02
Na_2O	0.01	0.00	0.00	0.00	0.01	0.00	0.00	0.00	0.00	0.00
K_2O	0.00	0.00	0.00	0.00	0.00	0.00	0.00	0.00	0.00	0.00
Total	102.03	100.91	100.81	100.32	101.02	100.77	100.56	100.67	100.94	100.73
Mg#	90.7	90.7	90.9	90.8	90.1	90.4	86.2	89.9	89.9	89.8

Appendix 5.1: Average major and minor elements composition of mineral phases from studied IVZ lherzolites and pyroxenites (contd.)

Location	Premosello				Balmuccia			Baldissero		
Rock type	Sp-Lhz.	Sp-Lhz.	Sp-Lhz.	Sp-Lhz.	Sp-Lhz.	Sp-Lhz.	Cr-Di pyx	Sp-Lhz.	Sp-Lhz.	Sp-Lhz.
Sample ID	PR22S01A	PR22S02A	PR22S09	PR22S16	BAL02A	BAL05	BAL01	BAD01	BAD02	BAD05
Phase	Spinel	Spinel	Spinel	Spinel	Spinel	Spinel	Spinel	Spinel	Spinel	Spinel
No. of analysis	4	3	2	3	6	3	1	4	2	2
SiO_2	0.02	0.00	0.00	0.00	0.01	0.00	0.06	0.00	0.01	0.00
TiO_2	0.07	0.06	0.06	0.11	0.04	0.10	0.08	0.07	0.06	0.04
Al_2O_3	48.86	45.72	49.97	34.14	56.72	45.88	47.03	55.56	55.49	55.48
Cr_2O_3	18.02	18.06	14.45	28.62	11.15	18.23	18.22	10.21	10.45	10.19
FeO_T	17.33	16.07	14.20	21.64	12.78	16.63	15.44	11.91	11.96	11.92
MnO	0.10	0.06	0.06	0.09	0.07	0.06	0.04	0.06	0.07	0.06
NiO	0.31	0.24	0.30	0.16	0.34	0.24	0.38	0.35	0.37	0.38
MgO	17.17	16.80	18.25	12.57	18.90	16.49	16.03	19.91	19.49	19.40
CaO	0.01	0.00	0.01	0.01	0.01	0.01	0.02	0.01	0.01	0.01
Na_2O	0.01	0.00	0.00	0.00	0.02	0.00	0.00	0.00	0.00	0.00
K_2O	0.01	0.00	0.00	0.00	0.00	0.00	0.00	0.00	0.00	0.00
Total	101.90	97.01	97.30	97.33	100.05	97.65	97.28	98.07	97.91	97.47
Mg#	63.8	65.1	69.6	50.9	72.5	63.9	64.9	74.9	74.4	74.4
Cr#	19.8	20.9	16.2	36.0	11.7	21.0	20.6	11.0	11.2	11.0

Appendix 5.2: Average trace element composition of clinopyroxenes from studied IVZ lherzolites and pyroxenites

Location	Premosello				Balmuccia				Baldissero		
Rock type	Sp-Lhz.	Sp-Lhz.	Sp-Lhz.	Sp-Lhz.	Sp-Lhz.	Sp-Lhz.	Cr-Di pyx	Websterite	Sp-Lhz.	Sp-Lhz.	Sp-Lhz.
Sample ID	PR22S01A	PR22S02A	PR22S09	PR22S16	BAL02A	BAL05	BAL01A	BAL18	BAD01	BAD02	BAD05
Phase	Cpx	Cpx	Cpx	Cpx	Cpx	Cpx	Cpx	Cpx	Cpx	Cpx	Cpx
No. of analysis	10	4	4	7	11	4	14	2	4	4	3
Li	4.03	5.13	3.00	3.54	4.07	3.72	2.01	2.20	2.06	2.59	3.46
Be	0.009	0.009	0.000	0.032	0.006	0.025	0.022	0.083	0.000	0.015	0.051
B	26.4	11.9	14.0	18.5	10.7	9.3	9.6	7.6	8.6	6.9	8.3
Sc	71.4	57.1	66.0	70.7	61.8	71.6	48.2	59.9	64.5	62.1	59.3
Ti	1012	760	785	530	1999	2208	937	1167	2343	2200	2307
V	218	226	198	193	263	248	194	254	262	261	268
Cr	4646	5130	4243	5611	5258	5468	5479	2730	4852	5178	4948
Mn	527	554	518	540	565	559	686	834	600	591	589
Co	17.1	17.9	16.6	17.7	17.1	16.9	19.9	28.4	17.0	16.8	17.2
Ni	279	338	285	302	269	260	286	305	267	253	277
Cu	1.63	0.37	4.34	0.33	0.63	0.57	0.24	2.38	1.39	3.21	0.69
Zn	15.3	8.5	8.7	12.5	10.8	8.6	6.9	14.1	9.2	7.9	10.2
Rb	0.023	0.009	0.013	0.014	0.014	0.009	0.011	0.013	0.019	0.030	0.012
Sr	7.7	6.7	6.3	12.7	5.2	26.4	29.7	28.3	13.6	3.4	2.8
Y	9.0	7.1	7.6	5.0	14.9	12.2	5.7	7.2	16.1	15.7	16.3
Zr	1.00	0.44	1.19	1.95	5.00	16.13	2.49	4.38	7.24	5.47	4.94
Nb	0.023	0.034	0.032	0.025	0.014	0.043	0.023	0.030	0.324	0.018	0.016
Cs	0.007	0.003	0.005	0.008	0.007	0.006	0.006	0.006	0.006	0.006	0.008
Ba	0.079	0.028	0.037	0.008	0.020	0.027	0.016	0.152	0.071	0.050	0.027
La	0.146	0.044	0.076	0.092	0.029	0.546	0.249	0.365	0.516	0.004	0.004
Ce	0.431	0.116	0.259	0.293	0.264	1.895	0.941	1.827	1.138	0.158	0.145
Pr	0.065	0.017	0.042	0.050	0.117	0.377	0.177	0.346	0.204	0.106	0.110
Nd	0.428	0.143	0.225	0.294	1.203	2.513	1.321	2.100	1.763	1.375	1.330
Sm	0.236	0.158	0.240	0.146	0.936	1.035	0.517	0.927	1.028	1.008	0.967
Eu	0.137	0.122	0.097	0.082	0.417	0.426	0.230	0.328	0.499	0.485	0.472
Gd	0.625	0.526	0.624	0.382	1.535	1.360	0.746	1.136	1.830	1.795	1.873
Tb	0.182	0.147	0.130	0.094	0.350	0.300	0.164	0.202	0.392	0.396	0.393
Dy	1.320	1.117	1.152	0.833	2.499	2.095	1.053	1.345	2.788	2.758	2.837
Ho	0.354	0.288	0.288	0.196	0.578	0.489	0.246	0.288	0.657	0.612	0.614
Er	1.126	0.842	0.789	0.621	1.615	1.443	0.636	0.783	1.800	1.743	1.767
Tm	0.167	0.122	0.146	0.096	0.237	0.191	0.091	0.096	0.268	0.247	0.266
Yb	1.148	0.879	0.923	0.617	1.681	1.300	0.619	0.728	1.720	1.770	1.743
Lu	0.170	0.128	0.144	0.089	0.228	0.196	0.075	0.101	0.233	0.247	0.239
Hf	0.091	0.062	0.081	0.063	0.415	0.738	0.136	0.193	0.505	0.407	0.430
Ta	0.004	0.002	0.000	0.006	0.001	0.006	0.000	0.002	0.015	0.000	0.000
Pb	0.095	0.178	0.050	0.142	0.040	0.060	0.120	0.145	0.062	0.034	0.045
Th	0.005	0.002	0.004	0.006	0.004	0.020	0.010	0.011	0.019	0.001	0.000
U	0.002	0.000	0.000	0.001	0.003	0.002	0.003	0.002	0.005	0.000	0.000

Appendix 5.3: Present-day Nd-Hf isotopic composition of clinopyroxenes from studied IVZ lherzolites and pyroxenites

Locality	Sample ID	Lithology	Phase	$^{147}Sm/^{144}Nd$	$^{143}Nd/^{144}Nd$	±2σ	εNd	$^{176}Lu/^{177}Hf$	$^{176}Hf/^{177}Hf$	±2σ	εHf
Premosello	PR22S01A	Sp-lherzolite	Cpx	0.3523	0.513236	0.000012	11.8	0.2710	0.284589	0.000019	63.8
	PR22S02A	Sp-lherzolite	Cpx	0.7332	0.514181	0.000026	30.3	0.3057	0.284859	0.000144	73.3
	PR22S09	Sp-lherzolite	Cpx	0.6858	0.513196	0.000008	11.0	0.2212	0.284139	0.000024	47.9
	PR22S16	Sp-lherzolite	Cpx	0.3257	0.513279	0.000012	12.7	0.1962	n.d.	n.d.	n.d.
Balmuccia	BAL02A	Sp-lherzolite	Cpx	0.4938	0.513653	0.000009	20.0	0.0780	0.283547	0.000009	26.9
	BAL05	Sp-lherzolite	Cpx	0.2583	0.513017	0.000007	7.5	0.0385	0.283110	0.000008	11.5
	BAL01	Cr-Di pyroxenite	Cpx	0.2452	0.513038	0.000006	8.0	0.0648	0.283381	0.000026	21.1
	BAL18	Websterite	Cpx	0.2778	0.512982	0.000006	6.9	0.0727	0.283284	0.000016	17.6
Baldissero	BAD01	Sp-lherzolite	Cpx	0.3732	0.513318	0.000006	13.4	0.0649	0.283426	0.000006	22.7
	BAD02	Sp-lherzolite	Cpx	0.4639	0.513307	0.000008	13.2	0.0865	0.283113	0.000201	11.6
	BAD05	Sp-lherzolite	Cpx	0.4598	0.513423	0.000004	15.5	0.0814	0.283262	0.000042	16.9

Normalized to LaJolla $^{143}Nd/^{144}Nd = 0.51185$

Normalized to JMC475 $^{176}Hf/^{177}Hf = 0.282150$

Appendix 5.4: Results of partial melting modeling of the Depleted Mantle (DM) at 370 Ma using the dynamic melting model of Stracke et al. (2003)

(A) Melting under garnet-facies condition

											370 Ma					
(F %)	La	Ce	Nd	Hf	Sm	Gd	Dy	Er	Yb	Lu	$^{147}Sm/^{144}Nd$	$^{143}Nd/^{144}Nd$	εNd	$^{177}Lu/^{176}Hf$	$^{177}Hf/^{176}Hf$	εHf
DM	0.234	0.772	0.713	0.199	0.270	0.395	0.531	0.371	0.401	0.063						
1%	0.076	0.478	0.536	0.172	0.231	0.374	0.511	0.361	0.394	0.062	0.2604	0.513086	8.9	0.0514	0.283149	12.9
2%	0.025	0.294	0.402	0.149	0.196	0.353	0.491	0.351	0.387	0.062	0.2960	0.513172	10.6	0.0589	0.283201	14.7
3%	0.008	0.180	0.300	0.129	0.167	0.334	0.472	0.342	0.380	0.061	0.3369	0.513271	12.5	0.0676	0.283261	16.8
4%	0.003	0.109	0.224	0.111	0.142	0.315	0.452	0.332	0.373	0.061	0.3838	0.513385	14.7	0.0777	0.283332	19.3
5%	0.00079	0.066	0.166	0.095	0.120	0.297	0.434	0.322	0.366	0.060	0.4379	0.513516	17.3	0.0896	0.283414	22.2
6%	0.00019	0.035	0.111	0.072	0.092	0.259	0.382	0.288	0.338	0.056	0.5063	0.513681	20.5	0.1101	0.283556	27.3
7%	0.000060	0.020	0.079	0.057	0.074	0.231	0.343	0.261	0.316	0.052	0.5720	0.513840	23.6	0.1309	0.283701	32.4
8%	0.000014	0.011	0.052	0.042	0.057	0.201	0.301	0.233	0.291	0.048	0.6629	0.514061	27.9	0.1614	0.283913	39.9
9%	0.0000044	0.006	0.037	0.033	0.046	0.178	0.269	0.212	0.272	0.045	0.7505	0.514273	32.0	0.1925	0.284129	47.5
10%	0.00000102	0.003	0.024	0.025	0.035	0.155	0.236	0.188	0.251	0.042	0.8722	0.514568	37.8	0.2351	0.284424	58.0
11%	0.000000302	0.002	0.017	0.020	0.028	0.136	0.210	0.170	0.235	0.039	0.9897	0.514852	43.4	0.2783	0.284724	68.6
12%	0.0000000699	0.0009	0.011	0.015	0.021	0.117	0.183	0.150	0.217	0.036	1.1534	0.515249	51.1	0.3413	0.285161	84.0
13%	0.0000000160	0.0005	0.007	0.011	0.016	0.100	0.159	0.132	0.200	0.033	1.3463	0.515716	60.2	0.4192	0.285703	103.2
14%	0.0000000046	0.0003	0.005	0.009	0.013	0.088	0.141	0.119	0.187	0.031	1.5335	0.516170	69.1	0.4983	0.286252	122.6

F % - Degree of partial melting

Appendix 5.4 (contd.): (B) Melting under spinel-facies condition

											370 Ma					
(F %)	La	Ce	Nd	Hf	Sm	Gd	Dy	Er	Yb	Lu	$^{147}Sm/^{144}Nd$	$^{143}Nd/^{144}Nd$	εNd	$^{177}Lu/^{176}Hf$	$^{177}Hf/^{176}Hf$	εHf
DM	0.234	0.772	0.713	0.199	0.27	0.395	0.531	0.371	0.401	0.063						
1%	0.060	0.368	0.434	0.139	0.194	0.331	0.451	0.321	0.362	0.057	0.2710	0.513221	11.5	0.0581	0.283395	21.6
2%	0.015	0.173	0.261	0.097	0.139	0.276	0.382	0.278	0.326	0.052	0.3212	0.513343	13.9	0.0755	0.283516	25.9
3%	0.0046	0.089	0.168	0.071	0.103	0.235	0.331	0.245	0.298	0.047	0.3726	0.513467	16.3	0.0950	0.283652	30.7
4%	0.0011	0.041	0.099	0.048	0.073	0.195	0.278	0.210	0.268	0.043	0.4447	0.513642	19.7	0.1250	0.283860	38.0
5%	0.00027	0.018	0.058	0.033	0.051	0.160	0.232	0.180	0.240	0.038	0.5325	0.513855	23.9	0.1654	0.284141	47.9
6%	0.000062	0.008	0.033	0.022	0.035	0.131	0.192	0.154	0.214	0.035	0.6400	0.514115	29.0	0.2202	0.284521	61.4
7%	0.000011	0.003	0.017	0.014	0.023	0.103	0.154	0.128	0.188	0.030	0.7933	0.514486	36.2	0.3051	0.285110	82.2
8%	0.0000025	0.0013	0.010	0.010	0.016	0.083	0.126	0.109	0.169	0.027	0.9614	0.514894	44.2	0.4004	0.285772	105.6
9%	0.00000055	0.00054	0.0054	0.0065	0.0104	0.066	0.103	0.091	0.151	0.024	1.1701	0.515399	54.0	0.5300	0.286672	137.4
10%	0.00000012	0.00022	0.00295	0.00432	0.00696	0.052	0.084	0.076	0.135	0.022	1.4306	0.516031	66.3	0.7057	0.287892	180.6
11%	0.0000000198	0.00008	0.00145	0.00271	0.00432	0.040	0.066	0.062	0.119	0.019	1.8108	0.516952	84.3	0.9868	0.289844	249.6
12%	0.0000000040	0.000029	0.00076	0.00178	0.00281	0.031	0.053	0.051	0.106	0.017	2.2388	0.517988	104.5	1.3336	0.292252	334.8
13%	0.0000000006	0.0000093	0.00035	0.00108	0.00168	0.023	0.041	0.041	0.092	0.015	2.8789	0.519539	134.8	1.9043	0.296214	474.9
14%	0.0000000001	0.0000028	0.00016	0.00065	0.00098	0.017	0.031	0.032	0.080	0.013	3.7417	0.521630	175.6	2.7576	0.302138	684.4

(C) Starting peridotite compositions are derived from Depleted Mantle (DM) estimates (Salters and Stracke, 2004) differentiated at 3.5 Ga

$^{143}Nd/^{144}Nd$	0.51311
$^{177}Hf/^{176}Hf$	0.28330
$^{147}Sm/^{144}Nd$	0.22512
$^{177}Lu/^{176}Hf$	0.04436

Appendix 5.4 (contd.): (D) Partition coefficients of mineral phases used for the melting and melt-rock reaction modeling (Salters and Stracke, 2004; Stracke et al., 2013; Sani et al., 2023)

	3 GPa				2 GPa		
	Olivine	Opx	Cpx	Garnet	Olivine	Opx	Cpx
La	0.0005	0.004	0.015	0.0007	0.0005	0.003	0.030
Ce	0.0005	0.004	0.038	0.017	0.0005	0.004	0.080
Nd	0.0004	0.012	0.088	0.064	0.0004	0.012	0.088
Hf	0.0011	0.024	0.14	0.40	0.0022	0.030	0.284
Sm	0.0011	0.020	0.15	0.23	0.0011	0.020	0.299
Gd	0.0011	0.065	0.16	1.2	0.0011	0.007	0.350
Dy	0.0027	0.065	0.17	2.0	0.0027	0.011	0.400
Er	0.013	0.065	0.18	3.0	0.013	0.045	0.420
Yb	0.020	0.080	0.25	5.5	0.020	0.080	0.450
Lu	0.020	0.120	0.28	7.0	0.020	0.120	0.511

Appendix 5.5: Initial compositions and results of melt-rock reaction modeling of DM residues and MORB melt at 370 Ma

(A) Starting peridotite compositions (DM, F = 5 %)

	Assimilant	Melt 1	AFC (F) – Whole-rock composition										
(ppm)	(DM, F=5%)	(E-MORB)	1%	10%	20%	30%	40%	50%	60%	70%	80%	90%	99%
La	0.00079	12.02	0.006	0.031	0.053	0.073	0.093	0.111	0.128	0.146	0.162	0.178	0.193
Ce	0.066	25.52	0.071	0.071	0.073	0.080	0.100	0.140	0.210	0.322	0.489	0.726	1.014
Nd	0.166	14.86	0.159	0.159	0.159	0.159	0.160	0.163	0.176	0.216	0.326	0.587	1.078
Sm	0.120	3.73	0.108	0.108	0.108	0.108	0.108	0.108	0.108	0.109	0.118	0.186	0.502
Gd	0.297	4.26	0.269	0.269	0.269	0.269	0.269	0.269	0.269	0.270	0.275	0.332	0.689
Dy	0.434	4.62	0.400	0.400	0.400	0.400	0.400	0.400	0.400	0.400	0.403	0.452	0.870
Er	0.322	2.75	0.302	0.302	0.302	0.302	0.302	0.302	0.302	0.302	0.304	0.328	0.569
Yb	0.366	2.59	0.346	0.346	0.346	0.346	0.346	0.346	0.346	0.346	0.347	0.365	0.588
Lu	0.060	0.38	0.058	0.058	0.058	0.058	0.058	0.058	0.058	0.058	0.058	0.060	0.098
Hf	0.095	2.54	0.087	0.087	0.087	0.087	0.087	0.087	0.087	0.088	0.095	0.140	0.333
$^{147}Sm/^{144}Nd$	0.4379	0.1521	0.4105	0.4105	0.4105	0.4103	0.4088	0.4008	0.3720	0.3052	0.2203	0.1919	0.2823
$^{177}Lu/^{176}Hf$	0.0897	0.0213	0.0942	0.0942	0.0942	0.0942	0.0942	0.0942	0.0941	0.0932	0.0864	0.0607	0.0416
(370 Ma)													
$^{143}Nd/^{144}Nd$	0.513626	0.512800	0.513559	0.513559	0.513559	0.513559	0.513554	0.513532	0.513451	0.513263	0.513020	0.512917	0.513117
$^{177}Hf/^{176}Hf$	0.283613	0.282900	0.283644	0.283644	0.283644	0.283644	0.283644	0.283644	0.283643	0.283634	0.283564	0.283294	0.283050

	AFC (F) – Clinopyroxene composition										
	1%	10%	20%	30%	40%	50%	60%	70%	80%	90%	99%
La	0.0028	0.005	0.014	0.030	0.055	0.089	0.133	0.187	0.251	0.326	0.403
Ce	0.205	0.206	0.208	0.220	0.250	0.312	0.421	0.597	0.861	1.237	1.694
Nd	0.471	0.471	0.471	0.472	0.475	0.489	0.532	0.642	0.887	1.384	2.194
Sm	0.322	0.322	0.322	0.322	0.322	0.322	0.325	0.337	0.387	0.563	1.016
Gd	0.787	0.787	0.787	0.787	0.787	0.787	0.788	0.795	0.835	1.012	1.575
Dy	1.133	1.133	1.133	1.133	1.133	1.133	1.133	1.138	1.173	1.375	2.166
Er	0.811	0.811	0.811	0.811	0.811	0.811	0.811	0.813	0.829	0.936	1.419
Yb	0.895	0.895	0.895	0.895	0.895	0.895	0.896	0.896	0.907	0.993	1.456
Lu	0.147	0.147	0.147	0.147	0.147	0.147	0.147	0.147	0.149	0.160	0.238
Hf	0.255	0.255	0.255	0.255	0.255	0.256	0.257	0.263	0.289	0.371	0.570

Appendix 5.5 (contd.): (B) Starting peridotite compositions (DM, F = 11 %)

	Assimilant	Melt 1	AFC (F) – Whole-rock composition										
(ppm)	(DM, F=11%)	(E-MORB)	1%	10%	20%	30%	40%	50%	60%	70%	80%	90%	99%
La	0.0000003	12.02	0.004	0.029	0.052	0.072	0.092	0.110	0.128	0.145	0.162	0.178	0.193
Ce	0.002	25.52	0.002	0.002	0.004	0.012	0.034	0.076	0.151	0.270	0.449	0.703	1.011
Nd	0.017	14.86	0.016	0.016	0.016	0.016	0.017	0.021	0.035	0.082	0.207	0.506	1.067
Sm	0.028	3.73	0.025	0.025	0.025	0.025	0.025	0.025	0.025	0.026	0.038	0.117	0.489
Gd	0.136	4.26	0.124	0.124	0.124	0.124	0.124	0.124	0.124	0.124	0.131	0.204	0.663
Dy	0.210	4.62	0.194	0.194	0.194	0.194	0.194	0.194	0.194	0.194	0.198	0.264	0.828
Er	0.170	2.75	0.159	0.159	0.159	0.159	0.159	0.159	0.159	0.159	0.161	0.195	0.537
Yb	0.235	2.59	0.222	0.222	0.222	0.222	0.222	0.222	0.222	0.222	0.224	0.249	0.559
Lu	0.039	0.38	0.037	0.037	0.037	0.037	0.037	0.037	0.037	0.037	0.037	0.040	0.092
Hf	0.020	2.54	0.018	0.018	0.018	0.018	0.018	0.018	0.018	0.019	0.028	0.084	0.323
$^{147}Sm/^{144}Nd$	0.9897	0.1521	0.9276	0.9276	0.9275	0.9235	0.8878	0.7313	0.4314	0.1956	0.1099	0.1402	0.2778
$^{177}Lu/^{176}Hf$	0.2787	0.0213	0.2927	0.2927	0.2927	0.2927	0.2927	0.2926	0.2911	0.2752	0.1898	0.0683	0.0406
(370 Ma)													
$^{143}Nd/^{144}Nd$	0.514962	0.512800	0.514812	0.514812	0.514812	0.514801	0.514710	0.514308	0.513537	0.512931	0.512707	0.512774	0.513105
$^{177}Hf/^{176}Hf$	0.284922	0.282900	0.285018	0.285018	0.285018	0.285018	0.285018	0.285018	0.285006	0.284883	0.284218	0.283268	0.283035

	AFC (F) – Clinopyroxene composition										
	1%	10%	20%	30%	40%	50%	60%	70%	80%	90%	99%
La	0.0002	0.014	0.040	0.072	0.110	0.152	0.198	0.247	0.300	0.355	0.408
Ce	0.008	0.012	0.032	0.079	0.162	0.286	0.460	0.689	0.978	1.333	1.714
Nd	0.068	0.068	0.069	0.075	0.096	0.151	0.266	0.481	0.847	1.433	2.216
Sm	0.102	0.102	0.102	0.103	0.103	0.106	0.118	0.158	0.267	0.528	1.023
Gd	0.493	0.493	0.493	0.493	0.494	0.495	0.502	0.532	0.633	0.926	1.578
Dy	0.744	0.744	0.744	0.744	0.744	0.744	0.749	0.772	0.873	1.232	2.169
Er	0.567	0.567	0.567	0.567	0.567	0.567	0.569	0.578	0.626	0.825	1.416
Yb	0.754	0.754	0.754	0.754	0.754	0.754	0.754	0.759	0.790	0.942	1.467
Lu	0.125	0.125	0.125	0.125	0.125	0.125	0.125	0.126	0.129	0.151	0.240
Hf	0.073	0.073	0.073	0.073	0.073	0.075	0.083	0.107	0.168	0.308	0.563

Starting peridotite compositions are melting residues under garnet facies at F=5 and 11 % from Appendix 5.4A

Partition coefficients at 2 GPa used for the modeling are from Appendix 5.4D

Appendix 6.1: Average major and minor elements composition of mineral phases from selected Finero phlogopite peridotite and websterite

Rock type	Phl-peridotite					Phl-peridotite*					
Sample ID	FI2203	FI2203	FI2203	FI2203	FI2203	FIN5	FIN5	FIN5	FIN5	FIN5	FIN5
Phase	Ol	Opx	Sp	Amph	Phl	Ol	Opx	Cpx	Sp	Amph	Phl
SiO_2	40.14	57.48	0.03	45.62	39.34	41.67	58.11	54.92	0.22	45.76	40.48
TiO_2	0.00	0.08	0.25	0.64	1.10	0.07	0.03	0.06	0.15	0.43	0.76
Al_2O_3	0.58	1.06	19.81	10.83	15.73	0.08	1.14	0.84	18.87	10.69	16.65
Cr_2O_3	0.00	0.32	44.08	2.00	1.45	0.00	0.30	0.43	42.73	1.89	1.17
FeO_T	9.30	6.40	27.40	3.59	3.02	8.71	5.81	1.69	26.41	3.20	3.02
MnO	0.14	0.15	0.15	0.05	0.01	0.13	0.15	0.12	0.07	0.04	0.03
NiO	0.31	0.08	0.15	0.08	0.19	n.d.	n.d.	n.d.	n.d.	n.d.	n.d.
MgO	50.30	34.94	8.94	18.95	24.00	49.59	34.83	17.77	9.89	19.17	23.61
CaO	0.03	0.46	0.01	12.25	0.01	0.04	0.41	24.40	0.00	12.30	0.00
Na_2O	0.00	0.00	0.02	2.53	0.96	0.00	0.12	0.27	0.00	1.90	0.73
K_2O	0.00	0.00	0.00	0.93	8.89	0.00	0.00	0.00	0.00	0.83	8.20
Total	100.81	100.98	100.83	97.46	94.67	100.29	100.90	100.50	98.34	96.21	94.65
Mg#	90.60	90.70	36.80	90.40	93.40	91.00	91.40	94.90	40.00	91.40	93.30
Cr#			59.90						60.30		

*The major element dataset for FIN5 and FIN6 are from Zanetti et al. (1999)

Appendix 6.1: Average major and minor elements composition of mineral phases from selected Finero phlogopite peridotite and websterite (contd.)

Rock type	Phl-websterite*				
Sample ID	FIN6	FIN6	FIN6	FIN6	FIN6
Phase	Opx	Cpx	Sp	Amph	Phl
SiO_2	58.78	55.12	0.11	46.00	41.41
TiO_2	0.09	0.11	0.19	0.67	1.03
Al_2O_3	0.91	1.26	20.44	11.71	16.09
Cr_2O_3	0.27	0.75	44.52	2.00	1.38
FeO_T	5.75	1.92	22.81	3.55	3.10
MnO	0.16	0.09	0.00	0.09	0.02
NiO	n.d.	n.d.	n.d.	n.d.	n.d.
MgO	35.87	17.32	11.56	19.00	24.01
CaO	0.33	24.24	0.00	11.49	0.01
Na_2O	0.55	0.42	0.00	2.76	0.70
K_2O	0.00	0.00	0.00	0.84	7.19
Total	102.71	101.23	99.63	98.11	94.94
Mg#	91.70	94.10	47.50	90.50	93.20
Cr#			59.40		

Appendix 6.2: Average trace element composition of mineral phases from selected Finero phlogopite peridotite and websterite

Rock type	Phl-peridotite						Phl-peridotite				
Sample ID	FI2203	FI2203	FI2203	FI2203	FI2203	FI2203	FIN5	FIN5	FIN5	FIN5	FIN5
Phase	Ol	Opx	Cpx	Sp	Amph	Phl	Ol	Opx	Sp	Amph	Phl
No. of analysis	5	5	5	3	10	4	3	5	2	6	3
Li	3.96	0.54	2.32	0.49	5.07	6.98	3.05	0.65	0.75	0.72	2.49
Be	0.00	0.13	0.29	0.04	0.85	0.16	0.00	0.09	0.00	1.24	0.10
B	17.94	18.29	17.33	31.70	19.42	35.24	8.13	8.05	20.88	8.95	19.78
Sc	1.14	4.31	19.04	0.56	26.26	3.14	1.73	10.87	2.14	100	8.37
Ti	5.58	329	419	1307	3863	7096	6.62	212	1646	2821	4331
V	0.25	20.47	50.98	652	177	132	0.41	29.34	1238	295	180
Cr	10.51	2075	3734	329153	13578	10826	8.96	1627	329921	12008	7697
Mn	1087	1224	482	2595	366	92.36	851	989	2149	310	62.06
Co	150	54.56	15.50	592	33.11	55.69	137	49.30	555	29.80	44.03
Ni	2617	500	218	669	640	1464	3121	582	1020	768	1528
Cu	0.07	0.05	0.22	0.07	1.28	0.77	0.08	0.06	0.17	0.98	0.50
Zn	78.80	66.30	11.99	6997	24.40	41.31	49.17	41.89	3758	15.92	21.60
Rb	0.03	0.02	0.02	0.11	5.76	553	0.43	0.20	1.37	5.60	539.95
Sr	0.06	0.19	145	0.13	301	118	0.03	0.07	0.17	250	79.26
Y	0.01	0.13	2.15	0.00	7.11	0.08	0.01	0.07	0.00	6.19	0.06
Zr	0.02	0.35	9.54	0.65	37.22	3.59	0.02	0.52	0.59	65.08	3.05
Nb	0.01	0.00	0.01	0.75	3.11	2.98	0.01	0.01	0.54	4.06	2.96
Cs	0.01	0.01	0.01	0.01	0.01	16.48	0.02	0.01	0.09	0.01	15.75
Ba	0.03	0.05	0.10	0.30	113	5764	0.01	0.00	0.17	65.74	2542
La	0.01	0.01	3.14	0.02	11.51	0.01	0.00	0.00	0.02	16.15	0.00
Ce	0.00	0.01	8.19	0.03	28.02	0.01	0.00	0.01	0.03	29.30	0.00
Pr	0.00	0.00	1.26	0.01	4.03	0.00	0.00	0.00	0.00	3.69	0.00
Nd	0.01	0.02	5.91	0.00	19.56	0.00	0.00	0.01	0.00	16.89	0.00
Sm	0.02	0.01	1.44	0.01	4.81	0.01	0.00	0.01	0.01	3.88	0.00
Eu	0.01	0.01	0.38	0.00	1.39	0.04	0.00	0.00	0.00	0.91	0.00
Gd	0.01	0.02	1.09	0.00	3.56	0.00	0.00	0.00	0.00	2.68	0.00
Tb	0.00	0.00	0.13	0.00	0.42	0.00	0.00	0.00	0.00	0.34	0.00
Dy	0.01	0.02	0.59	0.01	1.82	0.00	0.00	0.01	0.00	1.44	0.00
Ho	0.00	0.00	0.08	0.00	0.27	0.00	0.00	0.00	0.00	0.26	0.00
Er	0.03	0.03	0.16	0.00	0.55	0.00	0.00	0.02	0.00	0.49	0.01
Tm	0.00	0.00	0.02	0.00	0.07	0.00	0.00	0.00	0.00	0.07	0.00
Yb	0.01	0.01	0.12	0.00	0.39	0.00	0.00	0.02	0.00	0.49	0.00
Lu	0.00	0.01	0.02	0.00	0.05	0.00	0.00	0.00	0.00	0.06	0.00
Hf	0.00	0.02	0.42	0.00	1.43	0.03	0.00	0.01	0.00	1.76	0.06
Ta	0.00	0.00	0.00	0.00	0.16	0.15	0.00	0.00	0.00	0.27	0.16
Pb	0.03	0.05	0.64	0.08	1.92	4.53	0.01	0.03	0.03	2.00	4.28
Th	0.01	0.02	0.10	0.05	0.50	0.00	0.00	0.01	0.11	1.83	0.02
U	0.01	0.01	0.03	0.03	0.11	0.00	0.01	0.01	0.11	0.41	0.01

Appendix 6.2: Average trace element composition of mineral phases from selected Finero phlogopite peridotite and websterite (contd.)

Rock type	Phl-websterite					
Sample ID	FIN6	FIN6	FIN6	FIN6	FIN6	FIN6
Phase	Ol	Opx	Cpx	Sp	Amph	Phl
No. of analysis	3	2	9	2	7	5
Li	2.66	0.65	2.12	0.83	0.95	0.79
Be	0.00	0.00	0.27	0.34	1.50	0.19
B	8.00	7.24	10.67	16.36	13.08	24.59
Sc	1.85	7.11	36.40	1.98	64.68	6.66
Ti	7.21	208	519	2009	3515	5336
V	0.67	24.34	82.30	1093	258	174
Cr	19.19	1617	4503	241874	13283	7742
Mn	1070	1151	645	2379	390	92.82
Co	150	53.39	20.54	584	36.49	50.71
Ni	2400	457	257	902	660	1203
Cu	0.07	0.06	0.38	0.22	1.25	0.54
Zn	70.39	57.21	13.64	6448	20.42	30.33
Rb	0.03	0.02	0.02	0.09	5.99	608
Sr	0.53	0.11	187	0.06	398	135.90
Y	0.03	0.07	2.47	0.00	7.86	0.06
Zr	0.28	0.31	15.96	0.45	71.57	5.45
Nb	0.01	0.00	0.02	0.34	3.85	3.10
Cs	0.01	0.01	0.01	0.01	0.01	19.90
Ba	0.48	0.01	0.10	0.33	91.77	4211
La	0.03	0.01	6.47	0.01	23.55	0.01
Ce	0.08	0.02	17.43	0.00	57.81	0.02
Pr	0.00	0.00	2.30	0.00	7.38	0.00
Nd	0.01	0.01	10.02	0.00	31.84	0.00
Sm	0.00	0.00	1.91	0.00	5.88	0.00
Eu	0.00	0.00	0.46	0.00	1.48	0.03
Gd	0.00	0.00	1.15	0.00	3.55	0.00
Tb	0.00	0.00	0.14	0.00	0.43	0.00
Dy	0.01	0.00	0.55	0.00	1.70	0.00
Ho	0.00	0.00	0.10	0.00	0.30	0.00
Er	0.00	0.00	0.22	0.00	0.72	0.00
Tm	0.00	0.00	0.02	0.00	0.08	0.00
Yb	0.00	0.00	0.15	0.00	0.50	0.00
Lu	0.00	0.00	0.03	0.00	0.07	0.00
Hf	0.00	0.00	0.51	0.00	2.38	0.11
Ta	0.00	0.00	0.00	0.00	0.27	0.22
Pb	0.02	0.00	0.71	0.02	1.98	4.33
Th	0.00	0.00	0.11	0.03	0.47	0.00
U	0.01	0.00	0.03	0.00	0.09	0.01

Appendix 6.3: Nd-Hf-Sr-Pb isotopic composition of amphiboles from selected Finero phlogopite peridotite and websterite

Sample ID	FI2203	FIN5	FIN6
Rock type	Phl-peridotite	Phl-peridotite	Phl-websterite
$^{147}Sm/^{144}Nd$	0.1550	0.1430	0.1171
$^{143}Nd/^{144}Nd$	0.512454	0.512362	0.512331
$^{143}Nd/^{144}Nd_{(i)}$	0.512150	0.512081	0.512101
±2σ	0.000004	0.000004	0.000004
$\varepsilon Nd_{(i)}$	-1.9	-3.2	-2.8
$^{176}Lu/^{177}Hf$	0.0052	0.0049	0.0045
$^{176}Hf/^{177}Hf$	0.282628	0.282570	0.282598
$^{176}Hf/^{177}Hf_{(i)}$	0.282599	0.282542	0.282573
±2σ	0.000005	0.000005	0.000006
$\varepsilon Hf_{(i)}$	0.1	-1.9	-0.8
$^{87}Rb/^{86}Sr$	0.0540	0.0610	0.0420
$^{87}Sr/^{86}Sr$	0.707015	0.707893	0.706925
$^{87}Sr/^{86}Sr_{(i)}$	0.706785	0.707632	0.706746
±2σ	0.000008	0.000011	0.000012
ΔSr	67.8	76.3	67.5
$^{206}Pb/^{204}Pb$	18.4808	18.9531	18.4551
±2σ	0.0004	0.0005	0.0005
$^{207}Pb/^{204}Pb$	15.6431	15.6685	15.6404
±2σ	0.0004	0.0005	0.0005
$^{208}Pb/^{204}Pb$	38.5935	39.1867	38.5555
±2σ	0.0013	0.0015	0.0015
Δ7/4	14.88	12.30	14.89
Δ8/4	62.33	64.54	61.63

Normalized to LaJolla $^{143}Nd/^{144}Nd = 0.51185$

Normalized to JMC475 $^{176}Hf/^{177}Hf = 0.282150$

Normalized to NBS 981 6/4 = 16.9356, 7/4 = 15.4891, 8/4 = 36.7006

Subscript (i) represents correction to 300 Ma

Δ7/4, Δ8/4 and ΔSr calculated according to Hart (1984)